Walter Lacarbonara
Balakumar Balachandran
Michael J. Leamy · Jun Ma
J. A. Tenreiro Machado
Gabor Stepan   *Editors*

Advances in Nonlinear Dynamics

Proceedings of the Second International
Nonlinear Dynamics Conference
(NODYCON 2021), Volume 2

Springer

NODYCON Conference Proceedings Series

Series Editor
Walter Lacarbonara ⓘ, Sapienza University of Rome, Rome, Italy

The NODYCON Conference Proceedings Series presents early findings and case studies from a wide range of fundamental and applied work across multidisciplinary fields that encompass Nonlinear Dynamics. Series volumes follow the principle tracks or focus topics featured in the biennial International Nonlinear Dynamics Conference. Volumes in the series feature both well-established streams of research as well as novel areas and emerging fields of investigation.

More information about this series at https://link.springer.com/bookseries/16666

Walter Lacarbonara • Balakumar Balachandran
Michael J. Leamy • Jun Ma • J. A. Tenreiro Machado
Gabor Stepan

Editors

Advances in Nonlinear Dynamics

Proceedings of the Second International
Nonlinear Dynamics Conference
(NODYCON 2021), Volume 2

Springer

Editors

Walter Lacarbonara (iD)
Department of Structural
and Geotechnical Engineering
Sapienza University of Rome
Rome, Italy

Michael J. Leamy (iD)
Department of Mechanical Engineering
Georgia Institute of Technology
Atlanta, GA, USA

J. A. Tenreiro Machado (iD)
ISEP-Institute of Engineering
Polytechnic of Porto
Porto, Portugal

Balakumar Balachandran (iD)
Department of Mechanical Engineering
University of Maryland
College Park, MD, USA

Jun Ma (iD)
Department of Physics
Lanzhou University of Technology
Lanzhou, Gansu, China

Gabor Stepan (iD)
Department of Applied Mechanics
Budapest University of Technology and
Economics
Budapest, Hungary

Preface

This volume is part of three volumes collecting the *Proceedings of the Second International Nonlinear Dynamics Conference (NODYCON 2021)* held as a virtual (online) conference, February 16–19, 2021. NODYCON was launched in 2019 to foster the tradition of the conference series originally established by Prof. Ali H. Nayfeh in 1986 at Virginia Tech, Blacksburg, VA, USA, as the Nonlinear Vibrations, Stability and Dynamics of Structures Conference. With the passing in 2017 of Prof. Nayfeh, NODYCON 2019 was organized as a collective tribute to Prof. Nayfeh. NODYCON 2019 received an extraordinary response from the community with 408 abstracts (out of 450 submissions) presented by nearly 400 participants from 68 countries.

After the successful launch of NODYCON, NODYCON 2021, originally planned to be held in Rome, was hosted as a virtual (online) conference given the uncertainties related to the COVID-19 world crisis. The online conference was creatively designed to help corroborate and cement the sense of cohesiveness and liveliness of the NODYCON community. The NODYCON 2021 online conference featured 16 keynotes and mini-keynotes of broad interest, a panel, two workshops, and 442 oral presentations covering recent advances in the rich spectrum of topics covered by *Nonlinear Dynamics*, including new frontiers and challenges. The Special Session and Panel entitled "*Complex dynamics of COVID-19: modeling, prediction and control*" offered important outlooks into the nonlinear dynamic evolution and prediction of the global disease spreading across different scales by using a variety of analysis tools and modeling approaches.

For NODYCON 2021, the Organizing Committee received 478 abstracts and, after rigorous review cycles, 442 one-page abstracts were accepted and published in the Conference Book of Abstracts.

The diverse topics covered by the papers were clustered along the following four major themes to organize the technical sessions:

A. Concepts and methods in nonlinear dynamics
B. Nonlinear dynamics of mechanical and structural systems
C. Nonlinear dynamics and control
D. Recent trends in nonlinear dynamics

The authors of a selection of approximately 60 papers were invited to publish in the Special Issue of *Nonlinear Dynamics* entitled "NODYCON 2021 Second International Nonlinear Dynamics Conference." At the same time, about 200 full papers were submitted to *Advances in Nonlinear Dynamics – Proceedings of the Second International Nonlinear Dynamics Conference (NODYCON 2021)* within the newly established *NODYCON Conference Proceedings Series*. One hundred and eighty-one papers were accepted. These papers have been collected into three volumes, which are listed below together with a sub-topical organization.

Volume 1: Nonlinear Dynamics of Structures, Systems, and Devices

A. Fluid-structure interaction
B. Mechanical systems and structures
C. Computational nonlinear dynamics
D. Analytical techniques
E. Bifurcation and dynamic instability
 F. Rotating systems
G. Modal interactions and energy transfer
H. Nonsmooth systems

Volume 2: Nonlinear Dynamics and Control

A. Nonlinear vibration control
B. Control of nonlinear systems and synchronization
C. Experimental dynamics
D. System identification and SHM
E. Multibody dynamics

Volume 3: New Trends in Nonlinear Dynamics

A. Complex dynamics of COVID-19: modeling, prediction and control
B. Nonlinear phenomena in bio- and eco-systems
C. Energy harvesting
D. MEMS/NEMS
E. Multifunctional structures, materials and metamaterials
 F. Nonlinear waves
G. Chaotic systems, stochasticity and uncertainty

I wish to acknowledge the work and dedication of the co-editors of the NODY-CON 2021 Proceedings: Prof. Bala Balachandran (University of Maryland, College Park, USA), Prof. Michael J. Leamy (Georgia Institute of Technology, USA), Prof. Jun Ma (Lanzhou University of Technology, China), Prof. Jose Antonio Tenreiro Machado (Instituto Superior de Engenharia do Porto, Portugal), and Prof. Gabor Stepan (Budapest University of Technology and Economics, Hungary).

The success of the fully online conference NODYCON 2021 is due to the efforts, talent, energy, and enthusiasm of all researchers in the field of nonlinear dynamics who wrote, submitted, and presented their papers in a very lively way. Special praise is also deserved for the reviewers who invested significant time in reading, examining, and assessing multiple papers, thus ensuring a high standard of quality for this conference proceedings.

NODYCON 2021 Chair

Walter Lacarbonara, Rome, Italy
May 2021

Preface for Volume 2: Nonlinear Dynamics and Control

Volume 2 of the NODYCON 2021 Proceedings is composed of 50 chapters, which are spread across the following groupings: i) nonlinear vibration control (19 papers), ii) control of nonlinear systems and synchronization (8 papers), iii) experimental dynamics (4 papers), iv) system identification and SHM (10 papers), and v) multibody dynamics (9 papers). Due to the cross-cutting nature of the topics, the editors acknowledge that a paper placed in one grouping could have easily been placed in another grouping as well. As one reads through these 50 contributions, one will note the use of a wide range of experimental, analytical, and numerical techniques for studying the nonlinear dynamics of a wealth of systems across different space and time scales.

In the area of nonlinear dynamics concerning nonlinear vibration control, the reader will find studies concerning nonlinear damping mechanisms using friction, viscoelasticity, inerters, magnetic springs, tuned mass dampers, and nonlinear energy sinks (E. Denimal *et al.*; C. Silva *et al.*; J. Dekemele *et al.*; S. Pagliaro and A. Di Egidio; M. Cabral *et al.*; Z. Dong *et al.*; R. Philip *et al.*; M. Bednarek *et al.*; H.J. da Cruz Neto and M.A. Trindade, A.L. Silva *et al.*; S. Ikkurthi *et al.*; N. Menga *et al.*; D. De Domenico *et al.*) and applications such as turbine blades, twin rotor systems, airfoils, heavy chains, high-speed railway vehicles, and cart-pendulum systems (Y. Fahmy and A. El-Badawy; A. Chelihi *et al.*; G. Pepe *et al.*; E.A.R. Ribeiro *et al.*; Y. Zhao *et al.*; J.C. Basilio *et al.*).

In the area of control of nonlinear systems and synchronization, the reader will find works concerning control of cantilever beams, load hoisting, offshore cranes, bipedal walkers, chaotic systems, and riser re-entry (E. A. Petrocino *et al.*; A. Morock *et al.*; A. Rustico *et al.*; Y. Luo *et al.*; S. Lal De and S.F. Ali; I. Adamiec-Wójcik *et al.*) and studies on synchronization control (D.L. Xuan *et al.*; T. Chen).

In the area of experimental dynamics, the reader will find measurement results and their analyses to characterize nonlinear vibrations occurring in vibro-impact systems (G. Stefani *et al.*), in flight simulators (G. Avon *et al.*) and during greyhound galloping (H. Hayati *et al.*). The design of a Foucault pendulum of extreme sensitivity is also presented here (M.P. Cartmell *et al.*).

In the area of system identification and structural health monitoring (SHM), the reader will find identification techniques for nonlinear damping (H. P. Chintha and A. Chatterjee; R. Zhu *et al.*), for nonlinear stiffness (Q. Liu *et al.*), and for inertia and control delay (M. Ghani and A. Banazadeh). Nonlinear parameter identification techniques are applied and developed for MEMS resonators (R. T. Rocha *et al.*), for mine clearance (F. Mezzani *et al.*), and also for damage detection of large structures (M. Pinto *et al.*), for the gait analysis of robot quadrupeds (M. Laurenza *et al.*), for monitoring gear systems in rotating machinery (Z. Liu *et al.*), and for the Duffing oscillator (D. M. S. Lopes and A. Cunha Jr).

In the area of multibody dynamics, the reader will find the analysis of multibody models of bicycles (A. G. Agùndez *et al.*) and systems with nonlinear components or with frictional impacts (S. Natsiavas *et al.*). Multibody modelling is applied for legged robots (G. Chen *et al.*), in robot-trajectory processes (F. Pfeiffer), also in vehicle road dynamics (W.V. Wedig), and for the wear analysis of knee arthroplasties (E. Askari and M.S. Andersen). Efficient algorithms are discussed for the dynamic analysis of non-smooth multibody systems (A. Tasora *et al.*) and autonomous vehicles (S. Benatti *et al.*).

In conclusion, this volume represents a multifaceted cross section of recent advances in nonlinear vibration control, control of nonlinear systems and synchronization, experimental dynamics, system identification and SHM, and multibody dynamics. We hope that readers will benefit from the rich work portrayed here on nonlinear dynamics and control, and that this work will spur and inspire new ideas and future contributions.

Co-editors of the NODYCON 2021 Proceedings

Bala Balachandran, College Park, MD, USA
Walter Lacarbonara, Rome, Italy
Michael J. Leamy, Atlanta, GA, USA
Jun Ma, Lanzhou, China
J. A. Tenreiro Machado, Porto, Portugal
Gabor Stepan, Budapest, Hungary
May 2021

Contents

Part IV   System Identification and SHM

Part V   Multibody Dynamics

Part I
Nonlinear Vibration Control

Topological Optimisation of Friction Dampers for Nonlinear Resonances Mitigation

Enora Denimal, Ludovic Renson, and Loic Salles

1 Introduction

In the design of aircraft turbines, vibration analysis is of major importance to avoid high-cycle fatigue failures. Due to the high modal density, resonance cannot be avoided. A classic solution to limit the vibration amplitudes at resonance consists of introducing dry friction damping in the system to dissipate energy. This dissipation can take place in different locations, as shrouds, blades tips, or roots, but the most efficient solution is the use of underplatform dampers (UPDs) [1]. Located between adjacent blades and maintained in contact due to the centrifugal loading, UPD dissipates energy through friction contact when the blades are vibrating. The UPD geometry at the interface has a significant impact on the damping characteristics and on the overall nonlinear dynamic behaviour of the structure [2]. With the coming of additive manufacturing, new breakthrough UPD geometries could be obtained to improve their efficiency.

Topological optimisation (TO) of continuum structures consists of identifying the part of a given space occupied by material when only the boundary conditions are known [3–5]. It is mostly employed in pre-design stage to identify efficient layouts. The topology of a component is defined by its boundaries between the interior and the exterior, as well as by the number and the location of inner holes. They are optimised simultaneously to minimise an objective function with respect to constraints defined by the user. Two main approaches exist to solve such problems, namely density-based methods and level-set methods. In the density-based approach, the density of each element of a mesh is optimised based on their sensitivity to the objective function [3]. In the second approach, the geometry

E. Denimal (✉) · L. Renson · L. Salles
Dynamics Group, Imperial College London, London, UK
e-mail: enora.denimal@inria.fr; l.renson@imperial.ac.uk; l.salles@imperial.ac.uk

is described implicitly by a level-set function (LSF) propagated by solving an Hamilton–Jacobi equation [3, 5]. These two approaches require the sensitivities of the densities or of the shape with respect to the objective function and the constraints. If the sensitivities are analytically unknown, they might be too expensive to determine numerically. In a recent framework called the Moving Morphable Component (MMC), proposed by Guo et al [4], the LSF of the structure is defined as an assembly of several local LSFs. Each of this local LSF is described explicitly through few parameters, which reduces drastically the number of optimisation parameters and makes possible the use of standard optimisation methods such as global optimisation [6].

TO has been used for linear vibrations by optimising the structure eigenvalues [7]. In [8], the cross section of a beam with a geometrical nonlinearity has been optimised to reduce the nonlinear resonant response using a gradient-based approach. Contact problems have been addressed mostly in a quasi-static context [9] using both LSM and density-based approaches. In [10], the MMC framework coupled with Kriging-based optimisation was employed to optimise the nonlinear frequency response of blades with a UPD. If promising results were obtained, the computation of the full dynamic response over a large frequency range was required, which resulted in large computational times. Moreover, the contact law was simplistic and did not allow for contact separation, so the variability of the nonlinear dynamic response with regard to the UPD geometry was limited making the optimisation easier.

This chapter proposes to reduce the computational cost associated with the nonlinear resonance calculation by directly solving for responses that are in phase quadrature with the applied excitation [11]. A more complex and realistic contact law is considered where contact separation is possible, bringing a softening behaviour and large variations of the nonlinear dynamic response when the UPD geometry varies. Directly tracking the resonance with this approach will allow for exploiting the sensitivity of the resonance and perform robust topological optimisation in the future. Global optimisation is performed, and new UPD geometries that divide the level of vibrations by 8 are found at reasonable computational costs.

2   Mechanical System Under Study

The system under study is a 2D system that simulates the dynamic behaviour of a pair of high-pressure turbine blades [12]. It is displayed in Fig. 1a and is composed of two blades represented by two beams with platforms. They are connected to a basis that represents the disc. Between the two blades sits the damper that is in contact with the two platforms. In normal working conditions, the latter is kept in this position due to the centrifugal loading. When the blades vibrate, a relative displacement between the platforms and the damper appears. Energy is dissipated by friction, which damps the vibrations. In the rest of the study, the system is excited at the basis of blade 1 (see blue point in Fig. 1a), with an amplitude of 8 N to

(a) Scheme of the system under study

(b) IP mode

(c) OOP mode
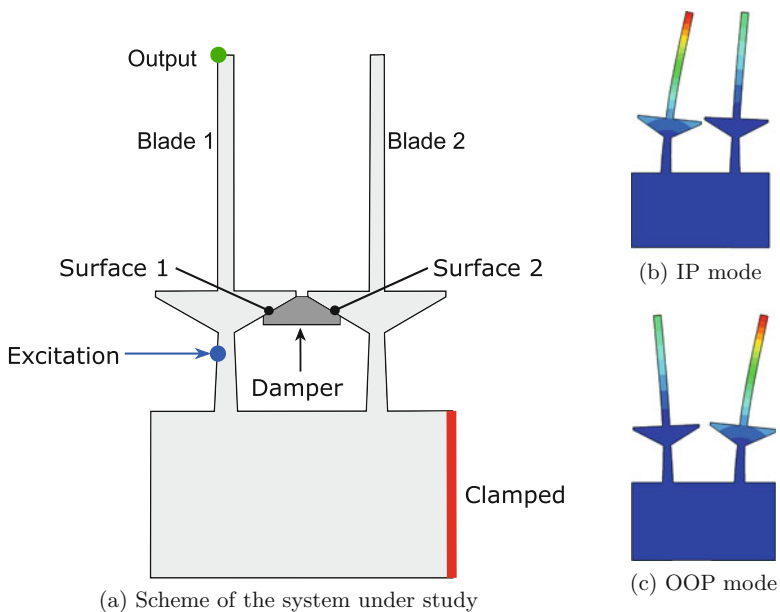
Fig. 1 System under study (**a**) and the two first bending modes of the blades (**b,c**)

activate the contact nonlinearity, and displacements are considered at the blade 1 tip (see green point in Fig. 1a). The finite-element model of the blades is composed of 3324 8-nodes bi-quadratic plane strain elements. The structure is composed of steel with a Young modulus of 197 GPa and a density of 7800 kg/m^3. The first two bending modes of the system correspond to in-phase (IP) and out-of-phase (OOP) motions of the blades and take place at 246.73 Hz and 247.51 Hz, respectively. They are represented in Fig. 1b,c, respectively. These natural frequencies are determined without the presence of the damper. An initial mesh for the damper is created and is composed of 3604 elements with the same material properties than the blades. The mesh is constructed to ensure matching at the contact points between the platforms and the damper. This mesh will be updated during the topological optimisation as it will be explained in the following.

The two contact surfaces are discretised, and a node-to-node contact modelling approach is employed. 2D friction contact elements are employed, one of them consisting of one Jenkins element and one normal spring to allow normal load variations [13]. Each contact element is characterised by four parameters, namely the friction coefficient μ, the tangential contact stiffness k_t, the normal contact stiffness k_n, and the normal pre-load N_0. This contact element allows for three different states: stuck, stick/slip, and separation. Energy is dissipated by friction during stick/slip. This contact formulation allows the analytical evaluation of the Jacobian matrix. The initial contact pressure is supposed to be homogeneous over the contact surface and depends directly on the centrifugal loading C_F and the

number of contact points n_{co} [14]. In the case of a full damper, 51 contact points are present at each contact surface, and the normal pre-load is equal to $N_0 = 9.8987$ N. The friction coefficient μ is equal to 0.5, and the normal contact stiffness is taken equal to $k_n = 20000$ N/m for this case. The tangential contact stiffness is chosen equal to the normal contact stiffness.

3 Geometry Description and Optimisation Process

3.1 Geometry Parametrisation

The geometry of the damper is described by a level-set function (LSF) Ψ [3]. This LSF is defined on the design space $\mathcal{D}$ and gives an implicit description of the domain Ω occupied by the material. Ψ is defined as follows:

$$\Psi(x, y) = \begin{cases} \Psi(x, y) > 0, \text{ if } x \in \Omega \\ \Psi(x, y) = 0, \text{ if } x \in \delta\Omega \\ \Psi(x, y) < 0, \text{ if } x \in \mathcal{D}\backslash\Omega, \end{cases} \tag{1}$$

where (x, y) is a point of the design space. Hence, the void is characterised by negative values of the LSF, and the material domain by positive values. The 0-iso-line marks the limit of the material domain. The MMC framework proposes to see this LSF as the union of several "local" LSFs ψ_i defined explicitly by few parameters [4]. Each local LSF describes an elementary beam that can be moved and deformed. Finally, each local LSF ψ_i describes a domain Ω_i occupied by the material, and the total domain Ω occupied by the material is equal to the union of the different subdomains, i.e., $\Omega = \cup_i \Omega_i$. More concretely, each component i is described by the explicit LSF ψ_i given by Guo et al. [4]:

$$\psi_i(x, y) = -\left[\left(\frac{\cos\theta_i(x - x_{0,i}) + \sin\theta_i(y - y_{0,i})}{L_i/2} \right)^m \right.$$
$$\left. + \left(\frac{-\sin\theta_i(x - x_{0,i}) + \cos\theta_i(y - y_{0,i})}{t_i/2} \right)^m - 1 \right], \tag{2}$$

where (x, y) are the coordinates of a point of the design space, θ_i is the inclination angle of the component, L_i its length, t_i its thickness, $(x_{0,i}, y_{0,i})$ its centre, and m is an even number taken equal to 6 here [4]. It describes the sharpness of the LSF. As an example, the geometry of an elementary component is shown in Fig. 2a, and its LSF is displayed in Fig. 2b, where negative values are set to zero for better readability. Hence, each component is described by a set of five parameters, namely θ_i, $x_{0,i}$, $y_{0,i}$, L_i, and t_i. By modifying these parameters, one can translate, rotate, shrink, or spread the component. And by assembling several components, complex geometries
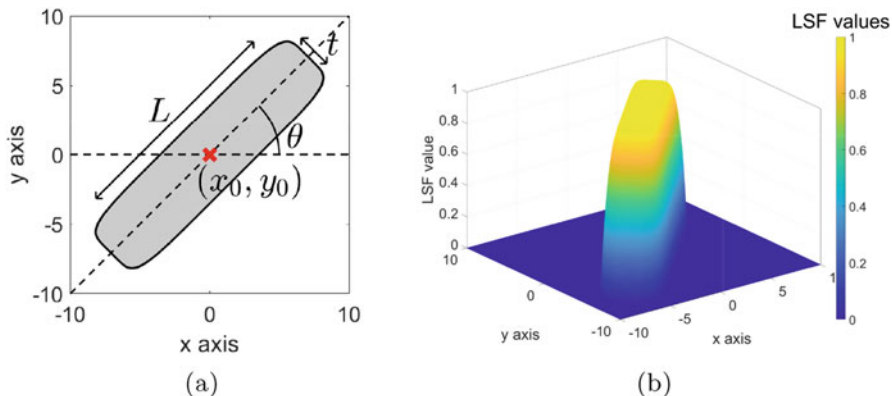
Fig. 2 (**a**) A component and its parameters and (**b**) its level-set function (negative values are set to zero for better readability)

can be described [4] with a very low number of parameters, hence making the use of gradient-free optimisation methods possible [6].

To get a mechanical translation of the geometry, the global LSF Ψ is then mapped on a mesh. An initial mesh of the damper is created, and it is composed of 3604 elements. The LSF is discretised in the centre of each element of the damper mesh [5]. Elements that correspond to material (positive value of the LSF) are kept, when elements that correspond to void (negative value of the LSF) are removed to avoid any residual modes in the mode computation. The connectivity of the local LSF is checked, and discontinuous geometries are avoided through a penalisation in the optimisation process, explained in the following.

3.2 Efficient Global Optimisation (EGO) Algorithm

Considering the strong non-convexity of the optimisation problem and the difficulty of the evaluation of the gradients, a global gradient-free optimisation method is adopted, namely the Efficient Global Optimisation (EGO) algorithm [15] that exploits a Kriging meta-model of the objective function together with an adaptive sampling process. The general idea is the following: an initial set of inputs (i.e., damper geometries denoted by $\mathbf{x}$) and outputs (i.e., the amplitude of vibration at resonance peak, denoted by u_{peak}, of these geometries) is generated. This set is often called an initial learning set. Then, an iterative process is adopted. At each iteration, a Kriging meta-model of the objective function is generated first, based on the set of inputs and outputs. Second, this meta-model is exploited to find the point that satisfies a given criterion. The objective function is evaluated for this new point, and the learning set is extended with this new point. The iterative process is often stopped when a limit number of iterations are reached. The choice of the

criterion to find a new point is important and must balance local and global search to be more precise around possible minima but also to explore unknown parts of the design space. A classic and efficient criterion is the expected improvement (EI) defined as [15]:

$$E[I(\mathbf{x})] = \left(u_{peak}^{(min)} - \tilde{u}_{peak}(\mathbf{x}) \right) \Phi \left(\frac{u_{peak}^{(min)} - \tilde{u}_{peak}(\mathbf{x})}{s(\mathbf{x})} \right)$$
$$+ s(x)\phi \left(\frac{u_{peak}^{(min)} - \tilde{u}_{peak}(\mathbf{x})}{s(\mathbf{x})} \right), \tag{3}$$

where $\mathbf{x}$ is the point of the input space in which the EI is computed, $u_{peak}^{(min)}$ is the minimum of the outputs observed so far, $\tilde{u}_{peak}(\mathbf{x})$ is the Kriging prediction at $\mathbf{x}$, $s(\mathbf{x})$ is the prediction standard deviation at $\mathbf{x}$, $\Phi(.)$ is the normal distribution function, and $\phi(.)$ is the normal density function. The new point added in the learning set is the point that maximises the EI. Some geometries defined by some parameters might not be connected. To face this issue, in the evaluation of the EI, first the connectivity of the different local LSFs ψ_i is checked. If the geometry defined by $\mathbf{x}$ is not connected, the EI is penalised with a negative value [6]. This EI maximisation problem is solved with the rgenoud algorithm [16], which couples a genetic algorithm with a gradient evaluation of the EI.

For each new damper geometry, the contact conditions are updated. More particularly, the centrifugal loading directly related to the damper mass is calculated as well as the new contact loading N_0. The normal contact stiffness k_n is also updated so that the ratio k_n/N_0 remains constant over the different geometries [17]. The tangential contact stiffness k_t is taken equal to k_n.

3.3 Nonlinear Analysis

For each damper geometry, the nonlinear dynamic response is computed. The equation of motion of the problem is given by

$$\mathbf{M}\ddot{\mathbf{q}}(t) + \mathbf{C}\dot{\mathbf{q}}(t) + \mathbf{K}\mathbf{q}(t) + \mathbf{F}_{nl}(\mathbf{q}(t), \dot{\mathbf{q}}(t)) = \mathbf{F}_{exc}(t), \tag{4}$$

where $\mathbf{q}$ is the displacement vector, $\mathbf{M}$ is the mass matrix, $\mathbf{C}$ is the damping matrix, $\mathbf{K}$ is the stiffness matrix, $\mathbf{F}_{nl}$ is the vector of the nonlinear forces due to contact, and $\mathbf{F}_{exc}$ is the excitation force vector. A Craig–Bampton reduction is applied on the damper and on the platform mass and stiffness structural matrices. The number of retained modes is kept constant for numerical convenience and taken high to ensure the quality of the reduction basis on the frequency range of interest. Thus, 12 modes are kept for the platform and 30 for the damper. Contact points, as well as excitation and output points for the platform, are taken as reduction nodes. To

take into consideration the structural damping [12], a Rayleigh damping of 0.2% is added for each component. These different matrices are then assembled to form the global mass, damping, and stiffness matrices $\mathbf{M}$, $\mathbf{C}$, and $\mathbf{K}$. It is worth emphasising here that the size of the matrices is directly related to the damper geometry and to the number of contact nodes. The largest possible size for the system is for the full damper case and is of size 454. During optimisation, the size of the matrices is smaller as less contact points are usually present.

The nonlinear dynamic response of the blades is determined with the Harmonic Balance Method [18]. The displacements are written as a truncated Fourier series including N_h harmonics. The equation of movement can then be written in the frequency domain and transformed into the problem:

$$\mathbf{J}_1(\mathbf{Q}, \omega) = \mathbf{Z}(\omega)\mathbf{Q} + \tilde{\mathbf{F}}_{nl}(\mathbf{Q}) - \tilde{\mathbf{F}}_{exc} = \mathbf{0}, \tag{5}$$

where $\mathbf{Q} = [\mathbf{a}_0, \mathbf{a}_1, \mathbf{b}_1, \ldots, \mathbf{a}_{N_h}, \mathbf{b}_{N_h}]^T$ denotes the vector of the cosine and sine coefficient. The resonant solution is directly sought by adding a constraint on the phase ϕ between the response and the excitation [11], i.e., the phase must be equal to $\pi/2$ between the two:

$$\mathbf{J}_2(\mathbf{Q}, \omega) = \phi - \pi/2 = \mathbf{0}. \tag{6}$$

By adding this constraint, the resonant peak is directly assessed, which avoids the computation of the full FRF. The angular frequency also becomes an unknown, and the vector of unknown is $\boldsymbol{\alpha} = [\mathbf{Q}; \omega]$. The problem $\mathbf{J}(\mathbf{Q}, \omega) = [\mathbf{J}_1(\mathbf{Q}, \omega), \mathbf{J}_2(\mathbf{Q}, \omega)] = 0$ is then solved with a Trust-Region-Dogleg algorithm.

4 Results

4.1 Optimisation Parameters Presentation

The number of components describing the damper geometry is chosen equal to five here. To reduce the size of the optimisation problem, a few assumptions are made. First, a component is set to be horizontal and thin at the top of the damper, to ensure that the damper seals the platforms. Second, the damper is assumed to be symmetric about its vertical central axis, which divides by two the number of optimisation parameters. To ensure the existence of the contact between the damper and the platforms, the centre of one component must be on the contact line (i.e., the vertical and horizontal coordinates of one component are linked). Finally, with these choices, the optimisation problem is of dimension 9.

The optimisation problem is a minimisation problem, where the objective function is the vibration amplitude at resonance, determined according to Sect. 3.3. This approach might seem unrealistic as there is no constraint on the damper

volume. However, putting a constraint could lead to missing some interesting features. For this reason, no volume constraints are added here.

To ensure a good convergence and a better efficiency of the optimisation, the objective function is slightly modified. Instead of minimising the vibration amplitude at resonance, denoted by u_{peak}, the opposite of the inverse of the vibration amplitude at resonance is minimised (i.e., $f_{obj} = -1/u_{peak}$). This choice is motivated by the fact that the vibration amplitude is low as well as their variation. This makes the optimisation difficult as all the points are "compacted". By using the transformation proposed, the points are spread, and a small improvement in vibration amplitude corresponds to large variation of the objective function.

4.2 Optimisation Results

Results are illustrated for one optimisation case. Similar results were obtained for other cases and are not presented here for the sake of concision. The initial learning set is generated based on a Latin Hypercube Sampling of 200 points of the input space. The non-connected geometries are removed, so it remains 53 initial points. The optimisation loop is stopped after 100 iterations.

Results are shown in Fig. 3 where the evolution of the objective function is displayed versus the iteration number (see Fig. 3a). The current minimum in the optimisation is displayed with red points. The initial learning set is composed of 53 points, the minimum observed in this set is equal to $-2.1 \, \text{mm}^{-1}$ (blue triangle), and it corresponds to a vibration amplitude equal to 0.47 mm. The corresponding damper geometry is given in Fig. 3d, which corresponds to a very light damper. After that, in 100 iterations, the algorithm has identified new more efficient geometries and the final minimum is equal to $-2.49 \, \text{mm}^{-1}$ (light blue triangle). It corresponds to a vibration amplitude equal to 0.4 mm, i.e., the vibrations at resonance have been divided by about 15%. The best identified geometry is the light blue one where a large amount of material have been removed. An intermediary geometry is also given (see the green one), and the material distribution is somewhat between the blue and the light blue geometries. This demonstrates the good ability of the approach to identify efficient UPD geometries, but also its capacity to optimise with precision this geometry. This example also shows how sensitive is the dynamic behaviour to the damper geometry.

Another interest of this approach is that many configurations are tested and a map is obtained. It is then possible to observe the properties of other geometries. For example, the resonance frequency and the mass ratio (mass of the considered UPD over the mass of the full damper) are given in Fig. 3b,c. For example, a geometry with a mass reduction of about 50% with good damping properties is given in yellow. Compared to the other geometries, the total contact surface is present here. As an illustration, the damper geometry associated to the largest vibration amplitude is also given in orange. Its shape is very similar to the optimised one, but a large difference in the dynamic response is observed. As a reference, the full damper case

(a) Evolution objective function -
(●) current minimum

(b) Resonance frequency versus vibration amplitude

(c) Mass ratio versus vibration amplitude
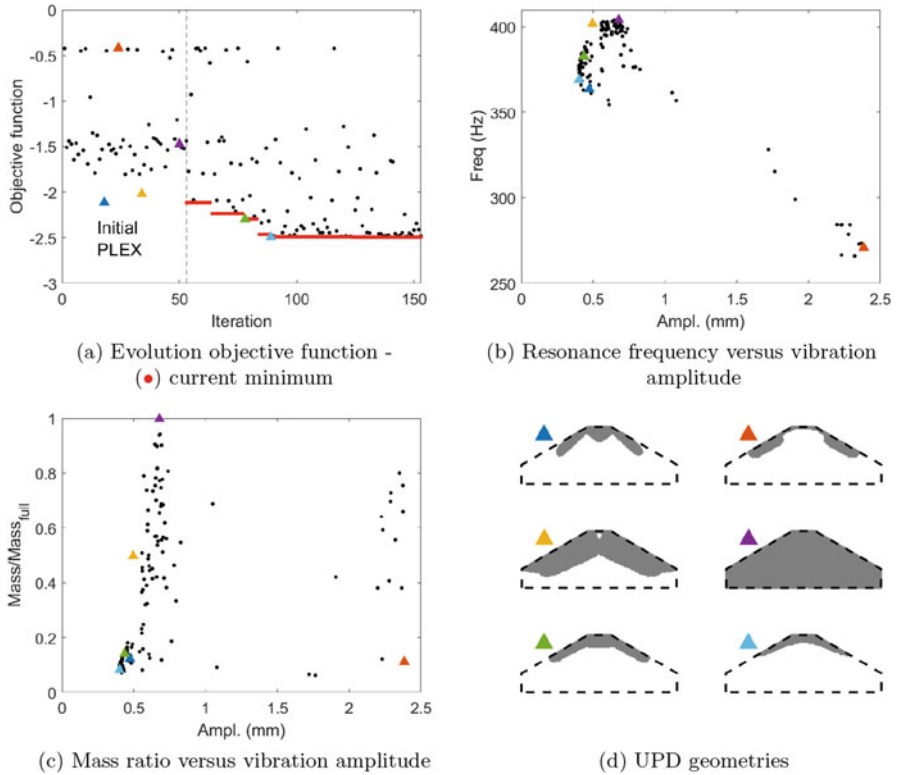
(d) UPD geometries

Fig. 3 Evolution of the objective function (**a**)—Resonance frequency (**b**) and mass ratio (**c**) of the tested configurations—UPD geometries (**d**) of some cases

is also illustrated in purple. One can notice that the different geometries presented here (the blue geometries, the yellow and the green ones) have better damping properties (up to 42% of vibration reduction) and are also lighter (up to 90% mass reduction). The frequency shift between these geometries is about 50 Hz. Finally, one can identify different geometries with different features and make conception choices based on criterion such as mass reduction, vibration reduction, or frequency shift.

5 Conclusions and Perspectives

Through this example, we illustrated the good capacity of the MMC approach coupled with EGO algorithm to optimise UPD geometry precisely at reasonable computational costs even with a complex contact law. Because many geometries are tested during the optimisation, it also gives tools for the analysis of the impact of

the UPD geometry on the nonlinear dynamic behaviour of the blades. The approach has shown promising results on a simple academic case for global optimisation, and more realistic optimisation problems will be considered in the future, by considering a volume constraint for example. The low numerical cost associated to the method and its formulation could be exploited to optimise other nonlinear dynamic features as bifurcation points [19] or to expand the optimisation to robust optimisation.

References

1. M. Krack, L. Salles, F. Thouverez, Vibration prediction of bladed disks coupled by friction joints. Arch. Comput. Meth. Eng. **24**(3), 589–636 (2017)
2. L. Panning, W. Sextro, K. Popp, Optimization of inter-blade friction damper design. Turbo Expo Power Land Sea Air 78576 (2000)
3. O. Sigmund, K. Maute, Topology optimization approaches. Struct. Multidiscip. Optim. **48**(6), 1031–1055 (2013)
4. X. Guo, W. Zhang, W. Zhong, Doing topology optimization explicitly and geometrically – a new moving morphable components based framework. J. Appl. Mech. **81** (2014)
5. V.J. Challis, A discrete level-set topology optimization code written in Matlab. Struct. Multidiscip. Optim. **41**(3), 453–464 (2010)
6. E. Raponi, M. Bujny, M. Olhofer, N. Aulig, S. Boria, F. Duddeck, Kriging-assisted topology optimization of crash structures. Comput. Methods Appl. Mech. Eng. **348**, 730–752 (2019)
7. A.R. Díaaz, N. Kikuchi, Solutions to shape and topology eigenvalue optimization problems using a homogenization method. Int. J. Numer. Methods Eng. **35**(7), 1487–1502 (1992)
8. S. Dou, J.S. Jensen, Optimization of nonlinear structural resonance using the incremental harmonic balance method. J. Sound Vib. **334**, 239–254 (2015)
9. A. Myźliński, Topology optimization of quasistatic contact problems. Int. J. Appl. Math. Comput. Sci. **22**(2), 269–280 (2012)
10. E. Denimal, F. El Haddad, C. Wong, L. Salles, Topological optimization of under-platform dampers with moving Morphable components and global optimization algorithm for nonlinear frequency response. ASME. J. Eng. Gas Turbines Power. **143**(2), 021021 (2021). https://doi.org/10.1115/1.4049666
11. L. Renson, T.L. Hill, D.A. Ehrhardt, D.A.W. Barton, S.A. Neild, Force appropriation of nonlinear structures. Proc. R. Soc. **A.474**, 20170880 (2018)
12. L. Pesaresi, L. Salles, A. Jones, J.S. Green, C.W. Schwingshackl, Modelling the nonlinear behaviour of an underplatform damper test rig for turbine applications. Mech. Syst. Signal Proces. **85**, 662–679 (2017)
13. J. Guillen, C. Pierre, An efficient, hybrid, frequency-time domain method for the dynamics of large-scale dry-friction damped structural systems, in *IUTAM Symposium on Unilateral Multibody Contacts* (1999), pp. 169–178
14. E.P. Petrov, D.J. Ewins, Advanced modeling of underplatform friction dampers for analysis of bladed disk vibration. J. Turbomach. **129**(1), 143–150 (2007)
15. D.R. Jones, M. Schonlau, W.J. Welch, Efficient global optimization of expensive black-box functions. J. Global Optim. **13**, 455-492 (1998)

16. W. Mebane, J. Sekhon, Genetic optimization using derivatives: the rgenoud package for R. J. Stat. Softw. **42**(11), 1–26 (2011)
17. W. Sextro, *Dynamical Contact Problems with Friction: Models, Methods and Applications*. (Springer, Berlin, 2002)
18. T. Detroux, L. Renson, L. Masset, G. Kerschen, The harmonic balance method for bifurcation analysis of large-scale nonlinear mechanical systems. Comput. Meth. Appl. Mech. Eng. **296**, 18–38 (2015)
19. R. Alcorta, S. Baguet, B. Prabel, P. Piteau, J.-G. Richardet, Period doubling bifurcation analysis and isolated sub-harmonic resonances in an oscillator with asymmetric clearances. Nonlin. Dyn. **98**(4), 2939–2960 (2019)

Experimental Demonstration of the Use of a Nonlinear Energy Sink with Rigid Lateral Boundaries as an Attenuator for Impulsive Vibrations

Christian E. Silva, Amin Maghareh, James M. Gibert, and Shirley J. Dyke

1 Introduction

In this chapter, we extend the results presented in [1], and [2] on the assessment and performance of a class of nonlinear energy sinks (NES) whose physical realization consists of a cantilevered beam with bounded lateral vibrations by means of two specially shaped rigid surfaces placed on both sides of the beam (in the vibration direction) thus providing nonlinear characteristics to the force–displacement response of the system. Nonlinear energy sinks are a category of passive vibration absorbers that use nonlinear energy pumping principles: A transference of vibratory energy from the point of occurrence in the host structure to a point of dissipation in the energy sinking device, where energy ideally travels irreversibly and dissipates entirely [3, 4].

Nonlinear energy sinks have received notable attention in recent years, due to some advantageous features in their performance when compared with their linear counterparts (tuned mass dampers, TMD). Among these advantages lie their capability to resonate at broadband frequencies, which makes them less prone to

C. E. Silva (✉)
Facultad de Ingeniería Mecánica y Ciencias de la Producción, Escuela Superior Politécnica del Litoral, ESPOL, Guayaquil, Ecuador
e-mail: chrsilva@espol.edu.ec
http://www.fimcp.espol.edu.ec/es/cv/christian_eduardo_silva_salazar

A. Maghareh · J. M. Gibert
School of Mechanical Engineering, Purdue University, West Lafayette, IN, USA
e-mail: amagare@purdue.edu; jgibert@purdue.edu

S. J. Dyke
School of Mechanical Engineering, Purdue University, West Lafayette, IN, USA

Lyles School of Civil Engineering, Purdue University, West Lafayette, IN, USA
e-mail: sdyke@purdue.edu

detuning and thus reducing the need of inspection and maintenance. A second characteristic of such devices is their capability of locally transfer and fully dissipate energy by means of a "controlled one-way channeling of the vibratory energy" as was stated by Gendelman et. al in a seminal paper in the topic [3]. Another interesting feature is the wide range of sources for geometric nonlinearities that can be exploited. These sources of nonlinear behavior can be even combined accordingly to produce different types of energy dissipation characteristics: e.g., nonlinear stiffness, nonlinear damping, or a combination thereof [5].

Despite the widespread variety of NES, within a large range of physical principles, few researchers have attempted to construct NES devices based on cantilevered beams, probably due to the fact that cantilever beams are classic examples of linear oscillators when the amplitudes of oscillation are small, which is usually the case for beams. Looking specifically at nonlinear springs based upon cantilevered beams, a number of researchers have reported the use of such devices in applications more related with energy harvesting, which use the opposite principle of energy collection instead of energy dissipation, but the physical principles are similar (e.g., same equations of motion). Among these studies rise the reports by Kluger et al. [6], who used a prototype of beam-based nonlinear spring as an energy harvesting device and load cell. In their study, they explored how the level of nonlinearity changes when the boundary surface order is modified. Along the same line of analysis, Liu et al. [7] expanded Kluger's study by presenting a comparative study with different curve fixtures, but adding a magnet to the tip of the beam for increasing the nonlinear behavior by changing the potential of the system. Furthermore, Wang et al. [8] proposed a similar idea with two sources of induced current that produced a four-well potential in the system. This device was also used in energy harvesting applications. Yuan et al. [9] explored a technique of expanding the bandwidth of beam-based energy harvesters by using optimization methods.

An extension of the concept of energy harvester was reported by Shmulevich et al. [10], in a study focused on a mechanical battery that used energy harvesting principles for generating energy produced by vibratory response of a linear host structure, and further storage of such energy that provided their system rechargeable battery features. To the best of the authors' knowledge, few researchers have indeed studied the vibration absorption phenomena with these types of systems in linear motion. Most of the existing studies are related with rotational motion vibration absorbers, where centrifugal pendulum vibration absorbers have been proved to reduce excessive torsional vibration in rotating systems [11], particularly in light aircraft, helicopter rotors, and automotive applications. One example is the study proposed by Borowski et al. [12], of the application of pendulums for reducing excessive vibrations in four-cylinder engines. Such pendulums were to be carefully designed for their optimal trajectories through the variation of a parameter that defines the curvature of the path followed by the pendulum, from circular to cycloidal. Following this finding, several other researchers proposed similar solutions for different cases of rotating systems [13–15].

2 Problem Definition

The proposed nonlinear spring to be used as an NES is comprised of a long homogeneous beam with one of its ends fixed between two rigid surfaces as shown in Fig. 1a. The spring has a linear damping coefficient, c, and an equivalent nonlinear stiffness κ. Quantity ϕ is the angle defining the angular displacement of the device with respect to the equilibrium position, and $\ddot{x}_b$ is the linear base excitation that perturbs the system.

The host structure consists of a two-DOF structure with the nonlinear spring attached to the second mass, as shown in Fig. 1b, for this case, $\ddot{u}_b = \ddot{X}_2$, and the NES is idealized as an inverted pendulum with a linear rotational dashpot of damping coefficient c_{NES}, and equivalent rotational spring of stiffness $\kappa = k_L(l\phi) + k_{NL}(l\phi)^9$, which will be defined shortly.
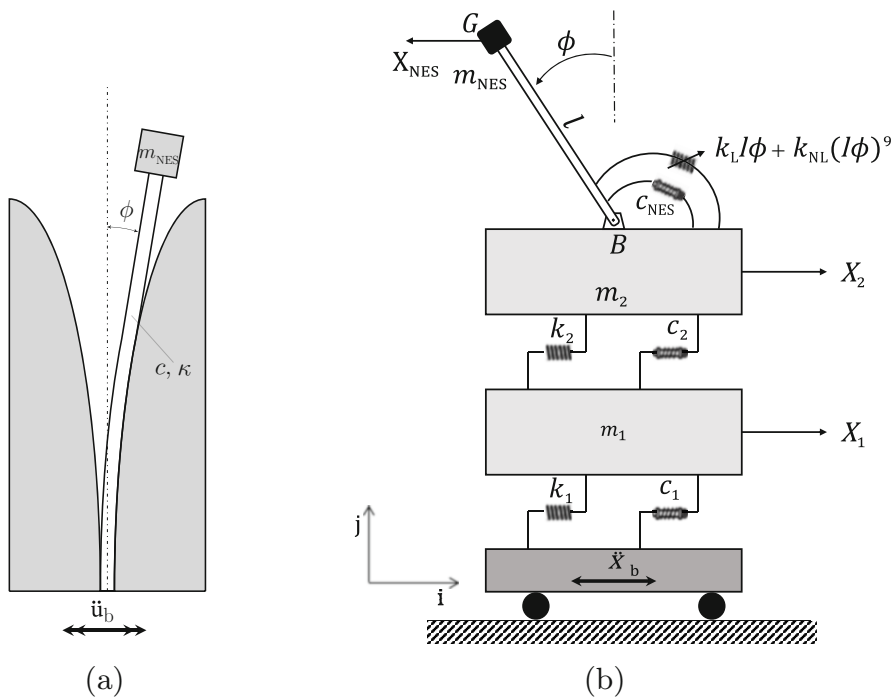
Fig. 1 Schematic diagrams (**a**) beam NES; (**b**) full system including host structure and NES

2.1 Model of the NES

It was demonstrated in [2] that this system can be modeled by using a rotational equation of motion with a ninth order polynomial nonlinearity, given by

$$(I_{\mathrm{B}} + ml^2)\ddot{\phi} + cl(l\dot{\phi}) + f_{\mathrm{sp}}(l\phi) - mgl(l\phi) = -ml\ddot{x}_{\mathrm{b}}, \tag{1}$$

where l, I_{B}, and g are the length, rotational moment of inertia of the mass, and gravitational acceleration, respectively. The quantity f_{sp} is the nonlinear spring force, associated with the equivalent stiffness of the beam, κ, defined by

$$f_{\mathrm{sp}} = k_{\mathrm{L}} l\phi + k_{\mathrm{NL}} (l\phi)^9, \tag{2}$$

where k_{L} and k_{NL} are the linear and nonlinear stiffness coefficients of the device. For the purposes of the present study, the gravitational effects are dropped as the device is installed in the horizontal plane.

2.2 Model of the Beam NES Coupled to the Primary System

The proposed nonlinear spring is now treated as an NES attached to the second mass of a linear system as schematically shown in Fig. 1b. The equations of motion of this system are derived using Lagrangian mechanics. The first step is to establish the position and velocity of the center of mass at the tip of the beam NES (point G), with respect to the coupling point at the second DOF (point B). From kinematics of rigid bodies, and choosing

$$x_{\mathrm{G/B}} = x_{\mathrm{NES}} = -l\sin(\phi)\mathbf{i} + l\cos\phi\mathbf{j} + X_2\mathbf{i}, \tag{3}$$

where X_2 is equivalent to the velocity of point B, and after taking the first time derivative, the velocity of B is obtained:

$$\dot{x}_{\mathrm{NES}} = [\dot{X}_2 - \dot{\phi}l\cos(\phi)]\mathbf{i} - \dot{\phi}l\sin\phi\mathbf{j}. \tag{4}$$

To construct the Lagrangian, the energy quantities of the system need to be obtained. The total kinetic energy of the system is

$$T = \tfrac{1}{2}m_1\dot{X}_1^2 + \tfrac{1}{2}m_2\dot{X}_2^2 + \tfrac{1}{2}m_{\mathrm{NES}}|\dot{X}_{\mathrm{NES}}|^2 + \tfrac{1}{2}I_{\mathrm{B}}\dot{\phi}^2, \tag{5}$$

where I_{B} is the rotational moment of inertia of the mass of the beam NES with respect to the connecting point B ($I_{\mathrm{B}} = I_{\mathrm{G}} + ml^2$), and the magnitude of the velocity vector of the NES is given by

$$|X_{\text{NES}}|^2 = \dot{X}_2^2 + l^2\dot{\phi}^2 + 2\dot{X}_2 l\dot{\phi}\cos\phi, \tag{6}$$

and the remaining quantities are defined in Fig. 1b. The potential energy is

$$V = \tfrac{1}{2}k_1(X_1 - x_{\text{b}})^2 + \tfrac{1}{2}k_2(X_2 - X_1)^2 + \tfrac{1}{2}k_{\text{L}}(l\phi)^2 + \tfrac{1}{10}k_{\text{NL}}(l\phi)^{10}. \tag{7}$$

Finally, the third element of Lagrange's formulation is to determine the non-conservative forces. The Rayleigh dissipation function is

$$D = \tfrac{1}{2}c_1\dot{X}_1^2 + \tfrac{1}{2}c_2(\dot{X}_2 - \dot{X}_1)^2 + \tfrac{1}{2}c_{\text{NES}}(l\dot{\phi})^2. \tag{8}$$

The Lagrangian of the system is then $\mathcal{L} = T - V$. Applying Lagrange's equations produces a system of equations of motion of the entire 3-DOF system. Considering that the acceleration obtained by taking the time derivative of the velocities is absolute (i.e., $\ddot{X}_1 = \ddot{x}_1 + \ddot{x}_{\text{b}}$, $\ddot{X}_2 = \ddot{x}_2 + \ddot{x}_{\text{b}}$, and so forth), the resulting EOMs of the system are given by

$$m_1\ddot{x}_1 + c_1\dot{x}_1 + c_2(\dot{x}_1 - \dot{y}_2) + k_1 x_1 + k_2(x_1 - x_2) = -m_1\ddot{x}_{\text{b}} \tag{9a}$$

$$(m_2 + m_{\text{NES}})\ddot{x}_2 + c_2(\dot{x}_2 - \dot{y}_1) + k_2(x_2 - x_1) - m_{\text{NES}}l\ddot{\phi} + m_{\text{NES}}lx_2\dot{x}_2^2$$
$$= -(m_2 + m_{\text{NES}})\ddot{x}_{\text{b}} \tag{9b}$$

$$(I_G + m_{\text{NES}})\ddot{\phi} - m_{\text{NES}}l\ddot{x}_2 + c_{\text{NES}}l^2\dot{\phi} + kl^2\phi + k_{\text{NL}}l^{10}\phi^9 = +m_{\text{NES}}l\ddot{x}_b. \tag{9c}$$

This constitutes the model of a two-DOF linear oscillator host structure, with masses m_1 and m_2, stiffness coefficients k_1 and k_2, and damping coefficients c_1 and c_2, coupled to a beam NES of mass m_{NES}, damping coefficient c_{NES}, linear component of stiffness k_{L}, and nonlinear component of stiffness k_{NL}, which is of order 9. To properly analyze this system numerically, by evaluating the relative contribution of terms in Eqns. (9), it is convenient to express them in nondimensional form. Choosing the inverse of the first linear natural frequency $\omega_1 = \sqrt{\frac{k_1}{m_1}}$ and the length of the beam l as time and length scales, respectively, such that $\tau = \omega_1 t$, and $x_i = z_i l$, $i = 1, 2$, the resulting nondimensional equations of motion are

$$z_1'' + 2\lambda_1 z_1' + \lambda_2(z_1' - z_2') + z_1 + \eta_1(z_1 - z_2) = -\frac{m_1}{k_1}lz_{\text{b}}''(\tau) \tag{10a}$$

$$\mu_2 z_2'' + 2\lambda_2(z_2' - z_1') + \eta_1(z_2 - z_1) - \mu_{\text{NES}}l\varphi'' + \mu_{\text{NES}}l^3\varphi(\varphi')^2 = -\frac{\mu_2}{m_1 k_1}lz_{\text{b}}(\tau)'' \tag{10b}$$

$$\mu_\varphi\varphi'' - \mu_{\text{NES}}lz_2'' + \lambda_{\text{NES}}l^2\varphi' + \eta_{\text{NL}}l^{18}\varphi^9 = +\frac{m_{\text{NES}}}{k_1}z_{\text{b}}(\tau)''. \tag{10c}$$

Here, z is the nondimensional displacement, and the new parameters are now

$$\lambda_i = \frac{c_i}{2\sqrt{m_1 k_1}}, (i = 1, 2, \text{NES}) \qquad \eta_1 = \frac{k_2}{k_1}, \qquad \eta_{\text{NL}} = \frac{k_{\text{NL}}}{k_{\text{L}}},$$

$$\mu_2 = \frac{m_2 + m_{\text{NES}}}{m_1}, \qquad \mu_\varphi = \frac{I_G + m_{\text{NES}} l_{\text{b}}^2}{m_1}, \qquad \mu_{\text{NES}} = \frac{m_{\text{NES}}}{m_1}.$$

3 Numerical Simulations

A comprehensive numerical study of the response of the developed model of the NES was presented in [2] with the aid of techniques proposed in [1]. Here, we extend the study by coupling the device to a physics-based model of a two-DOF base structure with the following characteristics [1]:

$$\mathbf{M} = \begin{bmatrix} m_1 & 0 \\ 0 & m_2 \end{bmatrix} = \begin{bmatrix} 23 & 0 \\ 0 & 24.0 \end{bmatrix} \text{kg}; \quad \mathbf{Z} = \begin{bmatrix} k_1 + k_2 & -k_2 \\ -k_2 & k_2 \end{bmatrix} = \begin{bmatrix} 58 & -29 \\ -29 & 29 \end{bmatrix} \text{kN/m}.$$

The higher mass on the second DOF accounts for the NES mounting bracket. The eigenvalue problem determined the natural frequencies of the system to be 3.4 and 9.2 Hz, and mode shapes to be $[0.66 \quad 1]^{\mathsf{T}}$, and $[1 \quad -0.56]^{\mathsf{T}}$. The system is initially at rest and then excited with an experimentally obtained base excitation signal that produces an effect similar to an impulse excitation. The development of the technique to carry out blast simulations (equivalent to initial velocity impulses to the structure), using ground motions such as those produced by shake tables, was reported by [16]. Here, the base excitation is dependent on several parameters that need to be designed. The base acceleration should generate a bounded displacement response. A sample of the shape of the ground motion that produces a valid impulse excitation to a structure is shown in Fig. 2a. The designed signal is

$$t_{\text{hold}}^+ = \frac{1}{\alpha E_{\text{acc}}} (E_{\text{acc}} t_{\text{hold}}^+ + a_{\text{max}} - a_{\text{max}} \alpha^2), \tag{11}$$

where all the variables are indicated in Fig. 2a. This function produces a bounded displacement, similar to a Haversine ramp with time $t_{\text{hold}}^+ + t_{\text{hold}}^-$.

4 Experimental Procedure

The experimental setup is a 2DOF system with the NES attached on the top floor as shown in Fig. 2b. A six-DOF servohydraulic shake table with an internal PID controller, model SC6000, manufactured by Shore Western is used to
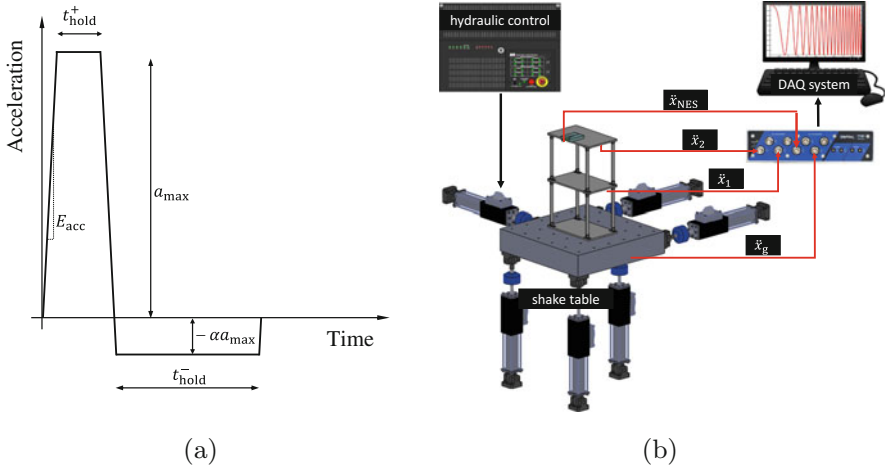
Fig. 2 Simulation and experimental setup: (**a**) Ground acceleration signal; (**b**) experimental schematic

perform this experiment. Four ceramic capacitive accelerometers, model 333B40, manufactured by PCB are used for measuring the accelerations of the system, with a frequency range of 0.5–3000 Hz, a measurement range of ± 98 m/s^2, and a broadband resolution of 0.0005 m/s^2. One accelerometer is fixed to each DOF. The base displacement generated by the shake table is measured using an LVDT located internally in the hydraulic actuator. Data is acquired using an analog, 8 channel input, 18-bit precision data acquisition box, model VibPilot-8 manufactured by m+p International, with built-in anti-aliasing filter and sampling time capacity of up to 104 kHz (for this experiment, data is sampled at 256 Hz).

Out of the original six cases of study presented in [2], corresponding to low, moderate, and high levels of excitation after the NES activation threshold has been surpassed, for two different boundary curvature orders, two limiting cases are selected: Limiting Case 1 (LC1), which has a total base displacement of 30 mm, an initial velocity $v_0 = 0.21$ m/s, and a curvature order 3; Limiting Case 2 (LC2), which has a total base displacement of 50 mm, an initial velocity $v_0 = 0.233$ m/s, and a curvature order 5. For both cases, the value of t_{hold} is set to 0.3 s.

4.1 Limiting Case 1 Results

The acceleration time histories of the NES with a rigid boundary whose curvature follows a function of third order are presented in Fig. 3 (top plot), and of both DOFs of the host structure (middle and bottom), when the NES is locked or inactive (light thick line) and unlocked or active (dark thin line). Figure 3a corresponds to the case of the numerical simulation, and Fig. 3b, of the experimental measurement.
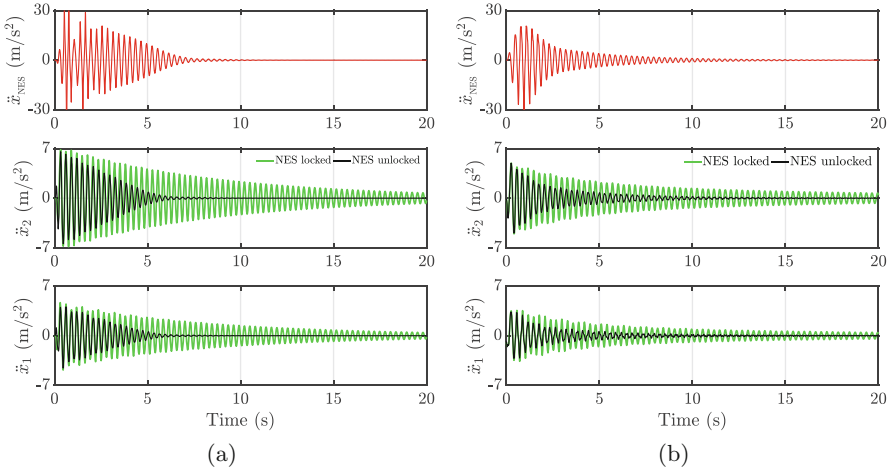
Fig. 3 Time and frequency modulation responses (LC1): (**a**) Numerical. (**b**) Experimental

Acceptable agreement is observed between numerical simulations and experiments. Significant reduction in the responses of the two DOFs of the host structure is also observed, and a response decay to near-zero values, when the NES is active, occurs before 5 s in the simulated case and at approximately 8 s in the experimental case. Despite the low excitation level, it is observed that the NES engages in resonance capture rapidly, contributing to a response reduction of the whole structure. Both DOFs of the structure experience response reduction due to the effect of the NES, suggesting that high energetic activity occurs on both modes of vibration. These results show that though the excitation level is in the low range, the NES is very effective at passively extracting and locally dissipating energy from the PO as a result of its nonlinear characteristics.

4.2 Limiting Case 2 Results

The simulated and measured results corresponding to an amplitude of excitation associated to a high level of impulsive energy (LC2) are now analyzed. The acceleration time histories of this case are shown in Fig. 3a, for the numerical simulation case, and in Fig. 3b, for the measured response case. This is an extreme case of impulsive excitation where the NES acceleration history shows very high peak amplitudes of acceleration. The acceleration of the beam NES can be exacerbated by the fact that the mass tends to impact the edges of the boundaries at high amplitudes of oscillation. The responses of the 1st and 2nd DOFs of the PO show a decay rate comparable with the previous case, reaching a near-zero response after about 9 s, only a second later than the previous case, but here with
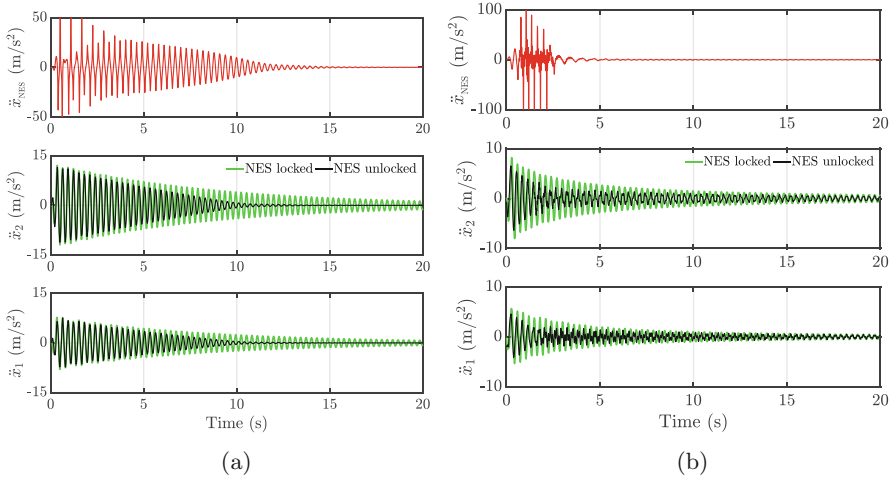
Fig. 4 Time and frequency modulation responses (LC2): (**a**) Numerical. (**b**) Experimental
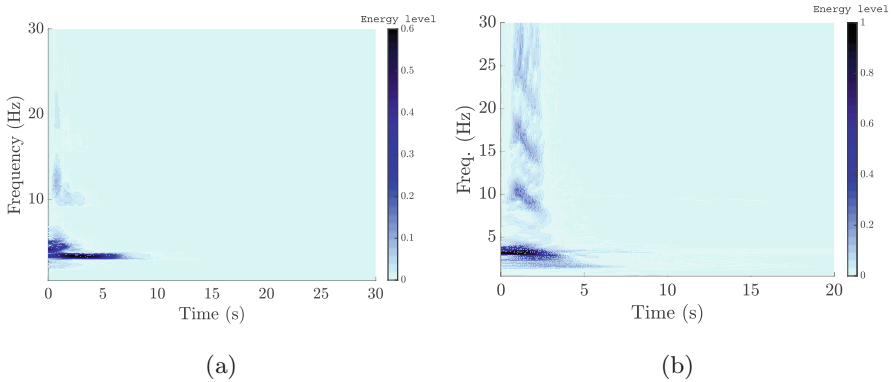
Fig. 5 Wavelet spectra associated with velocity response: (**a**) LC1; (**b**) LC2

a higher amplitude of impulsive excitation. The characteristic hardening behavior of the spring can be clearly noticed in Fig. 4a (top plot).

Further demonstration of the capacity of the NES in engaging in energy transfer with the PO is presented in Fig. 5, for both study cases (LC1 and LC2), where the wavelet spectra associated with the velocity of the systems are shown. In Fig. 5a, high-frequency activity can be observed where a small region of bandwidth starts to appear from 4 to 12 Hz, which suggests, as expected, that the NES has the nonlinear characteristics that allow it to engage in TET through resonance captures with the host structure, whose first resonant frequency is 3.4 Hz. It can also be observed that the frequency bandwidth of the device is not concentrated around a single frequency but dispersed from low- to high-frequency values, though the energy levels for the higher frequencies are low, as indicated by light shades of

activity. In Fig. 5b, the broadband energetic activity of the device of LC2 is rather more apparent, reaching up and beyond 30 Hz, and the linear natural frequency of the device appearing very dispersed without a clear constant value, consistent with the behavior of a hardening nonlinear spring, acting as an NES, and also with the modeled and experimental results of the NES characterization presented in [2]. The simulated velocity was obtained from the state-space model, whereas the experimental velocity was obtained by numerically integrating the acceleration response with intermediate steps of filtering and detrending of the signal.

5 Concluding Remarks

The development of a refined, physics-based model for a proposed NES configuration, which predicts its behavior and energy absorption capacity with reasonable accuracy, is further investigated and correlated with a series of experimental realizations. Both responses of the model and physical setup confirm the nonlinear energy absorption properties of this beam NES device.

References

1. C.E. Silva, A. Maghareh, H. Tao, S.J. Dyke, J. Gibert, Evaluation of energy and power flow in a nonlinear energy sink attached to a linear primary oscillator. J. Vib. Acoust. **141**(6), 061012 (2019). https://doi.org/10.1115/1.4044450
2. C.E. Silva, J.M. Gibert, A. Maghareh, S.J. Dyke, Dynamic study of a bounded cantilevered nonlinear spring for vibration reduction applications: a comparative study. Nonlin. Dyn. **101**(2), 893–909 (2020). https://doi.org/10.1007/s11071-020-05852-8
3. O.V. Gendelman, L.I. Manevitch, A.F. Vakakis, R. M'closkey, Energy pumping in nonlinear mechanical oscillators: part I–dynamics of the underlying Hamiltonian systems. J. Appl. Mech. **68**(1), 34 (2001). https://doi.org/10.1115/1.1345524
4. A.F. Vakakis, O. Gendelman, Energy pumping in nonlinear mechanical oscillators, part II: resonance capture. J. Appl. Mech. **68**(1), 42–48 (2001). https://doi.org/10.1115/1.1345525
5. Z. Lu, Z. Wang, Y. Zhou, X. Lu, Nonlinear dissipative devices in structural vibration control: a review. J. Sound Vib. **423**(June 9), 18–49 (2018). https://doi.org/10.1016/j.jsv.2018.02.052
6. J.M. Kluger, T.P. Sapsis, A.H. Slocum, Robust energy harvesting from walking vibrations by means of nonlinear cantilever beams. J. Sound Vib. **341**(April 14), 174–194 (2015). https://doi.org/10.1016/J.JSV.2014.11.035
7. W. Liu, C. Liu, X. Li, Q. Zhu, G. Hu, Comparative study about the cantilever generators with different curve fixtures. J. Intel. Mat. Syst. Struct. **29**(9), 1884–1899 (2018). https://doi.org/10.1177/1045389X17754274
8. C. Wang, Q. Zhang, W. Wang, J. Feng, A low-frequency, wideband quad-stable energy harvester using combined nonlinearity and frequency up-conversion by cantilever-surface contact. Mech. Syst. Signal Process. **112**(11), 305–318 (2018). https://doi.org/10.1016/j.ymssp.2018.04.027
9. Z. Yuan, W. Liu, S. Zhang, Q. Zhu, G. Hu, Bandwidth broadening through stiffness merging using the nonlinear cantilever generator. Mech. Syst. Signal Process. **132**, 1–17 (2019). https://doi.org/10.1016/j.ymssp.2019.06.014

10. S. Shmulevich, A. Joffe, I.H. Grinberg, D. Elata, On the notion of a mechanical battery. J. Microelectromech. Syst. **24**(4), 1085–1091 (2015). https://doi.org/10.1109/JMEMS.2014.2382638

11. T.M. Nester, P.M. Schmitz, A.G. Haddow, S.W. Shaw, Experimental observations of centrifugal pendulum vibration absorbers, in *The 10th International Symposium on Transport Phenomena and Dynamics of Rotating Machinery* (2004), pp. 7–11

12. V.J. Borowski, H.H. Denman, D.L. Cronin, S.W. Shaw, J.P. Hanisko, Brooks, L.T., D.A. Mikulec, W.B. Crum, M.P. Anderson, Reducing vibration of reciprocating engines with crankshaft pendulum vibration absorbers. SAE Trans. **100**(2), 376–382 (1991). https://doi.org/10.4271/911876

13. T.M. Nester, A.G. Haddow, S.W. Shaw, J.E. Brevick, V.J. Borowski, Vibration reduction in a variable displacement engine using pendulum absorbers, in *SAE Technical Papers. SAE International* (2003). https://doi.org/10.4271/2003-01-1484. https://www.sae.org/publications/technical-papers/content/2003-01-1484/

14. C.T. Lee, S.W. Shaw, V.T. Coppola, A subharmonic vibration absorber for rotating machinery. J. Vib. Acoust. Trans. ASME **119**(4), 590–595 (1997). https://doi.org/10.1115/1.2889766

15. R.P. Eason, C. Sun, A.J. Dick, S. Nagarajaiah, Steady-state response attenuation of a linear oscillator-nonlinear absorber system by using an adjustable-length pendulum in series: Numerical and experimental results. J. Sound Vib. **344**, 332–344 (2015). https://doi.org/10.1016/j.jsv.2015.01.030

16. N.E. Wierschem, Targeted energy transfer using nonlinear energy sinks for the attenuation of transient loads on building structures. Ph.D. Thesis, University of Illinois at Urbana-Champaign (2014)

Equivalence of Grounded and Non-grounded NES Tuning and Performance in Mitigating Transient Vibrations

Kevin Dekemele, Lennert De Knop, Patrick Van Torre, and Mia Loccufier

1 Introduction

When a nonlinear energy sink (NES) is attached to a mechanical system, the vibration energy is irreversibly transferred from the mechanical system to the NES through targeted energy transfer (TET). This occurs because of highly localized nonlinear normal modes, where the vibration energy is mainly localized in the NES. The first research about these NESs focused on grounded NESs (GNESs) (Fig. 1a). It was investigated in the context of the redistribution of energy between a highly nonlinear and a linear oscillator, connected by a weak linear stiffness [1]. Later, non-grounded NESs (NGNESs) (Fig. 1b) were given more attention in the literature, primarily as vibration absorbers [2]. As a NGNES rests on the vibrating mechanical system, the NES mass is typically only a fraction of the mechanical system, e.g., 2%. Yet in [3], it was shown that increasing the NES mass expedited vibration transfer. GNESs do not have this limitation and additionally have more design freedom with the weak connecting spring. In engineering applications, the NGNES has been widely applied to civil structures [4], (rotating) machinery [5, 6], and aerospace [7], but GNES applications are few and far between. In [8], a GNES was developed to suppress lateral vibrations in a rotor system. An equivalent GNES model also appears when shunting piezoelectric material with a nonlinear impedance for vibration absorption [9]. In the research presented here, the GNES's dynamics will be analyzed by deriving its slow invariant manifold (SIM), expressing

K. Dekemele (✉) · L. De Knop · M. Loccufier
Ghent University, Department of Electromechanical, Systems and Metal Engineering, Ghent, Belgium
e-mail: kevin.dekemele@ugent.be; Lennert.DeKnop@UGent.be; mia.loccufier@ugent.be

P. Van Torre
Ghent University, Department of Information Technology, Ghent, Belgium
e-mail: patrick.vantorre@ugent.be

27
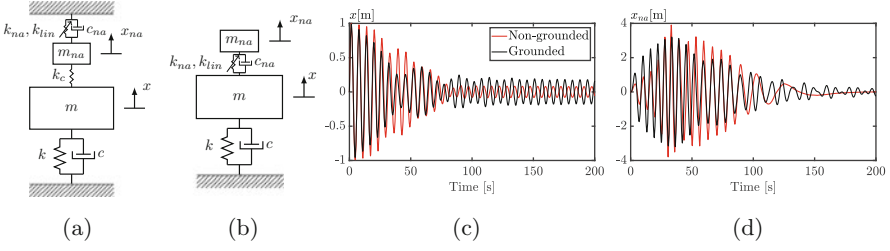
Fig. 1 The grounded (**a**) and non-grounded (**b**) NES coupled to an SDOF system. Mechanical system's (**c**) and NES's vibrations (**d**)

the evolution of the vibrations envelope on a slow time scale. The contributions are 1) the SIM is found to be equivalent to the SIM derived for the NGNES in [3], 2) the GNES performance can be predicted from simple formulae that solely depend on properties of the mechanical system and GNES, 3) the introduction of a novel *beating* measure, expressing the degree of back-and-forth vibration reflection between the GNES and the mechanical system, and 4) a tuning methodology based on maximizing GNES performance by increasing mitigation speed while steering clear of beating.

This chapter is structured in the following manner: in the next section, the SIM for the GNES is derived and compared to NGNES's SIM. Then in Sect. 3, analytical performance measures are derived, expressing the mitigation speed, dissipated energy, and beating. Section 4 presents the novel tuning methodology balancing the aforementioned performance measure, and finally, in Sect. 5, the conclusions are made.

2 System Dynamics

The dynamics of a GNES coupled to a mechanical system (Fig. 1a) is described by the following differential equations:

$$\begin{cases} m\ddot{x} + c\dot{x} + kx + k_c(x - x_{na}) = 0 \\ m_{na}\ddot{x}_{na} + c_{na}\dot{x}_{na} + k_{na}x_{na}^3 + k_{lin}x_{na} + k_c(x - x_{na}) = 0. \end{cases} \tag{1}$$

Similarly for the NGNES:

$$\begin{cases} m\ddot{x} + c\dot{x} + kx + c_{na}(\dot{x} - \dot{x}_{na}) + k_{na}(x - x_{na})^3 + k_{lin}(x - x_{na}) = 0 \\ m_{na}\ddot{x}_{na} + c_{na}(\dot{x}_{na} - \dot{x}) + k_{na}(x_{na} - x)^3 + k_{lin}(x_{na} - x) = 0. \end{cases} \tag{2}$$

A first numerical simulation is presented in Fig. 1c,d. Here the mechanical system has a mass $m = 1$ kg, a stiffness $k = 1$ N/m, and no damping. It has an initial speed

of $x(0) = 1$ m/s. The NGNES has an NES mass $m_{na} = 0.02$ kg, a damping $c_{na} = 0.002$ Ns/m, and a cubic nonlinear stiffness of $k_{na} = 0.004$ N/m^3 and the GNES $m_{na} = 0.04$ kg, $c_{na} = 0.002$ Ns/m, and $k_{na} = 0.004$ N/m^3. For this particular set of parameters, the vibrations are highly similar. The vibrations in the mechanical system decrease until about 70 s, after which a residual amount of energy is dissipated very slowly, typical of NESs. To clarify why they are similar, the SIM for both the GNES and the NGNES is derived next.

2.1 Grounded Absorber

Dividing (1) by mass m yields

$$
\begin{cases}
\ddot{x} + \epsilon\lambda\dot{x} + \omega_0^2 x + \epsilon\omega_0^2(x - x_{na}) = 0 \\
\epsilon\mu\ddot{x}_{na} + \epsilon\lambda_{na}\dot{x}_{na} + \epsilon\Omega_3\omega_0^4 x_{na}^3 + \epsilon\kappa\omega_0^2 x_{na} + \epsilon\omega_0^2(x_{na} - x) = 0,
\end{cases}
$$

where

$$
\epsilon\lambda = \frac{c}{m} \quad \omega_0^2 = \frac{k}{m} \quad \epsilon = \frac{k_c}{k} \quad \mu = \frac{m_{na}}{k_c}\omega_0^2
$$

$$
\kappa = \frac{k_{lin}}{k_c} \quad \lambda_{na} = \frac{c_{na}}{k_c}\omega_0^2 \quad \Omega_3 = \frac{k_{na}}{k_c\omega_0^2}
$$

(3)

with $\epsilon \ll 1$. For $\kappa < -\frac{1}{1+\epsilon}$, the NES is bistable. Bistable NESs have two stable resting positions where $x \neq 0$ and $x_{na} \neq 0$, which may strain the system at rest. Furthermore, unoptimal chaotic vibrations may occur [10]. This will not be considered in this chapter.

The slow flow dynamics are obtained by applying the following steps:

- A 1:1 resonance with frequency ω_0 is assumed.
- A complexification of the dynamic variables to $\varphi(t)e^{j\omega_0 t} = \dot{x} + j\omega_0 x$ and $\varphi_{na}(t)e^{j\omega_0 t} = \dot{x}_{na} + j\omega_0 x_{na}$ is applied with φ_{na} and $\varphi \in \mathbb{C}$ the dynamic envelopes.
- The complex variables are expressed as a perturbation series in ϵ, $\varphi = \varphi_0 + \epsilon\varphi_1$, and $\varphi_{na} = \varphi_{na,0} + \epsilon\varphi_{na,1}$.
- The dynamics are regarded on two time scales, $T_0 = t$, the fast time, and $T_1 = \epsilon t$, the slow time.
- The complex, slow time variables are expressed in their polar notation: $\varphi_0(T_1) = R_0 e^{j\delta_0}$ and $\varphi_{na,0}(T_1) = R_{na}e^{j\delta_{na}}$.
- Dimensionless envelope variables $Z_0 = \Omega_3 E_0$ and $Z_{na} = \Omega_3 E_{na}$ are introduced, with $E_0 = R_0^2 = |\varphi_0(T_1)|^2$ and $E_{na} = R_{na}^2 = |\varphi_{na}(T_1)|^2$.
- Damping is made dimensionless with $\xi = \frac{\lambda}{\omega_0}$ and $\xi_{na} = \frac{\lambda_{na}}{\omega_0}$.

A more thorough derivation is found in [3]. While applying these steps, all terms $O(\epsilon^2)$ were neglected.

The result is the slow flow dynamics:

$$\frac{\partial Z_0}{\partial T_1} = -\lambda Z_0 - \lambda_{na} Z_{na}$$

$$Z_0 = \left[\xi_{na}^2 + \left(\mu - \kappa - 1 - \frac{3}{4} Z_{na} \right)^2 \right] Z_{na}. \tag{4}$$

The set of equations in (4) has a dynamic and static relation between the dimensionless envelope of the mechanical system Z_0 and the NES's vibration Z_{na}. The dynamic relation dictates that Z_0 decreases if there is damping (λ and λ_{na}). The static relation is called the slow invariant manifold (SIM) and constrains the relation between Z_{na} and Z_0. Next, the SIM for the NGNES is derived.

2.2 Non-grounded Absorber

Dividing (2) by mass m:

$$\begin{cases} \ddot{x} + \epsilon \lambda \dot{x} + \omega_0^2 x + \epsilon \ddot{x}_{na} = 0 \\ \epsilon \ddot{x}_{na} + \epsilon \lambda_{na} (\dot{x}_{na} - \dot{x}) + \epsilon \Omega_3 \omega_0^4 (x_{na} - x)^3 + \epsilon \kappa \omega_0^2 (x_{na} - x) = 0 \end{cases} \tag{5}$$

with

$$\epsilon \lambda = \frac{c}{m} \quad \omega_0^2 = \frac{k}{m} \quad \epsilon = \frac{m_{na}}{m}$$

$$\kappa = \frac{k_{lin}}{m_{na} \omega_0^2} \quad \lambda_{na} = \frac{c_{na}}{m_{na}} \quad \Omega_3 = \frac{k_{na}}{m_{na} \omega_0^4}. \tag{6}$$

Although these parameters share the same symbols as in (3), their physical meaning is different.

To derive the slow flow dynamics, similar steps are applied as above, except the complexified variables are now defined as $\varphi(t)e^{j\omega_0 t} = \dot{x} + \epsilon \dot{x}_{na} + j\omega_0(x + \epsilon x_{na})$ and $\varphi_{na}(t)e^{j\omega_0 t} = \dot{x}_{na} - \dot{x} + j\omega_0(x_{na} - x)$. The slow flow dynamics for the NGNES are

$$\frac{\partial Z_0}{\partial T_1} = -\lambda Z_0 - \lambda_{na} Z_{na}$$

$$Z_0 = \left[\xi_{na}^2 + \left(1 - \kappa - \frac{3}{4} Z_{na} \right)^2 \right] Z_{na}. \tag{7}$$

The dynamic relation is equivalent as in (4), while the SIM is slightly different. The SIM is now generalized for both NESs.

2.3 Slow Dynamics

The slow flow dynamics and SIM for both NESs, (4) and (7) are generalized as

$$\frac{\partial Z_0}{\partial T_1} = -\lambda Z_0 - \lambda_{na} Z_{na}$$
$$Z_0 = \left[\xi_{na}^2 + \left(\Gamma - \frac{3}{4} Z_{na}\right)^2\right] Z_{na} \tag{8}$$

with $\Gamma = 1 - \kappa$ for the non-grounded absorber, and $\Gamma = \mu - \kappa - 1$ for the grounded absorber. Note that the dimensionless constants have a different physical meaning for the GNES (3) and NGNES (6). The simulations in Figs. 1c,d are compared to their slow flow dynamics in Fig. 2. For the GNES, $\mu = 2$ and $\kappa = 0$, and for the NGNES, $\kappa = 0$. Thus for both NESs, $\Gamma = 1$, $\xi_{na} = 0.1$, and $Z_0(0) = 0.2020$, and as such their SIM and slow flow evolutions are equivalent. The actual vibrations of the NESs follow the slow flow on average. The SIM as seen in Fig. 2c has a fold and two local extrema:

$$\begin{cases} Z_{na\pm} = \frac{4}{9}\left(2\Gamma \pm \sqrt{\Gamma^2 - 3\xi_{na}^2}\right) \\ Z_0^{\pm} = \left[\xi_{na}^2 + \left(\Gamma - \frac{3}{4} Z_{na\mp}\right)^2\right] Z^{na\mp} \end{cases} \tag{9}$$

with $\{Z_0^+, Z_{na}^-\}$ a local maximum and $\{Z_0^-, Z_{na}^+\}$ a local minimum that exists for

$$\xi_{na} < \frac{\Gamma}{\sqrt{3}}. \tag{10}$$
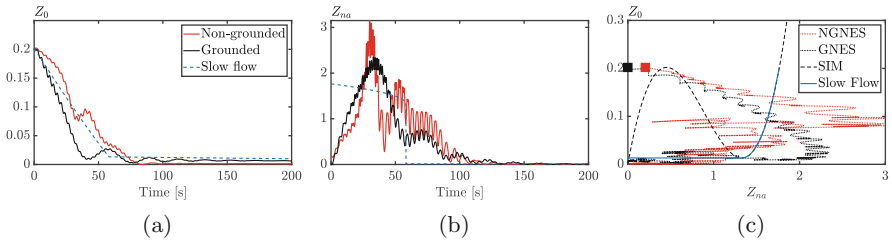
Fig. 2 Comparison of slow flow dynamics and simulation of complete dynamics with (**a**) the envelope of the mechanical system Z_0, (**b**) the envelope of the NES Z_{na} and (**c**) the phase plane of Z_0 and Z_{na} with the SIM

   The condition (10) for the existence of the extrema and thus the fold is required for efficient energy transfer [3, 10]. Optimal energy transfer occurs when the dynamics initiate on the right branch of the SIM, where according to the dynamic relation of (8), the decay rate of Z_0 is the highest. The SIM also has a local minimum. The vibrations decay efficiently to the minimum and then jump to the left branch. This explains the residual energy.

3   Performance

Observing the slow flow evolution in Fig. 2 reveals that Z_0 decays almost linearly at a high rate until a change of slope. The remaining Z_0 after the slope change is the residual energy that is dissipated slowly. At the same time, Z_{na} drops to a low value. On the SIM in Fig. 2c, this drop in NES efficiency corresponds to the jump from the right branch to the left branch. Now, simple analytic formulae expressing the duration of efficient energy transfer (or pumping time) and the residual energy are derived from (8).

3.1   Analytical Performance Measures

3.1.1   Residual Energy

The residual energy is the vibration energy left after the slow flow dynamics jump from the right to the left branch. Relative to the initial energy, it is found as

$$E_{res} = \frac{Z_0^-}{Z_0(0)} = \frac{E_0^-}{E_0(0)}. \tag{11}$$

These energy measures are calculated from the compound system's parameters (9) and the initial energy $Z_0(0) = \Omega_3(\dot{x}(0)^2 + \omega_0^2 x^2(0))$.

3.1.2   Pumping Time

From (4), the expression for $\frac{\partial Z_{na}}{\partial T_1}$ can be determined. By neglecting system damping, $\xi \approx 0$, the expression is integrated to obtain:

$$\overbrace{\frac{27}{32} Z_{na}^2 - 3\Gamma Z_{na} + \left(\Gamma^2 + \xi_{na}^2\right) \ln(Z_{na})}^{I(Z_{na})} = C - \omega_0 \xi_{na} T_1. \tag{12}$$

The duration between two values of Z_{na} can be calculated from (12). The pumping time can then be calculated as

$$\epsilon T_{pump} = \frac{1}{\omega_0 \xi_{na}} \Big(I(Z_{na}(0)) - I(Z_{na}^+) \Big). \tag{13}$$

This expression also depends only on the compound system's parameters and the initial energy. Here $Z_{na}(0)$ is the value on the right branch corresponding with $Z_0(0)$. The pumping time is inversely proportional to ϵ. For the NGNES, this is the mass ratio, which has hard upper limit. For the GNES, this is the stiffness ratio, which does not have a hard constraint.

3.1.3 Prediction of Performance

For the coefficient and initial conditions of simulations in Figs. 1 and 2, the pumping time T_{pump} is 58.2 s, and the residual energy is 0.066. These can be calculated before a numerical simulation, to predict the performance.

3.2 Beating Index

A vibration consisting of two closely spaced frequencies ω_1 and ω_2 has a significant amplitude modulating beat of frequency $\frac{\omega_2 - \omega_1}{2}$. In the simulations in Fig. 1, the GNES shows some slight beating, where vibration energy is reflected back and forth from NES to mechanical system.

The linear eigenfrequencies of the grounded absorber are derived from the following determinant, obtained from a linearized version of (1):

$$\begin{vmatrix} (1+\epsilon)\omega_0^2 - \omega^2 & -\epsilon\omega_0^2 \\ -\epsilon\omega_0^2 & \epsilon\omega_0^2(1+\kappa) - \epsilon\mu\omega^2 \end{vmatrix} = 0$$

$$\implies \omega^2 = \frac{1 + \mu(1+\epsilon) + \kappa \pm \sqrt{(1+\mu(1+\epsilon)+\kappa)^2 - 4\mu(1+\kappa+\epsilon\kappa)}}{2\mu} \omega_0^2$$

$$\approx \frac{1 + \mu + \kappa \pm (\mu - 1 - \kappa)}{2\mu} \omega_0^2 \implies \omega_{1,2}^2 \approx \{\frac{1+\kappa}{\mu}, 1\} \cdot \omega_0^2. \tag{14}$$

Similar, for the non-grounded absorber:

$$\begin{vmatrix} (1+\epsilon\kappa)\omega_0^2 - \omega^2 & -\epsilon\kappa\omega_0^2 \\ -\epsilon\kappa\omega_0^2 & \epsilon\kappa\omega_0^2 - \epsilon\omega^2 \end{vmatrix} = 0 \implies \omega_{1,2}^2 = \{\kappa, 1\} \cdot \omega_0^2. \tag{15}$$

The following measures express the proximity of the eigenfrequencies:

$$I_{beat}^2 = \frac{\omega_2^2 - \omega_1^2}{\omega_0^2} \overset{\text{GNES}}{=} \frac{\mu - \kappa - 1}{\mu} \qquad \overset{\text{NGNES}}{=} 1 - \kappa. \tag{16}$$

For the simulation in Fig. 1, I_{beat}^2 is 0.5 for the GNES and 1 for the NGNES. The linearized eigenfrequencies for the GNES are closer, explaining the *higher degree of beating* in the GNES.

4 Tuning

Although the GNES and NGNES have an equivalent SIM and performance measures, tuning and designing the physical parameters of both NESs are different. While the NGNES has a hard constraint on the absorber mass, directly impacting ϵ and thus the performance (it is in the denominator in (13)), this is less of an issue for the GNES. Moreover, the ϵ for the GNES, the stiffness ratio, generally does not have a hard constraint. The only real tuning parameters for the NGNES are thus the damping ξ_{na} and κ. For the GNES, ϵ, μ, κ, and ξ_{na} can be considered to be design parameters. However, this high-dimensional design space increases the complexity of finding suitable GNES parameters. Therefore, a novel tuning methodology is presented next.

4.1 Tuning Plane GNES

To obtain a suitable choice for μ and κ, the tuning plane is presented in Fig. 3. The choice for μ and κ is constrained by the conditions for the fold in the SIM, (10), $\mu > \kappa + 1 + \sqrt{3}\xi_{na}$, by the condition for bistability and chaotic vibrations $\kappa > -\frac{1}{1\epsilon}$ and by an optional mass constraint $\mu < \mu_{max}$. These constraints form a triangle of admissible μ and κ values, within the black lines in Fig. 3.

The class of GNESs with equal Γ, or where $\mu - \kappa = C$, $C > 1$ have the same analytical performance, (13) and (11). Two equi-performance lines are drawn in Fig. 3. Additionally, lines for constant beating index, $\mu = \frac{1+\kappa}{1 - I_{beat}^2}$, are also shown. For the same predicted performance, GNES more to the right on the tuning plane suffers more from beating.

Fig. 3 Tuning plane for grounded NES for $\epsilon = .02$ and $\xi_{na} = 0.1$
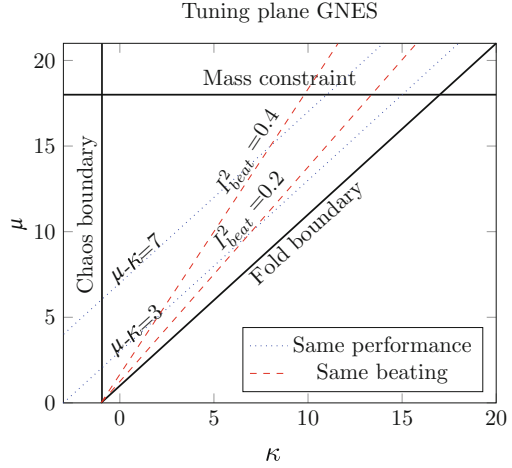
Table 1 NES parameters and static performance

	Ω_3	μ	κ	ϵ	E_{res}	T_{pmp}	I_{beat}^2
1	10.7	4	0	0.02	0.003	1021 s	0.75
2	10.7	24	20	0.02	0.003	1021 s	0.125
3	0.404	1.1	−0.9	0.02	0.03	112 s	0.9
4	0.404	5	3	0.02	0.03	112 s	0.2
5	10.7	4	0	0.12	0.003	170 s	0.75

4.2 Simulations

For the mechanical system presented in Sect. 2, several GNESs are now tuned, with parameters given in Table 1. Each time, Ω_3 is chosen such that $Z_0(0) = 2 \cdot Z_0^+$ to ensure the dynamics attract to the right branch of the SIM. Five NESs will be simulated for $\dot{x}(0) = 1$ m/s. The first two NESs, where $\mu - \kappa = 4$, lay on an equi-performance line but have a different beating index. The simulations in Fig. 4a,d reveal a similar performance, but significant beating for the second NES. The next 2 NESs have $\mu - \kappa = 2$, and a faster GNES is predicted with the pumping time and is confirmed in Fig. 4b,e. However, the NES with the lower beating index has significantly more residual energy in the simulation, not predicted by (11). From these simulations, one might suggest that an as small $\mu - \kappa$ with an as small μ is the optimal choice. As a counterexample, NES 5 is simulated, having an $\epsilon = 0.12$ and a $\mu = 4$, or $m_{na} = 0.48$. It is compared to NES 3 in Fig. 4c,f and has comparable performance. Additionally, NES 5 has a lower stroke. The high absorber mass of this NES, 0.48 kg, would not be feasible for NGNESs.
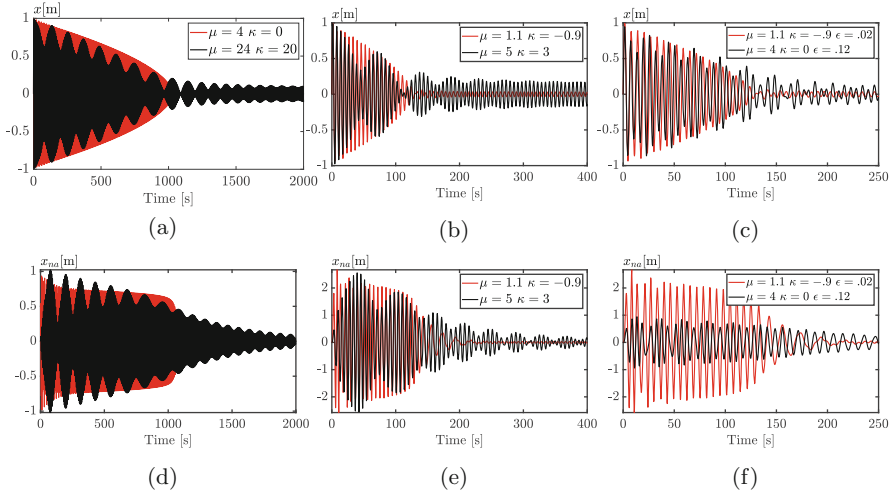
Fig. 4 Simulation of NES in Table 1, NESs 1 and 2 (**a**)(**d**), 3 and 4 (**b**)(**e**), and 3 and 5 (**c**)(**f**)

5 Conclusions

This chapter presented a thorough research of the grounded nonlinear energy sink (GNES) based on its slow invariant manifold (SIM). It was shown that the SIM has an equivalent shape as the SIM of non-grounded NESs, but where the GNES mass and coupling spring have a different role. The performance of the GNES could be predicted with static performance measures and the novel beating index. These allowed to construct a tuning plane GNES, constrained by constant lines of performance and beating. It was shown that for GNESs with distant linear eigenfrequencies or a high beating index, the static performance measures are good predictors of the duration of energy transfer and residual energy. The opposite was true GNESs with close eigenfrequencies or low beating index. The increased design freedom of the GNES allows a performant vibration mitigation for both small NES mass with weak coupling spring and higher NES mass with stronger coupling spring. The latter configuration has a smaller stroke.

References

1. O.V. Gendelman, Transition of energy to a nonlinear localized mode in a highly asymmetric system of two oscillators. Nonlin. Dyn. **25**(1–3), 237–253 (2001)
2. G. Kerschen, Y.S. Lee, A.F. Vakakis, D.M. McFarland, L.A. Bergman, Irreversible passive energy transfer in coupled oscillators with essential nonlinearity. SIAM J. Appl. Math. **66**(2), 648–679 (2005)

3. K. Dekemele, R. De Keyser, M. Loccufier, Performance measures for targeted energy transfer and resonance capture cascading in nonlinear energy sinks. Nonlin. Dyn. **93**(2), 259–284 (2018)
4. S. Lo Feudo, C. Touzé, J. Boisson, G. Cumunel, Nonlinear magnetic vibration absorber for passive control of a multi-storey structure. J. Sound Vib. **438**, 33–53 (2019)
5. G. Habib, G. Kerschen, G. Stepan, Chatter mitigation using the nonlinear tuned vibration absorber. Int. J. Nonlin. Mech. **91**, 103–112 (2017)
6. A. Haris, P. Alevras, M. Mohammadpour, S. Theodossiades, M. O'Mahony, Design and validation of a nonlinear vibration absorber to attenuate torsional oscillations of propulsion systems. Nonlin. Dyn. **100**(1), 33–49 (2020)
7. B. Bergeot, S. Bellizzi, B. Cochelin, Passive suppression of helicopter ground resonance using nonlinear energy sinks attached on the helicopter blades. J. Sound Vib. **392**, 41–55 (2017)
8. H. Yao, Y. Cao, Z. Ding, B. Wen, Using grounded nonlinear energy sinks to suppress lateral vibration in rotor systems. Mech. Syst. Signal Proces. **124**, 237–253 (2019)
9. R. Viguié, G. Kerschen, M. Ruzzene, Exploration of nonlinear shunting strategies as effective vibration absorbers, in *Active and Passive Smart Structures and Integrated Systems 2009*, vol. 7288 (International Society for Optics and Photonics, Bellingham, 2009), p. 72882B
10. K. Dekemele, P. Van Torre, M. Loccufier, Performance and tuning of a chaotic bi-stable NES to mitigate transient vibrations. Nonlin. Dyn. **98**(3), 1831–1851 (2019)

Dynamic Performances of a 2 DOF System Coupled with Rigid Block and Inerters

Check for updates

Stefano Pagliaro and Angelo Di Egidio

1 Introduction

Recently, many papers have studied the coupling between mechanical systems, where rigid blocks are combined with devices or structures. An interesting work is [1], where the effectiveness of base anchorages is studied. In [2, 3], the effects of base isolated systems are investigated. Another interesting technique to improve the behaviour of rigid block-like structures is the mass-damper dynamic absorber, as highlighted in [4, 5]. Instead, a safety device can be the mass damper, where in [6, 7] it is modelled as a single degree of freedom that runs on the top of the block. The use of semi-active anchorages was investigated in [8], whereas an active control technique was used to protect the rigid block from overturning [9].

An interesting issue is the protection of frame structures or bridges by using rocking rigid blocks. The paper [10] investigated the effects of a structure placed on a rocking podium, whereas [11] discussed the rocking isolation. An interesting technique to protect frame structures by using a rigid block can be carried out using a rigid coupling between a frame and a rocking wall, as showed in [12]. Instead, [13] studied an elastic link between the frame structure and the block.

Recent papers deal with the use of inerter devices to improve the dynamic and seismic response of structures. For instance in [14, 15], Tuned Mass Damper Inerter devices were used to improve the behaviour of base isolated structures. Instead, in [16, 17], the controlled dynamics of two adjacent structures linked by a spring-dashpot-inerter was investigated.

S. Pagliaro (✉) · A. Di Egidio
University of L'Aquila, DICEAA, L'Aquila, Italy
e-mail: stefano.pagliaro@graduate.univaq.it; angelo.diegidio@univaq.it
http://ing.univaq.it/diegidio

The coupling between a frame structure and an external rocking wall is examined in this chapter with the purpose of improving the dynamical behaviour. A multi-storey frame structure is modelled by means of an equivalent two-degree-of-freedom linear system, whereas the classical model of rigid block is used to represent the wall. The top of the block is connected to the first storey of the frame structure with an elastic device. The inerter devices considered in this chapter are connected to the vertical sides of block and to the ground as investigated in [18] for stand-alone rigid blocks. The inerter devices possess the ability to increase the inertial mass of the mechanical system introducing apparent inertial mass, which depends only on the acceleration.

The dynamical behaviour of coupled system is analyzed by means of numerical integrations of the equations of motion. Simulations are performed using several earthquakes records as forcing term. A parametric analysis is carried out, and the results are organized in gain maps. The maps show the ratio between the maximum displacements or drifts of coupled and uncoupled systems in the system's parameters. Wide regions of the maps, where coupling is effective, are found. Results also show that the effectiveness of the coupling can be increased with the use of inerters and makes possible the use of blocks with smaller dimensions.

2 Mechanical System

The mechanical system is portrayed in Fig. 1. It is a planar structural system composed of a 2-*DOF* linear system, which represents the frame structure, and a rocking block whose purpose is to reduce the horizontal displacement derived from a base motion. The mass of the rocking block is $M = \rho \times 2b \times h_1 \times s$, where $\rho = 2500 \, \text{kg/m}^3$ and s is the length (orthogonal to the plane of the figure). An elastic device represents the connection between the first level of the 2-*DOF* system and block. Two inerter devices, whose apparent inertial mass is m_R, are considered. They connect the ground and the vertical sides of the block. The inerter devices posses the notably ability to behave as virtual added masses since they can transform the rotational inertia of a flywheel in translational inertia.

As observed in previous paper [13], the effectiveness of the coupling depends on the ratio between the mass of the block and the mass of the frame, in particular to achieve good results the mass of the block should be about 10–30% of the total mass of the structure to be protected. The introduction of inerter devices is intended to make coupling effective by using relatively small block, since the inerter devices can provide the additional mass needed.

The procedure developed in [19] allows the two-degree-of-freedom system to represent the main dynamic characteristics of a general multi-storey frame structure. Such a dynamic equivalence refers to stand-alone frame structures. It is based on two main assumptions: (*i*) the frequency of the first mode of the multi-*DOF* system is
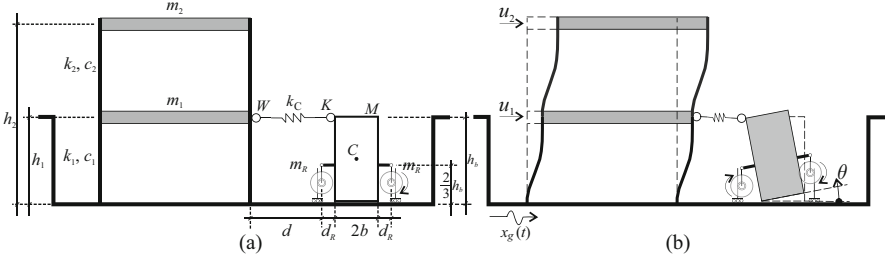
Fig. 1 Coupling of a frame with rocking block: (**a**) Mechanical and geometrical characteristics of the reduced-order model; (**b**) Positive directions of the Lagrangian parameters

the same of the 2-*DOF* system and (*ii*) the modal components of the 2-DOF system and those ones associated to the two reference storeys of the multi-DOF system are equal. These assumptions implicitly require that the frame structure has to be sufficiently regular. It is reasonably assumed that, if the dynamic equivalence works correctly for stand-alone structures, it works correctly for the same structures also after the coupling with an external rocking block.

2.1 Equations of Motion

The dynamic response of the reduced-order model is defined by three Lagrangian parameters: two displacements u_1 and u_2, and the rotation θ of the block. In order to represent the motion of the system when block rocks around either left corner or right corner, two sets of three nonlinear equations of motion are derived through a Lagrangian approach, whose positive directions of Lagrangian parameters u_1, u_2, and θ are shown in Fig. 1b. In this section, only the first set of equations, which describes the motion of the system when the block is rocking around left corner, are reported. The second set of equations, which describe the rocking motion around the right corner, can be found in [20]. The two sets of equations that describe the motion of the system without inerter devices are reported in [13].

The introduction of the inerter devices modifies the equations by adding supplemental inertia terms, since they introduce apparent inertial masses in the system (underlined term). The equations of motion are

$$-k_C \left(d - h_1 \sin\theta - u_1\right) \times Q_1 + \left(c_1 + c_2\right) \dot{u}_1 -$$
$$c_2 \dot{u}_2 + \left(k_1 + k_2\right) u_1 - k_2 u_2 + m_1 \left(\ddot{x}_g + \ddot{u}_1\right) = 0$$
$$- - - - - - - -$$
$$c_2 \left(\dot{u}_2 - \dot{u}_1\right) + k_2 \left(u_2 - u_1\right) + m_2 \left(\ddot{x}_g + \ddot{u}_2\right) = 0 \qquad (1)$$
$$- - - - - - - - -$$
$$k_C h_1 \left((u_1 - d) \cos\theta + h_1 \sin\theta\right) \times Q_1 -$$
$$\ddot{x}_g \left(h_b M \cos\theta + b M \sin\theta\right) + b g M \cos\theta - h_b g M +$$
$$\left(J_A + m_R \left((2b + d_R)\cos(\theta) - \tfrac{2}{3} h_b \sin(\theta)\right)^2\right) \ddot{\theta} = 0,$$

where m_R is the apparent inertial mass of the inerter devices; $J_A = J_C + M(b^2 + h_b^2)$ and J_C are the total polar inertia of block with respect to left base corner and to its centre, respectively; quantity Q_1 reads

$$Q_1 = \frac{-d + \sqrt{d^2 - 2\left(d - u_1\right) h_1 \sin\theta - 2du_1 - 2h_1{}^2 \cos\theta_1 + 2h_1^2 + u_1^2}}{\sqrt{d^2 - 2\left(d - u_1\right) h_1 \sin\theta - 2du_1 - 2h_1{}^2 \cos\theta + 2h_1^2 + u_1^2}}. \qquad (2)$$

2.2 Uplift and Impact Conditions

When the stabilizing moment $M_R = M g b$, which depends on the weight of the block, is smaller than the overturning moment $M_O = -M \ddot{x}_g(t) h_b + k_C u_1(t) h_1$ that depends on inertial forces and elastic reaction of the coupling device, the uplift of the block around left base occurs. If uplift does not take place, the elastic reaction of coupling device depends only on the displacement of the 2-*DOF* system. By simplifying the sum of two previous moments, the uplift acceleration $\ddot{x}_g = a_{UP}$ around base left corner is obtained. The uplift acceleration reads

$$a_{UP}(t) = \frac{g}{\lambda} + \frac{k_C u_1(t) h_1}{M h_b}, \qquad (3)$$

where $\lambda = h_b/b$ is the slenderness of the block. If there is no coupling, the same uplift condition of a stand-alone block is obtained. The uplift condition around the right corner can be found in [20].

During rocking motion, when the rotation $\theta(t)$ approaches zero, an impact between the block and the support takes place. The impact condition provides the angular velocity $\dot{\theta}^+$ as a function of the pre-impact velocity $\dot{\theta}^-$, $(\dot{\theta}^+/\dot{\theta}^-)^2 = \eta^2 \cdot r$, where $r = (J_O - 2bS_y/J_O)^2$ is the restitution coefficient. Quantity J_O represents polar inertia of block with respect to one of the two base corners, whereas the static moment of the block with respect to a vertical axis passing through one of the two base corners is defined by $S_y = \pm M b$ (sign $+$ refers to a block that re-uplifts around the left corner, sign $-$ refers to a block that re-uplifts around the right corner). The

coefficient η represents an additional loss of mechanical energy. In case the impact is perfectly rigid, then $\eta = 1$; otherwise, it is less than unity. Such a coefficient can be experimentally obtained as in [5]. In the analyses carried out in this chapter, the value of η is fixed ($\eta = 0.9$). Finally, it is worth to notice that the restitution coefficient r is the same as that of the classical stand-alone rigid block model [21].

3 Parametric Analysis

The dynamical behaviour of the coupled mechanical system is investigated by means of an extensive parametric analysis, in which three parameters have been varied: (i) the base dimension of the block $2b$, (ii) the coupling stiffness ratio $\beta = k_C/k_1$, and (iii) the apparent inertial mass ratio of the inerter devices $\gamma = m_R/M$ (see Fig. 1).

In the parametric analyses, the 2-DOF system refers to two buildings whose proprieties are shown in Table 1. Considering the values reported in Table 1, the dynamical characteristics of the equivalent model, shown in Table 2, are obtained from the procedure described in [19].

The two modes of the 2-*DOF* system have a modal damping ratio ξ, that is reported in Table 2.

3.1 Gain Coefficients

The displacement u_1 and the drift $u_2 - u_1$ of the system with coupling and inerters are compared to those obtained from the stand-alone frame in order to provide an indication of the efficiency of the method. The comparison is carried out introducing two gain coefficients as follows:

$$\alpha_1 = \frac{\max |u_1(t)|}{\max |\tilde{u}_1(t)|}, \quad \alpha_2 = \frac{\max |u_2(t) - u_1(t)|}{\max |\tilde{u}_2(t) - \tilde{u}_1(t)|}, \tag{4}$$

Table 1 Proprieties of the two reference buildings

Storeys	Connection level	Storey area	Storey mass m_s	Storey height
3	1	$100\,\mathrm{m}^2$	$120.6 \times 10^3\,\mathrm{kg}$	$3\,\mathrm{m}$
5	1	$250\,\mathrm{m}^2$	$301.5 \times 10^3\,\mathrm{kg}$	$3\,\mathrm{m}$

Table 2 Characteristics of the reduced-order models

Storeys	k_1 [N/m]	k_2 [N/m]	m_1 [kg]	m_2 [kg]	ξ
3	2.194415×10^8	0.940463×10^8	120.6×10^3	241.2×10^3	0.05
5	7.641287×10^8	1.819354×10^8	301.5×10^3	1206.0×10^3	0.05

where the displacements $\tilde{u}_1$ and $\tilde{u}_2$ refer to the stand-alone frame. Equation (4) shows that the effectiveness of the coupling increases when α_1 and α_2 decrease. Specifically, values of the gain coefficients less than unit represent good performances of the coupling.

The purpose of parametric analysis is to evaluate gain coefficients α_1 and α_2 in a specific parameter plane and summarize the results in gain maps.

3.2 Seismic Excitation

Four earthquake records were used as exciting input. The earthquake records (later called with underlined name) are listed below:

– *Kobe*, Takarazuka-000 station, ground motion recorded during the 1995 Japan earthquake
– *L'Aquila*, IT.AQV.HNE.D.20090406.013240.X.ACC station, ground motion recorded during the 2009 Italian earthquake
– *Pacoima*, Dam-164 ground motion recorded during the 1971 San Fernando, California earthquake
– *Parkfield*, CO2-065 ground motion recorded during the California earthquake 1966

4 Discussion of the Results

The gain maps summarize the results of the simulations and represent the contour plots (for a single earthquake) of gain coefficients α_1 and α_2 in a specific parameter plane. When gain parameters are less than unity, the region is coloured in light grey. These regions are named gain regions and define the optimal design parameters.

Figure 2 shows the maps obtained for the three-storey frame (first rows of Tables 1 and 2) in the parameter plane γ-β, whose geometrical scheme is portrayed in Fig. 2a. The maps in Fig. 2b refer to two earthquakes. In particular, the first row refers to Pacoima and the second row to Parkfield earthquakes. The maps show that the ability of coupling with external wall to reduce displacement increases when the apparent inertial mass ratio γ grows up, since the gain regions become wider and the value of gain coefficients reduces. Moreover, when $\gamma = 0$ (i.e., when there are no inerters), the coupling is not able to reduce the displacement of the frame because gain coefficients are higher or close to unity. The minimum values of the α_1 gain coefficient are located along the straight dotted lines, whereas the minimum values of the α_2 coefficient are along the dash-dotted straight lines. It is possible to observe that the minimum values of the α_1 coefficient do not depend on the seismic excitation. Several numerical simulations, carried out using many other earthquake records, have confirmed this assertion. Instead, the straight lines of minimum values of the α_2 coefficient change with the earthquake.
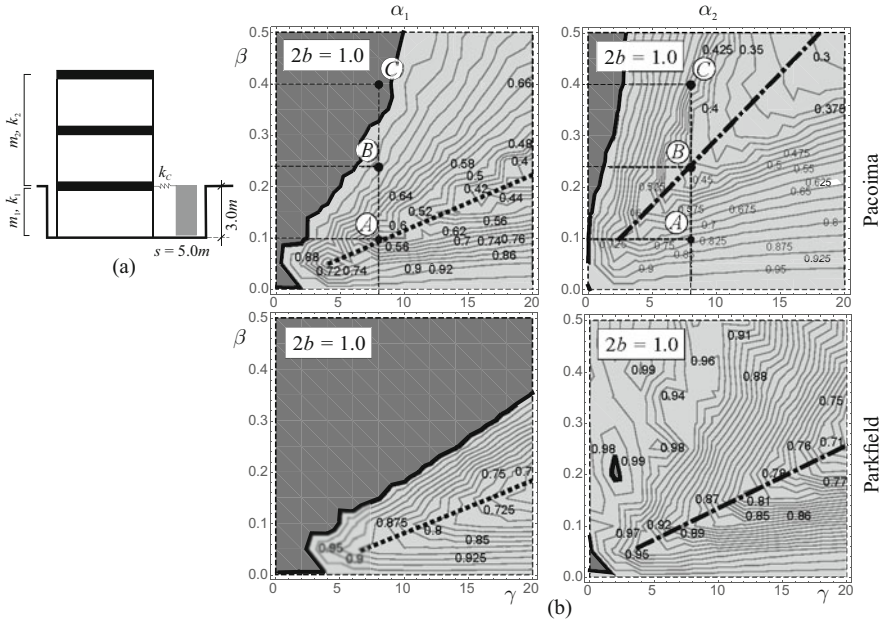
Fig. 2 Gain maps: (**a**) Geometrical coupling scheme; (**b**) Gain maps α_1 and α_2 for a fixed base dimension of the block $2b = 1.0$ m and two different earthquakes (Pacoima and Parkfield)

The effects of the coupling with an external rocking wall equipped with vertical inerters are investigated by means of the observation of some time histories. In particular, the parameters of the coupled system are indicated with the letters A, B, and C in Fig. 2b. The time histories of displacement u_1 and of rocking angle θ of a system whose proprieties are labelled with A, are shown in Fig. 3a. The point A ($\gamma = 8$, $\beta = 0.10$) lies on the dotted line and is inside the gain regions of both gain coefficients. The time histories of u_1 and θ (Fig. 3a) reveal that the block and the first storey of frame move in counter phase (see the signs convention of the Lagrangian parameters in Fig. 1b). Therefore, the rocking block behaves as a tuned mass damper with respect to the first storey of the frame and is able to reduce the displacements of the structure. Figure 3b shows the time histories of a coupled frame whose parameters are labelled with B. Point B ($\gamma = 8$, $\beta = 0.24$) lies on a dash-dotted line and is inside the gain regions of both maps. The examination of the graph of Fig. 3b) reveals that motion of block and first storey is slightly out of phase. Therefore, wall does not behave correctly as a tuned mass damper; nevertheless, it is still able to reduce the displacements. Lastly, point C ($\gamma = 8$, $\beta = 0.40$) is outside the gain region of the first gain coefficient (but is inside the gain region of the second gain coefficient). In fact, Fig. 3c displays that the block and the first storey are approximately in phase and an increase of the displacement of the first storey with respect to the stand-alone frame occurs.

The analyses are carried out also for a five-storey frame as shown in Fig. 4a (second rows of Tables 1 and 2), coupled with a block whose base is $2b = 1.5$ m.
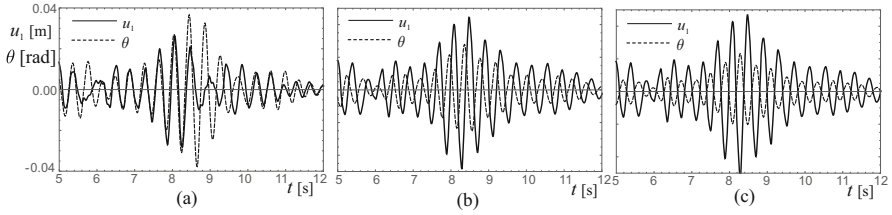
Fig. 3 Time histories under Pacoima earthquake: (**a**) Point A; (**b**) Point B; (**c**) Point C
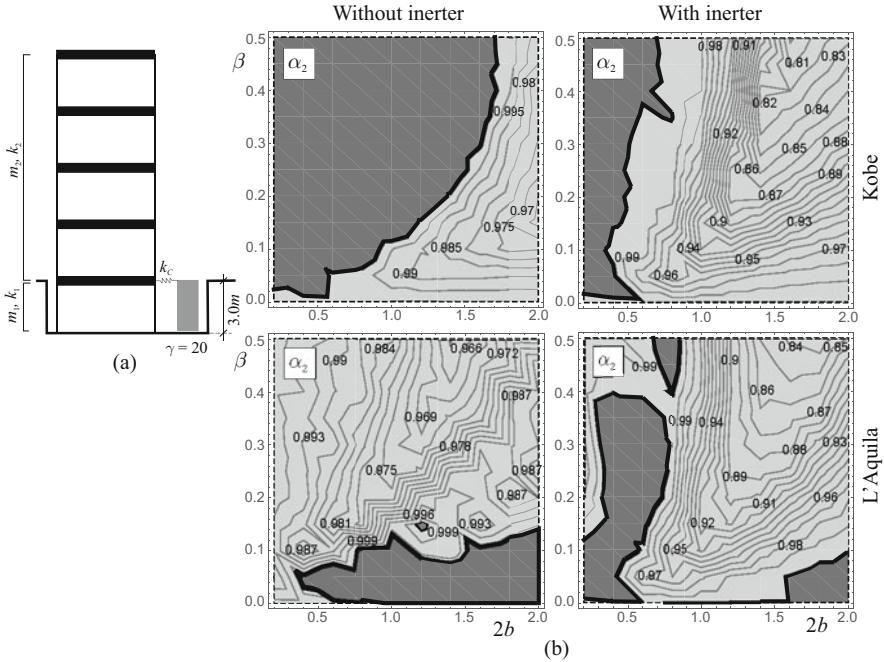
Fig. 4 Gain maps: (**a**) Geometrical coupling scheme; (**b**) Gain maps α_2 for Kobe and L'Aquila (left column $\gamma = 0$; right column $\gamma = 20$)

The α_1 and α_2 gain maps, built for two different earthquakes (Kobe and L'Aquila), are showed in Fig. 4b. The seismic records used in this analysis are different from those used in Fig. 2 to show that the proposed method works correctly with different seismic records. Differently from Fig. 2, the maps of Fig. 4b show the gain coefficient α_2 in the parameter plane $2b$-β. The maps on the left column refer to the coupling without inerters, whereas those on the right column consider a coupling with inerters, with apparent mass ratio $\gamma = 20$. The performance of the coupled system with rocking block grows up when the apparent inertial mass ratio γ increases; in fact, the gain regions may become larger and the value of the gain coefficients decreases.

As further consideration, the oscillation period of rigid blocks depends on the rocking amplitude because of their natural nonlinearity. When the block starts to move in counter-phase motion, it can keep moving in counter phase also if a change of characteristics of motion occurs in time by appropriately adapting the rocking amplitude. The block acts almost as a hysteretic mass damper [22], being able to work properly in wide ranges of frequencies.

5   Conclusions

In this chapter, the coupling between a 2-DOF system and an external rocking block was investigated with the aim to improve the behaviour of the coupled system under base excitations. An inerter device was introduced to add virtual mass to the system. The connection of the top of block to the first level of the of 2-DOF system is carried out by means of an elastic device. Under sufficient regularity of the multi-DOF frame structure, the main dynamical characteristics of such multi-DOF system can be represented by an equivalent 2-DOF model. The behaviour of coupled system was studied by numerically integrating the nonlinear equations of motion. The coupling with block and the use of inerters were considered effective for the structure when there is a reduction in the displacements and drifts of the coupled system with respect to the stand-alone frame. Many analyses were carried out considering four earthquakes records. The gain maps, which provide the ratio between maximum displacement (or the drift) of coupled and uncoupled system, were used to collect the results of an extensive parametric analysis.

The analysis showed that wide gain regions, where the coupling improves the dynamical behaviour of the coupled system with respect to the stand-alone frame, exist in the parameter plane. In these gain regions, the block behaves as a tuned mass damper for the frame system. The size of the gain regions strongly depend on the apparent inertial mass of the inerter devices. In fact, higher is the value of the apparent inertial mass, smaller can be the dimensions of the block to achieve the same reduction of the displacements.

References

1. E. Dimitrakopoulos, M. DeJong, Overturning of retrofitted rocking structures under pulse-type excitations. J. Eng. Mech. **138**, 963–972 (2012)
2. A. Contento, A. Di Egidio, On the use of base isolation for the protection of rigid bodies placed on a multi-storey frame under seismic excitation. Eng. Struct. **62–63**, 1–10 (2014)
3. M. Vassiliou, N. Makris, Analysis of the rocking response of rigid blocks standing free on a seismically isolated base. Earthq. Eng. Struct. Dyn. **41**(2), 177–196 (2012)
4. P. Brzeski, T. Kapitaniak, P. Perlikowski, The use of tuned mass absorber to prevent overturning of the rigid block during earthquake. Int. J. Struct. Stab. Dyn. **16**(10) (2016)

5. A. Di Egidio, R. Alaggio, A. Aloisio, A. de Leo, A. Contento, M. Tursini, Analytical and experimental investigation into the effectiveness of a pendulum dynamic absorber to protect rigid blocks from overturning. Int. J. Nonlin. Mech. **115**, 1–10 (2019)
6. G. Simoneschi, A. Geniola, A. de Leo, A. Di Egidio, On the seismic performances of rigid blocks coupled with an oscillating mass working as TMD. Earthq. Eng. Struct. Dyn. **46**, 1453–1469 (2017)
7. A. Di Egidio, A. de Leo, G. Simoneschi, Effectiveness of mass-damper dynamic absorber on rocking block under one-sine pulse ground motion. Int. J. Nonlin. Mech. https://doi.org/10.1016/j.ijnonlinmec.2017.10.015 (2016)
8. R. Ceravolo, M. Pecorelli, L.Z. Fragonara, Comparison of semi-active control strategies for rocking objects under pulse and harmonic excitations. Mech. Syst. Signal Proces. **90**, 175–188 (2017)
9. A. Di Egidio, C. Olivieri, A. de Leo, Protection from overturning of rigid block-like objects with linear quadratic regulator active control. Struct. Control. Health Monit. **27** (2020)
10. J. Bachmann, M. Vassiliou, B. Stojadinović, Dynamics of rocking podium structures. Earthq. Eng. Struct. Dyn. **46**(14), 2499–2517 (2017)
11. N. Makris, A half-century of rocking isolation. Earthq. Struct. **7**(6), 1187–1221 (2014)
12. N. Makris, M. Aghagholizadeh, The dynamics of an elastic structure coupled with a rocking wall. Earthq. Eng. Struct. Dyn. **46**, 945–954 (2017)
13. A. Di Egidio, S. Pagliaro, C. Fabrizio, A. de Leo, Seismic performance of frame structures coupled with an external rocking wall. Eng. Struct. **224**, 111207 (2020)
14. D. De Domenico, G. Ricciardi, An enhanced base isolation system equipped with optimal tuned mass damper inerter (TMDI). Earthquake Engineering and Struct. Dyn. **47**, 1169–1192 (2018)
15. M. De Angelis, A. Giaralis, F. Petrini, D. Pietrosanti, Optimal tuning and assessment of inertial dampers with grounded inerter for vibration control of seismically excited base-isolated systems. Eng. Struct. **196**, 109250 (2019)
16. M. Basili, M. De Angelis, D. Pietrosanti, Modal analysis and dynamic response of a two adjacent single degree of freedom systems linked by spring-dashpot-inerter elements. Eng. Struct. **174**, 736–752 (2018)
17. M. Basili, M. De Angelis, D. Pietrosanti, Defective two adjacent single degree of freedom systems linked by spring-dashpot-inerter for vibration control. Eng. Struct. **188**, 480–492 (2019)
18. R. Thiers-Moggia, C. Málaga-Chuquitaype, Seismic protection of rocking structures with inerters. Earthq. Eng. Struct. Dyn. **48**(5), 528–547 (2018)
19. C. Fabrizio, A. de Leo, A. Di Egidio, Tuned mass damper and base isolation: a unitary approach for the seismic protection of conventional frame structures. J. Eng. Mech. **145**(4) (2019). https://doi.org/10.1061/(ASCE)EM.1943--7889.0001581
20. A. Di Egidio, S. Pagliaro, C. Fabrizio, Combined use of rocking walls and inerters to improve the seismic response of frame structures. J. Eng. Mech. **147**(5) (2021). https://doi.org/10.1061/(ASCE)EM.1943--7889.0001920
21. G. Housner, The behaviour of inverted pendulum structures during earthquakes. Bull. Seismol. Soc. Am. **53**(2), 404–417 (1963)
22. N. Carpineto, W. Lacarbonara, F. Vestroni, Hysteretic tuned mass dampers for structural vibration mitigation. J. Sound Vib. **333**(5), 1302–1318 (2014)

Fuzzy Model Predictive Pitch Control of Flexible Wind Turbine Blade

Youssef Fahmy and Ayman El-Badawy

1 Introduction

Renewable systems in general and wind turbines (WTs) in particular have gained recently a high research interest. This is due to the natural problems the world is facing nowadays such as limited fossil fuels, climate changes, and the carbon dioxide emissions. Thereby, the worldwide wind energy capacity has reached about 600 GW with 53.9 GW at the end of 2018, with an annual installations of an average 50 GW each year since 2014 [1]. This growth rate gives a good motivation to put more effort into developing advanced and reliable control algorithms in order to enhance their performance.

The operation of the WT can be classified into 3 regions, depending on the wind speed, and the control objectives are different for each region. Region 1 is where the wind speed is less than the cut-in speed where the control objective is to accelerate the rotor for start-up, as for Region 2, defined between the cut-in and rated wind speeds where the control objective is to extract maximum available power. Region 3 is defined by wind speeds above the rated speed and below the cut-out speed. The control objectives are to regulate the generator speed and power to their rated values and to reduce the mechanical loads induced by the wind on the blades.

Significant challenges are being investigated throughout the research to guarantee the energy sustainability of WTs. One of the most complex challenges is the turbine model because of its highly nonlinear nature. The problem gets more complicated when the blades' deflections are taken into consideration in the model that makes the control algorithm very challenging. Furthermore, region 3 rotor over-speed scenario represents another major challenge regarding the pitch-regulated WTs.

Y. Fahmy · A. El-Badawy (✉)
German University in Cairo, Cairo, Egypt
e-mail: youssef.fahmi@guc.edu.eg; ayman.elbadawy@guc.edu.eg

49

Thus, it experiences the risk of flutter instability due to the interaction of the elastic vibrations and the unsteady aerodynamic forces on the blades[2]. Moreover, the design of recent WTs tends to increase in size and capacity to reduce the energy cost compared to the other energy resources [3]. However, lighter structures design is required in order to overcome the weight limitation issue. Accordingly, WT blades turn out to be longer and more flexible; this could result in large deformations under aerodynamic loading, even under nominal operating conditions due to the reduction of the blade torsional stiffness [4].

There is a broad literature that addresses the control of the WTs across its different operating regions. Also, it tackled a major challenge of the WTs regarding the flutter instability at rotor over-speed situations in region 3. Jonkman et al. developed a gain-scheduled PI controller based on a linearized one-mass drive-train model, since speed and power regulations are his main control objectives. The controller was investigated on the NREL reference 5MW WT [5]. Duong et al. carried out a comparative study between the conventional PI controller, fuzzy controller, and a hybrid fuzzy,PI based on linearized one-mass drive-train model. This chapter aimed to handle the different operating points due to varying wind speeds [6].

Several approaches used optimal control techniques, and the authors in [7, 8] demonstrated that using model predictive control (MPC) can lead to a better load mitigation and optimal power tracking than using a PI controller that is still widely used in the industry. MPC can avoid unnecessary shutdowns, due to over-speed limits, for its effective use of information about system constraints and predicted behavior. In [8], Soliman et al. implemented multiple MPC based on the NREL WT linearized model for drive train and generator degrees of freedom (DOFs) at different wind speeds. The main drawbacks for such a controller are the computational complexity and the sharp switching behavior. Lasheen et al. [9] proposed a collective pitch control using MPC with fuzzy logic rules, where the prediction model is based on FAST linearized model for drive train and generator DOFs, to regulate the power to its rated value in region 3. The MPC is coupled with individual PI pitch controllers, one for each blade, to reduce the moment acting on the blade. However, the flap-wise deflections were not considered in the prediction model. Also, the controller was not tested under flutter conditions. The authors in [10] approximated the model of the WT by a T–S fuzzy model and proposed parallel distributed compensation and fuzzy observe-based H_∞ controller to stabilize the generator speed. Their model did not include the flap-wise deflections of the blades. Moodi et al. introduced a T–S model of the WT while including the blade flap-wise and tower fore-aft deflections. However, they did not test their H_∞ controller under flutter conditions [11]. The authors in [12] developed a robust H_∞ controller based on a T–S fuzzy model for the WT's generator, to control a variable speed WT. In [13], the author used genetic algorithm to optimize the fuzzy controller designed to stabilize the WT power.

The nonlinear aspect of the WT's operating problems is handled by the implementation of nonlinear MPC (NMPC). A suitable reduced-order model for computational efficiency should therefore be developed to capture enough degrees

of freedom that are of interest to the control objectives. The authors in [14] implemented an NMPC with a reduced nonlinear model that represents a one-mass drive train together with the first tower fore-aft bending mode. Their approach was motivated by the objectives of the controller, which were to regulate the generated power, generator speed, and reduction of the tower mechanical loads. Flutter is a particularly important aspect for pitch-regulated HAWTs [15]. Lobitz in [16] has shown that flutter can occur in rotor over-speed situations where tip speeds are high enough for aerodynamic forces to have sufficient energy. This instability occurs because the angle of attack changes due to torsion deflection that changes the lift force in an unfortunate condition with flap-wise bending. The authors in [17, 18] present an aero-elastic model that governs the extensional, chordwise, flap-wise, and torsional vibrations of an isolated HAWT blade in addition to investigation of the blade's flutter stability limit that was carried out. El-Baklish et al. [19] implemented an NMPC algorithm based on an aero-elastic rotor nonlinear prediction model for regulating the WT performance, alleviating mechanical loads on the blades, and avoiding flutter instability.

This chapter presents a collective pitch control using fuzzy-based MPC algorithm capable of regulating the WT performance and reducing blades flap-wise deflections through feedback while operating in region 3. The proposed prediction model takes into consideration the generator, drive train, and flap-wise deflections of the blades. In order to demonstrate the effectiveness of including the flap-wise deflections in the prediction model, the proposed controller was compared to the GSPI controller under steady wind, turbulent wind, and conditions inducing flutter instability.

2 T–S Fuzzy Wind Turbine Model

The WT system is highly nonlinear, and it is difficult to develop a perfect mathematical model that can effectively capture all its dynamics and more difficult to design a controller based on the nonlinear model that would have low computational time. In this chapter, linear models for the wind turbine are used to develop the T–S fuzzy model to combine the advantage of low computational time of linear controllers and a wide range of operations of nonlinear controllers.

FAST (Fatigue, Aero-dynamics, Structure, and Turbulence) is used to model and simulate a 5 MW Horizontal Axis 3-bladed WT [20]. Linearized models of the WT were extracted through FAST linearization capabilities for wind speed range from 12 m/s to 24 m/s with a step of 1 m/s. The linearized model that FAST provides around specific operating point is in the form of state-space representation as stated in Eq. (1). The operating point was specified by the main variables that are: generator speed, azimuth angle of the rotor, the hub height wind speed, and the steady-state pitch angle [20].

$$\Delta \underline{\dot{x}} = A \Delta \underline{x} + B \Delta \underline{u}_{cpc}, \tag{1}$$

where $\Delta \underline{u}_{cpc}$ is the perturbation in the collective pitch control input. $\Delta \underline{x}$ describes the perturbation in the system states. Since the blades are controlled collectively, the model that undergoes the control investigation is presenting one blade rather than three blades to decrease the computational time. The perturbation in system states vector is expressed as

$$\Delta \underline{x} = \begin{bmatrix} \theta_{gen} & \theta_{DrTr} & w_{b1} & \dot{\theta}_{gen} & \dot{\theta}_{DrTr} & \dot{w}_{b1} \end{bmatrix}^T, \tag{2}$$

where $\theta_{gen}, \dot{\theta}_{gen}$ are the angular displacement and angular velocity of generator, respectively. θ_{DrTr} and $\dot{\theta}_{DrTr}$ represent the angular displacement and angular velocity of drive-train rotational flexibility, respectively. w_{b1} and $\dot{w}_{b1}$ are the displacement and velocity of flap-wise bending mode of blade 1, respectively.

$$\Delta \underline{\dot{x}} = \begin{bmatrix} 0 & 0 & 0 & 1 & 0 & 0 \\ 0 & 0 & 0 & 0 & 1 & 0 \\ 0 & 0 & 0 & 0 & 0 & 1 \\ 0 & 172.6 & 0 & 0 & 1.23 & 0 \\ 0.004 & -195.4 & 0.011 & -0.083 & -1.48 & 0.0002 \\ 3.19 & 525.1 & -21.85 & 27.59 & 31.33 & -5.71 \end{bmatrix} \begin{bmatrix} \theta_{gen} \\ \theta_{DrTr} \\ w_{b1} \\ \dot{\theta}_{gen} \\ \dot{\theta}_{DrTr} \\ \dot{w}_{b1} \end{bmatrix} + \begin{bmatrix} 0 \\ 0 \\ 0 \\ 0 \\ -0.14 \\ -519.4 \end{bmatrix} \Delta \underline{u}_{cpc}. \tag{3}$$

The T–S fuzzy model was developed to represent the WT model considering the wind speed variation in region 3. This was achieved by blending of linear system models. First, the gap metric approach was applied to select the minimum number of models that are capable of representing the dynamics of the WT in region 3 using Eq. (4) [21].

$$\delta \left(G_i, G_j \right) = \left\| \frac{\left(G_i - G_j \right)}{\sqrt{1 + G_i \bar{G}_i} \sqrt{1 + G_j \bar{G}_j}} \right\|_\infty, \tag{4}$$

where G_i and G_j are the transfer functions of the models obtained at the wind speeds i m/s and j m/s, respectively. $\bar{G}_i$ and $\bar{G}_j$ are their conjugates. The models were approximated according to a prescribed level of gap metric measure δ between two models, and the measure δ decides either they can be sufficiently represented in one model or not.

The results of the gap metric approach are shown in Table 1. The entries of the table represent the gap metric measure $\delta \left(G_i, G_j \right)$ between two transfer functions (G_i, G_j). The results are obtained ranging between zero and one. The closer the value to the zero the better in terms of model dynamics equality.

Table 1 Gap metric approach results on the wind turbine linearized models

	G12	G13	G14	G15	G16	G17	G18	G19	G20	G21	G22	G23	G24
G12	0	0.162	0.261	0.345	0.411	0.470	0.530	0.578	0.610	0.646	0.677	0.712	0.746
G13	0.162	0	0.102	0.188	0.259	0.332	0.402	0.454	0.490	0.529	0.564	0.603	0.642
G14	0.261	0.102	0	0.087	0.160	0.239	0.313	0.367	0.404	0.445	0.482	0.524	0.566
G15	0.345	0.188	0.087	0	0.074	0.155	0.230	0.286	0.324	0.367	0.405	0.449	0.493
G16	0.411	0.259	0.160	0.074	0	0.082	0.157	0.214	0.253	0.297	0.336	0.382	0.427
G17	0.470	0.332	0.239	0.155	0.082	0	0.076	0.133	0.173	0.217	0.258	0.305	0.352
G18	0.530	0.402	0.313	0.230	0.157	0.076	0	0.057	0.097	0.142	0.184	0.231	0.279
G19	0.578	0.454	0.367	0.286	0.214	0.133	0.057	0	0.045	0.085	0.127	0.175	0.224
G20	0.610	0.490	0.404	0.324	0.253	0.173	0.097	0.045	0	0.045	0.087	0.135	0.184
G21	0.646	0.529	0.445	0.367	0.297	0.217	0.142	0.085	0.045	0	0.041	0.090	0.139
G22	0.677	0.564	0.482	0.405	0.336	0.258	0.184	0.127	0.087	0.041	0	0.048	0.098
G23	0.712	0.603	0.524	0.449	0.382	0.305	0.231	0.175	0.135	0.090	0.048	0	0.049
G24	0.746	0.642	0.566	0.493	0.427	0.352	0.279	0.224	0.184	0.139	0.098	0.049	0

Based on the gap metric approach results, three models that correspond to wind speeds 12 m/s, 16 m/s, and 20 m/s have been chosen to represent the dynamics of the WT covering the operating region. These three models were selected to balance between the overall T–S fuzzy model simplicity and the computational efficiency. The T–S fuzzy WT model is represented as a weighted sum of the linearized models as shown in the linear parameter-varying (LPV) representation in Eq. (5).

$$x(k+1) = \sum_{j=1}^{n} Q_j(k) \left\{ A_{dj} x(k) + B_{dj} u_{cpc}(k) \right\}$$

$$y(k) = \sum_{j=1}^{n} Q_j(k) \left\{ C_{dj} x(k) \right\},$$

(5)

where $Q_j(k)$ is the membership function value at a certain sample time, and n is the number of fuzzy rules. The matrices A_{dj}, B_{dj}, and C_{dj} are the system dynamics matrices having constant coefficients. x and u_{cpc} represent the vectors of the system states and the control input, respectively. y represents the output vector states.

There are three fuzzy rules corresponding to each of the mentioned models. When a measurement of the wind speed is received, the fuzzy rules are fired calculating the rules' strength, which are obtained by direct substitution of the measured wind speed into the membership functions (6, 7, 8). The resulting rule strength is a weight between 0 and 1 as shown in Fig. 1. The output of each rule is the product of the rule strength and the rule consequent, which is the linearized model. Finally, the outputs of the rules are aggregated to form the fuzzified model (5).
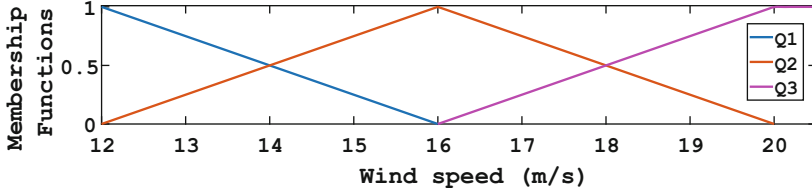
Fig. 1 Fuzzy membership functions

$$Q1(W_i) = \frac{W_{max} - W_i}{W_{max} - W_{min}}; \; 12 \le W_i \le 16 \tag{6}$$

$$Q2(W_i) = \begin{cases} \frac{W_i - W_{min}}{W_{max} - W_{min}} & ; \; 12 \le W_i \le 16 \\ \frac{W_{max} - W_i}{W_{max} - W_{min}} & ; \; 16 \le W_i \le 20 \end{cases} \tag{7}$$

$$Q3(W_i) = \frac{W_i - W_{min}}{W_{max} - W_{min}}; \; 16 \le W_i \le 20. \tag{8}$$

As a verification for the T–S fuzzy model, the linear model, extracted from FAST at wind speed 14 m/s, G_{14} was compared to the fuzzified model $\hat{G}_{14}$ using the gap metric approach $\delta(G_{14}, \hat{G}_{14}) = 0.044$, which shows a good agreement with the system dynamics at that wind speed.

3 Control Approach

Model predictive control (MPC) is used in this chapter as it tackles the multivariable control problem with the ability of working with constraints and due to its predicted behavior. MPC is a model-based optimal control method that utilizes the system's model to predict the future response of the plant. The goal of the optimal control problem (OCP) is to find the vector of manipulated inputs, $[\Delta u^*(k) \; \Delta u^*(k + 1) \ldots \Delta u^*(k + N - 1)]$, which is obtained by optimizing the objective function in (9) over prediction horizon N based on the Karush–Kuhn–Tucker (KKT) optimality conditions. Only the first control input of the optimal sequence is used according to the receding horizon policy. The obtained control input is added to the nominal pitch angle and applied to the system as illustrated in Fig. 2.

The T–S fuzzy model developed in (5) is used as the prediction model for the MPC algorithm. At every sample step, the model is obtained and then simulated for targeting the optimal control input to achieve the desired behavior by solving the OCP in Eq. (9). In addition, pitching the blades is subjected to magnitude and rate constraints [5], by which the collective pitch angle must not exceed 90 deg and must not be below 0 deg and its rate of change must not exceed 8 deg/sec. Therefore, the
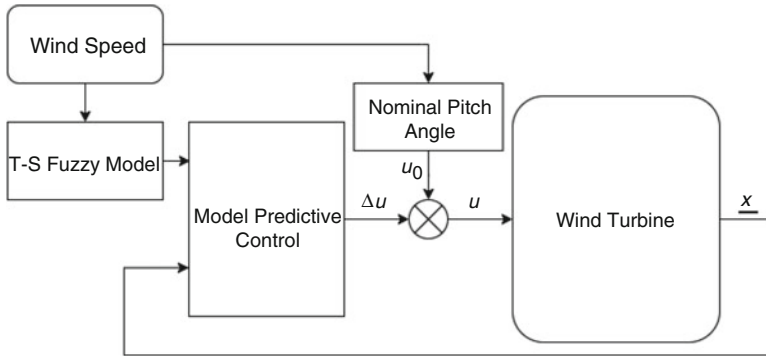
Fig. 2 Pitch control diagram

OCP is formulated as

$$\Delta \underline{U}^* = \min_{\Delta \underline{x}, \Delta u} \Delta \underline{x} \left(T_p\right)^T \boldsymbol{P} \Delta \underline{x} \left(T_p\right) + \int_0^{T_p} \Delta \underline{x}(t)^T \boldsymbol{Q} \Delta \underline{x}(t) + \Delta u(t)^T \boldsymbol{R} \Delta u(t) \, dt \tag{9}$$

$$\text{s.t.} \Delta \underline{\dot{x}} = A \Delta \underline{x} + B \Delta u, \quad \Delta \underline{x}(0) = \Delta \underline{x}(t), \quad -u_0 \le \Delta u \le \frac{\pi}{2} - u_0, \quad \frac{-8\pi}{180} \le \Delta \dot{u} \le \frac{8\pi}{180}, \tag{10}$$

where T_p is the time horizon, $\Delta \underline{x}(t)$ is the vector of perturbation in the system states, $\Delta u(t)$ is the perturbation in the input to the system, $\Delta \dot{u}(t)$ is the rate of change of the perturbation in the input, u_0 is the nominal blade pitch, $\boldsymbol{Q}$ is the weight function of the stage cost penalizing the perturbation in system states, $\boldsymbol{R}$ is the weight function of the stage cost penalizing the control effort, and $\boldsymbol{P}$ is the weight function of the terminal cost that is calculated by solving the Riccati equation.

The OCP is then converted by the direct multiple shooting method into a nonlinear program and solved by the ACADO toolkit, which is an open-source software framework for automatic control and dynamic optimization [22].

4   Simulation Results

The wind turbine nonlinear model was simulated on MATLAB/SIMULINK with all the turbine DOFs enabled, with ElastoDyn for structural dynamics and BeamDyn for the blades structural model. The FMPC algorithm was investigated on the WT model and then compared to FAST baseline GSPI controller [5], on three test cases: steady and uniform wind, turbulent wind, and conditions that induce flutter.

A steady wind speed of 15 m/s was applied with an initial rotor speed of 12.1 rpm. Then, the wind speed stepped up to 17 m/s. The two controllers managed to
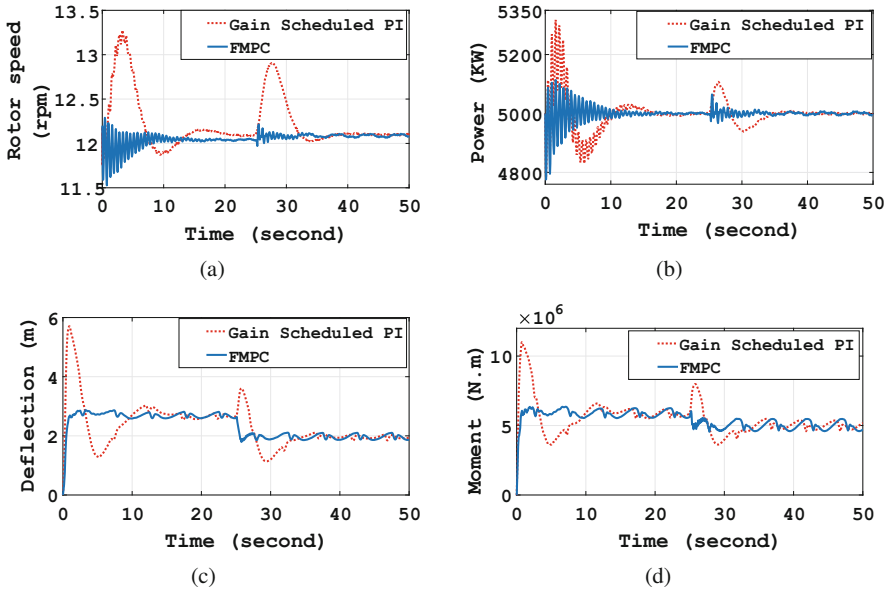
Fig. 3 Wind turbine response using both the FMPC and baseline GSPI controller under steady wind profile. (**a**) Rotor speed response. (**b**) Power response. (**c**) Blade flap-wise deflection response. (**d**) Blade flap-wise moment response

Fig. 4 Flap-wise deflection response under two controllers with different prediction models
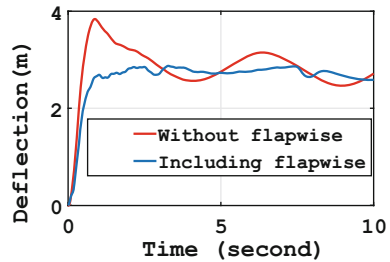
regulate the generator speed and power to their rated values 1173.1 rpm and 5 MW, respectively, and the flap-wise deflection and moment to remain bounded as shown in Fig. 3. The proposed FMPC showed better response in terms of less overshoot and settling time due to the utilization of the T–S fuzzy model as prediction, in contrast with the baseline controller, which showed higher overshoot and settling time at the beginning of the simulation and after stepping up the wind speed as well.

For further investigation, a model excluding the flap-wise flexibility DOF was used as prediction for the MPC and compared to the prediction model proposed that includes the flap-wise deflections. Both controllers were simulated at wind speed 15 m/s, and the result is shown in Fig. 4.
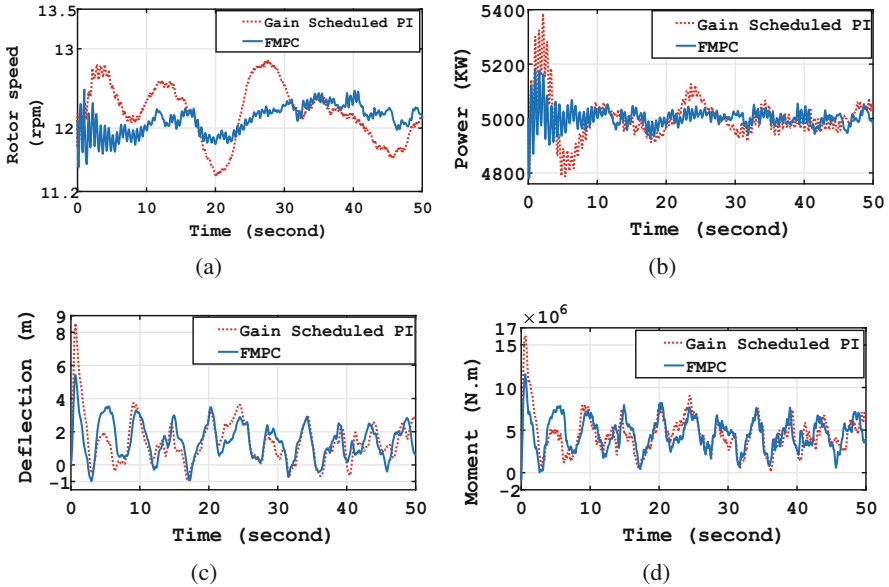
Fig. 5 Wind turbine response using both the FMPC and the baseline GSPI controller under turbulent Von Karman wind profile. (**a**) Rotor speed response. (**b**) Power response. (**c**) Blade flap-wise deflection response. (**d**) Blade flap-wise moment response

Additionally, a von Karman turbulent wind profile with a mean speed of 18 m/s is generated using TurbSim software [23] and applied to the WT. The two controllers were capable of regulating the WT performance as shown in Fig. 5. However, the proposed FMPC showed better performance with less deviations from the WT rated values. The simulations data for the first two cases were analyzed and summarized in Table 2.

The proposed FMPC was tested on the WT using the ElastoDyn module for the blades structural model and the turbulent wind profile used in [9]. The comparison results showed that the standard deviation of the flap-wise moment improved by 13.1% due to the inclusion of the flap-wise deflections in the objective function of the MPC, with the advantage of using one controller that governs the drive train, generator, and flap-wise deflections of the blades.

Finally, the WT model was simulated under conditions inducing flutter instability, with a constant wind speed of 24 m/s and a rotor over-speed of 14 rpm, adopted from the case study on the NREL 5MW WT in [2]. The results are shown in Figs. 6 and 7.

In which, the baseline GSPI controller failed to handle the instability after approximately 0.07 s as shown in Fig. 6, where the torsional deflection is increased to 4 of the Wiener–Milenkovic-dimensional rotation parameter corresponding to 120 degrees, which is structurally unstable and features flutter, while the FMPC in Fig. 7 succeeded in suppressing flutter due to the utilization of the proposed

Table 2 Result summary of the FMPC and the baseline GSPI controller under steady and turbulent wind profiles

Parameter	Performance measure	Steady wind			Turbulent wind		
		GSPI	FMPC	Improvement	GSPI	FMPC	Improvement
Rotor speed (rpm)	Max abs (error)	1.175	0.573	51.2%	0.755	0.599	20.7%
	Sum of squared error	0.0015	0.0004	73.3%	0.0017	0.0008	52.94%
Power (KW)	Max abs (error)	317.53	223.84	29.5%	386.14	219.48	43.16%
	Sum of squared error	0.264	0.121	54.1%	0.339	0.155	54.3%
Flap-wise deflection (m)	Max. overshoot	5.70	2.87	49.6%	8.53	5.14	39.7%
Flap-wise moment (KN.m)	Max. overshoot	10997	6353	42.2%	16038	11563	27.9%

(a)   (b)

Fig. 6 Wind turbine response using baseline GSPI controller under risk of flutter conditions. (**a**) Rotor speed response. (**b**) Blade tip torsional deflection response

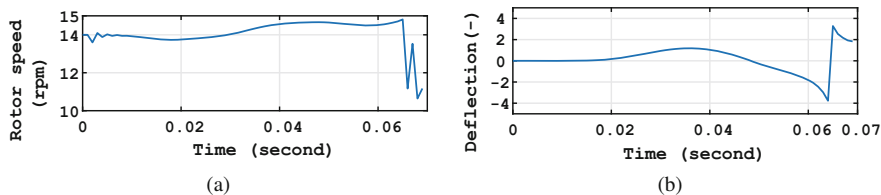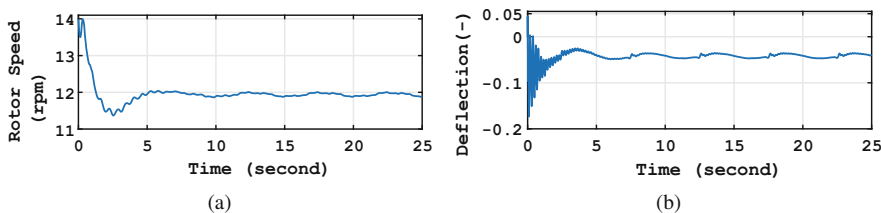(a)   (b)

Fig. 7 Wind turbine response using the fuzzy MPC under risk of flutter conditions. (**a**) Rotor speed response. (**b**) Blade tip torsional deflection response

prediction model. The computational time of the controller was 0.5 ms, which is less than the sample time of the system; therefore, the controller is applicable for practical implementation.

5 Conclusions

In conclusion, the FMPC algorithm was able to utilize the T–S fuzzy model to have a good approximation of the nonlinear wind turbine model and showed promising performance compared to the baseline GSPI controller, for regulating the turbine performance and suppressing flutter instability. Moreover, including the flap-wise deflections in the prediction model of the MPC showed improvements in reducing mechanical loads compared to [9]. The proposed control algorithm has a low computational time that could be implemented on embedded hardware.

References

1. Global Wind Energy Council. Global wind statistics report. Brussels, Technical Report, 4 (2018)
2. M.H. Hansen, Aeroelastic instability problems for wind turbines. Wind Energy An Int. J. Prog. Appl. Wind Power Conver. Technol. **10**(6), 551–577 (2007)
3. N. Fichaux, J. Beurskens, P.H. Jensen, J. Wilkes, S. Frandsen, J. Sorensen, P. Eecen, Upwind: Design limits and solutions for very large wind turbines, in Sixth Framework Programme (2011)
4. M.M. Rezaei, M. Behzad, H. Haddadpour, H. Moradi, Aeroelastic analysis of a rotating wind turbine blade using a geometrically exact formulation. Nonlin. Dyn. **89**(4), 2367–2392 (2017)
5. J. Jonkman, S. Butterfield, W. Musial, G. Scott, Definition of a 5-MW reference wind turbine for offshore system development (No. NREL/TP-500-38060). National Renewable Energy Lab. (NREL), Golden (2009)
6. M.Q. Duong, F. Grimaccia, S. Leva, M. Mussetta, E. Ogliari, Pitch angle control using hybrid controller for all operating regions of SCIG wind turbine system. Renew. Energy **70**, 197–203 (2014)
7. A. Korber, R. King, Model predictive control for wind turbines, in *European Wind Energy Conference* (2010)
8. M. Soliman, O.P. Malik, D.T. Westwick, Multiple model MIMO predictive control for variable speed variable pitch wind turbines, in *Proceedings of the 2010 American Control Conference* (IEEE, Piscataway, 2010), pp. 2778–2784
9. A. Lasheen, A.L. Elshafei, Wind-turbine collective-pitch control via a fuzzy predictive algorithm. Renew. Energy **87**, 298–306 (2016)
10. N. Hamrouni, S. Younsi, Modeling and fuzzy command approach to stabilize the wind generator. Int. J. Elect. Eng. Inf. **10**(4), 648–660 (2018)
11. H. Moodi, D. Bustan, Wind turbine control using TS systems with nonlinear consequent parts. Energy **172**, 922–931 (2019)
12. A.V. Hemeyine, A. Abbou, N. Tidjani, M. Mokhlis, A. Bakouri, Robust takagi sugeno fuzzy models control for a variable speed wind turbine based a DFI-generator. Int. J. Intell. Eng. Syst. **13**(3), 90–100 (2020)
13. Z. Civelek, Optimization of fuzzy logic (Takagi-Sugeno) blade pitch angle controller in wind turbines by genetic algorithm. Eng. Sci. Technol. Int. J. **23**(1), 1–9 (2020)
14. S. Gros, A. Schild, Real-time economic nonlinear model predictive control for wind turbine control. Int. J. Control **90**(12), 2799–2812 (2017)
15. G. Bir, J. Jonkman, Aeroelastic instabilities of large offshore and onshore wind turbines, in *Journal of Physics: Conference Series*, vol. 75, No. 1 (IOP Publishing, Bristol, 2007), p. 012069

16. D.W. Lobitz, Parameter sensitivities affecting the flutter speed of a MW-sized blade. J. Sol. Energy Eng. **127**, 538–543 (2005)
17. M.M. Abdel Hafeez, A.A. El-Badawy, Effect of mass and shear center offset on the dynamic response of a rotating blade. J. Vib. Control **23**(14), 2235–2255 (2017)
18. M.M. Abdel Hafeez, A.A. El-Badawy, Flutter limit investigation for a horizontal axis wind turbine blade. J. Vib. Acoust. **140**(4) (2018)
19. S.K. El-Baklish, A.A. El-Badawy, G. Frison, M. Diehl, Nonlinear model predictive pitch control of aero-elastic wind turbine blades. Renew. Energy **161**, 777–791 (2020)
20. J. Jonkman, The new modularization framework for the FAST wind turbine CAE tool, in *51st AIAA Aerospace Sciences Meeting Including the New Horizons Forum and Aerospace Exposition* (2013), p. 202
21. G. Vinnicombe, Frequency domain uncertainty and the graph topology. IEEE Trans. Auto. Control **38**(9), 1371–1383 (1993)
22. B. Houska, H.J. Ferreau, M. Diehl, ACADO toolkit—An open-source framework for automatic control and dynamic optimization. Optimal Control Appl. Methods **32**(3), 298–312 (2011)
23. N.D. Kelley, B.J. Jonkman, Overview of the TurbSim stochastic inflow turbulence simulator (No. NREL/TP-500-36971). National Renewable Energy Lab. (NREL), Golden (2005)

Nonlinear Flutter Suppression of Composite Panels with Nonlinear Energy Sinks

Myrella V. Cabral, Flávio D. Marques, and António J. M. Ferreira

1 Introduction

Aerospace structures subjected to supersonic flow can undergo aeroelastic instability, such as panel flutter. These vibrations imposed on aerospace skin make it susceptible to fatigue failure. Thus, various techniques have been designed to passively or actively manage this undesired phenomenon. Passive methods do not need additional energy and sensors to function, being more stable and simple to design. In this context, the NES has been receiving growing attention due to its simplicity and ability to extract energy from the system [1]. NES is an oscillator connected to a structure to extract and dissipate the energy input by external loads. A nonlinear spring prevents the energy transferred to the NES from returning to the primary structure, and a linear damper dissipates such energy. Zhang Y et al. [2] analyzed a 4-layered cross-ply composite plate with a nonlinear energy sink. They concluded that this technique can effectively suppress the plate's excessive vibration in a short time. However, their study comprises only pre-flutter conditions, leaving aside the flutter suppression and the NES's capability to reduce limit cycle oscillation (LCOs) amplitudes. Pacheco et al. [3] analyzed the pre- and post-flutter conditions of isotropic plates and provided an energy pumping quantification. He showed that even a non-optimized NES manages to suppress flutter for an extent of flow velocities and significantly diminish the LCO amplitudes of isotropic plates subjected to higher flow velocities.

M. V. Cabral (✉) · F. D. Marques
São Carlos School of Engineering, University of São Paulo, São Carlos, SP, Brazil
e-mail: myrella@usp.br; fmarques@sc.usp.br
https://eesc.usp.br/en/

A. J. M. Ferreira
Faculty of Engineering, University of Porto, Porto, Portugal
e-mail: ferreira@gcloud.fe.up.pt

This chapter investigates the use of NES for suppressing flutter of composite laminated plates under supersonic flow regimes. The main goal is to assess the NES's effectiveness for angle-ply laminates, which is not available in the current literature. The Mindlin theory is coupled with von Kármán's nonlinear strain–displacements to form the structural panel model. The NES is attached to a certain point of the panel, including a small mass, a linear damper, and a purely cubic spring. The first-order piston theory is applied to model the supersonic aerodynamic loads. The iterative Newmark method solves the second-order nonlinear equation system that results from the aeroelastic model discretized with the finite-element method. The numerical study comprises motion analysis and mechanical energy quantification to assess the NES's capability to passively control panel flutter. Pre- and post-flutter conditions are analyzed for different angle-ply laminates, and a parametric study is presented.

2   Aeroelastic Model

The structural model is described by the Mindlin theory combined with the von Kármán's nonlinear strain–displacement relations, which can be written as Pica et al. [4]

$$
\varepsilon = \begin{Bmatrix} \varepsilon_x \\ \varepsilon_y \\ \gamma_{xy} \\ \gamma_{xz} \\ \gamma_{yz} \end{Bmatrix} = \begin{Bmatrix} \frac{\partial \hat{u}}{\partial x} \\ \frac{\partial \hat{v}}{\partial y} \\ \frac{\partial \hat{u}}{\partial y} + \frac{\partial \hat{v}}{\partial x} \\ \frac{\partial \hat{w}}{\partial x} - \phi_x \\ \frac{\partial \hat{w}}{\partial y} - \phi_y \end{Bmatrix} + z \begin{Bmatrix} -\frac{\partial \phi_x}{\partial x} \\ -\frac{\partial \phi_y}{\partial y} \\ -\frac{\partial \phi_x}{\partial y} - \frac{\partial \phi_y}{\partial x} \\ 0 \\ 0 \end{Bmatrix} + \begin{Bmatrix} \frac{1}{2}(\frac{\partial \hat{w}}{\partial x})^2 \\ \frac{1}{2}(\frac{\partial \hat{w}}{\partial y})^2 \\ \frac{\partial \hat{w}}{\partial x} \frac{\partial \hat{w}}{\partial y} \\ 0 \\ 0 \end{Bmatrix}, \tag{1}
$$

in which $\hat{w}$, $\hat{u}$, $\hat{v}$ are the translational midsurface degrees of freedom; and ϕ_x and ϕ_y are the rotation DOFs with respect to y and x directions, respectively [4]. To derive the equations of motion, the principle of virtual work (PVW) is employed:

$$
\delta W_{int} - \delta W_{ext} = 0. \tag{2}
$$

The virtual work done by internal forces due to a virtual strain $\delta \epsilon$ over the entire structural volume can be written as

$$
\delta W_{int} = \int_V \sigma^T \delta \epsilon \, dV = \int_V \delta \epsilon^T \sigma \, dV = \int_V \delta \epsilon^T \bar{Q} \epsilon \, dV, \tag{3}
$$

where σ is the stress vector and $\bar{Q}$ is the plane-stress constitutive matrix with respect to the (x, y, z) system adopted, as in Reddy [5].

The aerodynamic pressure to which the panel is subjected during flight operations will be obtained by the first-order piston theory. Recently, Alder [6] and

Vedeneev [7] proved, through comparisons between theory and high-fidelity models, that the piston theory produces results with good precision for the panel flutter for Mach> 1.7. The formulation of the piston theory applied to panel flutter can also be found in Pacheco et al. [3].

The virtual external work is composed by a term from the pressure field due to the aerodynamic loads and another term derived from the inertial forces:

$$\delta W_{ext} = \int_A \delta\hat{w}\,\Delta p\ \mathrm{dA} - \int_A \rho\left[h\left(\delta\hat{u}\frac{\partial^2\hat{u}}{\partial t^2} + \delta\hat{v}\frac{\partial^2\hat{v}}{\partial t^2} + \delta\hat{w}\frac{\partial^2\hat{w}}{\partial t^2}\right)\right.$$
$$\left. + \frac{h^3}{12}\left(\delta\phi_x\frac{\partial^2\phi_x}{\partial t^2} + \delta\phi_y\frac{\partial^2\phi_y}{\partial t^2}\right)\right]\ \mathrm{dA}, \tag{4}$$

in which ρ and h are the panel's density and thickness, respectively. The PVW is applied to combine the aerodynamic and structural models. The four-node Lagrangian finite element was used to discretize the domain. If all the elemental participations were put together, the PVW allows [3]

$$\delta\mathbf{U}^T\left([M]\ddot{\mathbf{U}} + g_a[C_a]\dot{\mathbf{U}} + (\lambda[K_a] + [K_0] + [K_1] + [K_2])\mathbf{U}\right) = 0, \tag{5}$$

in which $\ddot{\mathbf{U}}$ and $\dot{\mathbf{U}}$ are the derivatives of the total DOF vector, $\mathbf{U}$; $[M]$ is the mass matrix; $[K_0]$, $[K_1]$, and $[K_2]$ are the structural stiffness of zero, first, and second order, respectively. $\lambda[K_a]$ and $g_a[C_a]$ are the aerodynamic stiffness and damping matrices, where

$$\lambda = \frac{2qL^3}{D\sqrt{M^2 - 1}}, \tag{6}$$

$$D = \frac{E_1 h^3}{12\left(1 - \frac{E_1}{E_2}\nu_{12}\right)}, \tag{7}$$

and

$$g_a = \sqrt{\frac{\lambda\mu}{\sqrt{M^2 - 1}}}\left(\frac{M^2 - 2}{M^2 - 1}\right) \simeq \sqrt{\frac{\mu\lambda}{M}}, \tag{8}$$

in which $\mu = \frac{L\rho_\infty}{h\rho}$.

The NES is designed as a small mass, a purely cubic spring, and a linear damping attached to a certain point (x_q, y_q) in the panel midplane, Fig. 1. Since the mass, m, can move, it is necessary to introduce one new displacement, q, as the $(N + 1)$-th DOF to the plate model to obtain the final coupled model. Thereby, the instantaneous force imposed by the NES to the panel is [3]
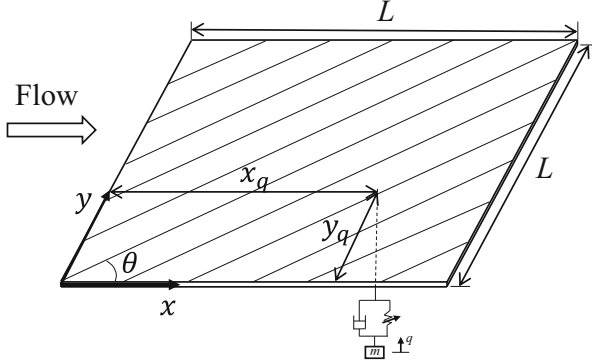
Fig. 1 Illustration of a composite panel with a NES

$$F = c(\dot{q} - \dot{w}_q) + k(q - w_q)^3, \tag{9}$$

where c and k are the damping and stiffness constants, and w_q is the plate's transverse displacement at (x_q, y_q). Therefore, the virtual work δW done by the NES upon the plate is

$$\delta W = F \delta w_q = \delta w_q [c(\dot{q} - \dot{w}_q) + k(q - w_q)^3], \tag{10}$$

in which w_q is defined as the n-th DOF in $\mathbf{U}$, then Eq. (5) should be extended to add the virtual work done by the NES. A new vector of DOFs was defined, in which the last value corresponds to the NES vertical displacement, q. The stiffness and damping matrix due to the NES, $[C_q]$, and $[K_q]$, were also defined as

$$\bar{\mathbf{U}} = \begin{Bmatrix} \mathbf{U} \\ q \end{Bmatrix}, \quad [C_q] = c[T], \quad [K_q] = k(q - w_q)^2[T], \tag{11}$$

in which $[T]$ is a $(N+1) \times (N+1)$ matrix defined as

$$T_{ij} = \begin{cases} 1, & \text{if } (i, j) = (n, n); \\ -1, & \text{if } (i, j) = (n, N+1); \\ 0, & \text{otherwise.} \end{cases} \tag{12}$$

Therefore, Eq. (5) is rewritten including the NES as

$$\delta \bar{\mathbf{U}}^T \left\{ \begin{bmatrix} [M] & 0 \\ 0 & \dots & 0 \end{bmatrix} \ddot{\bar{\mathbf{U}}} + \left(\begin{bmatrix} g_a[C_a] & 0 \\ 0 & \dots & 0 \end{bmatrix} + [C_q] \right) \dot{\bar{\mathbf{U}}} + \left(\begin{bmatrix} [\mathbf{K}] & 0 \\ 0 & \dots & 0 \end{bmatrix} + [K_q] \right) \bar{\mathbf{U}} \right\} = 0, \tag{13}$$

in which $[\mathbf{K}]$ is the sum of the plate stiffness matrices and aerodynamic matrix. Based on the PVW, Eq. (13) maintains its validity for any compatible $\delta\bar{\mathbf{U}}$. Consequently, the aeroelastic equations of motion of a plate coupled with a NES are

$$\begin{bmatrix} [M] & 0 \\ 0 \dots & 0 \end{bmatrix} \ddot{\bar{\mathbf{U}}} + \left(\begin{bmatrix} g_a[C_a] & 0 \\ 0 \dots & 0 \end{bmatrix} + [C_q] \right) \dot{\bar{\mathbf{U}}} + \left(\begin{bmatrix} [\mathbf{K}] & 0 \\ 0 \dots & 0 \end{bmatrix} + [K_q] \right) \bar{\mathbf{U}} = 0. \quad (14)$$

The equation of motion of the NES can be expressed as

$$m\ddot{q} + c(\dot{q} - \dot{w}_q) + k(q - w_q)^2(q - w_q) = 0, \quad (15)$$

which substitutes the line of zeros in Eq. (14). The results presented in Sect. 3 are nondimensionalized. Considering the plate's mass, $m_p = \rho h L^2$, the NES mass, damping, and stiffness coefficients are

$$\bar{m} := \frac{m}{m_p}, \quad \bar{c} := \frac{c}{2m_p\omega_0}, \quad \text{and} \quad \bar{k} := \frac{k}{D/(hL)^2}, \quad (16)$$

in which $\omega_0 = \sqrt{\frac{D}{\rho h L^4}}$ is the reference frequency. The final nonlinear system of ordinary differential equations in Eq. (14) is solved by the Newmark method with an effective treatment of nonlinear terms and an iterative scheme with a constant coefficient matrix as proposed by Akay [8]. The integration time step Δt is the one also used by Pacheco [9], namely:

$$\Delta t = \frac{1}{\omega_0} \left(\frac{\overline{\Delta d}}{2L} \right)^2, \quad (17)$$

where $\overline{\Delta d}$ is the minimum element size in the mesh.

The mechanical energy is computed to evaluate the NES's effectiveness and performance. By pumping the input energy from the flow, the NES yields the plate a considerably less energetic motion. The total mechanical energy instantaneously contained in the plate, E_p, is the amount of the panel strain and kinetic energies as defined by Pacheco et al. [3], which can be nondimensionalized as

$$\bar{E}_p := \frac{E_p}{D(h/L)^2}. \quad (18)$$

3 Results and Discussion

This section reports and discusses the results regarding the nonlinear dynamic analysis of composite laminate panels with an attached NES at the $\frac{3}{4}$ position. The length of the square plate is L, and the boundary condition is simply supported:

Table 1 Analysis cases determined from LHS

#	$\bar{m}$	$\bar{k}$	$\bar{c}$	#	$\bar{m}$	$\bar{k}$	$\bar{c}$	#	$\bar{m}$	$\bar{k}$	$\bar{c}$
1	0.08	76	286	8	0.60	33	33	15	0.09	41	743
2	0.12	53	388	9	0.12	56	777	16	0.09	21	958
3	0.13	2	164	10	0.14	63	888	17	0.06	10	843
4	0.106	85	669	11	0.08	17	514	18	0.06	85	221
5	0.10	92	420	12	0.14	26	307	19	0.07	68	632
6	0.11	73	917	13	0.073	45	586	20	0.126	97	60
7	0.10	69	148	14	0.13	38	463				

$\hat{u}(x, y, t) = \hat{v}(x, y, t) = \hat{w}(x, y, t) = 0$ for all edges, $\phi_y(x, 0, t) = \phi_y(x, L, t) = 0$, and $\phi_x(0, y, t) = \phi_x(L, y, t) = 0$. The composite square panel used in this chapter is Graphite-epoxy AS-3002 with the following properties: $h = L/100$, $E_1/E_2 = 26.5$, $\nu_{12} = 0.21$, $G_{12} = 1.184 E_2$, $G_{13} = G_{12}$, $G_{23} = G_{12}$, $\mu/M = 0.01$. The initial condition for the time solution corresponds to the static deflections due to the application of a uniform pressure $\Delta p = 0.01 E_2 (h/L)^4$ field. The mesh used for all the analysis was $\Delta x = L/32$, which was the same used by Pacheco et al. [3] to guarantee highly accurate results.

The analyzed lamination scheme was the 10-layered $[+\theta, -\theta, +\theta, -\theta, +\theta]_s$ symmetric laminate. Three values of θ were evaluated: 10°, 30°, and 60°. Pre-flutter and post-flutter conditions are surveyed, and a parametric study concerning the stiffness and damping constants is performed to appraise the system sensitivity to the NES parameters.

The Latin hypercube sampling (LHS) was applied to select a n number of combinations of NES constants: mass, stiffness, and damping from a range of chosen values of these constants. The LHS is one popular modern design of experiments (DOE) method that has found wide computational application [10]. The ranges of chosen values were: 0.05 to 0.15 for $\bar{m}$, 1 to 100 for $\bar{k}$, and 1 to 1000 for $\bar{c}$. The number of samples was $n = 20$; hence, 20 different combinations of mass, stiffness, and damping constants were simulated, as presented in Table 1. All these cases were simulated for $\theta = 30$ and $\lambda = 300$ to found that the NES is capable to withhold flutter for the following cases: 3, 10, 14, and 20. The cases 10 and 20 were picked to analyze the other θ, 10° and 60°, for a post-flutter condition to determine which case has the best parameters for these angle-ply laminates. As done for $\theta = 30°$, the dynamic pressure $\lambda \approx 1.1 \lambda_{f_{30}}$ was chosen to simulate cases 10 and 20 for $\theta = 10°$ and 60°. The critical flutter dynamic pressures are $\lambda_{f_{10}} = 354.2$, $\lambda_{f_{30}} = 271.5$, and $\lambda_{f_{60}} = 144.5$, where the subscript numbers represent the θ angle of the lamination scheme. Therefore, $\lambda = 390$ ($\theta = 10°$) and $\lambda = 160$ ($\theta = 60°$) were used to analyze these laminates and, finally, the following parameters: $\bar{m} = 0.14$, $\bar{k} = 63$, and $\bar{c} = 888$ were chosen for the NES attached to all angle-ply laminates.

3.1 Motion and Energy Analysis

The reference point for measuring displacements was $[x, y] = [0.75, 0.5]L$, which is well known from previous studies as the position where the maximum oscillation amplitudes occur. Figure 2 shows the vertical displacements at the aforementioned reference point, with and without NES, for a pre-flutter and a post-flutter condition, for $\theta = 10°$. The NES leads to a faster return to equilibrium for $\lambda = 352$ (pre-flutter) and reduces the LCO amplitudes for $\lambda = 390$ (post-flutter) in approximately 78.5%. This reduction in amplitude implies in smaller strains and stress, leading to a longer lifetime for fatigue-life design of structural skins.

Figure 3 shows the panel's response for a pre-flutter and a post-flutter condition for $\theta = 30°$. In the pre-flutter condition, the plate with NES achieves stability faster, similarly to the previously laminated angle, $\theta = 10°$. As stated before, for $\lambda = 1.1\lambda_{f_{30}}$, the NES parameters lead the plate to static equilibrium, indicating the NES's ability to postpone the flutter onset. By increasing λ to 350, the NES is no longer able to suppress the flutter, although it reduces the LCO amplitudes in approximately 30%.

The last analyzed laminate concerns $\theta = 60°$. Once again, the NES allows a faster return to stability for the pre-flutter condition, Fig. 4a. For the post-flutter condition, $\lambda = 1.1\lambda_{f_{60}}$, the NES dissipates the energy input by the flow, prompting the structure to return to equilibrium, as shown in Fig. 4b. By increasing the dynamic pressure to $\lambda = 175$, the NES leads the plate to chaotic motion, Fig. 5a. Although the oscillation amplitudes reduce, the chaotic motion is associated with much more energy than the limit cycle oscillations, as can be verified through Fig. 5b. Consequently, the potential for causing fatigue failure in the structure greatly increases by adding a NES with these parameters. Therefore, either the dynamic pressure of operation must comprise values lower than 175 or the NES parameters
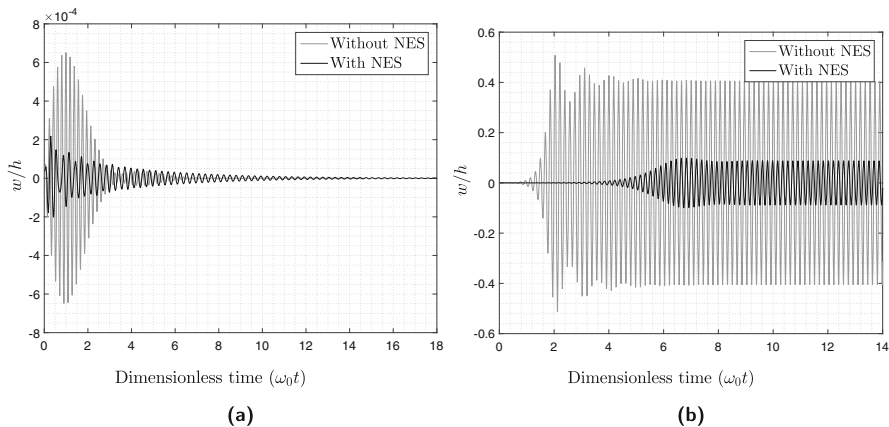

Fig. 2 Panel's response for $\theta = 10°$. (**a**) Pre-flutter, $\lambda = 352$. (**b**) Post-flutter, $\lambda = 390$
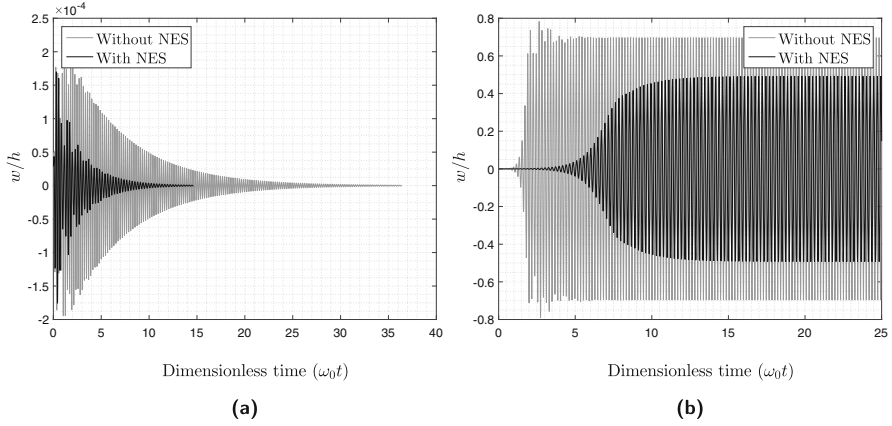
Fig. 3 Panel's response for $\theta = 30°$. (**a**) Pre-flutter, $\lambda = 270$. (**b**) Post-flutter, $\lambda = 350$
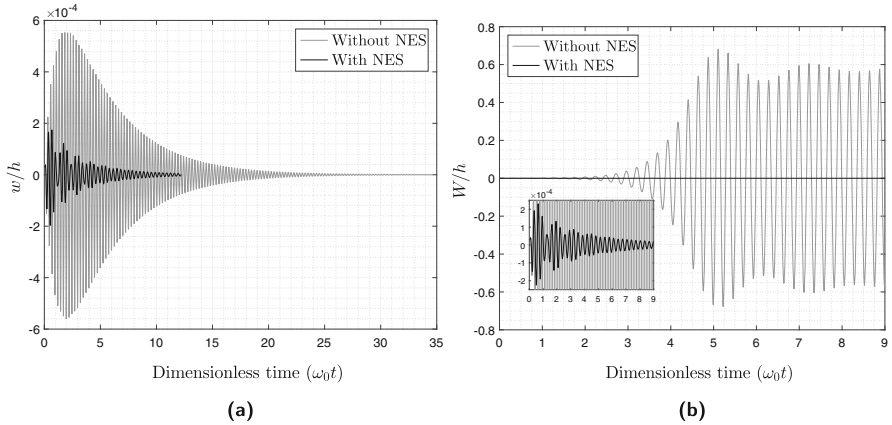
Fig. 4 Panel's response for $\theta = 60°$. (**a**) Pre-flutter, $\lambda = 144$. (**b**) Post-flutter, $\lambda = 160$

must properly change, since a suitably engineered NES must operate by passively extracting the energy input to the structure.

3.2 Parametric Study

To assess how distinct parameters of the NES affect its performance, this section provides a simple parametric study for the $\theta = 10°$ angle-ply laminate. For this study, the mass and position of the NES remain constant ($\bar{m} = 0.14$, and $[x_q, y_q] = [0.75, 0.5]L$); $\bar{k}$ and $\bar{c}$ vary, one at a time. The reference parameters are set as before, $\bar{m} = 0.14$, $\bar{k} = 63$, and $\bar{c} = 888$. Moreover, the dynamic pressure is also fixed for

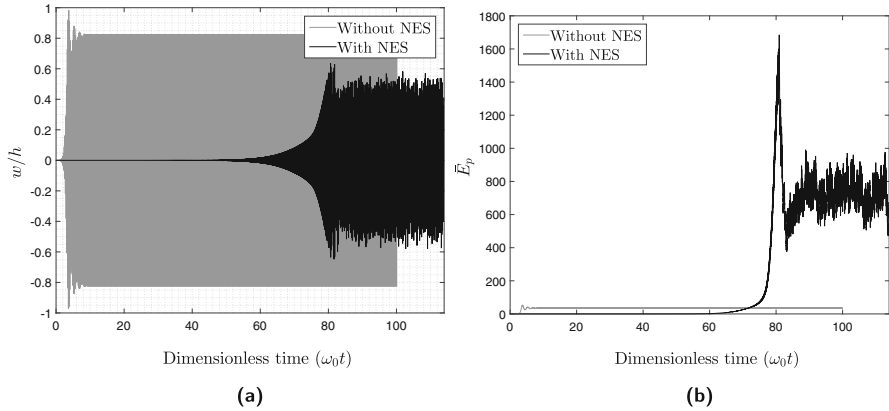**Fig. 5** Time history for $\theta = 60°$ and $\lambda = 175$ ($\bar{c} = 888$ and $\bar{k} = 63$). (**a**) Vertical displacements. (**b**) Mechanical energy
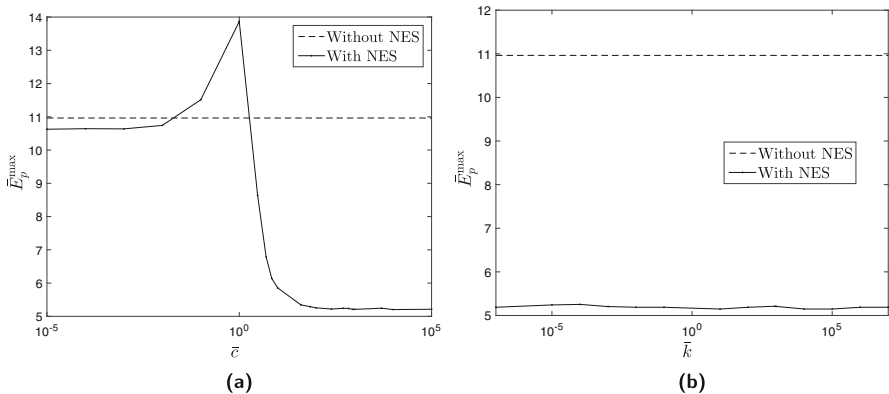

Fig. 6 Effect of damping and stiffness coefficients on the maximum LCO energy for $\lambda = 380$ and $\theta = 10°$. (**a**) Damping. (**b**) Stiffness

each laminate, which corresponds to determine a critical operational flight condition for aircraft design. The measure used to evaluate the NES's performance was the upmost energy held in the panel while having LCO, $\bar{E}_p^{\max}$, as the principle of a NES is to extract energy from the structure.

Figure 6a shows the high-peak LCO energy for various damping coefficients. The graphic presents two horizontal asymptotes and a peak of maximum energy. The lower horizontal asymptote comprises the NES parameters that better provide energy pumping, which corresponds to higher values of $\bar{c}$. The higher horizontal asymptote, achieved when $\bar{c}$ tends to zero, approaches the upmost LCO energy of a panel without NES. Figure 6b shows the influence of the nonlinear stiffness coefficient in the NES's efficiency for a broad range of values: $10^{-7} \leq \bar{k} \leq 10^7$. The LCO energy is minimized in approximately 50% in relation to the case without

NES. For a NES with this damping coefficient: $\bar{c} = 888$, the stiffness coefficient seems not to have an imperative role in the behavior of the system.

The purpose of this parametric analysis is to assess how the NES's effectiveness concerning flutter application of composite laminate panels can be affected by such parameters. Hence, the aim of this chapter is not to perform an optimization analysis, although it provides some insights indicating that the panel flutter design with this passive control technique may highly benefit from optimization study.

4   Conclusions

This chapter presented a numerical investigation on the nonlinear aeroelastic behavior of composite laminate panels endowed with a passive controller, namely nonlinear energy sinks. The Mindlin theory coupled with the von Kármán's strain–displacement is applied to model the geometrically nonlinear structural behavior of the panel, and the first-order piston theory is used to determine the aerodynamic loads. The analyzed lamination scheme was the 10-layered $[+\theta, -\theta, +\theta, -\theta, +\theta]_s$ symmetric laminate, for three different values of θ.

The panel's time responses have shown that the NES's efficiency varies with the lamination scheme if the same parameters are used. Moreover, as the dynamic pressure increases from the flutter onset, the NES's effectiveness decreases. An interesting result is found for $\theta = 60°$. When λ increases from $1.1\lambda_{f_{60}}$ to $1.21\lambda_{f_{60}}$, the NES that once suppressed the flutter leads the system to chaotic motion when the dynamic pressure goes up. Hence, besides affecting the NES performance, the NES parameters have demonstrated to have an impact on the dynamic behavior of the panel. This shows the necessity to define an operational range of λ to properly design an efficient NES. It also indicates that an optimization study would greatly benefit the design of this passive control technique. The parametric study—varying only the $\bar{c}$ and $\bar{k}$ coefficients—reassures the importance of properly determining the NES parameters to provide maximum energy pumping.

The study of nonlinear panel flutter suppression with NES is performed for the first time regarding composite laminates through this chapter. The investigation of different angle-ply laminates provided some insights on how different NES parameters affect the nonlinear aeroelastic response of angle-ply laminates.

References

1. S.A. Hubbard, R.L. Fontenot, D.M. McFarland, P.G.A. Cizmas, L.A. Bergman, T.W. Strganac, A.F. Vakakis, Transonic aeroelastic instability suppression for a swept wing by targeted energy transfer. J. Aircraft. **51**, 1467–1482 (2014). https://doi.org/10.2514/1.C032339
2. Y. Zhang, H. Zhang, S. Hou, K. Xu, L. Chen, Vibration suppression of composite laminated plate with nonlinear energy sink. Acta Astronaut. **123**, 109–115 (2016). https://doi.org/10.1016/j.actaastro.2016.02.021
3. D.R.Q. Pacheco, F.D. Marques, A.J.M. Ferreira, Panel flutter suppression with nonlinear energy sinks: numerical modeling and analysis. Int. J. Nonlin. Mech. **106**, 108–114 (2018). https://doi.org/10.1016/j.ijnonlinmec.2018.08.009
4. A. Pica, R.D. Wood, E. Hinton, Finite element analysis of geometrically nonlinear plate behaviour using a Mindlin formulation. Comput. Struct. **11**, 203–215 (1980). https://doi.org/10.1016/0045-7949(80)90160-1
5. J.N. Reddy, *Mechanics of Laminated Composite Plates and Shells: Theory and Analysis*, 2nd edn. (CRC press, New York, 2003)
6. M. Alder, Development and validation of a fluid–structure solver for transonic panel flutter. JAIAA J. **53**, 3509–3521 (2015). https://doi.org/10.2514/1.J054013
7. V.V. Vedeneev, Panel flutter at low supersonic speeds. J. Fluids Struct. **29**, 79–96 (2012). https://doi.org/10.1016/j.jfluidstructs.2011.12.011
8. H.U. Akay, Dynamic large deflection analysis of plates using mixed finite elements. Comput. Struct. **11**, 1–11 (1980). https://doi.org/10.1016/0045-7949(80)90142-X
9. D.R.Q. Pacheco, Nonlinear finite element aeroelastic modelling of reinforced skin panels in supersonic flows. Carlos School of Engineering, University of São Paulo, São Paulo (2018)
10. A. Giunta, S. Wojtkiewicz, M. Eldred, Overview of modern design of experiments methods for computational simulations, in *41st Aerospace Sciences Meeting and Exhibit* (AIAA, Reston, 2003), pp. 649. https://doi.org/10.2514/6.2003-649

Dynamic Analysis of a Coupled System with a Nonlinear Inerter-Based Device

Zhuang Dong, Jian Yang (ORCID), **and Dimitrios Chronopoulos**

1 Introduction

The inerter is a relatively recently proposed passive device with the property that the applied force at its two terminals is proportional to the relative acceleration between them, that is, $F_b = b\left(\dot{V}_1 - \dot{V}_2\right)$, where F_b is the coupling inertial force, b is the inertance, an intrinsic parameter of the inerter, $\dot{V}_1$ and $\dot{V}_2$ are the accelerations of the two terminals [1]. Benefits of introducing the inerter in vibration mitigation have been demonstrated in many applications including automobile shock absorbers [2], building vibration control systems [3], and landing gear shimmy vibration suppression systems [4]. Some studies have also been reported on the performance of inerter-based single degree-of-freedom (DOF) vibration isolators [5], dual-stage isolators [6], coupled oscillators with an inerter-based joint [7], laminated composite plates with inerter-based suppression configurations [8], and metamaterial beam structures with an embedded inerter-based configuration [9]. Basili et al. [10–12] studied the dynamics of coupled two-degree-of-freedom (2-DOF) systems linked by linear spring-damper-inerter elements. Masri and Caffrey [13] presented a damped linear 2-DOF system, which resembles a primary system provided with an auxiliary mass damper as well as an inerter.

Nonlinearities are often encountered in the design and analysis of physical systems and engineering structures [14]. Nonlinear isolators are considered to obtain low amplitude response and low vibration transmission in a wide range of

Z. Dong · J. Yang (✉)

Faculty of Science and Engineering, University of Nottingham Ningbo China, Ningbo, People's Republic of China

e-mail: jian.yang@nottingham.edu.cn

D. Chronopoulos

Institute for Aerospace Technology & The Composites Group, University of Nottingham, Nottingham, UK

excitation frequencies [15–17]. Yang et al. [18] presented a nonlinear absorber with cubic stiffness and damping nonlinearities attached to a nonlinear primary system. Nonlinearities are usually introduced into dynamical systems through restoring or damping forces as nonlinear smooth functions of the dynamic response. For instance, the restoring force of the Duffing oscillator is a smooth cubic function of the displacement [19]. However, only few studies have considered the nonlinearities arising from the use of the inerter. Papageorgiu et al. [20] and Gonzalez Buelga et al. [21] used experimental tests to analyze the nonlinear effects on two types of inerters including the friction. Very recently, Yang et al. [22] proposed a nonlinear geometric configuration of inerters and examined its dynamics and performance in nonlinear vibration isolators. They showed that the addition of a nonlinear inertance mechanism (NIM) to a quasi-zero-stiffness isolator enhances vibration isolation performance by providing a wider frequency band of low amplitude response and force transmissibility. It was also found that the frequency response curves of the nonlinear inerter-based isolation system bend toward the low-frequency range in contrast to a linear inerter-based system.

In this work, the influence of a nonlinear inerter on the dynamic response of a coupled system is studied. The nonlinearity in the inerter is introduced through nonlinear geometric configuration. In Sect. 2, the NIM and the coupled oscillator system are briefly introduced and modelled. The analysis method is also introduced to obtain the steady-state response. In Sect. 3, the response of each subsystem for two different locations of nonlinear inerter is obtained. Also, the effects of different levels of inertance on the dynamic response are investigated. Conclusions are drawn in at the end of the paper.

2 Mathematical Modelling

2.1 NIM

Figure 1 provides a schematic representation of the NIM created by using a pair of oblique inerters proposed by Yang et al. [22]. Two inerters are hinged together at terminal A and their other terminals are fixed at points C and D, which are separated horizontally by $2l_0$. The two inerters are assumed to be ideal with inertance b so that the inertance force in the axial direction AB is proportional to the relative acceleration across the terminals. The displacement, velocity, and acceleration of the moving terminal A are x_2, $\dot{x_2}$, and $\ddot{x_2}$, whereas, x_1, $\dot{x_1}$, and $\ddot{x_1}$ are the displacement, velocity, and acceleration of terminal B. The dynamic displacement between the two terminals is defined as $\delta = x_1 - x_2$. Hence, a geometric nonlinearity is introduced by the NIM, with the total force between A and B expressed by [22]:

$$f_b = 2b \left(\frac{\delta^2 \ddot{\delta}}{l_0{}^2 + \delta^2} + \frac{l_0{}^2 \delta \dot{\delta}^2}{\left(l_0{}^2 + \delta^2\right)^2} \right). \tag{1}$$

Fig. 1 Schematic model of
the NIM
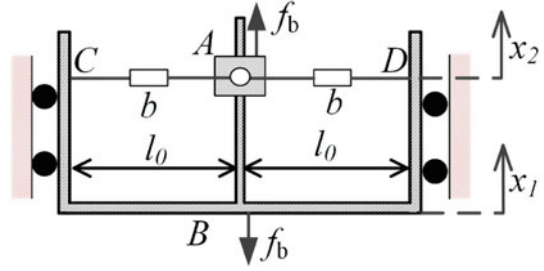
2.2 Coupled Oscillators

Figure 2 shows a model of the coupled oscillators comprising of two subsystems connected through a mechanical joint characterized by a spring with stiffness coefficient k_0. Subsystem 1 is a single-DOF system consisting of mass m_1 subjected to an external harmonic excitation of amplitude f_0 with frequency ω, a linear spring with stiffness coefficient k_1, and a viscous damper of damping coefficient c_1. Subsystem 2 is another single-DOF system consisting of mass m_2, a linear spring k_2, and a viscous damper c_2. It is assumed that both masses move horizontally without friction and their static equilibrium positions are taken as reference where $x_1 = x_2 = 0$ and the springs are unstretched. The influence of NIM on the dynamic behavior of the coupled system is studied by placing it at different locations. When the nonlinear inerter is placed at P, the dynamic governing equations of the system could be expressed as follows:
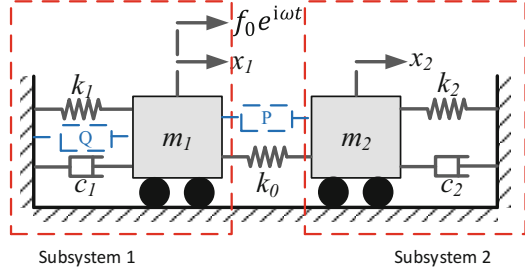
$$m_1 \ddot{x}_1 + c_1 \dot{x}_1 + k_1 x_1 + f_b + k_0 (x_1 - x_2) = f_0 e^{i\omega t}, \tag{2a}$$

$$m_2 \ddot{x}_2 + c_2 \dot{x}_2 + k_2 x_2 - f_b - k_0 (x_1 - x_2) = 0, \tag{2b}$$

where

$$f_b = 2b \left(\frac{\delta^2 \ddot{\delta}}{l_0^2 + \delta^2} + \frac{l_0^2 \delta \dot{\delta}^2}{\left(l_0^2 + \delta^2 \right)^2} \right). \tag{3}$$

Fig. 2 A schematic of the coupled oscillators with a nonlinear inerter-based joint

Subsystem 1   Subsystem 2

To facilitate later formulations, the following parameters are introduced:

$$\omega_1 = \sqrt{\frac{k_1}{m_1}}, \quad \omega_2 = \sqrt{\frac{k_2}{m_2}}, \quad \mu = \frac{m_2}{m_1}, \quad X_1 = \frac{x_1}{l_0}, \quad X_2 = \frac{x_2}{l_0},$$

$$\Delta = X_1 - X_2, \quad \gamma = \frac{k_2}{k_1}, \quad \varphi = \frac{k_0}{k_1}, \quad \zeta_1 = \frac{c_1}{2m_1\omega_1},$$

$$\zeta_2 = \frac{c_2}{2m_2\omega_1}, \quad \lambda = \frac{b}{m_1}, \quad F_0 = \frac{f_0}{k_1 l_0}, \quad \Omega = \frac{\omega}{\omega_1}, \quad \tau = \omega_1 t,$$

where ω_1 and ω_2 are the natural frequencies of subsystems 1 and 2, respectively, μ is the mass ratio, X_1 and X_2 are the nondimensional displacements of masses m_1 and m_2, respectively, Δ is the relative displacement between m_1 and m_2, γ is the stiffness ratio, ζ_1 and ζ_2 are the damping ratios, λ is the inertance-to-mass ratio, F_0 is the nondimensional force amplitude, and Ω and τ are the dimensionless frequency and time. By using these parameters, Eqs. (2) and (3) can be rearranged as follows:

$$X_1'' + 2\zeta_1 X_1' + X_1 + F_b + \varphi\Delta = F_0 e^{i\Omega\tau}, \tag{4a}$$

$$\mu\left(X_1'' - \Delta''\right) + 2\mu\zeta_2\left(X_1' - \Delta'\right) + \gamma\left(X_1 - \Delta\right) - F_b - \varphi\Delta = 0, \tag{4b}$$

respectively, where the nonlinear force arising from the NIM is

$$F_b = 2\lambda\left(\frac{\Delta^2\Delta''}{1+\Delta^2} + \frac{\Delta\Delta'^2}{\left(1+\Delta^2\right)^2}\right). \tag{5}$$

Similarly, when the nonlinear inerter is placed at position Q, the governing equations of the system can be derived as

$$m_1\ddot{x}_1 + c_1\dot{x}_1 + k_1 x_1 + f_{b2} + k_0\left(x_1 - x_2\right) = f_0 e^{i\omega t}, \tag{6a}$$

$$m_2\ddot{x}_2 + c_2\dot{x}_2 + k_2 x_2 - k_0 (x_1 - x_2) = 0, \tag{6b}$$

where

$$f_{b2} = 2b \left(\frac{x_1^2 \ddot{x}_1}{l_0^2 + x_1^2} + \frac{l_0^2 x_1 \dot{x}_1^2}{\left(l_0^2 + x_1^2\right)^2} \right). \tag{7}$$

By using the previously defined parameters, the nondimensional equations can be obtained:

$$X_1'' + 2\zeta_1 X_1' + X_1 + F_{b2} + \varphi\Delta = F_0 e^{\mathrm{i}\Omega\tau}, \tag{8a}$$

$$\mu \left(X_1'' - \Delta'' \right) + 2\mu\zeta_2 \left(X_1' - \Delta' \right) + \gamma \left(X_1 - \Delta \right) - \varphi\Delta = 0, \tag{8b}$$

where the nonlinear force induced by the addition of the NIM is

$$F_{b2} = 2\lambda \left(\frac{X_1^2 X_1''}{1 + X_1^2} + \frac{X_1 X_1'^2}{\left(1 + X_1^2\right)^2} \right). \tag{9}$$

2.3   Alternating-Frequency-Time (AFT) Scheme

In this paper, the dynamic responses of the coupled system are obtained using the harmonic balance (HB) method with alternating-frequency-time (AFT) scheme [23, 24]. For complex systems, the determination of the Fourier coefficients of the nonlinear force (i.e., Eq. (5)) is the primary challenge in the implementation of the HB method. The AFT scheme is one of the most efficient ways to determine the Fourier coefficients associated with a general nonlinear force, which may be smooth or non-smooth functions of the displacement, velocity, or the acceleration. The main idea of the AFT scheme is to replace the continuous Fourier transform of the nonlinear forces by a discrete Fourier transform so that samples of the nonlinear forces at equidistant time instants within one period of oscillation are taken. This scheme is one of the general and efficient numerical methods to solve nonlinear governing equations within the HB method and is thus used in the current study.

3   Response Analysis

3.1   Nonlinear Inerter at Position P

By using the HB method, the steady-state response amplitudes of the oscillator masses are obtained and shown in Figs. 3 and 4. Four different values of the inertance-to-mass ratio with $\lambda = 0, 1, 5, 10$ are selected and the corresponding results are shown by solid, dashed, dash-dot, and dotted lines. The other parameters are set as $\mu = 1$, $\gamma = 1$, $\varphi = 10$, $\zeta_1 = \zeta_2 = 0.01$, $F_0 = 0.05$. Figure 3 plots the response amplitude R_1 of mass m_1. When the nonlinear inerter is added in between the two subsystems, two resonant peaks are observed in the response curve. With the increase of the inertance-to-mass ratio λ, the second peak for each curve bends to the lower frequency range. However, the first peak in the response curve remains at the same frequency with the change of inertance-to-mass ratio λ. An anti-peak is also observed in Fig. 3, which remains almost the same with the change in the value of λ. An explanation for the effects of the nonlinear inerter is that when the response amplitude is large, the nonlinearity introduced by the nonlinear inerter becomes stronger. In contrast, when the response amplitude is low, as is the case at the anti-peak, the nonlinearity is small, leading to negligible effects of the NIM on the response. The figure also shows that the response amplitude at the original second peak of the corresponding linear system is reduced by adding the NIM. This behavior demonstrates that the NIM may be used to suppress vibration at prescribed excitation frequencies. As shown in Fig. 4, the response behavior of mass m_2 is analyzed by investigating the response amplitude R_2. The figure shows a similar
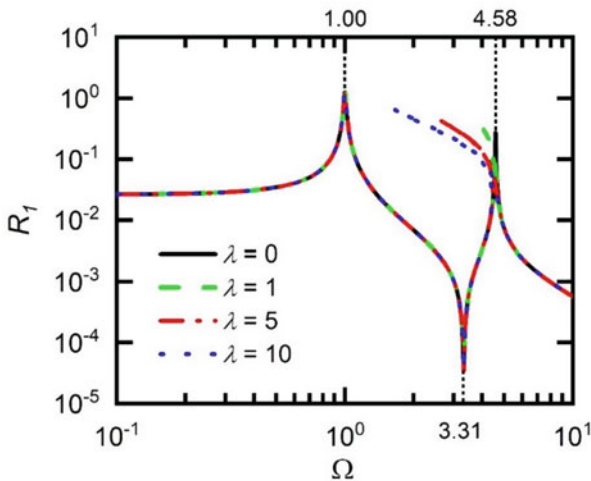

Fig. 3 Effects of the NIM on the response amplitude of mass m_1 when the nonlinear inerter is added at position P ($\mu = 1$, $\gamma = 1$, $\varphi = 10$, $\zeta_1 = \zeta_2 = 0.01$, $F_0 = 0.05$)
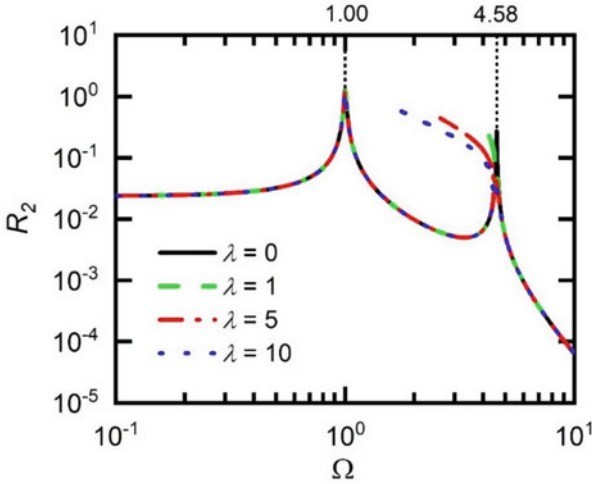
Fig. 4 Effects of the NIM on the response amplitude of mass m_2 when the nonlinear inerter is added at position P ($\mu = 1$, $\gamma = 1$, $\varphi = 10$, $\zeta_1 = \zeta_2 = 0.01$, $F_0 = 0.05$)

bending of the second peak to the left toward the low-frequency range. The first peak value and the peak frequency change a little. Also, no clear anti-peak is found in this case.

3.2 Nonlinear Inerter at Position Q

The effects of inertance on the response amplitudes of the oscillator masses with the nonlinear inerter added at position Q in Fig. 2 are obtained, and the results are shown in Figs. 5 and 6. Four different values of the inertance-to-mass ratio with $\lambda = 0, 1, 5, 10$ are selected and the corresponding results are shown by solid, dashed, dash-dot, and dotted lines. The other parameters are set as $\mu = 1$, $\gamma = 1$, $\varphi = 10$, $\zeta_1 = \zeta_2 = 0.01$, $F_0 = 0.05$. Figure 5a plots the response amplitude curves of mass m_1. When NIM is added in the subsystem 1, both peaks on each curve of the response amplitude X_1 bend toward the lower frequency range. With the increase in the value of λ from 1 to 10, the response curve bends further to the low frequencies. Compared with the effects of the NIM on the first peak found at a lower frequency, there are weaker effects of the nonlinearity on the second peak found at higher frequencies. Figure 5b provides an enlarged view of the first peak shown in Fig. 5a. It shows that on the bending resonance response branch found at low frequencies, another local anti-peak is introduced with the increase of inertance-to-mass ratio λ. This behavior indicates that the vibration suppression is possible in particular range of the excitation frequency for $\lambda = 5$ and $\lambda = 10$ cases.
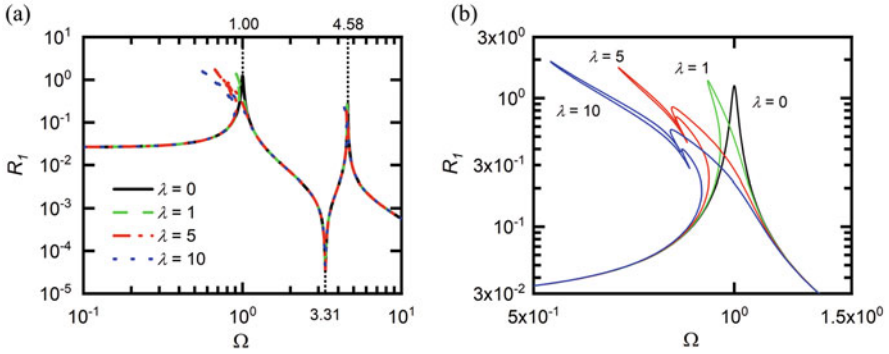
Fig. 5 Effects of the NIM on the response amplitude of mass m_1 (**a**), and enlargement (**b**), when the nonlinear inerter is added to position Q ($\mu = 1$, $\gamma = 1$, $\varphi = 10$, $\zeta_1 = \zeta_2 = 0.01$, $F_0 = 0.05$)
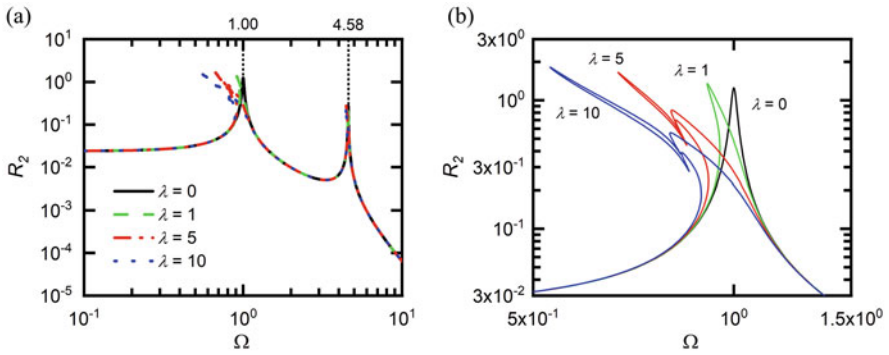

Fig. 6 Effects of the NIM on the response amplitude of mass m_2 (**a**), and enlargement (**b**), when the nonlinear inerter is added to position Q ($\mu = 1$, $\gamma = 1$, $\varphi = 10$, $\zeta_1 = \zeta_2 = 0.01$, $F_0 = 0.05$)

Figure 6a plots the steady-state response amplitude R_2 of mass m_2 under different values of inertance. When the nonlinear inerter is added into subsystem 1, both peaks of response amplitude R_2 bend toward the lower frequency range. With the increase in the value of λ from 1 to 10, the response curve bends further to the left. The second peak is relatively less affected by the change in λ. Figure 6b provides a better view of the neighborhood of the first peak. It shows that another anti-peak may appear when the inertance-to-mass ratio λ increases to 5 or 10. This behavior demonstrates the rich nonlinear phenomenon arising from the using of NIM. The figure also shows that for $\lambda = 5$ and 10, at specific excitation frequencies, it is possible to reduce the response amplitude by adding NIM.

4   Conclusions

This study investigated the effects of adding a nonlinear inerter on the vibration behavior of a coupled system. The nonlinear inerter is created by a pair of linear inerters resulting in a geometric nonlinearity. The steady-state response amplitudes of the two subsystems were obtained for two different positions of the nonlinear inerter. When the nonlinear inerter is added between two subsystems as a mechanical joint, it was shown that with the increase of the inertance-to-mass ratio, the second peak in the response amplitude curves can bend toward the lower frequency range. When the nonlinear inerter is added to the force-excited subsystem 1, both peaks of the response amplitude curve bend toward lower frequencies with the increase of the inertance-to-mass ratio. The effects of the nonlinearity on the first peak were found to be stronger than those on the second peak. It was found that an extra anti-peak could be generated in the first peak response branch due to the addition of the nonlinear inerter. The study showed that the vibration response amplitude of the coupled oscillators can be reduced at predetermined excitation frequencies by the addition of the nonlinear inerter. These findings improve the understanding of the dynamic properties of NIM and provide insights for enhancing vibration attenuation using the nonlinear inerter element.

References

1. M. Smith, Synthesis of mechanical networks: The inerter. IEEE Trans. Autom. Control **47**(10), 1648–1662 (2002)
2. M. Smith, F. Wang, Performance benefits in passive vehicle suspensions employing inerters. Veh. Syst. Dyn. **42**(4), 235–257 (2004)
3. I. Lazar, S. Neild, D. Wagg, Using an inerter-based device for structural vibration suppression. Earthq. Eng. Struct. Dyn. **43**(8), 1129–1147 (2013)
4. Y. Li, J. Jiang, S. Neild, Inerter-based configurations for main-landing-gear shimmy suppression. J. Aircr. **54**(2), 684–693 (2017)
5. J. Yang, Force transmissibility and vibration power flow behaviour of inerter-based vibration isolators. J. Phys. Conf. Ser. **744**, 012234 (2016)
6. J. Yang, J. Jiang, X. Zhu, H. Chen, Performance of a dual-stage inerter-based vibration isolator. Procedia Eng. **199**, 1822–1827 (2017)
7. Z. Dong, D. Chronopoulos, J. Yang, Suppression of vibration transmission between oscillators coupled with an inerter-based joint. Proc. Int. Conf. Struct. Dyn. (EURODYN) **1**, 1521–1528 (2020)
8. C. Zhu, J. Yang, C. Rudd, Vibration transmission and power flow of laminated composite plates with inerter-based suppression configurations. Int. J. Mech. Sci. **190**, 106012 (2020)
9. Z. Dong, D. Chronopoulos, J. Yang, Enhancement of wave damping for metamaterial beam structures with embedded inerter-based configurations. Appl. Acoust. **178**, 108013 (2021)

10. M. Basili, M. De Angelis, D. Pietrosanti, Modal analysis and dynamic response of two adjacent single-degree-of-freedom systems linked by spring-dashpot-inerter elements. Eng. Struct. **174**, 736–752 (2008)
11. M. Basili, M. De Angelis, D. Pietrosanti, Defective two adjacent single degree of freedom systems linked by spring-dashpot-inerter for vibration control. Eng. Struct. **188**, 480–492 (2019)
12. M. Basili, M. De Angelis, D. Pietrosanti, Dynamic response of a viscously damped two adjacent degree of freedom system linked by inerter subjected to base harmonic excitation. Procedia Eng. **199**, 1586–1591 (2017)
13. S. Masri, J. Caffrey, Transient response of a SDOF system with an inerter to nonstationary stochastic excitation. J. Appl. Mech. **84**(4), 041005 (2017)
14. A.H. Nayfeh, D.T. Mook, *Nonlinear Oscillations* (John Wiley & Sons, New York, 1979)
15. R. Ibrahim, Recent advances in nonlinear passive vibration isolators. J. Sound Vib. **314**(3–5), 371–452 (2008)
16. J. Yang, Y.P. Xiong, J.T. Xing, Dynamics and power flow behaviour of a nonlinear vibration isolation system with a negative stiffness mechanism. J. Sound Vib. **332**(1), 167–183 (2013)
17. J. Yang, Y.P. Xiong, J.T. Xing, Vibration power flow and force transmission behaviour of a nonlinear isolator mounted on a nonlinear base. Int. J. Mech. Sci. **115-116**, 238–252 (2016)
18. J. Yang, Y.P. Xiong, J.T. Xing, Power flow behaviour and dynamic performance of a nonlinear vibration absorber coupled to a nonlinear oscillator. Nonlinear Dyn. **80**(3), 1063–1079 (2015)
19. J. Yang, Y.P. Xiong, J.T. Xing, Nonlinear power flow analysis of the Duffing oscillator. Mech. Syst. Signal Process. **45**(2), 563–578 (2014)
20. C. Papageorgiou, N. Houghton, M. Smith, Experimental testing and analysis of inerter devices. J. Dyn. Syst. Meas. Control **131**(1), 011001 (2008)
21. A. Gonzalez-Buelga, I.F. Lazar, J.Z. Jiang, S.A. Neild, D.J. Inman, Assessing the effect of nonlinearities on the performance of a tuned inerter damper. Struct. Control Health Monit. **24**, e1879 (2017)
22. J. Yang, J.Z. Jiang, S. Neild, Dynamic analysis and performance evaluation of nonlinear inerter-based vibration isolators. Nonlinear Dyn. **99**(3), 1823–1839 (2020)
23. G. Von Groll, D.J. Ewins, The harmonic balance method with arc-length continuation in rotor/stator contact problems. J. Sound Vib. **241**(2), 223–233 (2001)
24. M. Krack, J. Gross, *Harmonic Balance for Nonlinear Vibration Problems* (Springer, Cham, 2019)

Optimal Direct Adaptive Model-Free Controller for Twin Rotor MIMO System Using Legendre Polynomials and PSO Algorithm

Abdelghani Chelihi, Gabriele Perozzi, and Chouki Sentouh

1 Introduction

TRMS is widely used by researchers and engineers as benchmark for exploring, testing, and validating flight control and optimization schemes in the recent technologies, i.e., helicopters, airplanes, spacecraft, unmanned aerial vehicles, as well as broad-ranging multiple-input multiple-output (MIMO) systems with varying degrees of nonlinearities and complexities. These control and estimation methods are first validated on the TRMS test bed using the real-world online sensors' data.

Different control techniques and architectures were developed [1]. Fractional-order proportional–integral–derivative (PID) controllers with optimized tuning parameters (i.e., neuro-based, swarm-based, genetic-based, and bacterial-foraging-based) were discussed in [2–5]. In [6], a robust H_∞ controller was designed. The Takagi–Sugeno fuzzy modeling and fuzzy controllers were applied in [7]. Linear quadratic regulator, linear quadratic Gaussian, and sliding mode controllers were discussed in [8–10]. Using the Lie derivatives, the TRMS model is transformed and a model reference adaptive controller was applied in [11]. The main drawback of the cited works is that they all require a previous knowledge of the platform dynamics. For this reason, the model-free controllers have increased in popularity in the last years. Motivated by the previous discussion, we propose in this chapter an optimal

A. Chelihi (✉)
Department of Electronics, Faculty of Technology, Constantine 1 University, Constantine, Algeria

G. Perozzi
Inria, University of Lille, CNRS, UMR 9189 – CRIStAL, Lille, France

C. Sentouh
LAMIH-UMR CNRS 8201, Department of Automatic Control, Hauts-de-France Polytechnic University, Valenciennes, France
e-mail: chouki.sentouh@univ-valenciennes.fr

model-free controller based on Legendre polynomials (LP) and particle swarm optimization (PSO) algorithm for attitude control of the TRMS in the presence of disturbances. The originality of the proposed approach lies in the design of a simple robust control law without any prior knowledge of the system's dynamics, unlike to the most of model-free intelligent control approaches that are complex and difficult to be implemented in real time, see [2, 12]. Therewith, in some works as in [13, 14], the stability proof of TRMS control system is not studied, which decreases the reliability of the controller.

In this chapter, the TRMS is considered as large-scale system that can be decoupled into two SISO subsystems describing its motion in vertical and horizontal planes. For each subsystem, an adaptive model-free controller is designed using LPs to approximate directly the ideal control law. Then, the tuning parameters of our controllers are selected by PSO algorithm to maintain best performance of the TRMS even in the presence of unknown dynamics and disturbances. The overall stability of the closed-loop control system and boundedness of signals is demonstrated.

2   Dynamical Model

The TRMS, as shown in Fig. 1, is a laboratory setup designed for flight control experiments. It consists of a beam with main and tail rotors driven by direct current (DC) motors. The two rotors are connected perpendicularly and controlled by their variable speeds enabling the TRMS to rotate in vertical and horizontal planes with pitch and yaw angles denoted as θ_v and θ_h, respectively. The TRMS is constructed such that the aerodynamic force is controlled by varying the speed of the rotors that are ensured by their supply voltages denoted as u_v and u_h. As supplied by the manufacturer [15], the dynamic motion of the TRMS in vertical and horizontal planes is given by the following equations:

$$
\begin{cases}
\dot{\theta}_v = \Omega_v \\
\dot{\Omega}_v = \sigma_v \\
\Omega_v = (S_v + J_{tr}\omega_t)/J_v \\
\dot{S}_v = l_m F_v(\omega_m) + g\left((A-B)\cos\theta_v - C\sin\theta_v\right) - \Omega_v k_v + g_{hv} \\
\dot{u}_{vv} = (K_{mr}u_v - u_{vv})/T_{mr}
\end{cases}
\tag{1}
$$

$$
\begin{cases}
\dot{\theta}_h = \Omega_h \\
\dot{\Omega}_h = \sigma_h \\
\Omega_h = (S_h + J_{mr}\omega_m\cos\theta_v)/J_h \\
\dot{S}_h = l_t F_h(\omega_t)\cos\theta_v - \Omega_h k_h \\
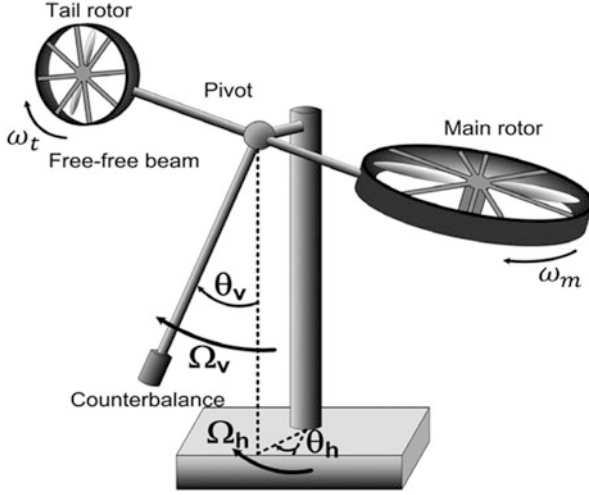u_{hh} = (K_{tr}u_h - u_{hh})/T_{tr},
\end{cases}
\tag{2}
$$

Fig. 1 Twin rotor MIMO system [17]

where Ω_v (Ω_h) is the angular velocity around the vertical (horizontal) axis, σ_v (σ_h) is the beam acceleration in the vertical (horizontal) plane, S_v (S_h) is the angular momentum in vertical (horizontal) plane of the beam, u_{vv} (u_{hh}) is the rotation angle of the main (tail) DC motor. F_v (F_h) is the propulsive force generated by the DC motor rotational speed ω_m (ω_t) of the main (tail) rotor, with

$$\begin{cases} F_v = \mathcal{L}_v(\omega_m) \quad and \quad F_h = \mathcal{L}_h(\omega_t) \\ \omega_m = \mathcal{P}_v(u_{vv}) \quad and \quad \omega_t = \mathcal{P}_h(u_{hh}), \end{cases} \tag{3}$$

where $\mathcal{L}_v$, $\mathcal{L}_h$, $\mathcal{P}_v$, and $\mathcal{P}_h$ are nonlinear functions identified experimentally with the model parameters provided by the manufacturer, which are available in [16]. From the previous development, we can conclude that the TRMS model is a MIMO complex nonlinear system composed of two single-input single-output (SISO) interconnected subsystems models. Thus, the model of TRMS can be decoupled to simplify the design of our controller. The vertical and horizontal sub-models are derived, respectively, from the coupled model by setting $\theta_h = 0$ and substituting $u_h = 0$ in Eq. (1), and by fixing $\theta_v = \theta_v(0)$ and substituting $u_v = 0$ in Eq. (2). These two models can be rewritten in a generalized state form as follows:

$$\begin{cases} \dot{x}_{i,1} = x_{v,2} \\ \dot{x}_{i,2} = x_{v,3} \\ \dot{x}_i(t) = \mathcal{F}_i(x_i) + \mathcal{G}_i(x_i)u_i(t) + \mathcal{R}_i(x, t) \\ y_i(t) = x_{i,1}(t), \ i \in \{v, h\}, \end{cases} \tag{4}$$

where $x = \begin{bmatrix} x_v, x_h \end{bmatrix}^T$ denotes the total state variables vector of TRMS, $x_i = \begin{bmatrix} x_{i,1}, x_{i,2}, x_{i,3} \end{bmatrix}^T = \begin{bmatrix} \theta_i, \Omega_i, \sigma_i \end{bmatrix}^T$ are the local state vectors, u_i are the control inputs, $y_i = \theta_i$ are the output variables, $\mathcal{F}_i(x_i)$, $\mathcal{G}_i(x_i)$, and $\mathcal{R}_i(x, t)$ are nonlinear functions that represent the dynamic functions, input gains, and disturbance effects including the interactions between subsystems, respectively, with

$$\begin{cases} \mathcal{F}_v(x_v) = -\frac{g}{J_v} \left((A - B) \sin x_{v,1} + C \cos x_{v,1} \right) x_{v,2} - \frac{K_v}{J_v} x_{v,3} \\ \mathcal{G}_v(x_v) = \frac{l_m K_{mr}}{J_v} \Delta_v, \quad \mathcal{R}_v(x_v) = -\frac{l_m}{J_v T_{mr}} \Delta_v u_{vv}, \quad \Delta_v = \frac{\partial \mathcal{L}_v}{\partial \omega_m} \cdot \frac{\partial \mathcal{P}_v}{\partial u_{vv}} \end{cases} \quad (5)$$

$$\begin{cases} \mathcal{F}_h(x_h) = -K_h x_{h,3}, \quad \mathcal{G}_h(x_h) = \frac{l_t K_{tr}}{J_{h0}} \cos x_{v,1}(0) \Delta_h \\ \mathcal{R}_h(x_h) = -\frac{l_t \cos x_{v,1}(0)}{J_{h0} T_{tr}} \Delta_h u_{hh}, \quad \Delta_h = \frac{\partial \mathcal{L}_h}{\partial \omega_m} \cdot \frac{\partial \mathcal{P}_h}{\partial u_{hh}}. \end{cases} \quad (6)$$

The control problem considered in this chapter is to develop a simple and robust controller for the model (3) ensuring that the TRMS angles θ_i for $i \in \{v, h\}$ track asymptotically and optimally the desired signals θ_i^*. In addition, it should guarantee the stability and boundedness of all closed-loop signals even in the presence of unknown nonlinear dynamics, parameter variations, and external disturbances. Both goals may be achieved by means of the chosen controller in the next section.

3 Control System Design

This section presents the proposed optimal direct adaptive model-free control (ODAMFC) strategy for controlling the attitude TRMS angles, θ_i for $i \in \{v, h\}$. The control structure is made by two independent parallel control loops for the vertical and horizontal subsystems where the interconnections between them are considered as model uncertainties or disturbances. Each control loop is performed into two steps. In the first step, a direct adaptive model-free control (DAMFC) law is developed for the two subsystems using Legendre polynomials (LP). In the second step, the accelerated PSO meta-heuristic algorithm is introduced to find the optimal design parameters of the DAMFC law that are then applied to the DC motors of the main and tail rotors. The closed-loop structure of the TRMS control system is shown in Fig. 2. First, let us define the reference signal vectors x_i^* and the tracking error vectors e_i as

$$\begin{cases} e_i = x_i^* - x_i \ for \ i = v, h; \\ with \ x_i^* = \begin{bmatrix} \theta_i^*, \Omega_i^*, \sigma_i^* \end{bmatrix}^T = \begin{bmatrix} \theta_i^*, \dot{\theta}_i^*, \ddot{\theta}_i^* \end{bmatrix}^T. \end{cases} \quad (7)$$
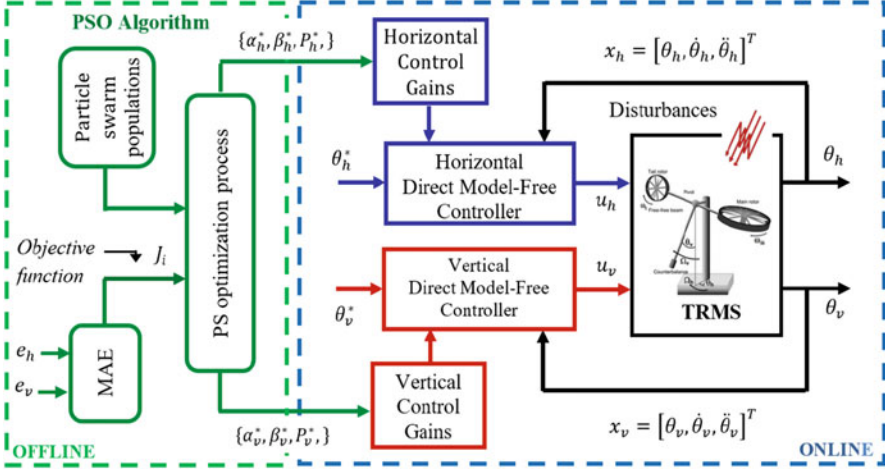
Fig. 2 Block diagram of the proposed optimal direct model-free control scheme

From (4) and (7), the error dynamics is defined by the following equations:

$$\begin{cases} \dot{e}_{i,1} = e_{i,2}; \\ \dot{e}_{i,2} = e_{i,3}; \\ \dot{e}_{i,3} = \ddot{\theta}_i^* - \mathcal{F}_i(x_i) - \mathcal{G}_i(x_i)u_i(t) - \mathcal{R}_i(x, t). \end{cases} \tag{8}$$

Using feedback linearization technique, the control law takes the form

$$u_i^* = \mathcal{G}_i(x_i)^{-1} \left[-\mathcal{F}_i(x_i) + \ddot{\theta}_i^* + K_i^T e_i \right], \tag{9}$$

where $K_i = \begin{bmatrix} k_{i,1}, k_{i,2}, k_{i,3} \end{bmatrix}^T$ are gain vectors designed to have a stable closed-loop system, i.e., $e_i \to 0$ when $t \to 0$. The control objective can be obtained with (9) if the functions $\mathcal{F}_i$ and $\mathcal{G}_i$ are known exactly and the TRMS subsystems are free of disturbances, $\mathcal{R}_i = 0$. To deal with the nonlinear problems, traditionally the proposed works in the literature use neural networks and/or fuzzy networks to estimate directly or indirectly the ideal control law u_i^*. Despite their universal approximation property and linear parameterization, these approaches increase the computational burden of the controller that can lead to the convergence problem and consequently limits their applicability in real time. As a solution in this chapter, we have employed LP to replace (9) by a simple robust controller.

3.1 Direct Adaptive Model-Free Control

The LPs are approximation techniques used in general for uncertainty estimation. They have simple structures and few tuning parameters and can approximate continuous-time functions with an arbitrary accuracy. In our case, a direct adaptive control of TRMS using LP is developed, in which the ideal control law (10) is replaced by its LP approximation as follows [18]:

$$u_i^* = \varphi_i^T(z_i(t))\pi_i^*(e_i) + \varepsilon_i(t), \tag{10}$$

where $\varphi_i^T = \left[\varphi_{i,0}(z_i), \ldots, \varphi_{i,m}(z_i)\right]^T$ are the vectors of Legendre functions in which $z_i(t)$ are the time functions chosen by the user to be mutually orthogonal on the interval $[-1, 1]$. In our case, they are chosen as $z_i(t) = \sin(2t)$. The elements of ϕ_i are calculated from the following orthogonal basis algorithm [18]:

$$\begin{cases} \varphi_{i,0}(z_i) = 1 \\ \varphi_{i,1}(z_i) = z_i \\ (j+1)\varphi_{i,j+1}(z_i) = (2j+1)\varphi_{i,j}(z_i) - j\varphi_{i,j}(z_i) \quad for \quad j = 1, \ldots, m-1, \end{cases} \tag{11}$$

where $\pi_i^* = \left[\pi_{i,0}^*, \ldots, \pi_{i,m}^*\right]^T$ are the optimal Legendre coefficients minimizing the approximation errors $\varepsilon_i(t)$ that are assumed small and bounded according to the theory of the universal approximation, i.e., $|\varepsilon_i(t)| < \varepsilon_{i0}$, for $\varepsilon_{i0} > 0$ and $t > 0$, since π_i^* are unknown and hence u_i^* cannot be computed explicitly according to (10). The convergence of the tracking errors e_i is influenced by the approximation errors and the disturbances. The control law (10) is approximated by

$$u_i = \varphi_i^T(z_i)\hat{\pi}_i(e_i) + u_{ri}(t), \tag{12}$$

where $\hat{\pi}_i$ are the estimation of π_i^*, and u_{ri} are the robust control terms that should be designed to deal with the disturbances and approximation errors. From (8), (9), and by expliciting (12), the error equations of the closed-loop TRMS become

$$\dot{e}_i(t) = \left(\Lambda_i - \Gamma_i K_i^T\right) e_i(t) + \Gamma_i \psi_i(t) \tag{13}$$

with $\Lambda_i = \begin{bmatrix} 0 & 1 & 0 \\ 0 & 0 & 1 \\ 0 & 0 & 0 \end{bmatrix}$, $\Gamma_i = \begin{bmatrix} 0 \\ 0 \\ 1 \end{bmatrix}$ and

$$\psi_i = \mathcal{G}_i(x_i) \left[\varphi_i^T(z_i)\tilde{\pi}_i(e_i) - u_{ri} + \mathcal{D}_i(x, t)\right], \tag{14}$$

where $\mathcal{D}_i(x, t) = \varepsilon_i(t) - \mathcal{G}_i^{-1}(x_i)\mathcal{R}_i(x, t)$ and $\tilde{\pi}_i = \pi_i^* - \hat{\pi}_i$ are the estimation errors.

To investigate the stability of the overall TRMS control system, the Lyapunov method is used with the following assumptions:

Assumption 1 According to [11], the control gains are positive and bounded on all the operating space as $0 < \mathcal{G}_i(x_i) < \mathcal{G}_{i0}$, where $\mathcal{G}_{i0}$ are positive constants.

Assumption 2 There exist positive definite matrices P_i and Q_i for horizontal and vertical subsystems, such as $P_i \left(\Lambda_i - \Gamma_i K_i^T \right) + \left(\Lambda_i - \Gamma_i K_i^T \right)^T P_i = -Q_i$.

Theorem 1 *Consider the TRMS system (4) with the proposed DAMFC law (12). The closed-loop signals are bounded, and the tracking errors e_i asymptotically converge to zero if Assumptions 1 and 2 are satisfied and*

$$\dot{\hat{\pi}}_i = \alpha_i e_i^T P_i \Gamma_i \varphi_i (z_i) \tag{15}$$

$$u_{ri} = \hat{\mathcal{D}}_i sgn \left(e_i^T P_i \Gamma_i \right), \ \dot{\hat{\mathcal{D}}}_i = \beta_i \left| e_i^T P_i \Gamma_i \right|, \tag{16}$$

where sgn(.) denotes the sign function replaced in simulations by tanh(.) to avoid chattering problem, $\hat{\mathcal{D}}_i$ are the estimates of $\mathcal{D}_i$, and α_i and β_i are the positive constants.

The stability analysis of the proposed controller has been analyzed and given in [19]. It is established based on rigorous proof that leads to imply that the signals e_i, $\dot{e}_i$, $\tilde{\pi}_i$, and $\tilde{\omega}_i$, and u_i are bounded. Furthermore, e_i and $\dot{e}_i$ for $i \in \{v, h\}$ converge asymptotically to zero when $t \to \infty$.

Remark 1 From a practical point of view, these assumptions are reasonable and acceptable. Assumption 1 is standard for system control designing, and it is made to ensure the controllability of TRMS system (4). This assumption is proved in [11], in which the knowledge of precise value of upper bounded $\mathcal{G}_{i0}$ is not necessary for developing our controller. The Lyapunov equation in Assumption 2 is quite natural and is common in the robust nonlinear control literature to prove the stability of closed-loop system. It also allows to find the tuning parameters so that $\Lambda_i - \Gamma_i K_i^T$ in (13) are Hurwitz matrix and the tracking errors converge exponentially to zero.

3.2 Optimal Control Based on Accelerated PSO

From the laws given by (15) and (16), it is clear that the TRMS performances are influenced by the setting parameters α_i, β_i, and P_i for $i \in \{v, h\}$. So, we propose an accelerated PSO algorithm for autonomous tuning and to find the best values, i.e., α_i^*, β_i^*, and P_i^*. The goal is to make maximum performances even with changing the reference trajectory. To describe the process of the accelerated PSO algorithm, let us put $\rho_\mu(t) \in \{\alpha_v, \beta_v, P_v, \alpha_h, \beta_h, P_h\}$ as a position vector and $v_\mu(t)$ as a velocity vector of the particle μ. The new velocity vector $v_\mu(t + 1)$ is defined through the current global best $G = \min \left\{ J \left(\rho_\mu(t) \right) \right\}$ as [20]:

Algorithm 1 Pseudocode of the acceleration PSO

Objective cost function Min J_i for $i \in \{v, h\}$
Initialize ρ_μ and v_μ with random solution.
Find the best position G^* in the initial population, at $t = 0$.
while t < Max Generation **do**
    Generate new velocities $v_\mu(t + 1)$ using eq (17)
    Generate new locations $\rho_\mu(t + 1)$ using eq (18)
    Evaluate objective functions $J(\rho(t + 1))$ using eq (19)
    Rank the swarms and find the current best solution S^*.
end while
Final result optimal output ($\rho_\mu^* \in \{\alpha_i^*, \beta_i^*, P_i^*\}$)

$$v_\mu(t+1) = w v_\mu(t) + \gamma_t(\epsilon - 1/2) + C_1 r_1 \left(\rho_\mu^* - \rho_\mu(t)\right) + C_2 r_2 \left(G - \rho_\mu(t)\right), \quad (17)$$

where $\epsilon \in [0, 1]$ is a random variable, $\gamma_t = \gamma_0 e^{-\lambda t}$ the cognition decreasing function with $\gamma_0 = 0.5, 0 < \lambda < 1$, w is the inertia weight, C_1 and C_2 represent the cognition learning and the social learning factors, respectively, and $r_1, r_2 \in [0, 1]$ are generated random numbers. The new position is then computed as

$$\rho_\mu(t + 1) = \rho_\mu(t) + v_\mu(t + 1). \quad (18)$$

The optimal required parameters must minimize the mean absolute error (MAE) as a fitness function J_i

$$J_i = \frac{\sum_{j=1}^{N} \left(\theta_i^* - \theta_i\right)}{N}, \quad (19)$$

where j^{th} is a sampling time and N is the sampling size. Also, it can be seen from (1) and (2) that the main and tail subsystems have the same dimension. So, we propose to consider the global objective function during the optimization process as $J = \sum_{i \in \{v,h\}} J_i/2$. The main steps of accelerated PSO process applied to the TRMS are summarized in Algorithm 1.

4 Simulation Results

To show the performance of the proposed control scheme, numerical simulation tests on the phenomenological model of the TRMS system are carried out for different reference signals in regulation and tracking problems. All tests are performed using the same initial states $x_v = [-0.63, 0, 0]^T$ and $x_h = [0, 0, 0]^T$, which represent the static equilibrium point at rest. The robustness against external disturbances is evaluated with external force applied to the system from $t = 40$ s. to $t = 100$ s. For both horizontal and vertical controllers, the parameters of the accelerated PSO algo-
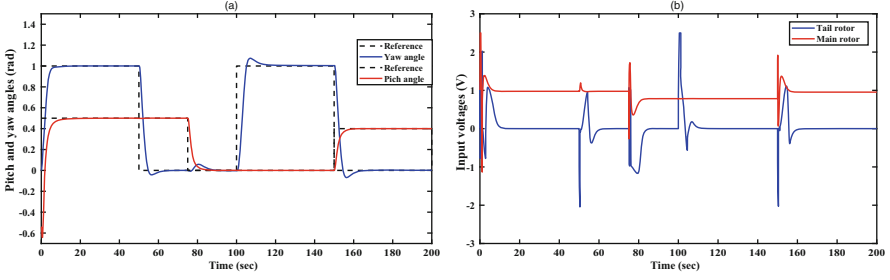
Fig. 3 Simulation results for square wave references. (**a**) Pitch and yaw angles (θ_v,θ_h), (**b**) main and tail input voltages (u_v, u_h)
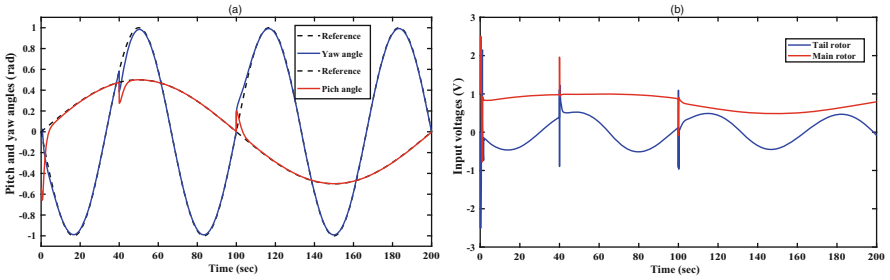
Fig. 4 Simulation results for sin wave references. (**a**) Pitch and yaw angles (θ_v,θ_h), (**b**) main and tail input voltages (u_v, u_h)

rithm are chosen as: swarm size $n = 10$, $w = 2$, $C_1 = 2$, $C_2 = 2$ and the number of iterations is set to 100. The optimal values minimizing MAE are $\alpha_v^* = 0.1682$, $\beta_v^* = 0.8891$, $\alpha_h^* = 0.0686$, $\beta_h^* = 0.9997$, $Q_v^* = diag\,\{62.6771; 20.0237; 5.0053\}$, and $Q_h^* = diag\,\{205.6015; 200.3968; 10.0657\}$.

By solving the Lyapunov equation for $K_v = K_h = [1, 2.24, 1.89]^T$, we can compute P_v^* and P_h^*. These values have been determined through offline simulation tests, and they work well under all conditions.

The simulation results for the two scenarios are sketched in Figs. 3 and 4. Figure 3 shows the responses of the control system according to square reference signals for pitch and yaw angles. Figure 4 depicts the performance of the controller for sine reference signals with disturbance injections. From the results, it is evident that the proposed control scheme leads to excellent tracking performance, despite the presence of nonlinearities and cross-coupling effects in TRMS device. The input control voltages do not show any chattering phenomenon and saturation, while the occurrence of peaks represents the transient of the adaptation to compensate the sudden change of TRMS angles and disturbances injection. Besides, the control input signal of each subsystem is computed only from local measurements without the knowledge of the precise dynamic model.

5   Conclusions

The results of this chapter can be summarized as follows. First, the extracted TRMS model is decoupled into vertical and horizontal subsystems. Then, for each subsystem, a DAMFC law is designed using LP to drive the TRMS to the desired position trajectory with null steady-state errors. Finally, the design parameters of DAMFC are tuned by using accelerated PSO algorithm to find optimal control law that leads to best performances. This approach does not require a prior knowledge of the model, it is simple to implement, and it deals with unknown dynamics system, coupling effects, and external disturbances. The simulation results show that the proposed controller improves the overall tracking performance and robustness of TRMS control system. In future, the controller will be tested on a real device dealing with the time discretization and the limits of the control saturation.

Funding

References

1. D.M. Ezekiel, R. Samikannu, O. Matsebe, Pitch and Yaw Angular Motions (Rotations) Control of the 1-DOF and 2-DOF TRMS: A Survey. Arch Computat Methods Eng 28, 1449–1458 (2021). https://doi.org/10.1007/s11831-020-09423-3.
2. N.M.H. Norsahperi, K.A. Danapalasingam, Particle swarm-based and neuro-based FOPID controllers for a twin rotor system with improved tracking performance and energy reduction. ISA Trans. **102**, 230–244 (2020)
3. D. Sain, S.K. Swain, A. Saha, S.K. Mishra, S. Chakraborty, Real-time performance analysis of FOI-PD controller for twin rotor MIMO system. IETE Tech. Rev. **36**(6), 547–567 (2019)
4. T. Dogruer, N. Tan, Decoupling control of a twin rotor MIMO system using optimization method, in *11th International Conference on Electrical and Electronics Engineering (ELECO)*, Bursa (2019), pp. 780–784
5. S.K. Pandey, J. Dey, S. Banerjee, Design of optimal PID controller for control of twin rotor MIMO system (TRMS), in *Advances in Power and Control Engineering. Lecture Notes in Electrical Engineering* (Springer, Singapore, 2020), pp. 93–106
6. Ayush, H. Prabha, R. Kumar, Robust H_∞ control approach for trajectory tracking of twin rotor MIMO system, in *International Conference on Emerging Trends in Communication, Control and Computing (ICONC3)* (Lakshmangarh, Sikar, 2020), pp. 1–4
7. O. Castillo, F. Kutlu, O. Atan, Intuitionistic fuzzy control of twin rotor multiple input multiple output systems. J. Intell. Fuzzy Syst. **38**(1), 821–833 (2020)
8. S.K. Valluru, M. Singh, Ayush, A. Dharavath, Design and experimental implementation of multi-loop LQR, PID, and LQG controllers for the trajectory tracking control of twin rotor MIMO system, in *Intelligent Communication, Control and Devices, Advances in Intelligent Systems and Computing* (Springer, Singapore, 2020), pp. 599–608

9. Y. Coskunturk, Design of a robust controller using sliding mode for two rotor aerodynamic system. Int. J. Innov. Techn. Int. Discip. Sci. **2**(2), 119–132 (2019)
10. A.J. Humaidi, A.F. Hasan, Particle swarm optimization-based adaptive super-twisting sliding mode control design for 2-degree-of-freedom helicopter. Meas. Control **52**(9–10), 1403–1419 (2019)
11. A. Chelihi, M. Chemachema, Model reference adaptive control for twin rotor multiple-input and multiple-output system via minimal controller synthesis. Proc. Instit. Mech. Eng. Part I J. Syst. Contr. Eng. **228**(6), 406–418 (2014)
12. Y.A. Younes, A. Rabhi, H. Al-Wedyan, Intelligent controller design for MIMO systems using model-free control and LMI approaches applied on a twin rotor MIMO system, in *2019 Advances in Science and Engineering Technology International Conferences (ASET)*, Tokyo (2019), pp. 1–6
13. R.-C. Roman, R.-E. Precup, M.-B. Radac, Model-free fuzzy control of twin rotor aerodynamic systems, in *2017 25th Mediterranean Conference on Control and Automation (MED)*, Valletta (2017), pp. 559–564
14. R.-C. Roman, M.-B. Radac, R.-E. Precup, Multi-input-multi-output system experimental validation of model-free control and virtual reference feedback tuning techniques. IET Contr. Theory Appl. **10**(12), 1395–1403 (2016)
15. Feedback Instruments Limited: Twin Rotor MIMO System. Advanced teaching manual (33-007-04M5). Crowborough, E. Sussex (1998)
16. S. Miah, M.R. Kafi, H. Chaoui, Generalized cascaded control technology for a twin-rotor MIMO system with state estimation. J. Contr. Auto. Elect. Syst. **30**(2), 170–180 (2019)
17. P. Witczak, M. Witczak, J. Korbicz, Ch. Aubrun, A robust predictive actuator fault-tolerant control scheme for Takagi-Sugeno fuzzy systems. Bull. Pol. Acad. Sci. Tech. Sci. **63**(4), 977–987 (2015)
18. R. Zarei, S. Khorashadizadeh, Direct adaptive model-free control of a class of uncertain nonlinear systems using Legendre polynomials. Trans Inst. Meas. Contr. **41**(11), 3081–3091 (2019)
19. H.E. Glida, L. Abdou, A. Chelihi, C. Sentouh, Optimal direct adaptive fuzzy controller based on bat algorithm for UAV quadrotor, in *2019 8th International Conference on Systems and Control (ICSC)*, Marrakesh (2019), pp. 52–57
20. X.-S. Yang, *Nature-Inspired Optimization Algorithms* (Elsevier, Amsterdam, 2014)

Dynamics and Performance Analysis of a Nonlinear Energy Sink with Geometric Nonlinear Damping

Rony Philip, B. Santhosh, and Bipin Balaram

1 Introduction

Performance of linear dampers is limited under certain conditions such as detuning effect of tuned mass dampers under non-stationary excitations and at high velocities when excessive damping forces are generated [1]. In the absence of a generic computational framework and the difficulty with comprehending complex dynamics, the conventional design techniques ignored the impact of nonlinearity. With the advancement in computational technology, efficient algorithms, and experiments, there is a paradigm shift in the conventional thought process and it leads to a new research direction "Exploiting the nonlinear behavior in physical systems to improve its performance." Nonlinear vibration absorbers have been recognized to be able to efficiently absorb and disperse the vibration energy of the primary structure over a frequency band and have been extensively used in different engineering applications [2].

Over the last two decades, it has been shown that nonlinear energy sink (NES), which is an essentially nonlinear element, when attached to a vibrating system can provide a unidirectional flow of energy through targeted energy transfer (TET) [3]. NES has been used widely in engineering applications from vibration suppression and isolation to harvesting energy, due to their exceptional properties and robustness [4]. To study the harmonically excited NES system, Gendelman et al. [5, 6] suggested a standardized analysis and numerical procedure. In [7, 8], Gendelman et al. revealed that there is a response regime near the 1:1 resonance termed as strongly modulated response (SMR), which can be described as a jump between two stable branches in a slow invariant manifold (SIM). A SIM is developed using

R. Philip · B. Santhosh (✉) · B. Balaram
Department of Mechanical Engineering, Amrita School of Engineering, Amrita Vishwa
Vidyapeetham, Coimbatore, India
e-mail: b_santhosh@cb.amrita.edu; b_bipin@cb.amrita.edu

the complex-averaging (CX-A) methodology by partitioning between slow and fast dynamics, leading to a reduced-order system dynamics. The SIM topology is used to predict the NES response in all of the above studies. The NES is very sensitive to the excitation amplitude. Most of the previous studies were mainly based on NES with linear viscous damping [9, 10].

Later studies that examine the dynamics of NES with both nonlinear damping and stiffness reveal that the inclusion of nonlinearity in damping will lead to complex dynamics, like transient disturbance. In most cases, geometric nonlinear damping NES has been used because these nonlinear damping conditions can be easily fabricated and physically realized through the geometry of the deformation of linear components. The transient instability induced by nonlinear damping results in a strong energy transfer facilitates its use in various applications, such as vibration isolation, energy localization, and energy harvesting. It was also observed that the NES with a nonlinear damper could provide better energy absorption of the main structure than that of a linear viscous damper. Andersen et al. [11] investigated the dynamics of a coupled oscillator model for strong nonlinear stiffness and damping, and a continuous vibration dispersion phenomenon was noted. Previous studies showed that the nonlinear damping, which is normally ignored in most research, has a crucial role in vibrating systems with NES. However, the previous studies were concentrated on single-degree-of-freedom systems, and limited works were carried out on multi-degree-of-freedom systems.

In this chapter, the work is extended to the study of two-degree-of-freedom systems with a NES, coupled with a nonlinear damping mechanism, and is investigated analytically and numerically to reveal the dynamics, including the evolution of the different energy transfer regimes involved in the system. In Sect. 2, the equations of motion in the non-dimensional form are derived, and an analytical study by the complex-averaging method is explained. The dynamics of the NES with nonlinear damping is discussed in Sect. 3. The complex response regimes in slow and fast dynamics are described in Sect. 4. Section 5 offers a comparison of the performance of a system with NES having linear and nonlinear damping using the harmonic balance method.

2   Problem Formulation

2.1   Modeling

In this section, a harmonically excited linear oscillator consisting of masses m_i, linear springs k_i, and dampers c_i ($i = 1, 2, 3$) with an NES absorber attached to the mass m_1 as shown in Fig. 1 is considered. The NES is induced by cubic nonlinear stiffness (k_n) and geometric nonlinear damping (c_n). Geometrically nonlinear damping is in the form $c_n (x_1 - x_3)^2 (\dot{x}_1 - \dot{x}_3)$. A thorough understanding of this form of geometric nonlinear damping by two linear viscous dampers was given

Fig. 1 Model of 2-dof oscillator with NES
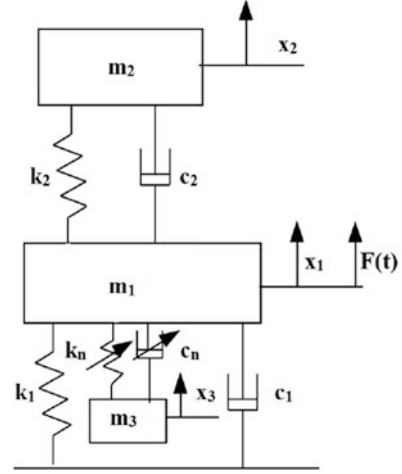
by Andersen et al. [11]. The equations of motion of this system can be expressed in a non-dimensional form by defining the following non-dimensional parameters: $\mu_i = \frac{m_i}{m_1}$, $\beta_i = \frac{k_i}{k_1}$, $\zeta_i = \frac{c_i}{m_1\omega_1}$, $\beta_n = \beta_3 X_{st}^2$, $\zeta_n = \zeta_3 X_{st}^2$, $f = \frac{F}{k_1 X_{st}}$, $\omega = \frac{\Omega}{\omega_1}$, $\tau = \omega_1 t$, $X_{st} = \frac{F}{k_1}$. The non-dimensional equations of motion are given by

$$\ddot{x}_1 + x_1 + \zeta_1 \dot{x}_1 + \beta_2 (x_1 - x_2) + \zeta_2 (\dot{x}_1 - \dot{x}_2) + \beta_n (x_1 - x_3)^3$$

$$+ \zeta_n (\dot{x}_1 - \dot{x}_3)(x_1 - x_3)^2 = f \cos(\omega\tau)$$

$$\mu_2 \ddot{x}_2 + \beta_2 (x_2 - x_1) + \zeta_2 (\dot{x}_2 - \dot{x}_1) = 0 \tag{1}$$

$$\mu_3 \ddot{x}_3 + \zeta_n (\dot{x}_3 - \dot{x}_1)(x_3 - x_1)^2 + \beta_n (x_3 - x_1)^3 = 0.$$

The system undergoing study is assumed to be in the nearby area of 1:1 resonance, where the excitation force frequency is near the eigenfrequency of the primary oscillator.

2.2 Analytical Study Using Complex Averaging

The complex-averaging method (CX-A) [9] is used to determine the analytical approximation for the system dynamics. It is difficult to explore directly Eq. (1), to understand the system dynamics. The two assumptions in Eq. (2) are as follows: the dynamics of the system are studied in the vicinity of the fundamental transient resonance; hence, the fast frequency for all three masses is ω and the excitation amplitudes considered are low-to-medium energy levels [12].

$$\psi_j = \dot{x}_i + i\,\omega\,x_i. \tag{2}$$

Introducing new complex variables [13] and substituting Eq. (2) as $\psi_j = \phi_i e^{i\omega t}$, $j = 1, 2, 3$, across the fast time scale, Eq. (1) can be averaged. It yields

$$\dot{\phi}_1 + \frac{i\,\phi_1\,(\omega^2 - 1)}{\omega} + \frac{\zeta_1\,\phi_1}{2} - \frac{i\beta_2\,(\phi_1 - \phi_2)}{2\omega} + \frac{\zeta_2\,(\phi_1 - \phi_2)}{2}$$

$$+ \frac{\zeta_n\,(\phi_1 - \phi_3)^2\,(|\,\phi_1 - \phi_3\,|)}{8\,\omega^2} - \frac{3i\,\beta_n\,|\,\phi_1 - \phi_3\,|\,(\phi_1 - \phi_3)^2}{8\,\omega^3} = f/2$$

$$\mu_2\,\dot{\phi}_2 + \frac{i\,\mu_2\,\omega\,\phi_2}{2} + \frac{i\,\beta_2\,(\phi_1 - \phi_2)}{2\omega} - \frac{\zeta_2\,(\phi_1 - \phi_2)}{2} = 0 \qquad (3)$$

$$\mu_3\,\dot{\phi}_3 + \frac{i\,\mu_3\,\omega\,\phi_3}{2} - \frac{\zeta_n\,(\phi_1 - \phi_3)^2\,|\,\phi_1 - \phi_3\,|}{8\,\omega^2} + \frac{3i\,|\,\phi_1 - \phi_3\,|\,\beta_n\,(\phi_1 - \phi_3)^2}{8\,\omega^3} = 0.$$

Now another set of new variables u, v, and w are introduced into Eq. (3). Define $u = \phi_1 - \phi_2$, $v = \phi_1 - \phi_3$, and $w = \phi_1 + \mu_2\,\phi_2 + \mu_3\,\phi_3$. The differential equations in new variables u, v, and w can now be derived from Eq. (3) and are given below

$$\dot{u} + \frac{\zeta_1\,(w + \mu_2 u + \mu_3 v)}{2\,(1 + \mu_2 + \mu_3)} + \frac{u\,(1 + \mu_2)\,(\zeta_2\,\omega - i\,\beta_2)}{2\,\mu_2\,\omega} - \frac{i\,(w + \mu_2 u + \mu_3 v)}{2\,(1 + \mu_2 + \mu_3)\,\omega}$$

$$+ \frac{i\,\omega\,u}{2} + \frac{(\zeta_n\,\omega - 3i\,\beta_n)\,v^2\,|\,v\,|}{8\omega^3} = \frac{f}{2}$$

$$\dot{v} + \frac{\zeta_1\,(w + \mu_2 u + \mu_3 v)}{2\,(1 + \mu_2 + \mu_3)} + \frac{(\zeta_2\,\omega - i\beta_2)\,u}{2\,\omega} - \frac{i\,(w + \mu_2 u + \mu_3 v)}{2\,(1 + \mu_2 + \mu_3)\,\omega}$$

$$+ \frac{i\,\omega\,v}{2} + \frac{(1 + \mu_3\,(\zeta_n\omega - 3\,i\beta_n))\,v^2\,|\,v\,|}{8\,\mu_3\omega^3} = \frac{f}{2} \qquad (4)$$

$$\dot{w} + \frac{\zeta_1\,(w + \mu_2\,u + \mu_3\,v)}{2\,(1 + \mu_2 + \mu_3)} - \frac{i\,(w + \mu_2 u + \mu_3 v)}{2\,(1 + \mu_2 + \mu_3)\,\omega} + \frac{i\,\omega\,w}{2} = \frac{f}{2}.$$

Equation (4) is known as the averaged flow of the system shown in Fig. 1.

3 Dynamics of the NES with Nonlinear Damping

In this section, the dynamics introduced in the system due to the inclusion of nonlinear damping element in the NES, which helps to identify the evolution of the different energy transfers in the system, is discussed. It is possible to incorporate slow time-scale variables in time and to define different energy transfers that occur among the primary oscillator and the NES using Eq. (4). The time-series plot of
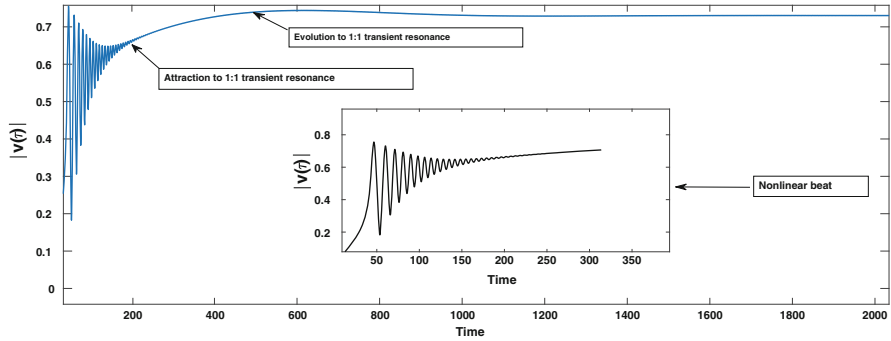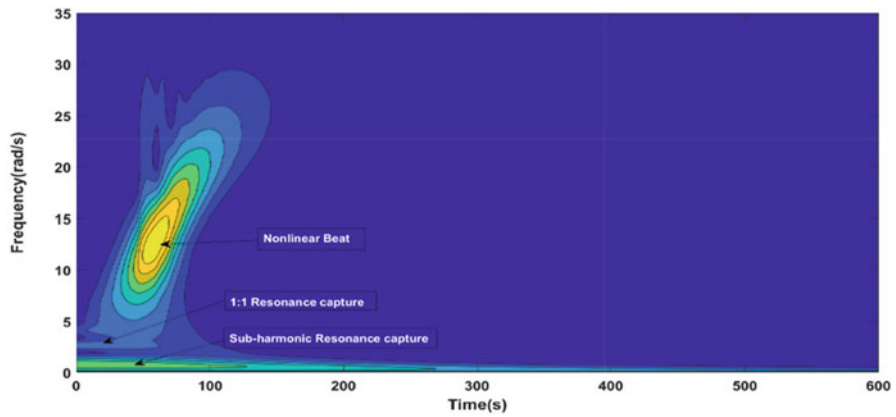
Fig. 2 Evolution of $| \, v(\tau) \, |$

Fig. 3 Wavelet spectrum of the system

$| \, v(\tau) \, |$ for a specific set of model parameters $\zeta_1 = 0.009, \zeta_2 = 0.06, \zeta_n = 0.01, \beta_2 = 1.1429, \beta_n = 0.15, \mu_2 = 0.2, \mu_3 = 0.04$, and $f = 0.0159$ is shown in Fig. 2. Since the fundamental resonance capture and sub-harmonic orbits energy transfer regimes cannot be directly triggered by the excitation force, there is a nonlinear beat phenomenon that occurs at the initial stages of the response that helps the system to get captured into 1:1 transient resonance and eventually transfers all energies to NES.

Figure 3 shows the wavelet spectrum of the relative response. After the preliminary high-frequency nonlinear beat phenomenon, the damped dynamics adopt the 1:1 resonance branch as energy decreases as a result of the action of the damping components. Shortly after the initial 1:1 resonance capture, the system settles itself into a sub-harmonic resonance capture state. During this complex transition, the primary masses oscillate mostly with its own natural frequency, and the existence of lower frequencies in the wavelet spectrum is mainly due to the oscillation of the NES. It is found that this transformation is due to the nonlinear damping present in

the NES. Though these transitions were observed for the NES with only nonlinear stiffness, it is evident from Figs. 2 and 3 that in this case the geometric nonlinearity in damping triggers the transition and changes the system's dynamic behavior even without triggering any of the impulsive orbits of the system.

4 Response Regimes (Slow Invariant Manifold)

The complex response regime in the system that arises due to the presence of strongly modulated response (SMR) and the transient orbits projected in the slow invariant manifold (SIM) is described in this section. Eq. (4) can be analyzed by the method of multiple scales with respect to a small parameter ϵ ($0 << \epsilon = \mu_3 << 1$). Define $u = u(\tau_0, \tau_1)$, $v = v(\tau_0, \tau_1)$, $w = w(\tau_0, \tau_1)$, $\tau_n = \epsilon^n \tau$, $\frac{d}{d\tau} = \frac{\partial}{\partial \tau_0} + \epsilon \frac{\partial}{\partial \tau_1}$ and $n = 0, 1$. Substituting in Eq. (4), equating the coefficients of ϵ^0, and making its time derivatives to zero lead to

$$\frac{\zeta_1 (w + \mu_2 u)}{2 (1 + \mu_2)} + \frac{(1 + \mu_2)(\zeta_2 \omega - i\beta_2) u}{2 \mu_2 \omega} + \frac{(\zeta_n \omega - 3 i\beta_n) v (|v|)^2}{8 \omega^3} - \frac{i (w + \mu_2 u)}{2 \omega (1 + \mu_2)}$$
$$+ \frac{i \omega u}{2} = \frac{f}{2}$$

$$\frac{\zeta_1 (w + \mu_2 u)}{2 (1 + \mu_2)} + \frac{(\zeta_2 \omega - i\beta_2) u}{2 \omega} + \frac{(2 + \mu_2)(\zeta_n \omega - 3 i\beta_n) v (|v|)^2}{8 \omega^3 (1 + \mu_2)} - \frac{i (w + \mu_2 u)}{2 \omega (1 + \mu_2)}$$
$$+ \frac{i \omega v}{2} = \frac{f}{2} \tag{5}$$

$$\frac{\zeta_1 (w + \mu_2 u)}{2 (1 + \mu_2)} - \frac{i (w + \mu_2 u)}{2 \omega (1 + \mu_2)} + \frac{i \omega w}{2} = \frac{f}{2},$$

where u, v, and w indicate the fixed points of the system. Eq. (5) can be simplified and combined in terms of w and v into a single equation of the form

$$\alpha_1 N_3{}^3 + \alpha_2 N_3{}^2 + \alpha_3 N_3 = N_1, \tag{6}$$

where $N_1 = | w^2 |$ and $N_3 = | v^2 |$; α_1, α_2, and α_3 are the coefficients of N_3. Such a SIM topology indicates that there exists SMR in the system near to its resonance frequency. It can also lead directly to relaxation oscillations. There are three solutions for Eq. (6) among which, two of them are stable and one is unstable with respect to time τ_0. Variations of system responses, where the jump phenomenon exists between the stable branches that are marked by firm lines, are shown in Fig. 4. However, this motion is only feasible unless the system is capable of reaching the boundary of stable branches when moving along the SIM about the slow time

Fig. 4 SIM topology of the system with nonlinear damping
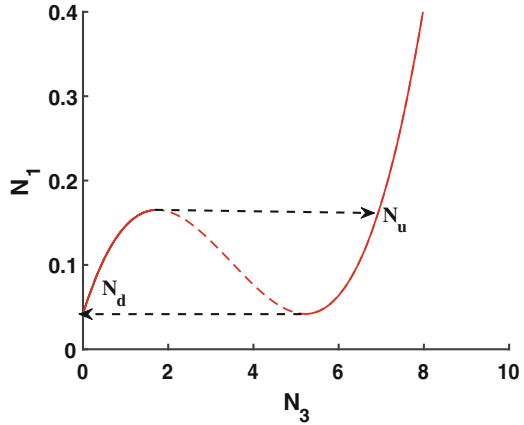
scale. A linearized analysis can obtain the stability of the branches, as described in previous works [8]. Thus, correctly to the approximation of the slow time scale, the dynamics will be drawn to any one of the stable branches. If the SIM has turning points, there seems to be a significant chance of jump phenomena as the orbits on the SIM encounter abrupt shifts among stable branches as shown by the black dashed lines where N_u and N_d in Fig. 4 represent the landing points on the SIM. This opens the way for forced dynamics relaxation oscillations and tends to create SMR. The indication of such SMRs is advantageous for the objective of vibration suppression of harmonically excited systems and energy localization from linear oscillators to the NES. It is clear from the SIM topology in Fig. 4 that the localization of energy to the NES takes place, where the NES oscillates with much higher amplitude than the primary system under consideration.

An illustration of SIM with NES having viscous damping and the one with nonlinear damping is shown in Fig. 5. The two different SIMs were plotted for a specific set of parameters $\zeta_1 = 0.009, \zeta_2 = 0.06, \zeta_n = 0.01, \beta_2 = 1.1429, \beta_n = 0.15, \mu_2 = 0.2, \mu_3 = 0.04$, and $f = 0.0159$. The comparison is made between normal NES and NES with nonlinear damping. The topological shape of the SIM for both NES looks similar, but the SIM for normal NES is larger and the unstable branch is pushed to the right.

The stable branches of NES with nonlinear damping shift slightly closer to each other compared to the normal NES. To determine the response, the orbital motion of the system is projected into the SIM as shown in Fig. 6. For the model described in Fig. 1, under harmonic excitation, the transient modulus of the primary mass and NES is defined as $N_1 = | (\dot{w} + i \, \omega \, w) \exp^{-i\omega \tau} |^2$ and $N_3 = | (\dot{v} + i \, \omega \, v) \exp^{-i\omega \tau} |^2$. Figure 6 clearly explains the difference in the dynamic behavior of the two types of NES. In normal NES, the horizontal orbits representing the projection of motion of the system clearly show that the system's motion is confined to one of SIM's stable branches. But in the case of NES with nonlinear damping, a quasi-periodic response is observed with both linear oscillator and NES

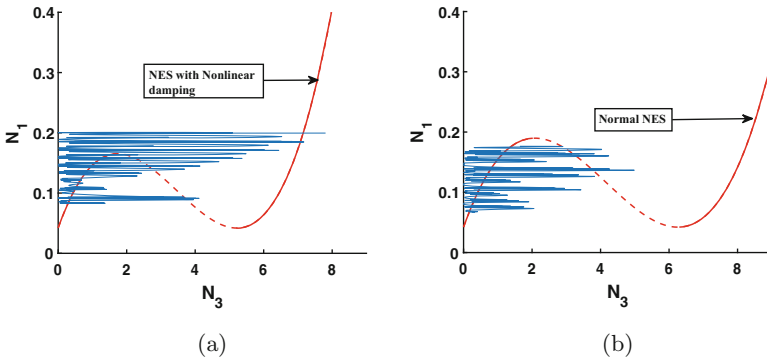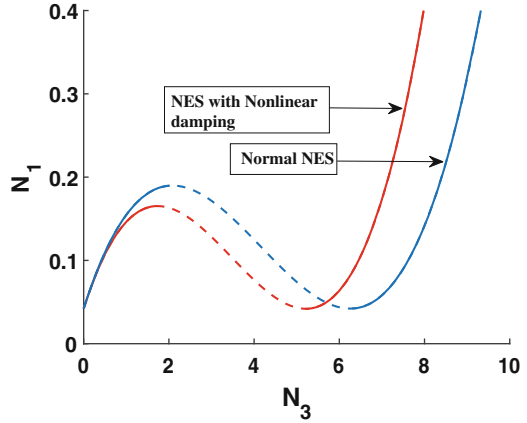**Fig. 5** Comparison of SIM topology for NDNES with NES

(a)

(b)

Fig. 6 Time–displacement response of linear oscillator and NES projected into SIM. (**a**) NES with nonlinear damping. (**b**) Normal NES

amplitudes. Even at low excitation amplitude, the system's orbital motion shows the jump phenomenon. This opens a way for relaxation oscillations to occur and leads to the SMR regime.

5 Periodic Solutions of the System

The method of harmonic balance is a semi-analytical approach that can generate the periodic solutions directly from the steady-state response of a system that are excited harmonically. Harmonic balance method (HBM) can be extended to nonlinear systems that are strongly nonlinear or discontinuous [14]. The method outlined in [15] is used here to obtain the periodic solution. To construct the frequency response of the system under consideration, HBM is used together with the arc-length continuation for $\zeta_1 = 0.009, \zeta_2 = 0.06, \zeta_n = 0.01, \beta_2 = 1.1429, \beta_n =$
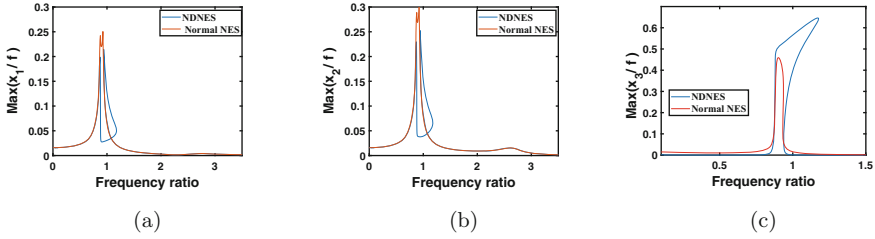
Fig. 7 Frequency response plot to compare the proposed NDNES with normal NES. (**a**) Frequency response plots of primary system amplitude. (**b**) Frequency response plots of the mass (m_2) amplitude. (**c**) Frequency response plots of the NES amplitude

0.15, $\mu_2 = 0.2$, $\mu_3 = 0.04$, and $f = 0.0159$. For comparison, the frequency response of the system with the normal NES and NES with nonlinear damping is shown in Fig. 7. The frequency response in Fig. 7a indicates that there are multiple stable periodic solutions and jump phenomenon at $\omega = 0.875$, which is nearer to the resonance frequency, where exactly the SMR regime occurs. It is evident from Fig. 7c that the energy from the main mass (m_1) is more efficiently transmitted to the NES with nonlinear damping. This effective localization of energy is due to the occurrence of relaxation oscillations leading to the SMR regime as discussed in Sect. 4. In the frequency response of the NES, it also appears that the NES with nonlinear damping has high amplitudes not only at the near-resonance frequency but even after it the NES with nonlinear damping has carried forward with a higher amplitude value. It is due to the motion of the system crosses the boundary of the low-amplitude stable branch when moving along the SIM, it jumps to the N_u point, which is on the high-amplitude stable branch, and it continues its motion on that branch until it crosses the next jump point to the low-amplitude branch of the SIM (Fig. 4). In the case of normal NES, the energy is transferred only at the neighborhood of resonance frequency, and the displacement amplitude of the NES is much lower than the NES with nonlinear damping as shown in Fig. 7c. It means that in normal NES the energy transmitted from mass m_1 to m_2 is relatively greater than to the NES and clearly visible in Fig. 7b.

6 Conclusions

In this chapter, using a combination of analytical and numerical approaches, a framework for the computation of system parameters leading to the efficient transfer of energy in a two-degree-of-freedom system with geometric damping is discussed. The results obtained from the dynamics of the system with nonlinear damping show that nonlinear damping can lead to different bifurcations and response regimes. The SMR and SIM topologies also explain the formation and dynamic behavior of the system. The SMR of the system under study paves the way for relaxation

oscillations that lead to the effective energy transfer to the NES from the main structure. Analytical approximations of the dynamics governing the evolution of the energy transfer due to resonance capture have been determined by complex-averaging method. This chapter shows that NES with nonlinear damping results in higher energy transfer from the linear oscillator to the NES compared to the standard NES that signals the potential for various applications. The findings also show that even at low excitation amplitude, the NES with nonlinear damping is superior to the standard NES in its efficiency and robustness.

References

1. M.F. Daqaq, R. Masana, A. Erturk, D.D. Quinn, On the role of nonlinearities in vibratory energy harvesting: a critical review and discussion. Appl. Mech. Rev. **66**(4) (2014)
2. D. Wagg, L. Virgin (eds.), *Exploiting Nonlinear Behavior in Structural Dynamics*, vol. 536 (Springer Science & Business Media, Berlin, 2012)
3. A.F. Vakakis, Inducing passive nonlinear energy sinks in vibrating systems. J. Vib. Acoust. **123**(3), 324–332 (2001)
4. Z. Lu, Z. Wang, Y. Zhou, X. Lu, Nonlinear dissipative devices in structural vibration control: a review. J. Sound Vib. **423**, 18–49 (2018)
5. O.V. Gendelman, Transition of energy to a nonlinear localized mode in a highly asymmetric system of two oscillators. Nonlin. Dyn. **25**(1–3), 237–253 (2001)
6. Y. Starosvetsky, O.V. Gendelman, Response regimes of linear oscillator coupled to nonlinear energy sink with harmonic forcing and frequency detuning. J. Sound Vib. **315**(3), 746–765 (2008)
7. O.V. Gendelman, E. Gourdon, C.-H. Lamarque, Quasiperiodic energy pumping in coupled oscillators under periodic forcing. J. Sound Vib. **294**(4–5), 651–662 (2006)
8. O.V. Gendelman, Y. Starosvetsky, M. Feldman, Attractors of harmonically forced linear oscillator with attached nonlinear energy sink I: description of response regimes. Nonlin. Dyn. **51**(1–2), 31–46 (2008)
9. Y.S. Lee, G. Kerschen, A.F. Vakakis, P. Panagopoulos, L. Bergman, D.M. McFarland, Complicated dynamics of a linear oscillator with a light, essentially nonlinear attachment. Phys. D Nonlin. Phenom. **204**(1–2), 41–69 (2005)
10. G. Kerschen, Y.S. Lee, A.F. Vakakis, D.M. McFarland, L.A. Bergman, Irreversible passive energy transfer in coupled oscillators with essential nonlinearity. SIAM J. Appl. Math. **66**(2), 648–679 (2005)
11. D. Andersen, Y. Starosvetsky, A. Vakakis, L. Bergman, Dynamic instabilities in coupled oscillators induced by geometrically nonlinear damping. Nonlin. Dyn. **67**(1), 807–827 (2012)
12. A. Tripathi, P. Grover, T. Kalmár-Nagy, On optimal performance of nonlinear energy sinks in multiple-degree-of-freedom systems. J. Sound Vib. **388**, 272–297 (2017)
13. L.I. Manevitch, The description of localized normal modes in a chain of nonlinear coupled oscillators using complex variables. Nonlin. Dyn. **25**(1–3), 95–109 (2001)
14. B. Santhosh, C. Padmanabhan, S. Narayanan, Numeric-analytic solutions of the smooth and discontinuous oscillator. Int. J. Mech. Sci. **84**, 102–119 (2014)
15. P.V.R. Raj, B. Santhosh, Parametric study and optimization of linear and nonlinear vibration absorbers combined with piezoelectric energy harvester. Int. J. Mech. Sci. **152**, 268–279 (2019)

Aeroelastic Dynamic Feedback Control of a Volterra Airfoil

Gianluca Pepe (iD)**, Elena Paifelman, and Antonio Carcaterra**

1 Introduction

Dynamic behavior analysis of the nonlinear aeroelastic system is one of the interesting topics among researchers that have been studied in recent years. Nonlinear airfoil instability and behavior analysis in subsonic flow are one of the main parts in this field. Aeroelastic systems are characterized by complex nonlinear phenomena due to structural oscillations coupled with the fluid dynamic. The coexistence of phenomena, such as limit cycle oscillation and chaotic vibrations induced by the fluid, can lead the dynamic systems to instability such as flutter which can decrease the system performance, as well as the damage of the structure itself.

Historically, the main approach to analyze the dynamic instability of nonlinear aeroelastic systems has been developed by Theodorsen [1] in the frequency domain. His theory aimed to model the aerodynamic loads on an airfoil when the wake releasing is considered as a memory effect on the global fluid-structure interaction dynamic. Wagner proposed a time-domain analysis where the memory effects are represented by convolution Volterra integrals [2]. Both these traditional models are linear, but, in many cases, the dynamic equations of an airfoil became nonlinear due to the presence of nonlinear elements (dampers, stiffness) or for the instabilities generated from the fluid-structure interaction. The nonlinear aerodynamic model in the time domain can be solved by numerical techniques or analytical methods. In the first case, the solutions such as the finite difference method, Runge–Kutta,

G. Pepe · A. Carcaterra (✉)
Department of Mechanical and Aerospace Engineering, Sapienza University of Rome, Rome, Italy
e-mail: gianluca.pepe@uniroma1.it; antonio.carcaterra@uniroma1.it

E. Paifelman
Italian National Research Council, Institute of Marine Engineering of Rome, Rome, Italy
e-mail: elena.paifelman@inm.cnr.it

and cyclic method were employed to solve differential equations of a nonlinear system. Moreover, analytical and semi-analytical solutions including describing function technique were used to analyze the instability of control surfaces of a wing with nonlinear stiffness [3]. In the last decade, different methods have been used to investigate nonlinear dynamic systems [4, 5], some, based on perturbation method and stochastic approach [6], have been developed to analyze nonlinear aeroelastic systems such as perturbation incremental or transformation point method and homotropy method [7, 8].

In the literature, several authors have provided extensive reviews about nonlinear control methods for the minimization of oscillations of elastic wings and aircraft; moreover, in recent years, many control strategies for flutter avoidance have been developed. Partial feedback linearization methodology was also applied to the design of nonlinear controllers for the nonlinear aeroelastic system [9]. The state-dependent Riccati equation (SDRE) method was developed for nonlinear control problems and used to design suboptimal control laws of nonlinear aeroelastic systems considering both quasi-steady [10] and unsteady aerodynamics. Recently, an output feedback and an adaptive decoupled fuzzy sliding-mode control laws have been implemented for suppressing flutter and reducing the vibrational level in the subcritical flight speed range [11]. Moreover, based on the tensor-product model transformation and the parallel distributed compensation, a control law for the prototypical aeroelastic wing section was designed and presented in [12].

This work aims to develop a novel variational optimal control strategy to control the aerodynamic behavior of an aerofoil which presents a memory effect from wake production. Integral memory terms, representing, in this case, the release of wake, are normally not included in variational control algorithms. From the control point of view, the Volterra models are solved through direct methods, discretizing the equations, and then the optimal problem is solved through nonlinear programming [11]. The proposed optimal control, called Proportional-Nth-order-Integral control, PI(N), fills this gap and it belongs to the category of Variational Feedback Controls (VFCs) [13–18]. The solution of the optimal problem is provided through a particular solution of Riccati's equation including the memory terms generated by the past system evolution [19, 20]. The structure of the control law shows how the optimal solution is related to the kernel function order, that is, of the Volterra integral typology.

Finally, the analytical solution PI(N) is tested on a prototypical wing and the numerical results show how is possible to reach the best performance of the proposed controller in comparison with the classical Linear Quadratic Regulator (LQR) method.

2 Mathematical Model of Wagner's Controlled Wing

Theodorsen's theory is widely used to achieve the mathematical model of the aerodynamic problem [1]. It provides the generalized unsteady aerodynamic forces
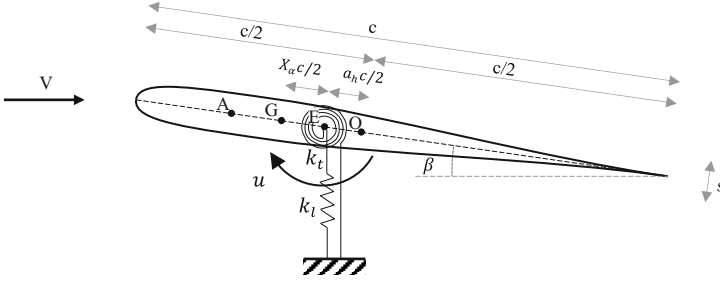
Fig. 1 Theodorsen's airfoil section geometry

due to an arbitrary motion of the airfoil, which generates a vortex wake. The time-domain counterpart of the Theodorsen's theory, formulated by Wagner [2], is considered in this work to formulate an optimal control law which includes Volterra's memory effects.

The engineering control application of a two-degree-of-freedom airfoil is here investigated, where the pitch degree of freedom is actively controlled.

The sketch in Fig. 1 shows the geometry of the typical Theodorsen airfoil section where the x-axis is chord-wise axis (positive towards the trailing edge) and E is the center of rotation. The airfoil is a simple two degree-of-freedom system, elastically constrained by a pair of springs, k_l and k_t, oscillating in plunge and pitch. The actuation force, u, is meant here as dimensionless torque applied on the pitch rotation degree-of-freedom β. By using standard notations, the nondimensional plunge deflection at the elastic center is denoted by w, while β represents the pitch motion. The elastic center, E, is located at a distance $OE = a_h c/2$ from the mid-chord (a_h is the dimensionless distance, considered with respect to the half-cord length, $c/2$, between the center of the foil O, and the elastic axis), while the mass center, G, is located at a distance $EG = x_\alpha c/2$. With these assumptions, the aeroelastic equations of the typical wing are:

$$\begin{cases} \ddot{w} + x_\alpha \ddot{\beta} + \Omega^2 w = -p(w, \beta) \\ \frac{x_\alpha}{r_\alpha^2} \ddot{w} + \ddot{\beta} + \beta = r(w, \beta) + u \end{cases} \tag{1}$$

where the overdot denotes differentiation with respect to a dimensionless time $\tau = \omega_\alpha t$; $\Omega = \omega_w/\omega_\alpha$ is the heave stiffness, being ω_w and ω_α the uncoupled natural frequencies of heave and pitch modes; $r_\alpha = \sqrt{4I_\beta/mc^2}$ is the dimensionless radius of gyration about the elastic axis and m, I_β, c are the mass, the moment of inertia per unit length with respect to the elastic center, and the wing chord. For an incompressible two-dimensional flow, Wagner defines the aerodynamic loads as the sum of two contributions [2]: (i) a linear composition of degree-of-freedom which represents the added mass, damping, and stiffness due to the fluid-structure interaction and (ii) a convolution term including the memory effects defined as follows:

$$p(w, \beta) = \frac{1}{\mu}\left(\ddot{w} - a_h\ddot{\beta} + U\dot{\beta}\right) + \frac{2U}{\mu}\int_{-\infty}^{t} K_W(t-\tau)\,\dot{\tilde{w}}_{3/4}(\tau)\,d\tau$$

$$r(w, \beta) = \frac{1}{\mu r_\alpha^2}\left[a_h\left(\ddot{w} - a_h\ddot{\beta}\right) - \frac{1}{2}U(1-a_h)\dot{\beta} - \frac{1}{8}\ddot{\beta}\right] \tag{2}$$

$$+ \frac{U(1+2a_h)}{\mu r_\alpha^2}\int_{-\infty}^{t} K_W(t-\tau)\,\dot{\tilde{w}}_{3/4}(\tau)\,d\tau$$

where p and r are the lift and pitching moment, respectively, $\mu = \pi\rho c^2/4m$ is the mass ratio, and $U = 2V/c\omega_\alpha$ is the dimensionless inflow velocity and V is the inflow velocity, oriented along the x-axis. The time-dependent known function $\tilde{w}_{3/4}(\tau) = \dot{w}(\tau) - \left(\frac{1}{2} - a_h\right)\dot{\beta}(\tau) + U\beta(\tau)$ and $K_W(t-\tau) = \sum_{k=1}^{N}\alpha_k e^{-\beta_k(t-\tau)}$ are the downwash and the Wagner function, respectively. Using a standard notation in control theory, by defining a new state vector $x = [w, \beta, \dot{w}, \dot{\beta}]^T$, the system can be arranged in its matrix notation:

$$\dot{x} = Ax + K(t) * x + Bu \tag{3}$$

where the following definitions are used:

$$A = \begin{bmatrix} 0_{2\times2} & I_{2\times2} \\ -M^{-1}\Omega & -M^{-1}C \end{bmatrix}; \ M = \begin{bmatrix} 1 + \frac{1}{\mu} & x_\alpha - \frac{a_h}{\mu} \\ \frac{x_\alpha}{r_\alpha^2} - \frac{a_h}{\mu r_\alpha^2} & 1 + \frac{a_h^2}{\mu r_\alpha^2} + \frac{1}{8\mu r_\alpha^2} \end{bmatrix}; \ C = \begin{bmatrix} 0 & \frac{U}{\mu} \\ 0 & \frac{U(1-a_h)}{2\mu r_\alpha^2} \end{bmatrix}$$

$$K(t) = \begin{bmatrix} 0_{2\times2} & 0_{2\times2} \\ -M^{-1}\Phi(t) & 0_{2\times2} \end{bmatrix}; \ B = \begin{bmatrix} 0_{2\times1} \\ 8\mu r_\alpha^2(a_h - \mu x_\alpha)/\epsilon \\ 8\mu r_\alpha^2(\mu + 1)/\epsilon \end{bmatrix}$$

$$\Omega = \begin{bmatrix} \Omega^2 & 0 \\ 0 & 1 \end{bmatrix}; \ \Phi(t) = \begin{bmatrix} \frac{2U}{\mu}\ddot{K}_w & \frac{2U}{\mu}\left[\left(a_h - \frac{1}{2}\right)\ddot{K}_w + U\dot{K}_w\right] \\ -\frac{(1+2a_h)U}{\mu r_\alpha^2}\ddot{K}_w & -\frac{(1+2a_h)U}{\mu r_\alpha^2}\left[\left(a_h - \frac{1}{2}\right)\ddot{K}_w + U\dot{K}_w\right] \end{bmatrix}$$

$$\epsilon = 8a_h^2\mu + 16a_h\mu x_\alpha + 8r_\alpha^2\mu(\mu + 1) - 8\mu^2 x_\alpha^2 + \mu + 1 \tag{4}$$

and I is indicating the identity matrix. The term expressed by the operator $*$ indicates the convolution integral or Volterra integral between the element i-row j-column of K matrix and the state x.

$$K_{ij} * x_i = \int_0^t K_{ij}(t-\tau)\,x_i(\tau)\,d\tau \tag{5}$$

This work aims to find an optimal control that can minimize a given objective function J under the constraint hypotheses of the differential system (3). Usually, the Pontryagin problem is not easily solved except through numerical approaches based on the discretization of the equations making use of direct control methods

such as single-multiple shooting or collocation methods. In this case, the open-loop control solution is founded by the solution of a nonlinear programming system, which requires high computational efforts and therefore cannot be used for real-time applications. Here, the authors propose an indirect and analytical solution of the Pontryagin problem for Volterra equations, which can be used in feedback, making the algorithm suitable for real-time applications. The objective function is defined as the classical quadratic form in terms of both the state x and the control u, and the constraint expressed by the integral differential equation of first species Volterra:

$$\min J = \min \left\{ \int_0^T \tfrac{1}{2} x^T Q x + \tfrac{1}{2} R u^2 + \lambda^T \left(\dot{x} - Ax - K * x - Bu \right) dt \right\} \tag{6}$$

$$i.c. \ x(0) = x_0$$

Equation (6) represents a typical optimal problem in which the integral differential constraint is considered using the Lagrange multiplier λ. The matrix Q and the coefficient R are generally gains of the objective function or also called penalty parameters suitably selected to best tune the optimal control solution.

3 Theory of the Proportional Integrative N-Order PI(N) Control

The proposed optimal control theory of the Volterra Eq. (3) is here presented in a scalar formulation without loss of generality for more clarification. Therefore, starting with the minimizing of the following cost function:

$$\min J = \min \left\{ \int_0^T \frac{1}{2} q x + \frac{1}{2} r u^2 + \lambda \left(\dot{x} - ax - k * x - bu \right) dt \right\} \tag{7}$$

and doing the δ variations and imposing $\delta J = 0$, a set of differential equations in x and λ is found (see Ref. [16] for more details):

$$\begin{cases} \dot{x} = ax + bu + \int_0^\infty k \left(t - \tau \right) x \left(\tau \right) d\tau \\ \dot{\lambda} = qx - a\lambda - \int_0^\infty k \left(\tau - t \right) \lambda \left(\tau \right) d\tau \\ \lambda(T) = 0, \quad u = \frac{b}{r} \lambda \end{cases} \tag{8}$$

The first integral of (8) is the convolutional term $k * x$; instead, the second integral is associated to the δ-variation of $k * x$ in the x variable that is a nontrivial problem. Both can be derived under the kernel causality proprieties $k(t - \tau) = 0$ for $t < 0$ and $\tau > t$ (see Ref. [16] for more details). The transversality condition of Eq. (8), $\lambda(T) = 0$, makes the problem difficult to solve, and only an open loop control solution is naturally stated, precluding the chance of a direct feedback control. As it happens for physical systems described by differential equations, the infinite

time-horizon presents the chance of a direct feedback control passing through some assumptions. The proposed method is based on the use of a specific exponential kernel function, which may well represent most convolutional memory phenomena or hysteresis models:

$$k(t) = \sum_{k=1}^{N} \alpha_k e^{-\beta_k t} \tag{9}$$

where α_k and β_k are general coefficients of the exponential series. Now, eliminating u through the third of Eq. (8) and considering the Eq. (9), one can easily obtain

$$\begin{cases} \dot{x} = ax + \lambda \frac{b^2}{r} + \int_0^\infty \sum_{k=1}^{N} \alpha_k e^{-\beta_k t} x(\tau) \, d\tau \\ \dot{\lambda} = qx - a\lambda - \int_0^\infty \sum_{k=1}^{N} \alpha_k e^{-\beta_k t} \lambda(\tau) \, d\tau \end{cases} \tag{10}$$

Thanks to the special form of k, the two integral terms of (10) can be easily Laplace-transformed $\mathcal{L}\{\}$ with variable s:

$$(sX(s) - x_0) = (a - d_{N-1}) X(s)$$

$$+ \sum_{j=1}^{N} \left(a d_{N-j} X(s) + p_{N-j} X(s) + \frac{b^2}{r} d_{N-j} \Lambda(s) + x_0 d_{N-j} \right.$$

$$\left. - d_{N-1-j} X(s) \right) s^{-j} + \frac{b^2}{r} \Lambda(s)$$

$$(s\Lambda(s) - \lambda_0) = - \left(a + \tilde{d}_{N-1} \right) \Lambda(s)$$

$$+ \sum_{j=1}^{N} \left(q \tilde{d}_{N-j} X(s) + \tilde{p}_{N-j} \Lambda(s) - a \tilde{d}_{N-j} \Lambda(s) + \lambda_0 \tilde{d}_{N-j} \right.$$

$$\left. - \tilde{d}_{N-1-j} \Lambda(s) \right) s^{-j} + q X(s) \tag{11}$$

where d_j, $\tilde{d}_j, p_j, \tilde{p}_j$ are general coefficients. Now Laplace antitransforming $\mathcal{L}^{-1}\{\}$ and reducing the integral-differential equation to a set of first order, the Eq. (11) can be reduced to an LTI system with the state vector $\boldsymbol{q} = [\boldsymbol{\xi}, \boldsymbol{\eta}]^T$, $\boldsymbol{\xi} = [\xi_1, \ldots, \xi_{N+1}]^T$, $\boldsymbol{\eta} = [\eta_1, \ldots, \eta_{N+1}]^T$ where $\xi_1 = \mathcal{L}^{-1}\{X(s)\}$ and $\eta_1 = \mathcal{L}^{-1}\{\Lambda(s)\}$; the following variables ξ_k, η_k present integrals of state and lambda up to the k-order and matrix $\boldsymbol{H} = [\boldsymbol{H}_{\xi\xi} \boldsymbol{H}_{\xi\eta}; \boldsymbol{H}_{\eta\xi} \boldsymbol{H}_{\eta\eta}] \in \mathbb{R}^{(2N+2) \times (2N+2)}$:

$$\dot{\boldsymbol{q}} = \boldsymbol{H}\boldsymbol{q} \tag{12}$$

Its solution can be expressed in function of its $2N + 2$ eigenvectors $\boldsymbol{\psi}_k \, \boldsymbol{\theta}_k$ and eigenvalues $\boldsymbol{p} = [p_1, \ldots p_k, \ldots, p_{2N+2}]$. Arranging the eigenvalues p_k with $\mathcal{R}$-positive and Y-negative real part, Eq. (12) can be written as follows:

$$\boldsymbol{q} = \begin{bmatrix} \boldsymbol{\xi} \\ \boldsymbol{\eta} \end{bmatrix} = \sum_{k=1}^{Y} c_k^{\{-\}} \begin{bmatrix} \boldsymbol{\psi}_k^{\{-\}} \\ \boldsymbol{\theta}_k^{\{-\}} \end{bmatrix} e^{p_k^{\{-\}}t} + \sum_{k=1}^{\mathcal{R}} c_k^{\{+\}} \begin{bmatrix} \boldsymbol{\psi}_k^{\{+\}} \\ \boldsymbol{\theta}_k^{\{+\}} \end{bmatrix} e^{p_k^{\{+\}}t} \tag{13}$$

where $Y + \mathcal{R} = 2N + 2$ and the superscript $\{+\}$ identify the set of values $\boldsymbol{\psi}_k$, $\boldsymbol{\theta}_k$, c_k referred to the positive real parts $\mathcal{R}e\{p_k\} \geq 0$ and vice versa the superscript $\{-\}$ is referred to the set of $\mathcal{R}e\{p_k\} < 0$. The c_k are the unknown coefficients found by imposing the boundary conditions. The system (13) can be solved assuming $\mathcal{R} \geq Y$ or the number of eigenvalues p_k with negative real part are more than the others. The solution can be found by imposing $c_k^{\{+\}} = 0$ to satisfy the boundary condition $\lim_{T\to\infty} \lambda(T) = 0$ and its derivatives, that is, $\lim_{T\to\infty} \boldsymbol{\eta}(T) = 0$. By selecting $N + 1$ equations with $p_k^{\{-\}}$, from Eq. (13), one obtains:

$$\boldsymbol{\eta} = \left[\boldsymbol{\theta}_1^{\{-\}}, \ldots, \boldsymbol{\theta}_{N+1}^{\{-\}} \right] \left[\boldsymbol{\psi}_1^{\{-\}}, \ldots, \boldsymbol{\psi}_{N+1}^{\{-\}} \right]^{-1} \boldsymbol{\xi} = \boldsymbol{P}\boldsymbol{\xi} \tag{14}$$

Finally, from Eq. (8), since $u = \frac{b}{r}\lambda$, extracting from $\boldsymbol{\eta}$ the last subvector $\eta_{N+1} = \lambda$, the optimal feedback control variable u can be found as follows:

$$u = -P_{1,1}x + \sum_{i=1}^{N} P_{1,i+1} \underbrace{\int \ldots \int}_{i} \left(\hat{d}_i x + \hat{p}_i u \right) \underbrace{dt \ldots dt}_{i} \tag{15}$$

$$+ \sum_{i=1}^{N} x_0 d_{N-i} \frac{t^{i-1}}{(j-1)!}$$

with $\hat{d}_i$, $\hat{p}_i$, $P_{1,j}$ are general coefficients. The structure of Eq. (15) shows the explicit optimal control solution of Volterra's differential equations here called PI(N). The form of u is mainly related to the structure of the kernel $k(t)$, because it presents a combination of state integral of order equal to the number of the k exponential terms. The explicit control solution has been obtained not only by satisfying the transversality condition stated in (8), but also imposing the same condition for its higher derivatives $\lim_{T\to\infty} \frac{d^i \lambda(T)}{dt^i} = 0$. Moreover, the control solution is also strictly related to the state initial condition x_0.

4   Results and Discussion

In this section, the numerical results are discussed. The proposed PI(N) controller is here developed to control the airfoil motion of Eq. (3) by minimizing the release of vortex wake. The novel algorithm is compared with the benchmarking LQR method, in terms of cost function $1/2(\,\boldsymbol{x}^T\boldsymbol{Q}\boldsymbol{x} + Ru^2)$. The benchmarking LQR method has been developed for the model in analysis by disregarding convolutive memory effects that cannot be included in the method $\boldsymbol{K}(t) * \boldsymbol{x} = \boldsymbol{0}$. Moreover, both controllers, LQR and PI(N), have been applied to the real Volterra wing model. Table 1 below shows the geometric and dynamic adimensional parameters considered as input for the numerical simulations.

Results in Fig. 2 show the behavior of heave (a) and pitch wing (b) motion, when the PIN and LQR controllers are, respectively, acting on the system. For both degree-of-freedom the novel PIN algorithm presents a faster attitude to reach the rest condition, that is, the minimization of memory wake effect, compared to the LQR, which is around 20% of the maximum reached value of the pitch degree-of-freedom. Particularly, the LQR solution presents discontinuity in the heave evolution possibly caused by the presence of memory effects generated by the kernel function. Indeed these effects, which take place during the first seconds of the simulation, are not taken into account in the LQR algorithm.

Also, the control in Fig. 3a underlying a lower effort for the PI(N) controller and in Fig. 3b the cost functions for both methods are compared. The PIN solution presents a lower value of the cost function J than the LQR, confirming a better behavior of the proposed control both in terms of minimization of memory wake effects and cost function itself. This result is due to the fact that the LQR method is not taking into account the memory effects differently from PIN whose behavior is favored by this feature.

Table 1   Dimensionless parameters (see [21] for more details)

Description	Parameters	Value
Dimensionless distance OE	a_h	0.2
Dimensionless mass	μ	26.18
Dimensionless radius of gyration	r_α	4.8
Dimensionless distance GE	x_α	0.2
Frequency	Ω	0.55
Dimensionless inflow velocity	U	2
Kernel function	K_W	$1 - 0.165e^{-0.0009Ut} - 0.335e^{-0.006Ut}$
Control gain	$\boldsymbol{Q}$; R	$diag(5e4; 250; 500; 40)$; 0.2
Initial displacement	$w(0),\, \beta(0),\, \dot{w}(0),\, \dot{\beta}(0)$	$[10, 0, 0, 0]$
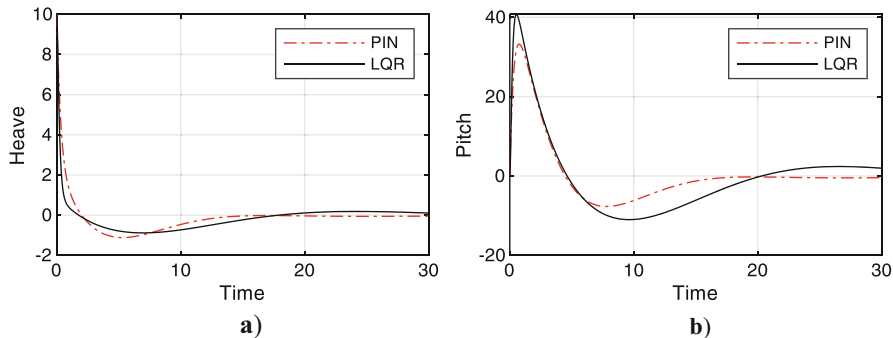
Fig. 2 Heave (**a**) and pitch (**b**) motion: PIN vs LQR
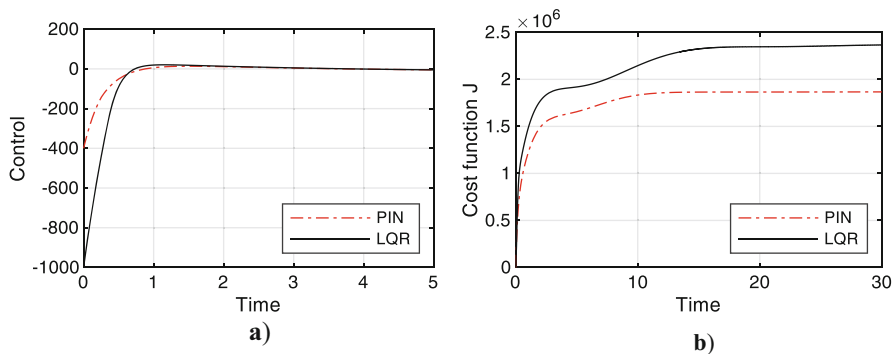
Fig. 3 Control law (**a**) and cost function (**b**) PI(N) vs LQR

5 Conclusions

This work aims to develop a novel optimal control strategy for Volterra models, based on the variational optimal control theory, which normally is applied only to differential equations. In this paper, the proposed algorithm is applied to the control of the aerodynamic behavior of an airfoil which presents a memory effect from wake production. The optimal control, called Proportional-Nth-order-Integral control, PI(N), is here proposed as the indirect solution of the Pontryagin theory applied to the Volterra equation of motions. The analytical control solution has an integral form of order equal to the order of the kernel function series expansion for modelling the wake vortex. Numerical results show the better performances of the proposed PI(N) controller compared with the classic LQR method in terms of reaching rest conditions and minimizing the cost function value.

References

1. T. Theodorsen, Theory of wing sections of arbitrary shape. Nasa Report (1933)
2. W. Olsen, J. Wagner, Effect of thickness on airfoil surface noise. AIAA J. **20**(3), 437–439 (1982)
3. Y.M. Chen, J.K. Liu, G. Meng, Equivalent damping of aeroelastic system of an airfoil with cubic stiffness. J. Fluids Struct. **27**(8), 1447–1454 (2011)
4. F. Mezzani, A.S. Rezaei, A. Carcaterra, Wave propagation phenomena in nonlinear elastic metamaterials, in *New Trends in Nonlinear Dynamics*, (Springer, Cham, 2020), pp. 31–40
5. A. Carcaterra et al., Long-range retarded elastic metamaterials: Wave-stopping, negative, and hypersonic or superluminal group velocity. Phys. Rev. Appl. **11**(1), 014041 (2019)
6. Y.M. Chen, J.K. Liu, G. Meng, An incremental method for limit cycle oscillations of an airfoil with an external store. Int. J. Non-Linear Mech. **47**(3), 75–83 (2012)
7. Q. Liu, Y. Xu, J. Kurths, Active vibration suppression of a novel airfoil model with fractional order viscoelastic constitutive relationship. J. Sound Vib. **432**, 50–64 (2018)
8. Q. Liu et al., The sliding mode control for an airfoil system driven by harmonic and colored Gaussian noise excitations. App. Math. Model. **64**, 249–264 (2018)
9. A.J. Kurdila et al., Nonlinear control methods for high-energy limit-cycle oscillations. J. Guid. Control Dynam. **24**(1), 185–192 (2001)
10. P. Baranyi, Tensor product model-based control of two-dimensional aeroelastic system. J. Guid. Control Dynam. **29**(2), 391–400 (2006)
11. M. Avriel, Nonlinear Programming: Analysis and Methods. Courier Corporation, Dover. (2003)
12. H. Xiong, W.Q. Zhu, A stochastic optimal control strategy for viscoelastic systems with actuator saturation. Probabilistic Eng. Mech. **45**, 44–51 (2016)
13. E. Paifelman, et al., Control of fluctuations of a tethered unmanned-underwater-vehicle. in *Proceedings of ISMA 2018 - International Conference on Noise and Vibration Engineering and USD 2018 - International Conference on Uncertainty in Structural Dynamics*, (2018)
14. E. Paifelman, G. Pepe, A. Carcaterra, Optimal control with memory effects: Theory and application to wings. in *2019 18th European Control Conference (ECC)*, (2019)
15. E. Paifelman, A comparison between mathematical models of stationary configuration of an underwater towed system with experimental validations for oceans'17 MTS/IEEE Aberdeen conferences. in *OCEANS 2017 – Aberdeen*, (2017)
16. E. Paifelman, G. Pepe, A. Carcaterra, An optimal indirect control of underwater vehicle. Int. J. Control, **94**(2), 312–326 (2021)
17. D. Antonelli, et al., A novel approach in optimal trajectory identification for autonomous driving in racetrack, in *2019 18th European Control Conference, ECC 2019*, (2019)
18. G. Pepe, N. Roveri, A. Carcaterra. Prototyping a new car semi-active suspension by variational feedback controller, in *Proceedings of ISMA 2016 - International Conference on Noise and Vibration Engineering and USD2016 - International Conference on Uncertainty in Structural Dynamics*, (2016)
19. G. Pepe, E. Paifelman, A. Carcaterra. Optimal feedback control law for viscoelastic materials with memory effects, in *Proceedings of the International Conference on Structural Dynamic, EURODYN2020. Athens, Greece*, (2020)
20. G. Pepe, E. Paifelman, A. Carcaterra, Volterra models of magnetorheological dampers and their application to vibrating systems, in *Proceedings of ISMA 2020 - International Conference on Noise and Vibration Engineering and USD 2020 - International Conference on Uncertainty in Structural Dynamics. 2020: Leuven, Belgium*, (2020)
21. A. Carcaterra, D. Dessi, F. Mastroddi, Hydrofoil vibration induced by a random flow: A stochastic perturbation approach. J. Sound Vib. **283**(1–2), 401–432 (2005)

Magnetic and Electromagnetic Springs Forces: Determination and Usage in Damping Vibrations

Maksymilian Bednarek, Donat Lewandowski, and Jan Awrejcewicz

1 Introduction

Springs are commonly used in the technical industry, thanks to their ability to store energy or, in certain cases, to damp some movement. Technological progress allows creating devices that act as a spring (e.g., rubber, hydro-pneumatic, magnetic, or electromagnetic springs). Electromagnetic spring has an advantage because its parameters can be controllable by changing the current in the coil. The idea of using an electromagnet to achieve varying stiffness has already found usage in biomechanics. Liang et al. [1] designed a finger exoskeleton with a variable stiffness which can be used in hand rehabilitation. Liu et al. [2] developed a controllable electromagnetic vibration isolator. Authors have introduced negative stiffness which opposes the excited movement in some working range. As a result, the amplitude of this vibration has been decreased. Since electromagnets can operate with varying forces, they can be successfully used for shock absorption [3, 4]. We can treat two or more magnets moving coaxially as a nonlinear magnetic spring. By electromagnetic spring we mean here a magnet moving coaxially in the vicinity of the powered coil. Usually, the identification of spring parameters, such as stiffness or damping coefficient, is biased with an error resulting from dry friction. Experimental stand consisting of aerostatic bearings allows us to minimize this error. There are numerous publications that try to model the strength of a magnet or powered coil depending on the distance from it [5–7]. In this work, the interaction between a pair of magnets and between a magnet and a coil has been described and experimentally validated. Sometimes in an application, one needs a spring with a particular characteristic, for example, linear or progressive. Finding

M. Bednarek · D. Lewandowski · J. Awrejcewicz (✉)
Department of Automation, Biomechanics and Mechatronics, Lodz University of Technology, Lodz, Poland
e-mail: maksymilian.bednarek@dokt.p.lodz.pl; jan.awrejcewicz@p.lodz.pl

a proper combination of springs to achieve the desired characteristic might be troublesome, especially for complex stiffness shapes. This work presents a method for tailoring any characteristic of electromagnetic spring. It should be emphasized that by changing characteristics of certain components of the system during its motion in an appropriate way, we can dampen or additionally force the motion. That property allows one to create active damping, which, unlike passive damping, can adapt to changing conditions in which the device is operated. In this article, we present the current controller with a feedback loop, which allows us to dampen any movement that appears as a result of some external excitation. This article extends our previous work [6] by introducing a new formula to approximate electromagnetic force. Furthermore, a concept of tailoring electromagnetic stiffness characteristic is introduced. This paper is constructed in the following way: Sect. 2 – description of the experimental setup, Sect. 3 – investigations of spring stiffness characteristic, Sect. 4 – shaping the electromagnetic stiffness characteristic, Sect. 5 – active damping.

2   Experimental Rig

Our experimental rig allows us to test a wide spectrum of properties of stiffness elements (springs). Thanks to the use of nonferromagnetic elements, we can study not only mechanical springs but also magnetic and electromagnetic springs. The setup consists of a guide 6 suspended in two closed aerostatic supports (see Fig. 1) which allows for full elimination of dry friction between the guide and the supports. Universal spring holders are placed at the ends of the guide 6 and on the brackets 7. The distance between the handles and the guide's face can be adjusted by axial movement of the brackets 7 in the t-slots of the base 9. It is possible to measure the displacement of the guide with an accuracy of 1 micrometer. Position of the guide is measured with Hall sensor 3 and gathered by data acquisition card. The value of force F is changed by setting the angle α, relative to the direction of gravity, with a self-locking worm gear 12. Inclinometer 2 ensures accurate angle reading.

3   Determining Spring Stiffness Characteristics

We study two different types of springs which will be subject to theoretical and experimental analysis: magnetic and electromagnetic (see Fig. 2). Their forces will be denoted as F_m and F_e, where F_m is the force of magnetic spring and F_e indicates the force of electromagnetic spring. Static stiffness characteristic was collected using a dynamometer.

Fig. 1 Photo (**a**) and diagram (**b**) of the experimental rig with aerostatic supports: 1 – coil, 2 – inclinometer, 3 – position sensor, 4 – aerostatic supports, 5 – air preparation system, 6 – guide, 7 – brackets, 8 – compressed air, 9 – base, 10 – magnet, 11 – angle adjustment locks, 12 – worm gear, 13 – magnetic ruler, 14 – supports, 15 – displacement display, 16 – angular scale, 17- rig frame, 18 – power supply, 19 – data acquisition card, 20 – H-bridge
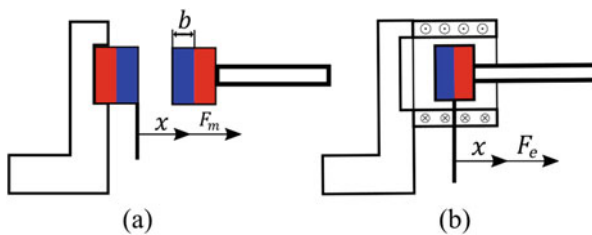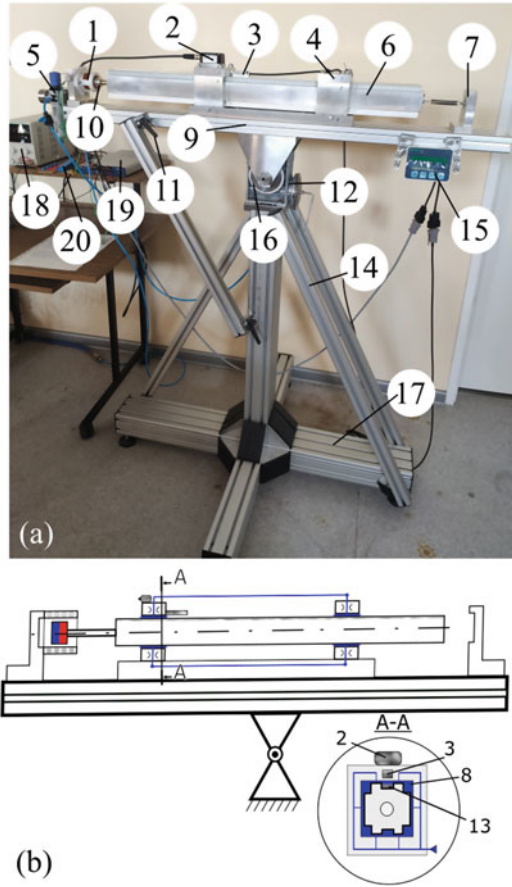
Fig. 2 Test objects: (**a**) magnetic spring (magnet - magnet), (**b**) electromagnetic spring (powered coil - magnet)

3.1 Magnetic Spring

A magnetic spring is defined as two magnets arranged coaxially with identical poles relative to each other as it is shown in Fig. 2a. One magnet was attached to the fixed
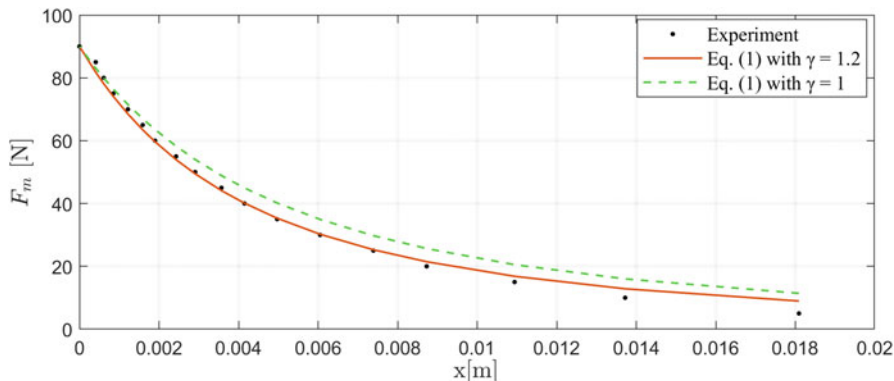
Fig. 3 Graph representing repulsive force vs. displacement of magnetic spring. For $x = 0$, the surfaces of magnets adjoin. Dots represent experimental values; red (green) curve represents Eq. (1) with (without) regard to environmental conditions

mounting, while the other to the guide. Repulsive force of two magnets moving coaxially on the guide without friction is nonlinear and can be determined by the formula:

$$F_m = A(\gamma x + 2b)^{-2}, \tag{1}$$

where A is a magnet constant, b is the distance between the center of the magnet and the magnet's front surface, while γ is a constant of distance influences for given conditions. Constant A can be determined from the formula:

$$A = F_0(2b)^2, \tag{2}$$

where F_0 is the value of force that occurs between connected identical poles of magnets. The green curve shown in Fig. 3 displays formula (1) without taking into consideration environmental conditions represented by parameter γ, while the red curve represents formula (1) with regard to them.

3.2 Electromagnetic Spring

An electromagnetic spring is defined as a pair of a magnet and powered coil arranged coaxially, so that magnet can move freely inside and outside the coil (see Fig. 2b). Depending on the polarization of the current, the magnet is repelled or attracted to the center of the coil. Measurement was carried out in the same way as magnetic spring. The coil used in the experiment has 30 mm in length, 26 mm on the inner diameter, and 45 mm in outer diameter. Static tests have shown that the stiffness of the electromagnetic spring is linear inside the coil and strongly nonlinear
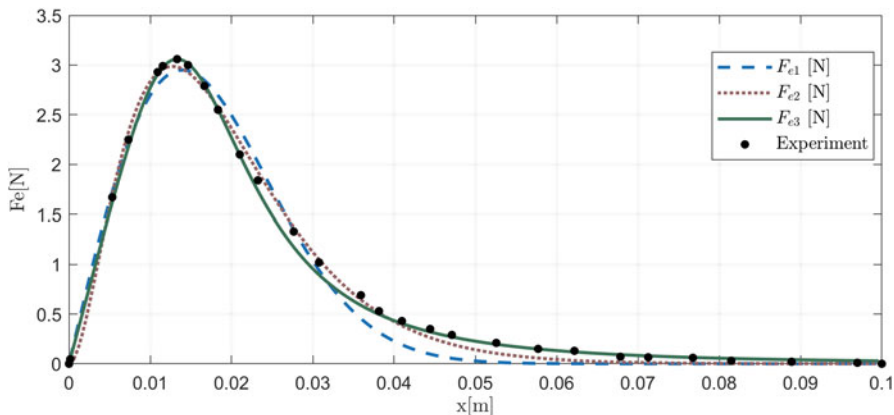
Fig. 4 Fitting of Eqs. (3), (4), and (5) to the experimental data for $I = 2A$

Table 1 Values of parameters used in Eqs. (3), (4), and (5)

a_1 [Nm]	$a_2[m^2]$	$b_1 \left[\frac{N}{m^{b_2}}\right]$	b_2	$b_3 \left[\frac{1}{m}\right]$	$c_1 \left[\frac{N}{A}\right]$	$c_2[m]$
0.6782	0.000388	106100	1.953	-153.6	2.6857	0.0175

outside the coil (see Fig. 4). Such a line can be approximated with many formulas. To distinguish and compare them, they are named F_{e1}, F_{e2}, and F_{e3}. In each of three mathematical descriptions of the electromagnetic force, the force reaches a maximum value when the center of magnet meets the frontal surface of the coil. Force is equal to 0 when center of the magnet is located in the center of the coil ($x = 0$). Figure 4 shows a correspondence between the experimental dots and an analytical curve in all three variants. The parameters in formulas of electromagnetic spring are purely mathematical. They have no physical meaning, unlike parameters in formula (1) and (2). All values have been adjusted by Matlab curve fitting tool, using nonlinear least squares method. Obtained values are given in Table 1.

Term F_{e1} is described by the expression [8]

$$F_{e1} = \frac{2a_1}{a_2} \cdot x \cdot e^{-\frac{x^2}{a_2}}, \tag{3}$$

where a_1 [Nm] and $a_2[m^2]$ are constant coefficients for the given current amplitude.

Term F_{e2} is described by the expression [6]

$$F_{e2} = b_1 x^{b_2} e^{b_3 x}, \tag{4}$$

where $b_1 \left[\frac{N}{m^{b_2}}\right]$, b_2, and $b_3 \left[\frac{1}{m}\right]$ are coil-current-dependent parameters.

Term F_{e3} we propose to describe by the following expression
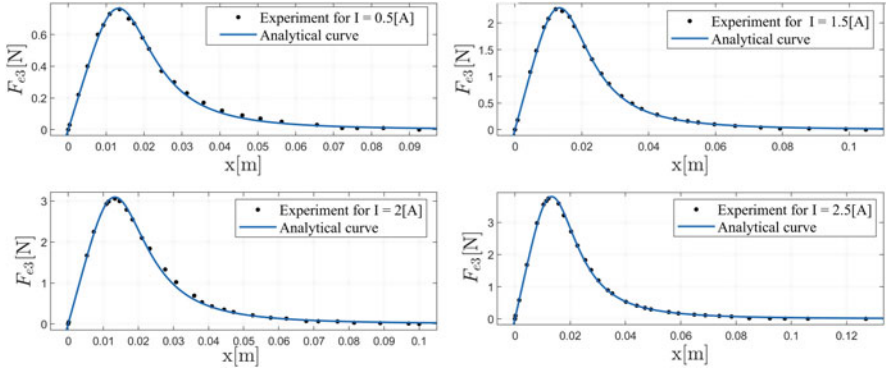
Fig. 5 Congruence of Eq. (5) for various values of current

$$F_{e3} = c_1 \cdot I \cdot \frac{\frac{x}{c_2}}{1 + \left(\frac{x}{c_2}\right)^4}, \tag{5}$$

where $c_1 \left[\frac{N}{A}\right]$ and $c_2 [m]$ are constant parameters for a given coil-magnet pair. In our case, $c_1 = 2.6857 \frac{N}{A}$ and $c_2 = 0.0175\ m$. The electric current in the coil is represented by I.

Analysis of all three mathematical description methods shows that F_{e3} has the best fitting with experimental data. To measure the value of fitness, coefficient of measurement(R^2) was determined. For F_{e1}: $R^2 = 0.9853$, for F_{e2}: $R^2 = 0.9971$, and for F_{e3}: $R^2 = 0.9985$. Moreover, the dependency between c_1 and c_2 parameters and current is linear, which is a very useful phenomenon for tailoring characteristic of electromagnetic spring. Figure 5 shows fitting F_{e3} to values of current from 0.5A to 2.5A.

4 Tailoring Characteristics of the Electromagnet

Knowing that the force of an arbitrary spring is denoted as $F = kx$, we can use it along with Eq. (5) to tailor the characteristic of the electromagnetic spring. Let us denote k_e as an established linear stiffness that we want to achieve in electromagnetic spring. Transforming Eq. (5), we achieve following expression:

$$\begin{cases} F_e = k_e \cdot x \\ I = \frac{F_e c_2}{c_1 x} \left(1 + \left(\frac{x}{c_2}\right)^4\right) \end{cases} . \tag{6}$$
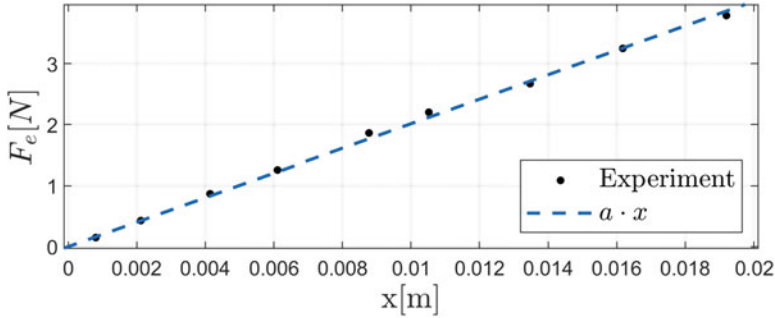
Fig. 6 Force vs. displacement chart of electromagnetic spring for the value of current calculated by Eq. (6), under assumption that $k_e = 200$ (dashed curve represents arbitrary linear function)
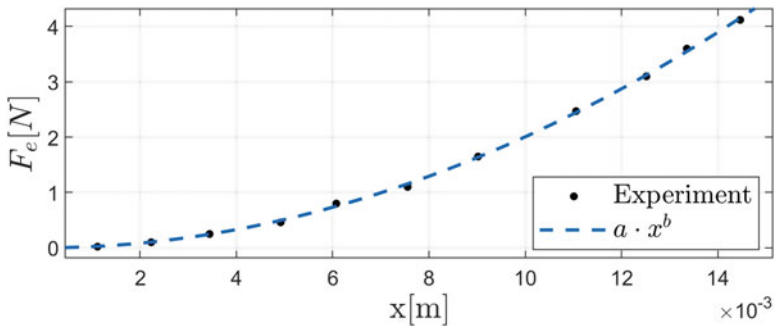
Fig. 7 Force vs. displacement chart of electromagnetic spring for the value of current calculated by Eq. (6), under assumption that $k_e = 20000x$ (dashed curve represents arbitrary progressive power function)

Figures 6, 7, and 8 show force versus displacement of an electromagnet with various linear and nonlinear set stiffness k_e. The idea is to make linear, progressive, and regressive characteristic.

This section has shown that by manipulating the current in a coil, we can use electromagnetic spring as a substitute for an arbitrary spring. Of course, above certain distance from the coil, needed current grows exponentially, so in order to use this solution efficiently, working space should be limited to double or triple of a coil length (depending on the specification of a coil).

5   Active Damping

Since force characteristic of electromagnetic spring can be tailored arbitrary, it can also be amplified or diminished in such a way, so that the resulting force will be opposite to the movement. To achieve such behaviour, a control system with a
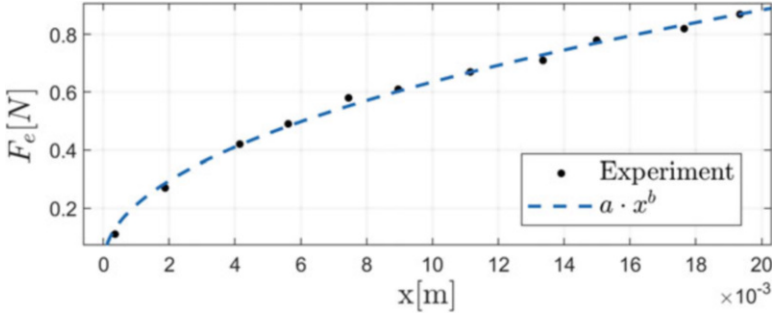
Fig. 8 Force vs. displacement chart of electromagnetic spring for the value of current calculated by Eq. (6), under assumption that $k_e = \frac{200000}{\sqrt{x}}$ (dashed curve represents arbitrary regressive power function)
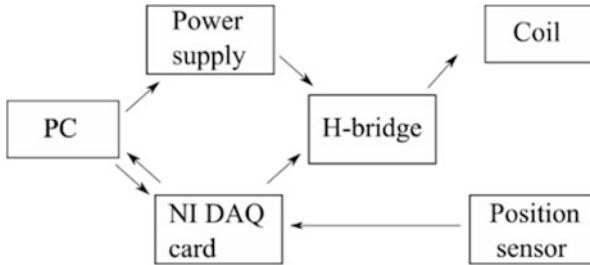
Fig. 9 Diagram showing communications between components of the control system

feedback loop has been developed. It allows data to be acquired and processed in real time. To acquire measurements, we use the NI USB-6341 device, sensors, and a computer connected to the card (see Fig. 9). In order for the current to flow in both directions, the H-bridge is used. The program shows parameters such as guide inclination, displacement, and current sent to the coil in runtime.

The algorithm, which controls the current, is represented by the following expression:

$$I(x, \dot{x}) = K_p x + K_d \dot{x} + K_i \int x \, dt, \tag{7}$$

where K_p, K_d, and K_i are coefficients of the proportional, derivative, and integral terms, respectively. All tune settings parameters have been adjusted experimentally by trails and error method. In each loop iteration, the displacement is numerically differentiated to obtain the velocity and it is proportionally converted to the coil current. The fourth order Runge-Kutta method was used to integrate displacement in time in order to get a second component of the algorithm which is first amplified by a tuning constant. Thanks to this, we achieve the effect in which the guide moving toward the electromagnet is repelled from it, while moving in the opposite
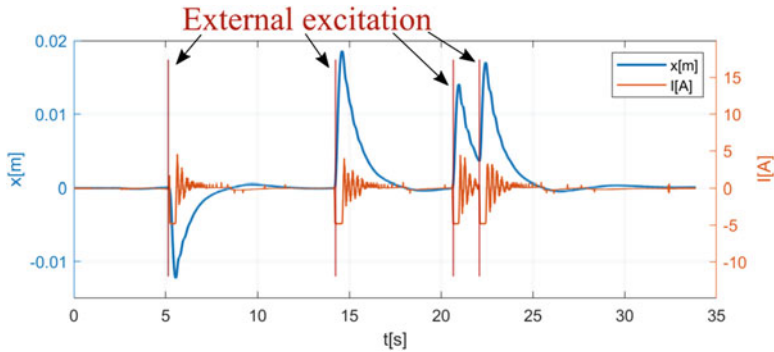
Fig. 10 Time history of the guide movement and value of the coil current. The blue curve stands for the displacement of the guide, whereas orange curve stands for coil current

direction, it is attracted. Figure 10 shows the damping of the guide movement using the presented algorithm. External excitation is an impulse force which is used for presentation purposes. Without active damping, the guide would move in the direction compatible with the direction of external excitation until it meets one of the brackets.

6   Concluding Remarks

The formula for the magnetic force between two magnets is proposed and experimentally validated. It might be very useful for engineers who need to calculate the force of a magnet in a given distance from each other, knowing only maximum force between them, and length of the magnets. The formula for tailoring characteristic of electromagnet has been presented and proven experimentally. It is shown that electromagnetic spring can also be a successful shock absorber. It may be useful for applications where there is a need for varying stiffness of the spring. For example, in suspension systems for active vibration damping or in systems where it is necessary to pass through resonance to achieve target rotational speeds.

References

1. R. Liang, G. Xu, M. Li, S. Zhang, A. Luo, T. Tao, A novel variable stiffness compliant finger exoskeleton for rehabilitation based on electromagnet control. Proc Annu Int Conf IEEE Eng Med Biol Soc EMBS 2018-July:3926–3929 (2018). https://doi.org/10.1109/EMBC.2018.8513288

2. S. Liu, L. Feng, D. Zhao, X. Shi, Y. Zhang, J. Jiang, Y. Zhao, C. Zhang, L. Chen, A real-time controllable electromagnetic vibration isolator based on magnetorheological elastomer with quasi-zero stiffness characteristic. Smart Mater. Struct. **28**, (2019). https://doi.org/10.1088/1361-665X/ab2e44

3. D.F. Ledezma-Ramirez, N.S. Ferguson, M.J. Brennan, An experimental switchable stiffness device for shock isolation. J. Sound Vib. **331**, 4987–5001 (2012). https://doi.org/10.1016/j.jsv.2012.06.010

4. F. Dohnal, Experimental studies on damping by parametric excitation using electromagnets. Proc. Inst. Mech. Eng. Part C J. Mech. Eng. Sci. **226**, 2015–2027 (2012). https://doi.org/10.1177/0954406212439515

5. K. Polczyński, A. Wijata, J. Awrejcewicz, G. Wasilewski, Numerical and experimental study of dynamics of two pendulums under a magnetic field. Proc. Inst. Mech. Eng. Part I J. Syst. Control Eng. **233**, 441–453 (2019). https://doi.org/10.1177/0959651819828878

6. M. Bednarek, D. Lewandowski, K. Polczyński, J. Awrejcewicz, On the active damping of vibrations using electromagnetic spring. Mech. Based Des. Struct. Mach. **49**(8), 1131–1144, (2021). https://doi.org/10.1080/15397734.2020.1819311

7. W. Robertson, B. Cazzolato, A. Zander, Axial force between a thick coil and a cylindrical permanent magnet: Optimising the geometry of an electromagnetic actuator, (2012). https://doi.org/10.1109/TMAG.2012.2194789

8. A. Wijata, K. Polczyński, J. Awrejcewicz, Theoretical and numerical analysis of regular one-side oscillations in a single pendulum system driven by a magnetic field. Mech. Syst. Signal Process. **150**, 107229 (2021). https://doi.org/10.1016/j.ymssp.2020.107229

A Novel Methodology for Controlling Stick–Slip Vibrations in Drill Strings

Hélio Jacinto da Cruz Neto and Marcelo Areias Trindade

1 Introduction

Oil-drilling systems have complex dynamics and can present vibrations in multiple directions. Vibrations during drilling are a major cause of loss of efficiency and damage to drill-string components. Indeed, statistics indicate that up to 25% of the annual non-productive time is caused by shocks and vibrations [1], and their presence can also increase drilling costs by up to 10% [2]. In the particular case of torsional vibrations, experimental studies have shown that the bit rotation is almost always irregular and the stick–slip phenomenon is present in nearly 50% of the drilling process [3]. Several approaches have been proposed to model and control drill-string torsional vibrations, many of them relying on active vibration control techniques. For instance, soft torque [4] and torsional rectification [5] techniques were developed specifically for the problem of drill-string vibrations. Later, general control techniques were also employed, such as LQR [6], feedback linearization [7], sliding mode [8], PI control [9, 10], and $\mathcal{H}_\infty$ control [11].

Recently, the authors proposed some changes in the optimal static output feedback (OSOF) control [12] involving the addition of sensor locations as optimization variables and a new way of dealing with the dependence of optimal variables on system initial conditions. When applied to vibration control problems in linear systems, this technique presented meaningful results, such as good performance using a reduced number of sensors and low sensitivity to uncertainties and spillover. In this contribution, we propose the application of this technique to suppress stick–slip oscillations in drilling systems. The continuous nature of the structure and the nonsmooth interaction between drill bit and rock formation are represented

H. J. da Cruz Neto (✉) · M. A. Trindade
São Carlos School of Engineering, University of São Paulo, Department of Mechanical
Engineering, São Carlos, SP, Brazil
e-mail: helio.neto@usp.br; trindade@sc.usp.br

by a finite element (FE) model and a non-regularized dry friction function. As required by the OSOF controller, a translated modal form removing the rigid-body modal displacement is developed to rewrite the original problem as a stabilization problem. In order to achieve robust regulation, the error integral is added as a system state. Although the control design is based on the deterministic linearized system, numerical simulations considering the nonlinear system in regions far from the linearization point and also subjected to uncertainties are performed in order to evaluate stability and performance of the proposed controller.

2 Drilling System Model

The torsional dynamics of the drilling system is represented in a simplified way considering three main components: the rotary table, the bottom hole assembly (BHA), and the drill string, which are depicted schematically in Fig. 1. The BHA contains the stabilizers, drill collars, and drill bit and, for modeling purposes, is represented as a rigid body with rotary inertia J_b. The hypothesis of rigid body is also assumed for the rotary table, which has a rotary inertia J_t. The drill string is modeled as a circular shaft using the fundamental torsional-deformation assumptions [13]. Additionally, the material is considered linear elastic with constant properties (Table 1).

Two main external sources are acting on this system: a drive torque on the rotary table and a reaction torque induced by the bit–rock interaction. The drive torque is taken as a control input variable, which will be determined later in the controller design. The reaction torque T_b is modeled as frictional force using Karnopp's model with an exponential decaying friction term

Fig. 1 Basic components of
a rotary drilling system
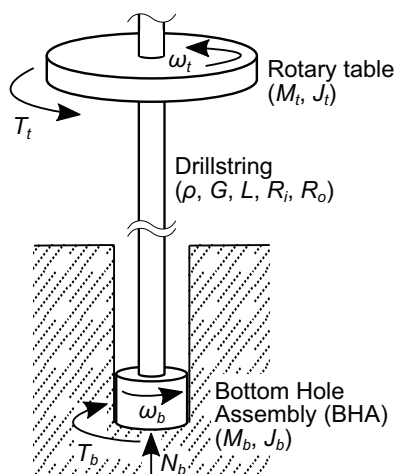
Table 1 Numerical values of the drilling system general parameters

Drill-string mass density (kg/m^3)	8010
Drill-string shear modulus (GPa)	79.6
Drill-string length (m)	3000
Drill-string inner radius—R_i (m)	0.0543
Drill-string outer radius—R_o (m)	0.0635
BHA effective rotary inertia ($kg.m^2$)	394
Driving table effective rotary inertia ($kg.m^2$)	500

$$T_b = \begin{cases} T, & \text{for } |\omega_b| \leq \delta \text{ and } |T| \leq a_2 N_b, \\ a_2 N_b sgn(T), & \text{for } |\omega_b| \leq \delta \text{ and } |T| > a_2 N_b, \\ \left[a_1 + (a_2 - a_1)e^{-\beta|\omega_b|} \right] N_b sgn(\omega_b), & \text{for } |\omega_b| > \delta \end{cases}$$

(1)

in which the values a_1 and a_2 are called dynamic and static friction coefficients, respectively, β is a positive exponential friction coefficient, T is the torque transmitted by the drill string to the bit, N_b is the normal force applied to the bit, and ω_b is the bit angular speed. The parameters for the dry friction model were taken from [9]: $a_1 = 0.029$, $a_2 = 0.079$, $\beta = 0.097$, $\delta = 10^{-4}$, which are associated with a WOB of 120 kN.

The frictional force is the element that makes the system nonlinear and non-smooth, bringing dynamical characteristics that were not present in its absence, such as new equilibrium points, self-excited oscillations, a lower limit for a stable constant angular speed, and so forth [8].

To represent this system using a FE model, a regular mesh was constructed and refined until there was a negligible variation in the natural frequencies up until 6 Hz, which, by rounding up, implied in the use of 30 elements with Hermite cubics as interpolation functions. To reduce computational effort, a modal reduction was performed retaining only the thirteen modes that were within the range of 6 Hz (including a rigid-body mode). The approximate eigenfunctions were determined in order to simplify sensors positioning in the implementation of the OSOF controller. An additional modal damping factor of 1% was added for each mode in order to represent the interaction between the drill string and drilling mud and other dissipation sources. Using these assumptions, the system equations were written using a state-space representation:

$$\dot{\mathbf{x}} = \mathbf{A}\mathbf{x} + \mathbf{B}_c T_t + \mathbf{B}_r T_b$$

$$\mathbf{x} = \begin{bmatrix} \boldsymbol{\eta} \\ \dot{\boldsymbol{\eta}} \end{bmatrix}, \quad \mathbf{A} = \begin{bmatrix} \mathbf{0} & \mathbf{I} \\ -\boldsymbol{\Lambda} & -\mathbf{D} \end{bmatrix}, \quad \mathbf{B}_c = \begin{bmatrix} \mathbf{0} \\ \boldsymbol{\phi}(0) \end{bmatrix}, \quad \mathbf{B}_r = \begin{bmatrix} \mathbf{0} \\ -\boldsymbol{\phi}(L) \end{bmatrix}$$

(2)

in which $\boldsymbol{\eta} \in \mathbb{R}^n$ is the vector of modal displacements, $\boldsymbol{\Lambda} \in \mathbb{R}^{n \times n}$ is a diagonal matrix of system eigenvalues or natural frequencies squared, $\mathbf{D} \in \mathbb{R}^{n \times n}$ is a diagonal matrix of damping, and $\boldsymbol{\phi} : \mathbb{R} \to \mathbb{R}^n$ is the vector of approximated eigenfunctions.

Some transformations were applied to Eq. (2) in order to make it suitable for the design of the OSOF controller. First, as the rigid-body displacement does not appear on the right side of Eq. (2), it does not affect system dynamics and can be eliminated. By doing this, we obtain

$$
\begin{aligned}
\dot{\mathbf{x}}' &= \mathbf{A}'\mathbf{x}' + \mathbf{B}'_c T_t + \mathbf{B}'_r T_b \\
\dot{\mathbf{x}}' &= \mathbf{f}(\mathbf{x}', T_t)
\end{aligned}
\tag{3}
$$

in which the apostrophe $'$ is used to indicate that all components associated with the rigid-body displacement were removed from matrices and vectors, for example, the first element of the vector $\mathbf{x}$ and the first row and column of the matrix $\mathbf{A}$. Henceforth, this notation will be used for all variables that do not have the component associated with the rigid-body displacement. Then, we denote the configuration corresponding to the drill-string rotating at the desired angular velocity (ω_{ref}) in terms of system states as $\mathbf{x}'_{eq} = [\boldsymbol{\eta}'_{eq} \ \dot{\boldsymbol{\eta}}_{eq}]^{\mathsf{T}}$. The applied torque is decomposed into a feedforward constant component $\tilde{u}$, inducing $\mathbf{x}'_{eq}$, and a feedback component u to avoid oscillations, such that $T_t = \tilde{u} + u$. The constant parameters $\boldsymbol{\eta}'_{eq}$ and $\tilde{u}$ can be obtained from the equilibrium condition of Eq. (3), $\mathbf{f}(\mathbf{x}'_{eq}, \tilde{u}) = \mathbf{0}$:

$$
\boldsymbol{\Lambda}'\boldsymbol{\eta}'_{eq} - \boldsymbol{\phi}(0)\tilde{u} + \boldsymbol{\phi}(L)T_b(\omega_{ref}) = \mathbf{0}.
\tag{4}
$$

Using these results and defining the change of coordinates

$$
\boldsymbol{\xi} = \begin{bmatrix} \boldsymbol{\xi}_d \\ \boldsymbol{\xi}_v \end{bmatrix} = \begin{bmatrix} \boldsymbol{\eta}' - \boldsymbol{\eta}'_{eq} \\ \dot{\boldsymbol{\eta}} - \dot{\boldsymbol{\eta}}_{eq} \end{bmatrix} = \mathbf{x}' - \mathbf{x}'_{eq},
\tag{5}
$$

we get the following system of equations in which the point $\mathbf{x}'_{eq}$ has been shifted to the origin:

$$
\dot{\boldsymbol{\xi}} = \mathbf{A}'\boldsymbol{\xi} + \mathbf{B}'_c u + \mathbf{B}'_r \left[T_b \left(\boldsymbol{\phi}^{\mathsf{T}}(L)\boldsymbol{\xi}_v + \omega_{ref} \right) - T_b \left(\omega_{ref} \right) \right].
\tag{6}
$$

Thus, the original problem of keeping the system rotating with constant angular speed and applied torque is transformed into a stabilization problem in coordinate $\boldsymbol{\xi}$. Examining Eq. (4), we see that the constant feedforward torque $\tilde{u}$ that induces the desired drilling operating condition is a function of the bit–rock interaction model. The variables that characterize the bit–rock interaction are rarely known and are subject to changes according to the rock formation lithology. Therefore, these uncertainties may yield a steady-state error. To achieve robust regulation, Eq. (6) is augmented with the integrator:

$$
\dot{e} = \boldsymbol{\phi}^{\mathsf{T}}(0)\boldsymbol{\xi}_v = \omega_t - \omega_{ref}
\tag{7}
$$

such that the augmented system is rewritten as

$$\dot{e} = \boldsymbol{\phi}^{\mathsf{T}}(0)\boldsymbol{\xi}_v$$
$$\dot{\boldsymbol{\xi}} = \mathbf{A}'\boldsymbol{\xi} + \mathbf{B}'_c u + \mathbf{B}'_r \left[T_b \left(\boldsymbol{\phi}^{\mathsf{T}}(L)\boldsymbol{\xi}_v + \omega_{ref} \right) - T_b \left(\omega_{ref} \right) \right]. \tag{8}$$

The augmented system is represented by the state $\boldsymbol{\psi} = [e \quad \boldsymbol{\xi}]^{\mathsf{T}}$. In the OSOF controller design, the state e is feed back to the system, providing an integral action that regulates the error to zero if the closed-loop system is structurally stable [14].

3 OSOF Control

The optimal static output feedback (OSOF) is a control technique based on the linear quadratic regulator (LQR) formulation. Despite having some substantial frequency margins and reduced sensitivity, the LQR control has a disadvantage of requiring, in most cases, measurement of all states for feedback. A common approach to solve this problem is to use linear quadratic Gaussian (LQG) control, which consists of using an observer to estimate unmeasured states. However, LQG control does not have guaranteed stability margins [15], and the loop transfer recovery procedures are limited to minimum phase plants and tend to produce high gains [16]. The OSOF control, initially proposed by Levine and Athans [17], appears as a simple alternative that uses the quadratic cost function of LQR, but with the constraint of using only measured signals for feedback.

Recently, some contributions to the OSOF control have been proposed in [12]. Initially, aiming to apply the OSOF control to distributed parameter systems, sensor locations were included as optimization variables. Moreover, a new approach to deal with the dependence on system initial conditions was suggested. Since any output controller has a performance criterion below that of the full-state feedback controller, it would be desirable that the cost function values of both controllers would be as close as possible for any initial condition. Based on this statement, a new optimization was proposed

$$\min_{(\mathbf{K},\boldsymbol{\alpha})} \max_{\mathbf{x}_0} \quad \frac{\mathbf{x}_0^{\mathsf{T}} \mathbf{P}_o(\mathbf{K}, \boldsymbol{\alpha}) \mathbf{x}_0}{\mathbf{x}_0^{\mathsf{T}} \mathbf{P}_l \mathbf{x}_0} \tag{9a}$$

$$\text{subject to} \quad \mathbf{A}_c^{\mathsf{T}} \mathbf{P}_o + \mathbf{P}_o \mathbf{A}_c + \mathbf{Q} + (\mathbf{K}\mathbf{C}(\boldsymbol{\alpha}))^{\mathsf{T}} \mathbf{R}\mathbf{K}\mathbf{C}(\boldsymbol{\alpha}) = \mathbf{0}, \tag{9b}$$

in which $\mathbf{K}$ is the output control gain, $\boldsymbol{\alpha}$ represents sensor locations, $\mathbf{x}_0$ is the initial condition, $\mathbf{P}_o$ and $\mathbf{P}_l$ are positive definite matrices associated with the OSOF and LQR cost functions, $\mathbf{A}_c$ is the closed-loop state matrix, $\mathbf{C}(\boldsymbol{\alpha})$ is the output matrix, and $(\mathbf{Q}, \mathbf{R})$ are standard LQR weighting matrices. The criterion minimized is a ratio between the cost functions of the OSOF and LQR controllers and possesses the benefit of being independent of measurement and excitation locations. Additionally, as the cost function of the LQR is minimal for any initial condition, this ratio is

always greater than or equal to one, and it also gives a measure of the maximum difference between LQR and OSOF considering performance and control effort.

Since the problem given in Eq. (9a) is a ratio of quadratic forms, the initial condition that maximizes this ratio is the solution of the generalized eigenvalue problem involving matrices P_o and P_l [12]. Therefore, the optimization (9a) can be rewritten as

$$\min_{(\mathbf{K}, \boldsymbol{\alpha})} \lambda_m(\mathbf{P}_o, \mathbf{P}_l) \tag{10}$$

in which λ_m is the largest eigenvalue of the generalized eigenvalue problem:

$$\mathbf{P}_o \mathbf{v} = \lambda \mathbf{P}_l \mathbf{v}. \tag{11}$$

More details on the numerical solution of this problem are given in [12].

To apply this controller to the drilling system, Eqs. (8) are linearized at the origin. Since measurements along the whole drill string are available only in the minority of oil wells, only two sensors whose signals could be processed in order to obtain angular displacements and velocities are considered. Due to the need for an integrator at the rotary table, one of the sensors was fixed at this location, while the other could be positioned up to 10% of the total drill-string length. Under this assumption, the output matrix $\mathbf{C}(\boldsymbol{\alpha})$ is given by

$$\mathbf{C}(\boldsymbol{\alpha}) = \begin{bmatrix} 1 & 0 & 0 & 0 & 0 \\ \mathbf{0} & \boldsymbol{\phi}'(\alpha_1) & \boldsymbol{\phi}'(\alpha_2) & \mathbf{0} & \mathbf{0} \\ \mathbf{0} & \mathbf{0} & \mathbf{0} & \boldsymbol{\phi}(\alpha_1) & \boldsymbol{\phi}(\alpha_2) \end{bmatrix}^\mathsf{T} \tag{12}$$

and the OSOF control law is expressed as

$$u = -\mathbf{K}\mathbf{C}(\boldsymbol{\alpha})\boldsymbol{\psi}. \tag{13}$$

4 Numerical Results

In this section, the OSOF controller aforementioned is applied to the drill-string model described in Sect. 2. The first step in designing the OSOF controller is to choose the weighting matrices $(\mathbf{Q}, \mathbf{R})$ that yield a controller with reasonable trade-off between control effort and performance. The matrix $\mathbf{Q}$ is adopted such that $\mathbf{x}^\mathsf{T}\mathbf{Q}\mathbf{x}$ is the system total energy with an additional weighting factor (q_i) for the error integral:

$$\mathbf{Q} = \begin{bmatrix} q_i & \mathbf{0} & \mathbf{0} \\ 0 & \boldsymbol{\Lambda}' & \mathbf{0} \\ 0 & \mathbf{0} & \mathbf{I}. \end{bmatrix} \tag{14}$$
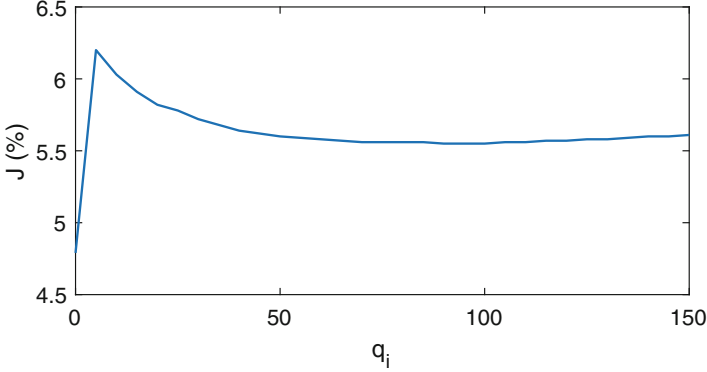
Fig. 2 J as a function of q_i for the closed-loop system using OSOF control

The constant q_i is chosen such that, when applying the OSOF controller, the average deviation from the drill-bit target angular velocity (criterion proposed in [9]) is minimized

$$J = \frac{1}{\Delta t} \int_0^{\Delta t} \frac{|\omega_b - \omega_{ref}|}{\omega_{ref}} dt. \tag{15}$$

To evaluate this criterion, the initial condition is established as the entire system rotating undeformed at a constant speed of 70 rpm and the simulation time is taken as 100 s. Figure 2 indicates how q_i influences the magnitude of J. For each value of q_i, the value of **R** (which is a scalar for this problem) has been adjusted to ensure that the highest value of control effort over time does not exceed 1.2×10^4 Nm.

For $q_i \approx 0$ (the Hamiltonian associated with the algebraic Riccati equation has eigenvalues on the imaginary axis for $q_i = 0$), the system has no integral gain; therefore, the time response is benefited by the absence of overshoot. However, this system is not robust to parameter variations, so the minimum desired is in the region after the first peak, which is around $q_i = 100$. The time response of the closed-loop systems with OSOF control for $q_i \approx 0$ and $q_i = 100$ is compared in Fig. 3. In both cases, one can observe that despite being designed based on the linearized system, the OSOF control was able to keep the nonlinear system stable even when the system's trajectory went to regions far from the linearization point. Indeed, for any simulated initial condition, it was found that the closed-loop system with the OSOF controller remained stable. For instance, the cases in which the drill string starts with null angular velocity undeformed and with a deformation $\eta' = \eta'_{eq}$ are shown in Fig. 4. For simulations corresponding to Fig. 4 and the subsequent ones, the closed-loop system is equipped with the OSOF obtained from $q_i = 100$, which is characterized by the output gain **K** $= [47.7 \ 697.7 \ 665.7 \ -263.2 \ 55.9]$ and sensors locations $\boldsymbol{\alpha} = [0.0 \ 300.0]$ m.
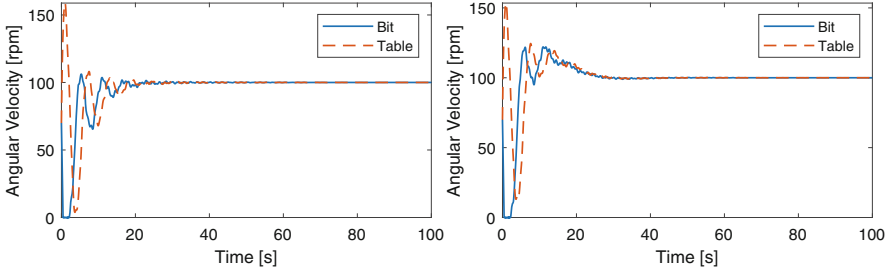
Fig. 3 Comparison of the closed-loop systems using the OSOF controllers obtained with $q_i \approx 0$ (left) and $q_i = 100$ (right)
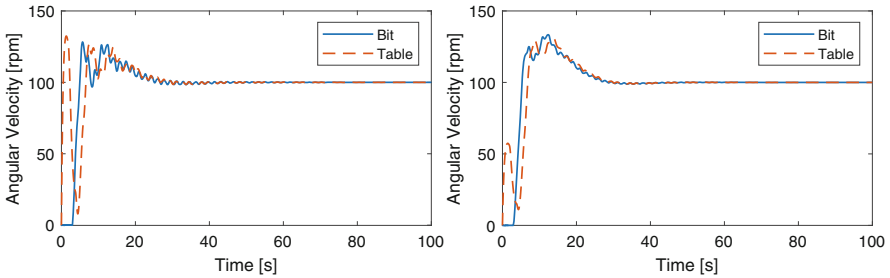
Fig. 4 Time response when the drill string starts with null angular velocity undeformed (left) and with a deformation $\eta' = \eta'_{eq}$ (right)

Another interesting aspect of the closed-loop system with OSOF is its behavior in the presence of uncertainties. To analyze this aspect, let $c_1 = (1 - \epsilon)a_1$ and $c_2 = (1 + \epsilon)a_2$ be the modified dynamic and static friction coefficients, respectively, with $\epsilon > 0$. Let also $\Upsilon(\mathbf{A_c})$ be the spectral abcissa of closed-loop system (6), linearized at $\boldsymbol{\xi} = \mathbf{0}$, using the OSOF controller without integral action. The influence of ϵ in the spectral abscissa $\Upsilon(\mathbf{A_c})$ is depicted in Fig. 5. The discontinuity in the derivative occurs due to a change in the eigenvector associated with the spectral abscissa.

From Fig. 5, we conclude that the closed-loop system is exponentially stable for $\epsilon < 0.47$. Therefore, there is a small enough integral gain k_i such that the closed-loop system is locally stable for all values of ϵ below 0.47 [18]. Two additional results were obtained numerically for this problem: 1. for each ϵ, the set of values that k_i can assume in order to make the system locally stable is an interval $(0, k_{max})$, with k_{max} decreasing as ϵ increases; 2. In agreement with the results obtained for the system without uncertainties, the stability of the closed-loop system seems to hold globally. Both of these results are highlighted in Fig. 6, in which the integral gain $k_i = k_{max}$ was applied to different ϵ values. These results indicate that, assuming that the occurrence of stick/slip is due to variations in friction coefficients, an alternative to avoid it would be to reduce the integral gain, as small k_i values ensure stability over a larger range of ϵ. It is also worth mentioning that, although the model tolerates a variation of 46% in both friction coefficients, it is noted that
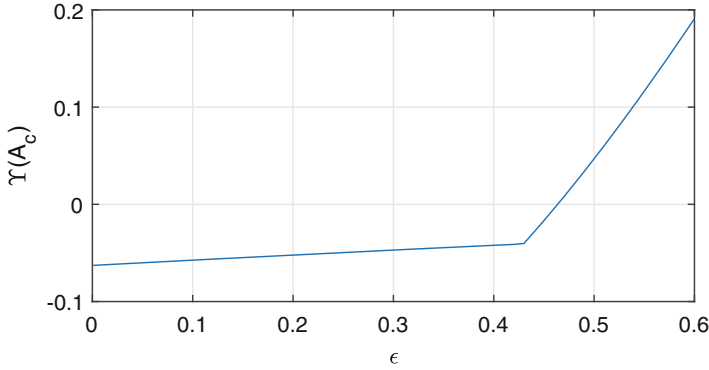
Fig. 5 $\Upsilon(\mathbf{A_c})$ as a function of ϵ for the linearized closed-loop system using OSOF control
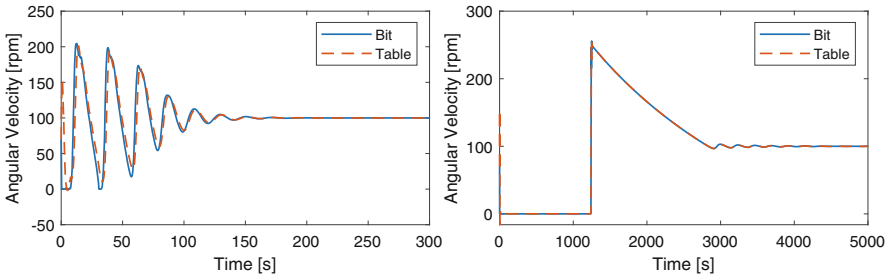
Fig. 6 Time response for the closed-loop system with $\epsilon = 0.2$, $k_i = 83.8$ (left) and $\epsilon = 0.46$, $k_i = 0.5$ (right)

the period in the stick region for this case is long, which indicates that the drill string is subjected to a large deformation, which may violate the assumptions adopted in modeling.

5 Conclusions

A novel strategy for the suppression of stick–slip oscillations in rotary drilling systems was proposed. As required by the strategy, the equations of motion were rewritten using a translated modal form without the rigid-body displacement, transforming the original problem into a stabilization problem. A change in the traditional design of the proposed controller is also developed, incorporating the integral action to ensure robust regulation. Numerical simulations indicate the proposed controller has good performance and can handle large uncertainties in the bit–rock interaction. It was also shown numerically that the analysis of stability using the linearized controlled system with OSOF may be reliable to characterize

the global stability of the nonlinear system. Further analytical analyses are required to corroborate or refute these results. Future works will be directed to the robust design of the proposed controller considering different types of uncertainties.

References

1. G.J. Dong, P. Chen, A review of the evaluation, control, and application technologies for drill string vibrations and shocks in oil and gas well, Shock Vib, p. 34 (2016)
2. S. Jardine, D. Malone, M. Sheppard, Putting a damper on drillings bad vibrations. Oilfield Rev. **6**(1), 15–20 (1994)
3. M.P. Dufeyte, H. Henneuse, Detection and monitoring of the slip-stick motion: field experiments. SPE/IADC Drilling Conference, p. 10 (1991)
4. G.W. Halsey, A. Kyllingstad, A. Kylling, Torque feedback used to cure slip-stick motion. SPE Annual Technical Conference and Exhibition, p. 6 (1988)
5. R.W. Tucker, C. Wang, On the effective control of torsional vibrations in drilling systems. J. Sound Vib. **224**(1), 101–122 (1999)
6. A.P. Christoforou, A.S. Yigit, Fully coupled vibrations of actively controlled drillstrings. J. Sound Vib. **267**(5), 1029–1045 (2003)
7. F. Abdulgalil, H. Siguerdidjane, Nonlinear control design for suppressing stick-slip oscillations in oil well drillstrings, in *2004 5th Asian Control Conference (IEEE Cat. No. 04EX904)*, vol. 2 (2004), pp. 1276–1281
8. E.M. Navarro-López, E. Licéaga-Castro, Non-desired transitions and sliding-mode control of a multi-dof mechanical system with stick-slip oscillations. Chaos, Solitons Fractals **41**(4), 2035–2044 (2009)
9. H.L.S. Monteiro, M.A. Trindade, Performance analysis of proportional-integral feedback control for the reduction of stick-slip-induced torsional vibrations in oil well drillstrings. J. Sound Vib. **398**, 28–38 (2017)
10. M.A. Trindade, Robust evaluation of stability regions of oil-well drilling systems with uncertain bit-rock nonlinear interaction. J. Sound Vib. **483**, 115481 (2020)
11. A.F.A. Serrarens, M.J.G. van de Molengraft, J.J. Kok, L. van den Steen, H infinity control for suppressing stick-slip in oil well drillstrings. IEEE Control Syst. Mag. **18**(2), 19–30 (1998)
12. H.J. Cruz Neto, M.A. Trindade, On the noncollocated control of structures with optimal static output feedback: initial conditions dependence, sensors placement, and sensitivity analysis. Struct. Control. Health Monit. **26**(10), e2407 (2019)
13. R.R. Craig, A.J. Kurdila, *Fundamentals of Structural Dynamics* (John Wiley & Sons, Hoboken, 2006)
14. H. Khalil, *Nonlinear Systems* (Prentice Hall, Hoboken, 2002)
15. J.C. Doyle, Guaranteed margins for LPG regulators. IEEE Trans. Automat. Control **23**(4), 756–757 (1978)
16. S. Skogestad, I. Postlethwaite, *Multivariable Feedback Control: Analysis and Design*, 2nd edn. John Wiley, Chichester (2005)
17. W. Levine, M. Athans, On the determination of the optimal constant output feedback gains for linear multivariable systems. IEEE Trans. Autom. Control **15**(1), 44–48 (1970)
18. G. Weiss, V. Natarajan, Stability of the integral control of stable nonlinear systems, in *2016 IEEE International Conference on the Science of Electrical Engineering (ICSEE)*, pp. 1–5 (2016)

Suppression of the Sommerfeld Effect in a Cantilever Beam Through a Viscoelastic Dynamic Neutralizer: An Experimental Study

Anderson L. Silva, Marcus Varanis, Eduardo M. O. Lopes, José M. Balthazar, and Carlos A. Bavastri

1 Introduction

Several efforts are made in order to generate more efficient methods for vibration control. In this sense, several studies have addressed the use of viscoelastic materials for viscoelastic dynamic neutralizers (VDN). Viscoelastic materials have been widely used in vibration control due to their high capacity to dissipate vibratory energy and the improvement of vulcanization techniques, which make it possible to manufacture devices of all sizes and shapes. These materials can be used in dynamic neutralizers and isolators. VDNs are simple resonant devices, composed of a mass and a viscoelastic material that connects it to the primary system and provides stiffness and damping [1].

A robust methodology for designing a set of VDNs to reduce the vibration levels of a geometrically complex, linear, and multiple-degree-of-freedom structure was proposed by Espíndola and Silva [2] and expanded by Espíndola and Bavastri [3]. The proposed methodology is based on the modal parameters of the system to be controlled, dynamic characteristics of the viscoelastic material, generalized equivalent parameters (GEP) of the dynamic neutralizer, and nonlinear optimization techniques. This methodology allows to design the optimal VDNs that minimize the system response in the desired frequency band. A comprehensive study on the

A. L. Silva (✉) · E. M. O. Lopes · C. A. Bavastri
Department of Mechanical Engineering, Federal University of Paraná, Curitiba, PR, Brazil
e-mail: anderson.langone@outlook.com; eduardo_lopes@ufpr.br; bavastri@ufpr.br

M. Varanis
Faculty of Engineering, Federal University of Grande Dourados, Dourados, MS, Brazil
e-mail: marcusvaranis@ufgd.edu.br

J. M. Balthazar
Department of Electronics, Federal University of Technology – Paraná, Ponta Grossa, PR, Brazil

methodology for the optimal design of VDNs by means of the GEP theory can be carried out in [1–9].

Some efforts are also made regarding the passive control of nonlinear systems. In [10, 11], the use of the similarity principle for the design of nonlinear neutralizers is proposed, obtaining good results in controlling the system's amplitude and also linearizing the system in some cases.

Recent works show that the use of VDNs in nonlinear one-degree-of-freedom primary systems also has excellent results, considerably reducing the amplitude of vibration and linearizing the primary system [4, 5]. These results are obtained due to the high-energy dissipation capacity of viscoelastic materials that considerably reduce the vibration amplitude of the system. Nonlinear phenomena related to non-ideal energy sources are quite interesting. Among them, the Sommerfeld effect, which has been the subject of several studies [12, 14–17], stands out. The Sommerfeld effect occurs when there is an interaction between an elastic system and its energy source. In this phenomenon, the power source does not have enough energy to pass through the resonance frequencies of the elastic system, and its operating frequency remains fixed at a resonance frequency of the system (for instance, the first one), which can be temporary. During the Sommerfeld effect, the system becomes unstable, so that small external excitations can fully change the system response.

The Sommerfeld effect can be easily seen in the system temporal response, in the form of sudden reductions in the amplitude of vibration. Another way to identify the phenomenon is through time–frequency analyzes, where a sudden increase in the frequency of the system response can be observed simultaneously with the reduction in amplitude. In [12, 13], the characterization of the Sommerfeld effect is performed using wavelet transform techniques, which highlights several characteristics of the phenomenon in the time–frequency plane.

Several works address the mathematical modeling of electromechanical systems where the Sommerfeld effect is present. In [14], a continuous linear beam model is presented to which two non-ideal DC motors are coupled. Some parameters of the model are analyzed for their influence on the Sommerfeld effect, and the model is validated experimentally, showing a good coherence with the experimental system. Models for similar systems can be found in [15–17].

The aim of this chapter is to design an optimal VDN to suppress the occurrence of the Sommerfeld effect on a linear metallic cantilever beam with a non-ideal unbalanced DC motor at its free end. For the VDN design, the coupling between the beam and the motor was disregarded, considering only the dynamics of the beam.

This chapter consists of five sections: in Sect. 1, a brief discussion was held on the topics covered in the present work; in Sect. 2, the experimental apparatus used is presented, as well as the experiments carried out; in Sect. 3, the experimental results are presented; and in Sect. 4, some final comments are made on the methodology presented in this chapter.

2 Methodology

Experiments were carried out on a stainless steel cantilever beam with an unbalanced DC motor coupled to its free end. The motor was manually controlled using a DC power supply. The beam dimension is $540 \times 37 \times 4.8$ mm, and the motor was unbalanced with 6.59 g at 15 mm of rotation axis. The total mass of the motor is 85 g. The system under study is shown in Fig. 1.

Initially, experiments were carried out to identify the Sommerfeld effect during the motor operation. The phenomenon was identified both in the time domain and in the frequency domain. Subsequently, a finite-element mathematical model was developed, which was calibrated experimentally. With this, it is possible to determine which modes interact with the DC motor and extract the modal parameters for the VDN design. Then, based on the modal parameters of the system and the characteristics of the viscoelastic material, the design of the VDN is carried out, which, after being manufactured, will be coupled to the primary system to carry out new experiments in order to verify the efficiency of the VDN.

2.1 Identification of the Sommerfeld Effect

Preliminary tests were carried out, in which the motor was accelerated to its working speed, 6600 RPM. In those tests, the system was instrumented using an accelerometer, model 32C68, PCB Piezotronics, and the DataPhysics Quattro signal analyzer. The accelerometer was positioned at 520 mm from the fixed end. A sampling frequency of 1000 Hz was used, and the signal was acquired for approximately 32 s.

The occurrence of the Sommerfeld effect was observed in the preliminary tests by means of the temporal signal and using the methodology proposed in [12, 13], with the occurrence of the resonance capture phenomenon at 72 Hz, the second natural frequency. In order to efficiently control the phenomenon, it was decided to perform
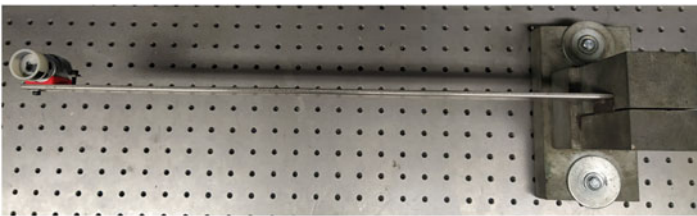
Fig. 1 Primary system to be controlled, stainless steel cantilever beam with an unbalanced DC motor coupled to its free end
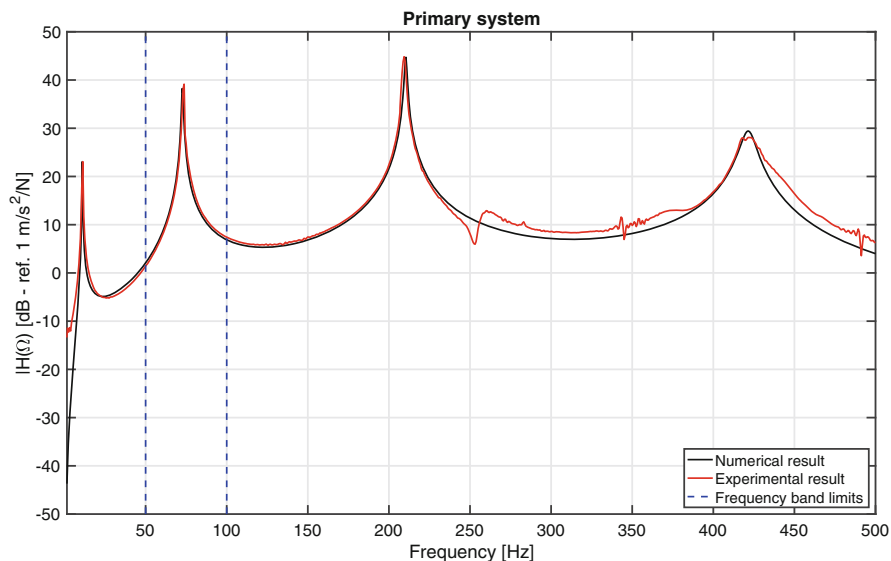
Fig. 2 Frequency response function of the primary system, obtained with excitation at 140 mm and measuring the response at 520 mm from the fixed end

passive vibration control in the range of 50 to 100 Hz, as highlighted in Fig. 2. The results for this experiment, in the time and frequency domains, are presented in the next section, Fig. 5.

2.2 Finite-Element Model

By using ANSYS software, a finite-element model was developed for the beam. The model parameters were calibrated in such a way that the system's numerical frequency response functions could match the experimental counterparts. The system was modeled using beam elements with three degrees of freedom per node. A total of 54 elements were generated. The torsional modes were neglected in the mathematical model, and it should be noted that the proposed mathematical model considers only the cantilever beam with a point mass at its free end, disregarding the nonlinear coupling between the DC motor and the beam.

Experimental FRFs were obtained using a DataPhysics Quattro signal analyzer, a PCB Piezotronics impact hammer, model 086C04, and a 32C68 accelerometer, also PCB Piezotronics. Excitation was performed at 140 mm of the fixed end, and the response was also measured at 520 mm from the fixed end. The experimental results were used to calibrate the finite-element model. The numerical and experimental FRFs are presented in Fig. 2.

As can be seen in Fig. 2, the mathematical model faithfully represents the structure, except for the torsional modes.

2.3 VDN Design

The VDN design was carried out using the LAVIBS-ND software, which is based on the methodology proposed in [3], considering only the dynamics of the cantilever beam with a point mass at its free end and omitting the coupling between the beam and the DC motor. Genetic algorithms were utilized to minimize the FRF amplitude in the control range, in this case 50 to 100 Hz. The viscoelastic material used to manufacture the device was the butyl rubber, and its parameters can be found in [18]. The device was designed to operate at 300 K.

The optimal parameters obtained in the LAVIBS-ND software were 0.044 kg and 60.31 Hz, and the manufactured VDN, as well as its drawing with designed dimensions, can be seen in Fig. 3.

After coupling the VDN to the primary system, new tests were performed to check the efficiency of the device in controlling the Sommerfeld effect. The results obtained are presented in the next section.
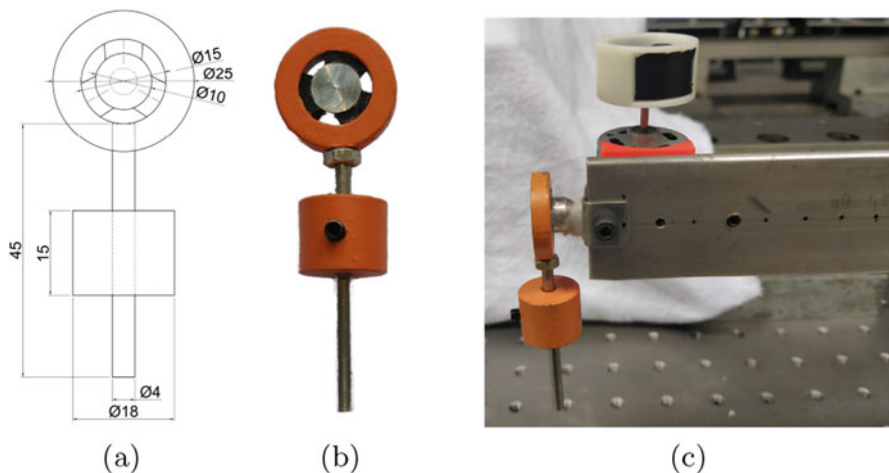
Fig. 3 Optimal VDN for the system control: (**a**) Drawing of the designed device, (**b**) Designed device, and (**c**) Device attached to the primary system

3   Results and Discussion

In the first tests, the DC motor was accelerated to its working speed, 6600 RPM. The Sommerfeld effect was identified in the tests through the analysis of the temporal signal, Fig. 4a, which shows a sudden reduction in the vibration amplitude of the system. In addition, the time–frequency analysis using wavelet synchrosqueezed transform—WSST, Fig. 4b, shows that the system response frequency remains constant at 72 Hz, between 7 and 12 s, which indicates the occurrence of the resonance capture phenomenon, characteristic of the Sommerfeld effect, as shown in [12].

The use of WSST for time–frequency analysis in this chapter is due to its anti-noise capability and high time–frequency resolution [14]. It should also be noted that, as it is based on empirical mode decomposition, the WSST does not depend on the mother wavelet used [19].

After coupling the VDN to the primary system, new tests were performed during the start-up of the DC motor. The vibration amplitude of the system decreased as expected, and there were no sudden changes in amplitude during the operation of the motor, as can be seen in Fig. 5a. In addition, in the analysis using the WSST, Fig. 5b, it is observed that the motor speed increases gradually, without stagnation regions.

The results presented in Fig. 5 show that the Sommerfeld effect was suppressed after coupling the VDN to the primary system. In addition, the amplitude of vibration decreases considerably, from 471 m/s^2 to just 58 m/s^2, an 8 times decrease, approximately 18 dB.
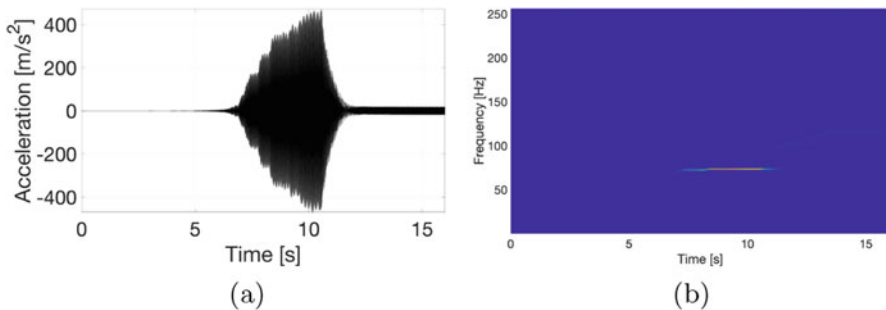
Fig. 4 System response without passive control: (**a**) Acceleration response, and (**b**) Time–frequency plane obtained with WST
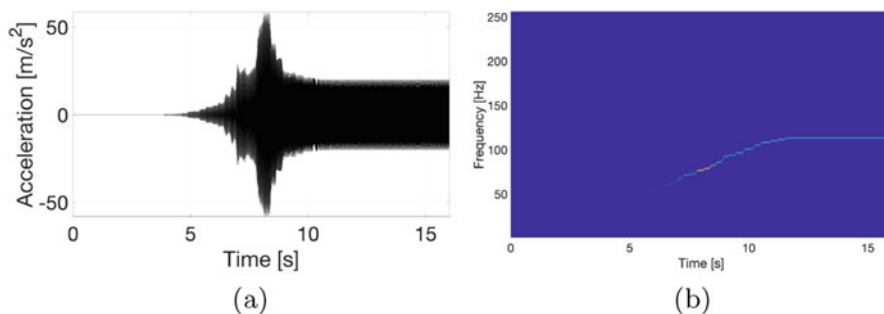
Fig. 5 System response after coupling the VDN to the primary system: (**a**) Acceleration response, and (**b**) Time–frequency plane obtained with WST

4 Conclusions

The results show that VDNs are excellent devices for the passive control of large amplitudes of vibrations, even during the Sommerfeld effect. This is due to the fact that the viscoelastic materials used in the manufacture of VDNs have high-energy dissipation capacities which, together with the optimal design of the VDN, provide an excellent reduction in the amplitude of vibration.

It is observed that the presented results were obtained with a VDN designed only considering the system composed by the beam with a point mass at the end, disregarding the interaction between the motor and the beam. In this way, a high mechanical impedance was added in the frequency range of the second mode, the occurrence mode of the phenomenon, by means of the VDN, which proved to be sufficient to suppress the occurrence of the Sommerfeld effect. The VDN could also be designed taking into account the electromechanical system in order to prevent the phenomenon from occurring in the motor operating range.

The main contribution of this chapter is the suppression of the Sommerfeld effect through VDNs. Despite the fact that VDNs are widely used in passive vibration control, the application of this device is unusual for the suppression of the Sommerfeld effect and nonlinear jumps.

In future work the goal is to extend the design methodology of VDNs to nonlinear systems with multiple degrees of freedom to evaluate the efficiency of the device in the control of the Sommerfeld effect in primary systems with stiffness nonlinearity.

Conflict of interest

The authors declare that they have no conflict of interest.

References

1. J.J. De Espíndola, C.A. Bavastri, E.M. De Oliveira Lopes, Design of optimum systems of viscoelastic vibration absorbers for a given material based on the fractional calculus model. J. Vib. Contr. **14**(9–10), 1607–1630 (2008)
2. J.J. Espíndola, H.P. Silva, Modal reduction of vibrations by dynamic neutralizers, in *Proceedings of the Tenth International Modal Analysis Conference*, San Diego (pp. 1367–1373) (1992)
3. J.J. Espíndola, C.A. Bavastri, Viscoelastic neutralisers in vibration abatement: a non-linear optimisation approach. J. Braz. Soc. Mech. Sci. **19**(2), 154–163 (1997)
4. K.B. Bronkhorst, M. Febbo, E.M. Lopes, C.A. Bavastri, Experimental implementation of an optimum viscoelastic vibration absorber for cubic nonlinear systems. Eng. Struct. **163**, 323–331 (2018)
5. C.A. Bavastri, M. Febbo, V.V. Goncalves, E.M. Lopes, Optimum viscoelastic absorbers for cubic nonlinear systems. J. Vib. Control **20**(10), 1464–1474 (2014)
6. E.d.C.F. Silva, C.A. Bavastri, A methodology for an optimal design of physical parameters, positions, and viscoelastic materials of simple dynamic absorbers for passive vibration control. J. Vib. Control **25**(6), 1133–1147 (2019)
7. J.J. de Espíndola, C.A. Bavastri, E.M. Lopes, On the passive control of vibrations with viscoelastic dynamic absorbers of ordinary and pendulum types. J. Frankl. Inst. **347**(1), 102–115 (2010)
8. J.J.D. Espíndola, P. Pereira, C.A. Bavastri, E.M. Lopes, Design of optimum system of viscoelastic vibration absorbers with a Frobenius norm objective function. J. Braz. Soc. Mech. Sci. Eng. **31**(3), 210–219 (2009)
9. C.A. Bavastri, M.L. Polli, D.R. Voltolini, F.A. Presezniak, A methodology to mitigate chatter through optimal viscoelastic absorber. Proc. Inst. Mech. Eng. B J. Eng. Manuf. **229**(8), 1348–1356 (2015)
10. G. Habib, T. Detroux, R. Viguié, G. Kerschen, Nonlinear generalization of Den Hartog's equal-peak method. Mech. Syst. Signal Proces. **52**, 17–28 (2015)
11. G. Habib, G. Kerschen, A principle of similarity for nonlinear vibration absorbers. Physica D **332**, 1–8 (2016)
12. M. Varanis, J.M. Balthazar, A. Silva, A.G. Mereles, R. Pederiva, Remarks on the Sommerfeld effect characterization in the wavelet domain. J. Vib. Contr. **25**(1), 98–108 (2019)
13. M. Varanis, A.L. Silva, J.M. Balthazar, R. Pederiva, A tutorial review on time-frequency analysis of non-stationary vibration signals with nonlinear dynamics applications. Braz. J. Phys. 1–19 (2021)
14. M. Varanis, A. Mereles, A.L. Silva, M.R. Barghouthi, J.M. Balthazar, E.M. Lopes, C.A. Bavastri, Numerical and experimental investigation of the dynamic behavior of a cantilever beam driven by two non-ideal sources. J. Braz. Soc. Mech. Sci. Eng. **42**(10), 1–18 (2020)
15. A. Mereles, M. Varanis, A.L. Silva, J.M. Balthazar, E.M.O. Lopes, C.A. Bavastri. Mathematical modelling of a cantilever beam driven by two unbalanced electric motors, in *Proceedings of the 25th International Congress of Mechanical Engineering*, Uberlândia (2019)
16. J.M. Balthazar, D.T. Mook, H.I. Weber, R.M. Brasil, A. Fenili, D. Belato, J.L.P. Felix, An overview on non-ideal vibrations. Meccanica **38**(6), 613–621 (2003)
17. P.J.P. Gonçalves, M. Silveira, B.P. Junior, J.M. Balthazar, The dynamic behavior of a cantilever beam coupled to a non-ideal unbalanced motor through numerical and experimental analysis. J. Sound Vib. **333**(20), 5115–5129 (2014)

18. D.R. Voltolini, S. Kluthcovsky, F.J. Doubrawa Filho, E.M.O. Lopes, C.A. Bavastri, Optimal design of a viscoelastic vibration neutralizer for rotating systems: flexural control by slope degree of freedom. J. Vib. Contr. **24**(16), 3525–3537 (2018)
19. I. Daubechies, J. Lu, H.T. Wu, Synchrosqueezed wavelet transforms: an empirical mode decomposition-like tool. Appl. Comput. Harmon. Anal. **30**(2), 243–261 (2011)

Stabilisation of a Heavy Chain Buckled Configuration Through Parametric Excitation

Eduardo A. R. Ribeiro (iD)**, Breno A. P. Mendes, and Carlos E. N. Mazzilli**

1 Introduction

Since Stephenson [1–3] firstly observed that the vibrations of inverted pendula could be stabilised in the upward configuration with the aid of high-frequency vertical base excitations, the theme of stabilisation has been studied in the context of different mechanical systems by many authors. Among them, we mention Hirsch [4], Kapitza [5], Chelomei [6, 7], Kalmus [8], Acheson and Mullin [9–11], Champneys and Fraser [12, 13], Butikov [14], Anderson and Tadjbakhsh [15], Thomsen [16], Galán and others [17], Seyrarian, Arkhipova and others [18–25]. For the sake of examples, in [17], the problem of stabilisation was applied to an inverted pendula chain. In [15], the same was done with a Ziegler's column. In [16], experimental results were obtained for an axially excited piano string. In [11–13], different authors tried to explain the so-called Indian rope trick. In [19], a parametrically excited beam was regarded and it was found that stabilisation could be also achieved from low forcing frequencies. Such works are just a small sample of the extensive literature about the role of parametric excitation for stabilisation of otherwise unstable configurations.

In this work, we address the same for the case study of a heavy chain (see Fig. 1). This model has been studied before [26–30], under the condition of modal asynchrony, which in this context refers to *localised* modes (for the sake of an illustration, see forthcoming Fig. 2a). In some cases, asynchronous modes may be unstable (they have a complex frequency) as a result of a supercritical statical loading. In fact, static instability and modal asynchronicity may, sometimes, be related. This was our motivation to further exploit such a relationship and investigate whether unstable configurations and ensuing motions can be stabilised with the

E. A. R. Ribeiro (✉) · B. A. P. Mendes · C. E. N. Mazzilli
Polytechnic School of Sao Paulo University, Sao Paulo SP, Brazil
e-mail: asceduardo@usp.br; brenoay@usp.br; cenmazzi@usp.br
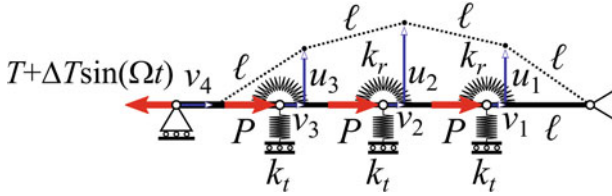
Fig. 1 Heavy chain
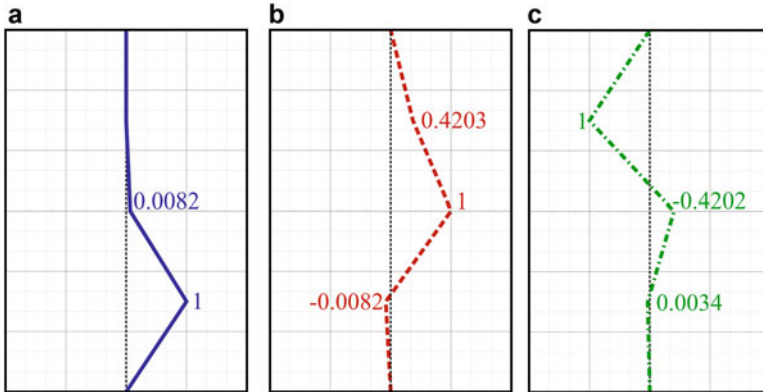
Fig. 2 Modes for $\alpha = 0.01$, $\sigma = 1.20$ and $\theta_3 = 2.3798$. Eigenvalues: (**a**) $\lambda = -0.1906$, (**b**) $\lambda = 1.7070$ and (**c**) $\lambda = 5.1222$

aid of parametric excitation. Heavy chains are convenient reduced-order models (ROMs) of slender structures subjected to variable axial tension, which is the case of buoying structures, risers, bridge cables, etc.enlargethispage-24pt

2   Problem Statement

Consider the heavy chain of Fig. 1, which is composed of four massless rigid bars of length ℓ, transverse and rotation springs of stiffness k_t and k_r. The heavy chain is subjected to a tensile force $T + \Delta T \sin \Omega t$, where Ω is the forcing frequency, and to dead weights $P = mg$, in which m stands for point masses and g refers to the gravity acceleration. This system has three degrees of freedom (DOFs) q_i – see (3) –

so that the following kinematical relationships between the bar x-axis displacements u_i, y-axis displacements v_i and rotations of bars φ_i can be written:

$$u_i = \ell \sin \varphi_i + u_{i-1} \tag{1}$$

and

$$v_i = \ell \left(1 - \cos \varphi_i\right) + v_{i-1}, \tag{2}$$

where $i = 1, \ldots, 3$ and $u_0 = v_0 = \varphi_0 = 0$. Defining

$$q_i = \frac{u_i}{\ell} \tag{3}$$

as the system's generalised co-ordinates and following the Lagrangian formulation, we obtain the system' equations of motion. To benefit from a dimensionless approach, we define

$$\tau = \sqrt{\frac{k_t}{m}}\,t, \tag{4}$$

which can be interpreted as the dimensionless time, and also.

$$\alpha = \frac{k_r}{k_t \ell^2}, \quad \sigma = \frac{P}{k_t \ell}, \quad \theta = \frac{T}{k_t \ell} \quad \text{and} \quad \Delta\theta = \frac{\Delta T}{k_t \ell}. \tag{5}$$

For small vibrations about the rest position, the linearised motion equations can be written in matrix form:

$$\mathbf{M}\mathbf{q}'' + \mathbf{K}\mathbf{q} = \mathbf{0}, \tag{6}$$

where $(\ )' = \frac{d(\ )}{d\tau}$ means differentiation with respect to the dimensionless time τ, and $\mathbf{M}$ and $\mathbf{K}$ are the dimensionless mass and stiffness matrices. In this case, $\mathbf{M} = \mathbf{I}$ is simply the identity matrix, and $\mathbf{K}(\tau) = \mathbf{K_s} + \mathbf{K_e}(\tau)$, in which

$$\mathbf{K_s} = \begin{bmatrix} 1 + 5\alpha - 5\sigma + 2\theta & -4\alpha + 2\sigma - \theta & \alpha \\ -4\alpha + 2\sigma - \theta & 1 + 6\alpha - 3\sigma + 2\theta & -4\alpha + \sigma - \theta \\ \alpha & -4\alpha + \sigma - \theta & 1 + 5\alpha - \sigma + 2\theta \end{bmatrix} \tag{7}$$

already incorporates the geometric stiffness due to the static loading, while

$$\mathbf{K_e} = \Delta\theta \sin \sqrt{\Lambda}\tau \begin{bmatrix} +2 & -1 & +0 \\ -1 & +2 & -1 \\ +0 & -1 & +2 \end{bmatrix} \tag{8}$$

accounts for the stiffness variation with time due to the harmonic excitation. The dimensionless parameter

$$\Lambda = \frac{m}{k_t}\Omega^2 \tag{9}$$

is related to the forcing frequency.

2.1 Modal Analysis

The modal analysis of discrete linear systems usually reduces to an eigenproblem, in which the eigenvalues λ supply the system's natural frequencies, while the eigenvectors $\boldsymbol{\phi}$ are the vibration modes, as indicated by

$$\left(\mathbf{M}^{-1}\mathbf{K_s} - \lambda\mathbf{I}\right)\boldsymbol{\phi} = \mathbf{0}, \tag{10}$$

which comes from the substitution of $\mathbf{q} = \boldsymbol{\phi}\sin\sqrt{\lambda}\tau$ into (6). In the above expression, the eigenvalue

$$\lambda = \frac{m}{k_t}\omega^2 \tag{11}$$

is proportional to the square of a natural frequency ω.

Usually, one departs from known structural parameters to calculate frequencies and modes. However, we actually want to fine-tune the system to display a given mode, namely, an asynchronous one. Therefore, we substitute

$$\boldsymbol{\phi} = \{1 \ q_2 \ 0\}^T, \tag{12}$$

which is knowingly asynchronous, into (10), and then we get the *admissibility conditions* for that mode to exist, from the resulting system of algebraic equations. They supply the unknown co-ordinate:

$$q_2 = \frac{\alpha}{4\alpha + \theta - \sigma}, \tag{13}$$

and two independent expressions for the eigenvalue appear, which must be identified to yield a cubic equation in α, σ and θ:

$$\theta^3 + (12\alpha - 4\sigma)\,\theta^2 + \left(46\alpha^2 - 34\alpha\sigma + 5\sigma^2\right)\theta + 56\alpha^3 - 69\alpha^2\sigma + 22\alpha\sigma^2 - 2\sigma^3 = 0. \tag{14}$$

Equation (14) is the *admissibility condition* to be satisfied for the asynchronous mode (12) to exist.

After adopting, for the sake of an illustration, $\alpha = 0.01$ and $\sigma = 1.20$, the three alternative solutions for θ come out from (14):

$$\theta_1 = 1.1361, \ \theta_2 = 1.1641 \text{ and } \theta_3 = 2.3798, \tag{15}$$

so that the respective eigenvalues are

$$\lambda_1 = -3.1903, \ \lambda_2 = 0.2809 \text{ and } \lambda_3 = -0.1906. \tag{16}$$

Notice that λ_1 and λ_3 are negative and thus lead to complex natural frequencies, which means that the corresponding modes are unstable. In Fig. 2, the asynchronous modes (blue) for $\alpha = 0.01$, $\sigma = 1.20$ and $\theta_3 = 2.3798$, with its almost asynchronous companion modes, are shown together with their corresponding eigenvalues.

2.2 Buckling Analysis

If all inertial effects are disregarded, the system's response becomes

$$\mathbf{K}_s \mathbf{q}_s = \mathbf{F}_s, \tag{17}$$

in which $\mathbf{q}_s$ refers to the static deflection, and $\mathbf{F}_s$ to the static forces acting upon the structure. If the axial compression along the structure is progressively increased, it will eventually reach a critical value ($\mathbf{F}_s = \mathbf{F}_{crit}$) and the heavy chain will buckle. From a mathematical viewpoint, buckling corresponds to a singular stiffness matrix, that is, to

$$\det \mathbf{K}_s = 0. \tag{18}$$

If we consider such a progressive increase of axial stress by means of

$$\sigma = (1 + \eta)\, \sigma_0, \tag{19}$$

then $\mathbf{K_s} = \mathbf{K_0} + \eta \mathbf{\Delta K_0}$, where

$$\mathbf{K_0} = \begin{bmatrix} 1 + 5\alpha - 5\sigma_0 + 2\theta & -4\alpha + 2\sigma_0 - \theta & \alpha \\ -4\alpha + 2\sigma_0 - \theta & 1 + 6\alpha - 3\sigma_0 + 2\theta & -4\alpha + \sigma_0 - \theta \\ \alpha & -4\alpha + \sigma_0 - \theta & 1 + 5\alpha - \sigma_0 + 2\theta \end{bmatrix} \tag{20}$$

and
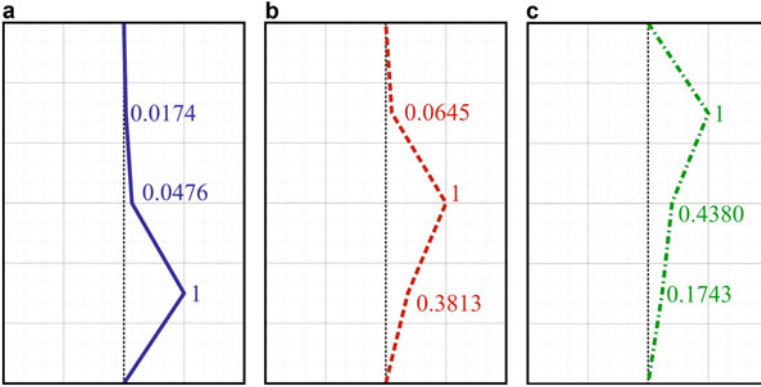
Fig. 3 Buckling modes for $\alpha = 0.01$, $\sigma = 1.20$ and $\theta_3 = 2.3798$. (**a**) $\eta_1 = -0.0325$, (**b**) $\eta_2 = 0.8182$ and (**c**) $\eta_3 = 6.0456$

$$\boldsymbol{\Delta K_0} = \begin{bmatrix} -5\sigma_0 & +2\sigma_0 & +0 \\ +2\sigma_0 & -3\sigma_0 & +\sigma_0 \\ 0 & +1\sigma_0 & -\sigma_0 \end{bmatrix}, \tag{21}$$

and (17) can be rewritten as an eigenvalue problem:

$$\left(-\boldsymbol{\Delta K_0^{-1} K_0} - \eta \boldsymbol{I} \right) \boldsymbol{\psi} = \boldsymbol{0}, \tag{22}$$

in which η gives the magnification factor of σ_0 for which the structure buckles, and $\boldsymbol{\psi}$ tells the respective buckling modes.

For the buckling analysis, we choose the same parameters of Fig. 2, namely, $\alpha = 0.01$, $\sigma_0 = 1.20$ and $\theta_3 = 2.3798$, which yield

$$\eta_1 = -0.0325, \ \eta_2 = 0.8182 \ \text{and} \ \eta_3 = 6.0456. \tag{23}$$

Observe that η_1 is negative, which means that for $\sigma_0 = 1.20$, the heavy chain has already buckled and, therefore, it is a supercritical loading. Furthermore, as illustrated in Fig. 3, two buckling modes are nearly localised, which suggests that, in this heavy chain, modal asynchronicity and buckling might be related.

3 Stabilisation of the Linear System Response

We now investigate the parametrically excited response of the linearised system when the system's parameters are $\alpha = 0.01$, $\sigma = 1.20$ and $\theta_3 = 2.3798$. They lead to an *unstable asynchronous mode* and also to a *supercritical load configuration*.
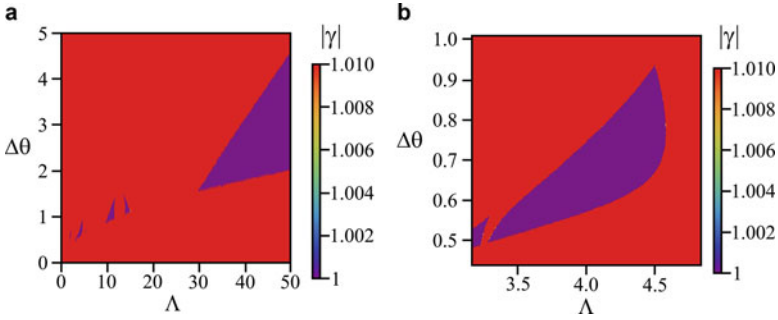
Fig. 4 Strutt-like diagram for the linear system, in which γ is the Floquet's multiplier for each $(\Lambda, \Delta\theta)$ pair. (**a**) General view. (**b**) Detail of the stabilised region for low parametric excitation frequency
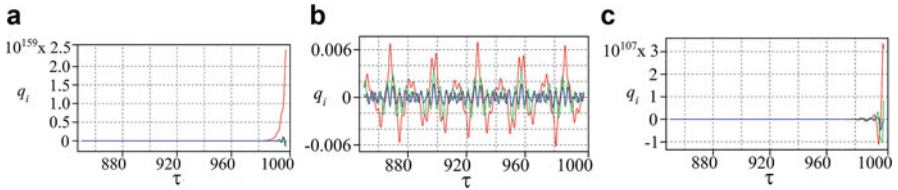
Fig. 5 Linear system time responses for $\Lambda = 4.0$ and (**a**) $\Delta\theta = 0.3$ (unstable), (**b**) $\Delta\theta = 0.7$ (stable) and (**c**) $\Delta\theta = 1.1$ (unstable)

Hence, for such an unfavourable scenario, large responses are to be expected. However, if we bear in mind that the parametric excitation brings additional energy to the system, it may happen that, for some combinations of $\Delta\theta$ and Λ, the instability can actually be reverted.

Figure 4 shows the Strutt-like diagram built for the chosen system parameters and several values for the pair $(\Lambda, \Delta\theta)$. For each pair, the highest Floquet's multiplier γ is computed. Notice the existence of regions (in purple) for which $|\gamma| \approx 1$. According to [29], for $|\gamma| = 1$, the equilibrium of a linear system will be stable if and only if the unitary Floquet's multipliers are simple or semi-simple. In this work, this feature will not be assessed. Instead, we will assume such purple zones are (potentially) stable. This assumption will be later confirmed in Sect. 5, after geometric non-linearities are regarded.

In Fig. 5, three responses for the linear system are regarded. Those of Fig. 5a, c are within the red zone; as expected, they are unstable. The one depicted in Fig. 5b is within the purple zone, and it is stable, conforming our expectations anticipated in Fig. 4. It is noteworthy that, although the potentially stable zone increases with the forcing frequency (which was expected), stable responses also appear at relatively small frequencies. For instance, for the stabilised response of Fig. 5b, the forcing frequency associated to $\Lambda = 4.0$ is lower than the system's highest natural frequency (corresponding to $\lambda = 5.1222$).
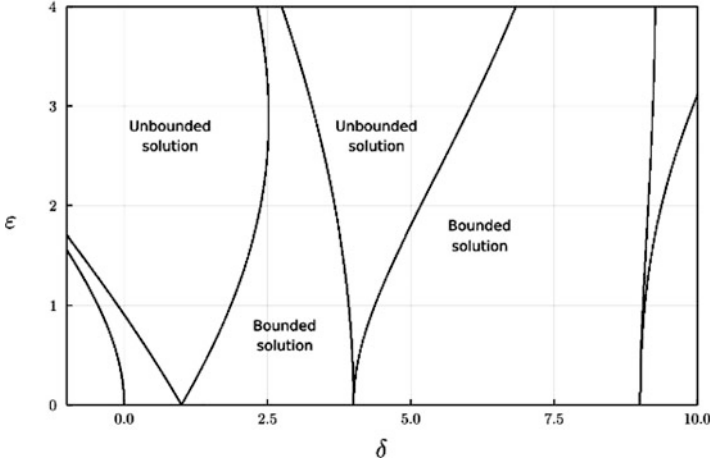
Fig. 6 Typical Strutt's diagram of systems governed by Mathieu's Eq. (29)

4 Reduced-Order Model

Figure 6 illustrates the typical Strutt's diagram of undamped systems governed by Mathieu's equation:

$$\ddot{q} + (\delta + 2\varepsilon \cos 2t)\, q = 0. \tag{24}$$

In the classical problem of a parametrically excited pendulum,

$$\delta = 4\left(\frac{\omega}{\Omega}\right)^2 \quad \text{and} \quad \varepsilon = \frac{2\Delta H}{\ell} \tag{25}$$

correlate the natural and forcing frequencies, support-excitation amplitude ΔH and the pendulum length ℓ. Notice that, on the left-hand side of the δ-axis (where ω is always complex), responses are predominantly unstable, except for those within a tiny region near the origin. This is precisely the region where statically unstable responses can be stabilised by parametric excitation.

In order to demonstrate that the potentially stabilised responses of Fig. 4 correspond to that tiny region of Fig. 6, we propose a ROM for the 3DOF model of the heavy chain. We again recall $\alpha = 0.01$, $\sigma = 1.20$ and $\theta_3 = 2.3798$, which, according to (12) and (13), yield the following asynchronous mode:

$$\boldsymbol{\phi} = \left\{ 1\ 0.0097\ 0 \right\}^T \sin \sqrt{\lambda}\tau, \tag{26}$$

and we then substitute it into (6), yielding
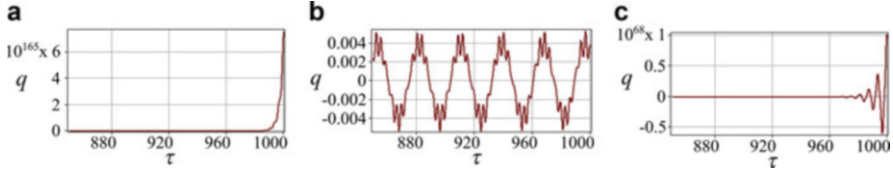
Fig. 7 ROM responses. $\delta = -0.1906$ and (**a**) $\varepsilon_1 = 0.2971$, (**b**) $\varepsilon_2 = 0.6932$ and (**c**) $\varepsilon_3 = 1.0893$

$$\mathbf{M}\boldsymbol{\phi}'' + \mathbf{K}\boldsymbol{\phi} = \boldsymbol{\epsilon}, \tag{27}$$

where $\boldsymbol{\epsilon}$ is the residual error inherent to Galerkin's projection. Next, we consider that $\boldsymbol{\epsilon}$ will be orthogonal to $\boldsymbol{\phi}$. This leads to an equation in the form of (24), in which

$$\delta = 1 + \frac{\left(6q_2^2 - 8q_2 + 5\right)\alpha + \left(-3q_2^2 + 4q_2 - 5\right)\sigma + \left(2q_2^2 - 2q_2 + 2\right)\theta}{1 + q_2^2} \tag{28}$$

and

$$\varepsilon = \left(1 + \frac{q_2}{1 + q_2^2}\right)\Delta\theta. \tag{29}$$

Let us now consider $\Lambda = 4.0$ and, alternatively, $\Delta\theta_1 = 0.3$, $\Delta\theta_2 = 0.7$ and $\Delta\theta_3 = 1.1$, that is, two unstable responses (1 and 3) and a stabilised one (2), as seen in Fig. 5. According to (28) and (29), such values correspond to

$$\delta = -0.1906 \tag{30}$$

and

$$\varepsilon_1 = 0.2971, \ \varepsilon_2 = 0.6932 \ \text{and} \ \varepsilon_3 = 1.0893, \tag{31}$$

which confirm that all cases fall within the left side of Strutt's diagram. Furthermore, as predicted, (δ, ε_2) is inside the stabilised-response region, as shown in Fig. 7b.

5 Stabilisation of Non-linear Responses

Since the stable responses obtained for the 3DOF linear model and for its ROM were very close to the instability boundary, it is convenient to further investigate the effect of geometric non-linearities upon the conclusions withdrawn for the linear system.

Fig. 8 Stability map for the non-linear system, in which q_1 is the RMS value of $q_1(\tau)$
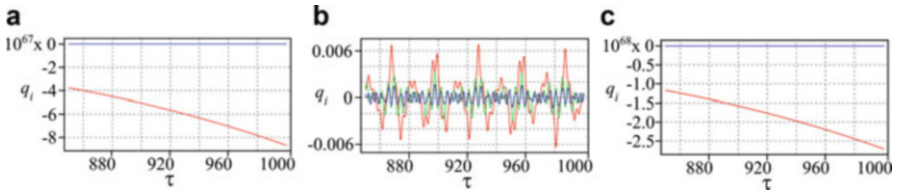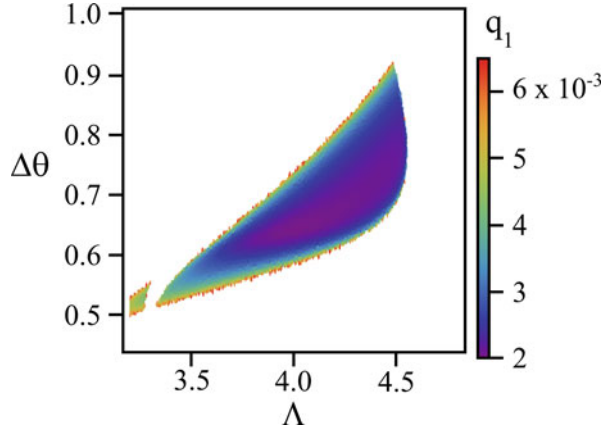
Fig. 9 Non-linear-system time responses for $\Lambda = 4.0$ and (**a**) $\Delta\theta = 0.3$, (**b**) $\Delta\theta = 0.7$ and (**c**) $\Delta\theta = 1.1$

The non-linear motion equations can be written as

$$\mathbf{M}(\mathbf{q})\,\mathbf{q}'' + (\mathbf{K_s} + \mathbf{K_e}\,(\tau))\,\mathbf{q} + \mathbf{K_{nl}}\left(\mathbf{q},\mathbf{q}',\tau\right) = \mathbf{0}. \tag{32}$$

For the sake of brevity, the terms of $\mathbf{M}(\mathbf{q})$ and $\mathbf{K_{nl}}(\mathbf{q},\mathbf{q}',\tau)$ are not shown explicitly here, but can be deduced from the expressions supplied in [30].

Figure 8 displays the non-linear system's stability map. It computes the root mean square (RMS) of $q_1(\tau)$ for different values of Λ and $\Delta\theta$. Blank regions refer to unbounded responses. The analysis of stable wells in Figs. 4 and 8 shows that the responses close to the stability boundary for the linear system are definitely stable for the non-linear system. Hence, the effect of parametric excitation to stabilise unbounded responses is enhanced by geometric non-linearities. Figure 9 confirms the same findings of Fig. 5 for the selected time responses.

6 Conclusions

In this work, a 3DOF heavy chain model was considered for the sake of investigating the role of parametric excitation on the stabilisation of unstable asynchronous responses. In the linear system, Strutt-like diagrams revealed that the parametric

excitation yields a large range of potentially stable responses. Nevertheless, such results must be seen with caution, as they are near the stability boundary (Floquet's multiplier near to unity). Still, stable time responses were successfully obtained, both in the 3DOF and in the associated 1DOF reduced-order model. More clearly stable responses were obtained for the non-linear system. This is due to the combined effect of geometric non-linearities and parametric excitation. Furthermore, stabilisation was achieved with relatively small forcing frequencies, in between the system's natural frequencies. Damping has not been considered throughout, but as in the case of the Mathieu's equation, its effect is expected to be favourable for stabilisation of the solutions.

References

1. A. Stephenson, On induced stability. Philos. Msg. **15**, 233–236 (1908)
2. A. Stephenson. A new type of dynamical stability. Proc. Manchester Literary Philos. Sot. 52, (1908)
3. A. Stephenson, On induced stability. Philos. Msg. **17**, 765–766 (1909)
4. P. Hirtsh, Das Pendel mit Oszillierendem Aufhängepunkt (In German). ZAMM **10**(1), 41–52 (1930)
5. P.L. Kapitsa, The dynamic stability of a pendulum with a vibrating point of suspension. J. Exp. Theor. Phys. **21**, 588–598 (1951)
6. V.N. Chelomei, On the possibility to increase an elastic systems stability by means of vibration (in Russian). Sov. Phys. Dokl. **110**, 345–347 (1956)
7. V.N. Chelomei, Mechanical paradoxes caused by vibrations. Sov. Phys. Dokl. **28**, 387–390 (1983)
8. H.P. Kalmus, The inverted pendulum. Am. J. Phys. **38**, 874 (1970)
9. D.J. Acheson, A pendulum theorem. Proc. Royal Soc. London. Ser. A Math. Phys. Sci. Royal Soc. **443**, 239–245 (1993)
10. D.J. Acheson, T. Mullin, Upside-down pendulums. Nature **366**, 215–216 (1993)
11. D.J. Acheson, T. Mullin. Ropy magic. New Scientist, 32–33 (1998)
12. W.B. Fraser, A.R. Champneys, The 'Indian rope trick' for a parametrically excited flexible rod: Linearized analysis. Proc. Royal Soc. London Ser. A Math. Phys. Eng. Sci. **456**, 553–570 (2000)
13. W.B. Fraser, A.R. Champneys, The 'Indian rope trick' for a parametrically excited flexible rod: Nonlinear and subharmonic analysis. Proc. Royal Soc. London Ser. A Math. Phys. Eng. Sci. **458**, 1353–1373 (2002)
14. E.I. Butikov, On the dynamic stabilization of an inverted pendulum. Am. J. Phys. Am. Assoc. Phys. Teachers (AAPT) **69**, 755–768 (2001)
15. G.L. Anderson, I.G. Tadjbakhsh, Stabilization of Ziegler's pendulum by means of the method of vibrational control. J. Math. Anal. Appl. **143**(1), 198–223 (1989)
16. J. Thomsen, Theories and experiments on the stiffening effect of high-frequency excitation for continuous elastic systems. J. Sound Vib., **260**, 117–139 (2003)
17. J. Galán, W. Fraser, D. Acheson, A. Champneys, The parametrically excited upside-down rod: An elastic jointed pendulum model. J. Sound Vib., **280**, 359–377 (2005)
18. A. Seyranian, A. Seyranian, The stability of an inverted pendulum with a vibrating suspension point. J. Appl. Math. Mech., **70**, 754–761 (2006)
19. A. Seyranian, A. Seyranian, Chelomei's problem of the stabilization of a statically unstable rod by means of a vibration. J. Appl. Math. Mech., **72**, 649–652 (2008)

20. A.A. Mailybaev, A.P. Seyranian, Stabilization of statically unstable systems by parametric excitation. J. Sound Vib., **323**, 1016–1031 (2009)
21. I.M. Arkhipova, A. Luongo, A.P. Seyranian, Vibrational stabilization of the upright statically unstable position of a double pendulum. J. Sound Vib., **331**, 457–469 (2012)
22. I.M. Arkhipova, On Stabilization of a Triple Inverted Pendulum via Vibration of a Support Point with an Arbitrary Frequency. Vestnik St. Petersb. Univ. Math. **52**(2), 194–198 (2019)
23. E.I. Kugushev, M.A. Levin, T.V. Popova, Holonomic systems on a rapidly oscillating plat-form. J. Appl. Math. Mech., **81**(5), 360–367 (2017)
24. C.E.N. Mazzilli, S. Lenci. Asynchronous modes of vibration in a heavy-chain model, in *17th International symposium on dynamics problems of mechanics. Sao Sebastiao*, (2017)
25. C.E.N. Mazzilli, S. Lenci. Asynchronous modes of vibration in a heavy-chain model with linear and rotational springs, in *9th European nonlinear dynamics conference, Budapest*, (2017)
26. E.A.R. Ribeiro, C.E.N. Mazzilli, S. Lenci, Influence of geometric nonlinearities on the asynchronous modes of an articulated prestressed slender structure. J. Vib. Acoust. **141**, 021007–0211–9 (2018)
27. B.A.P. Mendes, C.E.N. Mazzilli, E.A.R. Ribeiro. Parametric instability of a heavy-chain model with an asynchronous vibration mode, in *First international nonlinear dynamics conference, Rome*, (2019)
28. B.A.P. Mendes, C.E.N. Mazzilli, E.A.R. Ribeiro, Energy harvesting in a slender-rod model with modal asynchronicity. Nonlinear Dyn. **55**, 1–14 (2019)
29. A.A. Mailybaev, *Introduction to the Theory of Parametric Resonance (Lecture Notes)* (Instituto Nacional de Matemática Pura e Aplicada, Rio de Janeiro, 2019)
30. A.H. Nayfeh, D.T. Mook, *Nonlinear Oscillations* (Wiley, New York, 1979)

A New Semi-Active Control Method of Yaw Damper in High-Speed Railway Vehicle and Its Experiment in Hardware-in-the-Loop System

Yiwei Zhao, Shaopu Yang, Yongqiang Liu, and Ya Li

1   Introduction

With the rapid development of high-speed railway technology, many dynamic problems have been found and have been researched. In order to avoid hunting instability when the train is running at high speed on a straight line, greater longitudinal damping between the body and the frame is required in most cases, while the longitudinal damping should not be too large when the train passes through the curve to ensure the safety performance. Therefore, the contradiction between lateral stability and curving performance has always been difficult to solve in the process of increasing train speed. This is one of many problems. Engineers constantly optimize the suspension parameters and bogie structure to coordinate the relationship between them to finally achieve overall balance [1–5]. However, the process of parameter and structure optimization is not endless. When

Y. Zhao

School of Traffic and Transportation, Shijiazhuang Tiedao University, Shijiazhuang, Hebei, People's Republic of China

S. Yang (✉)

State Key Laboratory of Mechanical Behavior in Traffic Engineering Structure and System Safety, Shijiazhuang, Hebei, People's Republic of China
e-mail: Yangsp@stdu.edu.cn

Y. Liu

State Key Laboratory of Mechanical Behavior in Traffic Engineering Structure and System Safety, Shijiazhuang, Hebei, People's Republic of China

School of Mechanical Engineering, Shijiazhuang Tiedao University, Shijiazhuang, Hebei, People's Republic of China

Y. Li

School of Mechanical Engineering, Shijiazhuang Tiedao University, Shijiazhuang, Hebei, People's Republic of China

the optimization reaches a certain degree, the contradiction between lateral stability and curving performance will become a main bottleneck for further improving train speed.

Experts and scholars from all around the world have proposed a variety of solutions to the contradiction between lateral stability and curvilinear trafficability. A new type of radial bogie was proposed in [6]. According to the design principle of radial bogie, a breakthrough design of axle box positioning mode is carried out. The contradiction between curve negotiation performance and lateral stability of the bogie is solved with the least number of bars. The dynamic models of electric locomotive with radial bogies and conventional bogies are established by using multi-rigid body dynamics software in [7]. The two models are compared by simulation. The results show that the curving performance of the locomotive model with radial bogies is better than that of the other vehicle. At the same time, the wheel rail wear is reduced significantly. An independent wheelset structure with active control capability is proposed in [8]. The running ability on straight track and curving ability are simulated and analyzed. A curvature measuring method that can be implemented in a railway vehicle system is proposed to steer a railway vehicle in [9]. The field test is carried out by this method. The results show that the method can enhance the curving performance of trains and keep the lateral stability. The primary suspension stiffness is optimized to evaluate the curving performance and stability of trains to meet the operational requirements better in [10]. It can be concluded that the main ways to solve the problem are to use radial bogies and independent wheelsets, as well as parameter optimization, and so on. These solutions can solve the problem to a certain extent.

This chapter presents a semi-active control system of anti-hunting shock absorber, which can change the damping coefficient between straight track and curve track so as to solve the contradiction between lateral stability and curving performance of trains.

At present, semi-active control technology is a kind of control technology which scholars have studied extensively and deeply. Crosby and Karnopp [11] from the United States put forward the concept of semi-active suspension control in the 1970s. Its control mode was applied to actual vehicles in the early 1980s. Up to now, semi-active control technology has been applied in many fields [12–15] such as automobile, railway, and building. In 1983, Toyota developed an "on-off" semi-active suspension which can generate corresponding damping force by adjusting a switch and applied it to the 280GT car. In 1985, Dominy and Bulman designed a Formula One racing car with semi-active suspension. In 2014, Yutong Bus Company developed the semi-active suspension system with variable damping and variable stiffness, which greatly improved the ride comfort of the car. In order to verify the performance of semi-active vibration reduction and improve the ride comfort of high-speed trains, Japanese railway vehicle engineers carried out vehicle tests on 500 series EMUs at 300 km/h on Shanyang Shinkansen Line. The results showed a significant decrease in the energy spectrum of lateral acceleration and lateral acceleration of the vehicle body. Semi-active suspension has gradually become a standardized device on Shinkansen vehicles in Japan. Meanwhile, there are

many types of semi-active control strategies for adjusting the damping coefficient [16–20].

Generally speaking, semi-active control is a mature and reliable control method. It is feasible to apply semi-active control technology to anti-hunting shock absorbers, which can solve the problems described in the chapter. This method does not need to change the structure of the system and to optimize some parameters to redesign the components. This method only needs to replace the traditional oil damper, which can reduce costs.

The content of this work discussed in this chapter is based on the railway field, and the research object is a railway vehicle. The first purpose is to build a simple single wheelset model to study the influence of large damping and small damping on curving performance.

The second goal is to establish the UM-MATLAB co-simulation model of railway vehicles, to propose a new semi-active control strategy, and to study the influence of the control strategy on the dynamic performance of trains, such as ride comfort, safety, and stability.

The third purpose is to carry out the hardware-in-the-loop test and apply the semi-active control strategy to the actual MR damper to verify the effectiveness of the control method.

2 Establishment and Simulation of Single Wheelset Model

This work first considers the problem from a simple model. A single wheelset model used in curve track is established. The longitudinal positioning stiffness kx, lateral positioning stiffness ky, and anti-yaw damping cx of single wheelset are considered in the model as shown in Fig. 1.

The model includes lateral and yaw degrees of freedom. The parameters denoted in Table 1 are derived from a type of high-speed EMUs.

The differential equations of the model are established, which are as follows [21, 22]:

Fig. 1 Two freedom dynamics model of single wheelset
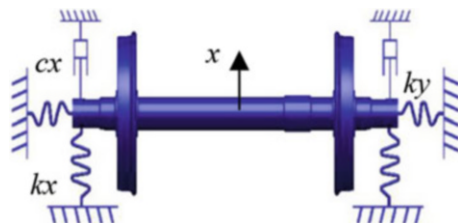
Table 1 The model parameters

Parameters	m/kg	J_w/kg	kx_l/(N·m^{-1})	ky_l/(N·m^{-1})	cx/(N·s·m^{-1})
Value	1901.8	685	9.8e06	9.8e05	2.45e06

$$m\ddot{y}_w + 2f_{22}\left(\frac{\dot{y}_w}{v} - \varphi_w\right) + 2k_y y_w + k_g\left(y_w - y_a\right) - mg\phi + m\frac{v^2}{R} + mr_0\ddot{\varphi} = 0$$
$$J_w\left(\ddot{\varphi}_w + vd\left(\frac{1}{R}\right)\right) + 2f_{11}\left(\frac{\lambda b}{r_0}y_w + \frac{b^2}{v}\dot{\varphi}_w\right) + 2k_x l^2 \varphi_w + 2c_x l^2 \dot{\varphi}_w + k_{g\varphi}\varphi_w - 2f_{11}\frac{\lambda b}{r_0}y_a = 0$$

$$\text{(1)}$$

where f_{11} is the longitudinal creep coefficient, 1e07 N; f_{22} is the lateral creep coefficient, 1e07 N; R is the radius of the curve track, 1500 m; λ is the equivalent conicity, 0.15; v is the running speed, 200 km/h; k_g is the gravity stiffness, 2e04 N/m; $k_{g\varphi}$ is the gravity angular stiffness, 1.1e04 N/m; r_0 is the rolling circle radius, 0.43 m; b is the half of the rolling circle distance, 0.7465 m; l is the half the length of axle, 1 m; and ϕ is the superelevation angle of track, 0.1 rad. y_a is input excitation, y_w is the lateral displacement of the wheelset, φ_w is the wheelset yaw angle.

According to the Eq. (1), the Simulink model of the single wheelset is established, and the parameters are input into the model for simulation. The radius of the curve track used in the model is 1500 m, and the random excitation is German lateral irregularity spectrum.

First, the lateral displacement curves of wheelset and longitudinal creep force under different yaw dampings are obtained, respectively, when the wheelset passes through the ideal curve track as shown in Fig. 2.

The lateral displacement curves of wheelset and longitudinal creep force under different yaw dampings are obtained under the random excitation condition as shown in Fig. 3.

The simulation results show that the larger the damping coefficient, the larger the wheel rail lateral displacement and longitudinal creep force. It is very obvious on the transition curve track. When the damping coefficient is too large, the safety of trains will be reduced, which is not conducive to passing through the curve track. Therefore, the damping coefficient should be smaller so that the train can easily pass through the curve track.

3   Research and Simulation of Semi-Active Control Based for a Whole Car Model

In the second section, the single wheelset is simulated under different damping coefficients. In this section, a vehicle model is built for more in-depth and accurate research. The model of a certain-type high-speed train is established as shown in Fig. 4 by using the UM dynamics simulation software.

The wheel tread is LMA type. The rail profile is T60. The train speed is 200 km/h. Dynamic simulation analysis is carried out using the UM software. The curve track is used. The radius is 1500 m.

(a) Lateral displacement of wheelset

(b) Longitudinal creep force
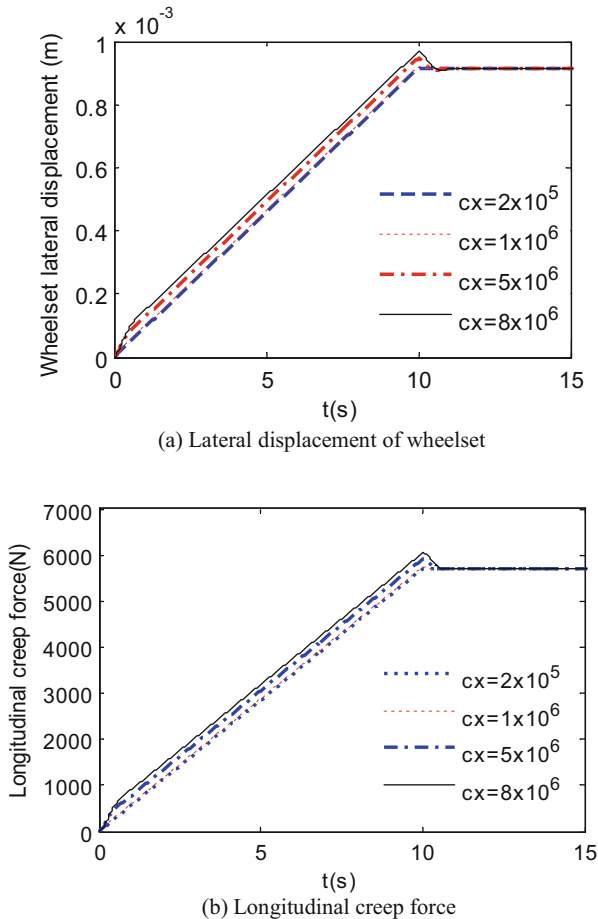
Fig. 2 Parameters using different damping coefficients under ideal track. (**a**) Lateral displacement of wheelset. (**b**) Longitudinal creep force

3.1 Control Strategy Design

Analyzing critical speed is a common way of evaluating train hunting stability. This chapter analyzes the stability of the train on the straight track and safety on the curve track. The critical speeds of the train are obtained under different damping coefficients of yaw dampers. The maximum derailment coefficients under different damping coefficients are obtained when the train runs on the curve track. Derailment coefficient which is used for evaluating train safety is defined as the vertical force on the wheel divided by the lateral force. In order to make the results clear and easy to understand, the simulation data are standardized to ensure them in the range of 0–1.The standardized formula is shown in (2). After normalization of simulation
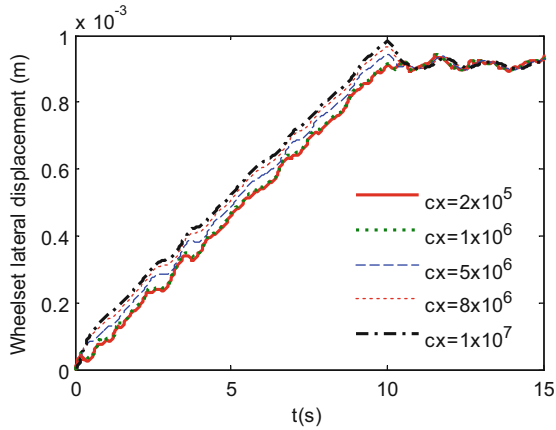
(a) Lateral displacement of wheelset under the random excitation
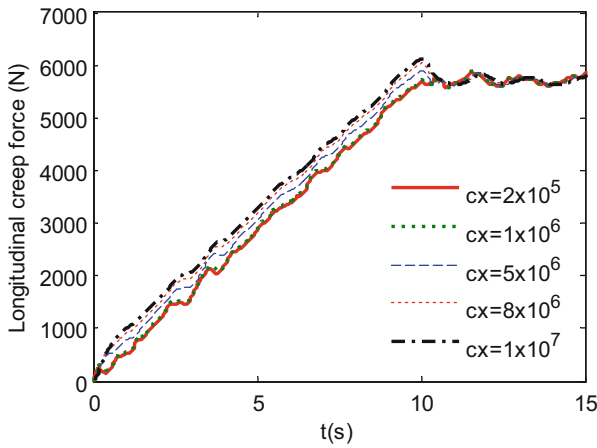
(b) Longitudinal creep force under the random excitation

Fig. 3 Parameters using different damping coefficients under random excitation. (**a**) Lateral displacement of wheelset under random excitation. (**b**) Longitudinal creep force under random excitation

data, the two indexes are put on a picture for analysis as shown in Fig. 5.

$$f_{(0\sim1)} = \frac{x - X_{\min}}{X_{\max} - X_{\min}} \tag{2}$$

where $X_{\min}$ is the minimum value of sample data, $X_{\max}$ is the maximum value of sample data, and x and f are the values before and after standardization, respectively.

Fig. 4 Vehicle model built by UM software
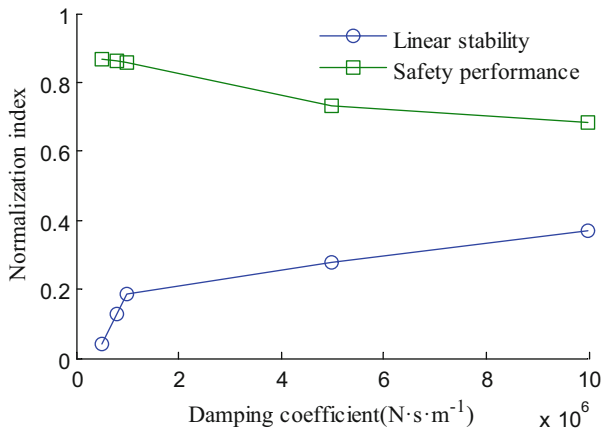
Fig. 5 Comparison chart of normalized indexes

It can be seen from Fig. 5 that the stability is getting higher and higher with the increase of damping coefficient, but the safety performance becomes worse and worse as the train passes through the curve track. Therefore, we need to control the damping coefficient. When a train passes through a straight track, in order to ensure the stability of the train, the damping coefficient needs to be increased, whereas when the train enters a curve track, the damping coefficient is reduced to improve the train running safety. Figure 6 shows the idea of damping control directly.

While, how to identify the train entering the curve track and control the damping has become a core problem of the semi-active control strategy. It is generally known that there will be a height difference between the two sides of a train when the train enters a curve track, while the height difference between the two sides of the train
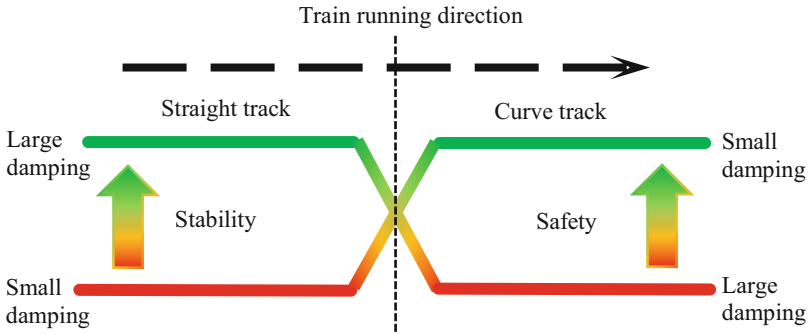
Fig. 6 Damping control diagram

Fig. 7 Comparison of height difference between two sides of frame on straight track and curve track
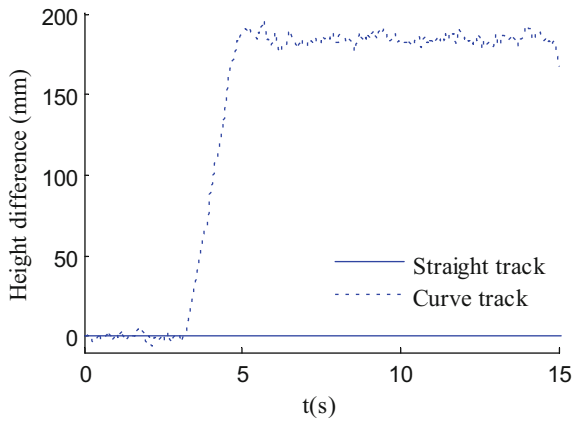
on the straight track is close to zero. Therefore, the height difference is used as a control strategy to adjust the damping coefficient as shown in Fig. 7.

Therefore, the control strategy is as follows:

$$c = \begin{cases} c_{\max} & \Delta h \leq 0 \\ c_{\min} & \Delta h > 0 \end{cases} \tag{3}$$

where Δh is the height difference between the two sides of the bogie.

When a train runs on a straight track with excitation, the height difference between the two sides will not be exactly equal to 0, and it will fluctuate within a threshold. After simulation, the threshold value obtained is 5 mm. Therefore, the control strategy is as follows:

$$c = \begin{cases} c_{\max} & \Delta h \leq \delta \\ c_{\min} & \Delta h > \delta \end{cases} \tag{4}$$

where δ is the threshold.

This kind of control strategy is a switch-type control strategy. When the damping coefficient is switched, the shock absorber may be impacted. The continuous control strategy is discussed in this chapter. In other words, an intermediate damping coefficient is added between the maximum and minimum damping coefficients to mitigate the impact, which is formed by a first-order function, the independent variable of which is height difference between the maximum and minimum damping coefficients to mitigate the impact. The control strategy is as follows:

$$c = \begin{cases} c_{\max} & \Delta h \leq \delta \\ a\,\Delta h + b & \Delta h > \delta \ \text{and} \ \Delta h < \sigma \\ c_{\min} & \Delta h \geq \sigma \end{cases} \tag{5}$$

where a and b are the slope and intercept values of the first-order function respectively, and σ is a threshold which is bigger than δ, 10 mm in this paper.

In order to apply semi-active control strategy to the vehicle, it is imported into MATLAB/Simulink in the form of S-function. The co-simulation model built is shown in Fig. 8. The control strategy is applied to the yaw dampers in Simulink.

In this work, different damping coefficients of yaw dampers are used to simulate when the model is running on the curve track. For each damping value, a corresponding peak value of derailment coefficient is obtained. The simulation curve is shown in Fig. 9.

When the damping coefficient is 2×10^5 N s m^{-1}, the peak value of derailment coefficient is minimum and the train safety is best. The minimum damping coefficient for the control strategy is obtained based on the maximum derailment coefficient in the simulations according to Fig. 9; the maximum damping coefficient obtained is 5×10^6 N s m^{-1}. It can be specifically expressed as follows:

$$c = \begin{cases} c_{\max} & \Delta h \leq 5 \\ -958000 & \Delta h + 9790000 \quad \Delta h > 5 \ \text{and} \ \Delta h < 10 \\ c_{\min} & \Delta h \geq 10 \end{cases} \tag{6}$$

3.2 The Simulation Based on Semi-Active Control

The control strategy is applied to the UM model and the semi-active control simulation is carried out. The curving performance of the model is analyzed, and the comparison curves of derailment coefficient, wheel axle lateral force, and wear work are obtained as shown in Fig. 10.

It can be seen from Fig. 10 that the maximum derailment coefficient decreases by 41.75%, the maximum value of wheel axle lateral force by 17.65%, and the maximum wear power by 57.67%. The safety is enhanced and the curving performance is improved by using the semi-active control strategy. Meanwhile, the
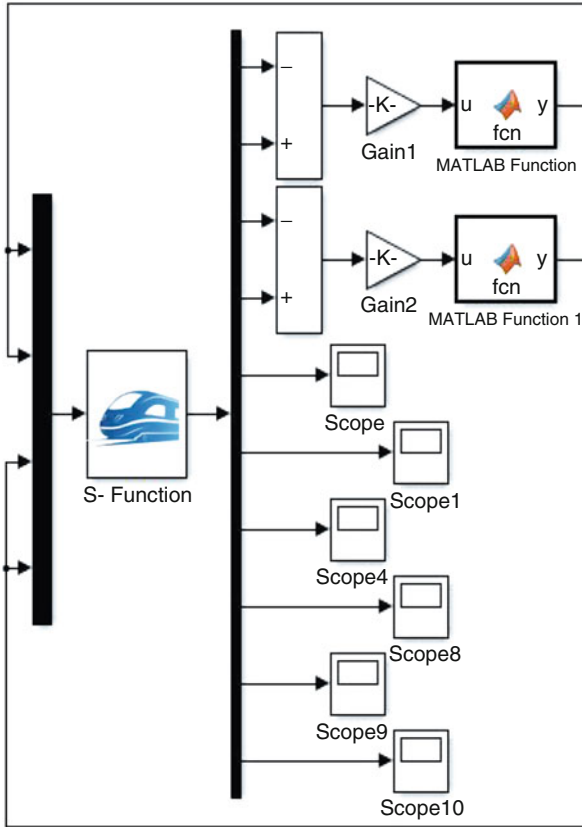
Fig. 8 The co-simulation model

wheel rail wear is reduced substantially. Therefore, the semi-active control strategy proposed in this chapter is effective.

The lateral acceleration curve of the train is obtained as shown in Fig. 11. Through comparison, it is found that the influence of semi-active control on the lateral acceleration is not obvious.

In general, the control strategy proposed in this chapter can improve the curving performance of the train. Meanwhile, it can ensure the stability of the train and the contradiction between the stability and curving performance is solved.

4 Hardware in the Loop Experiment

The semi-active control experiment is analyzed by the MR damper hardware in the loop test. Hardware in the loop (HIL) means that the research object is made into a
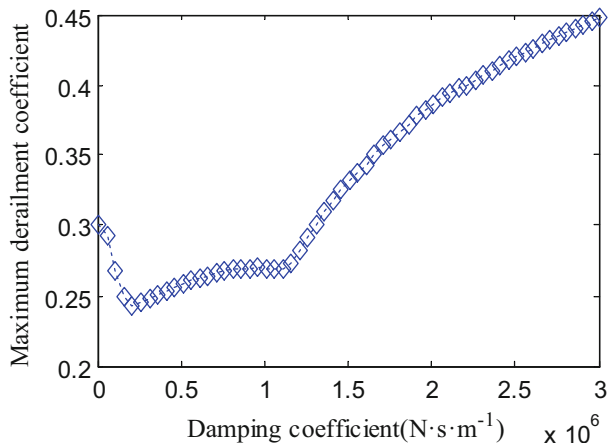
Fig. 9 Optimization of damping coefficient on curved track

real object instead of a virtual model. The shock absorber is embedded in the two degree of freedom model in the work. The real shock absorbers are used to verify the effectiveness of the control strategy. The schematic and physical configuration of HIL test are shown in Fig. 12.

The experimental platform system built by the research team mainly includes upper computer/lower computer, servo electric cylinder, drive controller, force sensor, magnetorheological damper, input/output board, and so on. In the experiment, the RTX real-time simulation system of the ADI company is adopted. The drive controller receives the analog voltages from I/O boards and sends them to the electric cylinder making the MR damper move. The signal received by the electric cylinder comes from the relative velocity at both ends of the shock absorber in the model. The force generated by the real damper is returned to the model through the sensor. Thus, the whole system forms a loop. It can be close to the real operating conditions. In order to apply the control strategy to the test system, damping values in the control strategy need to be represented by the current values.

The lateral displacement and longitudinal creep force of wheelset are obtained by using the test to evaluate the effectiveness of the control strategy as shown in Figs. 13 and 14. In order to match the real shock absorber, the model needs to be scaled and random excitation is applied.

It can be found in the test from the Figs. 13 and 14 that the control effect of semi-active control is better than passive control under the condition of random excitation. This proves the effectiveness of the control strategy proposed in this chapter.

Fig. 10 Comparison of curving performance under different control. (**a**) Comparison chart of derailment coefficient. (**b**) Comparison chart of wheel axle lateral force. (**c**) Comparison chart of wear power
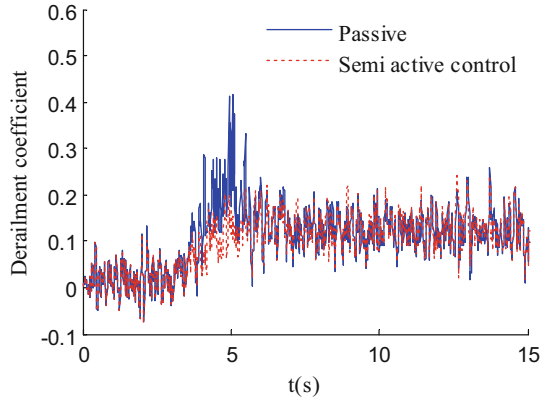
(a) Comparison chart of derailment coefficient
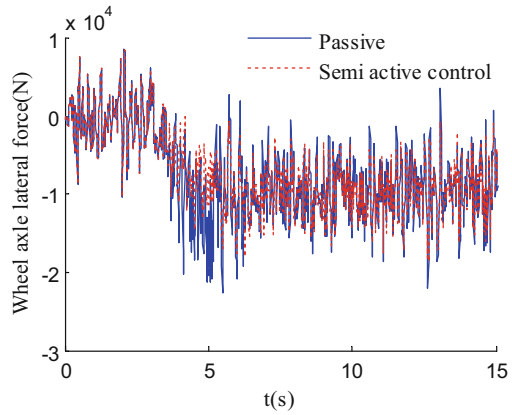
(b) Comparison chart of wheel axle lateral force
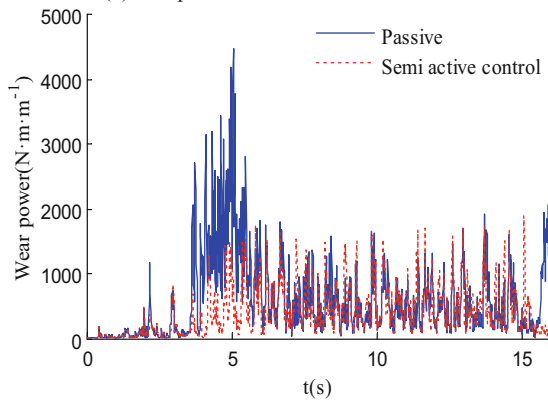
(c) Comparison chart of wear power

Fig. 11 Comparison of car body acceleration under different control
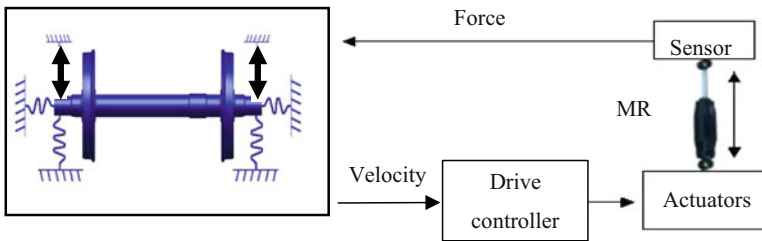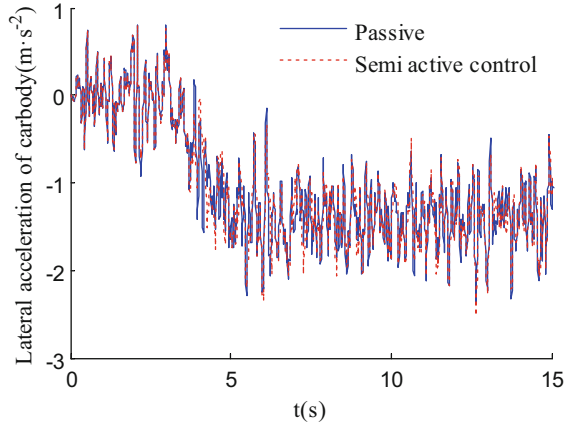
(a) Schematic diagram of hardware in the loop test
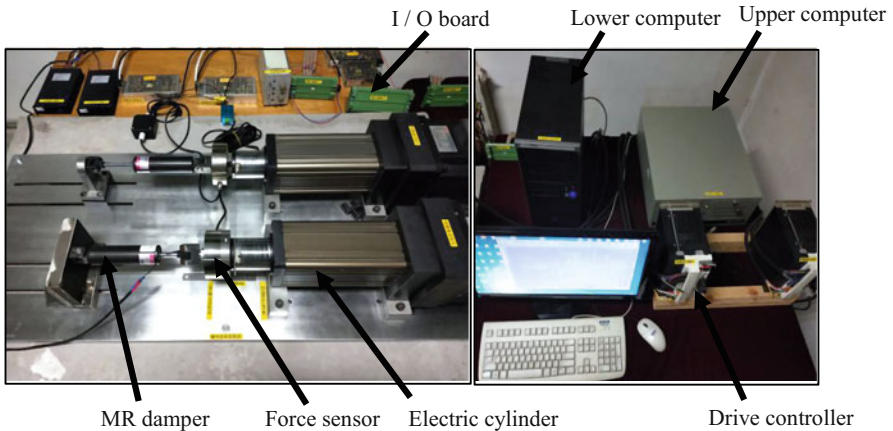
(b) Hardware in the loop test of MRD

Fig. 12 Physical and schematic diagrams of hardware in the loop test. (**a**) Schematic diagram of hardware in the loop test. (**b**) Hardware in the loop test of MRD
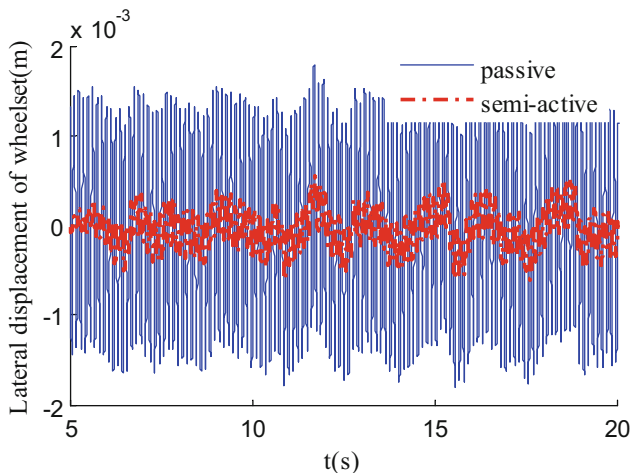
Fig. 13 Lateral displacement of wheelset obtained from the HIL test
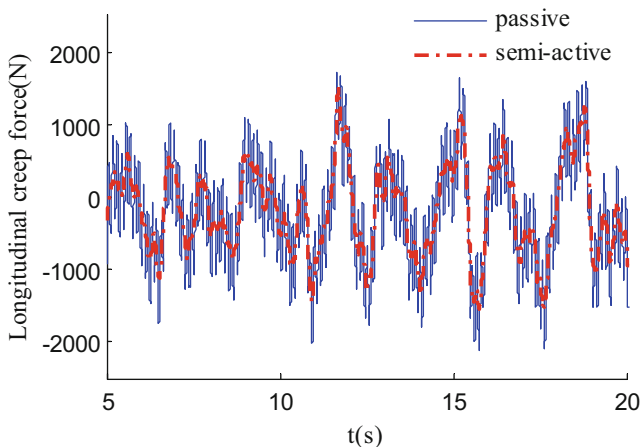
Fig. 14 Longitudinal creep force obtained from the HIL test

5 Conclusions

The results are here summarized.

1. The single wheelset model is established, and the curving performance of wheelsets is analyzed by changing the damping coefficient of yaw dampers. The results show that it is easy to pass the curve track by reducing the damping coefficient.

2. A new type of semi-active control is proposed through vehicle dynamics simulation. The UM-MATLAB simulation results show that the safety is enhanced and the curving performance is improved by using the semi-active control strategy. The contradiction between the stability and curving performance is solved.
3. In this chapter, the hardware in the loop method is used to analyze the new semi-active control strategy. The results show that the experimental results are consistent with the theoretical results, which prove that the control strategy proposed in this chapter is practical.
4. It is very interesting to study semi-active control strategies. The work discussed in this chapter is just the beginning. The most important thing is that the research results should be applied to the engineering practice. In the future, the control strategy will be materialized, the controller will be developed, and the real vehicle test will be carried out.

References

1. H.L. Li, F. Li, Y.H. Huang, Research on wheel hollow wear and dynamic performance of freight radial bogies[J]. Proc. Instit. Mech. Eng. Part F J. Rail Rapid Transit **231**(9), 1015–1021 (2017)
2. Y.X. Wen, W.X. Zhou, Y. Chen, et al., Study on passing curve of light rail vehicles with independent wheelsets [J]. Railway Locomotive Car **40**(02), 126–130 (2020). (in Chinese)
3. Y.X. Wen, W.X. Zhou, Y. Chen, et al., Study on curving pass of independent wheelset on light rail transit[J]. Electric Drive Locomotives **05**, 111–115 (2019). (in Chinese)
4. B. Fu, S.H. Luo, X.Y. Liu, et al., Steering characteristic of independent wheelset of articulated single-axle bogie with radial mechanism[J]. Electric Drive Locomotives **05**, 27–31 (2016). (in Chinese)
5. O. Polach, I. Kaiser, Comparison of methods analyzing bifurcation and hunting of complex rail vehicle models[J]. J. Comput. Nonlinear Dyn. **7**(4), 1–8 (2012)
6. Y. Shi, Research of principle and dynamic of pendulum type radial bogie[J]. Railway Locomotive Car **35**(05), 46–48 (2015). (in Chinese)
7. J. Wei, Y. Luo, K.Q. Wang, Dynamic performances comparison of type HX_D1C electric locomotives with traditional and radial bogies[J]. Railway Locomotive Car **34**(04), 24–28+65 (2014). (in Chinese)
8. H. Yin, T.F. Wang, M. Xiao, et al., Research on active control of new low floor independent wheelset bogies[J]. Machine Build. Automation **48**(05), 168–170+192 (2019). (in Chinese)
9. K.S. Sim, H.M. Hur, H.S. Song, et al., Study of the active radial steering of a railway vehicle using the curvature measuring method[J]. J. Mech. Sci. Technol. **28**(11), 4583–4589 (2014)
10. L.H. Ren, H. Leng, Y.P. Huang, et al., Radial mechanism and parameter influence of coupled bogie for the straddling monorail vehicle[J]. J. Tongji Univ. (Nat. Sci.) **48**(05), 743–750 (2020). (in Chinese)
11. D. Karnopp, M.J. Crosby, R.A. Harwood, Vibration control using semi-active force generators[J]. J. Manuf. Sci. Eng. **96**(2), 619–626 (1974)

12. I. Mihai, F. Andronic, Behavior of a semi-active suspension system versus a passive suspension system on an uneven road surface[J]. Mechanika **20**(1), 64–69 (2014)
13. X.L. Xu, Research on intelligent semi-active vibration control of tall building structure[D]. Hang zhou Zhejiang Univ. (2006) (in Chinese)
14. X.M. Dong, M. Yu, C.R. Liao, et al., Comparative research on semi-active control strategies for magneto-rheological suspension[J]. Nonlinear Dyn. **59**(3), 433–453 (2010)
15. W.S. Ding, S.J. Liu, J.L. Bu, Lateral suspension control mode and semi-active damper of high-speed train[J]. China Mech. Eng. **14**(12), 995–998 (2013)
16. Y.L. Liu, L. Zuo, Mixed skyhook and power-driven-damper: A new low-jerk semi-active suspension control based on power flow analysis[J]. J. Dyn. Syst. Measure. Control **139**(8), 1–10 (2016)
17. D. Sammier, O. Sename, L. Dugard, Skyhook and H∞control of semi-active suspensions: Some practical aspects[J]. Veh. Syst. Dyn. **39**(4), 279–308 (2003)
18. S.M. Savaresi, C. Spelta, Mix-1-sensor: A control strategy for semi-active suspension[J]. IFCA Proc. Vol. **40**(10), 367–374 (2007)
19. M. Ahmadian, X.B. Song, S.C. Southward, No-jerk skyhook control methods for semi-active suspensions[J]. J. Vib. Acoust. **126**(4), 580–584 (2004)
20. S.M. Savaresi, E. Silani, S. Bittanti, Acceleration-Driven-Damper(ADD): An optimal control algorithm for comfort-oriented semi-active suspensions[J]. J. Dyn. Syst. Measure. Control **127**(2), 218–229 (2005)
21. P.F. Liu, Research on dynamic interaction between heavy haul train and track under longitudinal impact [D]. Southwest Jiaotong University (2015)
22. X.N. Ma Study on lateral vibration control and dynamics of high speed locomotive based on magnetorheological damper [D]. Beijing Jiaotong University (2012)

Analysis of Half-Car Model with Nonlinear Damper Under Sinusoidal Road Excitation

Sivakoteswararao Ikkurthi, Priyank Prakash, and Ashok Kumar Pandey

1 Introduction

A road vehicle vibrates when running on sinusoidal road surface. For better passenger comfort, the vibration amplitude needs to be reduced using the dampers. The dampers are classified as passive, semi-active, and active dampers. The semi-active and active dampers are known to use control force to suppress the vibration of vehicle due to road excitation [1–4]; nevertheless, almost all the road vehicles use passive oil dampers due to their low cost.

The active suspension with full feedback control and optimization with respect to ride comfort, working space of the suspension, road holding, and control force of the suspension is studied by Hac [3] when the vehicle is traversing on random road surface. The quarter car model with MR dampers is studied by Prabakar et al. [4]. The stability and frequency analysis of quarter car model is carried out by Siewe [5], and they concluded that the periodic motion of the system becomes chaotic motion with the increasing force. The homoclinic bifurcation in quarter car model using Melnikov criterion is studied by Litak et al. [6] in which they found critical Melnikov amplitude of the road surface profile above which the system shows chaotic behaviour. The linear time delay active control in nonlinear quarter car model is studied by Naik et al. [7] where they used Melnikov technique to study onset of chaos from homoclinic bifurcation and concluded that there is effect of time delay on the critical forces that lead to Melnikov chaos. They also concluded that the delayed feedback prevents the stable and unstable manifolds from tangling.

S. Ikkurthi · P. Prakash · A. K. Pandey (✉)
Department of Mechanical and Aerospace Engineering, Indian Institute of Technology
Hyderabad, Kandi, Sangareddy, Telangana, India
e-mail: me13m15p000009@iith.ac.in; ME12M1022@iith.ac.in; ashok@mae.iith.ac.in

To capture the dynamics of front and rear wheels, the half-car model with time delay with MR dampers at the front and rear wheels is studied by Prabakar et al. [8]. The rms state variables for the control force, suspension length, and tyre deflection are computed using spectral decomposition methods by Thompson et al. [9]. Using the semi-active MR damper, the preview distance control is studied by Rao et al. [10], and they concluded that the overall performance improves with preview distance and has a limit after which the performance saturates. To include the nonlinear properties of suspension system, the half-car model is studied by Zhu et al [11] in which the stiffness and damping are assumed to be nonlinear. It is observed by Zhu et al. [11] that the unstable region in frequency response diagram could lead to chaotic response. From the bifurcation diagram, they concluded that the chaotic motion is sensitive to the damping value of the system. The full-car nonlinear model is studied by Zhu et al. [12] in which the full vehicle is studied with the nonlinear stiffness and damping. They concluded that the chaotic vibration of the system could be avoided by having the frequency of excitation away from the unstable regions of the frequency response diagram. Thus, due to nonlinear characteristics of these dampers, the influence of suspension characteristics with delay in road excitation of front and rear wheels should be studied to understand the vehicle dynamics.

In this chapter, nonlinear damper with cubic nonlinearity for the stiffness and damping is considered. The system is converted from heave and pitch motions into two degrees of freedom at the front and rear vertical vibrations. The method of multiple scales [13] is used to arrive at the envelope equations by equating the secular terms to zero. The frequency response curves are obtained by using the envelope equations.

2 Mathematical Model

The schematic diagram of half-car suspension is shown in Fig. 1. The equation of motion for the half-car can be derived using Newton's laws for transverse displacement y_c and pitch angle θ as [1]

$$M\ddot{y}_c + K_{1f}z_1 + F_{hf} + K_{1r}z_2 + F_{hr} = 0 \tag{1}$$

$$I\ddot{\theta} + aK_{1f}z_1 + aF_{hf} - bK_{1r}z_2 - bF_{hr} = 0, \tag{2}$$

where road excitation provided through sinusoidal road profile of amplitude A and frequency Ω at front and rear wheels as $y_f = A\sin(\Omega t)$, $y_r = A\sin(\Omega t - \phi)$, $z_1 = y_c + a\theta - y_f$, $z_2 = y_c - b\theta - y_r$, $F_{hf} = K_{2f}z_1^3 + C_{1f}\dot{z}_1 + C_{2f}\dot{z}_1^3$, $F_{hr} = K_{2r}z_2^3 + C_{1r}\dot{z}_2 + C_{2r}\dot{z}_2^3$. The above equations in $\ddot{y}_c$ and $\ddot{\theta}$ can be converted into equations in terms of transverse displacements $\ddot{z}_1$ and $\ddot{z}_2$ of front and rear wheels at distances a and b, respectively, from the centre of gravity subjected to sinusoidal
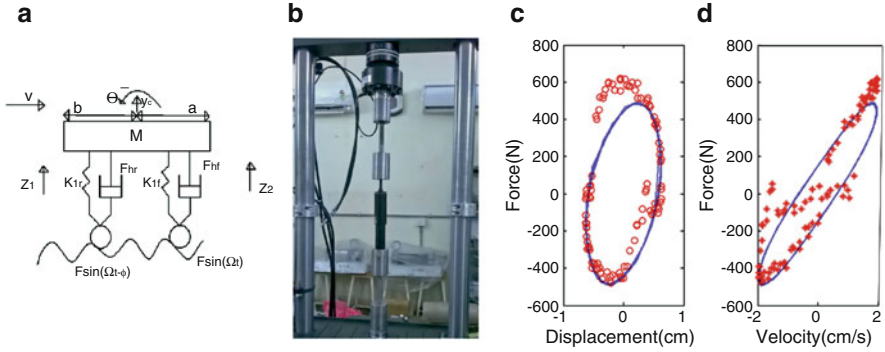
Fig. 1 (**a**) Half-car model with periodic excitation, (**b**) Experimental setup, (**c**) Force vs. displacement, and (**d**) Force vs. velocity

excitation of front and rear wheels with delay angle of ϕ. The equations can be non-dimensionalized by dividing them with ω_1^2, where $\omega_1 t = \tau$ and $\Omega' = \frac{\Omega}{\omega_1}$. The resulting equation can be written as

$$\ddot{z}_1 + z_1 + B_1 z_1^3 + B_2 \dot{z}_1 + B_3 \dot{z}_1^3 + B_4 z_2 + B_5 z_2^3 + B_6 \dot{z}_2 + B_7 \dot{z}_2^3 = F \sin(\Omega' \tau) \quad (3)$$

$$\ddot{z}_2 + \frac{\omega_2^2}{\omega_1^2} z_2 + B_8 z_1 + B_9 z_1^3 + B_{10} \dot{z}_1 + B_{11} \dot{z}_1^3 + B_{12} z_2^3 + B_{13} \dot{z}_2 + B_{14} \dot{z}_2^3$$

$$= F \sin(\Omega' \tau - \phi), \quad (4)$$

where $F = A\Omega'^2$ scaled version of road profile amplitude, $\omega_1^2 = (\frac{1}{M} + \frac{a^2}{I})K_{1f}$, $B_1 = (\frac{1}{M} + \frac{a^2}{I})\frac{K_{2f}}{\omega_1^2}$, $B_2 = (\frac{1}{M} + \frac{a^2}{I})\frac{C_{1f}}{\omega_1}$, $B_3 = (\frac{1}{M} + \frac{a^2}{I})C_{2f}\omega_1$, $B_4 = (\frac{1}{M} - \frac{ab}{I})\frac{K_{1r}}{\omega_1^2}$, $B_5 = (\frac{1}{M} - \frac{ab}{I})\frac{K_{2r}}{\omega_1^2}$, $B_6 = (\frac{1}{M} - \frac{ab}{I})\frac{C_{1r}}{\omega_1}$, $B_7 = (\frac{1}{M} - \frac{ab}{I})C_{2r}\omega_1$, $\omega_2^2 = (\frac{1}{M} + \frac{b^2}{I})K_{1r}$, $B_8 = (\frac{1}{M} - \frac{ab}{I})\frac{K_{1f}}{\omega_1^2}$, $B_9 = (\frac{1}{M} - \frac{ab}{I})\frac{K_{2f}}{\omega_1^2}$, $B_{10} = (\frac{1}{M} - \frac{ab}{I})\frac{C_{1f}}{\omega_1}$, $B_{11} = (\frac{1}{M} - \frac{ab}{I})C_{2f}\omega_1$, $B_{12} = (\frac{1}{M} + \frac{b^2}{I})\frac{K_{2r}}{\omega_1^2}$, $B_{13} = (\frac{1}{M} + \frac{b^2}{I})\frac{C_{1r}}{\omega_1}$, $B_{14} = (\frac{1}{M} + \frac{b^2}{I})C_{2r}\omega_1$. Suspension parameters are obtained from the silicon oil damper used in Tavera front suspension using MTS test machine as shown in Fig. 1b. The cubic nonlinearity of stiffness coefficient and linear and cubic nonlinearity of damping coefficients of damper are considered based on the curve fitting the experimental and analytical force displacement, and force velocity curves are shown in Fig. 1c, d. Now, the frequency analysis is done for half-car model under different resonance conditions: (a) $\omega_1 = 1, \Omega' = \omega_1 + \epsilon\sigma_1$ and $\omega_1 = \omega_2 + \epsilon\sigma_2$, (b) $\omega_1 = 1, \Omega' = \omega_1 + \epsilon\sigma_1$ and $3\omega_1 = \omega_2 - \epsilon\sigma_2$, (c) $\omega_1 = 1, 3\Omega' = \omega_1 + \epsilon\sigma_1$ and $3\omega_1 = \omega_2 + \epsilon\sigma_2$.

3 Modulation Equations

The solution to Eqs. (3) and (4) can be obtained using the method of multiple scales as follows:

$$z_1 = z_{10}(T_0, T_1) + \epsilon z_{11}(T_0, T_1) + O(\epsilon^2)$$
$$z_2 = z_{20}(T_0, T_1) + \epsilon z_{21}(T_0, T_1) + O(\epsilon^2), \tag{5}$$

where z_{10}, z_{11}, z_{20}, z_{21} are functions to be determined, $T_0 = t$, $T_1 = \epsilon t$, and $T_n = \epsilon^n t$. The differential operators become

$$\frac{d}{dt} = D_0 + \epsilon D_1 + ...; \quad \frac{d^2}{dt^2} = D_0^2 + \epsilon D_0 D_1 + \epsilon^2 (D_1^2 + 2D_0 D_2) + ... \tag{6}$$

3.1 Primary Resonance When Front Wheel and Rear Wheel Have Nearly Equal Resonance Frequencies

To determine the amplitude of oscillation at primary resonance, the force term and the nonlinear terms are assumed to be small and of the order of ϵ. Equating the coefficients of the like powers of ϵ gives the following differential equations.

$$D_0^2 z_{10} + \omega_1^2 z_{10} = 0, \ D_0^2 z_{20} + \omega_2^2 z_{20} = 0, \tag{7}$$

$$D_0^2 z_{11} + z_{11} = -2D_0 D_1 z_{10} - B_1 z_{10}^3 - B_2 D_0 z_{10} - B_3 (D_0 z_{10})^3 - B_4 z_{20}$$
$$- B_5 z_{20}^3 - B_6 D_0 z_{20} - B_7 D_0 z_{20}^3 + F \sin(\Omega' \tau),$$

$$D_0^2 z_{21} + \left(\frac{\omega_2^2}{\omega_1^2}\right) z_{21} = -2D_0 D_1 z_{20} - B_8 z_{10} - B_9 z_{10}^3 - B_{10} D_0 z_{10} - B_{11} (D_0 z_{10})^3$$
$$- B_{12} z_{20}^3 - B_{13} D_0 z_{20} - B_1 4 (D_0 z_{20})^3 + F \sin(\Omega' \tau - \phi). \tag{8}$$

The general solution to Eq. (7) is given by

$$z_{10} = A_1(T_1) e^{i\omega_1 T_0} + \bar{A_1}(T_1) e^{-i\omega_1 T_0}, \ z_{20} = A_2(T_1) e^{i\omega_2 T_0} + \bar{A_2}(T_1) e^{-i\omega_2 T_0}. \tag{9}$$

Substituting Eq. (9) into Eq. (8), collecting the secular terms with the conditions $\omega_1 = 1$, $\Omega' = \omega_1 + \epsilon \sigma_1$ and $\omega_1 = \omega_2 + \epsilon \sigma_2$, and equating the real and imaginary parts to zero give the following modulation equations for primary resonance at front wheel with internal resonance at rear wheel. Here, we substitute $A_m = \frac{1}{2} a_m e^{i\theta_m}$.

The ϕ is calculated using the time taken for the vehicle to travel its length of 2.5 m using 10 m/s speed. The corresponding modulation equations are

$$a_1' = \frac{B_2 a_1}{2} + \frac{3 B_3 a_1^3 \omega_1^2}{8} + \frac{B_4 a_2 \sin(\gamma_2)}{2\omega_1} + \frac{3 B_5 a_2^3 \sin(\gamma_2)}{8\omega_1}$$

$$+ \frac{B_6 a_2 \omega_2 \cos(\gamma_2)}{2\omega_1} + \frac{3 B_7 a_2^3 \omega_2^3 \cos(\gamma_2)}{8\omega_1} + \frac{F \cos(\gamma_1)}{2\omega_1} \tag{10}$$

$$\gamma_1' = \sigma_1 - \frac{3 B_1 a_1^3}{8 a_1 \omega_1} - \frac{B_4 a_2 \cos(\gamma_2)}{2 a_1 \omega_1} - \frac{3 B_5 a_2^3 \cos(\gamma_2)}{8 a_1 \omega_1}$$

$$+ \frac{B_6 a_2 \omega_2 \sin(\gamma_2)}{2 a_1 \omega_1} + \frac{3 B_7 a_2^3 \omega_2^3 \sin(\gamma_2)}{8 a_1 \omega_1} + \frac{F \sin(\gamma_1)}{2 a_1 \omega_1} \tag{11}$$

$$a_2' = \frac{B_8 a_1 \sin(\gamma_2)}{2\omega_2} + \frac{3 B_9 a_1^3 \sin(\gamma_2)}{8\omega_2} - \frac{B_{10} a_1 \omega_1 \cos(\gamma_2)}{2\omega_2} - \frac{3 B_{11} a_1^3 \omega_1^3 \cos(\gamma_2)}{8\omega_2}$$

$$- \frac{B_{13} a_2 \omega_2}{2\omega_2} - \frac{3 B_{14} a_2^3 \omega_2^3}{8\omega_2} - \frac{F \cos(\gamma_1 - \gamma_2 - \Omega\phi)}{2\omega_2} \tag{12}$$

$$\gamma_2' = -\sigma_2 + \frac{B_8 a_1 \cos(\gamma_2)}{2 a_2 \omega_2} + \frac{3 B_9 a_1^3 \cos(\gamma_2)}{8 a_2 \omega_2} + \frac{B_{10} a_1 \omega_1 \sin(\gamma_2)}{2 a_2 \omega_2} \tag{13}$$

$$+ \frac{3 B_{11} a_1^3 \omega_1^3 \sin(\gamma_2)}{8 a_2 \omega_2} + \frac{3 B_{12} a_2^3}{8 a_2 \omega_2} - \frac{F \sin(\gamma_1 - \gamma_2 - \Omega\phi)}{2 a_2 \omega_2}, \tag{14}$$

where $\gamma_1 = \sigma_1 T_1 - \theta_1$ and $\gamma_2 = -\sigma_2 T_1 + \theta_2 - \theta_1$.

3.2 Primary Resonance at the Front Wheel When Resonance Frequency of the Rear Wheel Is 3 Times That of the Front Wheel

To determine the amplitude of oscillation at primary resonance, the force term and the nonlinear terms are assumed to be small and are of the order of ϵ. Equating the coefficients of the like powers of ϵ, we get the following equations:

$$D_0{}^2 z_{10} + \omega_1{}^2 z_{10} = 0; \quad D_0{}^2 z_{20} + \omega_2{}^2 z_{20} = 0 \tag{15}$$

$$D_0{}^2 z_{11} + z_{11} = -2D_0 D_1 z_{10} - B_1 z_{10}{}^3 - B_2 D_0 z_{10} - B_3 (D_0 z_{10})^3 - B_4 z_{20}$$
$$- B_5 z_{20}{}^3 - B_6 D_0 z_{20} - B_7 D_0 z_{20}{}^3 + F \sin(\Omega' \tau)$$

$$D_0{}^2 z_{21} + \left(\frac{\omega_2{}^2}{\omega_1{}^2}\right) z_{21} = -2D_0 D_1 z_{20} - B_8 z_{10} - s B_9 z_{10}{}^3 - B_{10} D_0 z_{10} - B_{11}(D_0 z_{10})^3$$
$$- B_{12} z_{20}{}^3 - B_{13} D_0 z_{20} - B_1 4 (D_0 z_{20})^3 + F \sin(\Omega' \tau - \phi). \tag{16}$$

The general solution of Eq. (15) can be written as

$$z_{10} = A_1(T_1)e^{i\omega_1 T_0} + \bar{A_1}(T_1)e^{-i\omega_1 T_0}$$
$$z_{20} = A_2(T_1)e^{i\omega_2 T_0} + \bar{A_2}(T_1)e^{-i\omega_2 T_0}. \tag{17}$$

Substituting Eq. (17) into Eq. (16), collecting the secular terms with the conditions $\omega_1 = 1$, $\Omega' = \omega_1 + \epsilon\sigma_1$ and $3\omega_1 = \omega_2 - \epsilon\sigma_2$, and equating the real and imaginary parts to zero give the following modulation equations for primary resonance at front wheel with internal resonance at rear wheel. Here, we substitute $A_m = \frac{1}{2} a_m e^{i\theta_m}$. The ϕ is calculated using the time taken for the vehicle to travel its length of 2.5 m using 10 m/s speed.

$$a_1' = -\frac{B_2 a_1}{2} - \frac{3B_3 a_1^3}{8} - \frac{F\cos(\gamma_1)}{2}, \quad \gamma_1' = \sigma_1 - \frac{3B_1 a_1^2}{8} + \frac{F\sin(\gamma_1)}{a_1}$$
$$a_2' = -\frac{B_9 a_1^3 \sin(\gamma_2)}{24} - \frac{B_{11} a_1^3 \cos(\gamma_2)}{24} - \frac{B_{13} a_2}{2} - \frac{27 B_{14} a_2^3}{8}$$
$$\gamma_2' = -\sigma_2 + \frac{9B_1 a_1^2}{8} - \frac{F\sin(\gamma_1)}{2a_1} - \frac{B_9 a_1^3 \cos(\gamma_2)}{24a_2} + \frac{B_{11} a_1^3 \sin(\gamma_2)}{24a_2} - \frac{3B_{12} a_2^3}{24a_2}, \tag{18}$$

where $\gamma_1 = \sigma_1 T_1 - \theta_1$ and $\gamma_2 = -\sigma_2 T_1 + 3\theta_1 - \theta_2$.

3.3 Superharmonic Resonance at the Front Wheel with Internal Resonance at Rear Wheel

Now including the forcing term in Eq. (15) gives the below equations

$$D_0{}^2 z_{10} + \omega_1{}^2 z_{10} = F \sin(\Omega' \tau); \quad D_0{}^2 z_{20} + \omega_2{}^2 z_{20} = F \sin(\Omega' \tau - \phi) \tag{19}$$

$$D_0{}^2 z_{11} + z_{11} = -2D_0 D_1 z_{10} - B_1 z_{10}{}^3 - B_2 D_0 z_{10} - B_3 (D_0 z_{10})^3 - B_4 z_{20}$$

$$- B_5 z_{20}{}^3 - B_6 D_0 z_{20} - B_7 D_0 z_{20}{}^3$$

$$D_0{}^2 z_{21} + \left(\frac{\omega_2{}^2}{\omega_1{}^2}\right) z_{21} = -2D_0 D_1 z_{20} - B_8 z_{10}{}^3 - B_9 z_{10}{}^3 - B_{10} D_0 z_{10} - B_{11}(D_0 z_{10})^3$$

$$- B_{12} z_{20}{}^3 - B_{13} D_0 z_{20} - B_1 4 (D_0 z_{20})^3. \tag{20}$$

The general solution to Eq. (19) gives

$$z_{10} = A_1(T_1) e^{i\omega_1 T_0} + \bar{A_1}(T_1) e^{-i\omega_1 T_0} + \frac{F e^{i(\Omega T_0 - \frac{\pi}{2})}}{2(\omega_1{}^2 - \Omega'^2)} - \frac{F e^{-i(\Omega T_0 + \frac{\pi}{2})}}{2(\omega_1{}^2 - \Omega'^2)}$$

$$z_{20} = A_2(T_1) e^{i\omega_2 T_0} + \bar{A_2}(T_1) e^{-i\omega_2 T_0} + \frac{F e^{i(\Omega T_0 - \phi - \frac{\pi}{2})}}{2(\omega_2{}^2 - \Omega'^2)} - \frac{F e^{-i(\Omega T_0 - \phi + \frac{\pi}{2})}}{2(\omega_2{}^2 - \Omega'^2)}. \tag{21}$$

Substituting Eq. (21) into Eq. (20), collecting the secular terms with the conditions $\omega_1 = 1, 3\Omega' = \omega_1 + \epsilon \sigma_1$ and $3\omega_1 = \omega_2 + \epsilon \sigma_2$, and equating the real and imaginary parts to zero give the following envelope equations for superharmonic resonance at front wheel with internal resonance at rear wheel.

$$a_1' = -B_1 B_{111}^3 \cos(\gamma_1) - \frac{B_2 a_1}{2} - \frac{3B_3 a_1^3}{8} - 3B_3 B_{111}^2 \Omega'^2 a_1 - B_3 B_{111}^3 \Omega'^3 \sin(\gamma_1)$$

$$- B_5 B_{111}^3 \cos(\gamma_1 - 3\phi) - B_7 B_{111}^3 \Omega'^3 \sin(\gamma_1 - 3\phi)$$

$$\gamma_1' = \sigma_1 - \frac{3B_1 a_1^2}{8} - 3B_1 B_{111}^2 + \frac{B_1 B_{111}^3 \sin(\gamma_1)}{a_1} - \frac{B_3 B_{111}^3 \Omega'^3 \cos(\gamma_1)}{a_1}$$

$$+ \frac{B_5 B_{111}^3 \sin(\gamma_1 - 3\phi)}{a_1} - \frac{B_7 B_{111}^3 \Omega'^3 \cos(\gamma_1 - 3\phi)}{a_1}$$

$$a_2' = \frac{-B_9 a_1^3 \sin(\gamma_2)}{24} + \frac{B_{11} a_1^3 \cos(\gamma_2)}{24} - \frac{B_{13} a_2}{2} - \frac{27 B_{14} a_2^3}{8} - 3B_{14} B_{222}^2 \Omega'^2 a_2$$

$$\gamma_2' = \sigma_2 + \frac{9B_1 a_1^2}{8} + 9B_1 B_{111}^2 - \frac{3B_1 B_{111}^3 \sin(\gamma_1)}{a_1} + \frac{3B_3 B_{111}^3 \Omega'^3 \cos(\gamma_1)}{a_1}$$

$$- \frac{3B_5 B_{111}^3 \sin(\gamma_1 - 3\phi)}{a_1} + \frac{3B_7 B_{111}^3 \Omega'^3 \cos(\gamma_1 - 3\phi)}{a_1} - \frac{-B_9 a_1^3 \cos(\gamma_2)}{24 a_2}$$

$$- \frac{B_{11} a_1^3 \sin(\gamma_2)}{24} - \frac{B_{12} a_2^3}{8 a_2} - B_{12} B_{222}^2 a_2,$$

where $\gamma_1 = \sigma_1 T_1 - \theta_1, \gamma_2 = \sigma_2 T_1 + 3\theta_1 - \theta_2, B_{111} = \frac{F}{2(\omega_1^2 - \Omega^2)}$ and $B_{222} = \frac{F}{2(\omega_2^2 - \Omega^2)}$.

4 Results and Discussion

Modulation equations are obtained under different conditions and are used to obtain frequency response curves. Here, a_1, a_2, and σ_1, σ_2 are vibration amplitudes and detuning factors of front and rear wheels. They are plotted for different values of excitation amplitude F in order to show significant nonlinear effects under different resonance conditions.

4.1 Frequency Response Results

To obtain the amplitude versus frequency response curves at the front and rear wheels, we use the following parameter values from Popp et al. [14]. Approximate values of nonlinear coefficients and parameter values are $M = 1250\,\text{kg}$, $I = 2000\,\text{kgm}^2$, $a = 1.2\,\text{m}$, $b = 1.3\,\text{m}$, $K_{1f} = 50\,\text{kN/m}$, $K_{1r} = 50\,\text{kN/m}$, $K_{2f} = -5000\,\text{kN/m}^3$, $K_{2r} = -5000\,\text{kN/m}^3$, $C_{1f} = 3500\,\text{Ns/m}$, $C_{1r} = 3500\,\text{Ns/m}$, $C_{2f} = -350\,\text{Ns}^3/\text{m}^3$, $C_{2r} = -350\,\text{Ns}^3/\text{m}^3$, and $\epsilon << 1$. The vehicle is assumed to travel at a speed of 10 m/s to obtain the time delay between front and rear wheels of $\phi = 0.25\Omega^{'}\,\text{rad}$, where $\Omega^{'}$ is the road profile frequency. For nearly equal frequencies of front and rear wheels, we have limit cycles formed as amplitude vs. frequency response curves with two limit points $(-58.74, 0.531)$ and $(-58.39, 0.5294)$ in a_1 vs. σ. Similarly, for a_2 vs. σ, the limit points are observed at $(-58.39, 0.00623)$ and $(-58.74, 0.006226)$. For case in which the resonance of the rear wheel is three times the frequency of the front wheel, Fig. 2a shows the comparison between solution of modulation equation obtained using MATCONT and solution based on Runge–Kutta method for the primary resonance at the front wheel. Fig. 2b, c shows frequency response curves of front and rear wheels due to primary excitation at front wheel. Figure 2d shows frequency response curve of rear wheels when excitation is at rear wheel. Similarly, the response under superharmonic condition is observed in Fig. 3a–c.

4.2 Frequency Response Results with Parameters from Experiment

In this section, we obtain the solution under primary resonance and superharmonic resonance corresponding to the suspension parameters obtained from the experimental values [15] as $K_{1f} = 9\,\text{kN/m}$, $K_{1r} = 9\,\text{kN/m}$, $K_{2f} = -5000\,\text{kN/m}^3$, $K_{2r} = -5000\,\text{kN/m}^3$, $C_{1f} = 12\,\text{kNs/m}$, $C_{1r} = 12\,\text{kNs/m}$, $C_{2f} = -4\,\text{kNs}^3/\text{m}^3$, $C_{2r} = -4\,\text{kNs}^3/\text{m}^3$, and $\epsilon << 1$. Like previous case, for nearly equal frequencies of front and rear wheels, we get isolated limit cycles formed as amplitude vs. frequency response curves with two limit points in a_1 vs. σ as well as a_2 vs. σ
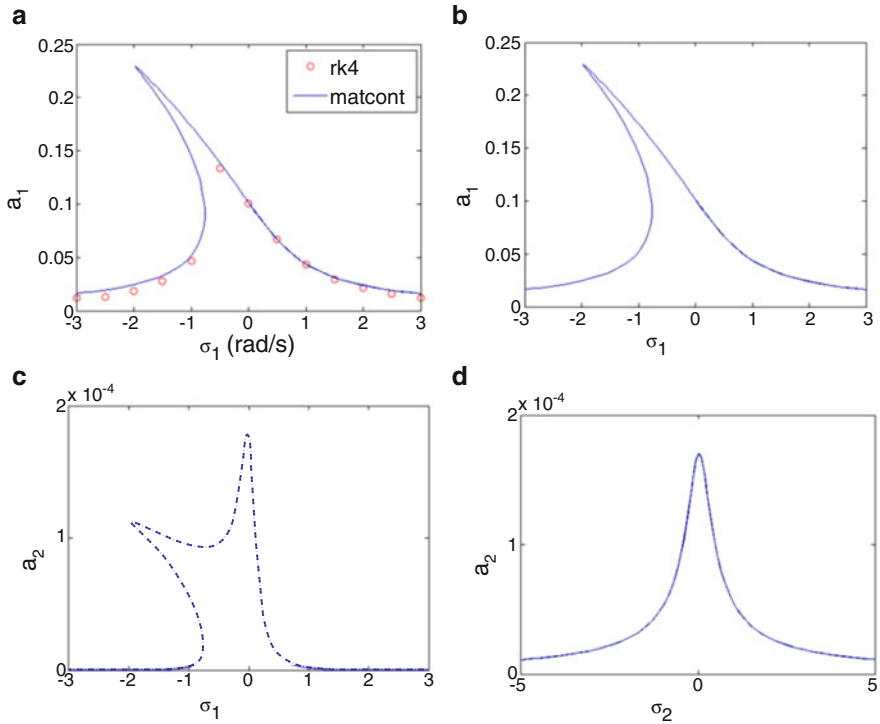
Fig. 2 (**a**) Validation of MMS solution with numerical results as per a_1 versus σ_1. Frequency response of (**b**) a_1 versus σ_1, (**c**) a_2 versus σ_1, and (**d**) a_2 versus σ_2 for $\Omega' = \omega_1 + \epsilon\sigma_1$, $3\omega_1 = \omega_2 - \epsilon\sigma_2$ and $F = 0.098N$
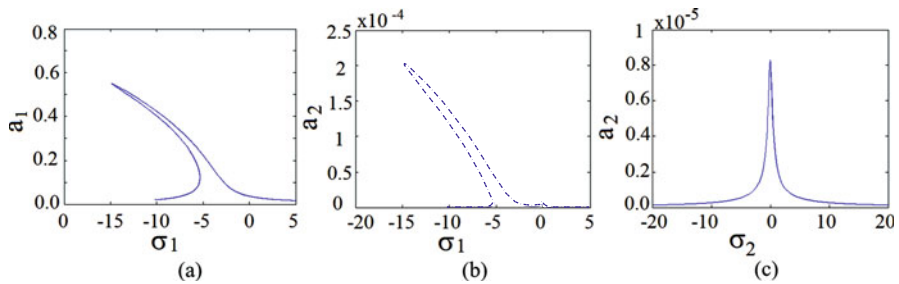
Fig. 3 Frequency response of (**a**) a_1 versus σ_1, (**b**) a_2 versus σ_1, and (**c**) a_2 versus σ_2 for $3\Omega' = \omega_1 + \epsilon\sigma_1$, $3\omega_1 = \omega_2 + \epsilon\sigma_2$ and $F = 0.2$

for the same speed and delay as in the previous case. For other cases, we obtain the response curve of front wheels and rear wheels in Fig. 4a, b when excitation is at front wheel under primary resonance condition. Figure 4c shows the response of rear wheel when excitation is near the resonance condition of rear wheel. Similarly, the
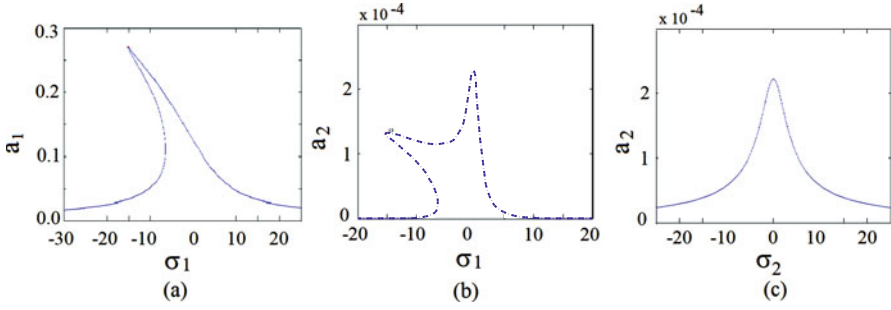
Fig. 4 Frequency response of (**a**) a_1 versus σ_1, (**b**) a_2 versus σ_1, and (**c**) a_2 versus σ_2 for $\Omega' = \omega_1 + \epsilon\sigma_1$, $3\omega_1 = \omega_2 - \epsilon\sigma_2$ and $F = 1$
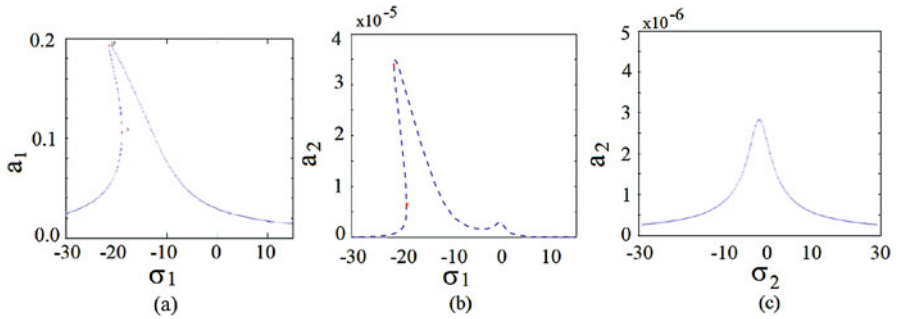
Fig. 5 Frequency response of (**a**) a_1 versus σ_1, (**b**) a_2 versus σ_1, and (**c**) a_2 versus σ_2 for $3\Omega' = \omega_1 + \epsilon\sigma_1$, $3\omega_1 = \omega_2 + \epsilon\sigma_2$ and $F = 0.16$

response of front and rear wheels under superharmonic condition is also obtained in Fig. 5.

Based on the observation of results, it is found that delay in road excitation between front and rear wheels induces coupled nonlinear response that should be controlled by tuning the vehicle parameters or damper characteristics.

5   Conclusions

The envelope equations are derived using the method of multiple scales for half-car model with nonlinear damper having cubic nonlinearity for the stiffness and damping coefficients. The frequency response curves are presented for primary and superharmonic resonances of front and rear wheel with periodic kinematic excitation from the road surface. The internal resonance effect between the front and rear wheels is present because of the damper nonlinearity.

References

1. I. Sivakoteswarrao, Performance characteristics of semi-active and passive damper using different car models. Master's thesis (2015). Indian Institute of Technology Hyderabad

2. V. Rajath, I. Sivakoteswarrao, A.K.P. Pandey, Performance characteristics of 2 and 3 dofs quarter car models with MR damper, in *24th International Congress on Sound and Vibration (ICSV24)*, 23–27 July 2017, London

3. A. Hac, Suspension optimization of a 2-dof vehicle model using a stochastic optimal control technique. J. Sound Vib. **100**(3), 343–357 (1985). https://doi.org/10.1016/0022-460X(85)90291-3

4. R.S. Prabakar, C. Sujatha, S. Narayanan, Response of a quarter car model with optimal magnetorheological damper parameters. J. Sound Vib. **332**, 2191–2206 (2013). https://doi.org/10.1016/j.jsv.2012.08.021

5. M. Siewe Siewe, Resonance, stability and period-doubling bifurcation of a quarter-car model excited by the road surface profile. Phys. Lett. A **374**(13–14), 1469–1476 (2010). https://doi.org/10.1016/j.physleta.2010.01.043

6. G. Litak, M. Borowiec, M.I. Friswell, K. Szabelski, Chaotic vibration of a quarter-car model excited by the road surface profile. Commun. Nonlinear. Sci. Numer. Simul. **13**, 1373–1383 (2008). https://doi.org/10.1016/j.cnsns.2007.01.003

7. R.D. Naik, P.M. Singru, Resonance, stability and chaotic vibration of a quarter-car vehicle model with time-delay feedback. Commun. Nonlinear. Sci. Numer. Simul. **16**, 3397–3410 (2011). https://doi.org/10.1016/j.cnsns.2010.11.006

8. R.S. Prabakar, C. Sujatha, S. Narayanan, Response of a half-car model with optimal magnetorheological damper parameters. J. Vib. Control **22**(3), 784–798 (2016). https://doi.org/10.1177/1077546314532300

9. A.G. Thompson, B.R. Davis, Computation of the rms state variables and control forces in a half-car model with preview active suspension using spectral decomposition methods. J. Sound Vib. **285**, 571–583 (2005). https://doi.org/10.1016/j.jsv.2004.08.017

10. L.V.V. Gopala Rao, S. Narayanan, Preview control of random response of a half car vehicle model traversing rough road. J. Sound Vib. **310**, 352–365 (2008). https://doi.org/10.1016/j.jsv.2007.08.004

11. Q. Zhu, M. Ishitobi, Chaos and bifurcations in a nonlinear vehicle model. J. Sound Vib. **275**, 1136–1146 (2004). https://doi.org/10.1016/j.ijsolstr.2005.06.070

12. Q. Zhu, M. Ishitobi, Chaotic vibration of a nonlinear full-vehicle model. Int. J. Solids Struct. **43**, 747–759 (2006). https://doi.org/10.1016/j.ijsolstr.2005.06.070

13. A.H. Nayfeh, D.T. Mook, *Nonlinear Oscillations* (Wiley, Hoboken, 2004). https://www.wiley.com/en-in/Nonlinear+Oscillations-p-9780471121428

14. K. Popp, W. Schiehlen, *Ground Vehicle Dynamics* (Springer, Berlin, 2010). https://www.springer.com/gp/book/9783540240389

15. P. Prakash, Experimental and analytical studies of MR damper under dynamic loading, MTech Thesis. Indian Institute of Technology Hyderabad (2014). https://doi.org/10.1177/1077546314532300

An Optimal Fractional LQR-Based Control Approach Applied to a Cart-Pendulum System

Julio Cesar Basilio, José Geraldo Telles Ribeiro, Americo Cunha Jr, and Tiago Roux Oliveira

1 Introduction

The idea of the fractional calculus was introduced in 1695, when L'Hôpital in a letter to Leibniz questions what would be the mathematical interpretation for the notation of the derivative $d^n f / dx^n$ (created by Leibniz) if it has a non-integer order ($n = 1/2$, for example). The search to find this interpretation involved many mathematicians like Euler, Fourier, Laplace, among others. Its first practical application was made in 1823 by Niels Henrik Abel, to solve problem of tautochrone curve, for which the time of descent of a body abandoned on it and subject to the action of gravity is the same regardless of the starting point where the body is abandoned [1, 2].

During the following centuries, many pure and applied mathematicians contributed to the development of the theory of fractional calculus, and many different fractional operators were proposed, including the fractional derivatives of Grünwald–Letnikov, Riemann–Liouville, and Caputo [3].

The Riemann–Liouville fractional integral [3] of order α, where $\alpha \in \mathbb{R}$ and $\alpha > 0$, is defined in terms of a convolution-type operation between the real-valued function $y(t)$ and the kernel $t^{\alpha-1}$

$$\mathcal{I}_{a,t}^{\alpha} y(t) = \frac{1}{\Gamma(\alpha)} \int_a^t (t - \tau)^{\alpha-1} y(\tau)\, d\tau , \quad t > a \tag{1}$$

being Γ the Gamma function, and the Riemann–Liouville fractional derivative [3] is defined in terms of the classical derivative of order $n \in \mathbb{Z}^+$ of this fractional-order integral

J. C. Basilio (✉) · J. G. T. Ribeiro · A. Cunha Jr · T. R. Oliveira
Rio de Janeiro State University – UERJ, Rio de Janeiro, Brazil
e-mail: basilio.julio@posgraduacao.uerj.br; jose.ribeiro@uerj.br; telles@eng.uerj.br;
americo.cunha@uerj.br; tiagoroux@uerj.br

185

$$_{RL}\mathcal{D}_{a,t}^{\alpha} y(t) = \frac{1}{\Gamma(n-\alpha)} \frac{d^n}{dx^n} \int_a^t (t-\tau)^{n-\alpha-1} y(\tau)\, d\tau \,, \tag{2}$$

which is a global operator (not local as in classical calculus) that presents "memory", being $t > a$ and $n - 1 < \alpha < n$.

The development of new definitions is an active field of research in mathematics [4, 5], including unified definitions [6]. On the other hand, the use in applications was possible mainly due to the development of numerical methods to simulate fractional systems [7], which also allowed the use of fractional operators in engineering analysis [8] and in control theory [9], especially when dealing with delays [10] or chaotic nonlinear systems [11].

In addition to the favorable feature of fractional-order operators in providing a natural framework for describing phenomena with memory, the fractional exponent in control theory also offers a type of additional degree of freedom to tune a controller, opening up opportunities for further performance improvements in the controller project. In this context, this chapter proposes a LQR-based control system with cross-entropy method to stabilize an inverted cart-pendulum system and analyzes the possibility of improving the performance of the controller using fractional integrators, comparing this with the integer-order. Performance is evaluated through indexes related to the control error, the settling time of the system output, and the control effort. To find the parameters that result in the best performance for the controller, including the possibility of fractional-order, and find the most efficient method to optimize systems that use fractional control, two methods of global optimization are used, the genetic algorithm [12] and the cross-entropy method [13, 14]. The inverted pendulum is chosen as a reference because it is a classic control problem, a nonlinear system widely studied using integer-order controllers [15], which has also started to be tested in the fractional control literature [16].

2 Nonlinear Dynamic System

An inverted pendulum has its center of mass above its pivot point, so when in the vertical position it is in its unstable equilibrium position, and a small disturbance can bring down the pendulum. Maintaining this equilibrium position or at a desired reference angle is done by changing the cart position. The inverted cart-pendulum used in this chapter is shown in Fig. 1 (left), where M is the cart mass; m is the inverted pendulum mass; L is the distance from the center of pendulum's mass to the fixation point; x is the cart's horizontal displacement; θ is the angle between the pendulum and a perpendicular axis through the cart's centroid; and u is the force applied to the cart to control the system. The mass of the rod is neglected, the surface is considered to be frictionless, and the mechanical joint is considered smooth.

The dynamics of the system evolve according to the nonlinear model

$$(J + m\,L^2)\,\ddot{\theta} - m\,g\,L\,\sin\theta = -m\,L\,\ddot{x}\,\cos\theta \tag{3}$$

$$(m + M)\,\ddot{x} + m\,L\,\ddot{\theta}\,\cos\theta - m\,L\,\dot{\theta}^2\,\sin\theta = u, \tag{4}$$

where J is the pendulum moment of inertia. As can be seen, the dynamics of the plant is nonlinear, and a suitable controller is needed to keep the pendulum in a certain position. In this chapter, we considered the values of m equal to 0.1 kg, M equal to 2 kg, L is the length of 0.5 m, and the moment of inertia J is equal to 0.006 kg.m^2. The upper dot is an abbreviation for time derivative.

3 Control Strategy

3.1 Controller Design

Figure 1 (right) shows the LQR-based controller proposed to control the inverted cart-pendulum system.

In this proposed controller, r is the reference input signal; e is the tracking error; u is the control signal; K_1, K_2, K_3, K_4, K_l are the control gains; $\mathcal{I}^{\alpha_1}$, $\mathcal{I}^{\alpha_2}$, $\mathcal{I}^{\alpha_3}$, $\mathcal{I}^{\alpha_l}$ are the integrators, if $\alpha \in \mathbb{Z}$ (integer order) and if $\alpha \notin \mathbb{Z}$ (fractional-order). In this plant, the feedback is done through two state variables, angular speed $\dot{\theta}$ and cart speed $\dot{x}$, chosen to be the observed states. Therefore, to obtain the angular position of the pendulum and the position of the car, these variables are integrated by $\mathcal{I}^{\alpha_1}$ and $\mathcal{I}^{\alpha_3}$, respectively, as defined by the fractional integral of Riemann–Liouville in Eq. (2). In addition, a feedback in the input through the integrals $\mathcal{I}^{\alpha_2}$ and $\mathcal{I}^{\alpha_l}$ of the car position is performed.
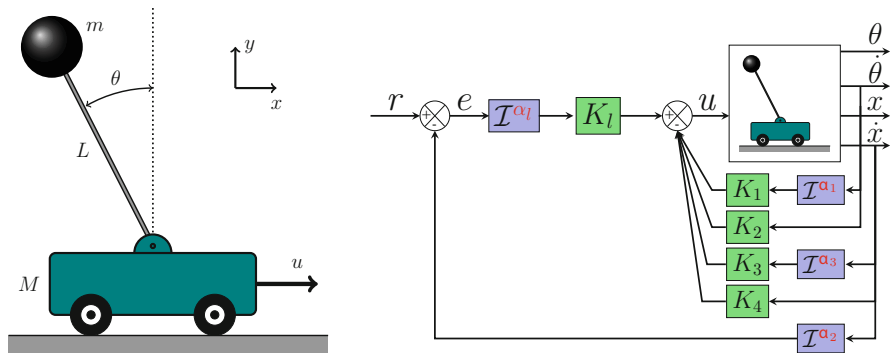
Fig. 1 Schematic illustration of the cart-pendulum system (left), and the proposed LQR-based controller (right)

To know the performance of an integer-order controller, used as a reference in the comparisons of this work, the pole placement method was used to obtain the controller gains K_i. This is a classic and widely used method, developed for linear systems using integer-order controllers, where the location of the poles is chosen based on the desired performance of the closed-loop system. Since this method is based on the linear system hypothesis, the inverted cart-pendulum model is linearized. Using the Matlab to calculate the gains, the following values are obtained: $K_1 = -200.6$; $K_2 = -50.3$; $K_3 = -70.1$; $K_4 = -46.8$; $K_l = -63.8$.

3.2 Controller Performance

Performance indexes of control systems are indicators of the quality of the elaborated project, being possible to evaluate quantitatively the performance of different controllers. Mathematically, a performance index is a function of system states, inputs, and time. In addition, performance indices can also be used as an objective function for obtaining controllers. In this chapter, the performance of the controllers is evaluated using the following criteria:

– Integrated square error: $ISE = \int_0^t e(t)^2 \, dt$
– Settling time (ST)
– Integrated square control signal: $ISU = \int_0^t u(t)^2 \, dt$

The first two indices refer to the state variables (θ, $\dot{\theta}$, x, and $\dot{x}$). The ISE index is related to the area displaced by the car or the pendulum during the evaluated period until reaching the reference. The settling time, as the name says, is the time it takes the signal to reach the reference. The latter, the ISU index, quantifies the control effort during the evaluated period.

4 Controller Optimization Problem

4.1 LQR-Based Fitness Function

The objective of this chapter is to find the set of controller parameters that maximize the performance of the controller. Thus, the design variables chosen for the optimization problem are the gains and the order of the integrators, especially the latter that define whether the controller will be fractional or integer.

The lower and upper bounds of the variables must be defined according to the computational capacity of the optimization method and in a way that allows the search for the global maximum, without one or more variables being close to the stipulated limit. This problem with the bounds of the variables is one of the reasons for using more than one optimization method.

As explained in Sect. 3.2, the performance evaluation is made through the indexes chosen here; however, for the optimization process, evaluating the indexes separately would make a multi-objective optimization of high computational cost, since the number of design variables is relatively high. Therefore, it is necessary to develop an objective function that takes into account all these performance indices, including the one that assesses the control effort. Control theory has an optimized controller design technique well known in the literature called linear quadratic regulator (LQR). This technique is used in linear systems and has a quadratic cost function that includes the state variables and the control signal, in order to find the optimized gains for the control project [17].

A fitness function based on the LQR was developed mainly because it also takes into account the state variables and the control signal in the formulation

$$
\mathcal{F} = \int_0^\tau \left(w_1 \frac{x^2(t)}{ISE_{x_I}} + w_2 \frac{\theta^2(t)}{ISE_{\theta_I}} + w_3 \frac{u^2(t)}{ISU_{u_I}} + w_4 \frac{\dot{x}^2(t)}{ISE_{\dot{x}_I}} + w_5 \frac{\dot{\theta}^2(t)}{ISE_{\dot{\theta}_I}} \right) dt,
\tag{5}
$$

where t is the time variable, τ is the final evaluation time, and the w's are the weights for each component of the objective function. It is worth mentioning that as the reference for the control is zero, the state variables used directly in the function quantify the error, one of the performance indices evaluated in this chapter. State variables are divided by the respective performance value (ISE and ISU) in integer-order control, minimizing the difference in order of magnitude of each component, trying to allow the weight to be defined as much as possible by $w_1 = w_2 = w_3 = 0.3$ and $w_4 = w_5 = 0.05$. Thus, the value of the fitness function for the classical controller is equal to 1.

Therefore, to obtain a better performance $\mathcal{F} < 1$ must be obtained, that is, the objective function must be minimized. To turn this minimization problem in a maximization problem, as is treated in the optimization methods applied in this chapter, it is considered $S = -\mathcal{F}$. The constraints are incorporated into the objective function through a penalty function

$$
P = 100 \left(\max(0, ST_\theta - ST_\theta^*) \right)^2 + 100 \left(\max(0, ST_x - ST_x^*) \right)^2,
\tag{6}
$$

where ST_θ and ST_x are the settling time of the angular position and the position of the car; ST_θ^* and ST_x^* are the respective values in the classic controller.

4.2 Genetic Algorithms

Genetic algorithms (GA) are heuristic search approaches applicable to a wide range of optimization problems. Invented by Holland (1975, 1992), this stochastic optimization and global search technique are successful methods for use in problems

with difficult solution spaces, for example, if no derivatives are available and if the fitness scenario suffers from poorly conditioned parts [12].

Using the principle of genetics and natural selection, evolution is the basis of genetic algorithms, together with their main genetic operators, which are crossover, mutation, and selection. Crossover operators combine the genomes of two or more solutions. The mutation operator adds randomness to the solutions. And finally, the selection operator chooses the best solutions in a population for survival [18].

4.3 Cross-Entropy Method

Global search methods like genetic algorithms are quite effective in overcoming local minimums or maximums, unlike gradient-based methods; however, its control parameters are not intuitive and most of the time its tuning is done through trial and error, which can lead to loss of performance and accuracy. In an attempt to overcome such difficulties and succeed in the search for the controller with the best performance, this work uses, in addition to the GA method, another global search algorithm known as the cross-entropy (CE) method. More robust and simple, it was proposed by R. Rubinstein in 1997 [13] initially for simulation of rare events, and then its effectiveness in application in optimization problems was observed [19, 20]. The idea of the method is to transform a non-convex optimization problem into a rare event estimation problem that can be solved by Monte Carlo sampling technique. The process consists of:

 (i) Sampling the feasible region according to a given probability distribution
 (ii) Evaluating the objective function in each of these samples
(iii) Identifying the samples that produced the highest values for the objective function, this subset being defined as the elite sample set
(iv) Updating the parameters of the probability distribution based on the mean and standard deviation of the elite sample set, modifying the distribution in order to try to make it as close as possible to the global optimum
 (v) Repeating steps (2) to (4) as long as a stop criterion is not met.

This iterative process can be classified into two stages: sampling (i and ii) and learning (iii to v). Furthermore, this process only requires the user to define the number of samples N_s, the number of elite samples $N_e < N_s$, a tolerance of convergence tol, and the maximum number of levels (iterations) $l_{\max}$ [14].

5 Numerical Experiments

The numerical experiments presented here consist of the execution of optimizations using GA and CE methods through numerical simulations in Matlab, where several evaluations of the objective function are performed and the ideal parameters of

the controller that result in its best performance are found. For the operations of fractional integrators, the FOMCON toolbox is employed [7].

The initial conditions for the numerical simulations are defined: $x_0 = 0$ m; $\dot{x}_0 = 0$ m/s; $\theta_0 = 10 \times \pi/180$ rad; $\dot{\theta}_0 = 0$ rad/s. Note that the initial condition of the angular position other than 0 (zero) will force the control system to act to find stabilization. The dynamics are integrated over the time interval $[0; \tau] = [0; 10]$ s.

The optimizations will be divided into two stages according to the choice of design variables to be analyzed. In the first round of optimization, it seeks to find the optimal values of α_1 and α_3, which results in the best performance for the controller, keeping the other parameters fixed. The strategy is to use the controller's gains, obtained by the linear pole placement method, and consider the order of the integers α_2 and α_l equal to 1. Then, optimizations are performed with all system parameters (gains and integrators) to find the one that results in the best control performance.

5.1 Optimization of α_1 and α_3

Initially, the GA and CE optimizations are made with the design variables being α_1 and α_3, keeping the other controller parameters fixed and equal to 1. The results obtained in each of these optimizations are presented in Table 1.

Table 1 Optimal values of the design variables (α_1 and α_3) with their respective performance indexes and fitness function value

		Integer controller	Fractional controller GA		Fractional controller CE	
Parameters	α_1	1.00	1.03		1.03	
	α_2	1.00	1.00		1.00	
	α_3	1.00	0.93		0.93	
	α_l	1.00	1.00		1.00	
	K_1	−200.60	−200.60		−200.60	
	K_2	−50.30	−50.30		−50.30	
	K_3	−70.10	−70.10		−70.10	
	K_4	−46.80	−46.80		−46.80	
	K_l	−63.80	−63.80		−63.80	
Performance index	$ISE\ \theta$	0.021	0.017	−20%	0.017	−20%
	$ISE\ \dot{\theta}$	0.190	0.204	7%	0.204	7%
	$ISE\ x$	0.257	0.230	−11%	0.230	−11%
	$ISE\ \dot{x}$	0.660	0.509	−23%	0.509	−23%
	$ISU\ u$	23.659	24.412	3%	24.411	3%
	$ST\ \theta$	4.873	4.088	−16%	4.088	−16%
	$ST\ x$	5.073	5.100	1%	5.100	1%
Fitness function		1.000	0.909	−9%	0.909	−9%
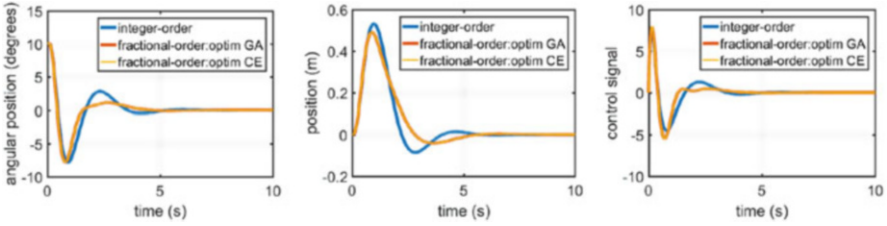
Fig. 2 Time series of the angular position (left), car position (center), and the control signal (right) for results for first optimization

Table 2 Bounds and performance of GA and CE algorithm for optimization evaluated

Method	Bounds			Levels	Function evaluation
	$\alpha_{1,2,3,l}$	K_1	$K_{2,3,4,l}$		
GA	[0.8 1.1]	[-250 -150]	[-90 -30]	327 generations	29,520
CE	[0.5 1.5]	[-350 -1]	[-150 -1]	88 iterations	4400

The first highlight can be made on the efficiency of the CE method compared to GA to obtain the same result more quickly and with less computational cost. Another observation is that the use of fractional-order integrators can improve the performance of the controller, with an optimization close to 10% of the overall performance (based on the fitness function) of the controller. The ISE of the angular position had a reduction of 20% compared to the integer order. The ISE of the angular velocity, the settling time of x, and the control effort were slightly higher; however, compared to the improvement obtained in the others, they are irrelevant. Some of these results are highlighted in Fig. 2, with the time series of the angular position, car position, and control effort.

5.2   Optimization of All Parameters

Based on the results of Sect. 5.1, the following question is asked: "if the gains are also optimized, will the integrators also have a fractional order?". To answer this question, new optimizations are developed with the GA and CE methods, now with all the parameters of the controller as design variables. The results are compared with the integer-order controller, as done previously. Table 2 shows the configuration of the methods, the bounds of all design variables, and the performance of each method for optimization evaluated with all parameters.

Unlike the previous optimization, the optimizations performed with all parameters required a higher computational cost. However, as shown in Table 3, the results of the performance indices and the fitness function of the optimized parameters show that the use of fractional-order integrators together with the optimal gains can further improve the performance of the controller designed through the method of

Table 3 Controller configuration with the optimal values of the design variables (all parameters) and their respective performance indexes and fitness function value

		Integer controller		Fractional controller GA		Fractional controller CE
Parameters	α_1	1.00		0.96		0.72
	α_2	1.00		0.94		0.79
	α_3	1.00		0.91		1.22
	α_l	1.00		0.97		0.80
	K_1	-200.60		-249.98		-205.68
	K_2	-50.30		-60.08		-86.97
	K_3	-70.10		-89.96		-67.54
	K_4	-46.80		-70.35		-124.60
	K_l	-63.80		-83.01		-65.56
Performance index	$ISE\ \theta$	0.021	0.012	-45%	0.009	-55%
	$ISE\ \dot{\theta}$	0.190	0.169	-11%	0.157	-17%
	$ISE\ x$	0.257	0.182	-29%	0.136	-47%
	$ISE\ \dot{x}$	0.660	0.357	-46%	0.283	-57%
	$ISU\ u$	23.659	22.158	-6%	21.497	-9%
	$ST\ \theta$	4.873	3.952	-19%	3.949	-19%
	$ST\ x$	5.073	4.899	-3%	5.100	1%
	Fitness function	1.000	0.730	-27%	0.630	-37%

pole placement. The optimization methods GA and CE allowed results in general (fitness function) with 27% and 37% better than the controller used as reference, respectively.

This difference in methods is linked to the better efficiency of the CE in relation to the operational cost (time/function evaluates). Because in GA, due to the CPU time and the number of variables in the problem, it was necessary to establish lower bound limits of each parameter/design variable for the method to run. This problem can be seen in the values of K_1 and K_3, which were very close to the lower bounds established for them. Another important highlight is how errors can be reduced by up to 50% with fractional integrators, yet requiring 9% less effort from the controller. The time series of the angular position, the car position, and the control effort is shown in Fig. 3, with the comparison of the result of each method with the integer controller.

6 Concluding Remarks

This chapter used the stability problem of an inverted cart-pendulum to develop a study on the performance of fractional controllers compared to those with integer-order integrators. So there is a nonlinear non-convex optimization problem that
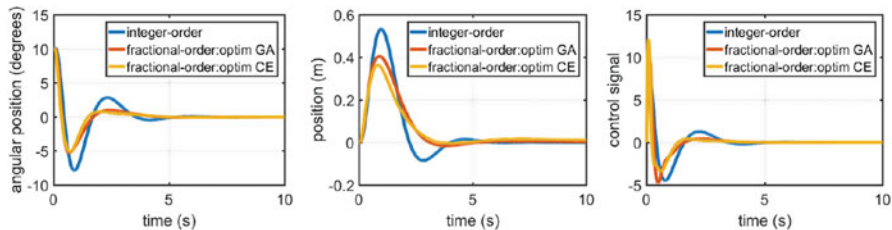
Fig. 3 Time series of the angular position (top-left), car position (top-right), and the control signal (bottom) for result optimization of all the parameters

aims to maximize the performance of the control system, taking into account the error, the settling time, and the control effort. For this, two different optimization methods were used: genetic algorithms and cross-entropy. The latter being faster and more robust for optimization that involves fractional-order integrators, i.e., the cross-entropy presents better performance for problems with many variables, which is the case of systems with fractional control.

As in [9], there is an improvement in the performance of the control circuit that has fractional-order operators, but in this chapter for a LQR-based controller using cross-entropy method. The results show that the use of controllers with fractional integrators instead of integer-order controllers makes the control more efficient and faster, approximately 20% faster to reach the benchmark ($\theta = 0$ rad), with less error and requiring less effort of control. With the reduction of all control parameters, integrators, and gains, the fitness function can be reduced by more than a third, allowing to find a better answer from the results of the pole placement method.

References

1. C.A. Monje, Y. Chen, B.M. Vinagre, D. Xue, V. Feliu-Batle, *Fractional-order Systems and Controls – Fundamentals and Applications* (Springer, Berlin, 2010)
2. M.D. Ortigueira, J.A.T. Machado, What is a fractional derivative? J. Comput. Phys. **293**, 4–13 (2015)
3. C. Li, W. Deng, Remarks on fractional derivatives. Appl. Math. Comput. **187**(2), 777–784 (2007)
4. M. Caputo, M. Fabrizio, A new definition of fractional derivative without singular kernel. Progr. Fract. Differ. Appl. **1**(2), 1–13 (2015)
5. Z. Zheng, W. Zhao, H. Dai, A new definition of fractional derivative. Int. J. NonLin. Mech. **108**, 1–6 (2019)

6. M. D'Elia, M. Gulian, H. Olson, G. Karniadakis, A unified theory of fractional, nonlocal, and weighted nonlocal vector calculus (2020). arxiv.org/abs/2005.07686
7. A. Tepljakov, E. Petlenkov, J. Belikov, FOMCOM: a MATLAB toolbox for fractional-order system identification and control. Int. J. Microelect. Comput. Sci. **2**(2), 51–62 (2011)
8. R.M. Lin, T.Y. Ng, Eigenvalue and eigenvector derivatives of fractional vibration systems. Mech. Syst. Signal Proces. **127**, 423–440 (2019)
9. A. Tepljakov, *Fractional-order Modeling and Control of Dynamic Systems*. Springer Theses (2017)
10. G. Martelli, Stability of PID-controlled second-order time-delay feedback systems. Automatica **45**(11), 2718–2722 (2009)
11. J. Niu, Y. Shen, S. Yang, S. Li, Analysis of duffing oscillator with time-delayed fractional-order PID controller. Int. J. NonLin. Mech. **92**, 66–75 (2017)
12. J.H. Holland, Genetic algorithms. Sci. Am. **267**, 66–73 (1992)
13. R.Y. Rubinstein, D.P. Kroese, *The Cross-Entropy Method: A Unified Approach to Combinatorial Optimization, Monte-Carlo Simulation and Machine Learning*. Information Science and Statistics (Springer, Berlin, 2004)
14. A. Cunha, Enhancing the performance of a bistable energy harvesting device via the cross-entropy method. Nonlin. Dyn. **103**(1), 137–155 (2021). https://doi.org/10.1007/s11071-020-06109-0
15. A. Kharola, P. Patil, S. Raiwani, D. Rajput, A comparison study for control and stabilisation of inverted pendulum on inclined surface (IPIS) using PID and fuzzy controllers. Perspect. Sci. **8**, 187–190 (2016)
16. M.E. Mousa, M.A. Ebrahim, M.M. Hassan, Optimal fractional-order proportional—integral—differential controller for inverted pendulum with reduced order linear quadratic regulator, in *Fractional-order Control and Synchronization of Chaotic Systems*, vol. 688 (Springer, Cham, 2017), pp. 225–252
17. B.D.O. Anderson, J.B. Moore, *Optimal Control: Linear Quadratic Methods* (Prentice-Hall Inc., Hoboken, 1990)
18. O. Kramer, *Genetic Algorithm Essentials* (Springer, Oldenburg, 2017)
19. D.P. Kroese, R.Y. Rubinstein, I. Cohen, S. Porotsky, T. Taimre, Cross-entropy method, in *Encyclopedia of Operations Research and Management Science* (Springer, Berlin, 2013). https://doi.org/10.1007/978-1-4419-1153-7_131
20. R.Y. Rubinstein, D.P. Kroese, *Simulation and the Monte Carlo Method*. Wiley Series in Probability and Statistics, 3rd edn. (Wiley, Hoboken, 2016)

Nonlinear Viscoelastic Damping for Seismic Isolation

Nicola Menga, Francesco Bottiglione, and Giuseppe Carbone

1 Introduction

Suppressing structural vibration has pushed the development of innovative devices and modelling methodologies tailored for the purpose up to the latest years. Since vibration is a common issue, several engineering applications have to face with it. It is the case, for instance, of wind energy converters which may undergo vibration due to internal sources (e.g., rotordynamics unbalance) or external forcing (e.g., wind blows, sea waves). Numerous techniques have been adopted to control the dynamic response of these structures [1], belonging to both families of the passive [2–6] and active systems [7]. Analogue issues exist aiming at isolating heavy mechanical equipment [8], in which case solutions span from hybrid spring-actuator complex [9] to specific actuators [10] and pneumatic suspensions [11]. Although higher performance is in most cases associated with active systems, these are unfeasible when dealing with enough large systems. In these cases, passive isolator is the preferred one. Power plants, as well as schools and medical institutions, require the highest degree of reliability; therefore, we need to enforce the structural integrity of large systems via vibrations control. Due to the broader input spectrum

N. Menga (✉)
Department of Mechanics, Mathematics and Management, Politecnico of Bari, Bari, Italy

Imperial College London, Department of Mechanical Engineering, London, UK
e-mail: nicola.menga@poliba.it

F. Bottiglione
Department of Mechanics, Mathematics and Management, Politecnico of Bari, Bari, Italy

G. Carbone
Department of Mechanics, Mathematics and Management, Politecnico of Bari, Bari, Italy

CNR - Institute for Photonics and Nanotechnologies U.O.S. Bari, Physics Department "M. Merlin", Bari, Italy

effectiveness, nonlinear passive isolation techniques are very promising; indeed, recent studies have focused on different kinds of nonlinearity [12, 13]. Base isolation techniques are mostly indicated in case of single or two storied buildings, with specific focus on rolling devices [14] with rolling path specifically shaped to promote nonlinear re-centering effects [15, 16]. The effectiveness of nonlinear damping is of primary interest as well [17, 18]. Nonlinear dampers can overcome typical limitations of linear ones [19] by acting as low-pass filters, thus being suitable for applications in which stochastic excitations are expected (e.g., wind and earthquakes). For example, nonlinear viscous dampers (NVDs), particle impact dampers (PIDs), and nonlinear energy sinks (NESs) are increasingly adopted in civil engineering applications [20–22] due to their ability to reduce both the relative displacement and the inertial loads acting on the structure [23]. Furthermore, since the overall behavior is nonlinear, higher energy dissipation can also be achieved through wider hysteretic cycles. Interestingly, by relying on viscoelastic NVDs, the overall nonlinear damping behavior can be combined with the nonmonotonic velocity-related dissipation of viscoelastic materials, in order to achieve a low-pass response of the NVD whose maximum damping force is limited.

Rubber-Layer Roller Bearings (RLRBs) are possible NVDs based on viscoelasticity. Indeed, in these systems, depending on the specific application, both metal balls [24–28] and cylinders [29–31] are in contact with viscoelastic coatings deposed onto rigid plates fixed to the ground and the superstructure. During the seismic shock, the relative oscillation between the ground and the superstructure leads to a rolling contact of the balls/cylinders and, in turn, to viscoelastic dissipation. A former investigation has shown promising results achievable with a viscoelastic RLRB with linear stiffness [32, 33] in comparison with linear base isolation, when the nonlinear damping is opportunely tuned for the seismic shock. However, the effectiveness of this kind of nonlinear isolation when dealing with excitation sources unknown a priori, as in the case of earthquakes, needs to be properly assessed. Indeed, in this case, their effectiveness relies on the ability to exhibit a convenient behavior with respect to the wider possible excitation bandwidth.

This study focuses on the isolation performance of an RLRB coupled to a nonlinear cubic spring. The effectiveness of such a nonlinear isolation scheme is investigated, with specific focus on the performance robustness. In order to accomplish this purpose, we focus on a set of three historical seismic shocks with different spectra. The nonlinear damping force is calculated via an accurate previously developed [34–38] model based on a Boundary Element Method (BEM) to formalize the viscoelastic contact behavior of the roller-coating interface. Finally, we compare the RLRB performance with that associated with a linear isolator.

2 Dynamic Model

Figure 1a shows a schematic of the system at hand. The inertial mass m_2 is connected by an elastic superstructure (bending stiffness k_S) to the RLRB, which isolates the superstructure from the ground horizontal seismic oscillation. The
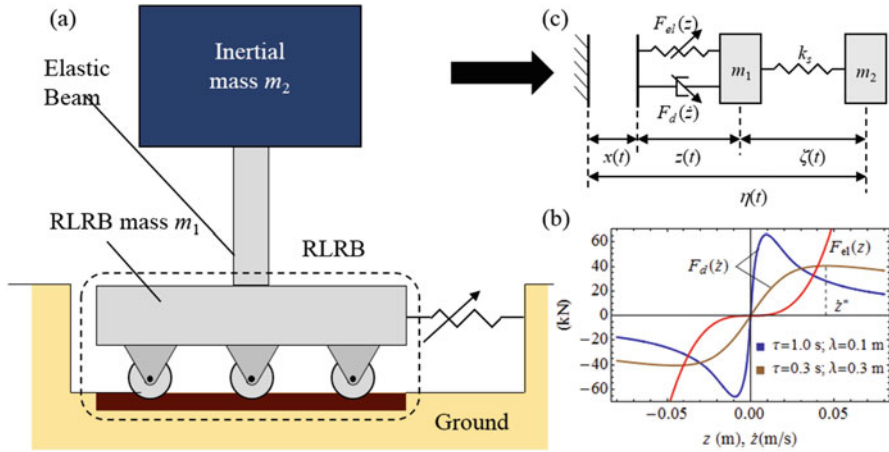
Fig. 1 (**a**) is the functional scheme of the isolator: an heavy mass m_2 is connected by an elastic beam to the RLRB body of mass m_1, which is in turn connected to the ground by means of a nonlinear spring and a nonlinear damper (i.e., the viscoelastic rolling contact between rigid cylinders and rubber pads). (**b**) shows the nonlinear elastic F_{el} and damping F_d forces, with $\mu = 2 \times 10^4$ kN/m^3. (**c**) reports the lumped scheme, showing that the connection to the ground occurs via the nonlinear elastic element and the nonlinear RLRB damper

RLRB mass is m_1, whereas the nonlinear damping force is $F_d(\dot{z})$ and the nonlinear elastic force is $F_{el}(z)$.

Specifically, we focus on the case of a cubic spring; therefore, the elastic force is $F_{el}(z) = \mu z^3$, where z is the relative displacement between the ground and the RLRB.

The RLRB is made of a linear array of rollers with equal radius R, axial length b, and spacing λ, moving in a reciprocating fashion on a viscoelastic layer of thickness h.

The nonlinear damper is a lumped representation of the nonlinear damping effect arising due to the rolling contact between the rigid rollers and the viscoelastic coating, as already shown in Refs. [32, 39].

In this study, we focus on the case of a viscoelastic material with relaxation time τ. Moreover, the damping force $F_d(\dot{z})$ arising from the viscoelastic contact is calculated by exploiting the contact solution already given for thin layers or coatings in Refs. [36–38, 40, 41]. Notably, we assume incompressible material behavior (i.e., $\nu = 0.5$).

In Fig. 1b, the nonlinear forces $F_{el}(z)$ and $F_d(\dot{z})$ are shown. The effects of two relevant parameters of the RLRB are emphasized: the relaxation time τ and the cylinder spacing λ. Interestingly, the effect of the term τ/λ is to shift velocity $\dot{z}^*$ corresponding to the force peak, whereas λ affects the peak amplitude.

Finally, assuming pure horizontal oscillation, with reference to the lumped parameters schematic given in Fig. 1c, the following linear momentum balance equations are derived:

$$m_1 \left(\ddot{x} + \ddot{z} \right) + \mu z^3 + F_d \left(\dot{z} \right) - k_s \zeta = 0$$

$$m_2 \left(\ddot{x} + \ddot{z} + \ddot{\zeta} \right) + k_s \zeta = 0 \tag{1}$$

With the total displacement of the inertial mass:

$$\eta(t) = x(t) + z(t) + \zeta(t) \tag{2}$$

We also considered a linearized version of the system for comparison. In this case, the governing equations are as follows:

$$m_1 \left(\ddot{x} + \ddot{z}_l \right) + k_l z_l + c_l \dot{z}_l - k_s \zeta_l = 0$$

$$m_2 \left(\ddot{x} + \ddot{z}_l + \ddot{\zeta}_l \right) + k_s \zeta_l = 0 \tag{3}$$

where the subscript l means *linear*.

3   Results

In our calculation, we set $E_0 = E_\infty/3 = 50$ MPa, where the subscripts 0 and ∞ refer to the low- and high-frequency elastic moduli of the viscoelastic material, respectively. Furthermore, we set $h/\lambda = 0.13$, $R/\lambda = 0.3$, and $b = 1$ m. For each set of requested values of λ and τ, the nonlinear damping force was therefore calculated following the procedure extensively described in [39].

The system physical parameters have been estimated from real civil applications. Indeed, we set [33] $m_1 = 1 \times 10^2$ kg, $m_2 = 1 \times 10^5$ kg, and $k_s = 6 \times 10^6$ N/m (i.e., the bending stiffness of a HEB 300 steel beam of length $L = 3$ m). The cubic spring stiffness is $\mu = \mu_0 \, 6.2 \times 10^7$ N/m³, with μ_0 being a dimensionless coefficient.

Furthermore, with reference to Eq. (3), the parameters of the linear stiffness have been also expressed in a more readable form. Specifically, $k_l = \kappa_l \times 3.1 \times 10^6$ N/m and $c_l = \psi_l \times 10^4$ N/m.

3.1   Seismic Dynamics

The robustness of the isolation performance is of primary importance when dealing with excitations whose spectra are unknown a priori, such as in the case of seismic events or wind and sea-wave forcing. Therefore, our goal is to understand if a

nonlinear system and, specifically, an RLRB isolator with both nonlinear damping and stiffness is more robust than an equivalent simpler linear one.

To achieve this goal, we perform a global optimization of both the systems assuming as inputs five different seismic events. After that, the isolation achieved by both systems in optimal conditions is compared for each seismic event here considered.

According to Refs. [33, 42–44], with reference to the force $F(t) = k_s \zeta(t)$ acting through the nonlinear spring on the structural mass m_2, we consider the following possible damages: (i) the instantaneous structural damage, correlated to the amplitude F_m of the force $F(t)$; (ii) the fatigue damage, correlated to the root-mean-square $F_{rms} = 1/T[\int_T F(t)^2 dt]^{1/2}$ of the force $F(t)$ (notably, T is the shock duration); (iii) the compatibility of the relative displacement between the ground and the superstructure base, correlated to the amplitude z_m of the displacement z(t). All these damage/compatibility parameters are collected to define the following cost function:

$$\varphi = \frac{1}{n} \sum_{k=1}^{n} \left(\frac{1}{3} \frac{F_{m,k}}{F_{m,0}} + \frac{1}{3} \frac{F_{rms,k}}{F_{rms,0}} + \frac{1}{3} \frac{z_{m,k}}{z_{m,0}} \right) \tag{4}$$

where n is the number of seismic events here considered (i.e., $n = 3$). In Eq. (4) $F_{m,0}$, $F_{rms,0}$, and $z_{m,0}$ are homogenization terms which represent the absolute maximum values assumed by F_m, F_{rms}, and z_m in the investigated domain. Since the focus of this study is on the physical effect of nonlinear base isolation more than on specific optimization strategies, here a brute force search has been implemented to solve the optimization process. The lower the cost function, the better the performance is. Therefore, the optimization consists of the cost minimization.

Figure 2 shows the effect of system parameters on the cost function for both (a) the linear isolator and (b) the nonlinear RLRB. For the linear system, we show the value of the cost function versus κ_l and c_l. For the nonlinear RLRB, it emerged interestingly that the stiffness parameter is less influential than the damping parameter in determining the isolation performance; thus, we show here the cost function versus μ_0 and λ with $\tau = 0.013$ s.

The relaxation time τ affects only and directly the damping force slope, whereas changing λ also leads to different peak values. This can be a reason for the observed behavior.

Similarly, we observe that effect of the nonlinear stiffness μ_0 on the overall behavior of the isolator is nonmonotonic, with the optimal conditions associated with relatively low values of μ_0.

The results in terms of optimal behavior are shown in Table 1. From them, we observe that the optimal tuning of the nonlinear RLRB is able to produce a more robust isolation behavior, as the seismic mass m_2 is subjected to lower loads during each seismic shock compared to the system equipped with linear isolation. The only drawback is the presence of slightly larger base displacements associated with the RLRB. The lower standard deviation of the achieved result indicates that the
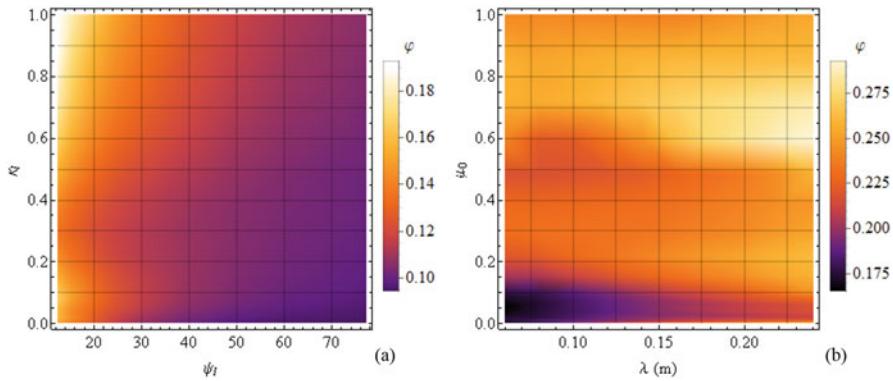
Fig. 2 The cost function maps. Figure (**a**) refers to the linear system, whereas figure (**b**) shows nonlinear system results with $\tau = 0.013$ s

Table 1 Linear and nonlinear system performance at optimal conditions. Optimal parameters are: $\kappa = 0.001$ and $\psi_l = 77.17$ for the linear system; $\mu_0 = 0.059$, $\lambda = 0.06$ m and $\tau = 0.013$ s for the RLRB

	Linear			Nonlinear		
	Force amplitude (kN)	Force rms (kN)	Displacement (cm)	Force amplitude (kN)	Force rms (kN)	Displacement (cm)
Irpinia 1980	84.2	18.0	18.6	175	25.6	9.1
Waianu 2016	122	21.9	26.6	500	52.0	10.7
Christchurch 2010	569	67.4	52.2	418	63.0	13.7

RLRB presents a higher robustness, since its performance is less affected by the actual spectral content of the excitation signal. This is remarkable property, which can be highly desirable when the input spectrum cannot be predicted as in several engineering applications requiring blind design of the isolation.

Finally, we report here the time history of η (Fig. 3a, c, e) for the three seismic events considered under optimal conditions (see Table 1). We observe that the data associated with the systems equipped with the RLRB show a smoother trend compared to the linear case. This is associated to lower peak displacement and lower acceleration, thus leading to lower inertial loads acting on the seismic mass m_2. We also observe that, due to the nonlinear recentering force (i.e., $F_{el}(z) \ll k_l z$ for $z \ll 1$), a residual offset is still present at the end of the shocks, which is expected to asymptotically decay for very long times.

Figure 3b, d, f shows the spectral contribution of the acceleration $\ddot{\eta}$ of the seismic mass m_2, under the same optimal conditions. A low-pass filter behavior is reported for both the RLRB and the linear isolator, with a more marked attenuation associated with the RLRB due to the nonmonotonic viscoelastic damping behavior (see Fig.
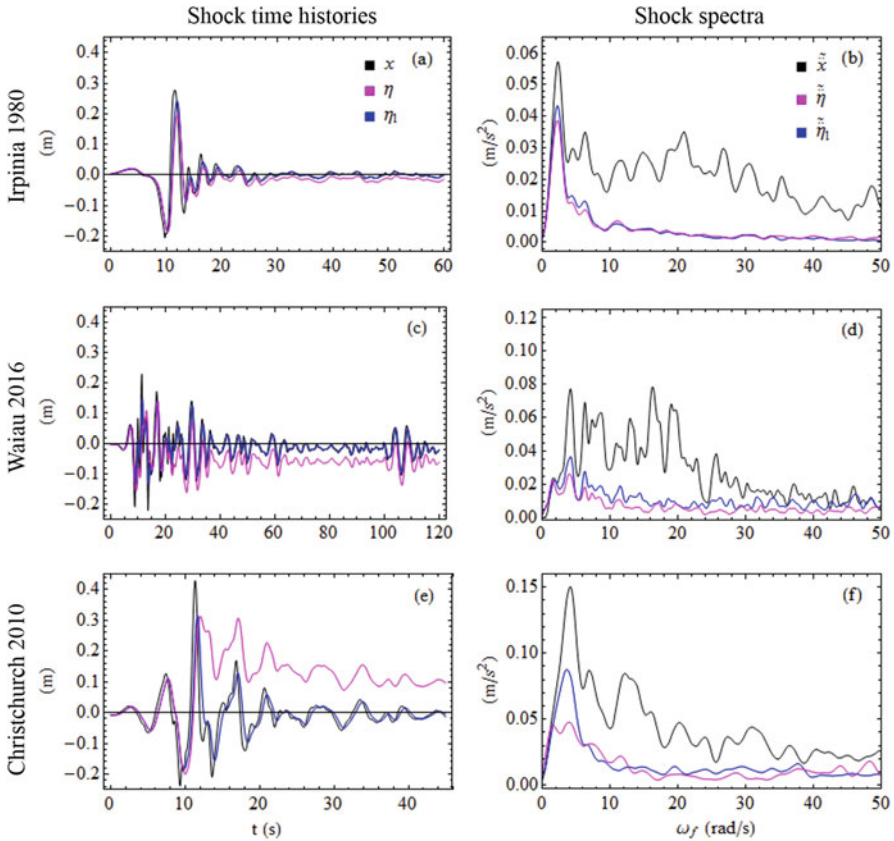
Fig. 3 (**a**, **c**, **e**) The seismic mass displacement η and (**b**, **d**, **f**) the spectrum of the seismic mass acceleration $\ddot{\eta}$. Data refers to systems under optimal conditions (see Table 1) isolated by a linear device (green curves) and an RLRB (red curves)

1b). Moreover, regardless of the specific seismic shock under consideration, the shock attenuation is particularly remarkable in the low-frequency range, where the largest differences are observed with respect to the linear isolator.

4   Conclusions

In this work, the isolation performance of an RLRB with viscoelastic nonlinear damping and nonlinear stiffness is investigated.

We investigate the robustness of the isolation effectiveness of a complex isolator composed of an RLRB coupled with a cubic spring under different seismic shocks, by tuning the system parameters (in terms of damping and stiffness) via a global

optimization procedure based on three different earthquakes. We performed the same optimization also in the case of a linear isolator, to compare the results of the nonlinear system in terms of isolation performance, with a simpler linear system as a reference. According to our results, a better load isolation is achieved by means of a nonlinear RLRB. In particular, our main result is that the system equipped with the RLRB is able to provide significantly higher isolation for a wider range of input spectra compared to the case where linear isolation is employed. Such a result may be of interest for several applications (e.g., seismic, marine, wind engineering) in which stochastic nonstationary excitation occurs. Indeed, in this case, the design of the isolation system can only count on statistical data, and isolators with the broadest effective frequency bandwidth are the preferred choice.

References

1. M. Rahman et al., Performance enhancement of wind turbine systems with vibration control: A review. Renew. Sustain. Energy Rev. **51**, 43–54 (2015)
2. H. Zuo, K. Bi, H. Hao, Using multiple tuned mass dampers to control offshore wind turbine vibrations under multiple hazards. Eng. Struct. **141**, 303–315 (2017)
3. J. Chen, C.T. Georgakis, Tuned rolling-ball dampers for vibration control in wind turbines. J. Sound Vib. **332**(21), 5271–5282 (2013)
4. J. Li, Z. Zhang and J. Chen, "Experimental study on vibration control of offshore wind turbines using a ball vibration absorber," Energy and Power Engineering, **4**(3), 153–157 (2012). https://doi.org/10.4236/epe.2012.43021
5. S. Colwell, B. Basu, Tuned liquid column dampers in offshore wind turbines for structural control. Eng. Struct. **31**(2), 358–368 (2009)
6. Z. Zhang et al., Performance evaluation of full-scale tuned liquid dampers (TLDs) for vibration control of large wind turbines using real-time hybrid testing. Eng. Struct. **126**, 417–431 (2016)
7. V. Maldonado et al., Active vibration control of a wind turbine blade using synthetic jets. Int. J. Flow Control **1**(4), 227–237 (2009)
8. S. Daley, I. Zazas, J. Hatonen, Harmonic control of a 'smart spring'machinery vibration isolation system. Proc. Inst. Mech. Eng. Part M J. Eng. Maritime Environ. **222.2**, 109–119 (2008)
9. E.I. Rivin, Vibration isolation of precision equipment. Precis. Eng. **17**(1), 41–56 (1995)
10. A. Farshidianfar, A. Saghafi, S.M. Kalami, I. Saghafi, Active vibration isolation of machinery and sensitive equipment using H control criterion and particle swarm optimization method. Meccanica **47**(2), 437–453 (2012)
11. A.J. Nieto et al., Unbalanced machinery vibration isolation with a semi-active pneumatic suspension. J. Sound Vib. **329**(1), 3–12 (2010)
12. S.T. De la Cruz, F. L'opez-Almansa, S. Oller, Numerical simulation of the seismic behavior of building structures equipped with friction energy dissipators. Comput. Struct. **85**, 30–42 (2007)

13. D. Foti, M. Diaferio, R. Nobile, Dynamic behavior of new aluminum–steel energy dissipating devices. Struct. Control Hlth. **20**, 1106–1119 (2013)
14. P.S. Harvey Jr., K.C. Kelly, A review of rolling-type seismic isolation: Historical development and future directions. Eng. Struct. **125**, 521–531 (2016)
15. P.S. Harvey Jr., H.P. Gavin, Assessment of a rolling isolation system using reduced order structural models. Eng. Struct. **99**, 708–725 (2015)
16. C.D. Casey, P.S. Harvey Jr., W. Song, Multi-unit rolling isolation system arrays: Analytical model and sensitivity analysis. Eng. Struct. **173**, 656–668 (2018)
17. Y. Starosvetsky, O.V. Gendelman, Vibration absorption in systems with a nonlinear energy sink: Nonlinear damping. J. Sound Vib. **324**, 916–939 (2009)
18. O.V. Gendelman, A. Alloni, Dynamics of forced system with vibro-impact energy sink. J. Sound Vib. **358**, 301–314 (2015)
19. A. Pazooki, A. Goodarzi, A. Khajepour, A. Soltani, C. Porlier, A novel approach for the design and analysis of nonlinear dampers for automotive suspensions. J. Vib. Control. **24**(14), 3132–3147 (2018)
20. Z. Lu et al., Nonlinear dissipative devices in structural vibration control: A review. J. Sound Vib. **423**, 18–49 (2018)
21. M.D. Symans, F.A. Charney, A.S. Whittaker, M.C. Constantinou, C.A. Kircher, M.W. Johnson, R.J. McNamara, Energy dissipation systems for seismic applications: Current practice and recent developments. J. Struct. Eng. **134**(1), 3–21 (2008)
22. D. Lee, D.P. Taylor, Viscous damper development and future trends. Struct. Des. Tall Build. **10**(5), 311–320 (2001)
23. X. Lu, Y. Zhou, F. Yan, Shaking table test and numerical analysis of RC frames with viscous wall dampers. J. Struct. Eng. **134**(1), 64–76 (2008)
24. N. Menga, D. Foti, G. Carbone, Viscoelastic frictional properties of rubber-layer roller bearings (RLRB) seismic isolators. Meccanica **52**, 2807–2817 (2017)
25. D. Foti, J.M. Kelly, Experimental analysis of a model isolated at the base with rubber-layer roller bearing (RLRB). Euro. Earthq. Eng. **10**, 3–13 (1996)
26. M. Mezzina, D. Raffaele, C. Dentamaro, D. Foti, P. Monaco. Seismic isolation with RLRB (Rubber Layer Roller Bearing), Proc. of the 1st European conference on Structural control, Barcelona 29–31 May (1996)
27. A.H. Muhr, M. Sulong, A.G. Thomas, Rolling-ball rubber-layer isolators. J. Nat. Rubber Res. **12**, 199–214 (1997)
28. A.H. Muhr, G. Bergamo. Shaking table tests on rolling-ball rubber-layer isolation system, in *14th European conference on earthquake engineering*, pp. 5703–5710 (2010)
29. L. Guerreiro, J. Azevedo, A.H. Muhr, Seismic tests and numerical modeling of a rolling-ball isolation system. J. Earthq. Eng. **11**, 49–66 (2007)
30. D. Foti, A. Catalan Goni, S. Vacca, On the dynamic response of rolling base isolation systems. Struct. Control Hlth. **20**, 639–648 (2013)
31. D. Foti, Isolatore sismico (Seismic Isolator), Italian Patent 0001414213, (2015)
32. D. Foti, Rolling devices for seismic isolation of lightweight structures and equipment. Design and realization of a prototype. Struct. Control Hlth. **26**, e2311 (2019)
33. N. Menga, F. Bottiglione, G. Carbone, The nonlinear dynamic behavior of a Rubber-Layer Roller Bearing (RLRB) for vibration isolation. J. Sound Vib. **463**, 114952 (2019)
34. N. Menga, L. Afferrante, G. Carbone, Effect of thickness and boundary conditions on the behavior of viscoelastic layers in sliding contact with wavy profiles. J. Mech. Phys. Solids **95**, 517–529 (2016)
35. N. Menga, L. Afferrante, G. Carbone, Adhesive and adhesiveless contact mechanics of elastic layers on slightly wavy rigid substrates. Int. J. Solids Struct. **88**, 101–109 (2016)
36. N. Menga, C. Putignano, L. Afferrante, G. Carbone, The contact mechanics of coated elastic solids: Effect of coating thickness and stiffness. Tribol Let **67**, 24 (2019)
37. N. Menga, F. Bottiglione, G. Carbone, The indentation rolling resistance in belt conveyors: A model for the viscoelastic friction. Lubricants **7**(7), 58 (2019)

38. N. Menga, L. Afferrante, G.P. Demelio, G. Carbone, Rough contact of sliding viscoelastic layers: Numerical calculations and theoretical predictions. Tribol. Int. **122**, 67–75 (2018)
39. N. Menga, Rough frictional contact of elastic thin layers: The effect of geometrical couplig. Int. J. Solids Struct. **164**, 212–220 (2019)
40. C.L. Ng, Y.L. Xu, Semi-active control of a building complex with variable friction dampers. Eng. Struct. **29**, 1209–1225 (2007)
41. A. Yanik, U. Aldemir, M. Bakioglu, A new active control performance index for vibration control of three-dimensional structures. Eng. Struct. **62**, 53–64 (2014)
42. F. Sadek, B. Mohraz, Semiactive control algorithms for structures with variable dampers. J. Eng. Mech. **124**, 981–990 (1998)
43. N. Menga, G. Carbone, D. Dini, Exploring the effect of geometric coupling on friction and energy dissipation in rough contacts of elastic and viscoelastic coatings. J. Mech. Phys. Solids **148**, 104273 (2021)
44. N. Menga, F. Bottiglione, G. Carbone, Nonlinear viscoelastic isolation for seismic vibration mitigation. Mech. Syst. Signal Process. **157**, 107626 (2021)

Optimal Design and Seismic Performance of a Nonlinear TMD with Pinched Hysteresis

Dario De Domenico, Giuseppe Quaranta, Giuseppe Ricciardi, and Walter Lacarbonara (iD)

1 Introduction

Tuned mass dampers (TMDs) can be an effective control strategy to mitigate wind- and earthquake-induced vibrations of the structures. In the linear version, a TMD consists of a secondary system (i.e., an oscillatory mass) connected to a main system (i.e., the structure to be protected) by means of a linear elastic spring and a linear dashpot. By properly calibrating the linear spring constant, it is possible to obtain an anti-resonant behavior for the secondary mass, which thus absorbs the kinetic energy transferred from the primary system (thereby justifying the alternative name of "dynamic vibration absorber"). The absorbed energy is then partially dissipated through the dashpot element.

The optimum design of the linear TMD has been thoroughly investigated in the past decades by considering different criteria and dynamic loading conditions. Deterministic, stochastic, and even hybrid fuzzy-stochastic design procedures have been also developed [1]. More recent attempts to improve the performance of the linear TMD have addressed the use of inerter-based amplification mechanisms [2]. On the other hand, nonlinear TMDs have been also studied in the past years. One of the first study in this field employs an additional cubic spring, besides the linear spring, to widen the operational bandwidth [3]. A TMD with Duffing-type (cubic) stiffness [4] and an inelastic TMD with bilinear hysteretic restoring force without viscous damper [5] have been investigated more recently.

D. De Domenico (✉) · G. Ricciardi
Department of Engineering, University of Messina, Messina, Italy
e-mail: dario.dedomenico@unime.it; gricciardi@unime.it

G. Quaranta · W. Lacarbonara
Department of Structural and Geotechnical Engineering, Sapienza University of Rome, Rome, Italy
e-mail: giuseppe.quaranta@uniroma1.it; walter.lacarbonara@uniroma1.it

Within this framework, the present contribution is concerned with a TMD featuring pinched hysteresis (TMD-PH) previously proposed by one of the co-authors. Unlike other nonlinear TMDs proposed in the literature, this device is characterized by a pinched hysteretic behavior offered by a combination of wire ropes made of shape memory alloy (SMA) and steel wires under axial-flexural loading [6]. The resulting behavior has been efficiently described by means of a modified Bouc–Wen model, where the main change basically concerns with an additional term tailored at simulating the contribution of the observed pinching phenomenon [7]. Notably, the hysteretic behavior of the device can be adjusted by modifying arrangement and proportion of SMA and steel wires [6]. This makes the TMD-PH very versatile and motivates the optimization of its features. Previous optimization strategies for such TMD-PH employed a deterministic definition of the seismic ground motion [7, 8]. In order to account for the uncertainties inherent in the seismic excitation, this contribution explores a stochastic-based optimum design procedure, wherein the ground motion is modeled as a zero-mean filtered non-stationary Gaussian random process. The nonlinear constitutive behavior of the TMD-PH is accounted for via stochastic linearization, where the expressions of the linearization coefficients are derived in the present study from the modified Bouc–Wen model describing the pinched hysteresis of the device. Final numerical results demonstrate the accuracy of the stochastic linearization and highlight the seismic performance of the TMD-PH optimized for a multi-storey reinforced concrete frame according to the proposed approach.

2 Constitutive Behavior of the TMD-PH

The TMD-PH under consideration is realized by an assembly of mixed NiTiNOL-steel wire ropes undergoing combined tension-flexure cycles [6, 7]. Based on previous experimental findings, a large variety of nonlinear constitutive behaviors can be obtained through different wire ropes arrangements by modulating concurrent interwire friction, phase transformation in the shape memory material, and geometric nonlinearities. The observed hysteretic behavior with pinching ranges from quasi-linear softening to strongly pinched hardening, and was described by means of a 6-parameter modified Bouc–Wen model [7]. In particular, without geometric nonlinearities, the restoring force f of the TMD-PH is given by the sum of a linear elastic force and a hysteretic contribution:

$$f = ku + z, \qquad (1)$$

where u is the TMD displacement relative to the main structure (i.e., TMD stroke). The evolution of the hysteretic force z is governed by the following first-order differential equation:
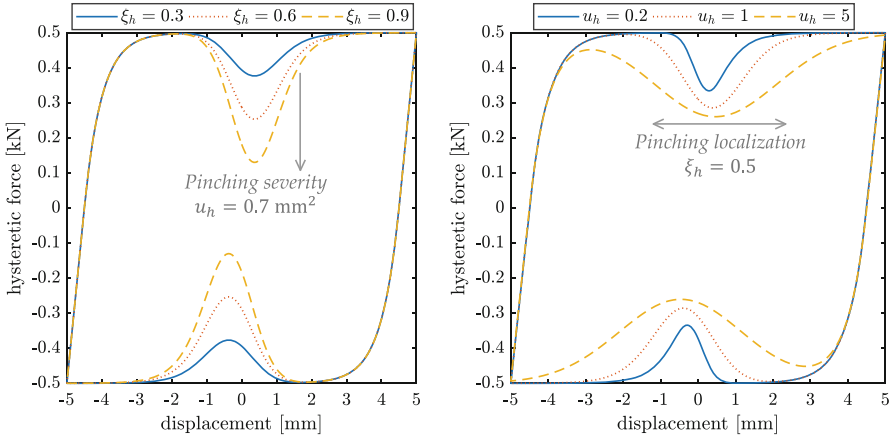
Fig. 1 Effect of pinching severity (left) and pinching localization (right) on the hysteretic force of the TMD-PH ($k_d = 1\,\text{kN/mm}$, $\gamma = \beta = 1\,\text{kN}^{1-n}/\text{mm}$, $n = 1$)

$$\dot{z} = \left[k_d \left(1 - \xi_h e^{-u^2/u_h} \right) - (\gamma + \beta \text{sgn}\,(\dot{u}z)) \, |z|^n \right] \dot{u}, \tag{2}$$

where the overdot denotes the derivative with respect to time, $k + k_d$ represents the tangent stiffness at the origin, the exponential function $H = 1 - \xi_h e^{-u^2/u_h}$ describes the pinching behavior in the neighborhood of the origin through the parameters $\xi_h \in [0, 1)$ (pinching severity parameter) and $u_h > 0$ (pinching localization parameter). Finally, γ and β are two hysteretic parameters that rule the softening or hardening behavior of the device ($\beta + \gamma > 0$ results in a softening restoring force), whereas n governs the smoothness of the transition between the elastic and the post-elastic phase. The influence of the pinching phenomenon on the hysteretic force exerted by a small-scale device is illustrated in Fig. 1 for different ξ_h values (for fixed u_h) and for different u_h values (for fixed ξ_h).

3 Stochastic Optimization of the TMD-PH

3.1 Equations of Motion

Let us consider a linear elastic structure with linear viscous damping whose dynamics are reduced to that of a single-degree-of-freedom (SDOF) system representative of its fundamental mode. The equations of motion of a linear elastic, viscously damped SDOF system equipped with the TMD-PH under base acceleration $\ddot{x}_g$ are:

$$m_1 \ddot{u}_1 + k_1 u_1 + c_1 \dot{u}_1 - k_2 u_2 - z = -m_1 \ddot{x}_g, \tag{3a}$$

$$m_2 \ddot{u}_2 + m_2 \ddot{u}_1 + k_2 u_2 + z = -m_2 \ddot{x}_g. \tag{3b}$$

where k_1, m_1, and c_1 denote stiffness, mass, and viscous damping coefficients of the SDOF system, respectively. The natural period of the SDOF system will be denoted by the term $T_1 = 2\pi/\omega_1$, where $\omega_1 = \sqrt{k_1/m_1}$ is the natural circular frequency while $\xi_1 = c_1/(2m_1\omega_1)$ is its damping ratio. Herein, u_1 represents the structural displacement of the SDOF system. On the other hand, m_2 and k_2 are mass and elastic stiffness of the TMD-PH, respectively; $\omega_2 = \sqrt{k_2/m_2}$ will denote the circular natural frequency of the TMD-PH associated with the stiffness k_2, while u_2 is the TMD stroke. Here and henceforth, the absorber mass is set according to $m_2 = \mu m_1$, where μ is the mass ratio of the TMD-PH. The evolution of the hysteretic force z is ruled by Eq. (2).

A stochastic approach is adopted to optimize the TMD-PH. In this context, the base acceleration is represented by a zero-mean filtered non-stationary (uniformly modulated) Gaussian random process whose evolutionary power spectral density (PSD) function $S_{\ddot{x}_g}(\omega, t)$ is the following:

$$S_{\ddot{x}_g}(\omega, t) = |\varphi(t)|^2 \bar{S}_{\ddot{x}_g}(\omega), \tag{4a}$$

$$\bar{S}_{\ddot{x}_g}(\omega) = \frac{\omega_k^4 + 4\zeta_k^2 \omega_k^2 \omega^2}{\left(\omega_k^2 - \omega^2\right)^2 + 4\zeta_k^2 \omega_k^2 \omega^2} \frac{\omega^4}{\left(\omega_p^2 - \omega^2\right)^2 + 4\zeta_p^2 \omega_p^2 \omega^2} S_0, \tag{4b}$$

where $\varphi(t)$ is the modulating function whereas ω_k, ξ_k, ω_p, and ξ_p are deterministic parameters of the Kanai–Tajimi/Clough–Penzien (KTCP) filter. These filter parameters can be chosen so as to represent different soil characteristics, thereby allowing the simulation of various frequency contents in the seismic excitation. Finally, S_0 is the constant PSD value of the white noise W. Among the alternative formulations available for the modulating function, without loss of generality, it is assumed $\varphi(t) = a_1 t\, e^{-a_2 t}$, with $a_1 = 0.45\, \text{s}^{-1}$ and $a_2 = 1/6\, \text{s}^{-1}$.

3.2   Stochastic Linearization

Linear random vibration theory is not applicable to Eq. (3) because of the nonlinear constitutive behavior of the TMD-PH. Therefore, the stochastic linearization technique (SLT) is employed to take into proper account the pinched hysteresis of the device. Assuming $n = 1$ in agreement with available experimental data, the nonlinear differential equation of the hysteretic force is first rewritten as follows:

$$g(u_2, \dot{u}_2, z) = 0 \rightarrow \dot{z} + \gamma \dot{u}_2 |z| + \beta |\dot{u}_2| z - k_{d2} \left(1 - \xi_h e^{-u_2^2/u_h}\right) \dot{u}_2 = 0. \tag{5}$$

The linearized expression corresponding to Eq. (5) is:

$$\dot{z} + c^{eq}\dot{u}_2 + k^{eq,z}z + k^{eq,u}u_2 = 0, \tag{6}$$

where $c^{eq} = \mathrm{E}\,[\partial g/\partial \dot{u}_2]$, $k^{eq,z} = \mathrm{E}\,[\partial g/\partial z]$, and $k^{eq,u} = \mathrm{E}\,[\partial g/\partial u_2]$ denote the linearization coefficients ($\mathrm{E}[\cdot]$ is the mean value operator).

Following the standard assumption of a multivariate Gaussian distribution for u_2, $\dot{u}_2$, z, the following expressions are obtained:

$$k^{eq,u} = -\frac{2k_{d2}}{u_h}\xi_h\left(\frac{u_h}{u_h + 2\sigma_{\dot{u}_2}^2}\right)^{3/2}\sigma_{u_2\dot{u}_2}, \tag{7a}$$

$$k^{eq,z} = \sqrt{\frac{2}{\pi}}\left(\gamma\frac{\sigma_{\dot{u}_2 z}}{\sigma_z} + \beta\sigma_{\dot{u}_2}\right), \tag{7b}$$

$$c^{eq} = -k_{d2}\left(1 - \xi_h\sqrt{\frac{u_h}{u_h + 2\sigma_{\dot{u}_2}^2}}\right) + \sqrt{\frac{2}{\pi}}\left(\beta\frac{\sigma_{\dot{u}_2 z}}{\sigma_{\dot{u}_2}} + \gamma\sigma_z\right), \tag{7c}$$

where σ_x denotes the standard deviation of the generic response x whereas σ_{xy} represents the cross-covariance of the generic responses x and y.

Note that Eq. (7) is valid under the assumption $n = 1$. This assumption, however, does not restrict the applicability of Eq. (7) since it is in good agreement with available experimental results [6].

3.3 Optimum Design

A time-domain stochastic dynamic analysis is performed in order to determine the covariance matrix of the system response upon which the linearization coefficients in Eq. (7) depend. By introducing the state-space vector of the filter parameters $\mathbf{y}_p = \{x_p\ \dot{x}_p\ x_k\ \dot{x}_k\}^\top$, the time-domain representation of the KTCP filter in Eq. (4) takes on the form:

$$\ddot{x}_g = \mathbf{a}_p^\top\mathbf{y}_p, \tag{8a}$$

$$\dot{\mathbf{y}}_p = \mathbf{D}_p\mathbf{y}_p + \mathbf{v}_p W, \tag{8b}$$

with

$$\mathbf{a}_p = \begin{Bmatrix} -\omega_p^2 \\ -2\xi_p\omega_p \\ \omega_k^2 \\ 2\xi_k\omega_k \end{Bmatrix}, \quad \mathbf{D}_p = \begin{bmatrix} 0 & 1 & 0 & 0 \\ -\omega_p^2 & -2\xi_p\omega_p & \omega_k^2 & 2\xi_k\omega_k \\ 0 & 0 & 0 & 1 \\ 0 & 0 & -\omega_k^2 & -2\xi_k\omega_k \end{bmatrix}, \quad \mathbf{v}_p = \begin{Bmatrix} 0 \\ 0 \\ 0 \\ -\varphi \end{Bmatrix}. \tag{9}$$

If the state-space vector of the mechanical states $\mathbf{y}_s = \{u_1 \; u_2 \; z \; \dot{u}_1 \; \dot{u}_2\}^\top$ is also introduced, then Eq. (3) can be arranged after stochastic linearization as:

$$
\underbrace{\begin{Bmatrix} \dot{\mathbf{y}}_s \\ \dot{\mathbf{y}}_p \end{Bmatrix}}_{\dot{\mathbf{y}}} = \underbrace{\begin{bmatrix} \mathbf{A}_s & \mathbf{H}_p \\ \mathbf{0}_{4\times5} & \mathbf{D}_p \end{bmatrix}}_{\mathbf{A}} \underbrace{\begin{Bmatrix} \mathbf{y}_s \\ \mathbf{y}_p \end{Bmatrix}}_{\mathbf{y}} + \underbrace{\begin{Bmatrix} \mathbf{0}_{5\times1} \\ \mathbf{v}_p W \end{Bmatrix}}_{\mathbf{f}},
\tag{10}
$$

with

$$
\mathbf{A}_s = \begin{bmatrix} 0 & 0 & 0 & 1 & 0 \\ 0 & 0 & 0 & 0 & 1 \\ 0 & -k^{eq,u} & -k^{eq,z} & 0 & -c^{eq} \\ -\dfrac{k_1}{m_1} & \dfrac{k_2}{m_1} & \dfrac{1}{m_1} & -\dfrac{c_1}{m_1} & 0 \\ \dfrac{k_1}{m_1} & -\dfrac{1+\mu}{\mu}\dfrac{k_2}{m_1} & -\dfrac{1+\mu}{\mu}\dfrac{1}{m_1} & \dfrac{c_1}{m_1} & 0 \end{bmatrix}, \quad \mathbf{H}_p = \begin{bmatrix} \mathbf{0}_{1\times4} \\ \mathbf{0}_{1\times4} \\ \mathbf{0}_{1\times4} \\ -\mathbf{a}_p^\top \\ \mathbf{0}_{1\times4} \end{bmatrix}.
\tag{11}
$$

The covariance matrix of the system response is thus the following:

$$
\mathbf{R} = \mathrm{E}\left[\mathbf{y}\mathbf{y}^\top\right] = \begin{bmatrix} \mathbf{R}_{\mathbf{y}_s\mathbf{y}_s} & \mathbf{R}_{\mathbf{y}_s\mathbf{y}_p} \\ \mathbf{R}_{\mathbf{y}_p\mathbf{y}_s} & \mathbf{R}_{\mathbf{y}_p\mathbf{y}_p} \end{bmatrix},
\tag{12}
$$

in which

$$
\mathbf{R}_{\mathbf{y}_s\mathbf{y}_s} = \mathrm{E}\left[\mathbf{y}_s\mathbf{y}_s^\top\right] = \begin{bmatrix} \sigma_{u_1}^2 & \sigma_{u_1u_2} & \sigma_{u_1z} & \sigma_{u_1\dot{u}_1} & \sigma_{u_1\dot{u}_2} \\ & \sigma_{u_2}^2 & \sigma_{u_2z} & \sigma_{u_2\dot{u}_1} & \sigma_{u_2\dot{u}_2} \\ & & \sigma_z^2 & \sigma_{z\dot{u}_1} & \sigma_{z\dot{u}_2} \\ & sym & & \sigma_{\dot{u}_1}^2 & \sigma_{\dot{u}_1\dot{u}_2} \\ & & & & \sigma_{\dot{u}_2}^2 \end{bmatrix}.
\tag{13}
$$

The covariance matrix of the system response $\mathbf{R}$ is determined by solving the following Lyapunov equation:

$$
\mathbf{A}\mathbf{R} + \mathbf{R}\mathbf{A}^\top + \mathbf{B} = \dot{\mathbf{R}},
\tag{14}
$$

where $\mathbf{B}$ is a 9×9 matrix whose $(9, 9)$ element is equal to $2\pi S_0\varphi^2$ and all the other entries are equal to 0. The solution of Eq. (14) provides the time-history of the covariance matrix of the system response. It is worth noting that an inner predictor–corrector cycle must be implemented at each time step of the analysis because the coefficients of the stochastic linearization depend, in turn, on the covariance matrix of the system response as per Eq. (7).

Finally, the optimal parameters of the TMD-PH are determined as the solution of the following box-constrained single-objective optimization problem:

$$\min_{\mathbf{d}_\ell \leq \mathbf{d} \leq \mathbf{d}_u} \{F\}. \tag{15}$$

In general, the objective function F can be defined according to one of the following formulations:

$$F = \int_0^T \sigma_{u_1}^2 \, dt \, , \underbrace{\qquad}_{\text{displacement} - \text{based}} F = \int_0^T \sigma_{\ddot{u}_{1,\text{tot}}}^2 \, dt, \underbrace{\qquad}_{\text{acceleration} - \text{based}} F = \int_0^T \sigma_{\dot{u}_1}^2 \, dt \, . \underbrace{\qquad}_{\text{energy} - \text{based}} \tag{16}$$

It is highlighted that these three objective function formulations reflect alternative design criteria, namely displacement-, acceleration-, and energy-based designs [9]. Additionally, $\mathbf{d}_\ell$ and $\mathbf{d}_u$ are lower and upper bounds of the design vector $\mathbf{d}$, with $\mathbf{d} = \{d_1 \ldots d_6\}^\top = \{k_2 \ k_{d2} \ \xi_h \ u_h \ \gamma \ \beta\}^\top$. These bounds are assumed according to available experimental results [6, 7], whereas $[0, T]$ represents the time window of the analysis (i.e., the seismic ground motion duration).

4 Numerical Results

The reliability of the stochastic-based optimum design of the TMD-PH depends on the correctness of the linearization coefficients in Eq. (7). Hence, the accuracy of the SLT is first estimated by comparison with Monte Carlo simulation (MCS).

The comparison between the results carried out analytically from the SLT and those obtained from MCS (considering 1000 samples) is reported in Fig. 2. For the sake of simplicity, a stationary, white Gaussian noise is considered as base excitation. A wide range of intensity levels is explored, e.g., $S_0 = 10^{-3} - 10^2 \, \text{m}^2/\text{m}^3$. A SDOF system with $T_1 = 0.5 \, \text{s}$, $m_1 = 1 \, \text{kg}$ and $\xi_1 = 0.05$ is assumed. On the other hand, a TMD-PH with $\mu = 0.05$, $\omega_2/\omega_1 = 0.9$, $\xi_h = 0.9$, $u_h = 0.5 \, \text{m}^2$, $\gamma = \beta = 0.5 \, \text{N}^{1-n}/m$ (given $n = 1$) is considered. The results plotted in Fig. 2 demonstrate a very good agreement between SLT and MCS for the entire range of seismic intensity levels and different values of the k_{d2}/k_2 ratio. It is pointed out that such wide range of values for S_0 is intended to trigger different levels of nonlinear behavior in the TMD-PH, even if $S_0 \gg 1 \, \text{m}^2/\text{m}^3$ is unrealistically high in earthquake engineering applications. The relative errors in the displacement and velocity do not exceed 10% in all simulations. This confirms the correctness of the linearization coefficients in Eq. (7).

Previous studies about the stochastic-based optimum design of a linear TMD attached to a linear elastic SDOF system suggest that the energy-based design leads to a satisfactory trade-off between the requirement of reducing displacement-induced damage in structural components and the needs of mitigating the damage in acceleration-sensitive equipment [9]. For the sake of conciseness, therefore, only the energy-based formulation of the objective function is plotted in Fig. 3. Filter parameters corresponding to firm soil condition are assumed [10], with $S_0 =$
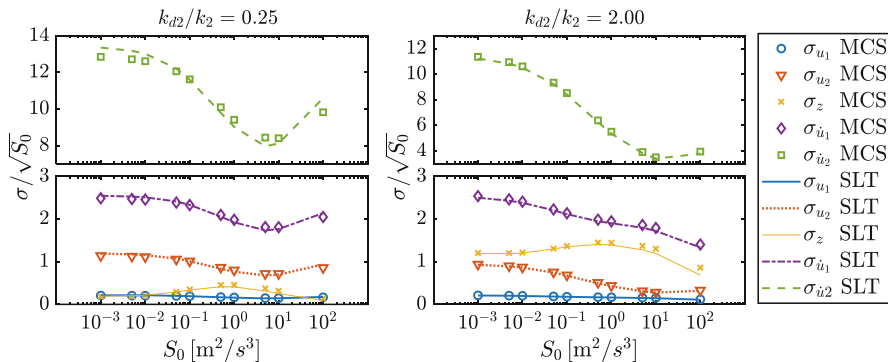
Fig. 2 Normalized standard deviations of the dynamic response: comparison between SLT (lines) and MCS (markers)
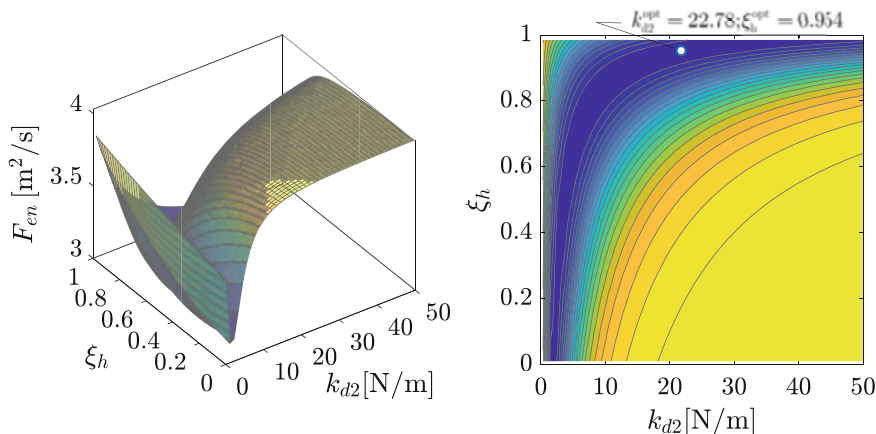
Fig. 3 Objective function for the energy-based design strategy, and identification of the global optimum

$0.03 \, \mathrm{m^2/s^3}$. The previous sets of data are adopted for, both, the SDOF system and the TMD-PH, except for k_{d2} and ξ_h. It is pointed out that the shapes of displacement- and acceleration-based objective function look like the one illustrated in Fig. 3, but their global optima do not coincide.

The seismic effectiveness of the TMD-PH optimized according to the proposed stochastic approach is finally assessed through time-history analyses. The case study is a 20-storey, 5-bay reinforced concrete framed building, whose geometrical and mechanical properties are described in [11]. The TMD-PH is installed on the top floor, and its optimum parameters (for $\mu = 0.05$) are calculated according to the proposed stochastic approach. The energy-based criterion is employed and the TMD-PH is designed to mitigate the seismic demand due to the fundamental mode of the structure. Considering firm and soft soil conditions according to [10]

Table 1 Optimum parameters of the TMD-PH for firm and soft soil conditions

Soil conditions	$k_2[\text{N/m}]$	$k_{d2}[\text{N/m}]$	$\xi_h[-]$	$u_h[\text{m}^2]$	$\beta[\text{N}^{1-n}/\text{m}]$	$\gamma[\text{N}^{1-n}/\text{m}]$
Firm soil	$3.73 \cdot 10^4$	$5.43 \cdot 10^6$	0.914	0.800	1.25	1.25
Soft soil	$2.79 \cdot 10^5$	$1.50 \cdot 10^6$	0.812	0.529	1.25	1.25
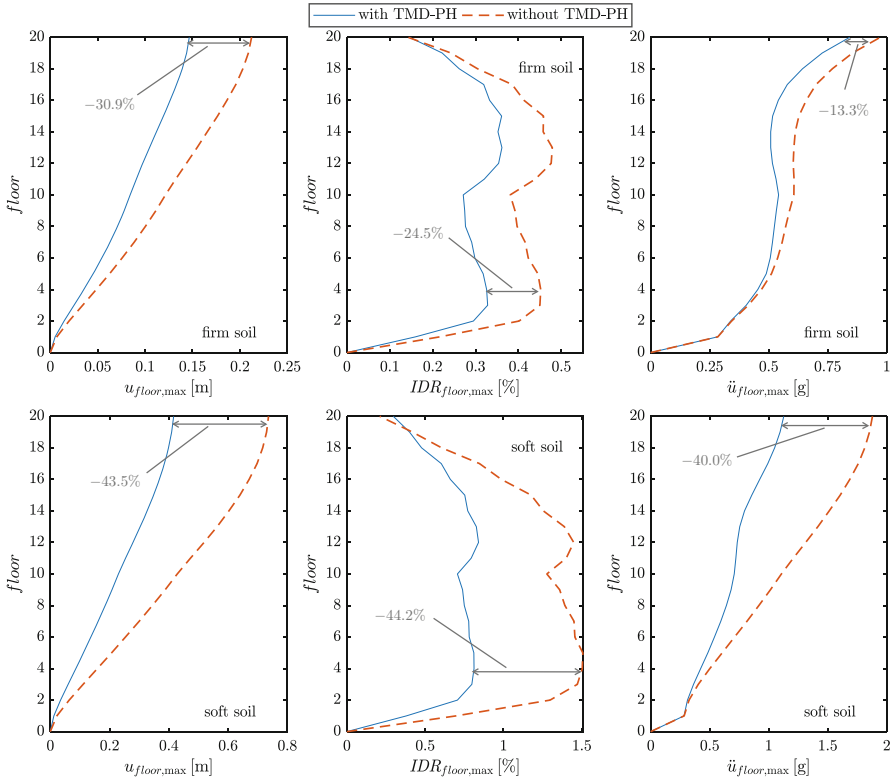
Fig. 4 Seismic performance of the TMD-PH for firm and soft soil conditions

and assuming a peak ground acceleration $\ddot{x}_{g,\max} = 0.3$ g (where g is the gravity acceleration), the optimum design parameters listed in Table 1 are obtained.

Figure 4 highlights the seismic performance of the TMD-PH in terms of floor displacements relative to the ground u_{floor}, inter-storey drift ratios IDR_{floor}, and floor accelerations $\ddot{u}_{\text{floor}}$, considering the average of the peak values carried out from time-history analyses based on 400 synthetic seismic ground motion records generated according to the specific soil conditions. The results in Fig. 4 demonstrate that the TMD-PH leads to a drastic reduction of the seismic demand in the reinforced concrete structure. This reduction is more evident for the soft soil condition because the frequency content of the corresponding seismic excitation is close to the natural period of the first mode of the building, whose period is $T_1 = 1.296$ s.

5   Conclusions

The stochastic-based optimum design of a tuned mass damper with pinched hysteresis (TMD-PH) for linear elastic, damped structures has been here addressed. The seismic excitation has been modeled as a non-stationary zero-mean filtered Gaussian random process, and the TMD-PH has been designed by solving a box-constrained single-objective optimization problem. The stochastic dynamic analysis has been performed by resorting to the stochastic linearization technique. The correctness of the stochastic linearization as applied to the peculiar pinched hysteresis of the device under consideration has been first demonstrated through a comparison with Monte Carlo simulations. A 20-story, 5-bay reinforced concrete framed building with the TMD-PH optimized according to the proposed stochastic procedure has been investigated. The obtained results for this case study demonstrated that the TMD-PH is effective in reducing floor displacements relative to the ground, inter-storey drift ratios, and floor accelerations under earthquakes.

This preliminary study will be extended in future studies. The main novelty will deal with the gradient-based solution of the design optimization problem, for which an analytical approach based on the explicit evaluation of the gradient will be implemented. More extensive parametric studies and larger numerical investigations will be further carried out.

References

1. G.C. Marano, G. Quaranta, Robust optimum criteria for tuned mass dampers in fuzzy environments. Appl. Soft. Comput. **9**(4), 1232–1243 (2009)
2. D. De Domenico, H. Qiao, Q. Wang, Z. Zhu, G. Marano, Optimal design and seismic performance of Multi-Tuned Mass Damper Inerter (MTMDI) applied to adjacent high-rise buildings. Struct. Des. Tall. Spec. Build. **29**(14), e1781 (2020)
3. R.E. Roberson, Synthesis of a nonlinear dynamic vibration absorber. J. Franklin Inst. **254**(3), 205–220 (1952)
4. N.A. Alexander, F. Schilder, Exploring the performance of a nonlinear tuned mass damper. J. Sound Vib. **319**(1–2), 445–462 (2009)
5. S. Bagheri, V. Rahmani-Dabbagh, Seismic response control with inelastic tuned mass dampers. Eng. Struct. **172**, 712–722 (2018)
6. B. Carboni, W. Lacarbonara, F. Auricchio, Hysteresis of multiconfiguration assemblies of nitinol and steel strands: experiments and phenomenological identification. J. Eng. Mech. **141**(3), 04014135 (2014)
7. B. Carboni, W. Lacarbonara, Nonlinear vibration absorber with pinched hysteresis: theory and experiments. J. Eng. Mech. **142**(5), 04016023 (2016)
8. A. Boccamazzo, B, Carboni, G. Quaranta, W. Lacarbonara, Seismic effectiveness of hysteretic tuned mass dampers for inelastic structures. Eng. Struct. **216**, 110591 (2020)
9. D. De Domenico, G. Ricciardi, An enhanced base isolation system equipped with optimal tuned mass damper inerter (TMDI). Earth Eng. Struct. Dyn. **47**(5), 1169–1192 (2018)

10. A. Der Kiureghian, A. Neuenhofer, Response spectrum method for multi-support seismic excitations. Earthq. Eng. Struct. Dyn. **21**, 713–740 (1992).
11. D. De Domenico, G. Ricciardi, Dynamic response of non-classically damped structures via reduced-order complex modal analysis: Two novel truncation measures. J. Sound Vib. **452**, 169–190 (2019)

Part II
Control of Nonlinear Systems and Synchronization

Vibration Control of a Cantilever Beam Coupled to a Non-ideal Power Source by Coil Impedance Matching

E. A. Petrocino, J. M. Balthazar, A. M. Tusset, P. J. Gonçalves, M. Silveira, W. M. Kuhnert, G. Kudra, and J. Awrejcewicz

1 Introduction

Ideal dynamic systems are those whose excitation is known and not influenced by the dynamics of the structure, that is, it is simply a function of time, whereas a non-ideal system is based on the interaction of the structure with the energy source of limited power supply, thus, the excitation depends not only on time, but also on coupling and behavior of the structure. One of these behaviors was investigated experimentally by Sommerfeld in 1902, where a motor coupled to a flexible structure had its energy converted into vibration of the structure instead of increasing the speed of rotation, keeping the rotation constant even with the energy increase, until the moment of the "jump" when it exceeds the resonance regime. Kononenko in 1969 [1] studied several engine situations as a non-ideal energy source, showing that the load on the rotor shaft depends on the oscillation of the structure and that in soft variations the forced oscillation curve is obtained as a function of the angular velocity, which together with the torque response as a function of the angular speed, the jumps are predicted with the increase and decrease

E. A. Petrocino (✉) · P. J. Gonçalves · M. Silveira · W. M. Kuhnert
São Paulo State University (UNESP), School of Engineering, Bauru, Brazil
e-mail: eduardo.petrocino@unesp.br; paulo.paupitz@unesp.br; marcos.silveira@unesp.br

J. M. Balthazar
São Paulo State University (UNESP), School of Engineering, Bauru, Brazil
Federal University of Technology at Ponta Grossa, Ponta Grossa, Paraná, Brazil

A. M. Tusset
Federal University of Technology at Ponta Grossa, Ponta Grossa, Paraná, Brazil

G. Kudra · J. Awrejcewicz
Lodz University of Technology, Lodz, Poland
e-mail: grzegorz.kudra@p.lodz.pl; jan.awrejcewicz@p.lodz.pl
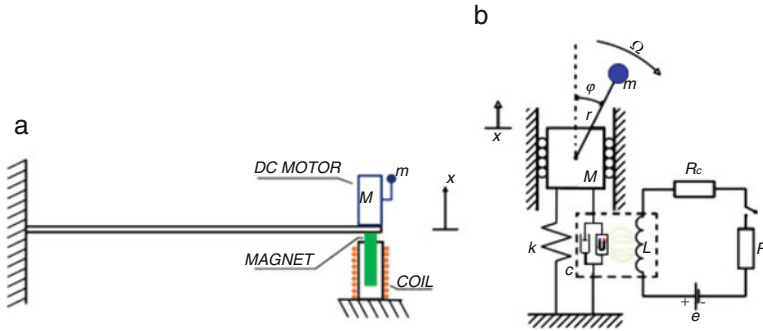
Fig. 1 Schematic representation of the system with clamped-free beam, DC motor, permanent magnet, and fixed coil (**a**); representative model of the system (**b**)

of the angular speed. A complete review of different aspects of non-ideal problems may be found in [2–7] without prejudice of others. The objective of this work is to perform numerical simulations, analytical and experimental modeling of the magnetic interaction [8, 9] in a non-ideal oscillatory system.

2 Mathematical Model

Figure 1a presents a schematic representation of the system, with an elastic beam with clamped-free boundary conditions, a DC motor with an unbalanced mass attached to the upper part of the free end of the beam, a permanent magnet attached to the lower side of the free end of the beam, and a coil fixed at the base. Figure 1b presents the simplified physical model of this system with a mass-spring-damper with unbalanced mass coupled to a RL circuit. In this model M is the equivalent mass of the beam, DC motor, and magnet, m is the unbalanced mass, k is the bending stiffness of the beam, c is the structural damping, L is the coil inductance, R is the external resistance, R_c is the coil resistance, x is the vertical displacement of the free end, φ is the angular displacement of the unbalanced mass, and e is the electrical voltage. If the electric circuit is open, the mechanical and electrical subsystems are decoupled. If the electric circuit is closed, the moving magnet inside the coil results in an electromotive force acting on the beam, and electrical current on the circuit, as energy from the mechanical vibrations is converted into electrical energy. The magnet-coil interaction acts as a vibration damper and can be used to mitigate resonance capture.

2.1 Governing Equations of Motion

The kinetic energy of the system is given by:

$$T = \frac{1}{2}(M + m)\dot{x}^2 + \frac{1}{2}(J_0 + mr^2)\dot{\phi}^2 - mr\dot{x}\dot{\phi}\sin\phi + \frac{1}{2}L_i\dot{q}^2 \tag{1}$$

in which r is the distance from unbalanced mass to the shaft center and J_0 is the motor shaft moment of inertia. The potential energy is given by:

$$V = \frac{1}{2}kx^2 + \frac{1}{2}\beta\dot{q}x \tag{2}$$

in which $\beta = Bl$ is the product of magnetic induction module and coil length. Applying Eqs. (1) and (2) to the Lagrange equations and considering the motive and damping forces, the equations of motion of the system are written as:

$$(M + m)\ddot{x} + c\dot{x} + kx - \beta\dot{q} = mr(\ddot{\varphi}\sin\varphi + \dot{\varphi}^2\cos\varphi)$$

$$(J_0 + mr^2)\ddot{\varphi} = \ddot{x}mr\sin\varphi + \mathfrak{M}(\dot{\varphi})$$

$$L_i\ddot{q} + R\dot{q} + \beta\dot{x} = V \tag{3}$$

The term $\ddot{x}mr\sin\varphi$ represents the action of the oscillating system on the source of the energy and the term $\mathfrak{M}(\dot{\varphi})$ defines the torque curve of a motor with limited power, given by $\mathfrak{M}(\dot{\varphi}) = L(\dot{\varphi}) - H(\dot{\varphi})$. The terms $L(\dot{\varphi})$ and $H(\dot{\varphi})$ respectively represent the driving torque and the resistive torque of the motor.

3 Analytical Modelling

Rewriting Eq. (3) in terms of the small parameter ϵ, one gets:

$$\ddot{x} + \omega^2 x = \epsilon(q_2\ddot{\varphi}\sin\varphi + q_2\dot{\varphi}^2\cos\varphi - h\dot{x} + q_4g\dot{x})$$

$$\ddot{\varphi} = \epsilon(q_3\ddot{x}\sin\varphi + \mathfrak{M})$$

$$\ddot{Q} = \epsilon(q_7 - q_5g\dot{x} - q_6\dot{x}) \tag{4}$$

in which $\omega^2 = \frac{k}{m+M}$; $\epsilon q_2 = \frac{mr}{m+M}$; $\epsilon q_3 = \frac{mr}{J}$; $\epsilon h = \frac{c}{m+M}$; $\epsilon q_4 = \frac{\beta}{m+M}$; $\epsilon q_5 = \frac{R}{L_i}$; $\epsilon q_6 = \frac{\beta}{L_i}$; $\epsilon q_7 = \frac{V}{L_i}$; $\epsilon\mathfrak{M} = \frac{\mathfrak{M}(\dot{\varphi})}{J}$; $\dot{Q} = -\frac{\beta}{R}\dot{x}$; $g = -\frac{\beta}{R}$.

To obtain the approximate solutions of Eq. (4), the method of averaging is used adopting $x = A\cos(\varphi + \Sigma)$; $\dot{x} = -A\omega\sin(\varphi + \Sigma)$; $\dot{Q} = -gA\omega\sin(\varphi + \Sigma)$; $\dot{\varphi} = \theta$.

Following Kononenko's proposal, the new variables A, Σ, and θ, respectively, the amplitude of the oscillations, the angular phase shift of the reference x, and the frequency of the exciting force, should vary slowly over time. Differentiating x; $\dot{x}$ and substituting in Eq. (4), a system of four equations in the standard form is obtained as:

$$\frac{dA}{dt} = -\frac{\epsilon}{\omega}\left[(hA\omega + \epsilon g\omega q_4 A)\sin(\varphi + \Sigma) + q_2\cos(\varphi)\theta^2\right]\sin(\varphi + \Sigma)$$

$$\frac{d\Sigma}{dt} = \epsilon\left\{\alpha_0 - \frac{1}{A\omega}\left[(\epsilon hA\omega + \epsilon g\omega q_4 A)\sin(\varphi + \Sigma) + q_2\cos(\varphi)\theta^2\right]\cos(\varphi + \Sigma)\right\}$$

$$\frac{d\Theta}{dt} = \epsilon\left[\mathfrak{M}(\theta) - q_3\theta A\omega\cos(\varphi + \Sigma)\sin(\varphi)\right]$$

$$\frac{d\dot{Q}}{dt} = \epsilon\left[q_7 + q_5 gA\omega\sin(\varphi + \Sigma) + q_6 A\omega\sin(\varphi + \Sigma)\right] \tag{5}$$

in which $\alpha_0 = \omega - \theta$. Using the Bogolyubov's perturbation method to calculate the approximate solution of Eq. (5), the following form can be used: $\theta = \Omega + \epsilon U_1(t, \Omega, a, \xi)$; $A = A + \epsilon U_2(t, \Omega, a, \xi)$; $\Sigma = \xi + \epsilon U_3(t, \Omega, a, \xi)$.

Realizing the method of averaging in Eq. (5) in the format $f_i(A, \Theta, \xi) = \frac{1}{2\pi}\int_0^{2\pi}\epsilon f_i(A, \Theta, \xi)dt$ results in:

$$\frac{d\Omega}{dt} = \epsilon\left(\mathfrak{M}(\Omega) + \frac{1}{2}q_3\omega a\Omega\sin(\xi)\right)$$

$$\frac{da}{dt} = -\frac{\epsilon}{2}\left(ha + agq_4 + \frac{q_2\Omega^2\sin(\xi)}{\omega}\right)$$

$$\frac{d\xi}{dt} = \epsilon\left(\alpha - \frac{\Omega^2 q_2\cos(\xi)}{2a\omega}\right)$$

$$\frac{d\dot{Q}}{dt} = \epsilon q_7 \tag{6}$$

Integrating Eq. (6) the results of which are shown in Figs. 2 and 3 with initial values $a_0 = 0$ mm and $\Omega_0 = 174$ rad/s for (a) increasing frequency, and with initial values $a_0 = 0$ mm and $\Omega_0 = 180$ rad/s for (b) decreasing frequency. It is observed that in the interval close to 0.1 s in which the amplitude increases rapidly, the angular velocity has smaller variations for the system without electromagnetic interaction, being reduced as the counter-electromotive force increases.

For stationary states of motions, i.e., $\dfrac{d\Omega}{dt} = 0$, $\dfrac{da}{dt} = 0$, $\dfrac{d\xi}{dt} = 0$, the following expressions are obtained:

$$\frac{\mathfrak{M}(\Omega)}{J} + \frac{1}{2}\frac{mr}{J}\omega a\Omega\sin(\xi) = 0 \qquad \frac{c}{m_0}a + ag\frac{\beta}{m_0} + \frac{\frac{mr}{m_0}\Omega^2\sin(\xi)}{\omega} = 0$$
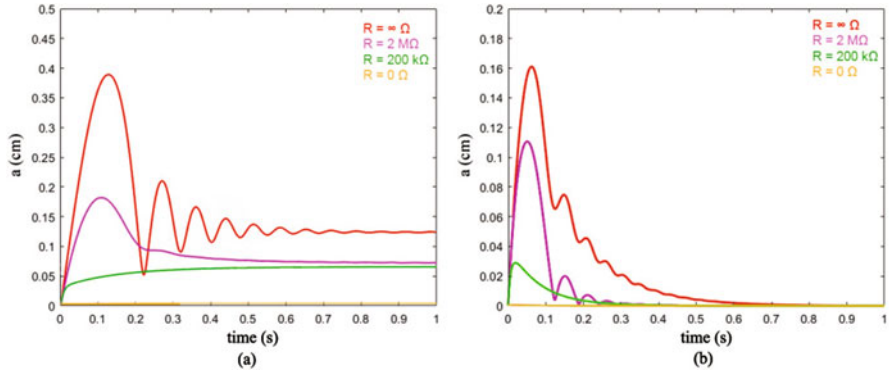
Fig. 2 Amplitude of the oscillations with transitions across a resonance for different resistor values with (**a**) increasing frequency and (**b**) decreasing frequency
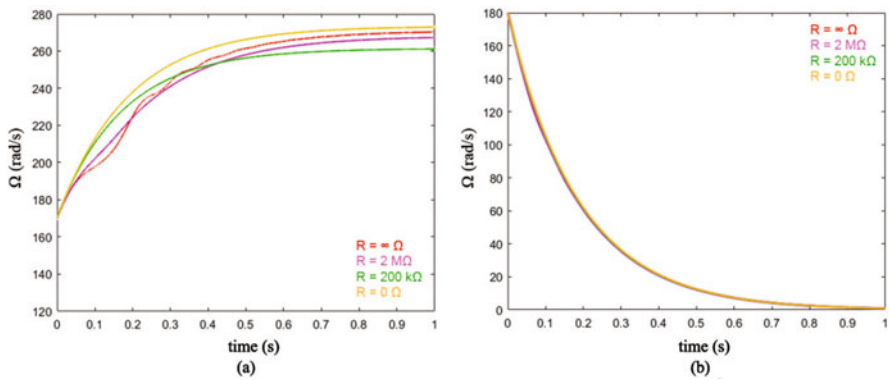
Fig. 3 Frequency of the oscillations with transitions across a resonance for different resistor values with (**a**) increasing frequency and (**b**) decreasing frequency

$$\omega - \Omega - \frac{\Omega^2 \frac{mr}{m_0} \cos(\xi)}{2a\omega} = 0 \tag{7}$$

Thus, the expressions for the amplitude and phase of the oscillation are obtained:

$$a = \frac{\Omega^2 mr}{\omega\sqrt{4m_0^2(\omega - \Omega)^2 + (\beta g + c)^2}} \qquad \tan(\xi) = \frac{\beta g - c}{2m_0(\Omega - \omega)}$$

$$S(\dot{\phi}) = H(\dot{\phi}) + \frac{\omega^3 m^2 r^2(\beta g + c)}{8m_0^2(\Omega - \omega)^2 + 2(\beta g + c)^2} \tag{8}$$
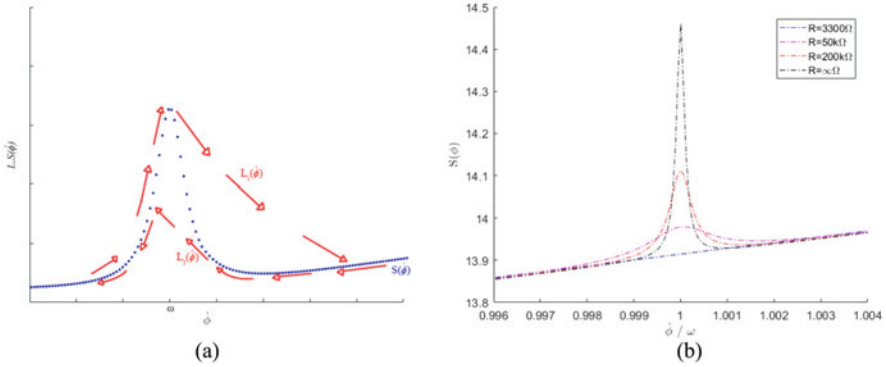
Fig. 4 (**a**) Frequency response curve and (**b**) Stationary conditions in the resonance region with resistance variations in the magnetic circuit

Figure 4a shows the amplitude of the oscillation in stationary condition $S(\dot{\phi})$, whose shape resembles an ideal energy source together with the motor drive torque $L_1(\dot{\phi})$ and $L_2(\dot{\phi})$, demonstrating the resonance capture jump. Figure 4b shows the changes in $S(\dot{\phi})$ varying the resistance of the electromagnetic circuit.

4   Numerical Simulations

For the implementation of numerical simulation, the dynamical equations (Eq. (3)) were rewritten in state space form. Assuming x, φ, and q as state variables, the state equations are obtaining using:

$$
\begin{aligned}
\ddot{x} &= \frac{L(mr^2 + J_0)(-c\dot{x} - kx + m\cos{(\varphi)}\varphi^2 r + \beta\dot{q})}{L(m + M)(mr^2 + J_0) - Lm^2\sin{(\varphi)}^2 r^2} \\
&+ \frac{Lm\mathfrak{M}(\dot{\varphi})\sin{(\varphi)}r}{L(m + M)(mr^2 + J_0) - Lm^2\sin{(\varphi)}^2 r^2} \\
\ddot{\varphi} &= \frac{Lm\sin{(\varphi)}r(-c\dot{x} - kx + m\cos{(\varphi)}\varphi^2 r + \beta\dot{q})}{L(m + M)(mr^2 + J_0) - Lm^2\sin{(\varphi)}^2 r^2} \\
&+ \frac{L(m + M)\mathfrak{M}(\dot{\varphi})}{L(m + M)(mr^2 + J_0) - Lm^2\sin{(\varphi)}^2 r^2} \\
\ddot{q} &= \frac{\left((m + M)(mr^2 + J_0) - m^2\sin{(\varphi)}^2 r^2\right)(-\beta\dot{x} - R\dot{q} + V)}{L(m + M)(mr^2 + J_0) - Lm^2\sin{(\varphi)}^2 r^2}
\end{aligned} \tag{9}
$$

The values of parameters are: $M = 0.1465$ kg, $m = 0.0048$ kg, $r = 0.003$ m, $k = 4.57$ kN/m, $c = 0.01$ Ns/m, $J_0 = 1e - 7$ Nm^2, $R_c = 3300$ Ω, $L = 10.8$ H.
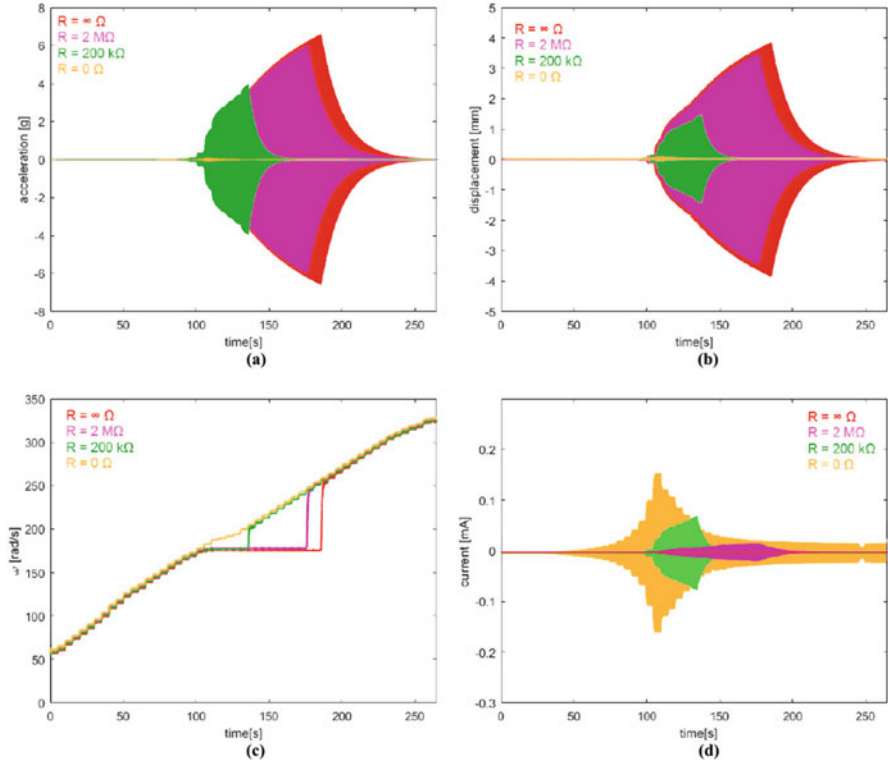
Fig. 5 Time history of (**a**) acceleration, (**b**) tip displacement of the beam, (**c**) angular velocity of the motor shaft, and (**d**) the current of the magnet circuit of the coil with increasing frequency

These values were determined based on the experimental setup, which is shown in the next section.

Simulations were performed to increase and decrease the voltage supplied to the motor so that the increase in the rotation of the shaft was linearly proportional, thus, the terms of coupling and energy limitation influence the rotation, characterizing a non-ideal system. Figure 5 shows the amplitude of (a) acceleration and (b) displacement of the tip, (c) angular velocity of the motor, and (d) electrical current for increasing voltage and the four different values of resistance. With open circuit ($R = \infty$), there is no electric current circulating through the coil, consequently there is no electromagnetic force acting on the beam. The term $\beta\dot{x}$ is not relevant, and terms $\beta\dot{q}$ and $R\dot{q}$ are null. With closed circuit, the amplitude of displacement and acceleration decreases with decreasing equivalent resistance in the electric circuit. Conversely, the current in the electrical circuit increases with decreasing resistance. The situation with short circuit ($R = 0$) results in very small resonance capture, and the Sommerfeld effect cannot be noticed on the motor velocity response, as there is no sudden jump. Figure 6 shows the simulation results for decreasing voltage.
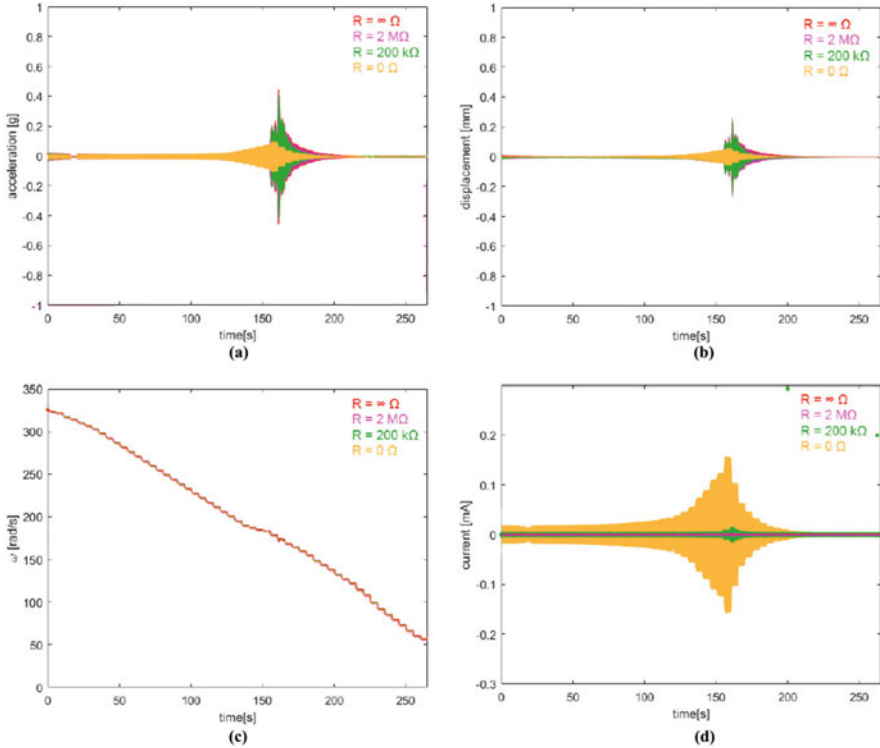
Fig. 6 Time history of (**a**) acceleration and (**b**) displacement of the beam, (**c**) angular velocity of the motor shaft, and (**d**) current in the magnet circuit with decreasing frequency

The Sommerfeld effect is seen near the natural frequency of the system at $\omega = 175.93$ rad/s, characterized by the rapid increase in acceleration and displacement.

5 Experimental Results

Figure 7 shows the experimental setup. A stainless steel beam is used with clamped-free boundary conditions. A DC motor with an unbalanced rotating mass is attached to the upper side of the free end of the beam, and a cylindrical neodymium magnet is attached to the lower side. A copper coil is fixed at the base. An accelerometer is placed on the motor, and an optical switch is used to measure the rotational speed of the unbalanced mass. Three voltage meters are used: one to measure the electric power supplied to the DC motor, another on an auxiliary resistor for current measurement of the DC motor, and a third to measure the voltage induced in the coil when it is open.
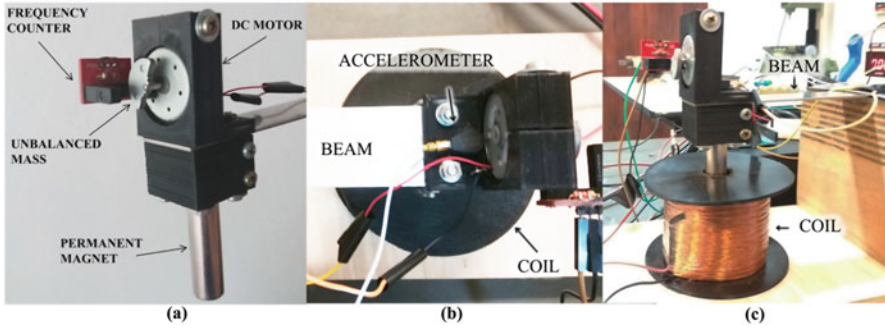
Fig. 7 The setup (**a**) beam free side, (**b**) top view, and (**c**) complete setup
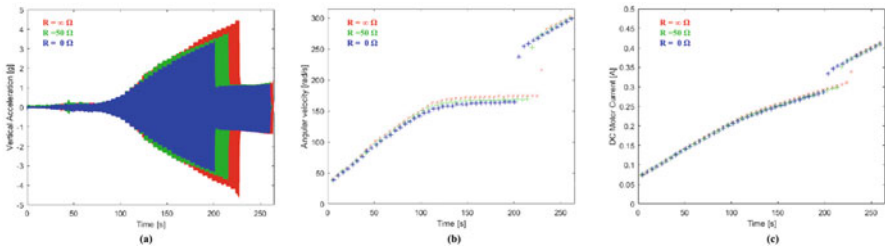
Fig. 8 Time history of (**a**) acceleration at the beam's tip, (**b**) angular velocity of the motor shaft and (**c**) DC motor current with electrical circuit resistance variation and increasing frequency

In order to study the behavior of the system, the experimental response is shown with varying motor voltage and current. A PWM controller is used in the range from 0 to 2.5 V, duty cycle from 18% to 60%, with 100% = 5V, step 0.8%, duration of 5 s each. Data acquisition was performed by a National Instruments USB-4431, with four simultaneous inputs. Data was acquired and recorded with National Instruments LabView, with sampling rate of 5 kHz, 1,325,000 total samples, and total time of 265 s.

The measurements made with the variations of the resistances in the magnetic circuit had an impact on the Sommerfeld effect. The coil current with the closed magnetic circuit was influenced by the measurement, so they were discarded. The displacement has the same characteristics as the acceleration measurements. Figure 8a shows the results with increasing voltage. It is observed that the amplitude of the acceleration is reduced with the reduction of the total resistance of the circuit. The jump occurred around 176 rad/s is advanced in time with the reduction of the impedance in the magnetic circuit observed in Fig. 8b, c. A similar procedure is performed to decrease the electrical voltage, with results shown in Fig. 9.
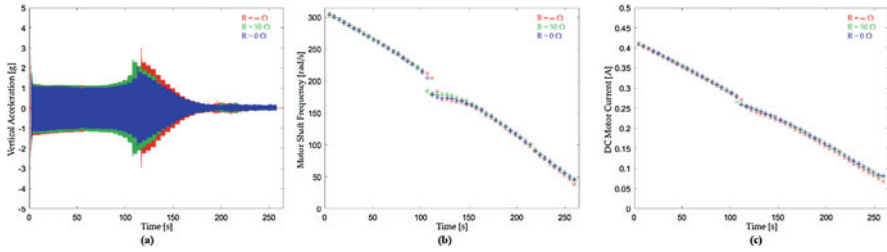
Fig. 9 Time history of (**a**) acceleration at the beam's tip, (**b**) angular velocity of the motor shaft and (**c**) DC motor current with electrical circuit resistance variation and decreasing frequency

6 Conclusions

The analytical and numerical results regarding the oscillatory behavior are similar to the experimental data. Some discrepancies occurred due to the way the voltage is increased and decreased using the PWM controller, and also by the non-linearity of the magnetic interaction between the elements, which was neglected. The effect of the magnetic field created by the oscillation does not affect the system in open circuit configuration. Therefore, the cantilever beam is limited only to its own structural parameters. However, when closing the magnetic circuit, the generated electromotive force produces a magnetic field proportional to the induced current. The magnetic field induced in the coil, when interacting with the permanent magnet, increases its damping in proportion to the oscillation speed. The various external resistances applied to the electrical circuit provide control over the acceleration and displacement amplitudes, maintaining the beam with its natural flexibility in situations far from the resonance frequency.

References

1. V.O. Kononenko, *Vibrating Systems with a Limited Power Supply* (Iliffe, Cambridgeshire, 1969)
2. J.M. Balthazar, A.M. Tusset, R.M.L.R.F. Brasil, et al., An overview on the appearance of the Sommerfeld effect and saturation phenomenon in non-ideal vibrating systems (NIS) in macro and MEMS scales. Nonlin. Dyn. **93**, 19–40 (2018). https://doi.org/10.1007/s11071-018-4126-0
3. L. Cveticanin, M. Zukovic, J.M. Balthazar, *Dynamics of Mechanical Systems with Non-Ideal Excitation*. Hardcover. ISBN: 978-3-319-54168-6 (2018). https://doi.org/10.1007/978-3-319-54169-3
4. P. Gonçalves, et al., The dynamic behavior of a cantilever beam coupled to a non-ideal unbalanced motor through numerical and experimental analysis. J. Sound Vib. **333**(20), 5115–5129 (2014)
5. M. Belhaq, A. Bichri, J. Der Hogapian, J. Mahfoud, Effect of electromagnetic actuations on the dynamics of a harmonically excited cantilever beam. Int. J. Non-Lin. Mech. **46**(6), 828–833 (2011)
6. M. Varanis, A.M. Tusset, J.M. Balthazar, G. Litak, C. Oliveira, R.T. Rocha, A. Nabarrete, V. Piccirillo, Dynamics and control of periodic and non-periodic behavior of Duffing vibrating

system with fractional damping and excited by a non-ideal motor. In press (2019). https://doi.org/10.1016/j.jfranklin.2019.11.048

7. P.J.P. Gonçalves, M. Silveira, E.A. Petrocino, J.M. Balthazar, Double resonance capture of a two-degree-of-freedom oscillator coupled to a non-ideal motor. Meccanica **51**(9), 2203–2214 (2016)

8. J. Awrejcewitz, D. Lewandowski, P. Olejnik, *Dynamics of Mechatronics Systems: Modeling, Simulation, Control, Optimization and Experimental Investigations* (World Scientific Publishing Co. Pte. Ltd, Singapore, 2017)

9. T. Chunawala, M. Ghandchi-Tehrani, J. Yan, An optimum design of a double pendulum in autoparametric resonance for energy harvesting applications. Vibroeng. Procedia **8**, 163–168 (2016)

Variable Length Sling Load Hoisting Control Method

Austin Morock, Andrea Arena, Mary Lanzerotti, Thomas Aldhizer, Jacob Capps, and Walter Lacarbonara ⓘ

1 Introduction

Understanding the behavior of the pendulum has captivated study for centuries [1–3]. When the bob of a pendulum is displaced above the lowest point of the stable equilibrium position and released from rest, the bob will typically swing indefinitely in the absence of external dissipative forces. The bob placed at the upper equilibrium point is unstable, and methods have been developed to induce stabilization of this case ("inverted pendulum") [4, 5] and related physical situations [6]. A bob attached to a shortening cable [7–10], driven pendulum [11, 12], and RLC circuits can exhibit unstable behavior. Stability in the pendulum is shown in this work to be induced making use of a parametric effect that has an analogy in other physical systems including parametric feedback cooling of atoms in optical cavities [13].

The aim of this work is to present a strategy to stabilize a low-mass sling load or hoist employing a variable length hoisting control method [14] and a hoisting control strategy that takes advantage of damping during the lengthening of a pendulum [15, 16] at the middle of the swing and of less harmful negative damping

A. Morock (✉)
U.S. Army, Fort Rucker, AL, USA
e-mail: austinmorock2@gmail.com

A. Arena · W. Lacarbonara
Sapienza University of Rome, Rome, Italy
e-mail: andrea.arena@uniroma1.it; walter.lacarbonara@uniroma1.it

M. Lanzerotti
Virginia Polytechnic Institute and State University, Arlington, VA, USA
e-mail: marylanzerotti@vt.edu

T. Aldhizer · J. Capps
United States Military Academy, West Point, NY, USA
e-mail: tom.aldhizer@gmail.com; jacob.capps@westpoint.edu

effects during the shortening phase near the maximum swing angles. Indeed, the cable is shortened when the swing angle nears its maximum value and the slowing pendulum has sufficiently low kinetic energy [17]. Lengthening the cable in the middle of the swing and shortening the cable at the end were shown with MATLAB simulations to decrease swing angle and cable length [17]. If a helicopter crew member does not observe the swinging payload, the cable could strike the helicopter, resulting in essentially a pulse input into the controls, likely resulting in a crash if the pilot cannot recover properly. In severe oscillation conditions, the hoist's contact with the frame could create a serrated edge, resulting in the sling being cut. Hoisting a rescued individual on a 6 m to 32 m cable in 90 s may be taken as a worst case scenario, implying a need for fast and precise control, as required in several rescue missions [18, 19]. Several models were proposed for the control problem of containers and slung loads [20–23]. Prior work presented control strategies to stabilize sling loads and hoists based on active and semi-active vibration control devices [24–26].

2   Mechanical Model

Figure 1 shows a photograph of a medical evacuation on the Matterhorn and schematic of a fixed Cartesian frame (O, $\mathbf{e}_1$, $\mathbf{e}_2$) with $\mathbf{e}_1$ and $\mathbf{e}_2$ collinear with the horizontal and the vertical directions, respectively. The position of the payload with respect to its suspension point is given, at time t, by the position vector $\mathbf{r}(t) = l(t) \sin \theta(t) \mathbf{e}_1 - l(t) \cos \theta(t) \mathbf{e}_2$, where $l(t)$ is the time-varying length of the cable, and $\theta(t)$ indicates the rotation of the hoisting sling. Finally, the payload weight is $\mathbf{w} = -M g \, \mathbf{e}_2$, where M represents the payload mass. The equation of motion of the one-degree-of-freedom (1 dof) mechanical system is obtained employing the Euler–Lagrange approach [27]. The potential energy $V = -Mgl(t) \cos \theta(t)$ and kinetic energy $T = \frac{1}{2} M \left\{ [\dot{l}(t)]^2 + [l(t) \dot{\theta}(t)]^2 \right\}$ are substituted into the Lagrangian $\mathcal{L} = T - V = \frac{1}{2} M \left\{ [\dot{l}(t)]^2 + [l(t) \dot{\theta}(t)]^2 \right\} + mgl(t) \cos \theta(t)$, from which the equation of motion is obtained [27]. The proposed mechanical model incorporates a real-time control system in which the cable length is alternatively constant or varied in time with a constant velocity proportional to the reference value v through the nondimensional gain $\alpha_{\mathrm{L,S}}(t)$, accordingly to a given control law. The system of equations including the pendulum nonlinear equation of motion and the time-rate of change of the cable length can be written as

$$
\begin{aligned}
&\ddot{\theta}(t) + \left[2\zeta\omega(t) + 2\frac{\dot{l}(t)}{l(t)} \right] \dot{\theta}(t) + \frac{g}{l(t)} \sin \theta(t) = 0, \\
&\dot{l}(t) = \alpha(t)\, v,
\end{aligned}
\tag{1}
$$

together with the initial conditions $\theta(0) = \theta_0$, $\dot{\theta}(0) = \dot{\theta}_0$, $l(0) = l_0$, where $\omega(t) = \sqrt{g/l(t)}$ is the time-varying frequency of the pendulum; and θ_0,
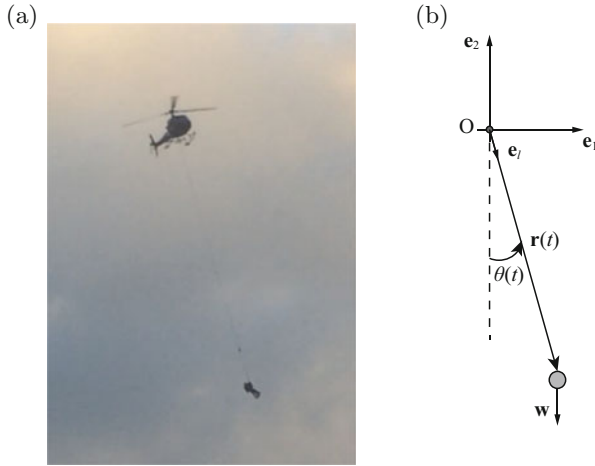
Fig. 1 (**a**) Photograph from a video of a medical evacuation rescue (MEDEVAC) with permission from Joseph Vanderlip, January 24, 2021. (**b**) Schematic representation of the hoisted payload and adopted fixed frame with variable cable length $l(t)$

$\dot{\theta}_0$, and l_0 are the initial angle, initial angular speed, and initial cable length, respectively. Moreover, $\alpha(t)$ is the nondimensional gain assuming the values $\alpha(t) = (\alpha_L, 0, -\alpha_S)$, respectively, during the time integration. Subscripts (L,S) indicate values prescribed during lengthening and shortening phases, respectively.

3 Variable Length Hoisting Control Strategy

In the hoist case, the cable length is varying in time, which produces a time-varying oscillation frequency. The aim of the control strategy is to shorten the cable length and reduce the oscillation amplitude so that the maximum allowed value θ_{ref} attained at the end of the hoisting phase is not exceeded. For a medical evacuation (MEDEVAC) rescue to hoist the payload into the helicopter, $\theta_{ref} = 5$ deg [19]. The goal is to obtain a minimum of the objective function F^{tar} defined by $F^{tar} = |\theta_{max}^{tar} - \theta_{ref}|$ according to an algorithm that provides new generations of parameters vectors $[\epsilon_\theta, \epsilon_{\dot{\theta}}, \alpha_L, \alpha_S]$. Here, ϵ_θ is the tolerance on the angle $\theta(t)$ that determines the switching from the free swinging phase to the lengthening phase, and vice versa. Also, $\epsilon_{\dot{\theta}}$ is the tolerance on the angular speed that decides the switching from the free swinging phase to the shortening phase, and vice versa. The objective function is evaluated for the parameters vector using a global optimization search. If $F^{tri} < F^{tar}$, the trial vector survives; otherwise, the target vector is selected for creating the new generation of parameters vectors which perform best in terms of control. This work adopts so-called Differential Evolution (DE) algorithm [28].

Fig. 2 Schematic
representation of the
shortening (S), lengthening
(L), and free swinging (F)
phases
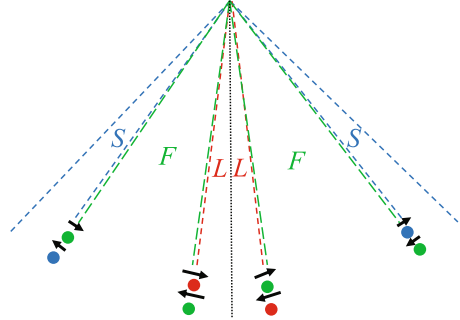
The set of n parameter vectors is generated from uniform probability distributions to ensure that the parameters span the space equally and respect the constraints. Time integration of the controlled system reproducing the entire retrieving maneuver is then performed for each set of vectors, and the maximum oscillation angle (that is, θ_{max}) is calculated for each simulation. The DE algorithm then perturbs a randomly selected vector chosen from among $n - 1$ vectors of the first generation and provides a new mutated parameters vector (that is, a trial vector); θ_{max}^{tri} is then calculated for the generated trial parameters vector, and the objective function $F^{tri} = |\theta_{max}^{tri} - \theta_{ref}|$ is compared with the objective function instance of the previous generation.

The following control laws are assigned for $t > t_{min}$ (see Fig. 2):

1. For $\theta = \epsilon_\theta$ and $\dot{\theta} < -\epsilon_{\dot{\theta}}$ then $\alpha = \alpha_L$,
2. For $\theta = -\epsilon_\theta$ and $\dot{\theta} < -\epsilon_{\dot{\theta}}$ then $\alpha = 0$,
3. For $\theta < -\epsilon_\theta$ and $\dot{\theta} = -\epsilon_{\dot{\theta}}$ then $\alpha = -\alpha_S$,
4. For $\theta < -\epsilon_\theta$ and $\dot{\theta} = \epsilon_{\dot{\theta}}$ then $\alpha = 0$,
5. For $\theta = -\epsilon_\theta$ and $\dot{\theta} > \epsilon_{\dot{\theta}}$ then $\alpha = \alpha_L$,
6. For $\theta = \epsilon_\theta$ and $\dot{\theta} > \epsilon_{\dot{\theta}}$ then $\alpha = 0$,
7. For $\theta > \epsilon_\theta$ and $\dot{\theta} = \epsilon_{\dot{\theta}}$ then $\alpha = -\alpha_S$,
8. For $\theta > \epsilon_\theta$ and $\dot{\theta} = -\epsilon_{\dot{\theta}}$ then $\alpha = 0$,

where t_{min} is the control starting time, and parameters α_L and α_S take on values lower than or equal to 1. The constraint prescribed on the cable length at all times t in the simulations is $l_{min} \leq l(t) \leq l_{max}$. The values of the mechanical parameters were adopted for a cable initially released from rest ($\dot{\theta}_0 = 0$) at the maximum angle $\theta_0 = 15$ deg at which a medical evacuation is initiated [14]: $g = 9.807$ m/s^2, $\zeta = 0$ (the case of no viscous damping), the maximum reeling speed in hoist rescues $v = 0.5$ m/s [14] with typical length $l_0 = 32$ m [14], and $l_{max} = l_0$. The final length is set to $l_{min} = 1.8$ m [14], and $t_{min} = 10$ s.

Without the control law, if no viscous damping is considered, the oscillations are stable only when the cable length is constant or when the cable is monotonically lengthening in time ($\dot{l}(t) \geq 0$); otherwise, for $\dot{l}(t) < 0$, the oscillations become unstable. In both cases, the time integration of the linearized equation of motion can be calculated in closed form expression through the combination of the Bessel

(a)

(b)
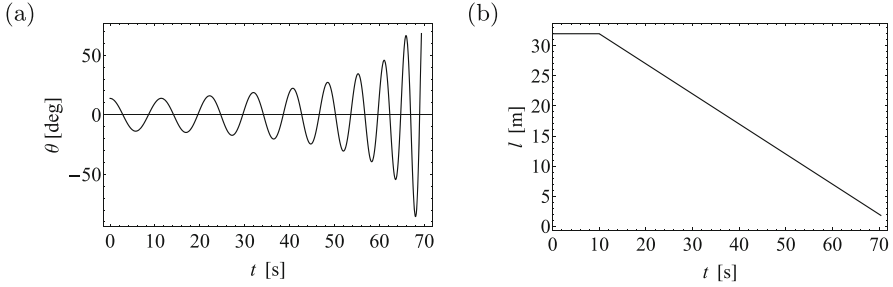
Fig. 3 (a) Unstable oscillations corresponding to the case in which the cable length is (b) monotonically shortening when a payload is released from rest with $\dot{\theta}_0 = 0$, where the reeling speed takes on the maximum value $v = 0.5$ m/s for a medical evacuation with $l_0 = 32$ m [14] and initial swing angle $\theta_0 = 15$ deg [14]

functions of the first kind $J_1(2\sqrt{g\,t/v})$ and of the second kind $Y_1(2\sqrt{g\,t/v})$ (for the lengthening case) and the combination of the modified Bessel functions of the first kind $I_1(2\sqrt{g\,t/v})$ and of the second kind $K_1(2\sqrt{g\,t/v})$ (for the shortening case), where $v > 0$. The unstable behavior is shown in Fig. 3 for the case of a cable that is shortening with a constant speed, such that $\dot{l}(t) = -v$ for $t > t_{\min}$.

3.1 Four-Parameter Optimization

The four control parameters (ϵ_θ, $\epsilon_{\dot{\theta}}$, α_L, α_S) are optimized via the DE algorithm. The effectiveness of the control is a tradeoff between different choices of these parameters/gains which also affect importantly the speed of the hoisting phase. Figure 4 displays the minimum value $F_{\min}$ of the objective function at every generation of the n four-dimensional parameters vectors and demonstrates that fewer than 50 generations are sufficient to determine a minimum. The optimal set of parameters corresponding to the last computed generation were found to be $[\epsilon_\theta, \epsilon_{\dot{\theta}}, \alpha_L, \alpha_S] = [2.8\,\text{deg}, 4.47\,\text{deg/s}, 0.29, 0.93]$ with the angle 12.6 deg corresponding to $\epsilon_{\dot{\theta}}$, and the angular speed 8.13 deg/s corresponding to ϵ_θ.

Figure 5a–d show the time histories of the swing angle θ and cable length l, respectively, in the case of controlled oscillations with the optimal parameters. Figure 5b shows the earliest 25 s of the time response as functions of θ and $\dot{\theta}$ (black and gray lines, respectively) by highlighting the switching conditions when the black curve θ reaches the tolerance ϵ_θ and when the gray curve $\dot{\theta}$ reaches the tolerance $\epsilon_{\dot{\theta}}$. Figure 5d shows the corresponding earliest 25 s of the time history of the cable length l. Dots in Figs. 2 and 5 indicate the onset of the shortening phase S (thresholds 1 and 5, blue), lengthening phase L (3 and 7, red), and free swinging phase F (2, 4, 6, 8, green) of the control law.

The computed ratio, at time t, between the frequency ω_c of the controlled length $l(t)$ assumed as the frequency at which the switching conditions 1 or 5 (blue
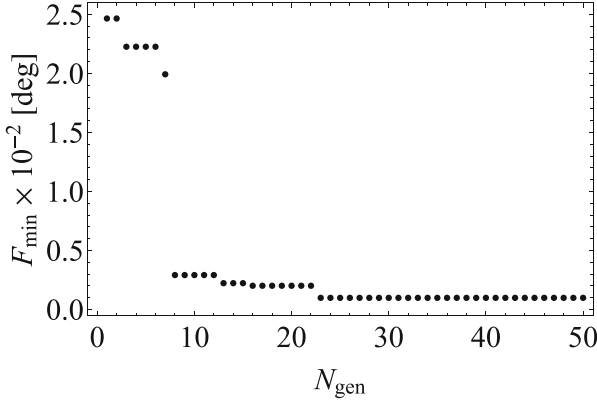
Fig. 4 Four-parameter optimization showing the minimum value of the objective function at each generation
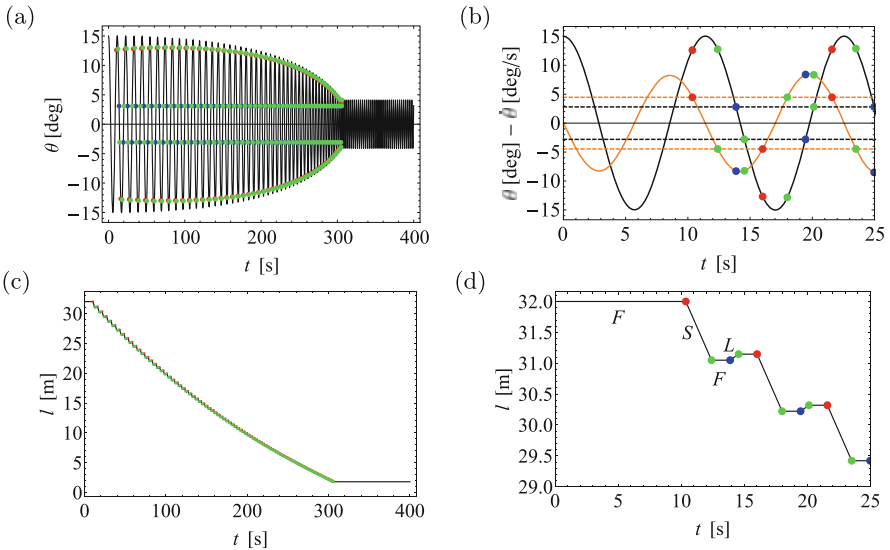
Fig. 5 Controlled θ (black line) and $\dot{\theta}$ (orange line) in (**a**) 400 s and (**b**) 25 s. In (**b**), the dashed black and orange lines indicate tolerances ϵ_θ and $\epsilon_{\dot{\theta}}$, respectively. Time history of the cable length in (**c**) 400 s and (**d**) 25 s

dots), or 3 or 7 (red dots), repeat, and the oscillation frequency $\omega(t) = \sqrt{g/l(t)}$ is equal to two. The time-varying length produces a parametric behavior of the oscillations as a result of parametric coupling between the length and swing angle. Figure 6 shows the payload position relative to the helicopter, where r_1 and r_2 are the component of the position vector $\mathbf{r}(t)$ along $\mathbf{e}_1$ and $\mathbf{e}_2$ directions, respectively. To show the robustness of the control method toward uncertainties related to the
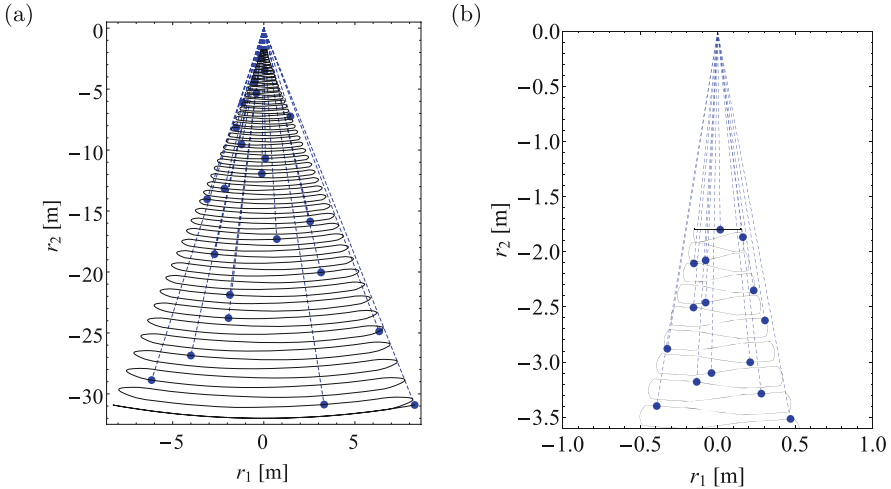
Fig. 6 (**a**) Payload position relative to the helicopter for the full length of the hoist for the proposed variable length control strategy. (**b**) Trajectory of the hoist cable from 3.5 m to 1.8 m. Blue circles indicate selected positions of the payload. Dashed lines indicate the corresponding cable configurations at selected time instants
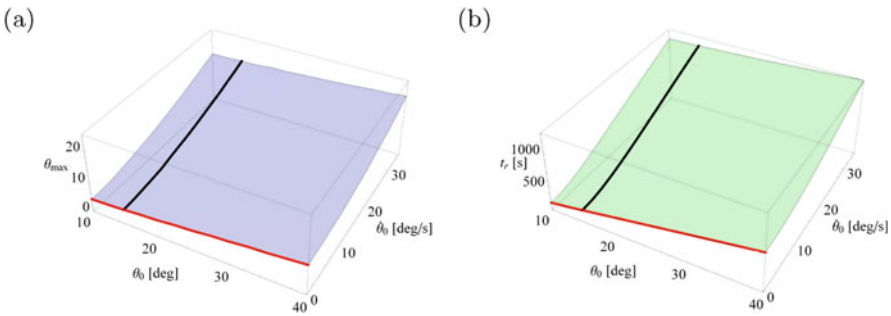
Fig. 7 (**a**) Residual oscillation amplitude θ_{max} of the controlled system varying the initial conditions θ_0 and $\dot{\theta}_0$. (**b**) Time t_r to achieve θ_{max} varying the initial conditions θ_0 and $\dot{\theta}_0$. The red (black) line indicates initial conditions in which the initial angle is changed (fixed to 15 deg) while the speed is constant and set to zero (changed)

initial conditions, the latter were varied in a feasible range of values. The maximum controlled oscillation amplitude θ_{max} was computed together with the time t_r at which θ_{max} is obtained. Figure 7a, b show the sensitivity to initial conditions in terms of the swing angle θ_{max} and time t_r to achieve the control. The results in this figure show that for the case in which θ_0 and $\dot{\theta}_0$ take on values that are greater than those for which the optimal parameters are calculated (that is, $\theta_0 = 15$ deg and $\dot{\theta}_0 = 0$), a loss of control efficiency occurs because both θ_{max} and t_r increase, thereby producing larger residual oscillations and longer times to hoist the payload.
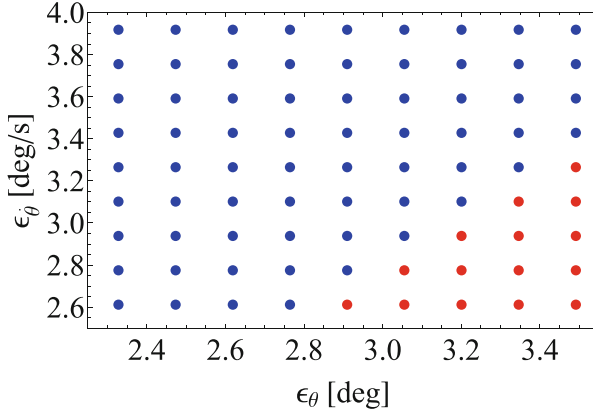
Fig. 8 Set of tolerances in angle and angular speed, ϵ_θ and $\epsilon_{\dot\theta}$, respectively, for stable control (blue points) and loss of control (red points)
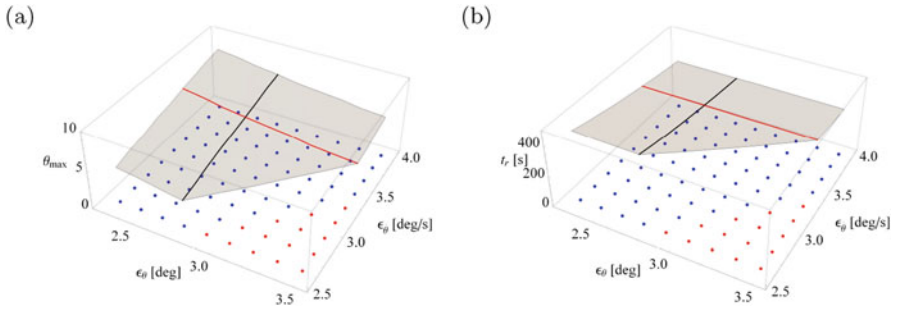
Fig. 9 (**a**) Residual oscillation amplitude θ_{max} of the controlled oscillation varying tolerances ϵ_θ and $\epsilon_{\dot\theta}$. (**b**) Time t_r to achieve θ_{max} varying tolerances ϵ_θ and $\epsilon_{\dot\theta}$

3.2   Two-Parameter Optimization and Sensitivity

This section discusses the case in which the control parameters α are fixed, and the different tolerances ϵ_θ and $\epsilon_{\dot\theta}$ are optimized via DE. In particular, it is assumed that the values of $\alpha_L = 0.2$ and $\alpha_S = 1$ are close to the optimal values calculated in the previous section. The optimal parameters turn out to be $\epsilon_\theta^{opt} = 2.91$ deg, and $\epsilon_{\dot\theta}^{opt} = 3.26$ deg/s, respectively. Sensitivity analyses on ϵ_θ and $\epsilon_{\dot\theta}$ are carried out by varying the tolerances in the range [0.8, 1.2] times the optimal values (that is, a 20% detuning from the optimal values). In Fig. 8, blue points indicate the set of tolerances ϵ_θ and $\epsilon_{\dot\theta}$ for which a stable solution is attained, and red points indicate the case in which the length of the cable shortens back to the initial length l_0. Figure 9a, b show the sensitivity to the tolerances in terms of the residual swing angle and time t_r at which the target residual controlled oscillation amplitude is obtained, respectively.

4 Conclusions

The proposed variable length control method is shown to be another effective and feasible approach [18] for reducing payload oscillations encountered during typical helicopter maneuvers. Further testing and modeling will be carried out to include time-varying cable length, scenarios for MEDEVAC rescues and 3D model of the controller, winch and hoist, and small-scale testing of the control feedback in a drone or advanced computer model. Future work will estimate downwash, or the velocity of air deflected downward by helicopter rotor blades.

References

1. L. da Vinci, *Of the Weight Distributed Over the Length of the Cord Which Supports It, The Notebooks of Leonardo da Vinci* (E. MacCurdy, New York, 1508)
2. C. Huygens, Correspondence 1664–1665, in *Ouvres Completes de Christiaan Huygens*, vol. V (La Societe Hollandaise Sciences, The Hague, 1893)
3. J.W. Strutt (Lord Rayleigh), XXXIV. On the pressure of vibrations. Philos. Mag. **3**, pp. 338–346 (1902)
4. A. Stephenson, XX. On induced stability. Philos. Mag., 233–236 (1908)
5. P. Kapitza, Dynamic stability of a pendulum when its point of suspension vibrates. Zhurnal eksperimental noi i teoreticheskoi fiziki **21**, 588–597 (1951)
6. B. Apffel, F. Novkoski, A. Eddi, E. Fort, Floating under a levitating liquid. Nature **585** (2020)
7. P. Langevin, M.D. Broglie (eds.), *La Theorie du Rayonnement et les Quanta* (Gauthier-Villars, Paris, 1912)
8. J.E. Littlewood, Lorentz's pendulum problem. Ann. Phys. **21**, 233–242 (1963)
9. D.K. Ross, The behaviour of a simple pendulum with uniformly shortening string length. Int. J. NonLin. Mech. **14**, 175–182 (1979)
10. L.L. Sanchez-Soto, J. Zoido, Variations on the adiabatic invariance: the Lorentz pendulum. Am. J. Phys. 57–62 (2013)
11. E.I. Butikov, Extraordinary oscillations of an ordinary forced pendulum. Eur. J. Phys. **29**, 215–233 (2008)
12. E.I. Butikov, Parametric excitation of a linear oscillator. Eur. J. Phys. **25**, 535–554 (2004)
13. J. Gieseler, B. Deutsch, R. Quidant, L. Novotny, Subkelvin parametric feedback cooling of a laser-trapped nanoparticle. Phys. Rev. Lett. **109**, 103603 (2012)
14. A. Morock, Variable length sling load hoisting control method, Honors Paper, Dept. Civil and Mech. Eng., U.S. Military Academy, West Point (2020)

15. M.N. Brearley, The simple pendulum with uniformly changing string length. Proc. Edinb. Math. Soc. **15**(1), 61–66 (1966)
16. A. Werner, C.J. Eliezer, The lengthening pendulum. J. Aust. Math. 331–336 (1969)
17. T. Aldhizer, A. Morock, K. Hughes, M.Y. Lanzerotti, S. Christoff, S. Lintelmann, J. Capps, Suspended load swing stabilization, in *IEEE Integrated STEM Education Conference* (2020). Virtual
18. A. Morock, A. Arena, M. Lanzerotti, J. Capps, B. Huff, W. Lacarbonara, Active sling load stabilization, in *Book of Abstracts, First International Nonlinear Dynamics Conference (NODYCON)*, Rome, Feb. 17–20 (Nodys Publications, 2019), pp. 549–550. ISBN 978-88-944229-0-0
19. A. Morock, T. Aldhizer, M.Y. Lanzerotti, A. Arena, W. Lacarbonara, J. Capps, Stabilization environment for swing stabilization and MEDEVAC hoists, in AIAA Aviation Forum (2021). https://doi.org/10.2514/6.2021-2430
20. A. Arena, A. Casalotti, W. Lacarbonara, M.P. Cartmell, Dynamics of container cranes: three-dimensional modeling, full-scale experiments, and identification. Int J. Mech Sci. **93**, 8–21 (2015)
21. A. Arena, W. Lacarbonara, M.P. Cartmell, Nonlinear interactions in deformable container cranes. P. I. Mech. Eng. C-J. Mec. **230**(1), 5–20 (2016)
22. L.S. Cicolani, G. Kanning, Equations of motion of slung load systems with results for dual life. NASA Technical Memorandum, 102246 (National Aeronautics and Space Administration, Washington, 1990), 39p
23. L.S. Cicolani, C. Ivler, C. Ott, R. Raz, A. Rosen, Rotational stabilization of cargo container slung loads. J. Am. Helicopter Soc. **60**, 042006-1-042006 (2015)
24. Z.N. Masoud, A.H. Nayfeh, Sway reduction on container cranes using delayed feedback controller. Nonlin. Dyn. **34**, 347–358 (2003)
25. A. Arena, W. Lacarbonara, A. Casalotti, Payload oscillations control in harbor cranes via semi-active vibration absorbers: modeling, simulations and experimental results. Procedia Eng. **199**, 501–509 (2017)
26. R.J. Henry, Z.N. Masoud, A.H. Nayfeh, Mook, D.T. Cargo, Pendulation reduction on ship-mounted cranes via boom-luff angle actuation. J. Vib. Control. **7**, 1253–1264 (2001)
27. M.L. Boas, *Mathematical Methods in the Physical Sciences*, 3rd edn. (Wiley, New York, 2005)
28. R. Storn, K. Price, Differential evolution a simple and efficient heuristic for global optimization over continuous spaces. J. Global Optim. **11**, 341–359 (1997)

Dynamic Actuation Model for Vibration Reduction in Offshore Cranes

Althea Rustico, Nicholas Fantuzzi, Massimiliano Formenti, and Antonio J. M. Ferreira

1 Introduction

Despite the high level of competence of skilled tower crane operators, it is hardly possible to completely remove payload oscillations in all possible circumstances [1]. External disturbances such as wind can easily initiate an oscillation. After a while, the oscillations can become larger, until the point is reached where the crane operations have to be stopped and the oscillation has to die out, which can take a very long time [2]. Even without these disturbances, due to the complex effects of the crane movements on the payload, oscillations are still hard to suppress [3]. Therefore, researchers have tried to find different ways to control the movement of the crane in order to prevent or reduce this payload swinging, with varying levels of success [4]. Tower cranes are one of the intricate pieces of machinery constructed and they exhibit complex dynamic behaviors [5]. Their design has to take into account diverse and various environmental conditions, such as on land or at sea, or in adverse weather conditions. Crane systems have been studied theoretically, along with its optimized control factors and non-linear dynamics behavior [6]. Most of the research to date has limited itself to several assumptions regarding the crane, such as it has a rigid structure or boom, and a simple beam [7]. Another interesting study was done about the dynamical behavior on the mobile elevating

A. Rustico · N. Fantuzzi (✉)
DICAM Department, University of Bologna, Bologna, Italy
e-mail: althea.rustico@studio.unibo.it; nicholas.fantuzzi@unibo.it

M. Formenti
Stephenson Academy, Rotterdam, NC, The Netherlands
e-mail: m.formenti@stephensonacademy.com

A. J. M. Ferreira
Faculty of Engineering, University of Porto, Porto, Portugal
e-mail: ferreira@fe.up.pt

work platform (MEWP). The study was inspired by an accident happened during a pruning operation. A big branch of three fell down and bumped the basket of MEWP. The consequent dynamical actions have made the operator jump out of the basket of MEWP [8]. Other works on the dynamics of big gantry crane subjected to different trolley motions [9] and cranes subjected to impulse loadings [10] have been recently presented. The present work focuses on the anti-sway reduction of hanging payloads. The oscillation reduction is led by the trolley motion which is able to reduce oscillations of hook and payload system (double-pendulum configuration) [11]. Several techniques have been presented in the past years [12]. However, in this work PID (proportional, integral, derivative) controllers are adopted. Such controllers are able to tailor an acting force according to three parameters which are proportional, integral, and derivative forms of a pre-defined error.

This work presents the mathematical development of a 2D and a 3D double-pendulum crane system with PID control. The crane system is displaced from its initial configuration, and it is left in free vibrations. Comparison between uncontrolled and PID controlled configurations is shown in terms of displacements. The actuation is performed by the introduction of a trolley which is able to reduce sway payload motion with its motion.

2   The 2D Double-Pendulum Model

Figure 1a illustrates the schematic representation of a 2D double-pendulum-type crane in the Cartesian space that is driven by the force F which moves along the x axis. Such crane system consists in a trolley, hook, and payload. The trolley position with respect to the origin is described by x. The double-pendulum motion is described by two angles, the hook angle with respect to the vertical line θ_1 and the
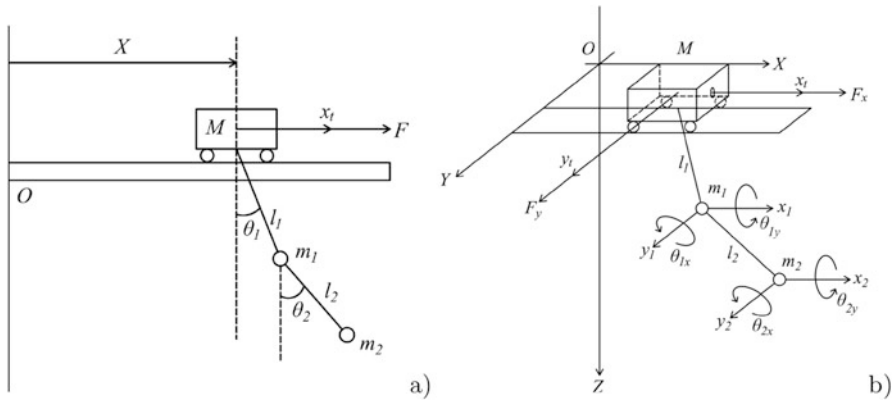
Fig. 1 (**a**) Schematic of two-dimensional double-pendulum-type overhead. (**b**) Schematic of three-dimensional double-pendulum-type overhead cranes

payload angle with respect to the vertical line θ_2. Other symbols in Fig. 1a are the trolley mass M, the hook mass m_1, the payload mass m_2, the cable length between the trolley and the hook l_1, and the cable length between the hook and the payload l_2.

Consider some mild and ideal assumptions such as no friction, mass-less cables, mass-point hook, and mass-point payload. Since the crane system in Fig. 1a contains three degrees of freedom, three generalized variables are needed to describe its dynamics. In Cartesian space, the trolley position x_t, the hook angle θ_1, and the payload angle θ_2 are adopted to describe the three degrees of freedom. Thus, the following Lagrangian equation can be obtained as

$$\frac{d}{dt}\left(\frac{\partial \mathcal{L}}{\partial \dot{q}_j}\right) - \frac{\partial \mathcal{L}}{\partial q_j} = F_j \tag{1}$$

where $j = 1, 2, 3$; q_j is the generalized coordinate, meaning x, θ_1, and θ_2; F_j is the external force; $\mathcal{L} = K - U$ indicates the Lagrangian of the crane system, where K is the kinetic energy, and U denotes the potential energy. From the aforementioned assumptions, the hook and payload are considered as point masses so that the kinetic energy K can be written as

$$K = \frac{1}{2}M\dot{x}^2 + \frac{1}{2}m_1\left(v_{1x}^2 + v_{1y}^2\right) + \frac{1}{2}m_2\left(v_{2x}^2 + v_{2y}^2\right) \tag{2}$$

where v_{1x}, v_{1y} and v_{2x}, v_{2y} are the hook and payload velocity components in the x and y directions, respectively.

In Fig. 1a, the potential energy of the trolley is kept unchanged. Due to the fact, the potential energy of the crane system is exhibited by the potential energies of the hook and payload determined as

$$U = m_1 g l_1 (1 - \cos\theta_1 + m_2 g [l_1(1 - \cos\theta_1 + l_2(1 - \cos\theta_2)] \tag{3}$$

where g denotes the gravity acceleration.

After several differentiation operations, the dynamic model of the crane system can be written as

$$\begin{aligned}
(M + m_1 + m_2)\ddot{x} + (m_1 + m_2)l_1\ddot{\theta}_1 \cos\theta_1 \\
-(m_1 + m_2)l_1\dot{\theta}_1^2 \sin\theta_1 + m_2 l_2\ddot{\theta}_2 \cos\theta_2 - m_2 l_2\dot{\theta}_2^2 \sin\theta_2 = F \\
(m_1 + m_2)l_1\ddot{x} \cos\theta_1 + (m_1 + m_2)l_1^2\ddot{\theta}_1 + m_2 l_1 l_2\ddot{\theta}_2 \cos(\theta_1 - \theta_2) \\
+ m_2 l_1 l_2\dot{\theta}_2^2 \sin(\theta_1 - \theta_2) + (m_1 + m_2)g l_1 \sin\theta_1 = 0 \\
m_2 l_2\ddot{x} \cos\theta_2 + m_2 l_2^2\ddot{\theta}_2 + m_2 l_1 l_2\ddot{\theta}_1 \cos(\theta_1 - \theta_2) \\
- m_2 l_1 l_2\dot{\theta}_1^2 \sin(\theta_1 - \theta_2) + m_2 g l_2 \sin\theta_2 = 0
\end{aligned} \tag{4}$$

For safe operations, the swing angle should be kept small $\sin\theta \approx \theta$, $\cos\theta \approx 1$, $\theta_1\theta_2 \approx 0$. So, considering also the damping factor B, the equations of motion (4)

become

$$(M + m_1 + m_2)\ddot{x} + B\dot{x} + (m_1 + m_2)l_1\ddot{\theta}_1 + m_2l_2\ddot{\theta}_2 = F$$
$$(m_1 + m_2)l_1\ddot{x} + (m_1 + m_2)l_1^2\ddot{\theta}_1 + m_2l_1l_2\ddot{\theta}_2 + (m_1 + m_2)gl_1\theta_1 = 0 \qquad (5)$$
$$m_2l_2\ddot{x} + m_2l_1l_2\ddot{\theta}_1 + m_2l_2^2\ddot{\theta}_2 + m_2gl_2\theta_2 = 0$$

In matrix form Eq. (5) are

$$
\begin{bmatrix} (M + m_1 + m_2) & (m_1 + m_2)l_1 & m_2l_2 \\ (m_1 + m_2)l_1 & (m_1 + m_2)l_1^2 & m_2l_1l_2 \\ m_2l_2 & m_2l_1l_2 & m_2l_2^2 \end{bmatrix} \begin{Bmatrix} \ddot{x} \\ \ddot{\theta}_1 \\ \ddot{\theta}_2 \end{Bmatrix} + \begin{bmatrix} B & 0 & 0 \\ 0 & 0 & 0 \\ 0 & 0 & 0 \end{bmatrix} \begin{Bmatrix} \dot{x} \\ \dot{\theta}_1 \\ \dot{\theta}_2 \end{Bmatrix}
$$
$$
+ \begin{bmatrix} 0 & 0 & 0 \\ 0 & (m_1 + m_2)gl_1 & 0 \\ 0 & 0 & m_2gl_2 \end{bmatrix} \begin{Bmatrix} x \\ \theta_1 \\ \theta_2 \end{Bmatrix} = \begin{Bmatrix} F \\ 0 \\ 0 \end{Bmatrix} \qquad (6)
$$

A numerical solution is carried out according to space-state approach, thus, the system of three equations of second order should be converted into a system of six equations of first order as

$$\dot{x} = y$$
$$(M + m_1 + m_2)\dot{y} + (m_1 + m_2)l_1\dot{\alpha} + m_2l_2\dot{\beta} = -By + F$$
$$\dot{\theta}_1 = \alpha$$
$$(m_1 + m_2)l_1\dot{y} + (m_1 + m_2)l_1^2\dot{\alpha} + m_2l_1l_2\dot{\beta} = -(m_1 + m_2)gl_1\theta_1 \qquad (7)$$
$$\dot{\theta}_2 = \beta$$
$$m_2l_2\dot{y} + m_2l_1l_2\dot{\alpha} + m_2l_2^2\dot{\beta} = -m_22gl_2\theta_2$$

In Table 1, the double-pendulum parameters are reported. The obtained results are reported in Fig. 2. Figure 2a represents the trolley, hook, and payload displacements without control system. Figure 2b represents the same displacements when the control based on the applied force F is active. The trolley force, that actuates the dynamic system, has been obtained via PID control system. This kind of control works according to the following formula:

Table 1 Double-pendulum crane parameters

Parameter	Symbol	Value	Unit
Trolley mass	M	500	kg
Hook mass	m_1	500	kg
Payload mass	m_2	40,000	kg
Wire 1 length	l_1	10	m
Wire 2 length	l_2	10	m
Gravity acceleration	g	9.81	m/s^2
Damping factor	B	10,000	Nm/s
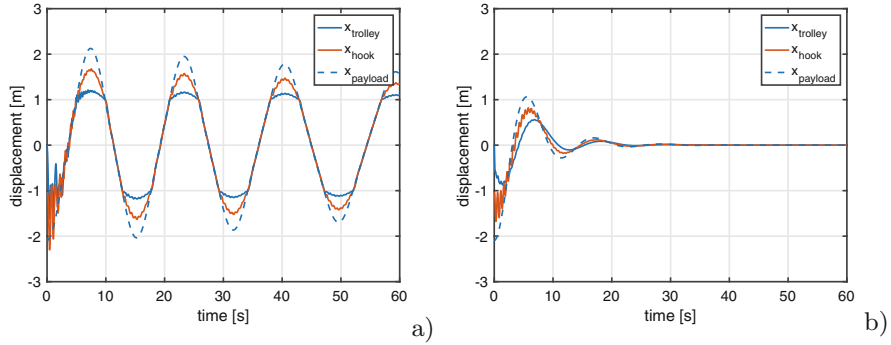
Fig. 2 (**a**) 2D Double-pendulum displacements w/o control. (**b**) 2D Double-pendulum displacements w/ control

Table 2 PID control parameters used in the computations

	k_p	k_i	k_d
Trolley x	1000	15	300
Trolley y	1500	20	700
Hook x	100	0	100
Hook y	1000	0	500
Payload x	100	0	100
Payload y	1000	0	200

$$f(t) = k_p e(t) + k_i \int_0^t e(\tau)d\tau + k_d \frac{de(t)}{dt} \qquad (8)$$

where the function $f(t)$ is optimized according to the proportional, integral, and derivative parameters which consider the error $e(t)$. The PID coefficients used in the computations below are listed in Table 2, where only values for x are considered for the 2D case. It is noted that for the hook and payload angles only PD control is necessary in order to avoid crane overshoot. Note that high damping is introduced with the coefficient k_d and to act on the velocity of the system k_i should be increased but for the present case equilibrium configuration is not achieved.

In order to study the actuation model, the double-pendulum is displaced from the equilibrium configuration of an angle of six degrees and let in free oscillations. Clearly the system with the control active is able to suppress vibrations in less than 20 seconds, whereas the system without control continues the oscillations for several minutes before stopping.

3 The 3D Double-Pendulum Model

The aforementioned case can be extended to the 3D case as depicted in Fig. 1b. In the $X-Y$ plane, the trolley can simultaneously move in both $x-$ and $y-$ directions. The reference system with coordinates $x_1-y_1-z_1$ is attached to the hook with z_1 pointing downward. The hook is connected to the trolley by a light, rigid cable of length l_2, with the cable mass considered negligible in comparison with that of the hook and the payload. The hook is assumed to be a point mass m_1. The rigid cable length between the hook and the trolley is l_1. In 3D space, the hook angle has two components, θ_{1x} and θ_{1y}. The two variables are the projections of the cable onto the $X-Z$ and $Y-Z$ planes, respectively. In Fig. 1b, the second reference frame with coordinates $x_2-y_2-z_2$, parallel to the first reference system, has its origin at the payload. The second reference system is utilized to describe the swing rotation of the payload. Similarly, the payload rotation can be described by two angles, θ_{2x} and θ_{2y}, which are projections of the payload angle onto the $X-Z$ and $Y-Z$ planes, respectively. From Fig. 1b, the instantaneous location of hook $[x_1, y_1, z_1]^\top$ with respect to an inertial coordinate system can have the form

$$
\begin{aligned}
x_1 &= x_t + l_1 \sin\theta_{1x} \\
y_1 &= y_t + l_1 \cos\theta_{1x} \sin\theta_{1y} \\
z_1 &= l_1 \cos\theta_{1x} \cos\theta_{1y}
\end{aligned}
\tag{9}
$$

where x_t and y_t are the trolley positions in the inertial reference frame. The instantaneous location of the payload $[x_2 \ y_2 \ z_2]^\top$ has the form

$$
\begin{aligned}
x_2 &= x_t + l_1 \sin\theta_{1x} + \tfrac{l_2}{2} \sin\theta_{2x} \\
y_2 &= y_t + l_1 \cos\theta_{1x} \sin\theta_{1y} + \tfrac{l_2}{2} \cos\theta_{2x} \sin\theta_{2y} \\
z_2 &= l_1 \cos\theta_{1x} \cos\theta_{1y} + \tfrac{l_2}{2} \cos\theta_{2x} \cos\theta_{2y}
\end{aligned}
\tag{10}
$$

Differentiating Eq. (9) with respect to time t we have

$$
\overrightarrow{v}_1 : \begin{aligned}
\dot{x}_1 &= \dot{x}_t + l_1\dot{\theta}_{1x} \cos\theta_{1x} \\
\dot{y}_1 &= \dot{y}_t - l_1\dot{\theta}_{1x} \sin\theta_{1x} \sin\theta_{1y} + l_1\dot{\theta}_{1y} \cos\theta_{1x} \cos\theta_{1y} \\
\dot{z}_1 &= -l_1\dot{\theta}_{1x} \sin\theta_{1x} \cos\theta_{1y} - l_1\dot{\theta}_{1y} \cos\theta_{1x} \sin\theta_{1y}
\end{aligned}
\tag{11}
$$

where $\overrightarrow{v}_1 = [\dot{x}_1 \ \dot{y}_1 \ \dot{z}_1]^\top$ is the instantaneous velocity of the hook. Differentiating Eq. (10) with respect to time t we have

$$
\overrightarrow{v}_2 : \begin{aligned}
\dot{x}_2 &= \dot{x}_1 + \tfrac{l_2}{2}\dot{\theta}_{2x} \cos\theta_{2x} \\
\dot{y}_2 &= \dot{y}_1 - \tfrac{l_2}{2}\dot{\theta}_{2x} \sin\theta_{2x} \sin\theta_{2y} + \tfrac{l_2}{2}\dot{\theta}_{2y} \cos\theta_{2x} \cos\theta_{2y} \\
\dot{z}_2 &= \dot{z}_1 - \tfrac{l_2}{2}\dot{\theta}_{2x} \sin\theta_{2x} \cos\theta_{2y} - \tfrac{l_2}{2}\dot{\theta}_{2y} \cos\theta_{2x} \sin\theta_{2y}
\end{aligned}
\tag{12}
$$

where $\vec{v}_2 = [\dot{x}_2 \ \dot{y}_2 \ \dot{z}_2]^\top$ is the instantaneous velocity of the payload. Take the four variables θ_{1x}, θ_{1y}, θ_{2x}, and θ_{2y} into account as generalized coordinates. The following Lagrangian equation can be obtained:

$$\frac{d}{dt}\left(\frac{\partial \mathcal{L}}{\partial \dot{q}_i}\right) - \left(\frac{\partial \mathcal{L}}{\partial q_i}\right) = 0 \tag{13}$$

where q_i for $i = 1, 2, 3, 4$ is the generalized coordinate. The right-hand side in Eq. (13) is set to be zero because there are no external inputs applied to the hook as well as the payload. After several differentiation operations, the dynamic model of the crane system can be written as

$$
\begin{aligned}
(m_1 l_1^2 + m_2 l_1^2)\ddot{\theta}_{1x} + (m_1 + m_2)l_1\ddot{x}_T \cos\theta_{1x} \\
-(m_1 + m_2)l_1\ddot{y}_t \sin\theta_{1x}\sin\theta_{1y} + (m_1 + m_2)l_1^2(\dot{\theta}_{1y})^2 \cos\theta_{1x}\sin\theta_{1x} \\
+\tfrac{1}{2}m_2 l_1 l_2\ddot{\theta}_{2x} \cos\theta_{1x}\cos\theta_{2x} - \tfrac{1}{2}m_2 l_1 l_2(\dot{\theta}_{2x})^2 \cos\theta_{1x}\sin\theta_{2x} \\
+\tfrac{1}{2}m_2 l_1 l_2\ddot{\theta}_{2x} \sin\theta_{1x}\sin\theta_{2x}\cos(\theta_{1y} - \theta_{2y}) \\
+\tfrac{1}{2}m_2 l_1 l_2(\dot{\theta}_{2x})^2 + (\dot{\theta}_{2y})^2 \sin\theta_{1x}\cos\theta_{2x}\cos(\theta_{1y} - \theta_{2y}) \\
+\tfrac{1}{2}m_2 l_1 l_2\ddot{\theta}_{2y} \sin\theta_{1x}\cos\theta_{2x}\sin(\theta_{2y} - \theta_{1y}) \\
+m_2 l_1 l_2\dot{\theta}_{2x}\dot{\theta}_{2y} \sin\theta_{1x}\sin\theta_{2x}\sin(\theta_{1y} - \theta_{2y}) \\
+(m_1 + m_2)g l_1 \sin\theta_{1x}\cos\theta_{1y} = 0
\end{aligned}
\tag{14}
$$

$$
\begin{aligned}
(m_1 + m_2)l_1^2 \cos^2\theta_{1x}\ddot{\theta}_{1y} - 2(m_1 + m_2)l_1^2\dot{\theta}_{1x}\dot{\theta}_{1y}\cos\theta_{1x}\sin\theta_{1x} \\
+(m_1 + m_2)l_1\ddot{y}_t \cos\theta_{1x}\cos\theta_{1y} \\
+\tfrac{1}{2}m_2 l_1 l_2\ddot{\theta}_{2y} \cos\theta_{1x}\cos\theta_{2x}\cos(\theta_{1y} - \theta_{2y}) \\
+\tfrac{1}{2}m_2 l_1 l_2(\dot{\theta}_{2x})^2 + (\dot{\theta}_{2y})^2 \cos\theta_{1x}\cos\theta_{2x}\sin(\theta_{1y} - \theta_{2y}) \\
+\tfrac{1}{2}m_2 l_1 l_2\ddot{\theta}_{2x} \cos\theta_{1x}\sin\theta_{2x}\sin(\theta_{1y} - \theta_{2y}) \\
-m_2 l_1 l_2\dot{\theta}_{2x}\dot{\theta}_{2y} \cos\theta_{1x}\sin\theta_{2x}\cos(\theta_{1y} - \theta_{2y}) \\
+(m_1 + m_2)g l_1 \cos\theta_{1x}\sin\theta_{1y} = 0
\end{aligned}
\tag{15}
$$

$$
\begin{aligned}
\left(m_2\frac{l_2^2}{4} + I_{yy}\right)\ddot{\theta}_{2x} + \tfrac{1}{2}m_2 l_2\ddot{x}_t \cos\theta_{2x} \\
-\tfrac{1}{2}m_2 l_2\ddot{y}_t \sin\theta_{2x}\sin\theta_{2y} + \tfrac{1}{2}m_2 l_1 l_2\ddot{\theta}_{1x} \cos\theta_{1x}\cos\theta_{2x} \\
-\tfrac{1}{2}m_2 l_1 l_2(\dot{\theta}_{1x})^2 \sin\theta_{1x}\cos\theta_{2x} \\
+\tfrac{1}{2}m_2 l_1 l_2\ddot{\theta}_{1x} \sin\theta_{1x}\sin\theta_{2x}\cos(\theta_{1y} - \theta_{2y}) \\
+\tfrac{1}{2}m_2 l_1 l_2(\dot{\theta}_{1x})^2 + (\dot{\theta}_{1y})^2 \cos\theta_{1x}\sin\theta_{2x}\cos(\theta_{1y} - \theta_{2y}) \\
-m_2 l_1 l_2\dot{\theta}_{1x}\dot{\theta}_{1y} \sin\theta_{1x}\sin\theta_{2x}\sin(\theta_{1y} - \theta_{2y}) \\
+m_2\frac{l_2^2}{4}(\dot{\theta}_{2y})^2 \cos\theta_{2x}\sin\theta_{2x} + (I_{xx} - I_{zz})(\dot{\theta}_{2y})^2 \cos\theta_{2x}\sin\theta_{2x} \\
+m_2 g\frac{l_2}{2} \cos\theta_{2x}\sin\theta_{2y} = 0
\end{aligned}
\tag{16}
$$

$$\left(m_2 \frac{l_2^2}{4} \cos^2 \theta_{2x} + I_{xx} \cos^2 \theta_{2x} + I_{zz} \sin^2 \theta_{2x}\right) \ddot{\theta}_{2y}$$

$$
\begin{aligned}
-m_2 \frac{l_2^2}{2} \dot{\theta}_{2x} \dot{\theta}_{2y} \cos \theta_{2x} \sin \theta_{2x} + \frac{1}{2} m_2 l_2 \ddot{y}_t \cos \theta_{2x} \cos \theta_{2y} \\
+ \frac{1}{2} m_2 l_1 l_2 \ddot{\theta}_{1x} \sin \theta_{1x} \cos \theta_{2x} \sin (\theta_{2y} - \theta_{1y}) \\
+ \frac{1}{2} m_2 l_1 l_2 (\dot{\theta}^2_{1x} + \dot{\theta}^2_{1y}) \cos \theta_{1x} \cos \theta_{2x} \sin (\theta_{2y} - \theta_{1y}) \\
+ \frac{1}{2} m_2 l_1 l_2 \ddot{\theta}_{1y} \cos \theta_{1x} \cos \theta_{2x} \cos (\theta_{1y} - \theta_{2y}) \\
- m_2 l_1 l_2 \dot{\theta}_{1x} \dot{\theta}_{1y} \sin \theta_{1x} \cos \theta_{2x} \cos (\theta_{2y} - \theta_{1y}) \\
+ (I_{xx} - I_{zz}) \dot{\theta}_{2x} \dot{\theta}_{2y} \sin (2\theta_{2x}) + m_2 g \frac{l_2}{2} \cos \theta_{2x} \sin \theta_{2y} = 0
\end{aligned}
\tag{17}
$$

Regarding the trolley dynamics, taking into account an active control, the right-hand side is characterize by an external force $F = (F_x, F_y)$. As aforementioned, the external forces are obtained via PID control system. When the PID control system is not active, the system is studied in its free vibration configuration. The two equations of motion for the trolley along x and y can be written as

$$
\begin{aligned}
(M + m_1 + m_2)\ddot{x} + (m_1 + m_2)l_1\ddot{\theta}_{1x} \cos \theta_{1x} \\
-(m_1 + m_2)l_1\dot{\theta}_{1x}^2 \sin \theta_{1x} + m_2 l_2 \ddot{\theta}_{2x} \cos \theta_{2x} - m_2 l_2 \dot{\theta}_{2x}^2 \sin \theta_{2x} = F_x \\
(M + m_1 + m_2)\ddot{x} + (m_1 + m_2)l_1\ddot{\theta}_{1y} \cos \theta_{1y} \\
-(m_1 + m_2)l_1\dot{\theta}_{1y}^2 \sin \theta_{1y} + m_2 l_2 \ddot{\theta}_{2y} \cos \theta_{2y} - m_2 l_2 \dot{\theta}_{2y}^2 \sin \theta_{2y} = F_y
\end{aligned}
\tag{18}
$$

The obtained results are reported in Fig. 3. Figure 3a–c represents displacements of the trolley, the hook, and the payload along x and y. Figure 3b–d represents the same displacements with an active control based on the applied force $F = (F_x, F_y)$.

4 Conclusions

In this work, a dynamic actuation model for vibration reduction in double-pendulum crane type has been presented. Starting from a 2D double-pendulum model, all the equations of motion have been obtained through the Lagrange method, and later, a more refined model consisting of a 3D double-pendulum has been considered: its main anchor point being able to translate on a Cartesian plane integral to the crane's jib (called trolley), a first mass characterized by the hook, and a second mass characterized by the payload. For the payload, different masses were taken into consideration, with the lightest one being 4 tons and the heaviest one being 100 tons. The initial simulations involved a 2D model without any external control action being performed to control the payload's oscillations: Different boundary conditions in terms of characteristic angles and displacements were injected into the solver in order to understand the dynamic behavior of the system. In this phase of the work, all the calculations were performed by making use of the sole MATLAB environment, given the simplicity of the reduced 3 DOF model: These initial trials served as very valuable data to subsequently set the main stability goals for the controlled
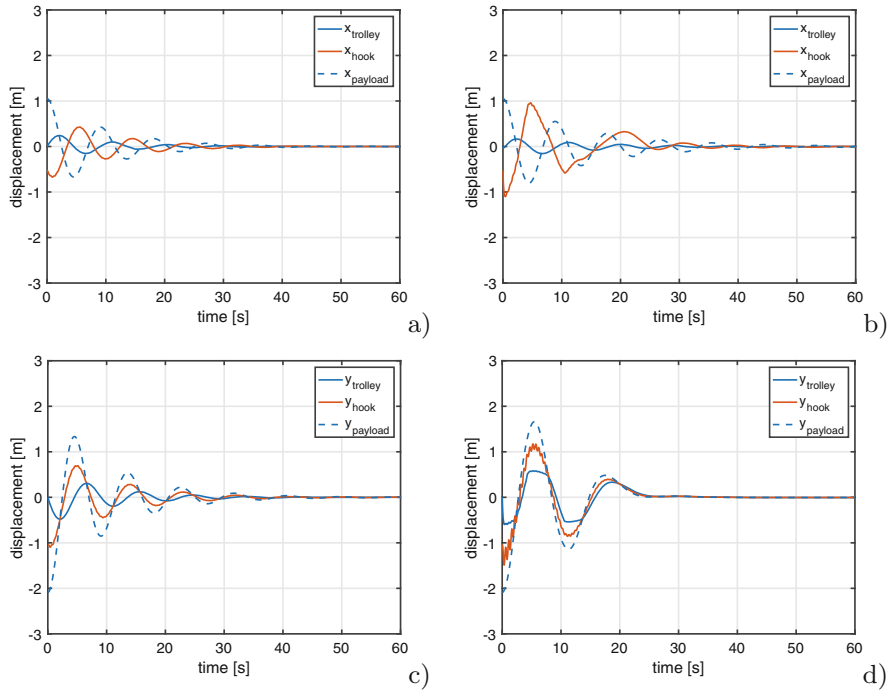
Fig. 3 (**a**) 3D Double-pendulum x displacements w/o control. (**b**) 3D Double-pendulum x displacements w/. (**c**) 3D Double-pendulum y displacements w/o control. (**d**) 3D Double-pendulum y displacements w/

system. With the increase in number of DOFs considered, it came to be the necessity of building and implementing a Simulink model that could better represent the increased level of complexity of the system. The second phase in this study has been characterized by such activity, including the verification and validation of the numerous output measures that came with it and their comparison with the outputs coming from analysis. After this crucial step, a PID control system was selected for the trolley actuation (displacement) in order to start the feasibility investigation that is object of this work. The control system was devised with the assumption that all the measurements concerning trolley, hook, and payload displacements are accessible in real-time by using appropriate sensors. In order to retrieve the PID values useful for a correct control of the payload oscillations, a manual method based on the system's characteristic step response was used: The results showed that, when considering a simplified 2D model, it is possible to suppress the payload's oscillations in a time-frame that ranges between 10 and 15 s with respect to the several minutes needed for the uncontrolled system, depending on the payload mass and the requested actuation force to be applied to the trolley. In conclusion, from this preliminary study it emerges that it is indeed possible to suppress or at least mitigate the payload's oscillations by means of a sliding trolley displaced through a PID controller.

References

1. R.L. Neitzel, N.S. Seixas, K.K. Ren, A review of crane safety in the construction industry. Appl. Occup. Environ. Hyg. **16**, 1106–1117 (2001)
2. F. Ju, Y. Choo, *Dynamics Characteristics of Tower Cranes* (World Scientific, Singapore, 2002), pp. 260–265
3. S. Kilicslan, T. Balkan, S. Ider, Tipping loads of mobile cranes with flexible booms. J. Sound Vib. **223**(4), 645–657 (1999)
4. L. Eriksson, V. Holtta, M. Misol, Modeling, simulation and control of a laboratory-scale trolley crane system, in *Conference: SIMS* (2006)
5. E.M. Abdel-Rahman, A.H. Nayfeh, Z.N. Masoud, Dynamics and control of cranes: a review. J. Vib. Control **9**, 863–908 (2003)
6. L. Cveticanin, Dynamic behavior of the lifting crane mechanism. Mech. Mach. Theory **30**(1), 141–151 (1995)
7. A. Maczynski, S. Wojciech, Dynamics of a mobile crane and optimisation of the slewing motion of its upper structure. Nonlin. Dyn. **32**(3), 259–290 (2003)
8. B. Jerman, J. Kramar, A study of the horizontal inertial forces acting on the suspended load of slewing cranes. Int. J. Mech. Sci. **50**(3), 490–500 (2008)
9. L. Solazzi, M. Cima, Structural dynamics of big gantry crane subjected to different trolley move laws. J. Phys. Conf. Ser. **1264**, 012046 (2019)
10. L. Solazzi, C. Remino, G. Incerti, Overhead crane subjected to impulse loading. J. Phys. Conf. Ser. **1264**, 012045 (2019)
11. Y. Tabata, K. Ichise, S. Ouchi, K.Z. Liu, *Anti-Sway Control System of a Rotational Crane Using a Nonlinear Controller* (IEEE, Piscataway, 2002)
12. R. Kondo, S. Shimahara, *Anti-Sway Control of a Rotary Crane via Switching Feedback Control*, vol. 1 (IEEE, Piscataway, 2004)

Improving Energy Efficiency of a Bipedal Walker with Optimized Nonlinear Elastic Coupling

Yinnan Luo, Ulrich J. Römer, Lena Zentner, and Alexander Fidlin

1 Introduction

Bipedal robots are capable of walking in many different environments and have therefore a wide range of applications. For example, humanoid robots are used for supporting rescue missions in many natural disaster scenarios that are demonstrated in the DARPA Robotics Challenge. Besides stabilizing the walking movements, improving the energy efficiency of locomotion is another major challenge in the development of these robots. An autonomous robot has to carry its energy source (e.g. a battery) which limits its operation time and range. Compared to humans, even the latest developed humanoid walking robots such as Boston Dynamics ATLAS and Honda Asimo show poorer energy efficiencies [1–3]. One of the main reasons of the less efficient walking lies on the control strategies, whose major task is to generate and stabilize the walking motion. There are many strategies focusing on different goals: e.g. the zero moment point (ZMP) principle enforces a nearly static stability of each robot body during the movement [4–6]. The controller focuses on giving the robot the capability to interact with the environments but may sacrifice the energy efficiency of the periodic movements like walking or running [7–9].

Other control strategies make use of the robot's natural dynamics and allow for higher efficiencies. For example, hybrid zero dynamics (HZD) based controllers stabilize periodic walking movements of underactuated robots. The dynamics are similar to human walking which utilizes the system's natural dynamics to achieve a high efficiency. The system's natural dynamics, which are preserved due to the

Y. Luo (✉) · U. J. Römer · A. Fidlin
Institute of Engineering Mechanics, Karlsruhe Institute of Technology (KIT), Karlsruhe, Germany
e-mail: yinnan.luo@kit.edu; ulrich.roemer@kit.edu; alexander.fidlin@kit.edu

L. Zentner
Compliant Systems Group, Ilmenau University of Technology, Ilmenau, Germany
e-mail: lena.zentner@tu-ilmenau.de

underactuation, are influenced by the mechanical design parameters. Coupling the robot's segments with linear elastic torsion springs significantly increases the energy efficiency [10–12]. A numerical optimization process simultaneously optimizes the walking gaits as well as the elasticity of the torsion spring to minimize the energy consumption of locomotion. This paper investigates the influence of the elastic coupling's nonlinearity on the efficiency of walking using cubic splines to describe and optimize the spring characteristics.

2 Model of the Robot and the Nonlinear Spring

Since the energy efficiency of locomotion mainly depends on the motion in the walking direction [13, 14], the focus of the presented research lies on a planer robot model whose lateral stabilizations are not considered. The robot model consists of five rigid segments, representing an upper body, two thighs, and two shanks, which are connected by ideal revolute joints. Four electric motors installed at each joint provide the driving torque for the motion. The robot's thighs are coupled by a nonlinear torsion spring, whose characteristics are described by cubic splines. The parameters of the cubic splines are considered as mechanical design parameters of the robot.

As depicted in Fig. 1, the robot has periodic walking gaits that can be mathematically described as a hybrid dynamic model including two alternating phases: a single support phase (SSP) and a double support phase (DSP). In both walking phases, point feet are modeled at the end of the shanks. Therefore, no torques can
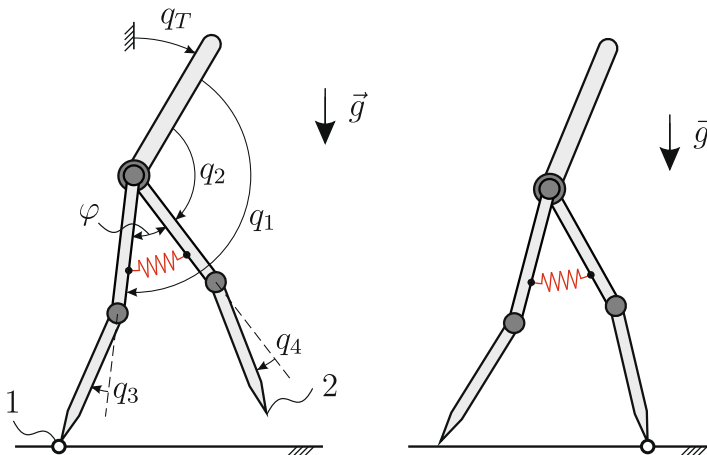
Fig. 1 Left: In the single support phase (SSP), leg 1 is in contact with the ground and leg 2 swings forward. Right: In the double support phase (DSP), both legs instantaneously touch the ground. The former swing leg impacts the ground and the former stance leg lifts off

be transmitted between the contacting leg and the ground. In the SSP, the stance leg is in contact with the ground and the other leg swings forward without scuffing. The contact of the stance foot is modeled as an ideal revolute joint without actuation, which gives the robot model one degree of underactuation. The continuous motion in the SSP is described via differential equations. In the DSP, a discrete mapping models an instantaneous impact of the swing leg with the ground; at the same time, the former stance leg lifts off. Physical conditions of walks without slipping, unilateral contacts, and static frictions at the contacting feet are ensured through further constraints.

A nonlinear controller generates and stabilizes the periodic walking gaits, namely a limit cycle of the hybrid dynamic system [15, 16]. The angles of the four actuated joints are synchronized to a set of time-invariant reference trajectories, described by Bézier polynomials with the parameters $\overline{\alpha}$. The remaining one degree of underactuation, namely the absolute rotation of the whole robot body about the contacting foot, is the controlled system's hybrid zero dynamics, if the error between the joint angles and the reference trajectories vanishes. Furthermore, the required driving torques $\overline{u} = [u_1, \ldots, u_4]^T$ in each electric motor are calculated through inverse dynamics, considering the elastic torques that are produced by the nonlinear torsion spring between the thighs.

In the mathematical description of the spring's nonlinearity, cubic splines show several advantages against high order polynomials. Cubic splines are smooth functions, combined by piecewise third-order polynomials, which pass through a set of control points (knots) [17]. Excluding the endpoints of the spline, whose second derivatives are set to zero, the first and the second derivatives of the knots are set equal to their neighborhoods. These boundary conditions uniquely define the complete spline, which is also known as a natural cubic spline.

It is assumed that the robot model is symmetric and its walking gaits are periodic. In this manner, the characteristic of the torsion spring between the thighs is supposed to be centrally symmetric. According to simulations, the maximal relative angle between the thighs of the robot without elastic couplings is 0.45 rad at the walking speed of 1.4 m/s. Thus, the active deflections of the nonlinear torsion spring are interpolated via splines in the interval of [-0.5, 0.5] rad; for larger deflections beyond this range a linear extrapolation is used. The spline is defined by a set of knots with the coordinates (φ_i, y_i) for $i = 0, \ldots, 10$: [$(-0.5, -m_5), (-0.4, -m_4), (-0.3, -m_3), (-0.2, -m_2), (-0.1, -m_1), (0, 0), (0.1, m_1), (0.2, m_2), (0.3, m_3), (0.4, m_4), (0.5, m_5)$]. The nonlinear characteristic $c(\varphi)$ of the nonlinear torsion spring has the property of central symmetry and is defined by the set of parameters $\overline{M}_{sp} = (m_1, m_2, \ldots, m_5)^T$.

3   Simultaneous Optimization

Solving the closed loop walking motion is formulated as an optimization problem. On the one hand, the robot's walking gaits are defined by the Bézier parameters $\overline{\alpha}$;

on the other hand, the nonlinear characteristics of the torsion spring are determined by the cubic spline with knots values $\overline{M}_{sp}$. While minimizing the energy consumption of walking, both parameter sets $\overline{\alpha}$ and $\overline{M}_{sp}$ are optimized simultaneously. The energy efficiency is optimized for different walking speeds from 0.2 m/s to 1.4 m/s. Sequential quadratic programming (SQP) is used as the optimization algorithms, which is mainly supported by the open source libraries "NLop.jl" and "OSQP.jl" in the programming language Julia. All derivatives required by the SQP algorithms are evaluated by automatic differentiation (AD) using the library "ForwardDiff.jl".

The objective of the numerical optimization is the energy consumption of locomotion. This is evaluated by a dimensionless quantity cost of transport (COT): the total supplied energy divided by the walking distance and the robot's weight. DC servo motors including gear transmissions convert the electrical energy into heat losses and mechanical energy. This work does not consider the heat losses, that are produced by the electric motor while it is maintaining static torques [11]. Furthermore, it is assumed that none of the generated electrical energy from the DC motors can be recovered during their braking operations (generator mode). So only positive mechanical power is considered in calculating

$$COT = \frac{\sum_{i=1}^{4} \int_{0}^{t^{-}} \max(u_i(t)\dot{q}_i(t), 0)\, \mathrm{d}t}{\ell_{\text{step}} mg} \tag{1}$$

with the step length ℓ_{step} and the total weight of the robot mg.

The physical conditions, which are introduced in Sect. 2, are considered as constraints in the numerical optimization [10–12]. Besides the walking speed v, which is enforced by an equality constraint $g(x)$, other conditions are guaranteed through a set of inequality constraints $\overline{h}(x)$. These are unilateral ground contacts; the condition of static frictions at the contact; no scuffing of the swing foot and no hyperextension of the knees.

The characteristics of the torsion spring are assumed to be constant once it has been manufactured and assembled. On the other hand, the walking gaits can be changed by reprogramming the controller according to the desired operating states. To identify the optimal elastic coupling for a range of walking speeds, the mean COT by considering different walking speeds $\overline{V} = [v_1 = 0.2, v_2 = 0.3, \ldots, v_n = 1.4]$ m/s with the same spring characteristic is minimized. An optimization problem is formulated for each desired walking speed v_i with the constraints $g_i(x)$ and $\overline{h}_i(x)$. These problems are combined into an extended optimization problem with $x = [\overline{M}_{sp}, \overline{\alpha}_1, \ldots, \overline{\alpha}_n]$. In this way, a nonlinear torsion spring is identified that increases the overall energy efficiency at different walking speeds.

4   Results and Discussion

The nonlinear elastic coupling shows significant improvements even compared to a linear characteristic, as depicted in Fig. 2. In comparison to the robot without any elastic couplings, the mean energy consumption is reduced by 78% for the investigated walking speeds. This is significantly better than using linear torsion springs, which results in a mean reduction of 62%. In Fig. 2, COT represents the total positive mechanical work that is supplied to the walking system from electric motors for compensating the energy losses to maintain the periodic walking gaits. From the aspect of the energy balance, less energy losses result in a high energy efficiency using nonlinear springs. Besides, the maximal power of the electric motors is also reduced through the elastic coupling: Without torsion springs the total maximal electrical power of four DC motors is 157.70 W at the speed 1.4 m/s; this is reduced to 71.63 W by using nonlinear springs. This makes the downsizing of the electric motors possible in an early development stage of any bipedal robots.

The optimal characteristic of the nonlinear torsion spring $c(\varphi)$ (the optimal parameter set $\overline{M}_{sp} = [-1.89, -6.89, -24.82, -183.35, -798.69]^T$ Nm) and the optimal stiffness ($k = 120.44$ Nm/rad) of the linear torsion spring are presented in Fig. 3. The deflections of the elastic couplings are equivalent to the relative angle φ between the thighs, which can be derived from the kinematical relationships. The simulations generally show an approximately linear relationship between the maximum relative angle of the thighs and the walking speed. At the walking speed of 1.4 m/s, the maximal deflection angle of the nonlinear torsion spring is 0.36 rad, which becomes 0.10 rad at 0.2 m/s; in the case of the optimal linear torsion spring, 0.33 rad is reached at 1.4 m/s and 0.05 at 0.2 m/s.

During one step, the optimal nonlinear torsion spring provides little elastic torques at smaller deflection angles, where the swing leg finds itself in the swing
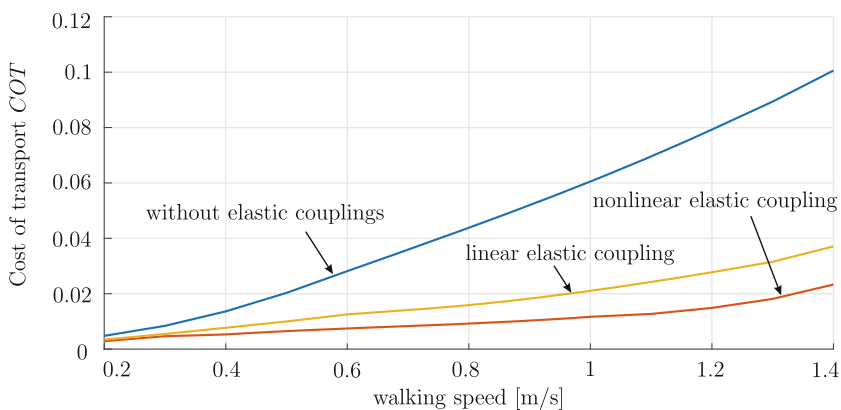
Fig. 2 The optimized cost of transport COT for different walking speeds from 0.2 m/s to 1.4 m/s with and without elastic couplings
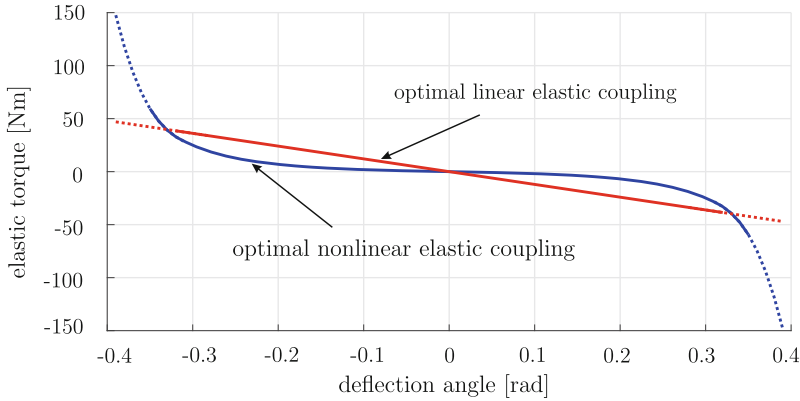
Fig. 3 The optimized linear and nonlinear torsion springs. The active operating ranges of the springs are plotted with solid lines

period. At the beginning as well as the end of the step, the deflection angle reaches its maximum in this step and the elastic torque increases dramatically. This implies that the nonlinear spring tends to be activated only at the beginning and the end of the step. According to the studies about the normal human walk in [18] and [19], the muscles of the swing leg are mainly activated just right at the beginning and end of one step. During the swing period in the middle of this step, the muscles are normally inactive. In this sense, the optimized nonlinear torsion spring acts in a way similar to the human muscles. The natural dynamics of the swing leg are less suppressed through a nonlinear torsion spring during the swing period. Also, this leads to a larger step length and therefore less steps required for the same walking distance: 0.20 m for using nonlinear torsion springs at the speed of 1.4 m/s; 0.18 m for linear torsion springs. The increased elastic torque decelerates the movement right before the swing leg touches the ground. In this process, kinetic energy is stored as potential energy into the torsion spring, which is reused for accelerating the robot at the beginning of the next step.

A closer study on the walking motion is employed based on a simplified compound pendulum model in Fig. 4: Both stance and swing leg are considered as rigid rods, whose mechanical parameters are derived from the thigh and shank of the formal complete robot model in Table 1. The stance leg is assumed to be firmly attached to the ground and connected to the swing leg by the torsion spring that is introduced in Fig. 3. The characteristic of the torsion spring therefore determines the free oscillations frequency of the simplified pendulum model. As the cubic spline $c(\varphi)$ is defined by piecewise cubic polynomials, the potential energy of the nonlinear spring is evaluated via integration:

$$V(\varphi) = -\int_0^\varphi c(\varphi)\, d\varphi. \tag{2}$$
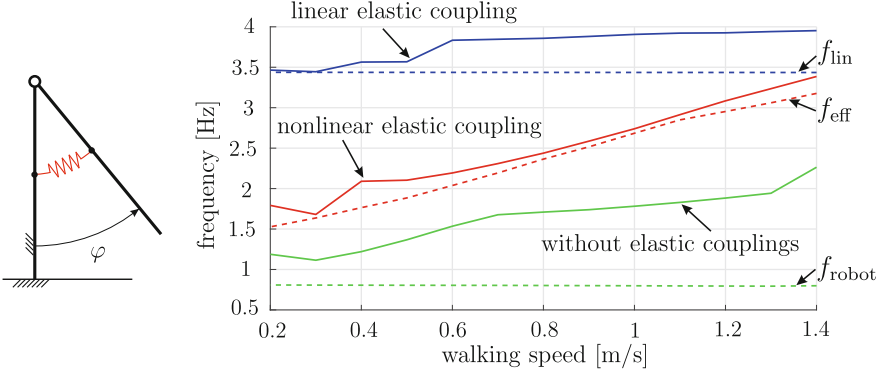
Fig. 4 Left: Simplified pendulum model for the analysis of the free oscillations frequency of the system consisting of two rigid bodies coupled by a nonlinear torsion spring. Right: Comparison of the derived free oscillations frequency of the pendulum model (dashed line) to the double step frequency of the complete robot (solid line)

Table 1 Model parameters

	Upper body	Thigh	Shank	Simplified model
Moment of inertia (in kgm^2)	0.15	0.02	0.01	0.27
Mass (in kg)	6.00	2.00	0.98	2.98
Length (in m)	0.55	0.30	0.30	0.60
Center of mass position (in m)	0.21	0.13	0.16	0.24

No energy dissipation is considered, the sum of the kinetic energy and the potential energy is constant

$$\frac{1}{2}J_o\dot{\varphi}^2 + mgr(1 - \cos(\varphi)) + V(\varphi) = mgr(1 - \cos(\varphi_{\text{MAX}})) + V(\varphi_{\text{MAX}}) \quad (3)$$

with the maximal deflection φ_{MAX} of the spring, where the velocity $\dot{\varphi}(\varphi_{\text{MAX}}) = 0$ and $J_o = J_{smp} + m_{smp}r_{smp}^2$, with the model parameters given in Table 1. The angular velocity $\dot{\varphi}$ is then given by

$$\dot{\varphi} = \sqrt{\frac{2(mgr(\cos(\varphi) - \cos(\varphi_{\text{MAX}})) + V(\varphi_{\text{MAX}}) - V(\varphi))}{J_o}}. \quad (4)$$

The swing period $\frac{T}{4}$, starting from the position $\varphi(0) = 0$ and ending at $\varphi(\frac{T}{4}) = \varphi_{\text{MAX}}$, of this nonlinear system can be determined via numerical integration

$$\frac{T}{4} = \int_0^{\varphi_{\text{MAX}}} \frac{1}{\dot{\varphi}} \, d\varphi = \sqrt{\frac{J_o}{2}} \int_0^{\varphi_{\text{MAX}}} \frac{1}{\sqrt{mgr(\cos(\varphi) - \cos(\varphi_{\text{MAX}})) + V(\varphi_{\text{MAX}}) - V(\varphi)}} \, d\varphi. \quad (5)$$
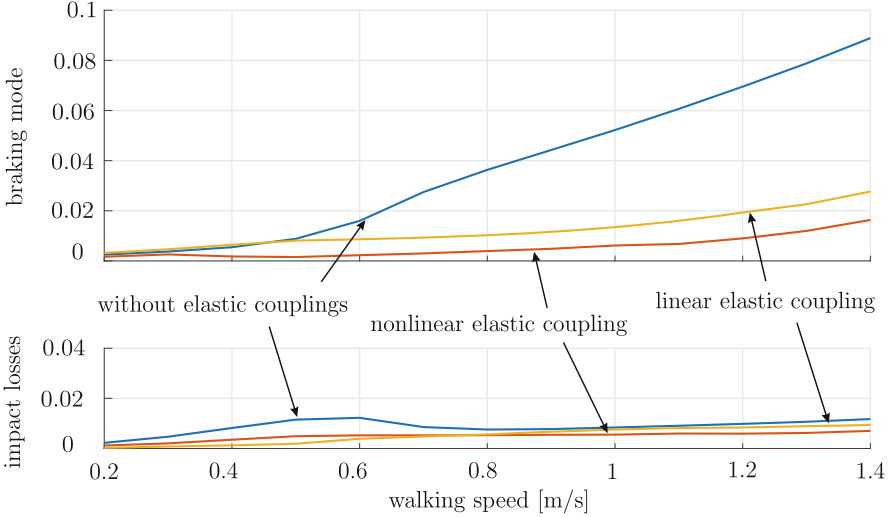
Fig. 5 Top: Removed energy due to the braking mode of the electric motors. Bottom: Energy losses due to the impact of the swing leg on the ground

The effective free oscillations frequency is given by $f_{\text{eff}} = \frac{1}{T}$. The effective frequencies for the linear torsion spring f_{lin} and without any elastic coupling f_{robot} also follow from equation (5) by changing the elastic potential energy $V(\varphi)$ accordingly.

As depicted in Fig. 4, the double step frequencies of the optimized gaits using nonlinear springs are very close to the effective frequency f_{eff} of the corresponding pendulum model at different walking speeds, i.e. at different amplitudes of the spring. In contrast, the pendulum model containing linear or no springs has an almost constant free oscillations frequency due to small oscillations amplitude. Studies in [20] and [21] approach a nearly linear relationship between the step frequency and the walking speed according to observations of the normal human walk. Thus, the major effect of the optimized nonlinear torsion spring is that the walking gaits and the characteristics of the spring are simultaneously optimized in such a way, that the robot always walks near the resonance of the system even at different walking speeds with a very high efficiency.

Figure 5 illustrates that both linear and nonlinear torsion springs reduce the energy losses while walking. These consist of two parts: the energy losses caused by the inelastic impact of the swing leg on the ground in the DSP, and the generated electrical energy from the electric motors in their braking operations, which is mainly turned into heat. Since the periodic walking gaits are limit cycles of the controlled system, any energy which is removed from the system due to braking or impact losses has to be supplied by the electric motors at some time. In all considered cases in Fig. 5, the impact losses are minimized by the optimization algorithm. After the numerical optimization, the robot always brakes its motion right

before the impact in order to minimize the impact losses. This braking torque must be provided through the electric motors in the case that the robot has no elastic couplings. As described in Fig. 3, the spring contributes to the braking operations at the right moments which greatly reduces the required energy input by the electric motors.

5 Conclusions

A method to improve the energy efficiency of a bipedal walking robot is investigated using nonlinear torsion springs characterized by cubic splines to couple its thighs. The underactuated robot is controlled by a nonlinear controller based on the hybrid zero dynamics approach. Its periodic walking gaits and the nonlinearity of the spring are determined simultaneously via numerical optimization, during the process of minimizing the energy consumption. Through the optimized nonlinear torsion spring, the mean energy consumption for walking speeds from 0.2 m/s to 1.4 m/s is reduced by 78%. This is significantly better than an optimal linear spring that reduces 62% of energy for the same conditions. The nonlinear spring tends to be activated only at the beginning and the end of one step, and remains silent during the swing period of the swing leg, which functions in a way similar to the human muscles. The free oscillations frequency of the swing leg is derived from a simplified pendulum model that is connected to the environment over the nonlinear spring. The free oscillations frequency of the pendulum model closely matches with the double step frequencies of the robot, that has optimum gaits generated by the optimization, i.e. the robot walks in resonance to achieve a very high energy efficiency at different walking speeds. According to simulations, not only the optimal step lengths but also step frequencies increase at larger walking speeds. This is in accordance with the studies about the relationship between the normal human step frequency and walking speeds.

   In future works, the nonlinear elastic couplings between the other segments of the robot will be investigated. The nonlinear characteristics are supposed to be realized in praxis through compliant smart mechanisms [22]. The simulation results will be validated on a prototype of the robot with the real nonlinear torsion springs.

References

1. S. Cotton, I.M.C. Olaru, M. Bellman, T.V.D. Ven, J. Godowski, J. Pratt, *2012 IEEE International Conference on Robotics and Automation* (2012)
2. A. Mazumdar, S.J. Spencer, C. Hobart, J. Salton, M. Quigley, T. Wu, S. Bertrand, J. Pratt, S.P. Buerger, IEEE/ASME Trans. Mech. **22**(2), 898–908 (2017)

3. N. Kashiri, A. Abate, S.J. Abram, A. Albu-Schaffer, P.J. Clary, M. Daley, S. Faraji, R. Furnemont, M. Garabini, H. Geyer, et al., Front. Robot. AI **5** (2018)
4. K. Hirai, M. Hirose, Y. Haikawa, T. Takenaka, *Proceedings of the 1998 IEEE International Conference on Robotics and Automation* (1998)
5. K. Nishiwaki, S. Kagami, Y. Kuniyoshi, M. Inaba, H. Inoue, *IEEE/RSJ International Conference on Intelligent Robots and System* (2002)
6. M. Vukobratovic, B. Borovac, I.J. Human. Robot. **1**(03), 157–173 (2004)
7. A.D. Kuo, IEEE Robot. Automat. Mag. **14**(2), 18–29 (2007)
8. S. Collins, A. Ruina, R. Tedrake, M. Wisse, Science **307**(5712), 1082–1085 (2005)
9. H. Shin, B.K. Kim, IEEE Trans. Indust. Elect. **62**(4), 2277–2286 (2015)
10. F. Bauer, U.J. Römer, A. Fidlin, W. Seemann, Nonlin. Dyn. **83**(3), 1275–1301 (2015)
11. F. Bauer, U.J. Römer, A. Fidlin, W. Seemann, Multibody Syst. Dyn. **38**(3), 227–262 (2016)
12. U.J. Römer, C. Kuhs, M.J. Krause, A. Fidlin, *2016 IEEE International Conference on Robotics and Automation (ICRA)* (2016)
13. L. Tesio, D. Lanzi, C. Detrembleur, Clin. Biomech. **13**(2), 77–82 (1998)
14. L. Tesio, V. Rota, Front, Neurol. **10** (2019)
15. E. Westervelt, J. Grizzle, D. Koditschek, IEEE Trans. Automat. Contr. **48**(1), 42–56 (2003)
16. C. Chevallereau, G. Abba, Y. Aoustin, F. Plestan, E.R. Westervelt, C. Canudas-De-Wit, J.W. Grizzle, IEEE Contr. Syst. Mag. **23**(5), 57–79 (2003)
17. E.W. Weisstein, MathWorld–A Wolfram Web Resource. https://mathworld.wolfram.com/CubicSpline.html (2020)
18. D. Winter, H. Yack, Electroencephalogr. Clin. Neurophysiol. **67**(5), 402–411 (1987)
19. S. Mochon, T.A. Mcmahon, J. Biomech. **13**(1), 49–57 (1980)
20. D.W. Grieve, R.J. Gear, Ergonomics **9**(5), 379–399 (1966)
21. J.E.A. Bertram, J. Experiment. Biol. **208**(6), 979–991 (2005)
22. M. Zirkel, Y. Luo, U.J. Römer, A. Fidlin, L. Zentner, Microactuators, Microsensors and Micromechanisms. MAMM 2020. Mechanisms Mach. Sci. **96** (2021)

Study on Control of Chaotic Systems

Srimanta Lal De and Shaikh Faruque Ali

1 Introduction

Chaos is one of the most interesting and widely studied subject in dynamical system after its initiation in 1963 [1] and with the advent of digital calculation. Soon it was evident that chaotic system exhibits much richer and intricate dynamics than a simple nonlinear system. After its initial inception a burst of research activities happened in the fields of mathematics, physics, biology, chemistry, economics, and various streams in engineering [2–4]. It has changed the way scientists and researchers have looked at the dynamical systems. Soon it was felt that for real engineering applications, one needs to tame chaotic system and drive them to periodic motions [5–7]. Therefore, 'Chaos control' came into existence [8, 9] with first application is unanimously considered to be the work of *Ott, Grebogi and Yorke* [8]. Following this a large volume of literature dedicated chaos control, to improve OGY technique and for possible applications [10–12]. Though many parallel works have been reported, OGY has been largely developed to control chaos [9]. This paper sheds light on the various aspects of this widely popular method through examples.

Section 2 briefs about OGY technique and its core philosophy. Section 3 describes some important extensions and generalized OGY algorithm. Implementation of these algorithms with well-known examples from dynamical systems and observation of some the key features are summarised in Sect. 4. Section 5 briefly discusses recent applications followed by a conclusion.

S. L. De · S. F. Ali (✉)
Applied Mechanics Department, IIT-M, Chennai, Tamil Nadu, India
e-mail: sfali@iitm.ac.in

263

2   OGY Technique: Basic Philosophy

A chaotic system shows the following properties which are essential for OGY implementation:

1. *System is highly sensitive to the initial condition:* Trajectories originated from almost same initial condition diverge exponentially with time.
2. *Existence of strange attractor:* Infinitely many *Unstable Periodic Orbits* (UPOs) are embedded inside chaotic attractor. UPOs are *saddle orbits* because they have both attracting and repulsing directions.
3. *Ergodicity:* Single trajectory originated from an arbitrary initial condition for a sufficiently long time represents the chaotic attractor containing all the possible evolutions.

With revolution in computational power, researchers were embolden to exploit these strange properties and to create control algorithm dealing with chaos. OGY algorithm exploits these properties of a chaotic system, to push trajectories into one of its UPOs by applying perturbation to a control parameter. Distinct UPOs represent distinct dynamical behaviour and seamless to switch from one dynamics to another using OGY for feasibility of application. One needs to understand though, which control parameter to use and how to identify one. The following section will detail such discussions.

3   OGY Technique: Implementation and Challenges

OGY control method was developed for discrete time systems or *maps* unlike real systems that are continuous in nature. Thus rather than working with a continuous time history of N-dimension, one takes transverse cuts through the chaotic attractor. This yields a set of cut points (say, $S \in \mathbb{R}^{N-1}$). Poincare section is the collection Σ where the set S lies, which can be represented as

$$x_{i+1} = P(x_i, p) \tag{1}$$

Here $x_i \in S$, $P(x_i) \in S$ is the *first return map*. Let us consider p as the system parameter (OGY control parameter) and it has a nominal value of $\bar{p}$.

For explaining the implementation of control on chaos, following four systems are considered:

1. Logistic Map:

$$x_{i+1} = r x_i (1 - x_i) \tag{2}$$

2. Henon Map:

$$x_{i+1} = y_i + 1 - ax_i^2; \quad y_{i+1} = bx_i \tag{3}$$

3. Ikeda Map:

$$x_{i+1} = a + u(x_i \cos(t_i) - y_i \sin(t_i)); \quad y_{i+1} = u(x_i \sin(t_i) + y_i \cos(t_i))$$

$$where\ t_i = c - \frac{d}{1 + x_i^2 + y_i^2}$$

$$\tag{4}$$

4. Duffing Oscillator:

$$\ddot{x} + \alpha \dot{x} + \beta x + \delta x^3 = \gamma \cos \omega t \tag{5}$$

Many often dynamical system responses are measured without a mathematical description. OGY can be extended to such systems as shown next. This has made OGY widespread in control of experimental systems [13, 14].

3.1 Delay-Coordinate Embedding

OGY technique is extended to time evolution data using Packard's algorithm [15] which can create phase space from time evolution data. The idea is extended to experimental systems [16]. As an example, phase space reconstruction of Eq. 5 is shown below.

Define t_i as discrete form for ith time step, t_F as time gap $(t_{i+1} - t_i)$ between two successive poincare sections. n is the number of time-delay coordinate used to reconstruct phase space with τ as time delay. Define a new state,

$$Z(t_i) = [x(t_i), x(t_i - \tau), \dots, x(t_i - (n-1)\tau)] \tag{6}$$

It is clear to see that when $(n-1)\tau > t_F$, the delay coordinate $Z(t_i)$ at time t_i contains information of the previous Poincare intersection. So the influence of parameter perturbation at time $(t_i - t_F) = t_{i-1}$ can be captured at time t_i. In fact, all parameter values $\{p_i, p_{i-1}, \dots, p_{i-r}\}$ have influence on the variable Z_i, where r is the smallest integer such that $(n-1)\tau < rt_F$. This observation leads to an alternative description of the system:

$$Z_{i+1} = P(Z_i, p_i, p_{i-1}, \dots, p_{i-r}) \tag{7}$$

Equation 7 is applied on data obtained from the system in Eq. 5, to generate Fig. 1. As shown, reconstructed phase captures the original phase.
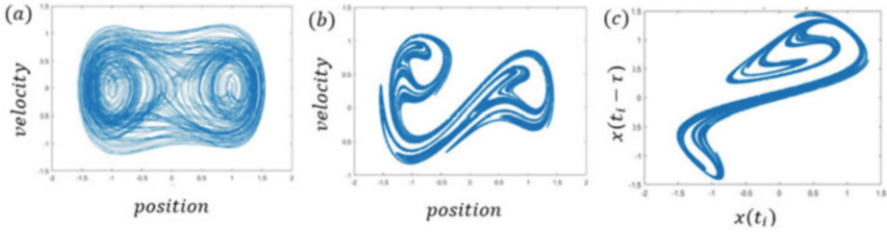
Fig. 1 Dynamics of Duffing oscillator showing (**a**) phase space, (**b**) poincare section, (**c**) poincare section using delay coordinate
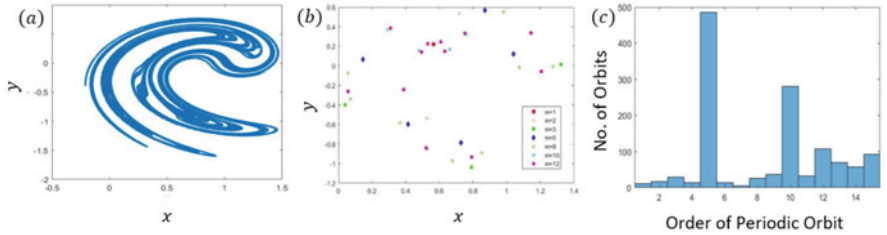
Fig. 2 Dynamics of Ikeda map showing (**a**) chaotic attractor at $u = 0.86$, (**b**) location of different m-periodic UPOs and (**c**) distribution of m-periodic orbits inside attractor

3.2 Determination of the UPOs Embedded Inside Chaotic Attractor

Once the phase space is determined, one needs to identify UPOs not required. Lathrop and Kostelich [17] reported a general procedure to identify UPOs (*periodic saddle orbit*) embedded inside a chaotic attractor reconstructed from experimental time-series data. The idea is when a random trajectory comes close to the UPO it moves with approximately same frequency of the orbit before diverging away.

Let x_i be a point in the reconstructed phase space and let $\varepsilon > 0$ be a sufficiently small scalar. Then following the subsequent map of x_i i.e., $x_{i+1}, x_{i+2}, ...$, find the smallest index k such that $\|x_k - x_i\| < \varepsilon$. x_i is a (m, ε) recurrent point where m is defined as $m = k - i$. In case of maps, m also represents the period of the located saddle orbit.

Figure 2 represents successful implementation of this identification algorithm in Ikeda Map by taking 10^5 sample points. The histogram depicts number of times trajectory comes near a particular UPO.

3.3   OGY as Pole-Placement Method

One of the simpler way to implement OGY is to augment it with pole placement. Romeiras et al. [18] first reported OGY as pole-placement method. For example, consider the system in Eq. 1, where p is considered as the control parameter that can be adjusted. A bound on p around its nominal value, $\bar{p}$ can be considered.

$$|p - \bar{p}| < \delta \tag{8}$$

Consider the fixed point $x_{i+1} = x_i = x_*$ of the system and linearizing it about the fixed point gives

$$x_{i+1} - x_*(\bar{p}) = A(x_i - x_*(\bar{p})) + B(p - \bar{p}) \tag{9}$$

Where A is a $n \times n$ Jacobian matrix and B is an n-dimensional column vector.

$$A = D_x P(x_*, \bar{p}); \quad B = D_p P(x_*, \bar{p}) \tag{10}$$

Define time dependence of control parameter p by giving it a linear dependence on state x_i of the system, as shown below

$$p - \bar{p} = -K^T(x_i - x_*) \tag{11}$$

Where $K^T_{1 \times n}$ is a vector of control gain obtained using pole placement [19], such that the fixed point x_* stabilize. Substituting Eq. 11 into Eq. 9,

$$x_{i+1} - x_*(\bar{p}) = (A - BK^T)(x_i - x_*(\bar{p})) \tag{12}$$

It is clear x_* will be a stable fixed point if the eigenvalues of $(A - BK^T)$ have modulus less than unity. K^T can be designed so that eigenvalues of matrix $(A - BK^T)$ have some specified value $\{\mu_1, \mu_2, \ldots, \mu_n\}$ (called *regular poles*).

Note that Eq. 9 is valid only in local region around fixed point $x_*(\bar{p})$. Equation 8 also gives a bound on the maximum allowable control.

$$|K^T(x_i - x_*(\bar{p}))| < \delta \tag{13}$$

This gives a slab of width $2\delta/|K^T|$ around the fixed point, and the control will be activated if x_i comes inside this slab otherwise $p = \bar{p}$. K^T is chosen such that n_s stable poles of A remain unchanged whereas the remaining $(n - n_s)$ unstable poles are fixed to 0. This choice of K^T orients the slab along with the stable manifold.

OGY algorithm has also been focused on reducing transient time, controlling fast dynamics, multiple parameters and higher periodic orbits [10, 20].

3.4   Determination of A and B on a Particular Orbit

Other than a few limited cases, typically it is not possible to determine A and B analytically from Eq. 10. Numerical techniques like linear curve fitting are generally applied to estimate the values of A and B in a least square sense [21].

3.4.1   Estimation of A

A is estimated from the time-series data of the nominal system (i.e. $p = \bar{p}$) with arbitrary initial conditions. As $\delta p = 0$, Eq. 9 becomes

$$\delta x_{i+1} = A \cdot \delta x_i \tag{14}$$

with $(\delta x_{i+1}, \delta x_i) = (x_{i+1} - x_*, x_i - x_*)$ and $\delta p = p - \bar{p}$. For a sufficiently small vicinity ξ (where $\xi > \varepsilon$), take a note of all such points for which both $\delta x_i < \xi$ and $\delta x_{i+1} < \xi$. For m periodic saddle orbits, defined as $x_{1*}, x_{2*}, \ldots, x_{m*}$, one has to check for the points for which $\|x_i - x_i*\| < \xi$ and its image $\|x_{i+1} - x_{i+1}*\| < \xi$.

$$E(\hat{A}) = \sum_{n=1}^{q} \left\| \delta x_{i+1} - \hat{A} \cdot \delta x_i \right\|_n^2 \tag{15}$$

A L_2 norm of the error (Eq. 15) is minimized for an optimal estimate $(\hat{A})$ of the matrix A. For a good estimate of A a large collection of points (q), is necessary.

3.4.2   Estimation of B

To estimate B with minimal computation, a strategy of alternate activation of control with each return of trajectory, is adopted. With an estimate $\hat{A}$, the linearized system is

$$\delta x_{i+1} = \hat{A} \cdot \delta x_i + B \delta p \tag{16}$$

Sampling the generated time series with alternate control on/off results in two separate series. δx_i results from the control turned off and δx_{i+1} from the other part. Collecting q such $(\delta x_{i+1}, \delta x_i)$ pairs, $\hat{B}$ is estimated using Eq. 17.

$$\hat{B} = \langle B \rangle = \left\langle \frac{1}{\delta p} (\delta x_{i+1} - \hat{A} \cdot \delta x_i) \right\rangle_{averaged\ over\ q\ samples} \tag{17}$$

In case of control using delay coordinate, parameters of Eq. 18 are estimated.

$$Z_{i+1} - Z_{i+1}^* = A_i(Z_i - Z_i^*) + B_i^1(p_i - \bar{p}) + \cdots + B_i^{r+1}(p_{i-r} - \bar{p}) \quad (18)$$

Where $B_i^j = D_{p_{i-(j-1)}}P(Z_i, p_i, p_{i-1}, \ldots, p_{i-r})$. For detailed discussion on estimation on B_j^i, refer to [16].

Once the A and B matrices are estimated, one can proceed with pole-placement technique to determine control requirement. In the next section, a few simulation results are shown.

4 Results and Discussion

This section implements OGY control on four dynamical systems (Eqs. 2–5) and reports the results and associated improvement over classical OGY [8].

Bifurcation diagram pictorially describes a system's transition from a stable equilibrium to a chaotic attractor with change in parameter value as in Fig. 3a. Methods described in Sect. 3 for identification of UPO and for design of controller have been applied on Ikeda map to restore its equilibrium from chaotic attractor by perturbing parameter at the correct instant as shown in Fig. 3b, c.

Logistic map (Eq. 2) has the most simplified form but has wide applications in population dynamics. OGY algorithm has been applied for two variation in maximum allowable perturbation of parameter, δ. Single realization of state evolution for two different control effort is shown in Fig. 4. Observation shows an increase in transition time before stabilization, with decrease in control effort.

Along with Ikeda and Logistic map, Henon map has been a popular choice in the literatures related to development of OGY algorithm [22, 23]. An extended version of the described method has been applied, to stabilize higher periodic orbit inside Henon attractor. A single realization, illustrated in Fig. 5 shows with increase in order of UPO, transition time decreases. Explanation of such observations comes from natural measures on chaotic attractor, which says average time spent by a random trajectory outside a control volume region of chaotic attractor, is inversely proportional to the volume of that region [21]. From Eq. 13 it can be inferred that
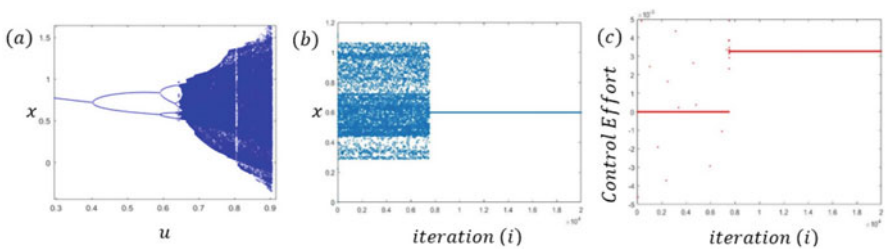
Fig. 3 Dynamics of Ikeda map showing (**a**) bifurcation with parameter u, (**b**) OGY control at fixed point at $u = 0.7$ and (**c**) control time history

a

b
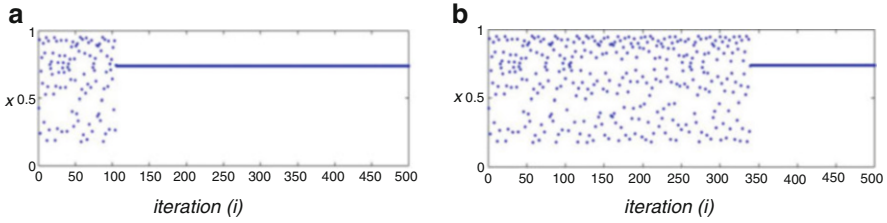
Fig. 4 OGY control of Logistic map at $r = 3.8$ with maximum parameter perturbation (**a**) $\delta r = 0.002r$, (**b**) $\delta r = 0.001r$
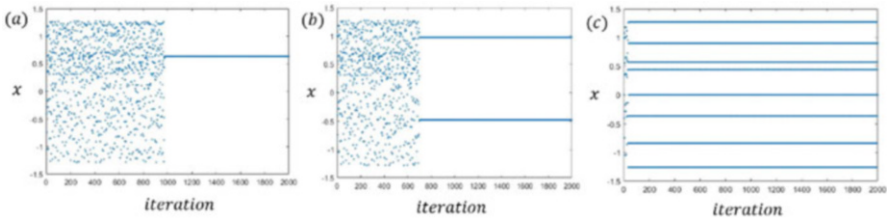
Fig. 5 OGY control of Henon Map at $a = 1.4$ and $b = 0.3$ showing (**a**) fixed point, (**b**) saddle orbit of period 2 and (**c**) saddle orbit of period 8

trajectory can only be stabilized inside $\delta/|K^T|$ region surrounding the UPO. In case of Logistic map, δ has been increased directly. In Henon map due to increase in orbit order, net control region is increased i.e. $\delta_{net} = \sum \delta_i > \delta_i$. So in both situations average transient time decreases. Our choice of realizations in these two systems represents this trend.

Duffing oscillator has been used widely in many literatures related to extension of OGY to continuous and non-autonomous systems [12, 16]. Such systems can be controlled by two methods, as described in Sect. 3. When state space model of a periodic non-autonomous system is available, it is recommended to create first return map by taking stroboscopic section as in Fig. 6a. In the absence of a model, delay-coordinate embedding method is used to create the first return map as in Fig. 6b. After identifying the UPO and acquiring data-set as discrete map, standard pole-placement method is applied to stabilize the orbits as in Fig. 6b–d.

5   Recent Trends in Application of OGY

This section briefs the relevance of OGY across fields. Gritli et al. [5] have studied characteristics of chaotic dynamics in biped robot walking on an inclined plane. Dynamics of simple and coupled mechanical impact oscillators have been studied under control of OGY algorithm [6, 24]. Biologists use discrete time models to study evolution and dynamics of biological systems. Some such biological system
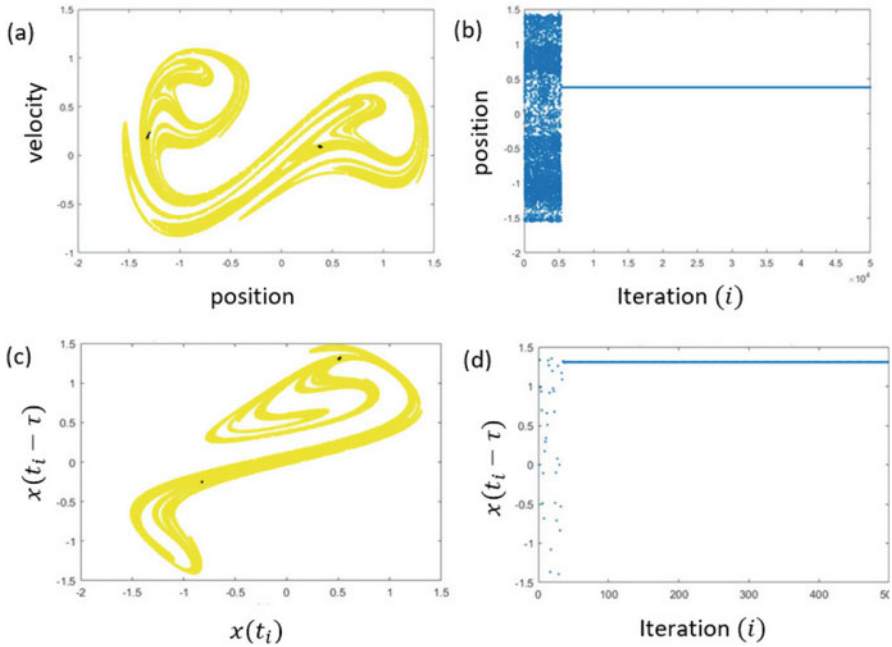
Fig. 6 Location of period-1 orbit in poincare section and OGY control of Duffing oscillator (**a**, **b**) based on known system dynamics, (**c**, **d**) based on phase space reconstruction using time-delay coordinate

models undergo bifurcation and become chaotic. Many such biological systems have found application of OGY algorithm in stabilizing their equilibrium viz. host–parasite models; prey–predator models; glycolysis model [3, 25, 26] and population dynamics [27]. Geiyer et al. [7] have found application of OGY in broadband energy harvesting using piezo-electric material. Kumar et al. have used OGY algorithm to enhance energy harvesting from nonlinear oscillator [28]. Salman et al. have studied and controlled theoretical model such as complex Riccati and logistic type map [4]. OGY based chaos control has tremendous potential for applications, we restricted to a very selected ones due to limitation in space.

6 Conclusions

The goal of writing this paper is to shed some light on the challenges in implementation of OGY algorithm for chaos control. It is a very short summary on the development of three decades of OGY, and a proper justification can be made with a longer and more thorough review of the subject. In discussion, OGY control is formulated as a variant of pole-placement method, which is much simpler

to understand and implement. This considers linearization of the system about UPOs. Application of OGY algorithm as a delayed feedback controller is also shown. Though researchers have investigated robustness and optimality of the OGY controller in the presence of noise, those remain outside the scope of this article [11]. The implementation of OGY on four example systems has been demonstrated.

Increasing the effective volume (in phase-space) around UPO inside which successful stabilization of a trajectory is possible, has remained the central idea behind further sophistication of OGY algorithm [10, 20]. Achieving it reduces average transient time, control gain and increases probability of successful control simultaneously. This article gives a short summary on early development of OGY algorithm and its recent applications.

References

1. E. N. Lorenz, Deterministic nonperiodic flow. J. Atmos. Sci. **20**, 130–141 (1963)
2. S. Strogatz, *Nonlinear Dynamics and Chaos* (Addison-Wesley, Reading, 1994)
3. Q. Din, Neimark-Sacker bifurcation and chaos control in Hassell-Varley model. J. Differ. Equations Appl. **23**, 741–762 (2017)
4. S.M. Salman, A.M. Yousef, A.A. Elsadany, Stability, bifurcation analysis and chaos control of a discrete predator-prey system with square root functional response. Chaos Solitons Fractals **93**, 20–31 (2016)
5. H. Gritli, S. Belghith, N. Khraief, OGY-based control of chaos in semi-passive dynamic walking of a torso-driven biped robot. Nonlinear Dyn. **79**, 1363–1384 (2014)
6. H. Gritli, S. Belghith, Mech. Mach. Theory **124**, 1–41 (2018)
7. D. Geiyer, J.L. Kauffman, Chaotification as a means of broadband energy harvesting with piezoelectric materials. J. Vib. Acoust. Trans. ASME **137**, 1–8 (2015)
8. E. Ott, C. Grebogi, J.A. Yorke, Controlling chaos. Phys. Rev. Lett. **64**, 1196–1199 (1990)
9. S. Boccaletti, C. Grebogi, Y. C. Lai, H. Mancini, D. Maza, The control of chaos: Theory and applications. Phys. Rep. **329**, 103–197 (2000)
10. T. Shinbrot, E. Ott, C. Grebogi, J.A. Yorke, Using chaos to direct trajectories to targets. Phys. Rev. Lett. **65**, 3215–3218 (1990)
11. H. Lenz, D. Obradovic, Stabilizing higher periodic orbits of chaotic discrete-time maps. Int. J. Bifurcat. Chaos **9**, 251–266 (1999)
12. H. Gritli, Chaos Solitons Fractals **127**, 127–145 (2019)
13. W.L. Ditto, S.N. Rauseo, M.L. Spano, Experimental control of chaos. Phys. Rev. Lett. **65**, 3211–3214 (1990)
14. V. Petrov, V. Gaspar, J. Masere et al., Controlling chaos in the Belousov–Zhabotinsky reaction. Nature **361**, 240–243 (1993)
15. N.H. Packard, J.P. Crutchfield, J.D. Farmer, R.S. Shaw, Geomerty from a time series. Phys. Rev. Lett. **45**, 725–728 (1979)
16. G. Nitsche, U. Dressler, Controlling chaotic dynamical systems using time delay coordinates. Phys. D **58**, 153–164 (1992)
17. D.P. Lathrop, E.J. Kostelich, Characterization of an experimental strange attractor by periodic orbits. Phys. Rev. A **40**, 4028–4031 (1989)
18. F.J. Romeiras, C. Grebogi, E. Ott, W.P. Dayawansa, Controlling chaotic dynamical systems. Phys. D Nonlinear Phenom. **58**, 165–192 (1992)
19. J. Ackermann, On the synthesis of linear control systems with specified characteristics. Automatica **13**, 89–94 (1977)

20. J.E.S. Socolar, D.W. Sukow, D.J. Gauthier, Stabilizing unstable periodic orbits in fast dynamical systems. Phys. Rev. E **50**, 3245–3248 (1994)
21. J.P. Eckmann, D. Ruelle, Ergodic theory of chaos and strange attractors. Rev. Mod. Phys. **57**, 617–656 (1985)
22. H. Lenz, D. Obradovic, Stabilizing higher periodic orbits of chaotic discrete-time maps. Int. J. Bifurcat. Chaos **9**, 251–266 (1999)
23. H. Lenz, D. Obradovic, Effectivity of the stabilization of higher periodic orbits of chaotic maps. Int. Conf. Control Oscil. Chaos Proc. **1**, 152–155 (1997)
24. G. Feng, P. Jian-Xun, M. Yong, J. Zhen-Dong, UPB Sci. Bull. Ser. D Mech. Eng. **80**, 29–42 (2018)
25. Q. Din, Bifurcation analysis and chaos control in discrete-time glycolysis models. J. Math. Chem. **56**, 904–931 (2018)
26. A.M.A. El-Sayed, S.M. Salman, Dynamic behavior and chaos control in a complex Riccati-type map. Quaest. Math. **39**, 665–681 (2016)
27. G. Feng, Controlling chaos of the Ricker population model by OGY method. Am. J. Biochem. Biotechnol. **16**, 424–431 (2020)
28. A. Kumar, S.F. Ali, A. Arockiarajan, Enhanced energy harvesting from nonlinear oscillators via chaos control. IFAC-PapersOnLine **49**, 35–40 (2016)
29. K. Pyragas, Continuous control of chaos by self-controlling feedback. Phys. Lett. A **170**, 421–428 (1992)
30. K. Pyragas, Control of chaos via extended delay feedback. Phys. Lett. A **206**, 323–330 (1995)

Stabilizing-Delay-Based Impulsive Control for Cluster Synchronization of Nonlinearly Coupled Lur'e Networks

Deli Xuan, Ze Tang, and Ju H. Park

1 Introduction

In recent years, the exploration on complex networks has received widespread attention due to its important applications in artificial and natural networks like biological networks and financial networks [1, 2]. As a typical collective behavior, synchronization has received extensive attention from scholars in various fields [3, 4]. For instance, Yu et al. in [5] studied the local synchronization for a class of complex networks. The global synchronization for the complex network with coupling delay was discussed by Li et al. in [6]. In addition, the impulsive synchronization [7] and cluster synchronization [8] were deeply investigated.

However, in most of existing results that discussed the cluster synchronization issues, such as [9, 10], they only focused on the cluster synchronization of the identically and linearly coupled complex networks. In particular, Ma et al. in [9] considered the cluster synchronization of complex networks with general linear couplings. Furthermore, as a kind of discontinuous control protocols, impulsive control [11, 12], which will be activated only at impulse time instants, efficiently reduces the control cost. Tang et al. in [11] investigated the impulsive synchronization for derivative coupled neural networks with the delay in impulsive controller. By the comparison principle, [12] discussed the synchronization for stochastic reaction–diffusion dynamical networks with impulsive delay.

To the best of authors' knowledge, the global and exponential cluster synchronization of nonlinearly coupled complex dynamical networks with nonidentical

D. Xuan · Z. Tang (✉)
School of Internet of Things Engineering, Jiangnan University, Wuxi, P.R. China
e-mail: tangze0124@gmail.com

J. H. Park
Department of Electrical Engineering, Yeungnam University, Kyonsan, Republic of Korea
e-mail: jessie@ynu.ac.kr

Lur'e systems and asymmetrical matrices, until now, receives little attention. It motivates us to investigate this work. In this chapter, the distinguished features different from other papers can be summarized as: (1) The global and exponential cluster synchronization of nonlinearly and nonidentically coupled Lur'e dynamical networks with an asymmetrical matrix is explored under the impulsive controller with stabilizing delay. (2) By considering the cluster-tree topology structures of the Lur'e networks, a kind of pinning feedback controllers is elaborately designed to be imposed on the Lur'e systems in the cluster that exist directed connections with the Lur'e systems in other clusters, which is more practical and closer to real situations than some previous works like [13]. (3) By introducing the average impulsive interval [14], sufficient conditions for the exponential cluster synchronization of nonlinearly coupled Lur'e dynamical networks are obtained in view of the Lyapunov stability theorem, mathematical induction method, and the projection method.

2 Model Description and Preliminaries

Before starting the theme, some assumptions for the nonlinearly coupled Lur'e dynamical networks with cluster-tree topology structure in the following are defined. Consider the coupled Lur'e networks with a total of m Lur'e systems and r clusters with $m > r \geq 2$. If the i-th Lur'e system belongs to the j-th cluster, it will be denoted as $\mu_i = j$. Let U_j be the set of all Lur'e systems in the j-th cluster and the set $\tilde{U}_j$ be all Lur'e systems in the j-th cluster that are directly connected to the Lur'e systems in other clusters. Therefore, we have: $(i).U_i \cap U_j = \emptyset$, for $i \neq j$ and $i, j = 1, 2, \cdots, r$; $(ii). \cup_{i=1}^{r} U_i = \{1, 2, \cdots, m\}$.

Consider the nonlinearly and nonidentically coupled Lur'e dynamical networks with r clusters and asymmetrical couplings

$$\dot{z}_i(t) = J_{\mu_i} z_i(t) + H_{\mu_i} \tilde{f}_{\mu_i}^1 (A z_i(t)) + K_{\mu_i} \tilde{f}_{\mu_i}^2 (Q z_i(t - \tau_1(t)))$$
$$+ c \sum_{j=1}^{m} b_{ij} \Gamma G(z_j(t)) + u_i(t), \tag{1}$$

where $z_i(t) = [z_i^1(t), z_i^2(t), \cdots, z_i^n(t)]^T \in \mathbb{R}^n, i = 1, 2, \cdots, m$, is the state variable of the i-th Lur'e system. $J_{\mu_i} \in \mathbb{R}^{n \times n}, H_{\mu_i} \in \mathbb{R}^{n \times l}, K_{\mu_i} \in \mathbb{R}^{n \times l}, A \in \mathbb{R}^{l \times n}, Q \in \mathbb{R}^{l \times n}$ are the constant matrices. The constant $c > 0$ is the coupling strength, and $\Gamma = \text{diag}\{\gamma_1, \gamma_2, \cdots, \gamma_n\} \in \mathbb{R}^{n \times n}$ is the inner connection matrix with $\gamma_i > 0$. In this chapter, it assumes that $\Gamma = I_n$ for simplicity; $\tilde{f}_{\mu_i}^\varsigma(\cdot) : \mathbb{R}^l \to \mathbb{R}^l$ are memoryless nonlinear vector-valued function that is continuously differentiable on $\mathbb{R}$ for $\varsigma = 2$. $\tau_1(t)$ is the system time-varying delay and satisfies $0 \leq \tau_1(t) \leq \hat{\tau}$. Matrix $B = (b_{ij})_{m \times m}$ represents the topology of a directed graph and is considered to be asymmetric and irreducible in this chapter. In addition, $b_{ij} > 0$ if and only if there is a connection from the j-th Lur'e system to the i-th Lur'e system for

$i \neq j$, and $b_{ij} = 0$, otherwise. Moreover, B satisfies the diffusive condition $\sum_{j=1}^{m} b_{ij} = 0$, i.e., $b_{ii} = -\sum_{j \neq i, j=1}^{m} b_{ij}$. $u_i(t)$ is the controller, which will be discussed later. $G(\cdot) : \mathbb{R}^n \to \mathbb{R}^n$ is the nonlinear coupling function with the form $G(z_i(t)) = [g_1(z_i^1(t)), g_2(z_i^2(t)), \cdots, g_n(z_i^n(t))]$, and it is assumed that $g_k(\cdot) \in NCF(\alpha, \nu)$ for $k = 1, 2, \cdots, n$ with positive constants α and ν [15]. Denote matrices $A = [a_1^T, a_2^T, \cdots, a_l^T]^T$ and $Q = [q_1^T, q_2^T, \cdots, q_l^T]^T$ with $a_j, q_j \in \mathbb{R}^{1 \times n}$ for $j = 1, 2, \cdots, l$. Then $Az_i(t) = [a_1 z_i(t), a_2 z_i(t), \cdots, a_l z_i(t)]^T$, $\tilde{f}_{\mu_i}^1(Az_i(t)) = [\tilde{f}_{\mu_i}^{11}(a_1 z_i(t)), \tilde{f}_{\mu_i}^{12}(a_2 z_i(t)), \cdots, \tilde{f}_{\mu_i}^{1l}(a_l z_i(t))]^T$ and $Qz_i(t - \tau_1(t)) = [q_1 z_i(t - \tau_1(t)), q_2 z_i(t - \tau_1(t)), \ldots, q_l z_i(t - \tau_1(t))]^T$, $\tilde{f}_{\mu_i}^2(Qz_i(t - \tau_1(t))) = [\tilde{f}_{\mu_i}^{21}(q_1 z_i(t - \tau_1(t))), \tilde{f}_{\mu_i}^{22}(q_2 z_i(t - \tau_1(t))), \cdots, \tilde{f}_{\mu_i}^{2l}(q_l z_i(t - \tau_1(t)))]^T$.

Let $s_{\mu_i}(t) = [s_{\mu_i}^1(t), s_{\mu_i}^2(t), \cdots, s_{\mu_i}^n(t)]^T \in \mathbb{R}^n, i = 1, 2, \cdots, r$ be the synchronization target in the i-th cluster satisfying

$$\dot{s}_{\mu_i}(t) = J_{\mu_i} s_{\mu_i}(t) + H_{\mu_i} \tilde{f}_{\mu_i}^1(As_{\mu_i}(t)) + K_{\mu_i} \tilde{f}_{\mu_i}^2(Qs_{\mu_i}(t - \tau_1(t))), \qquad (2)$$

where $\lim_{t \to +\infty} \|s_{\mu_i} - s_{\mu_j}\| \neq 0$. The delayed impulsive pinning controller is

$$u_i(t) = u_{0,i}(t) + u_{1,i}(t), \qquad i = 1, 2, \cdots, m, \qquad (3)$$

where the delayed impulsive control part is designed as

$$u_{0,i}(t) = \sum_{k=1}^{\infty} (\eta \delta z_i(t) + \rho \delta z_i(t - \tau_2(t))) \sigma(t - t_k), \qquad (4)$$

and the pinning feedback control part $u_{1,i}(t)$ is

$$u_{1,i}(t) = \begin{cases} -c\epsilon_i(G(z_i(t)) - G(s_{\mu_i}(t))) - c\sum_{j=1}^{m} b_{ij} G(s_{\mu_j}(t)), i \in \tilde{U}_{\mu_i}, \\ 0, \quad i \in U_{\mu_i} \setminus \tilde{U}_{\mu_i}, \end{cases} \qquad (5)$$

$\epsilon_i \geq 0$ is the feedback control gain, η and ρ represent impulsive effects and satisfy $0 < \eta, \rho < 1$. $\sigma(\cdot)$ is the Dirac function, and the time series $\xi = \{t_1, t_2, \cdots\}$ is a sequence of strictly increasing impulsive instants, which satisfy $\lim_{k \to \infty} t_k = +\infty$ for $k \in \mathcal{N}^+$. Let the control strength matrix be $D = \text{diag}\{\epsilon_1, \epsilon_2, \cdots, \epsilon_n\}$.

Define error vector $\delta z_i(t) = z_i(t) - s_{\mu_i}(t)$, $\delta z_i(t) = [\delta z_i^1(t), \delta z_i^2(t), \cdots, \delta z_i^n(t)]^T \in \mathbb{R}^n$ for $i = 1, 2, \cdots, n$. Therefore, the controlled error Lur'e network is

$$\begin{cases} \dot{\delta z}_i(t) = J_{\mu_i} \delta z_i(t) + H_{\mu_i} f_{\mu_i}^1(A\delta z_i(t)) + K_{\mu_i} f_{\mu_i}^2(Q\delta z_i(t - \tau_1(t))) \\ \quad + c\sum_{j=1}^{m} b_{ij}(G(z_j(t)) - G(s_{\mu_j}(t))) - c\epsilon_i(G(z_i(t)) - G(s_{\mu_i}(t))), \quad t \neq t_k, \\ \delta z_i(t_k^+) = (\eta + 1)\delta z_i(t_k^-) + \rho \delta z_i(t - \tau_2(t_k^-)), \quad t = t_k, \end{cases} \qquad (6)$$

where $0 \leq \tau_2(t) \leq \tau$, $f_{\mu_i}(A\delta z_i(t)) = \tilde{f}_{\mu_i}(Az_i(t)) - \tilde{f}_{\mu_i}(As_{\mu_i}(t))$ and $f_{\mu_i}^2(Q\delta z_i(t - \tau_1(t))) = \tilde{f}_{\mu_i}^2(Qz_i(t - \tau_1(t))) - \tilde{f}_{\mu_i}^2(Qs_{\mu_i}(t - \tau_1(t)))$. Throughout this chapter, $\delta z_i(t)$ is presumed to be right-hand continuous at $t = t_k$, $k \in \mathcal{N}^+$, and $\delta z_i(t_k) = \delta z_i(t_k^+) = \lim_{t \to t_k^+} \delta z_i(t)$, $\delta z_i(t_k^-) = \lim_{t \to t_k^-} \delta z_i(t)$. Then the solutions of the controlled error Lur'e network (6) are piecewise right-hand continuous functions with discontinuities at $t = t_k$ for $k \in \mathcal{N}^+$.

Definition 1 ([16]) The nonlinearly coupled Lur'e network (1) is globally and exponentially synchronized to the target Lur'e system (2), if and only if for any initial state $z_i(t_0) \in \mathbb{R}^n$, there exist constants $M_0, \lambda > 0$ and $t > t_0$ satisfying

$$\|z_i(t) - s(t)\| \leq M_0 \sup_{t_0 \in [t - \hat{\tau}, t]} \|z_i(t_0) - s(t_0)\| e^{-\lambda(t - t_0)}.$$

Lemma 1 ([17]) *Suppose that there exists a positive function $V(t)$ that satisfies the following impulsive differential inequalities:*

$$\begin{cases} D^+ V(t) \leq -\iota V(t) + \omega \sup_{\varrho \in [t - \hat{\tau}, t]} \{V(\varrho)\}, \\ V(t) = \psi(t), \qquad t \in [t_0 - \hat{\tau}, t_0] \end{cases}$$

for $\iota > \omega \geq 0$; then one may derive that $V(t) \leq \bar{V}(t_0) e^{-\lambda(t - t_0)}$, $t \geq t_0$, where $\psi(t)$ is a piecewise continuous function and $\bar{V}(t_0) = \sup_{\varrho \in [t_0 - \hat{\tau}, t_0]} \{V(\varrho)\}$, $\lambda > 0$ is the unique feasible solution to the equation $\lambda - \iota + \omega e^{\lambda \hat{\tau}} = 0$.

Assumption 1 *The two nonlinear system functions $\tilde{f}_{\mu_i}^1(\cdot)$ and $\tilde{f}_{\mu_i}^2(\cdot)$ are deemed to satisfy the Lipschitz condition. That is, there exist two related positive constants p_{μ_i} and q_{μ_i}, for any $a, b \in \mathbb{R}^n$, which satisfy*

$$\|f_{\mu_i}^1(a) - f_{\mu_i}^1(b)\| \leq p_{\mu_i} \|a - b\|, \qquad \|f_{\mu_i}^2(a) - f_{\mu_i}^2(b)\| \leq q_{\mu_i} \|a - b\|.$$

3 Main Result

In this section, the global and exponential cluster synchronization of the nonlinearly and nonidentically coupled Lur'e networks (1) is discussed. Then, sufficient conditions will be acquired under the delayed impulsive pinning controllers (3).

Theorem 1 *Suppose that Assumption 1 holds and the average impulsive interval is no larger than N_a for the impulsive sequence $\zeta = \{t_1, t_2, \cdots\}$. If there exist positive parameters c, α, v, υ and the control strength matrix D, such that:*

(i) The matrix inequality $\quad W - c(\alpha - v)D + \upsilon I_m \leq 0$.
(ii) For positive constant μ, the inequality $\quad \{\kappa + \beta e^{\lambda \tau}, e^{\lambda \hat{\tau}}\} \leq \mu$ holds,
where $W = c\alpha B + \frac{c}{2\varepsilon} B B^T + cv^2 \varepsilon (1 - \frac{1}{m}) I_m$, $\kappa = (1 + \eta)(1 + \eta + \rho)$, $\beta = \rho(1 +$

$\eta + \rho$) and λ is the unique feasible solution to the equation $\lambda - \iota + \omega e^{\lambda \hat{\tau}} = 0$ with parameters $\iota = -\min_{1 \leq i \leq m}\{\lambda_{\max}(J_{\mu_i}^s + H_{\mu_i} H_{\mu_i}^T + p_{\mu_i}^2 A^T A + K_{\mu_i} K_{\mu_i}^T - 2\upsilon I_n)\}$ and $\omega = \max_{1 \leq i \leq m}\{\lambda_{\max}(q_{\mu_i}^2 Q^T Q)\}$ satisfy $\iota \geq \omega$. Then, the controlled error Lur'e networks (6) are globally and exponentially stable with the convergence rate $\frac{1}{2}(\lambda - \frac{\ln \mu}{N_a})$. That is, the global and exponential cluster synchronization between the nonlinearly and nonidentically coupled Lur'e networks (1) and leader Lur'e system (2) is ultimately obtained by means of the delayed impulsive pinning controllers (3).

Proof Construct the suitable Lyapunov function: $V(t) = \frac{1}{2}\delta z(t)^T \delta z(t)$, where $\delta z(t) = [\delta z_1(t), \delta z_2(t), \cdots, \delta z_n(t)]^T$. For easy analysis later, denote $\tilde{\delta z}^k(t) = [\delta z_1^k(t), \delta z_2^k(t), \cdots, \delta z_m^k(t)]^T$, $\tilde{g}_k(z^k(t)) = [g_k(z_1^k(t)), g_k(z_2^k(t)), \cdots, g_k(z_m^k(t))]^T$, $\tilde{g}_k(s^k(t)) = [g_k(s_{\mu_1}^k(t)), g_k(s_{\mu_2}^k(t)), \cdots, g_k(s_{\mu_m}^k(t))]^T$, $\tilde{y}_k(z^k(t)) = [y_k(z_1^k(t)), y_k(z_2^k(t)), \cdots, y_k(z_m^k(t))]^T$, $\tilde{y}_k(s^k(t)) = [y_k(s_{\mu_1}^k(t)), y_k(s_{\mu_2}^k(t)), \cdots, y_k(s_{\mu_m}^k(t))]^T$.

On the one hand, for the impulsive time instant $t = t_k, k \in \mathcal{N}^+$, we have the following results based on the controlled error Lur'e networks(6):

$$
\begin{aligned}
V(t_k^+) &= \frac{1}{2}\delta z(t_k^+)^T \delta z(t_k^+) \\
&= \frac{1}{2}((1+\eta)\delta z(t_k^-) + \rho \delta z(t_k^- - \tau_2(t_k^-)))^T ((1+\eta)\delta z(t_k^-) \\
&\quad + \rho \delta z(t_k^- - \tau_2(t_k^-))) \\
&\leq \frac{1}{2}(1+\eta)(1+\eta+\rho)\delta z(t_k^-)^T \delta z(t_k^-) \\
&\quad + \frac{1}{2}\rho(1+\eta+\rho)\delta z(t_k^- - \tau_2(t_k^-))^T \delta z(t_k^- - \tau_2(t_k^-)) \\
&= \kappa V(t_k^-) + \beta V(t_k^- - \tau_2(t_k^-)).
\end{aligned}
\tag{7}
$$

On the other hand, for $t \in [t_{k-1}, t_k)$ $k \in \mathcal{N}^+$, calculating $D^+ V(t)$ along the controlled error Lur'e networks (6) under controllers (5) derives

$$
\begin{aligned}
D^+ V(t) &= \sum_{i=1}^{m} \delta z_i(t)^T \dot{\delta z}_i(t) \\
&\leq \frac{1}{2}\sum_{i=1}^{m} \delta z_i(t)^T \left(2 J_{\mu_i} + H_{\mu_i} H_{\mu_i}^T + p_{\mu_i}^2 A^T A + K_{\mu_i} K_{\mu_i}^T\right) \delta z_i(t) \\
&\quad + \frac{1}{2}\sum_{i=1}^{m} \delta z_i(t - \tau_1(t))^T q_{\mu_i}^2 Q^T Q \delta z_i(t - \tau_1(t)))
\end{aligned}
$$

$$+ c \sum_{i=1}^{m} \sum_{j=1}^{m} b_{ij} \delta z_i(t)^T (G(z_j(t)) - G(s_{\mu_j}(t)))$$

$$- c \sum_{i=1}^{m} \epsilon_i \delta z_i(t)^T (G(z_i(t)) - G(s_{\mu_i}(t)))). \tag{8}$$

In addition, the nonlinear coupling function $g_k(\cdot) \in NCF(\alpha, \nu)$ gives

$$c \sum_{i=1}^{m} \sum_{j=1}^{m} \delta z_i^T(t) b_{ij} (G(z_j(t)) - G(s_{\mu_j}(t)))$$

$$= c\alpha \sum_{k=1}^{n} \tilde{\delta} z_k(t)^T B \tilde{\delta} z_k(t) + c \sum_{k=1}^{n} \tilde{\delta} z_k(t)^T B(\tilde{y}_k(z^k(t)) - \tilde{y}_k(s^k(t))). \tag{9}$$

Furthermore, as B is a zero-row-sum matrix, it implies that

$$c \sum_{k=1}^{n} \tilde{\delta} z_k(t)^T B(\tilde{y}_k(z^k(t)) - \tilde{y}_k(s^k(t)))$$

$$= \sum_{k=1}^{n} \frac{c}{2\varepsilon} \tilde{\delta} z_k(t)^T B B^T \tilde{\delta} z_k(t) + \sum_{k=1}^{n} \frac{c\varepsilon}{2} (\tilde{y}_k(z^k(t)) - \tilde{y}_k(s^k(t)))^T$$

$$\times M(\tilde{y}_k(z^k(t)) - \tilde{y}_k(s^k(t))) = \sum_{k=1}^{n} \frac{c}{2\varepsilon} \tilde{\delta} z_k(t)^T B B^T \tilde{\delta} z_k(t)$$

$$- \frac{c\varepsilon}{2} \sum_{k=1}^{n} \sum_{i>j} m_{ij} (\tilde{y}_k(z_i^k(t)) - \tilde{y}_k(s_{\mu_i}^k(t)) + \tilde{y}_k(z_j^k(t)) - \tilde{y}_k(s_{\mu_j}^k(t)))^2$$

$$\leq \sum_{k=1}^{n} \frac{c}{2\varepsilon} \tilde{\delta} z_k(t)^T B B^T \tilde{\delta} z_k(t) - c\varepsilon \sum_{k=1}^{n} \sum_{i>j} m_{ij} ((\tilde{y}_k(z_i^k(t)) - \tilde{y}_k(s_{\mu_i}^k(t)))^2$$

$$+ (\tilde{y}_k(z_j^k(t)) - \tilde{y}_k(s_{\mu_j}^k(t)))^2) = \sum_{k=1}^{n} \frac{c}{2\varepsilon} \tilde{\delta} z_k(t)^T B B^T \tilde{\delta} z_k(t)$$

$$- c\nu^2 \varepsilon \sum_{k=1}^{n} \sum_{i>j} m_{ij} (\tilde{\delta}_i^k(t)^2 + \tilde{\delta}_j^k(t)^2)$$

$$= c \sum_{k=1}^{n} \tilde{\delta} z_k(t)^T \left(\frac{1}{2\varepsilon} B B^T + \nu^2 \varepsilon \left(1 - \frac{1}{m} \right) I_m \right) \tilde{\delta} z_k(t). \tag{10}$$

Define the matrix $W = c\alpha B + \frac{c}{2\varepsilon}BB^T + cv^2\varepsilon(1-\frac{1}{m})I_m$. By jointly considering the inequalities (8), (9), and (10), we can derive the following conclusion:

$$
\begin{aligned}
D^+V(t) \leq & \frac{1}{2}\sum_{i=1}^{m}\delta z_i(t)^T(2J_{\mu_i} + H_{\mu_i}H_{\mu_i}^T + p_{\mu_i}^2 A^T A + K_{\mu_i}K_{\mu_i}^T - 2vI_n)\delta z_i(t) \\
& + \frac{1}{2}\sum_{i=1}^{m}\delta z_i(t-\tau_1(t))^T q_{\mu_i}^2 Q^T Q \delta z_i(t-\tau_1(t))) \\
& + \sum_{k=1}^{n}\tilde{\delta} z_k(t)^T(W - c(\alpha-v)D + vI_m)\tilde{\delta} z_k(t) \\
\leq & -\iota V(t) + \omega \sup_{\varrho\in[t-\hat{\tau},t]} V(\varrho).
\end{aligned}
\tag{11}
$$

Therefore, in accordance with Lemma 1, for $\bar{V}(t_{k-1}) = \sup_{\varrho\in[t_{k-1}-\hat{\tau},t_{k-1}]} V(\varrho)$ at the impulsive time interval $t \in [t_{k-1} - t_k)$, we have

$$
V(t) \leq \bar{V}(t_{k-1})e^{-\lambda(t-t_{k-1})}.
\tag{12}
$$

Considering the inequality (12), for the given positive parameters μ and $t > t_0 > 0$, we will illustrate the following inequality:

$$
V(t) \leq \mu^{k-1}\bar{V}(t_0)e^{-\lambda(t-t_0)}
\tag{13}
$$

holds by introducing the mathematical induction method.

For the situation that $t \in [t_0, t_1)$ with $k = 1$, these is a positive parameter μ satisfying

$$
V(t) \leq \bar{V}(t_0)e^{-\lambda(t-t_0)} = \mu^{k-1}\bar{V}(t_0)e^{-\lambda(t-t_0)}.
$$

Next, assume that the inequality (13) holds for $t \in [t_{\varrho-1}, t_\varrho)$ with $k = \varrho$. Then, we have the following result in the light of condition (ii) in Theorem 1:

$$
\begin{aligned}
V(t_\varrho) \leq & \kappa V(t_\varrho^-) + \beta V(t_k^- - \tau_2(t_\varrho^-)) \\
\leq & \kappa\mu^{\varrho-1}\bar{V}(t_0)e^{-\lambda(t_\varrho-t_0)} + \beta\mu^{\varrho-1}\bar{V}(t_0)e^{-\lambda(t_\varrho-\tau_2(t_\varrho)-t_0)} \\
\leq & (\kappa + \beta e^{\lambda\tau})\mu^{\varrho-1}\bar{V}(t_0)e^{-\lambda(t_\varrho-t_0)} \leq \mu^\varrho\bar{V}(t_0)e^{-\lambda(t_\varrho-t_0)}.
\end{aligned}
$$

Finally, we will prove the inequality (13) is correct for $k = \varrho + 1$, i.e., $t \in [t_\varrho, t_{\varrho+1})$. Based on the above analysis, it derives

$$
V(t) \leq \bar{V}(t_\varrho)e^{-\lambda(t-t_\varrho)} = \sup_{\varpi\in[t_\varrho-\hat{\tau},t_\varrho]} V(\varpi)e^{-\lambda(t-t_\varrho)}
$$

$$= \max\{ \sup_{\varpi \in [t_\varrho - \hat\tau, t_\varrho)} V(\varpi), V(t_\varrho)\}e^{-\lambda(t-t_\varrho)}$$

$$\leq \max\{e^{\lambda\hat\tau}, \mu\}\mu^{\varrho-1}\bar V(t_0)e^{-\lambda(t-t_0)} \leq \mu^\varrho \bar V(t_0)e^{-\lambda(t-t_0)}.$$

Until now, it has explained the correctness of the inequality (13) for any $t \in [t_{k-1}, t_k)$ $k \in \mathcal{N}^+$. Considering that μ is a positive parameter, in the following, by applying the concept of the average impulsive interval [14], we study the global and exponential cluster synchronization of the nonlinearly coupled Lur'e networks according to the selection of the positive parameter μ.

First, if $\mu \in (0, 1)$, then for $t \in [t_{k-1}, t_k)$ $k \in \mathcal{N}^+$, it follows that

$$V(t) \leq \mu^{k-1}\bar V(t_0)e^{-\lambda(t-t_0)} \leq \mu^{\frac{t-t_0}{N_a} - N_0}\bar V(t_0)e^{-\lambda(t-t_0)}$$

$$= \mu^{-N_0}\bar V(t_0)e^{-(\lambda - \frac{\ln\mu}{N_a})(t-t_0)}. \tag{14}$$

Second, if $\mu \in (1, +\infty)$, then for $t \in [t_{k-1}, t_k)$ $k \in \mathcal{N}^+$, it implies that

$$V(t) \leq \mu^{k-1}\bar V(t_0)e^{-\lambda(t-t_0)} \leq \mu^{\frac{t-t_0}{N_a} + N_0}\bar V(t_0)e^{-\lambda(t-t_0)}$$

$$= \mu^{N_0}\bar V(t_0)e^{-(\lambda - \frac{\ln\mu}{N_a})(t-t_0)}. \tag{15}$$

Specially, when $\mu = 1$, for $t \in [t_{k-1}, t_k)$, we have

$$V(t) \leq \mu^{k-1}\bar V(t_0)e^{-\lambda(t-t_0)} = \bar V(t_0)e^{-(\lambda - \frac{\ln\mu}{N_a})(t-t_0)}. \tag{16}$$

Through the analysis of the above three situations on the positive parameter μ, we have three results (14), (15), and (16), which regards to the ultimate synchronization state. Then, according to Definition 1, it is obvious that there exist two positive parameters λ and M_0 satisfying

$$\|\delta z_i(t)\| \leq M_0\bar V(t_0)e^{-\frac{1}{2}(\lambda - \frac{\ln\mu}{N_a})(t-t_0)}.$$

Namely, it shows that the controlled error Lur'e network (6) is globally and exponentially stable with the convergence rate $\frac{1}{2}(\lambda - \frac{\ln\mu}{N_a})$. Moreover, the exponential cluster synchronization between the nonlinearly and nonidentically coupled Lur'e networks (1) and the leader Lur'e system (2) is finally realized under the delayed impulsive pinning controllers (3). Until now, we have finished the proof of Theorem 1.

4 Numerical Simulations

Consider the Chua's circuit with diverse system parameters [18]

$$\dot{z}(t) = J_i z(t) + H_i f_i^1(A_i z(t)) + K_i f_i^2(Q_i z(t - \pi_i(t))),$$

$$z(t) = \begin{bmatrix} z^1(t) \\ z^2(t) \\ z^3(t) \end{bmatrix}, \quad H_1 = H_2 = \begin{bmatrix} 3.247 \\ 0 \\ 0 \end{bmatrix}, \quad K_1 = K_2 = \begin{bmatrix} 0 \\ 0 \\ -3.906 \end{bmatrix},$$

$$J_1 = \begin{bmatrix} -\frac{13}{6} & 10 & 0 \\ 1 & -1 & 1 \\ 0 & -19.53 & -0.201 \end{bmatrix}, \quad J_2 = \begin{bmatrix} -2.169 & 10 & 0 \\ 1 & -1 & 1 \\ 0 & -19.53 & -0.1636 \end{bmatrix},$$

where $A_i = Q_i = [1, 0, 0], f_i^1(A_i z(t)) = (|z^1(t) + 1| - |z^1(t) - 1|)$ and $f_i^2(Q_i z(t)) = \sin(0.5z^1(t - \pi_i(t)))$, where $\pi_1 = \frac{0.01e^t}{1+e^t}$ and $\pi_2 = \frac{0.2e^t}{1+e^t}$. For two different Chua's circuits, the phase graphs are plotted in Fig. 1a.

(a)   (b)

(c)   (d)
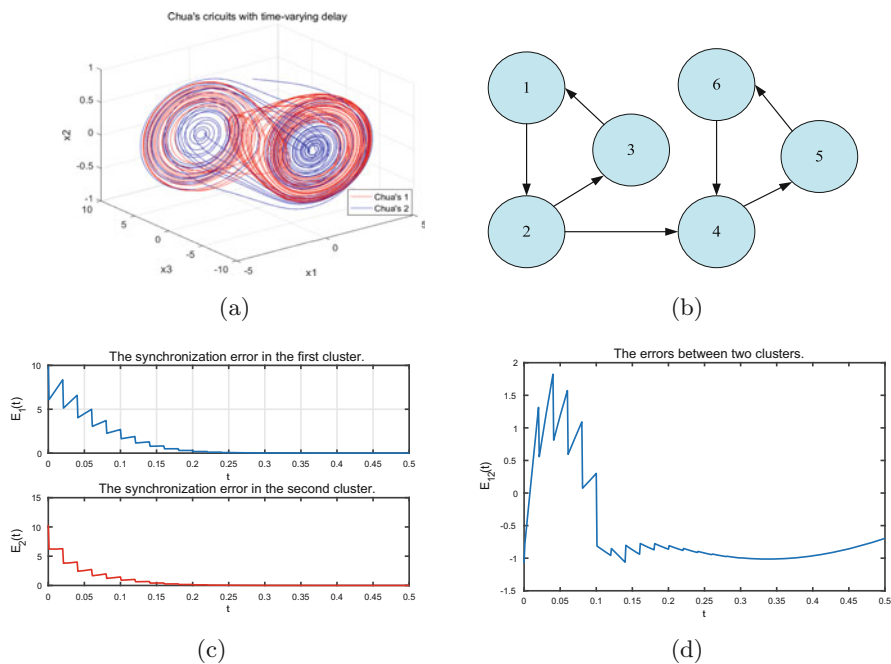
Fig. 1 (**a**) The phase graphs of two Chua's circuits with distinct parameters. (**b**) The structure of the Lur'e networks. (**c**) Synchronization error $E_j(t)(j = 1, 2)$ in each cluster. (**d**) The error curves between two clusters

In this numerical example, we orderly divided the complex network with six Lur'e systems into two distinct clusters $U_1 = \{1, 2, 3\}$ and $U_2 = \{4, 5, 6\}$ (see Fig. 1b). Therefore, the pinning feedback controllers (5) will be imposed on the second and fourth Lur'e systems because they are directly connected between two different clusters. Let $B = [-1, 1, 0, 0, 0, 0; 0, -2, 1, 1, 0, 0; 0, 1, -1, 0, 0, 0; 0, 0, 0, -1, 1, 0; 0, 0, 0, 0, -1, 1; 0, 0, 0, 0, 1, -1]$, $G(z_i(t)) = z_i(t) + 0.5 \sin(z_i(t))$, $c = 0.5$, and $D = diag\{0, 1.161, 0, 0.6157, 0, 0\}$. In addition, assume that the average impulsive interval N_a is less than 0.02.

The synchronization error evolution curves in two different clusters are plotted in Fig. 1c based on the definition $E_j(t) = \sqrt{\frac{1}{3} \sum_{i=1}^{3} (\|z_i(t) - s_{\mu_i}(t)\|)}$, $j = 1, 2$, which implies that cluster synchronization is realized. Define the state error between two clusters as $E_{12}(t) = \sqrt{1/3((z_1(t))^2 + (z_2(t))^2 + (z_3(t))^2)} - \sqrt{1/3((z_4(t))^2 + (z_5(t))^2 + (z_6(t))^2)}$. It is clearly shown from Fig. 1c–d that the synchronization error curves in the same cluster approach to zero at about 0.25 s, but the error $E_{12}(t)$ shows irregular oscillations between two different clusters.

5 Conclusions

This chapter has proposed an impulsive pinning control protocol with stabilizing delay for the cluster synchronization issue of a class of nonlinearly coupled Lur'e networks with an asymmetrical coupling matrix. By introducing the average impulsive interval and applying the Lyapunov stability theorem as well as mathematical induction method, sufficient conditions have been derived that ensure the realization of the global and exponential cluster synchronization for the Lur'e networks. Finally, a numerical example has been implemented to prove the correctness of the theoretical analyses and control schemes.

References

1. S.H. Strogatz, Exploring complex networks. Nature **410**(6825), 268–276 (2001)
2. W.L. He, F. Qing, J.D. Cao, Pinning-controlled synchronization of delayed neural networks with distributed-delay coupling via impulsive control. Neural Netw. **85**, 1–9 (2017)
3. Y.Q. Wang, J.Q. Lu, J.L. Ling, et al., Pinning synchronization of nonlinear coupled Lur'e networks under hybrid impulses. IEEE Trans. Circuit. Syst. II Exp. Briefs. **66**(3), 432–436 (2019)

4. T.P. Chen, X. Liu, W. Lu, Pinning complex networks by a single controller. IEEE Trans. Circuit. Syst. I Reg. Papers **54**(6), 1317–1326 (2007)
5. W.W. Yu, J.D. Cao, G.R. Chen, et al., Local synchronization of a complex network model. IEEE Trans. Syst. Man Cyber. B **39**(1), 230–241 (2009)
6. C.G. Li, G.R. Chen, Synchronization in general complex dynamical networks with coupling delays. Phys. A Stat. Mech. Its Appl. **343**, 263-278 (2004)
7. L.K. Gao, J. Xiao, X.X. Guo, et al., Adaptive variable impulsive synchronization of multi-agent systems. J. Elect. Eng. Tech. **15**(1), 259–268 (2020)
8. J.W. Feng, Z. Tang, Y. Zhao, et al., Cluster synchronisation of non-linearly coupled Lur'e networks with identical and non-identical nodes and an asymmetrical coupling matrix. IET Cont. Theory Appl. **7**(18), 2117–2127 (2013)
9. Z.J. Ma, Z.R. Liu, G. Zhang, A new method to realize cluster synchronization in connected chaotic networks. Chaos Interdiscip. J. Nonlin. Sci. **16**(2), 023103 (2006)
10. W. Wu, W.J. Zhou, T.P. Chen, Cluster synchronization of linearly coupled complex networks under pinning control. IEEE Trans. Circuit. Syst. I Reg. Papers **56**(4), 829–839 (2009)
11. Z. Tang, J.H. Park, Y. Wang, et al., Impulsive synchronization of derivative coupled neural networks with cluster-tree topology. IEEE Trans. Netw. Sci. Eng. **7**(3), 1788–1798 (2020)
12. H.B. Chen, P. Shi, C.C. Lim, Pinning impulsive synchronization for stochastic reaction-diffusion dynamical networks with delay. Neural Netw. **106**, 281–293 (2018)
13. W. Wu, W.J. Zhou, T.P. Chen, Cluster synchronization of linearly coupled complex networks under pinning control. IEEE Trans. Circuits Syst. I Reg. Papers **56**(4), 829–839 (2009)
14. J.Q. Lu, D.W.C. Ho, J.D. Cao, A unified synchronization criterion for impulsive dynamical networks. Automatica **46**(7), 1215–1221 (2010)
15. X. Liu, T.P. Chen, Synchronization analysis for nonlinearly-coupled complex networks with an asymmetrical coupling matrix. Phys. A Stat. Mech. Its Appl. **387**, 4429–4439 (2008)
16. X.Y. He, D.X. Peng, X.D. Li, Synchronization of complex networks with impulsive control involving stabilizing delay. J. Fran. Inst. **357**(8), 4869–4886 (2020)
17. J. Bebernes, Differential equations stability, oscillations, time lags. SIAM Rev. **10**(1), 93–94 (1968)
18. Z. Tang, J.H. Park, W.X. Zheng, Distributed impulsive synchronization of Lur'e dynamical networks via parameter variation methods. Int. J. Robust Nonlin. Control. **28**(3), 1001–1015 (2018)

Influence of Sea Currents on the Strategy of Riser Re-Entry

Iwona Adamiec-Wójcik (ID)**, Lucyna Brzozowska** (ID)
and Stanisław Wojciech (ID)

1 Introduction

Flexible risers used for transporting oil and gas from the seabed to platforms or ships become longer and longer as the water depths in exploration of hydrocarbons increase. Risers are long slender elements (with length up to 3000 m). Their diameters usually do not exceed 1 m, while the deformations caused by the sea environment (waves, sea currents, buoyancy, and hydrodynamic drag forces) can be large. Even in the case of hanging risers, the deflections can be hundreds of meters. For this reason, the mathematical models of risers have to take into account large deformations and consequently geometrical and sometimes physical nonlinearities. Sometimes the vibrations of the risers are influenced not only by the sea environment but also by internal fluid flow, which additionally complicates the equations of motion. Re-entry, namely, moving a free-hanging riser from a random position to the wellhead, is one of the most important operations on risers. The free-hanging riser is usually treated as a beam with a free bottom end, which has to be situated at a desired position by means of the movement of its upper end, while ensuring that the vibrations of the beam are substantially reduced. Figure 1 presents an illustration of the maneuver of re-entry for different directions of the sea-current with respect to plane *xy*.

A number of research papers are concerned [1–4] with the re-entry operation. The problem of the choice of movement of the top end of the riser without sea currents for a planar model is solved in [4]. The solution presented is obtained by means of the finite difference method for discretizing the riser and the ant colony algorithm for searching the optimal trajectory of the top end of the riser.

I. Adamiec-Wójcik (✉) · L. Brzozowska · S. Wojciech
University of Bielsko-Biala, Bielsko-Biała, Poland
e-mail: i.adamiec@ath.bielsko.pl
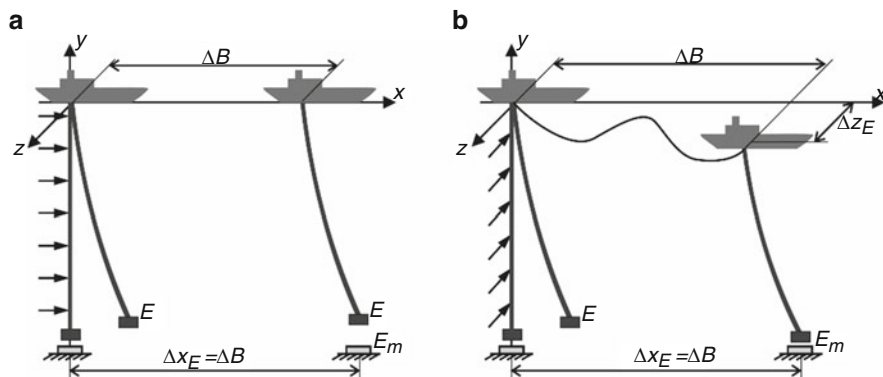
Fig. 1 Movement of the riser (**a**) sea current in-plane (**b**) sea current out of plane

In this paper, we use a modified formulation of the segment method (MS) [5, 6] for discretization of the riser and our own computer implementation of the method. It enables us to formulate the equations of motion using joint coordinates with consideration of bending, torsion, and elongation of the flexible riser. The possibility of elimination of some generalized coordinates is an important feature of the model, which can help to considerably improve the numerical effectiveness of the model and program. This is crucial since the choice of the base optimal trajectory ensuring realization of the required movement of the bottom end of the riser requires several integrations of the equations of motion. The equations of dynamics of the system are integrated for each combination of parameters defining the motion of the base in order to define the value of the objective function (minimal distance of the bottom end of the riser from the defined destination during a defined period of time and defined kinetic energy at the end of motion). The downhill simplex method is used for solving the optimization problem.

2 Discretization of the Riser and Equations of Motion

The segment method is one of the methods used for discretization of slender beam-like links. The finite element method [2], the finite difference method [1], and the lumped mass method [7] are examples of other methods used for this purpose. The most popular one – the finite element method – is implemented in commercial software packages, including those dedicated to analysis of offshore structures.

The extensive description of the method and the comparison of its numerical effectiveness in formulations using absolute and joint coordinates is presented in [8]. When using the absolute coordinates, the generalized coordinates of the i-th segment (rfe) are the components of a vector with six elements:

$$\mathbf{q}_{A,i} = \begin{bmatrix} \mathbf{r}_i \\ \boldsymbol{\varphi}_i \end{bmatrix} \tag{1}$$

where $\mathbf{r}_i = \begin{bmatrix} x_i \\ y_i \\ z_i \end{bmatrix}$ are coordinates of point A_i with respect to the global reference

system { }, $\boldsymbol{\varphi}_i = \begin{bmatrix} \varphi_i \\ \theta_i \\ \psi_i \end{bmatrix}$ are ZYX Euler angles (see Fig. 2) [9].

The vector of generalized coordinates of the flexible link consists of $N_A = 6(n + 1)$ components and takes the following form:

$$\mathbf{q}_A = \begin{bmatrix} \mathbf{q}_{A,0}^T & \cdots & \mathbf{q}_{A,i}^T & \cdots & \mathbf{q}_{A,n}^T \end{bmatrix}^T. \tag{2}$$

The vectors of generalized coordinates of the segments, when joint coordinates are used [8], take the following form:

$$\mathbf{q}_{J,i} = \boldsymbol{\varphi}_i, \tag{3}$$

where $\boldsymbol{\varphi}_i$ is defined in (1) and the vector of generalized coordinates of the whole link has $N_J = 3 + 3(n+1)$ components:
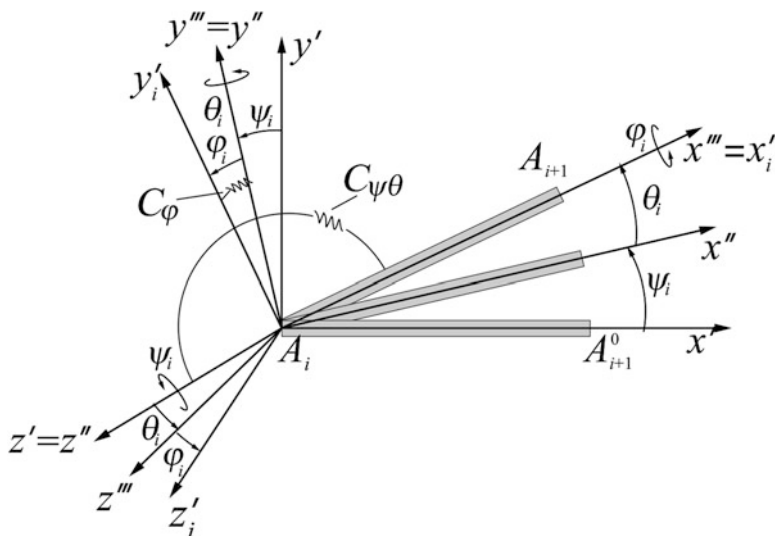
Fig. 2 ZYX Euler angles, c_φ – spring reflecting torsion, $c_{\theta\psi}$ – spring reflecting bending

$$\mathbf{q}_J = \begin{bmatrix} \mathbf{r}_0^T & \mathbf{q}_{J,0}^T & \cdots & \mathbf{q}_{J,i}^T & \cdots & \mathbf{q}_{J,n}^T \end{bmatrix}^T \tag{4}$$

where $\mathbf{r}_0 = \begin{bmatrix} x_0 & y_0 & z_0 \end{bmatrix}^T$ are coordinates of point A_0 with respect to global reference system { }.

For absolute coordinates, transformation of coordinates from local system $\{i\}'$ to the global system (Fig. 2) is carried out as follows:

$$\mathbf{r} = \mathbf{r}_i + \mathbf{R}_i \mathbf{r}', \tag{5}$$

where $\mathbf{r}$ is the vector of coordinates of a chosen point of segment i in global system { }, $\mathbf{r}'$ is the coordinate vector of this point with respect to local coordinate system $\{i\}'$, $\mathbf{R}_i = \mathbf{R}_i^{(\psi)} \mathbf{R}_i^{(\theta)} \mathbf{R}_i^{(\varphi)}$ is the rotation matrix.

When joint coordinates are used, coordinates $\mathbf{r}_i$ of point A_i can be calculated from the relation:

$$\mathbf{r}_i = \mathbf{r}_0 + \sum_{j=0}^{i-1} \mathbf{R}_j \begin{bmatrix} l_j \\ 0 \\ 0 \end{bmatrix} = \mathbf{r}_0 + \sum_{j=0}^{i-1} l_j \boldsymbol{\phi}_j \tag{6}$$

and vector $\boldsymbol{\phi}_j = \begin{bmatrix} c\theta_j c\psi_j & c\theta_j s\psi_j & -s\theta_j \end{bmatrix}^T$ is the first column of matrix $\mathbf{R}_i$ defined in (5).

Papers [10, 11] present a formulation of the method, in which, in order to consider elongation of a flexible link, each rfe from Fig. 3 is additionally divided into two parts connected by means of spring-damping element reflecting longitudinal flexibility. The vector of generalized coordinates of rfe i is then defined in the following form:

$$\mathbf{q}_{\Delta,i} = \begin{bmatrix} \mathbf{r}_i & \boldsymbol{\varphi}_i & \Delta_i \end{bmatrix}^T, \tag{7}$$

where $\mathbf{r}_i$, $\boldsymbol{\varphi}_i$ are defined by (1), Δ_i is the elongation of rfe i.

This paper presents a new formulation of the segment method with consideration of the elongation of a flexible link but by means of joint coordinates.

When discretizing the flexible link (Fig. 3), as in the Rigid Finite Element Method [9], primary division is carried out first. It is assumed that the generalized coordinates of the link are

$$\mathbf{r}_0 = \begin{bmatrix} x_0 & y_0 & z_0 \end{bmatrix}^T \quad - \text{ coordinates of point } A_0, \tag{8a}$$

$$\mathbf{q}_i = \begin{bmatrix} \boldsymbol{\Phi}_i & \Delta_i \end{bmatrix}^T - \text{generalized coordinates of rfe } i, \quad i = 0, \ldots, n-1, \tag{8b}$$
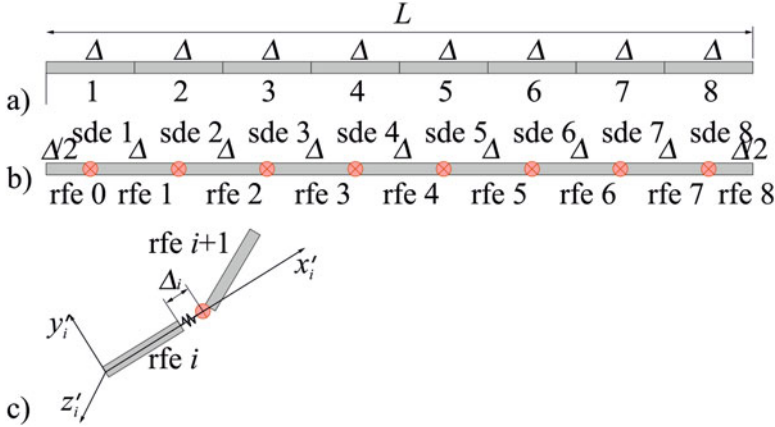
Fig. 3 Discretization of the flexible link (**a**) primary division (**b**) secondary division (**c**) translational coordinates Δ_i

$$\mathbf{q}_n = \mathbf{\Phi}_n - \text{generalized coordinates of rfe } n, \tag{8c}$$

where $\mathbf{\Phi}_i = \left[\psi_i \ \theta_i \ \varphi_i \right]^T$, $\psi_i, \theta_i, \varphi_i$ are ZYX Euler angles defining orientation of rfe i, Δ_i is the elongation of primary element i (Fig. 3).Coordinates of any point of rfe i with respect to global reference system can be defined by the relation:

$$\mathbf{r} = \mathbf{r}_0 + \sum_{j=0}^{i-1} \mathbf{T}_j + \mathbf{R}_i \mathbf{r}', \tag{9}$$

where $\mathbf{T}_j = \mathbf{R}_j^{(\psi)} \mathbf{R}_j^{(\theta)} \mathbf{R}_j^{(\varphi)} \overline{\mathbf{\Delta}}_j$, $\overline{\mathbf{\Delta}}_j = \left[l_{j-1} + \Delta_j \ 0 \ 0 \right]^T$, $\mathbf{r}'$ are the coordinates of the point in the local system of rfe i.

The equations of motion are derived from the Lagrange equations of the second kind. The kinetic energy of rfe, the potential energy of the spring damping elements (sde) as well as the sea environment such as drag, buoyancy forces, added mass (according to the Morison equation), and internal flow are included in the equations.

Having omitted laborious transformations, the equations of motion can be written as a set of $6 + 4n = N$ nonlinear differential equations of the second order in the following form:

$$\mathbf{M}(\mathbf{q}) \ddot{\mathbf{q}} = \mathbf{f}(t, \mathbf{q}, \dot{\mathbf{q}}), \tag{10}$$

where $\mathbf{q} = \left[\mathbf{r}_0^T \ \mathbf{q}_0^T \ \ldots \ \mathbf{q}_{n-1}^T \ \mathbf{q}_n^T \right]^T$; $\mathbf{r}_0 = \left[x_0 \ y_0 \ z_0 \right]^T$; $\mathbf{q}_i = \left[\mathbf{\Phi}_i^T \ \Delta_i \right]^T$ for $i = 0, 1, \ldots, n\text{-}1$; $\mathbf{q}_n = \mathbf{\Phi}_n$; $\mathbf{\Phi}_i$ defined in (8) for $i = 0, 1, \ldots, n$.

Table 1 Special cases of the equations of motion for the segment method in joint coordinates

Notation	$\mathbf{r}_0$	$\mathbf{q}_i$	$\mathbf{q}_n$	$\boldsymbol{\Phi}_i$	Description
M0	$\mathbf{r}_0 = \begin{bmatrix} x_0 \\ y_0 \\ z_0 \end{bmatrix}$	$\mathbf{q}_i = \begin{bmatrix} \boldsymbol{\Phi}_i \\ \Delta_i \end{bmatrix}$	$\mathbf{q}_n = \boldsymbol{\Phi}_n$	$\boldsymbol{\Phi}_i = \begin{bmatrix} \psi_i \\ \theta_i \\ \varphi_i \end{bmatrix}$	General case described above; consideration of bending, and torsional and longitudinal flexibilities.
M1	As above	$\mathbf{q}_i = \boldsymbol{\Phi}_i$	As above	As above	Classic case of MS described in [5, 8].
M2	As above	$\mathbf{q}_i = \begin{bmatrix} \boldsymbol{\Phi}_i \\ \Delta_i \end{bmatrix}$	As above	$\boldsymbol{\Phi}_i = \begin{bmatrix} \psi_i \\ \theta_i \end{bmatrix}$	Torsional flexibility is omitted, bending and longitudinal are taken into account.
M3	As above	$\mathbf{q}_i = \boldsymbol{\Phi}_i$	As above	As above	Only bending flexibility is considered [6]
M4	$\mathbf{r}_0 = \begin{bmatrix} x_0 \\ y_0 \end{bmatrix}$	$\mathbf{q}_i = \begin{bmatrix} \boldsymbol{\Phi}_i \\ \Delta_i \end{bmatrix}$	As above	$\boldsymbol{\Phi}_i = \begin{bmatrix} \psi_i \end{bmatrix}$	Bending in plane xy and extensibility are considered.
M5	As above	$\mathbf{q}_i = \boldsymbol{\Phi}_i$	As above	As above	Only bending in xy plane is taken into account [12].

Specific cases with smaller numbers of degrees of freedom can be obtained from Eq. (10), by appropriate modifications. They are presented in Table 1. Models M0, M1, M2, and M3 are spatial models (3D), while models M4 and M5 are planar (2D).

3   Validation of the Model

The model and formulae presented are implemented on a computer in Delphi 10.1. Validation of models and the computer program is carried out by comparison of our own results obtained for simulations of vibrations of the vertical riser with experimental measurements performed at MARITEK and presented in [13]. Paper [13] presents also results of numerical simulations using RIFLEX for a model of a riser with parameters as in Table 2.

Values of the first three frequencies of free vibrations are given in Table 3. The calculations were performed assuming $n = 25$.

The results obtained are very close to those obtained by RIFLEX, and the percentage error with reference to the experimental measurements does not exceed 5%.

Displacements and curvature of the riser were also measured in the experiment for harmonic motion imposed on the top end of the riser along the direction of axis x with amplitude $A = 0.013$ [m] and period $P = 0.677$ [s], which correspond to the

Table 2 Parameters of the riser analyzed

Riser analyzed	Parameter	Notation	Unit	Value
	Outer diameter	D_{out}	m	0.028
	Inner diameter	D_{inn}	m	0.017
	Bending stiffness	EI	Nm^2	120
	Spring stiffness	EA	Nm^2	1.819E+5
	Top tension	T_0	N	212
	Unit mass of the riser	ρ_r	kg/m	0.668
	Water density	ρ_w, ρ_F	kgm^{-3}	1025
	Normal drag coefficient	D'_x	–	0.1
	Tangential drag coeff.	D'_{yz}	–	1.0
	Added mass coefficient	c_M	–	2.1

Table 3 Frequencies of free vibrations

Mode	Experiment e f[Hz]	Riflex r f[Hz]	$\left\lvert \frac{e-r}{e} \right\rvert \cdot 100\%$	MS s f[Hz]	$\left\lvert \frac{e-s}{e} \right\rvert \cdot 100\%$
1	0.646	0.648	0.3	0.642	0.6
2	1.477	1.445	2.2	1.436	2.8
3	2.619	2.503	4.4	2.492	4.8

second frequency of the riser (according to measurements). Figure 4 presents the comparison of displacement amplitudes and curvature of the riser.

The comparison shows acceptable compatibility with the experiment and substantial agreement with the results of simulations by RIFLEX.

4 Optimization of the Base Trajectory in Re-Entry

Movement of the riser during its installation requires precise definition of the final position of the bottom end of the riser during a desired period of time t_m. This means that it is necessary to plan the motion of the base (vessel or platform) so that after desired time t_m, point E of the riser is as close as possible to the target position defined as E_m in Fig. 1. Moreover, the vibrations of the riser after time t_m should
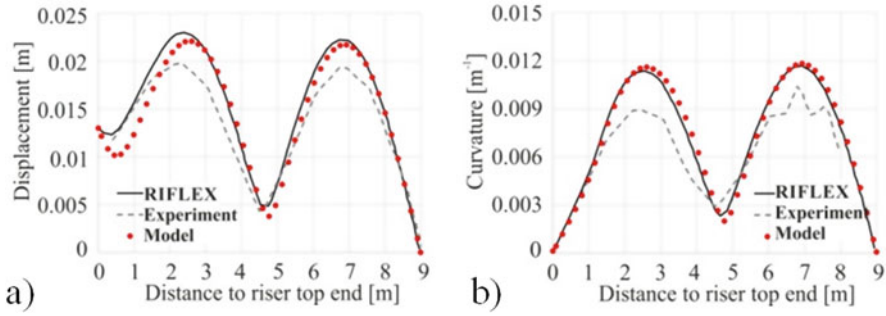
Fig. 4 Comparison of results obtained by experimental measurements, simulations by RIFLEX and the segment method (**a**) displacement amplitudes (**b**) curvature

also be reduced. According to the above requirements, the objective function in the optimization task is formulated in the form of the following functional:

$$\Omega = c_1 \left| \mathbf{r}_E(t_m) - \mathbf{r}_{E_m} \right|^2 + c_2 \int\limits_{t_m}^{t_k} E_k dt, \tag{11}$$

where $\mathbf{r}_E(t_m)$ is the vector defining the position of the bottom end of the riser (point E) at time moment t_m, $\mathbf{r}_{E_m}$ is the target position of point E of the riser at time t_m, $\int\limits_{t_m}^{t_k} E_k dt$ is the kinetic energy of the riser in time interval $<t_m, t_k>$, t_k defines the end of simulations, and c_1, c_2 are chosen constants.

The equations of motion (10) have to be integrated for each possible trajectory of the base, which is defined by vector $\mathbf{r}_0 = \mathbf{r}_0(t)$ in order to calculate the value of functional Ω. The problem defined is a 3D problem due to the sea current. It is assumed that the motion of the base is defined by the following functions $x_0 = x_0(t)$, $y_0 \equiv 0$, $z_0 = z_0(t)$, which means that the vertical movement is omitted. Time interval $<0, t_m>$ is divided into m subintervals and the courses of velocities $v_{0,x} = \dot{x}_0$ and $v_{0,z} = \dot{z}_0$ are defined as splines of the third order and fulfil the following conditions:

$$\begin{cases} x_0(0) = 0, \ x_0(t_m) = \Delta_E^x \\ v_{0,x}(0) = v_{0,x}(t_m) = 0 \end{cases} \begin{cases} z_0(0) = 0, \ z_0(t_m) = \Delta_E^z \\ v_{0,z}(0) = v_{0,z}(t_m) = 0 \end{cases}. \tag{12}$$

Values $v_{i,x} = \dot{x}_0(t_i)$, $v_{i,z} = \dot{z}_0(t_i)$ for $i = 1, \ldots, m-1$, defining courses of functions $x_0(t)$ and $z_0(t)$, which fulfil conditions (12) and functional Ω, are sought. For each combination of $2(m-1)$ parameters defining the trajectory of the base, the equations of motion of the riser (10) have to be integrated in order to calculate the value of functional $\Omega(v_{1,x}, \ldots, v_{m-1,z})$. The results presented below are obtained for the riser with parameters as in Table 4 identical to those in [4].

Table 4 Parameters of the riser

Parameter	Notation	Unit	Value
Length	L	m	1500
Outer diameter	D_{out}	m	0.406
Inner diameter	D_{inn}	m	0.375
Cross-section moment of inertia	I	m^4	3.63E-6
Mass in air per unit length	m	kg/m	229
Added mass per unit length	m_a	kg/m	137.4
Weight in water per unit length	W	N/m	1950
Young's module	E	N/m^2	2.07E+11
Drag coefficient	c_D	–	1.2
Added mass coefficient	c_M	–	1.5
Water density	ρ_w	kg/m^3	1025

Table 5 Static deflection of point E for $v_w = 0.8$ m/s

Static deflection of the riser	α_w	Δx_E [m]	Δz_E [m]
	0	122.11	0
	45	86.34	−86.34
	90	0	−122.11
	135	−86.34	−86.34
	180	−122.11	0

Point O (the upper end) of the riser is attached by means of a ball-joint with the base. Torsion and elongation deformations are omitted in the optimization calculations due to their negligible influence on the trajectory of point E. Thus, model M3 from Table 1 is considered. Table 5 presents static deflections Δx_E and Δz_E dependent on angle α_w for $v_w = 0.8$ m/s.

Values from Table 5 were used for defining boundary conditions from (12) assuming the following:

$$\begin{cases} x_0(t_m) - \Delta_E^x = 100 + \Delta x_E \\ z_0(t_m) - \Delta_E^z = \Delta z_E \end{cases}. \tag{13}$$

For optimization calculations, it was assumed that $t_m = 600$ s and $t_k = 900$ s. Courses of coordinates x_0 and z_0 as well as velocities of the base motion in this

directions after optimization for different angles α_w of the sea current acting on the riser are shown in Fig. 5.

Figure 6 presents the motion of the bottom end of the riser in both directions and its trajectory.

It can be seen that the position of the bottom end of the riser stabilizes in near proximity to the desired position ($x_E = 100, z_E = 0$) in the given time period and the final base velocity is equal to 0. In some cases, longer simulation time may be required (e.g., for $\alpha_w = 90^\circ$).
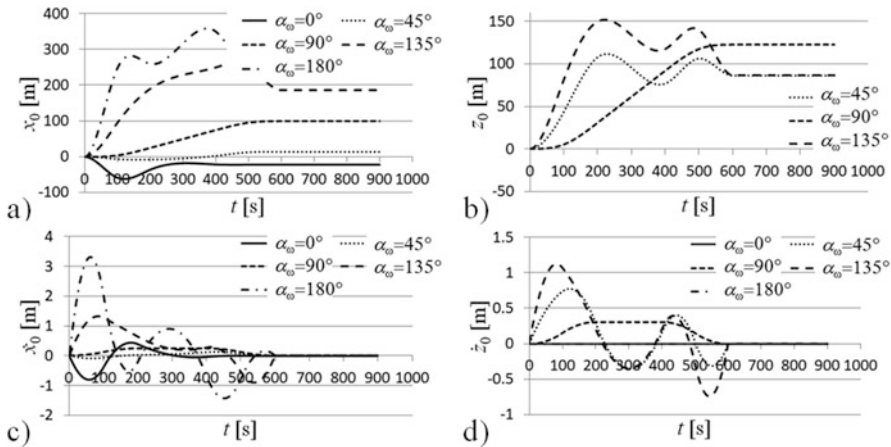
Fig. 5 Motion of the top end of the riser for different angles α_w (**a**) x_0 (**b**) z_0 (**c**) $\dot{x}_0$ (**d**) $\dot{z}_0$
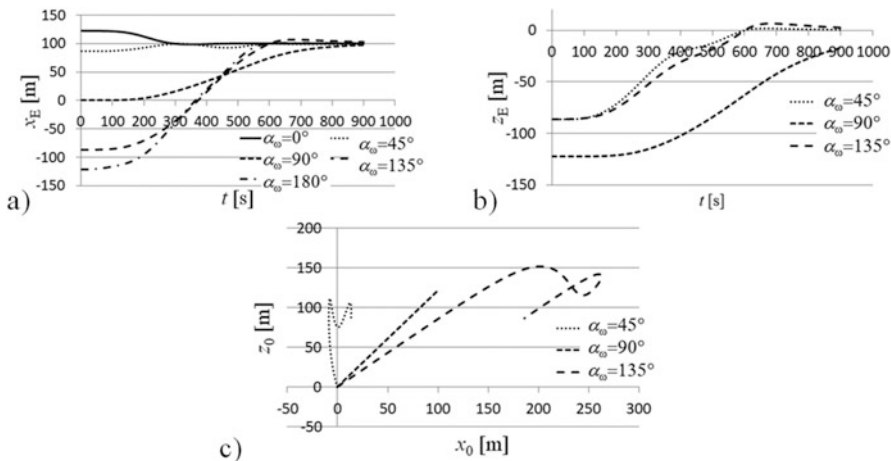
Fig. 6 Motion of the riser for different angles of sea current (**a**) x_E of the bottom end (point E) (**b**) z_E of the bottom end (point E) (**c**) trajectory of the top end of the riser (point O)

5 Closing Remarks

The paper applies the segment method to solve the dynamic optimization problem of choosing the trajectory of the base with an attached riser so that the bottom end of the riser is relocated to a defined destination during a given time. The equations of motion are integrated at each optimization step for each combination of motion parameters describing the trajectory of the base. Thus, the numerical effectiveness of the method used for discretization of the riser is crucial. The segment method proposed, due to its facility for simplifications (by elimination of bending and longitudinal vibrations), enables us to solve the equations of motion for a single combination of input parameters with a relatively large integration step. Integrating the equations of motion formulated for model M3 over the interval <0,900 s> with time step $\Delta t = 0.2$ s, for $n = 10$, (division of the riser into 11 rfes and 10 sdes) takes less than 1 s.

Validation of the method and the program is carried out by comparison of the authors' own results with experimental measurements presented by other researchers. Good compatibility of the results has been achieved.

The model presented has been used for several optimization simulations in which the trajectory of the base was calculated for different angles of the sea current acting on the riser.

References

1. S. Wang, X. Xu, B. Yao, L. Lian, A finite difference approximation for dynamic calculation of vertical free hanging slender risers in re-entry application. China Ocean Eng **26**, 637–652 (2012)
2. E. Fortaleza, Y. Creff, J. Lévine, Active control for the re-entry operation of flexible risers, in *Proc MATHMOD 09*, (Vienna, 2009), pp. 973–979
3. X. Xu, S. Wang, A flexible-segment-model-based dynamics calculation method for free hanging marine risers in re-entry. China Ocean Eng **26**, 139–152 (2012)
4. S. Wang, X. Xu, X. Lu, Movement optimization of freely-hanging Deepwater risers in reentry. Ocean Eng. **116**, 32–41 (2016)
5. J.D. Connelly, R.L. Huston, *The Dynamics of Flexible Multibody Systems: A Finite Segment Approach-I* (Theoretical aspects. Comput Struct, 1994)
6. I. Adamiec-Wójcik, S. Wojciech, Application of the finite segment method to stabilisation of the force in a riser connection with a wellhead. Nonlinear Dyn. **93**, 1853–1874 (2018)
7. L. Sun, B. Qi, Global analysis of a flexible riser. J. Mar. Sci. Appl. **10**, 478–484 (2011)
8. I. Adamiec-Wójcik, L. Brzozowska, S. Wojciech, Effectiveness of the segment method in absolute and joint coordinates when modelling risers. Acta Mech. **231**, 435–469 (2020)
9. E. Wittbrodt, I. Adamiec-Wójcik, S. Wojciech, *Dynamics of Flexible Multibody Systems* (Rigid Finite Element Method, Springer Verlag, Heildenberg, 2006)
10. Ł. Drąg, Application of dynamic optimisation to stabilise bending moments and top tension forces in risers. Nonlinear Dyn **88**, 2225–2239 (2017)
11. Ł. Drąg, *Modelling Ropes, Risers and Cranes with the Rigid Finite Element Method (Modelowanie Lin, riserów I żurawi metodą Sztywnych elementów Skonczonych) in Polish* (Bielsko-Biala University Press, Bielsko-Biała, First, 2017)

12. I. Adamiec-Wójcik, L. Brzozowska, S. Wojciech, Influence of sea current on stabilization of moments and forces in risers. J. Offshore Mech. Arct. Eng. **141**(6), 061701. (15 pages (2019)
13. D. Yin, E. Passano, H. Lie, et al., Experimental and numerical study of a top tensioned riser subjected to vessel motion. Ocean Eng. **171**, 565–574 (2019)

Continuous Leaderless Synchronization Control of Multiple Spacecraft on $SO(3)$

Ti Chen

1 Introduction

Attitude coordination is one key to some spacecraft formation flying missions, such as interferometry and inter-spacecraft communication. However, since the configuration space of the spacecraft attitude is the special orthogonal group $SO(3)$, the strongly nonlinear attitude dynamics poses great challenges for the controller design. Generally, attitude control is investigated based on some attitude parameterizations [1, 2], such as Euler angles, Modified Rodriguez Parameters (MRPs), or quaternions. The first two attitude representations cannot describe the rotation globally, i.e., the minimal attitude representations have singular points. Quaternions double cover $SO(3)$, i.e., two antipodal quaternions represent a single attitude [3]. As a result, quaternions are not unique in attitude representation. With continuous control laws, the undesirable unwinding phenomenon may happen. To avoid the singularities of Euler angles and Modified Rodriguez Parameters (MRPs) and the ambiguity associated with quaternions, some control algorithms have been developed directly on $SO(3)$. However, no continuous time-invariant control laws can globally stabilize the attitude maneuvering, and almost global asymptotic stability is the best result because $SO(3)$ is not diffeomorphic to any Euclidean space [4].

Furthermore, in the attitude consensus control, the leader–follower case has been widely studied with various attitude representations [5–7]. However, the leader–follower architecture relies heavily on the leader. The error or loss of a leader will cause the mission's failure. The leaderless consensus strategy can avoid this

T. Chen (✉)
Nanjing University of Aeronautics and Astronautics, Nanjing, Jiangsu, ChinaYork University, Toronto, ON, Canada
e-mail: chenti@nuaa.edu.cn; tichen@yorku.ca

problem. Hence, it is necessary to consider the leaderless consensus of multiple spacecraft [8]. However, all existing studies on leaderless attitude consensus are based on specified communication topologies or with local stability. The available methods with a distributed observer to estimate the leader's information do not work in the case of the leaderless consensus under a general undirected graph. For example, both the observers in [9] and [10] are proposed for a specified communication topology. It is almost impossible that the finite-time observer in [11] converges to a matrix on $SO(3)$ without the leader's information, i.e., the observer cannot provide a feasible reference trajectory. Hence, the leaderless attitude synchronization on $SO(3)$ under a general connected undirected graph is still unsolved. This work will provide a solution to such an open problem. Furthermore, the commonly used actuators, such as reaction wheels and control moment gyroscopes, can only provide continuous control torques. Hence, a continuous controller is desired for practical applications. The main contribution of this paper is that the leaderless consensus of multiple spacecraft is solved directly on $SO(3)$ under a general connected undirected graph. Compared with the existing studies [12] on leaderless consensus, the graph in this study is more general. Different from [13], an almost global stability is achieved.

2 Problem Formulation

2.1 Notations and Graph Theory

$SO(3) = \{R \in \mathbb{R}^{3\times3} | \det(R) = 1, R^T R = R R^T = I_3\}$ is a special orthogonal group in $\mathbb{R}^{3\times3}$ with determinant 1, where I_3 is the identity matrix of 3×3. Let SO(3) be the group of skew-symmetric matrices in $\mathbb{R}^{3\times3}$, i.e., SO(3) $= \{\bar{\Omega} | \bar{\Omega} \in \mathbb{R}^{3\times3}, \bar{\Omega} = -\bar{\Omega}^T\}$. SO(3) is referred as the Lie algebra of the Lie group $SO(3)$. The mapping $(\cdot)^\times : \mathbb{R}^3 \to$ SO(3) is defined such that $a^\times b = a \times b$ for vectors $a \in \mathbb{R}^3$ and $b \in \mathbb{R}^3$. The wedge mapping $(\cdot)^\vee :$ SO(3) $\to \mathbb{R}^3$ denotes the inverse mapping of $a^\times$, i.e., $(a^\times)^\vee = a$. For $a \in \mathbb{R}^3$ and $R \in SO(3)$, we have (i) $\text{tr}(Ra^\times) = -a^T(R - R^T)^\vee$; (ii) $(a^\times R + R^T a^\times)^\vee = (\text{tr}(R)I_3 - R)a$; and (iii) $(Ra)^\times = Ra^\times R^T$.

An undirected graph $\mathcal{G} = (\mathcal{V}, \mathcal{E})$ is adopted to describe the communication among N spacecraft. $\mathcal{V} = \{1, 2, \cdots, N\}$ and $\mathcal{E} \subset \mathcal{V} \times \mathcal{V}$ are the node set and the edge set, respectively. The element $(i, j) \in \mathcal{E}$ means that the jth node can receive information from node i. Nodes i and j are the parent and the child, respectively. The in-degree and out-degree of the ith node are the number of edges having node i as a head and having node i as a tail. The set of the neighbors of the ith node is denoted by $\mathcal{N}_i = \{j | (j, i) \in \mathcal{E}\}$. The number of neighbors of the ith node is equal to its in-degree. The adjacency matrix of the communication graph is represented by $A = [a_{ij}] \in \mathbb{R}^{N \times N}$, where $a_{ij} = 1$ if $(j, i) \in \mathcal{E}$ and $a_{ij} = 0$ otherwise. Note that $a_{ii} = 0$. For $(i, j) \in \mathcal{E}$ implies $(j, i) \in \mathcal{E}$ $\forall i, j$, the graph is said to

be undirected. A path is defined as a sequence of nodes $i_1, i_2, \cdots, i_r$ such that $(i_k, i_{k+1}) \in \mathcal{E}$ holds for $k = 1, \cdots, r - 1$. If there exists a path from node i to node j, the two nodes are said to be connected. The undirected graph $\mathcal{G}$ is said to be connected if any two distinct nodes are connected. A tree is defined as an undirected graph in which any two nodes are connected by exactly one path. Define the in-degree of node i as $d_i = \sum_{j \in \mathcal{N}_i} a_{ij}$. Denote the diagonal in-degree matrix as $\boldsymbol{D} = \mathrm{diag}\{d_i\}$ and the graph Laplacian matrix as $\boldsymbol{L} = \boldsymbol{D} - \boldsymbol{A}$. In this study, it is assumed that the undirected communication graph $\mathcal{G}$ is connected. Hence, the graph Laplacian matrix $\boldsymbol{L}$ is positive semidefinite and zero is a simple eigenvalue of $\boldsymbol{L}$, and $\mathbf{1} = [1, 1, \cdots, 1]^T \in \mathbb{R}^N$ is the associated eigenvector [14].

2.2 Spacecraft Dynamics

The dynamics equations of the ith spacecraft on $SO(3)$ are

$$\dot{\boldsymbol{R}}_i = \boldsymbol{R}_i \boldsymbol{\omega}_i^\times \tag{1}$$

$$\boldsymbol{J}_i \dot{\boldsymbol{\omega}}_i = -\boldsymbol{\omega}_i^\times \boldsymbol{J}_i \boldsymbol{\omega}_i + \boldsymbol{u}_i + \bar{\boldsymbol{d}}_i \tag{2}$$

where $\boldsymbol{R}_i \in SO(3)$ is the rotation matrix from the body frame to the inertial reference frame, $\boldsymbol{\omega}_i \in \mathbb{R}^3$ is the angular velocity, $\boldsymbol{J}_i \in \mathbb{R}^{3 \times 3}$ is the inertia matrix of the spacecraft, $\boldsymbol{u}_i$ is the control torque, and $\bar{\boldsymbol{d}}_i$ is the external disturbance. Suppose that the inertia matrix $\boldsymbol{J}_i$ is uncertain and $\bar{\boldsymbol{d}}_i$ is bounded by a positive constant μ_0, i.e, $\|\bar{\boldsymbol{d}}_i\|_2 \leq \mu_0$ holds.

3 Leaderless Consensus

This section aims to design a distributed controller to achieve the attitude and angular velocity synchronization of multiple spacecraft under a connected undirected graph. That is, the control input $\boldsymbol{u}_i$ is designed such that

$$\lim_{t \to \infty} \boldsymbol{R}_i = \lim_{t \to \infty} \boldsymbol{R}_j, \ \lim_{t \to \infty} \boldsymbol{\omega}_i = \lim_{t \to \infty} \boldsymbol{\omega}_j \tag{3}$$

hold for $\forall i, j \in \mathcal{V}$ and $i \neq j$. Note that the final synchronized angular velocity can be non-zero.

3.1 Generating an Undirected Tree Graph

Indeed, there are many algorithms [15] for traversing or searching tree structures, such as breadth-first search. However, usually, the global information is needed in these algorithms. Hence, in this subsection, to facilitate the design of a distributed controller, as shown in Algorithm 1, a method is proposed to generate an undirected tree graph based on the local information only. The generated undirected tree graph is referred as G' in what follows. Essentially, some communication edges are blocked based on the Algorithm 1 to obtain an undirected tree graph. Note that the information that flows in the edge contains layer number, friend flag (0 or 1), and its own attitude. Figure 1 gives one example to show how to generate an undirected tree graph based on the proposed algorithm. In Step A, the five nodes are divided into three layers. According to the rules in Step B, the red dotted communication should be blocked because their friend flags are equal to 0 and two possible tree graphs shown in Fig. 1(iii) and (iv) can be obtained.

Algorithm 1

Initialize:

  The 1st node is listed in Layer 1, i.e., $Ly_1 = 1$,

  The layer numbers of the other nodes are -1 i.e., $Ly_i = -1$, where $i = 2, \cdots, N$

  The friend flag F_k is initialized as 0 for each communication edge.

Algorithm Main():

  Step A: Assign Layer number for each node.

    For node i, if $Ly_i = -1$, the Layer number is set as 1 plus the minimum layer number that node i can receive.

  Step B: Extract an undirected tree graph.

    Rule 1: All nodes in Layer j must choose only one neighbor (friend) from the previous layer for $j \geq 2$ and change the friend flag of the relevant undirected edge to 1.

    Rule 2: All nodes drop the information received from the nodes in the same layer, i.e., the communication edges between two nodes in the same layer are with $F_k = 0$.
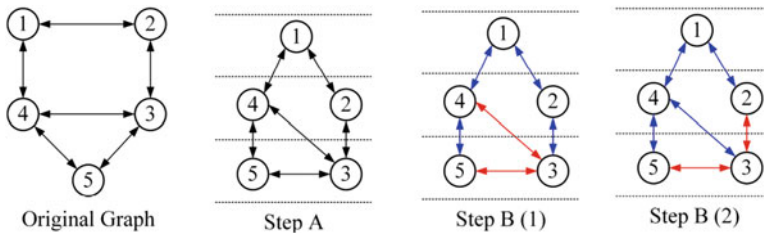
Fig. 1 An example of generating a tree graph using Algorithm 1

3.2 Distributed Observer

Based on the generated tree graph $\mathcal{G}'$ in Sect. 3.1, a distributed observer shown in the following equation is designed for each spacecraft in the group:

$$\dot{\hat{R}}_i = \hat{R}_i \hat{\omega}_{i\times}, \quad \dot{\hat{\omega}}_i = \hat{u}_i \tag{4}$$

where $\hat{R}_i \in \mathbb{R}^{3\times3}$ and $\hat{\omega}_i \in \mathbb{R}^3$ are the estimates of the final convergence attitude and angular velocity, respectively. $\hat{u}_i \in \mathbb{R}^3$ is a virtual control input of the designed observer and defined as $\hat{u}_i = -\kappa_1 \sum_{j=1}^N a'_{ij}(\hat{R}_j^T \hat{R}_i - \hat{R}_i^T \hat{R}_j)^\vee - \kappa_2 \sum_{j=1}^N a'_{ij}(\hat{\omega}_i - \hat{\omega}_j)$, where a'_{ij} is the (i, j) element of the adjacency matrix of the communication graph $\mathcal{G}'$. Note that the initial values of $\hat{R}_i$ and $\hat{\omega}_i$ are set as $R_i(0)$ and $\omega_i(0)$, respectively.

Lemma 1 *The synchronization of the N observers governed by Eq. (4) can be achieved almost globally asymptotically under the generated tree graph $\mathcal{G}'$. Furthermore, the acceleration $\dot{\hat{\omega}}_i$ will converge to zero asymptotically.*

Proof Consider the following Lyapunov function $V_1 = \frac{\kappa_1}{2} \sum_{i=1}^N \sum_{j=1}^N a'_{ij} \text{tr}(I_3 - \hat{R}_j^T \hat{R}_i) + \frac{1}{2}\hat{\Omega}^T \hat{\Omega}$, where $\text{tr}(\cdot)$ represents the trace of a matrix and $\hat{\Omega}$ is defined as $[\hat{\omega}_1^T, \cdots, \hat{\omega}_N^T]^T$. $V_1 = 0$ holds if and only if $\hat{R}_j = \hat{R}_i$ and $\hat{\omega}_i = \hat{\omega}_j = \mathbf{0}$ hold for $\forall i, j \in \mathcal{V}$. The time derivative of V_1 along Eq. (4) is $\dot{V}_1 = \kappa_1 \sum_{i=1}^N \sum_{j=1}^N a'_{ij} \left[\hat{\omega}_i^T (\hat{R}_j^T \hat{R}_i - \hat{R}_i^T \hat{R}_j)^\vee\right] + \sum_{i=1}^N \hat{\omega}_i^T [-\kappa_1 \sum_{j=1}^N a'_{ij}(\hat{R}_j^T \hat{R}_i - \hat{R}_i^T \hat{R}_j)^\vee - \kappa_2 \sum_{j=1}^N a'_{ij}(\hat{\omega}_i - \hat{\omega}_j)] = -\hat{\Omega}^T (L' \otimes I_3)\hat{\Omega} = -\hat{\Omega}_1^T L'\hat{\Omega}_1 - \hat{\Omega}_2^T L'\hat{\Omega}_2 - \hat{\Omega}_3^T L'\hat{\Omega}_3$, where $\hat{\Omega}_k \in \mathbb{R}^N$ is a column vector consisting of the kth element of $\hat{\omega}_1, \cdots, \hat{\omega}_N$ and L' is the Laplacian matrix of the graph $\mathcal{G}'$. The real symmetric matrix L' can be decomposed as $L' = Q\Lambda Q^T$, where Λ is a diagonal matrix whose entries are the eigenvalues of L' and Q is an orthogonal matrix whose columns are the eigenvectors of L'. Since zero is a simple eigenvalue of L', only the $(1,1)$ element of Λ is zero and the first column of Q is $1/\sqrt{N}$. Letting $Y_1 = Q^T \hat{\Omega}_1$, the solution to $\hat{\Omega}_1^T L'\hat{\Omega}_1 = \hat{\Omega}_1^T Q\Lambda Q^T \hat{\Omega}_1 = Y_1^T \Lambda Y_1 = 0$ is $Y_1 = [\alpha, 0, \cdots, 0]^T \in \mathbb{R}^N$ and $\hat{\Omega}_1 = \alpha\mathbf{1}$ with a constant α. The similar conclusions can be drawn for $\hat{\Omega}_2$ and $\hat{\Omega}_3$. Hence, the solution to $\dot{V}_1 = 0$ is $\hat{\omega}_i = \hat{\omega}_j$ for $\forall i, j \in \mathcal{V}$. In the case of $\hat{\omega}_i = \hat{\omega}_j$, one has $\dot{\hat{\omega}}_i = \dot{\hat{\omega}}_j$, i.e.,

$$\sum_{k=1}^N a'_{i_1 k}(\hat{R}_k^T \hat{R}_{i_1} - \hat{R}_{i_1}^T \hat{R}_k)^\vee = \sum_{k=1}^N a'_{i_2 k}(\hat{R}_k^T \hat{R}_{i_2} - \hat{R}_{i_2}^T \hat{R}_k)^\vee = \dot{\hat{\omega}}_1 \tag{5}$$

where (i_1, i_2) is one edge in $\mathcal{G}'$. Denote $\Delta_{ik} = (\hat{R}_k^T \hat{R}_i - \hat{R}_i^T \hat{R}_k)^\vee$. Note that $\Delta_{ik} = -\Delta_{ki}$. Since the undirected graph $\mathcal{G}'$ is a tree, a directed spanning tree $\bar{\mathcal{G}}'$ with the first node as the root can be obtained by designating a proper direction to each

undirected edge in $\mathcal{G}'$. Note that the graph $\bar{\mathcal{G}}'$ has N agents and $N - 1$ directed communication edges. Equation (5) can be expressed as $(\bar{C} \otimes I_3)\bar{\Delta} = 0$, where $\bar{\Delta} = [\Delta^T, \dot{\hat{\omega}}_1^T]^T$ with Δ as the column stack vector consisting of Δ_{ik} and $\bar{C} = [C \quad -1_N] \in \mathbb{R}^{N \times N}$ with $C \in \mathbb{R}^{N \times (N-1)}$ is the incidence matrix of $\bar{\mathcal{G}}'$. Note that each column of C only contains two non-zero elements, i.e., 1 or -1. Because $\bar{\mathcal{G}}'$ is a directed spanning tree, C is full column rank, i.e., the $N - 1$ columns of C are linearly independent. It is easy to verify that the inner product between the vector -1_N and each column of C is zero, i.e., -1_N is orthogonal to each column of C. Hence, the N columns of $\bar{C}$ are linearly independent. The only solution to $(\bar{C} \otimes I_3)\bar{\Delta} = 0$ is $\bar{\Delta} = 0$. As shown in [16], $(\hat{R}_k^T \hat{R}_i - \hat{R}_i^T \hat{R}_k)^\vee = 0$ has two solutions, i.e., $\hat{R}_k = \hat{R}_i$ and $\text{tr}(\hat{R}_k^T \hat{R}_i) = -1$. The two solutions corresponds to the minimum and the maximum of the potential function $\text{tr}(I_3 - \hat{R}_k^T \hat{R}_i)$. Considering that $\mathcal{G}'$ is an undirected tree graph, only $\hat{R}_1 = \cdots = \hat{R}_N$ is stable. According to LaSalle's invariance principle, the synchronization of the N observers can be achieved almost globally asymptotically.

Furthermore, since the N observer will be driven to the equilibrium $\{\bar{\Delta} = 0, \hat{\omega}_1 = \cdots = \hat{\omega}_N\}$, $\dot{\hat{\omega}}_i$ will converge to zero asymptotically according to Eq. (4).

Remark 1 Note that the convergence of the observers in Eq. (4) has nothing to do with the real-time state of the networked spacecraft and its responses are continuous. Essentially, the observer (4) provides the reference attitude and angular velocity for each node in spacecraft formation flying missions. Both $\hat{R}_i$ and $\hat{\omega}_i$ will start from the initial conditions of the ith spacecraft.

3.3 Controller Design

A synchronization controller is designed in this section under a connected undirected graph. Based on the distributed estimator governed by Eq. (4), for the ith spacecraft, a sliding variable can be defined as $s_i = \omega_i + \Phi_i$, where $\Phi_i = \beta_1(\hat{R}_i^T R_i - R_i^T \hat{R}_i)^\vee - R_i^T \hat{R}_i \hat{\omega}_i$ with a positive constant β_1. Note that the time derivative of Φ_i can be expressed as $\dot{\Phi}_i = \beta_1(\text{tr}(R_i^T \hat{R}_i)I_3 - R_i^T \hat{R}_i)\omega_i - \beta_1(\text{tr}(\hat{R}_i^T R_i)I_3 - \hat{R}_i^T R_i)\hat{\omega}_i + \omega_i^\times R_i^T \hat{R}_i \hat{\omega}_i - R_i^T \hat{R}_i \dot{\hat{\omega}}_i$. Note that the term $-R_i^T \hat{R}_i \dot{\hat{\omega}}_i$ goes to zero as time goes to infinity according to Lemma 1. Denote $\Phi_i^\circ = \dot{\Phi}_i + R_i^T \hat{R}_i \dot{\hat{\omega}}_i$. The controller can be designed as

$$u_i = -k_1 s_i + \omega_i^\times \hat{J}_i \omega_i - \hat{J}_i \Phi_i^\circ - \frac{\hat{d}_i s_i}{\|s_i\|_2 + \alpha_i^2}$$

$$- k_2 \sum_{j \in \mathcal{N}_i} [\beta_2(R_j^T R_i - R_i^T R_j)^\vee + s_i - s_j] \tag{6}$$

where k_1, k_2, and β_2 are three positive constants, and $\hat{J}_i$, $\hat{d}_i$, and α_i are three adaptive parameters. Note that the terms $-k_1 s_i$ and $-k_2 \sum_{j \in \mathcal{N}_i} a_{ij}[\beta_2(R_j^T R_i - R_i^T R_j)^\vee + s_i - s_j]$ are used to track the observer state and achieve the synchronization, respectively. Essentially, $\hat{J}_i$ is the estimate of the positive definite matrix J_i. Note that $J_i \Phi_i^\circ - \omega_i^\times J_i \omega_i$ can be expressed as $J_i \Phi_i^\circ - \omega_i^\times J_i \omega_i = \Psi_i J_i^\star$, where $\Psi_i \in \mathbb{R}^{3 \times 6}$ and $J_i^\star = [J_{i,11}, J_{i,12}, J_{i,13}, J_{i,22}, J_{i,23}, J_{i,33}]^T \in \mathbb{R}^{6 \times 1}$, where $J_{i,kr}$ represents the (k, r) element of J_i. Similarly, $\hat{J}_i^\star$ can be obtained for $\hat{J}_i$, i.e., $\hat{J}_i^\star = [\hat{J}_{i,11}, \hat{J}_{i,12}, \hat{J}_{i,13}, \hat{J}_{i,22}, \hat{J}_{i,23}, \hat{J}_{i,33}]^T$. The updating law of $\hat{J}_i^\star$ can be defined as

$$\dot{\hat{J}}_i^\star = \Gamma_0 \Psi_i^T s_i \tag{7}$$

where Γ_0 is a positive constant.

Since $R_j^T R_i$ is also one element of $SO(3)$, based on Rodrigues' rotation formula, one has $R_j^T R_i = I_3 + (1 - \cos\theta)\bar{n}^\times \bar{n}^\times + \sin\theta \bar{n}^\times$, where θ and $\bar{n}$ are the rotation angle and a unit vector, respectively. Hence, $(R_j^T R_i - R_i^T R_j)^\vee$ satisfies the inequality $\|(R_j^T R_i - R_i^T R_j)^\vee\|_2 = \|2\sin\theta\bar{n}\|_2 \leq 2$.

The closed-loop system can be expressed as

$$J_i \dot{s}_i = \tilde{J}_i \Phi_i^\circ - J_i R_i^T \hat{R}_i \dot{\hat{\omega}}_i - \omega_i^\times \tilde{J}_i \omega_i - k_1 s_i - \frac{\hat{d}_i s_i}{\|s_i\|_2 + \alpha_i^2}$$
$$- k_2 \sum_{j \in \mathcal{N}_i} (s_i - s_j) + d_i \tag{8}$$

where $\tilde{J}_i = J_i - \hat{J}_i$ and $d_i = \bar{d}_i - k_2 \sum_{j \in \mathcal{N}_i} \beta_2(R_j^T R_i - R_i^T R_j)^\vee$. Note that d_i is bounded by $\mu_0 + 2(N-1)\beta_2\kappa_2$. $\hat{d}_i$ is updated by the following law to estimate the bound of d_i:

$$\dot{\hat{d}}_i = \begin{cases} \Gamma_1 \|s_i\|_2 & \text{if } \hat{d}_i \leq \bar{\mu}_0 \\ \Gamma_1 \|s_i\|_2 (1 - \hat{d}_i^{\chi_1} + \bar{\mu}_0^{\chi_1}) & \text{otherwise} \end{cases} \tag{9}$$

where $\chi_1 > 0$ is a even number, $\Gamma_1 > 0$, and $\bar{\mu}_0$ is chosen large enough such that $\bar{\mu}_0 > \mu_0 + 2(N-1)\beta_2\kappa_2$ holds. α_i is introduced to avoid the possible control chattering with the following adaption law:

$$\dot{\alpha}_i = -\frac{\Gamma_2 \alpha_i \hat{d}_i \|s_i\|_2}{\|s_i\|_2 + \alpha_i^2} \tag{10}$$

with $\Gamma_2 > 0$.

Theorem 1 *With the observer in Eq. (4) and the updating laws (7), (9), and (10), if $\bar{\mu}_0 > \mu_0 + 2(N-1)\beta_2\kappa_2$ holds, the controller (6) can complete the attitude synchronization mission almost globally asymptotically.*

Proof Choose the following Lyapunov function $V_2 = \sum_{i=1}^{N}(\frac{1}{2}s_i^T J_i s_i + \frac{1}{2\Gamma_0}\tilde{J}_i^{\star T}\tilde{J}_i^{\star} + \frac{1}{2\Gamma_1}\tilde{d}_i^2 + \frac{1}{2\Gamma_2}\alpha_i^2)$, where $\tilde{d}_i = \bar{\mu}_0 - \hat{d}_i$.

In the case of $\hat{d}_i \leq \bar{\mu}_0$, $-s_i^T d_i + \frac{1}{\Gamma_1}\tilde{d}_i\dot{\tilde{d}}_i = -s_i^T d_i - \tilde{d}_i\|s_i\|_2 \leq \hat{d}_i\|s_i\|_2$ holds. Otherwise, one has $-s_i^T d_i + \frac{1}{\Gamma_1}\tilde{d}_i\dot{\tilde{d}}_i = -s_i^T d_i - (\bar{\mu}_0 - \hat{d}_i)\|s_i\|_2(1 - \hat{d}_i^{\chi_1} + \bar{\mu}_0^{\chi_1}) \leq \bar{\mu}_0\|s_i\|_2 - (\bar{\mu}_0 - \hat{d}_i)\|s_i\|_2(1 - \hat{d}_i^{\chi_1} + \bar{\mu}_0^{\chi_1}) = \bar{\mu}_0\|s_i\|_2 - \bar{\mu}_0\|s_i\|_2(1 - \hat{d}_i^{\chi_1} + \bar{\mu}_0^{\chi_1}) + \hat{d}_i\|s_i\|_2(1 - \hat{d}_i^{\chi_1} + \bar{\mu}_0^{\chi_1}) = \bar{\mu}_0\|s_i\|_2(-\hat{d}_i^{\chi_1} + \bar{\mu}_0^{\chi_1}) + \hat{d}_i\|s_i\|_2 + \hat{d}_i\|s_i\|_2(-\hat{d}_i^{\chi_1} + \bar{\mu}_0^{\chi_1}) < \hat{d}_i\|s_i\|_2$. Hence, $\dot{V}_2$ satisfies the following inequality:

$$
\begin{aligned}
\dot{V}_2 &\leq \sum_{i=1}^{N}\left[s_i^T(-J_i R_i^T \hat{R}_i\dot{\hat{\omega}}_i - k_1 s_i - \frac{\hat{d}_i s_i}{\|s_i\|_2 + \alpha_i^2} - k_2\sum_{j\in\mathcal{N}_i}(s_i - s_j))\right. \\
&\quad \left. + \hat{d}_i\|s_i\|_2 - \frac{\alpha_i^2\hat{d}_i\|s_i\|_2}{\|s_i\|_2 + \alpha_i^2}\right] \\
&\leq \sum_{i=1}^{N}\left[s_i^T(-J_i R_i^T \hat{R}_i\dot{\hat{\omega}}_i - k_1 s_i)\right]
\end{aligned}
\tag{11}
$$

If $\|s_i\|_2 > \|J_i\|_2\|\dot{\hat{\omega}}_i\|_2/k_1$, $\dot{V}_2 < 0$ holds. According to Lemma 1, $\|\dot{\hat{\omega}}_i\|_2 \to 0$ as time goes to infinity. Hence, s_i will go to zero as $t \to \infty$. From the definition of s_i, we have the system governed by $\omega_i - R_i^T\hat{R}_i\hat{\omega}_i + \beta_1(\hat{R}_i^T R_i - R_i^T\hat{R}_i)^{\vee} = s_i$, where s_i is considered as a decreasing control input with time. For such a system, a Morse–Lyapunov function is chosen as $V_{si} = \text{tr}(I_3 - \hat{R}_i^T R_i)$, whose time derivative is

$$
\begin{aligned}
\dot{V}_{si} &= \omega_i^T(\hat{R}_i^T R_i - R_i^T\hat{R}_i)^{\vee} + \hat{\omega}_i^T(R_i^T\hat{R}_i - \hat{R}_i^T R_i)^{\vee} \\
&= -\beta_1(\hat{R}_i^T R_i - R_i^T\hat{R}_i)^{\vee T}(\hat{R}_i^T R_i - R_i^T\hat{R}_i)^{\vee} + s_i^T(\hat{R}_i^T R_i - R_i^T\hat{R}_i)^{\vee}
\end{aligned}
\tag{12}
$$

In the case of $\|(\hat{R}_i^T R_i - R_i^T\hat{R}_i)^{\vee}\|_2 > \|s_i\|_2/\beta_1$, $\dot{V}_{si} < 0$ holds. Considering $s_i \to 0$ as $t \to \infty$, $(\hat{R}_i^T R_i - R_i^T\hat{R}_i)^{\vee}$ will go to zero as time goes to infinity. Note that $(\hat{R}_i^T R_i - R_i^T\hat{R}_i)^{\vee} = 0$ means $R_i = \hat{R}_i$ or $\text{tr}(R_i^T\hat{R}_i) = -1$, where V_{si} is equal to 0 or 4. Hence, only $R_i = \hat{R}_i$ is the stable equilibrium.

Hence, considering the conclusions in Lemma 1, the attitude synchronization of multiple spacecraft can be achieved almost globally asymptotically.

Remark 2 Note that the conclusion of Theorem 1 is attitude synchronization of multiple spacecraft, i.e., $R_i \to R_j$ and $\omega_i \to \omega_j$ as $t \to \infty$ almost globally. The final values of R_i can be time-varying and ω_i can converge to a non-zero value.

4 Simulations

In this section, a numerical simulation is presented to show the effectiveness of the proposed control scheme in Eq. (6) using five rigid spacecraft under the original graph in Fig. 1. The tree graph in Step B(1) in Fig. 1 is used as the generated graph $\mathcal{G}'$. The inertia matrix $\boldsymbol{J}_i$ is chosen as diag$\{25, 20, 8\}$. The external disturbance $\boldsymbol{d}_i$ is set as $0.1 \sin(5t)$ Nm. The initial attitudes and angular velocities of the five spacecraft are

$$\boldsymbol{R}_1(0) = \begin{bmatrix} 0.7474 & 0.5387 & -0.3887 \\ -0.5534 & 0.8287 & 0.0844 \\ 0.3676 & 0.1521 & 0.9175 \end{bmatrix}, \quad \boldsymbol{\omega}_1(0) = [0.0337, 0.0145, 0.0711]^T \tag{13}$$

$$\boldsymbol{R}_2(0) = \begin{bmatrix} 0.3478 & -0.7321 & -0.5858 \\ 0.5453 & 0.6662 & -0.5088 \\ 0.7627 & -0.1425 & 0.6309 \end{bmatrix}, \quad \boldsymbol{\omega}_2(0) = [0.3455, 0.0671, 0.2494]^T \tag{14}$$

$$\boldsymbol{R}_3(0) = \begin{bmatrix} -0.1476 & 0.346 & -0.9265 \\ 0.7834 & -0.5309 & -0.3231 \\ -0.6037 & -0.7735 & -0.1927 \end{bmatrix},$$

$$\boldsymbol{\omega}_3(0) = [-0.1604, -0.1939, -0.0512]^T \tag{15}$$

$$\boldsymbol{R}_4(0) = \begin{bmatrix} 0.7255 & -0.6582 & -0.2011 \\ 0.5594 & 0.7342 & -0.3848 \\ 0.4009 & 0.1667 & 0.9008 \end{bmatrix}, \quad \boldsymbol{\omega}_4(0) = [-0.2, -0.208, -0.0381]^T \tag{16}$$

$$\boldsymbol{R}_5(0) = \begin{bmatrix} 0.7822 & -0.5668 & -0.2586 \\ -0.5456 & -0.4229 & -0.7235 \\ 0.3007 & 0.707 & -0.6401 \end{bmatrix}, \quad \boldsymbol{\omega}_5(0) = [0.022, 0.0235, 0.0719]^T \tag{17}$$

Since the necessary and sufficient condition of $\operatorname{tr}(\boldsymbol{I}_3 - \boldsymbol{R}_j^T \boldsymbol{R}_i) = 0$ is $\boldsymbol{R}_j = \boldsymbol{R}_i$. Hence, $V_{\mathrm{syn}} = \operatorname{tr}(\boldsymbol{I}_3 - \boldsymbol{R}_1^T \boldsymbol{R}_2) + \operatorname{tr}(\boldsymbol{I}_3 - \boldsymbol{R}_2^T \boldsymbol{R}_3) + \operatorname{tr}(\boldsymbol{I}_3 - \boldsymbol{R}_3^T \boldsymbol{R}_4) + \operatorname{tr}(\boldsymbol{I}_3 - \boldsymbol{R}_4^T \boldsymbol{R}_5) \in [0, 16]$ is used to indicate the synchronization error of the five spacecraft. It is straightforward that $V_{\mathrm{syn}} = 0$ holds if and only if the synchronization of the networked spacecraft is achieved. $V_{t,i} = \operatorname{tr}(\boldsymbol{I}_3 - \hat{\boldsymbol{R}}_i^T \boldsymbol{R}_i) \in [0, 4]$ denotes the tracking error of the ith spacecraft with the attitude in the distributed observer as the reference trajectory.

The observer parameters κ_1 and κ_2 are chosen as 0.1 and 0.5, respectively. The remaining control parameters β_1, k_1, k_2, β_2, $\bar{\mu}_0$, Γ_0, Γ_1, and Γ_2 are 0.1, 2, 1, 0.1, 1, 0.01, 0.1, and 0.01, respectively. The initial value of the adaptive parameters $\hat{\boldsymbol{J}}_i^\star$, $\hat{d}_i$, and α_i are set as $\boldsymbol{0}$, 0, and 0.1. As shown in Figs. 2 and 3, the controller finishes

Fig. 2 The synchronization error V_{syn}
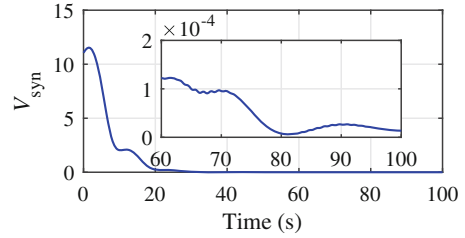
Fig. 3 The tracking error $V_{t,i}$
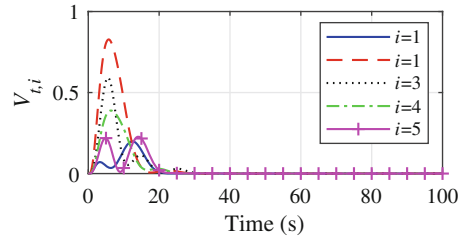
the leaderless consensus of the networked spacecraft at 70 s. Note that Fig. 3 gives the tracking error of each spacecraft. It can be found that the potential function $V_{t,i}$ is less than 1 during the whole mission, i.e., all five spacecraft are far from the undesired equilibriums, where $V_{t,i} = 4$ holds.

5 Conclusions

The leaderless consensus of multiple rigid spacecraft is studied directly on $SO(3)$ under connected undirected graphs. To provide the reference signal for each spacecraft, distributed observers are designed under an undirected tree graph. A control algorithm is presented to achieve leaderless consensus. The stability conditions are given based on the rigorous theoretical analyses. Since the controllers are continuous and developed directly on $SO(3)$, the singularities and ambiguities associated with other attitude representations can be avoided and the controllers' continuity facilitates its implementation in practice. How to extend the current work to the leaderless attitude synchronization on $SO(3)$ under a directed graph can be a future research direction.

References

1. N.A. Chaturvedi, A.K. Sanyal, N.H. McClamroch, Rigid-body attitude control. IEEE Control Syst. **31**(3), 30–51 (2011)
2. L.G. Gong, Q. Wang, C.Y. Dong, Spacecraft output feedback attitude control based on extended state observer and adaptive dynamic programming. J. Franklin Inst. **356**(10), 4971–5000 (2019)

3. J. Bohn, A.K. Sanyal, Almost global finite-time stabilization of rigid body attitude dynamics using rotation matrices. Int. J. Robust Nonlinear Control **26**(9), 2008–2022 (2016)
4. S. Berkane, A. Abdessameud, A. Tayebi, Hybrid global exponential stabilization on $SO(3)$. Automatica **81**, 279–285 (2017)
5. T. Chen, J. Shan, H. Wen, Distributed adaptive attitude control for networked underactuated flexible spacecraft. IEEE Trans. Aerospace Electron. Syst. **55**(1), 215–225 (2019)
6. W. Ren, Distributed cooperative attitude synchronization and tracking for multiple rigid bodies. IEEE Trans. Control Syst. Technol. **18**(2), 383–392 (2010)
7. H. Gui, G. Vukovich, Distributed almost global finite-time attitude consensus of multiple spacecraft without velocity measurements. Aerospace Sci. Technol. **75**, 284–296 (2018)
8. M. Nazari, E.A. Butcher, T. Yucelen, A.K. Sanyal, Decentralized consensus control of a rigid-body spacecraft formation with communication delay. J. Guidance Control Dyn. **39**(4), 838–851 (2016)
9. Y. Zou, Z. Meng, Velocity-free leader–follower cooperative attitude tracking of multiple rigid bodies on so (3). IEEE Trans. Cybern. **49**(12), 4078–4089 (2019)
10. X. Peng, Z. Geng, J. Sun, The specified finite-time distributed observers-based velocity-free attitude synchronization for rigid bodies on so(3). IEEE Trans. Syst. Man Cybern. Syst. **50**(4), 1610–1621 (2020)
11. T. Chen, J. Shan, Distributed adaptive fault-tolerant attitude tracking of multiple flexible spacecraft on $SO(3)$. Nonlinear Dyn. **95**(3), 1827–1839 (2019)
12. Y. Zou, Z. Meng, Z. Zuo, Rotation-matrix-based attitude synchronization of multiple spacecraft without velocity measurements, in *2017 11th Asian Control Conference (ASCC)* (2017, Dec), pp. 96–101
13. S. Weng, D. Yue, T. Yang, Coordinated attitude motion control of multiple rigid bodies on manifold $SO(3)$. IET Control Theory Appl. **7**(16), 1984–1991 (2013)
14. H. Du, M.Z. Chen, G. Wen, Leader–following attitude consensus for spacecraft formation with rigid and flexible spacecraft. J. Guid. Control Dyn. **39**(4), 944–951 (2016)
15. S. Kapoor, H. Ramesh, Algorithms for enumerating all spanning trees of undirected and weighted graphs. SIAM J. Comput. **24**(2), 247–265 (1995)
16. T. Chen, J. Shan, Rotation-matrix-based attitude tracking for multiple flexible spacecraft with actuator faults. J. Guid. Control Dyn. **42**(1), 181–188 (2019)

Part III
Experimental Dynamics

Preliminary Experimental Study on the Influence of the Gap in a Vibro-Impact System with Two-Sided Constraints

Giulia Stefani, Maurizio De Angelis, and Ugo Andreaus

1 Introduction

The impact phenomenon is ubiquitous in many engineering applications involving mechanical components or structures repeatedly colliding with one another or with obstacles. In the context of structural pounding, the occurrence of strong earthquakes can produce large horizontal displacements in base-isolated structures, which can damage the isolation system or can lead to pounding with the surrounding moat walls or adjacent structures, if the available clearance is not sufficient. A possible mitigation measure consists in the interposition of deformable shock absorbers (bumpers). The introduction of the bumpers limits the displacement of the structure, but the possible occurrence of the impact with the bumpers can involve an increase in acceleration which can be detrimental, not only for the structure itself, but also for any sensitive equipment housed in it. At the same time, the occurrence of impact can excessively deform the bumpers. The effect of the introduction of the obstacle depends on several factors, including the mechanical properties of the bumpers and the distance between them and the structure (gap).

The influence of the gap size on the system response was investigated by several authors. In general, the response decreases as the gap increases [1–5]. According to Polycarpou and Komodromos [4, 5], very small seismic gaps, in combination with strong ground excitation, not allowing the structure to develop high velocities before the impact, can lead to relatively milder consequences from pounding. According to Jankowski et al. [6], the optimal gap size to reduce the response is either a very small one or large enough to avoid collisions. The zero-gap configuration was recommended by Aguiar and Weber [7], since it allows to maximize the impact force

G. Stefani (✉) · M. De Angelis · U. Andreaus
Department of Structural and Geotechnical Engineering, Sapienza University of Rome, Rome, Italy
e-mail: giulia.stefani@uniroma1.it; maurizio.deangelis@uniroma1.it; ugo.andreaus@uniroma1.it

in a vibro-impact system without the occurrence of nonlinear jumps. Few works, on the contrary, deal with negative gaps, resulting in an initial pre-stress/pre-strain state in the bumpers. In [8] the authors studied the two cases of normal clearance and prepressing constraints in a two-degree-of-freedom periodically forced system and found that, if the constraints are initially prepressed, the observed behaviors are relatively simpler. The effect of the introduction of a prepressing constraint in a capsule system was investigated in [9].

The practical problem of excessive displacements in base-isolated structures inspired several works of the authors, of both numerical and experimental nature, in which a single-degree-of-freedom oscillator, impacting against two deformable and dissipative bumpers, was considered [10, 11]. The numerical analyses highlighted gradually more varied and complex behaviors, decreasing the gap between mass and bumpers [11]. Furthermore, the combination of small gaps with quite deformable bumpers appeared to be a good choice which allows to realize, compared to the free flight condition, a reduction of both accelerations and displacements or a good compromise between reduction of displacements and limited increase in accelerations [10].

Based on the results of these previous studies, a new laboratory campaign was designed and conducted to investigate, in particular, small positive, null, and small negative values of the total gap between mass and bumpers, not previously tested, in order to validate the numerical predictions. Furthermore, compared to the previous experimental investigations made by the authors, additional sensors were used to better characterize the experimentation. In particular, impact load cells were installed between the mass and the bumpers, to directly measure the contact force during the impact phases. In this work, some preliminary results of the new laboratory campaign will be presented. The attention is focused on the influence of the gap amplitude on the system (mass and bumpers) response, considering, in particular, small, null, and negative gaps. The selected response quantities are the relative displacement and the absolute acceleration of the mass, the contact forces, and the deformation of the bumpers. Although the impact problem has been the subject of several scientific works, there are not too much studies that address this topic in such a systematic way.

The paper is organized as follows. The experimental apparatus, together with the performed tests are introduced in Sect. 2; some preliminary experimental results are presented and discussed in Sect. 3; the conclusions and future developments of the work are finally drawn in Sect. 4.

2 Experimental Setup and Performed Tests

The experimental apparatus is shown in Fig. 1. It consists of a rigid body (mass $M =$ 550 kg), an elastomeric high damping rubber bearing (HDRB) isolator (denoted as "damper" in Fig. 1), and two elastomeric shock absorbers (denoted as right and left bumper, respectively), symmetrically mounted on steel moat walls.
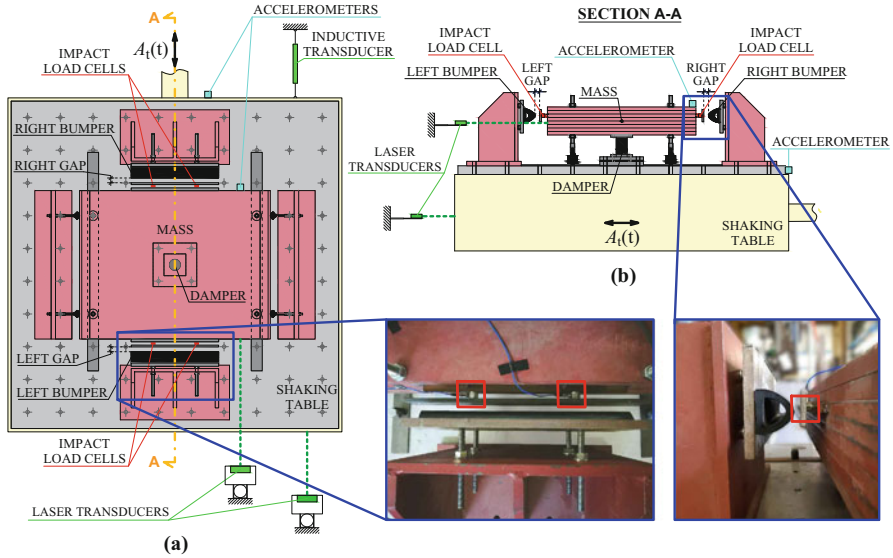
Fig. 1 Experimental setup: (**a**) plan view and (**b**) side view (Section A-A). The zoomed areas show two photos with details of the impact load cells, enclosed by red squares

2.1 Bumpers

Two configurations, namely with and without bumpers (the latter will be referred to as free flight condition), under the same base excitation, were considered. In the experimental laboratory campaign, to study the response of the system in the presence of obstacles, a single elastomeric bumper, with D-shape hollow section (denoted as B2), was tested.

2.2 Gap

Several values of the gap were considered, namely: G∞, G30, G16, G10, G4, G0, G-1, G-2, G-10, where the number, expressed in mm, denotes the amplitude of the total gap, defined as the sum of the right and left gaps (Fig. 1) and G∞ indicates the free flight condition. The negative gaps (G-1, G-2, G-10), obtained experimentally by slightly compressing the bumpers against the mass, involve, as a consequence, an initial pre-stress/pre-strain state in the bumpers. The investigation of small positive, null, and negative gaps represents one of the novelty elements of this laboratory campaign, compared to previous tests and works of the authors.

2.3 Input

The system was excited, using the shaking table, by a stepwise forward and backward sine sweep in displacement control, in order to impose a given value of peak table acceleration A, with a number of cycles n_c, in each sub-frequency range, such as to reach the steady state condition. In this work, some of the results corresponding to A $=$ 0.05g, where g is the gravity's acceleration, will be shown. For G $>$ 0, the investigated frequency range was between 0.5 and 5 Hz, with frequency step $\Delta f = 0.1$ Hz and $n_c = 10$. For G $\leq$ 0, the investigated frequency range was extended from 0.5 to 10 Hz, with frequency step $\Delta f = 0.1$ Hz and $n_c = 10$. In some cases, especially for small positive gaps, in order to better capture the experimental response of the system in the low frequency range, further input signals were imposed, characterized by reduced frequency steps Δf (up to 0.03 Hz) and greater number of cycles n_c (up to 30 cycles), depending on the performances of the shaking table.

2.4 Sensors

The measured quantities during the tests were the absolute (or total) accelerations and displacements of the mass and of the shaking table and the contact forces between mass and bumpers. The accelerations were measured by accelerometers and the displacements by laser transducers (Fig. 1). The forces developed at the moment of impact between mass and bumpers were measured by four impact load cells, symmetrically mounted on the mass, two on each side (see the two zoomed areas in Fig. 1). Between the impact load cells and the bumpers, steel plates were mounted to distribute the impact force. The use of impact load cells represents another novelty element of this laboratory campaign, compared to previous tests and works of the authors.

3 Preliminary Experimental Results

The evolution of the experimental forward (solid lines) and backward (dashed lines) Pseudo-Resonance Curves (PRCs) with the total gap G is represented in Fig. 2, where each color corresponds to a gap amplitude and the thickness of the lines is gradually reduced as G decreases. In Fig. 2a,b the black curves denote the free flight condition. The represented response quantities are: the normalized excursion of relative displacement of the mass $\eta_d = \frac{E_d}{E_{d0}} = \frac{u_{max} - u_{min}}{2u^*}$ (Fig. 2a), the normalized excursion of absolute acceleration of the mass $\eta_a = \frac{E_a}{E_{a0}} = \frac{a_{max} - a_{min}}{2a^*}$ (Fig. 2b), the normalized deformation $\eta_j = \frac{u_{j,max}}{u^*}$ (j = R, L) (Fig. 2c), and contact force $r_j = \frac{F_{j,max}}{Mg}$ (j = R, L) (Fig. 2d) of the right (B_R) and left (B_L) bumpers, respectively.
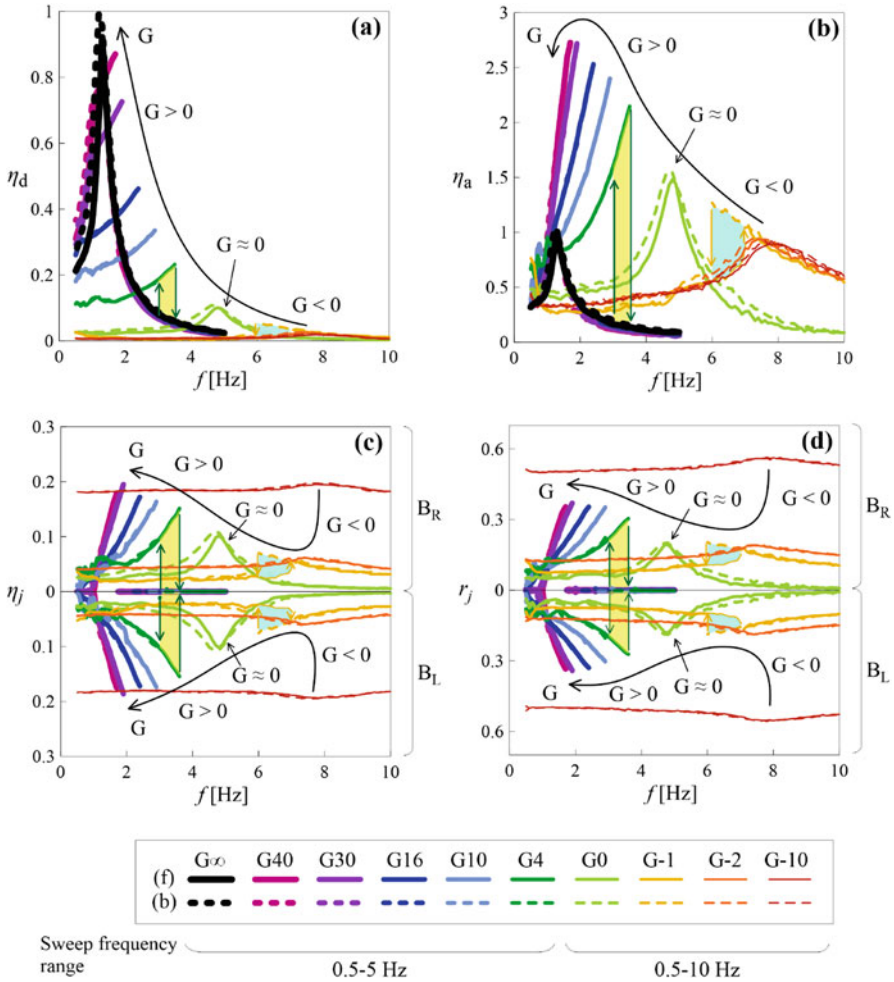
Fig. 2 Forward (*solid lines*) and backward (*dashed lines*) PRCs of: (**a**) η_d; (**b**) η_a; (**c**) η_j ($j = $ R, L) and (**d**) r_j ($j = $ R, L) for different values of the total gap G. In (**a**) and (**b**), the free flight condition (G∞) is represented with black curves and the PRCs corresponding to G-2 and G-10 are substantially superimposed on each other

In the first three cases, the normalization was made with respect to the free flight resonance condition (u^* and a^* denote the maximum relative displacement and absolute acceleration of the mass in free flight resonance condition).

As concerns the mass (Fig. 2a,b), it can be observed that, compared to the free flight condition (black curves), the hardening caused by the impact between the mass and the bumpers (G > 0) bends the PRCs to the right, causing the occurrence of jumps (represented with vertical arrows for G4), and thus of a *primary right hysteresis* (highlighted in yellow for G4). As G decreases, the maximum value of

η_d decreases due to the constrain exerted by the bumpers, whereas the acceleration, after an initial increase, starts to decrease. Gradually more complex scenarios at low frequencies, associated with *secondary resonances*, as G decreases were observed, confirming previous numerical results [11]. The situation returns to be smooth for bumpers initially more or less in contact with the mass (G ≃ 0), with the resonance shifted to higher frequencies and without jumps or hysteresis. For small negative values of the gap (G-1), PRCs bend to the left, due to a softening-like behavior, showing jumps (represented with vertical arrows) and a *primary left hysteresis* (highlighted in cyan). The softening is caused by the detachment of the mass from the bumpers, during its motion. For negative gaps exceeding a certain value which, for B2, is between G-1 and G-2, the mass, during its motion, always remains in contact with both bumpers and therefore, the resisting force is given by the sum of the forces exerted by the damper and the two bumpers. Consequently, for G-2 and G-10, since detachment never occurs, the PRCs of η_d and η_a are no longer bent and show neither jumps nor hysteresis. Furthermore, they appear to be substantially overlapped. This is due to the fact that, further increasing the negative gap, beyond a certain value, does not affect the mass response.

As concerns the two bumpers (Fig. 2c,d), the PRCs of the normalized deformation and contact force are symmetrical due to the mostly symmetric behavior of the studied system. It can be observed that the trends of both the deformation (Fig. 2c) and the contact force (Fig. 2d) are qualitative similar to each other and, for what concerns the cases where G ≥ 0, they are analogous to that of the acceleration of the mass (Fig. 2b). The jumps and hysteresis are still visible also in these curves. Compared to the PRCs of η_d and η_a, for G ≥ 0, the PRCs of η_j and r_j (j = R, L) are zero in the absence of impact. On the contrary, for negative gaps (G < 0) the PRCs assume non-zero values for all frequencies, due to the initial pre-stress/pre-strain state of the bumpers resulting from the negative gaps. Unlike what was seen for the mass (Fig. 2a,b), the PRCs of η_j and r_j (j = R, L) for G-2 and G-10 do not overlap, but they have shifted with respect to each other. Passing from G-2 to G-10, the PRCs move away from the frequency axis, with the extent of the shift related to initial pre-stress/pre-strain state caused by the negative gap. It can be observed that these PRCs, once the initial shift value has been removed, are substantially the same.

Analogous considerations can be made by looking at Fig. 3, in which the force-displacement cycles, in primary resonance condition, are represented, for both the mass (inertia force F_I vs. relative displacement u of the mass, Fig. 3a) and the two bumpers (contact force F_j vs. position v_j (j = R, L) of the bumper, Fig. 3b). As in Fig. 2, each color corresponds to a gap amplitude G and the vertical dashed lines represent the initial position of the bumpers for G > 0. These synthetic representations allow to see, in the same figure, the evolution of both the forces and the displacements with the amplitude of the gap. In Fig. 3a both the hardening-like behavior, caused by the occurrence of impact (for G > 0) and the softening-like behavior, caused by the detachment, for small negative gaps (G-1, light orange curve) are observable. For G-2 and G-10, the F_I-u cycles are substantially overlapped, since, as previously said, negative gaps beyond a certain value, do not affect the mass response. On the contrary, the pre-stress state induced in the bumpers
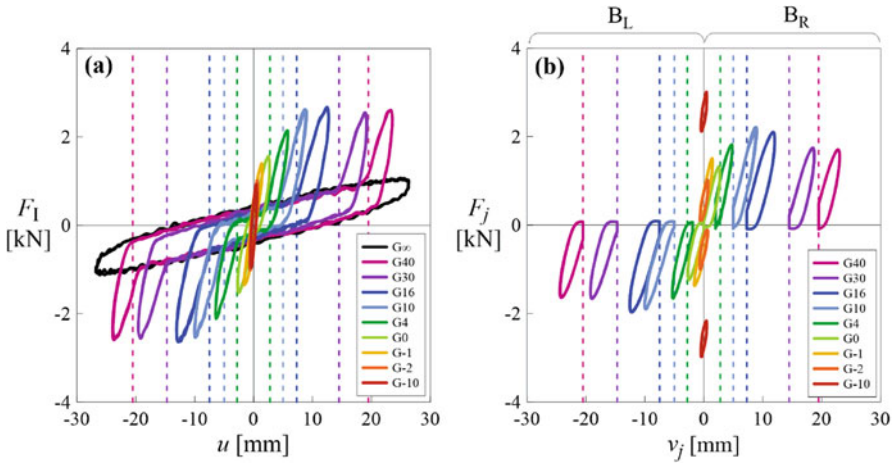
Fig. 3 Force-displacement cycles in primary resonance condition corresponding to the investigated values of the total gap G: (**a**) mass; (**b**) bumpers

by the negative gap causes the F_j-v_j ($j = $ R, L) cycles to move away from the x-axis (Fig. 3b).

4 Conclusions and Future Developments

Some preliminary results of an experimental laboratory campaign, designed based on the outcomes of previous studies of the authors, were presented. Compared to previous tests, also small positive, null, and small negative values of the total gap between mass and bumpers G were considered. Furthermore, impact load cells were used to directly measure the contact force between mass and bumpers during the impact phases. The preliminary experimental results confirmed the numerical outcomes.

The amplitude of the gap was found to influence the response of both the mass and the bumpers for G > 0, where the occurrence of impact causes a hardening-like behavior, characterized by the presence of jumps and a *primary right hysteresis* in the PRCs. In particular, referring to the primary resonance condition, the reduction of the gap causes the reduction of the relative displacement of the mass and an increase, followed by a decrease, of the absolute acceleration. A trend similar to the latter one was observed also in the deformation of the bumpers and in the impact force, which attain zero values in the absence of impact. By putting the bumpers initially, more or less, in contact with the mass (G $\simeq$ 0) the situation returns to be smooth, without jumps and hysteresis, although the behavior is still nonlinear. For small negative gaps (G-1), both the relative displacement and the absolute acceleration of the mass, the bumpers' deformation, and the contact force,

in resonance condition, continue to decrease. Compared to G > 0, a softening-like behavior was observed, characterized by the occurrence of jumps and a *primary left hysteresis*. Furthermore, due to initial pre-stress/pre-strain state resulting from the negative gap, the PRCs of both the bumpers' deformation and the contact forces are always greater than zero for each frequency value. In a dual manner with respect to G > 0, the softening-like behavior is caused by the detachment from the mass and the bumpers. For negative gaps exceeding a certain value which, for bumper B2, is between G-1 and G-2, the mass, during its motion, always remains in contact with both bumpers and therefore, the resisting force is given by the sum of the forces exerted by the damper and the two bumpers. In this case, further increasing the absolute value of the negative gap will only increase the stress and strain state of the bumpers without further affecting the response of the mass.

With regard to the future developments of this work, the authors intend to finish processing the recorded data and to extend the experimental laboratory campaign also considering the earthquake excitation. Furthermore, comparisons with the results obtained with a suitable numerical model will be carried out.

References

1. S.A. Anagnostopoulos, Pounding of buildings in series during earthquakes. Earthq. Eng. Struct. Dyn. **16**, 443–456 (1988)
2. P. Komodromos, P.C. Polycarpou, L. Papaloizou, M.C. Phocas, Response of seismically isolated buildings considering poundings. Earthq. Eng. Struct. Dyn. **36**, 1605–1622 (2007). https://doi.org/10.1002/eqe.692
3. P. Komodroms, Simulation of the earthquake-induced pounding of seismically isolated buildings. Comput. Struct. **86**, 618–626 (2008)
4. P.C. Polycarpou, P. Komodromos, On poundings of a seismically isolated building with adjacent structures during strong earthquakes. Earthq. Eng. Struct. Dyn. **39**, 933–940 (2010)
5. P.C. Polycarpou, P. Komodromos, Earthquake-induced poundings of a seismically isolated building with adjacent structures. Eng. Struct. **32**, 1937–1951 (2010)
6. R. Jankowski, K. Wilde, Y. Fujino, Reduction of pounding effects in elevated bridges during earthquakes. Earthq. Eng. Struct. Dyn. **29**, 195–212 (2000)
7. R.R. Aguiar, H. Weber, Impact force magnitude analysis of an impact pendulum suspended in a vibrating structure. Shock Vib. **19**, 1359—1372 (2012)
8. T. Luo, Z. Wang, Periodically forced system with symmetric motion limiting constraints: Dynamic characteristics and equivalent electronic circuit realization. Int. J. Nonlin. Mech. **81**, 283—302 (2016)
9. Y. Yan, Y. Liu, M. Liao, A comparative study of the vibro-impact capsule systems with one-sided and two-sided constraints. Nonlinear Dyn. **89**, 1063—1087 (2017)
10. U. Andreaus, M. De Angelis, Influence of the characteristics of isolation and mitigation devices on the response of single-degree-of-freedom vibro-impact systems with two-sided bumpers and gaps via shaking table tests. Struct. Control Heal. Monit. **27**(5), e2517 (2020)
11. G. Stefani, M. De Angelis, U. Andreaus, Scenarios in the experimental response of a vibro-impact single-degree-of-freedom system and numerical simulations. Nonlinear Dyn. 103, 3465–3488 (2021). https://doi.org/10.1007/s11071-020-05791-4

Experimental Investigation of Nonlinear Dynamics in Pilot Induced Oscillations Using FlightGear Flight Simulator

Giuseppe Avon, Arturo Buscarino, and Luigi Fortuna

1 Introduction

Pilot induced oscillation is the result of a detrimental collaboration between human and machine [1]. PIOs onset conditions are usually related to high gain tasks, which intuitively could be associated with abrupt and abnormal changes in flight envelope but also, counterintuitively, are part of standard and well-defined flight operations [2].

While high precision tasks are normal part of the pilot routine, the onset of severe PIO is an extraordinary event. This implies the need of a precursory trigger, which can be embodied in an unexpected event produced by the external environment [3]. Generating PIOs as a result of specific aircraft model input excitation allows the study of their onset, of their detection and eventual mitigation and/or suppression. Interesting results may be observed by feeding waveforms to pilot inputs and studying the response of the aircraft flying inside a simulator, which has several different physics models working together to calculate the overall vehicle dynamics.

Following recent results [4], the paper aims at investigating the onset of PIOs as a consequence of a nonlinear dynamical process. For the purpose of the work, pilot contribution is reduced to a simplified model which includes parametrizable delays, dead bands, gains and saturations. The artificial nature of the input waveforms represents a valid expedient to model the abrupt PIO triggering event. Feeding

G. Avon
DIEEI, University of Catania, Catania, Italy

A. Buscarino (✉) · L. Fortuna
DIEEI, University of Catania, Catania, Italy

CNR-IASI, Italian National Research Council Institute for Systems Analysis and Computer Science, A. Ruberti, Rome, Italy
e-mail: arturo.buscarino@unict.it

these as pilot actions to the simulator input endpoints finally allows their study and characterization.

The paper is organized as follows. In Sect. 2, the aircraft–pilot coupling is described, in Sect. 3, the system setup and in Sect. 4 the experimental setup are discussed. In Sect. 5 simulation setup and experimental results are discussed. Finally, conclusive remarks are reported in Sect. 6.

2 Aircraft–Pilot Coupling (APC)

Aircraft–Pilot coupling events are unwanted aircraft motions originating from the interactions between the craft itself and the pilot. These motions include changes in the flight path, which may result in sustained oscillatory motions. The APC term is used aside PIO, sometimes as a substitute, to remove the subtle presumption of blame on the human component of the loop. Although APC events have traces back in the history of the aviation, most of the severe events results from lacks in the aircraft design, especially regarding the flight control system. APC events are not necessarily oscillatory, giving another reason for the term substitution. However, even if is often difficult to pinpoint the cause of specific events, both oscillatory and non-oscillatory APCs result from a deviation between pilot intentions and aircraft response. Moreover, considering that aircraft (either by design or by the FCS actions) is dynamically stable, APCs events result only from the added collaboration of the pilot, which is misled in taking actions which derive in an adverse or catastrophic result.

3 System Setup Analysis

The setup phase, which led to this initial investigation, was aimed at finding a simplified model which can be fed to the flight simulator environment as pilot input, in order to recreate the oscillations. Key to the right model re-creation is the understanding of the cardinal points, which involves the aircraft part, the human part and their coupling, in order to create the oscillation.

Severe PIOs start from a triggering event, which generally involves the pilot, the craft or both. The trigger can be produced by the environment (wind gusts, turbulences) or from the aircraft (system failure, mode shifting of the flight control system). The trigger changes the pilot dynamic response to a high gain closed-loop mode, which may lead to a momentary excessive and exclusive concentration (the so-called tunnelling), which results in overreaction. The severity, which result in the increased gain, is inversely proportional to the expectance of the event (resulting from the adrenaline surge) or the stress of the task (refuelling, landing, take-off, evasive manoeuvres). The gain in pilot response application is also function of the experience of the pilot: novices attempt to control the aircraft with higher

gain, where experienced pilots tend to have a more developed mental model of the controlled dynamics. Moreover, a wrong control variable used by the pilot to recreate the mental process image may also represent a key to the PIO triggering. However, a trigger is a fundamental condition to the PIO onset.

From the aircraft side, the onset of PIOs is helped by some onboard mechanisms, which are in-between the pilot input and the control surfaces. Rate limiting has been recorded in most severe PIO events, alongside with time lags. Rate limiting is usually introduced explicitly by the command gain shaping (flight control system modes), and implicitly from the actuator and surface rate. Moreover, another source of nonlinearity in whole piloting process is due to the saturations: Starting from the flight stick and ending with the obvious surface, every element in the control chain has to deal with saturations. While these effects are limited in the primitive "manual" control systems, where pilot had direct (or quasi-direct) mechanical connection from the stick to the control surface, the problem is exacerbated in modern Fly-By-Wire flight control systems. In fact, in modern flight solutions, rate limiting, saturations and time lag may not be indicated (visually or by some sort of feedback) in the highly mediated control platform they propose. When the pilot has to deal with demanding tasks which require a higher gain, it becomes easy to enter the nonlinear rate limiting regions, which are immediately translated in sudden phase lag introduction, typical of the "jump resonance" phenomenon [5].

Another source of nonlinearity which is PIO related is intrinsic in the Fly-By-Wire systems. They in fact tend to apply a specific gain as a function of the pilot's command signal or on the current flight mode.

4 Experimental Setup

The experimental setup is essentially composed of two elements: the flight simulator and the pilot model. The pilot model is essentially a simplified pilot model, which has sensory input from the aircraft simulation platform, uses a setpoint to produce an output and sends it again to the flight simulator. FlightGear was chosen as simulator platform, essentially for two reasons: free availability and customization options. This allows a very fast setup of a test bench which can be further improved once assessed its validity.

4.1 The Flight Simulator Platform

FlightGear is an open-source flight simulator which can run on almost every major platform (Windows, MAC, Linux). Source code for the entire project is available and the purpose of the project is to create a framework which is suitable for use in research, academic environment, pilot training and other flight-related tasks. Among

the features, the main which is used in the experimental setup is called Generic Protocol and allows external programs to communicate with the flight simulator.

4.2 Pilot Model

The pilot action is modelled using a Python script, in which customization is allowed in terms of:

– Dead bands;
– Saturation;
– Rate limiting;
– Time-delay.

The pilot itself is modelled as a PID controller, in which a sinusoidal setpoint, in terms of roll or pitch, is given. The sinusoidal input in setpoint is given as a frequency sweep. The Python script is conceived as a listener from the UDP socket where the flight simulator is producing and streaming data. As long as samples arrive, they are parsed and an output is produced accordingly.

The pilot routine in the script requires the aircraft to be started from straight-and-level flight from an adequate flight level, in order to avoid terrain collision. The routine takes control of the aircraft and sustains the straight-and-level condition for a specified amount of time, before starting with the sinusoidal sweep. The initial straight and level is maintained to allow the dissipation of oscillations due to the mode switching. When the timeout expires, the script starts by changing the roll or the pitch setpoint, allowing for the pilot controller to do the adjustments. Aircraft response is observed, in order to understand what are the main factors that promote the PIO onset. Output data is saved locally, in order to allow further analysis and processing.

4.3 FlightGear Generic Protocol

As mentioned before, FlightGear supports a simple yet powerful interface to produce and consume data for the simulator. This is done essentially using an XML file where specifications on the variables produced or consumed, together with a protocol format specification can be given. In the experiment setup, format chosen was simply a CSV list of the values for roll/pitch/yaw (input) and normalized aileron/elevator/rudder position (outputs). Generic protocol definition also allows the use of binary or text modes, alongside with line separators, variable separators, pre-amble and post-ambles. The generic protocol input and outputs can be directed towards serial port or network; in the chosen testbench, UDP protocol was chosen. Moreover, the sampling frequency can be also chosen, which specifies the rate of production of data and was fixed to 10 Hz.

5   Simulation Setup and Results

The chosen aircraft, which is the default FlightGear one, is the Cessna 172. It was chose as it is one of the most detailed models (in terms of simulation and since it has no flight control systems or fly-by-wire, which can introduce further elements in the control chain. Simulation conditions are always chosen to be the best for the flight (fair day, noon). Manual take-off is carried on to bring the aircraft to a defined altitude. Script is started once the aircraft is in the straight-and-level condition. First test campaign was assessed on the roll axis. As the Cessna 172 is a propeller aircraft, every measurement has an offset which is due to the propeller torque factor. Initial or residual oscillations shown in figures are mainly due to the controller action compensation for the left bank/yaw tendency of the aircraft against the aforementioned propeller parasitic effect. The initial experimental campaign, which actually confirmed PIO literature, is proof of the platform setup suitability for analysis.

5.1   Pilot Gain

As mentioned before, pilot gain is not always constant and PIO onset is often associated with an increase of this value. This is mainly due to the increased attention, to the degree of the expectancy of the event and to the experience of the pilot. As expected, an increase on the pilot static gain, as in Fig. 1, is translated in a more pronounced oscillatory behaviour around the setpoints, as shown in
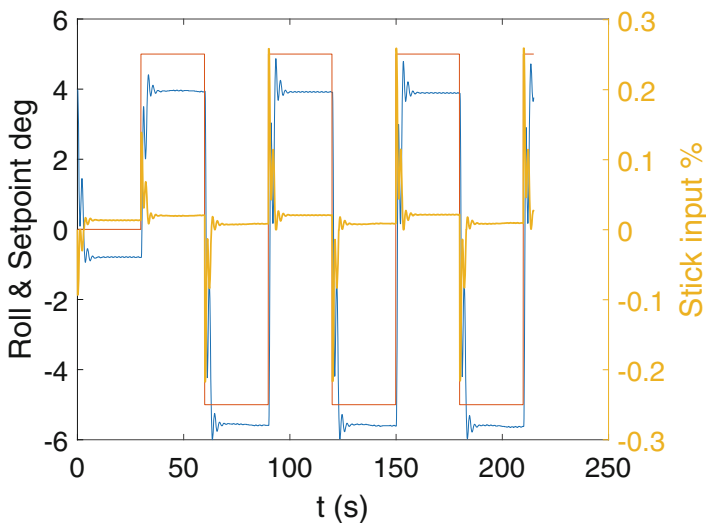
Fig. 1 Square wave input signal for roll under ideal conditions (Kp = 0.025 and delay 1 sample)
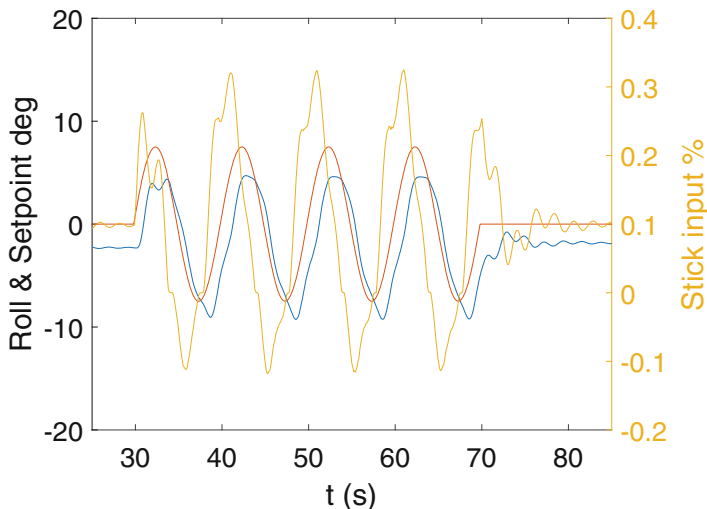
Fig. 2 Nonlinear effects enhanced by pilot gain, with Kp 0.055, deadband 0.5 and saturation 0.9 with 1 sample delay

Fig. 2. However, anomalous high gain control results in immediate aircraft loss of control, which translates into a crash without recovery possibility in the simulator. Breakdown values are observable for gain values around 0.06 on the specific setup. This value is however, as expected, extremely sensitive to other simulation parameters.

5.2 Delay Effect

Delay effect, as it may be introduced from a digital flight control system or by a real pilot has a detrimental effect on the oscillation onset. As pilot delay increases, its control action becomes more and more out of phase, with respect to the real aircraft situation. In the specific example, a delay of 10 samples (which is 1 s delay) in the control action has obviously a catastrophic effect on the aircraft flight, to the point where no straight-and-level condition can be achieved and a triggering event may lead to a total loss of control in about 3 cycles. Test campaigns which were conducted, has evidence that the maximum allowable delay is around 0.3 s. Figure 3 shows the detrimental effect of 10 samples delay in the controller, which unavoidably leads the aircraft to an out-of-control status. However, the exact breakdown point for maximum allowable delay has, again, dependency on the other controller parameters.
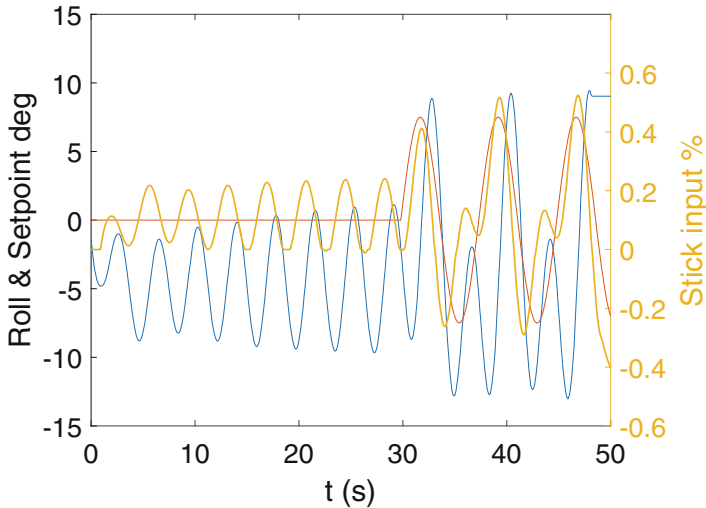
Fig. 3 Nonlinear effects enhanced by time-delay, Kp at 0.02625 with a time-delay of 10 samples

5.3 Saturation Effect

In this initial test campaign, the effect of saturation was simply modelled by putting a maximum on the allowed stick position for the pilot. The increment of the saturation width is also a detrimental effect on the PIO onset as increases the pilot feeling of aircraft non-responsiveness, which from the control point of view translates in missing or ineffective control action on the aircraft dynamics. Test campaign, summarized in Fig. 4, conducted evidence that a reduction of about 20% is allowable in sustaining triggering events, while losing the 25% of the stick effect is sufficient to lead to aircraft loss of control. The effect is more visible in one direction, due to the ease for the aircraft to bank in the p-factor induced preferential direction.

5.4 Deadband Effect

Deadband has, counterintuitively, a positive effect on the PIO mitigation. Deadband increase subtly implements the "stick-freezing" manoeuvre, which is commonly used to mitigate the aircraft oscillations. The introduction of deadbands in controls shows the rise of superimposed harmonics on the aircraft roll, as reported in Fig. 5.
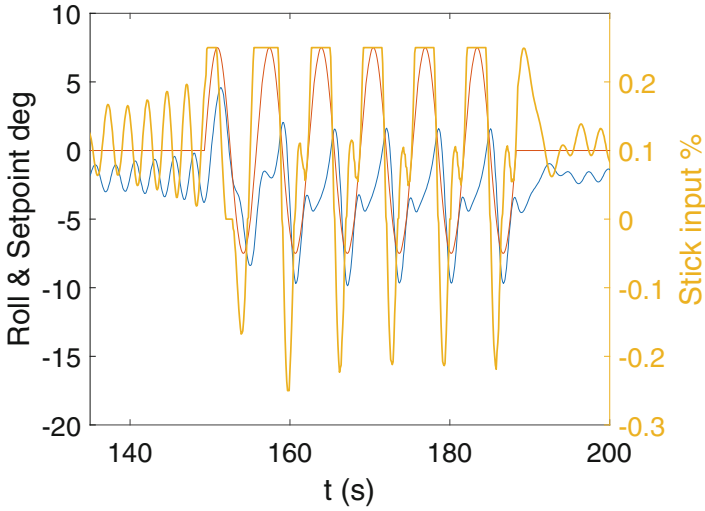
Fig. 4 Nonlinear effects enhanced by saturation, Kp at 0.0525, saturation at 0.25 and delay of three samples. Notice the saturation hitting during the left bank, due to the p-factor imbalance in banking ease
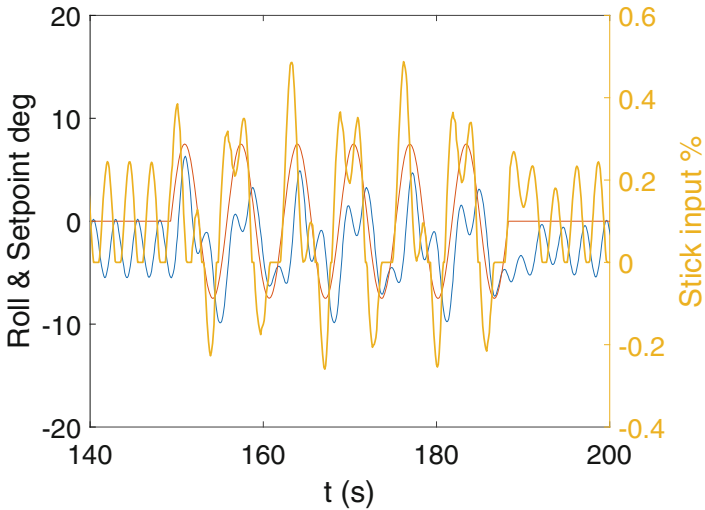
Fig. 5 Nonlinear effects enhanced by deadband, Kp at 0.0525, deadband at 1.5° of bank in both directions

6 Discussions and Conclusions

The study of PIOs as a result of oscillatory perturbation on flight sticks while observing the aircraft response is generally carried out as part of the aircrafts testing routine to assess their resilience, while PIO handling and suppression are part of the pilot knowledge base. The examination of the PIO phenomena as scenarios of nonlinear dynamics can give possible further explanations to their occurrence. Through the use of FlightGear simulator, which offers reasonably good flight dynamic models and superb integration possibilities, a simulation routine is established. The routine consists mainly of the setup of consistent conditions over all the experiments conducted, including weather, flight level, aircraft weights and other major flight-influencing aspects. Aircraft data are flowed out the simulator as a stream, which feeds the custom developed aircraft simulation model. First of all, a fixed amount of time pursuing the straight-and-level flight is given to allow decay of residual oscillations arising from the switch between manual and automated modes. After that, a setpoint variation waveform is fed into the pilot model, which translates into the related stick movement and, consequentially, into aircraft angles. The pilot model, which has configurable delays, setpoints, saturations and gains, flies the aircraft into pursuing the desired pitch and bank angles. The onset of oscillations is then studied, relating the frequency of occurrence, the amplitude and the oscillatory mode to the pilot model parameters. Results suggest relationships between deadband width, rate limitation and delay on pilot intervention which could, in turn, suggest mitigation and suppression strategies. Significant combinations for Kp, deadband, saturation and roll setpoint frequency were chosen among significant ones by systematically sweeping on them, with suitable ranges.

References

1. M.R. Anderson, Pilot-induced oscillations involving multiple nonlinearities. J. Guid. Control Dyn. **21**(5), 786–791 (1998)
2. R.A. Hess, P.W. Stout, Assessing aircraft susceptibility to nonlinear aircraft-pilot coupling/pilot-induced oscillations. J. Guid. Control Dyn. **21**(6), 957–964 (1998)
3. https://skybrary.aero/index.php/Pilot_Induced_Oscillation
4. M. Bucolo, A. Buscarino, L. Fortuna, S. Gagliano, Bifurcation scenarios for pilot induced oscillations. Aerospace Sci. Technol. **106**, 106194 (2020)
5. A. Buscarino, C. Famoso, L. Fortuna, M. Frasca, Multi-jump resonance systems. Int. J. Control **93**(2), 282–292 (2020)

Recurrence Plot Qualification Analysis of the Greyhound Rotary Gallop Gait

Hasti Hayati, David Eager, and Sebastian Oberst

1 Introduction

Accelerometry has been widely used in the field of biomechanics for different purposes from clinical setting [1, 2] to gait characteristics analysis [1, 3–7]. Inertial measurement units (IMU), which are usually equipped with accelerometers, gyroscope and magnetometer [8], can be used to study dynamics such as turning [9, 10], locomotion on difficult terrains [11] and amusement rides [12] where conventional measurement methods are not feasible. One common drawback of IMU is that their sampling rate is rather low as compared to high-end laboratory equipment, a trade-off to the versatility of these devices.

Accelerometry has been used to analyse the hunting dynamics of wild cheetah via a collar-shaped IMU. Using a conventional time-domain analysis, it is found that the spike in the anterior–posterior signals is approximately the stride-cuts and was due to the hind-leg impacts [13]. The same results have been observed, both through the time-domain and time-frequency-domain analysis on racing greyhounds [9, 10, 14]. Accelerometry has also been shown to be suited to study indirectly different terrains or the effect of different terrains on the dynamics of locomotion, a problem less often explored. Spence et al. used a custom designed accelerometer backpack attached close to the centre of mass (CoM) of a cockroach to study the effect of leaf-litter as complex terrain on the locomotion dynamics of rapid insects [11]. The peaks of the CoM dorsal-ventral acceleration on soft surfaces were smaller compared to those belonging to running on rigid surfaces [11].

While incredibly robust and fast to compute, frequency-domain approaches do not provide the same level of information as time-domain methods [15]. The latter

H. Hayati (✉) · D. Eager · S. Oberst
School of Mechanical and Mechatronic Engineering, University of Technology Sydney, Ultimo, NSW, Australia
e-mail: hasti.hayati@uts.edu.au

331

on the other hand, often fail to provide reliable measures or their ease of application is significantly hampered either due to missing analysis frameworks or due to the complexity of the analysis itself [16].

The greyhound racing pushes the dogs to their physical limits which sometimes results in injuries and subsequent euthanisation; to prevent this and to develop countermeasures, the biomechanics and dynamics of greyhound galloping gait including the relationship to ground reaction forces need to be better understood. This research uses an IMU to measure and then explain greyhound characteristics galloping over two different terrains, wet sand and natural grass. An IMU was chosen as it is capable of reliably recording field data for a galloping greyhound. In addition to conducting a frequency-domain analysis, we also conducted a continuous wavelet transform (CWT) and an extended time-domain analysis based on the reconstructed phase space (RPS), making use of nonlinear time series analysis, founded on nonlinear dynamics theory. While being more complex, we hypothesise that the CWT and especially the RPS will provide more information, beneficial to study the effect of different racing track grounds.

2   Methods

2.1   Experimental Setup

Two oval-shaped greyhound race tracks of different surface type–wet sand and natural grass–were selected.

Six randomly selected greyhounds ran individually on a track with a grass surface. The grass track was oval-shaped with a turn radius of 84 m. Six randomly selected greyhounds ran individually on a track with a wet sand surface. The sand track was also oval-shaped with a turn radius of 53 m.

Only galloping on the straight section of the tracks was analysed so as to eliminate the effect of other possible variables such as Turning.

To measure the dynamics, an in-house IMU device equipped with a 185 Hz tri-axial accelerometer capable of measuring acceleration up to 16G was used. The IMU allows tracking of tri-axial body rotation, tri-axial linear body acceleration and tri-axial magnetic heading. Only the tri-axial linear accelerations were analysed in this study. A simultaneous kinematics study was performed using two Sony DSC-RX10-III HFR cameras, one set to 50 fps to capture the entire race, the other set to 500 fps to capture at least two full strides of the greyhound with greater resolution. The HFR camera was mounted close to the finish line ensuring greyhounds were at their highest speed and at a steady-state gallop (Fig. 1).
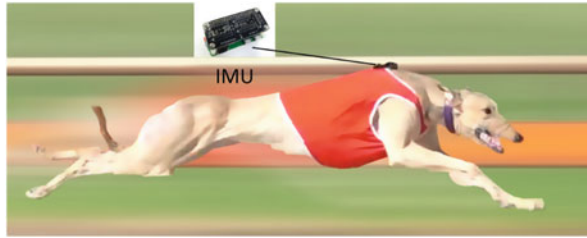
Fig. 1 A greyhound galloping over a sand track with the IMU mounted approximately above the greyhound's centre of mass

2.2 Frequency-Domain, Time-Frequency Domain Analysis and Phase-Space Analysis

2.2.1 Fast Fourier Transform (FFT)

This is a powerful tool in signal processing which is applied in numerous fields [17]. The FFT is based on the discrete Fourier transforms (DFT) but is much faster than DFT and allows to determine the dominant modes (resonances) in a vibrating system. The DFT is defined as

$$X(k) = \sum_{n=0}^{N-1} x(n) e^{-j2\pi n/k}, k = 0, 1, ..., N \tag{1}$$

where $x(n)$ is a finite data sequence in time-domain consisting of N elements and $e^{-j2\pi n/k}$ is a primitive Nth root of 1 [18].

2.2.2 Continuous Wavelet Transform (CWT)

This is another strong tool in signal processing which decomposes a time series into time-frequency space. In other words, using wavelets allows determining both the dominant modes and how those modes vary with time. The CWT is a type of wavelet analysis that provides an over-complete representation of a signal by letting the translation and scale parameter of the wavelets vary continuously and is defined as

$$W_n(s) = \sum_{n'=0}^{N-1} x(n') \sqrt{\frac{\delta t}{S}} \Psi_0^* \left[\frac{(n - n'\delta t)}{S} \right] \tag{2}$$

where S is the wavelet scale and Ψ is wavelet translation with $*$ symbolising a complex conjunction [19].

Although the use of FFTs and CWT, and linear-time-series analyses could provide informative data with regards greyhound gait, they are limited and are not the best tools to understand complex and highly nonlinear dynamics or transient processes of galloping greyhounds. Thus, frequency and wavelet analyses are compared to each other and complemented by a recurrence plot quantification analysis (RPQA) based on embedding the dynamics in the phase space which is suitable to study nonlinear dynamics but also allows a study of stochastic processes and non-stationary events [16]. These methods will be briefly introduced.

2.2.3 Phase-Space Reconstruction (RPS) and Recurrence Plots (RP)

Phase-space reconstruction is the foundation of nonlinear time series analysis that allows the reconstruction of complete system dynamics using a single time series [20]. The most common approach for RPS time series is based on Takens' delay embedding theorem [21]. Using this theorem, a single vector of the observations representing a chaotic system is used to reconstruct a multi-dimensional system. The regenerated vectors can thus display numerous essential properties of its real time series provided that the embedding dimension is sufficiently large [22].

RP is an advanced technique of nonlinear data analysis, introduced in late 1980s [16]. It is a visualisation (or a graph) of a square matrix, in which the matrix elements correspond to those times at which a state of a dynamical system recurs (columns and rows correspond then to a time-delayed pair of values) [16, 23].

3   Results and Discussion

FFT Results The frequency-domain results of a greyhound galloping on a grass track and on a sand track are shown in Fig. 2. There are three dominant frequencies at 3.5, 7 and 10 Hz, cf. Fig. 2a,c. The 3.5 Hz frequency is attributed to the gait frequency of the galloping greyhound (cycle) and 7 Hz frequency is the step frequency. The 12 Hz frequency attributes to paw strikes repeating four times each stride [14].

CWT Results The discrete wavelet transform was applied on data indicated as abrupt signal alterations shown in Fig. 2b,d, where the time-varying frequency (Hz) is plotted against time (s). Magnitude (indicated by colour gradient) refers to the value of the anterior–posterior acceleration. Abrupt changes in signals suggest anomaly in the gait, which may be caused by the design of the track, such as the lack of a transition into and out of the bend and inconsistency in the surface [14].

The CWT results of a greyhound galloping on a grass track and on a sand track are shown in Fig. 2b,d.

Three dominant frequencies were observed around 3, 6 and 10 Hz. The high-power frequency is at approximate 10 Hz. The similar patterns are observed in all
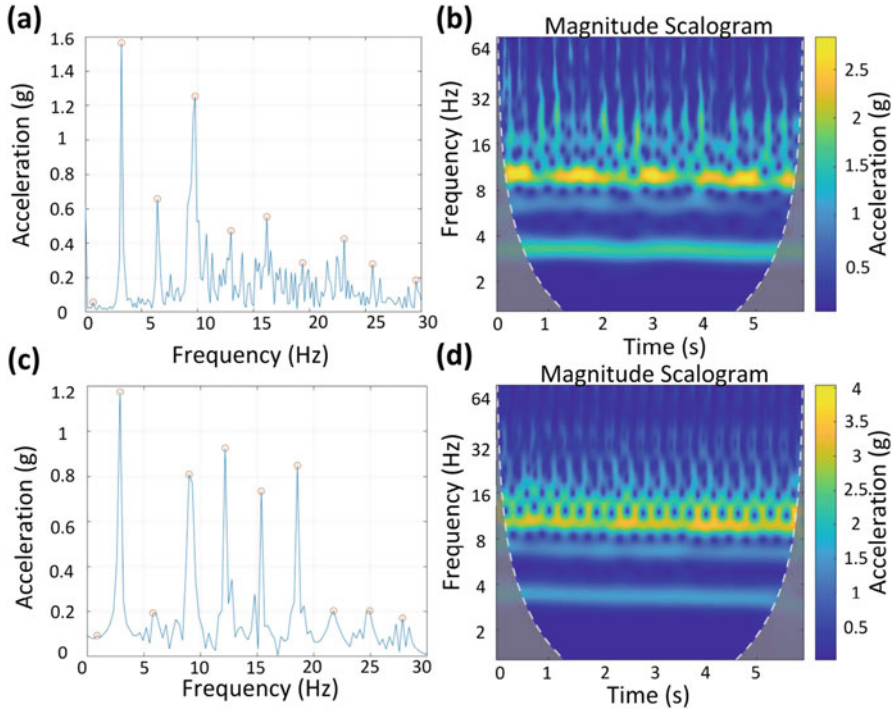
Fig. 2 (**a**) FFT plot of track with a grass surface. (**b**) CWT plot of track with a grass surface. (**c**) FFT plot of track with a sand surface. (**d**) CWT plot of track with a sand surface

data sets. Since the greyhounds are galloping straight, they are in a pseudo steady-state and no fluctuation in frequency and power is observed. However, there are few high-power spots on the plots.

A higher power stride frequency is observed on grass compared to sand. The CWT pattern on sand is more consistent which suggests a relative unchanging surface condition. Fatigue during racing, indicated as abrupt signal alterations has been observed from our recent work, where the CWT was applied on the whole race rather than isolated straight running sections of the race [14].

3.1 Nonlinear Time Series Method

3.1.1 RPS and RP Results

The averaged auto-mutual information (**mi**) determines a suitable delay τ and applying then the global false nearest neighbour (**fnn**) algorithm provides a suitable embedding dimension m to embed the time series into a n-dimensional phase space.

Table 1 The delay τ, the embedding dimension m and the phase-space size (*pss*) are given for accelerations of extracted track sections of grass (G) and sand (S)

Grass	m	τ	*pss*	Sand	m	τ	*pss*
G1	4	5	14.5	S1	5	4	14.7
G2	4	4	16.8	S2	4	4	14.7
G3	5	5	16.0	S3	4	4	17.7
G4	4	4	14.8	S4	3	3	17.7
G5	4	4	15.5	S5	4	5	12.3
G6	4	4	18.6	S6	4	4	16.3

Both, τ and m are needed to span up the phase space and to unfold the attracting set of the dynamics [24]. The phase space is required to set up the RP matrices, to study the phase-space diameter and to a conduct recurrence plot quantification analysis [16]. The **mi** as a general dependence (correlation) measure indicates how much of the information of the previous sample is contained in subsequent sample points [25]. Table 1 lists the identified delays τ and embedding dimensions m. As shown in [26], the delay and the dimension alone can already provide hints on how the phase-space size (*pss*) is calculated for the each RPS. From Table 1 it appears that the τ and m for grass are slightly larger, indicating a tendency for higher dimensionality. A higher sampling rate would facilitate the discrimination of different τ [1].

Figure 3 shows a sample of signal, represented in three different ways using the time-domain (Fig. 4a), RPS (Fig. 4b) and RP (Fig. 4c). The time-domain signals were synchronised with HFR videos in our recent work [14], which is now used to correlate with RPS and RP representations. The phase space indicates stable and unstable periodic orbits which are depicted in (c) as solid and interrupted diagonal lines [27, 28].

Figure 4 shows the RPS and RP on sand and grass. On the RSP plots, two trajectories lying in the negative quadrant are due to fore-leg strikes and the compressed flight. The trajectories in the first quadrant are attributed to the hind-leg strikes and the extended flight. The large trajectories in the third quadrant are attributed to the fore-leg strikes, and the second largest one is due to the compressed flight. The large trajectory in the first quadrant is attributed to the hind-leg strikes. The part with faster dynamics (high-frequency content) attributed to the extended flight its exact is, however, origin unknown.

The following patterns are generally seen in all recurrence plots of all twelve data sets. A solid black diagonal represents a clear periodicity, the main running cycle. The only clear periodicity in the current system is the main galloping cycle of the greyhound at 3.5 Hz, indicated as solid black diagonal line, which is also seen in the FFT and CWT plots. The two dashed-lines between each rigid diagonal lines are attributed to the compressed flight and hind-leg strikes, which have about half the sampling points of the main cycle. The dot-shaped pattern on the plots is also attributed to the extended flight (fast dynamics).

---

[1]The dimension estimate would not change.
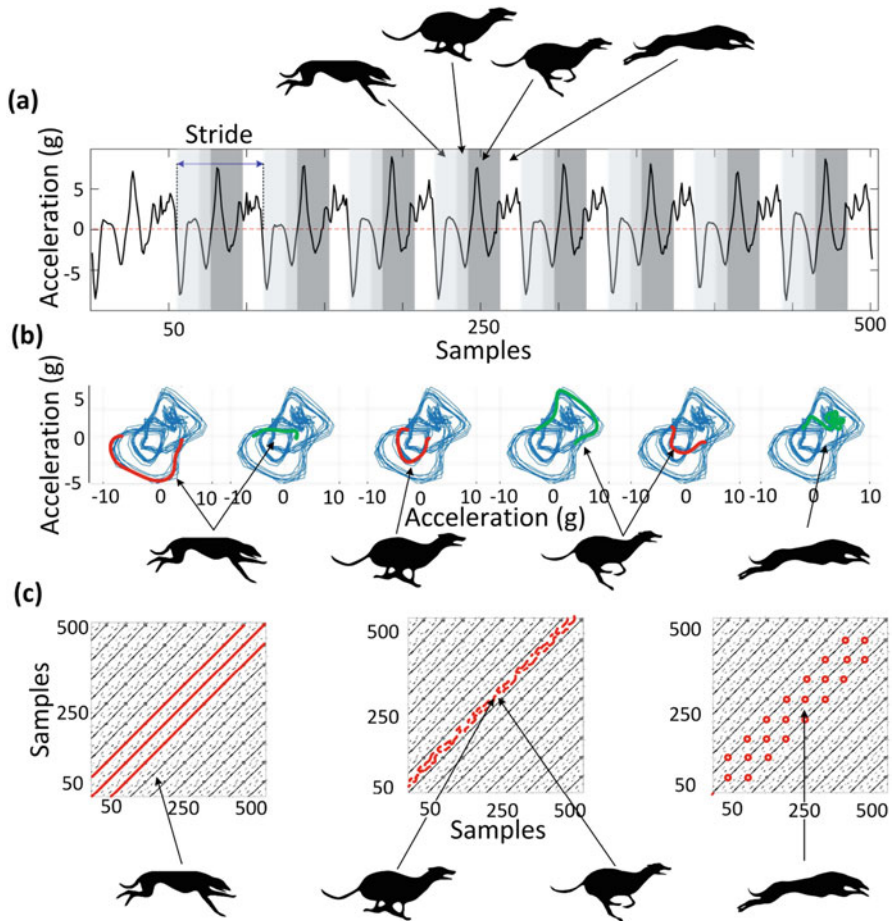
Fig. 3 (**a**) Time-domain signals, (**b**) RPS plots and (**c**) RP of a sample data set (greyhound galloping on a sand surface)
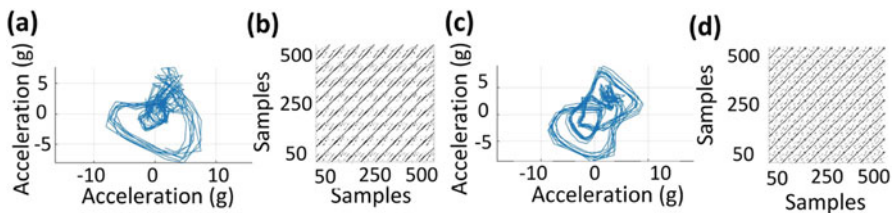
Fig. 4 (**a**) RPS plots of grass surface. (**b**) RPs of grass surface. (**c**) RPS plots of sand surface. (**d**) RPs of sand surface

The main observation based on Fig. 4 is that the RPS of sand surface appear clearer than that of grass. Sand surfaces are better maintained than grass surfaces in general resulting in a smoother arena ground and more consistent gallop. The large trajectories in the third quadrant, which are attributed to the fore-leg strikes, appear relatively larger on sand than on grass, which may suggest a harder surface. It has been observed in our recent work that sand surface is harder than the grass one but was not seen in the time-domain and frequency-domain analysis of the signal [14]. However, using RPS representations shows the potential to derive a method to estimate the difference in the surface stiffness relatively compared with each other.

It can be seen from Fig. 4 that the black rigid lines, attributed to stride frequency, are clear on both sand and grass surface. The extended flight dynamic is more distinguishable in RP representation than the RPS, where it was represented as more random appearing trajectories. The RP representation could reveal dynamics which could not be observed in other signal representations, i.e. extended flight dynamics which seems to be represented as positive random trajectories on RPS plots. However, the low frequency range does not allow to see more details. Also the correlation with other measurements (e.g. rotational sensors, videos) has not been conducted specifically for the purpose of studying these fast dynamics during extended flight, which is an outstanding task for the near future.

3.1.2 Cross Recurrence Quantification Analysis (CRQA)

Figure 5 shows the CRQA results of all samples via three different measurements of determinism (DET), divided by its laminarity (LAM); DET and LAM are calculated as percentage of recurrence points which form diagonal and vertical lines [16]. DET expresses how deterministic, i.e. predictable the data is as opposed to random data. For fully deterministic data, such as for a sinusoidal or a quasi-periodic signal, a value of one is obtained; for deterministic chaos, a value between 1 and 0 and for random data a value of 0 is expected. LAM indicates whether a system remains in a certain state or not. In both plots, the green lines attribute to the grass surface while the brown lines represent the sand surface. As can be observed from Fig. 5, the ratio of DET to LAM approximates unity which is indicative for having similarly high values. Both individual metrics were oscillating in phase at a value of around 0.8, which shows that the system is not fully predictable and that changes of states influence proportionally predictability. From Fig. 3 one can see that the main period, shown up at diagonal line (and related to the main frequency of the system) is predictable but that the subsequent motions are more recurrent than strictly periodic.

To test whether the measurements are significantly different, notched box plots are used. The notches indicate 95% confidence intervals (CI); non-overlapping confidence intervals indicate statistically significant results. The data related to sand has slightly higher values; S2 seems to be a very different measurement though and could be treated as outlier. Comparing the CI between the two groups (removing in both cases the boxplot with the minimum and the maximum median) indicates that
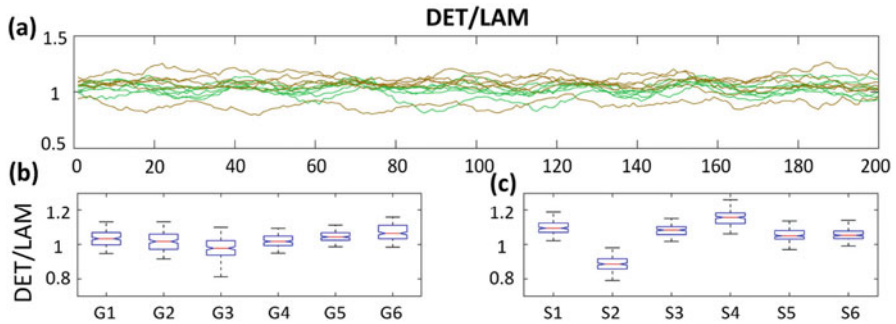
Fig. 5 (**a**) Determinism/laminarity of a greyhound galloping on grass (represented by green lines) and sand (represented by brown lines). (**b**) The notched box plots of grass. (**c**) The notched box plots of sand

the ratio DET/LAM for the sand tracks is significantly different to those of grass (average CI for grass is [1.033, 1.018] while that of sand is [1.09, 1.08]). Taking the median values of all DET/LAM for each of the two types of tracks and using a 1-way ANOVA test (assuming a parametric distribution) provides non-significant results ($df = 13$, $SS = 0.05002$, $F = 0.97$, $p = 0.3434$); removing the outliers, however, provides significant differences between sand and grass at the 5% significance level ($df = 7$, $SS = 0.01531$, $F = 6.11$, $p = 0.0484$).

4 Conclusions

In this work the nonlinear-time-series-analysis techniques of RPS and RP were applied for the first time to study greyhound dynamics. IMU signals measured from greyhounds galloping on grass surfaces were used to investigate whether these methods can detect a difference in the mechanical properties of the racing track surface. The results showed that using RPS and RP, the mechanical properties of the track surface can be generally be compared with each other. For the first time, the galloping gait segments of greyhounds were correlated with the RPS and RP representations. The overall motion can be classified as having a period-4 limit cycle, whereas only the main cycle is clearly periodic. RPS plots could identify the harder surface type; RP could identify dynamics on the system which were difficult to detect using other methods. Similar to identifying instabilities in technical systems long time before they occur [29], RP and RPQA may be used to extract otherwise hidden information to identify motion components from the attractor's trajectory as potential source of injuries. Using RPQA measures, we showed that the ratio of determinism and laminarity shows significantly different results between grass and sand. Using a Bonferroni correction would explicitly allow to study the group differences. While the different parts of the gait cycle have

been distinguished, a closer look at the recurrence plots and their quantification analysis may reveal differences in step pattern. The high-frequency content in the flight phase has not yet been fully analysed, for which potentially a higher sampling rate would be required.

References

1. E. Barrey, P. Galloux, Analysis of the equine jumping technique by accelerometry. Equine Vet. J. **29**(S23), 45–49 (1997)
2. A. Muro-De-La-Herran, B. Garcia-Zapirain, A. Mendez-Zorrilla, Gait analysis methods: An overview of wearable and non-wearable systems, highlighting clinical applications. Sensors **14**(2), 3362–3394 (2014)
3. T. Witte, K. Knill, A. Wilson, Determination of peak vertical ground reaction force from duty factor in the horse (Equus caballus). J. Exp. Biol. **207**(21), 3639–3648 (2004)
4. H. Chateau, L. Holden, D. Robin, S. Falala, P. Pourcelot, P. Estoup, J. Denoix, N. Crevier-Denoix, Biomechanical analysis of hoof landing and stride parameters in harness trotter horses running on different tracks of a sand beach (wet to dry) and on an asphalt road. Equine Vet. J. **42**, 488–495 (2010)
5. S.D. Starke, T.H. Witte, S.A. May, T. Pfau, Accuracy and precision of hind limb foot contact timings of horses determined using a pelvis-mounted inertial measurement unit. J. Biomech. **45**(8), 1522–1528 (2012)
6. S. Viry, R. Sleimen-Malkoun, J.-J. Temprado, J.-P. Frances, E. Berton, M. Laurent, C. Nicol, Patterns of horse-rider coordination during endurance race: a dynamical system approach. PloS One **8**(8), e71804 (2013)
7. A.-M. Pendrill, D. Eager, Velocity, acceleration, jerk, snap and vibration: forces in our bodies during a roller coaster ride. Phys. Educ. **55**(6), 065012 (2020)
8. N.F. Ribeiro, C.P. Santos, Inertial measurement units: A brief state of the art on gait analysis, in *2017 IEEE 5th Portuguese Meeting on Bioengineering (ENBENG)* (IEEE, Piscataway, 2017), pp. 1–4
9. H. Hayati, D. Eager, T. Brown, *A Study of Rapid Tetrapod Running and Turning Dynamics Utilizing Inertial Measurement units in Greyhound Sprinting* (American Society of Mechanical Engineers, New York, 2017)
10. H. Hayati, P. Walker, F. Mahdavi, R. Stephenson, T. Brown, D. Eager, *A Comparative Study of Rapid Quadrupedal Sprinting and Turning Dynamics on Different Terrains and Conditions: Racing Greyhounds Galloping Dynamics* (American Society of Mechanical Engineers, New York, 2018)
11. A.J. Spence, S. Revzen, J. Seipel, C. Mullens, R.J. Full, Insects running on elastic surfaces. Exp. Biol. **213**(11), 1907–1920 (2010)
12. D. Eager, A.-M. Pendrill, N. Reistad, Beyond velocity and acceleration: Jerk, snap and higher derivatives. Eur. J. Phys. **37**(6), 65–68 (2016)
13. A.M. Wilson, J. Lowe, K. Roskilly, P.E. Hudson, K. Golabek, J. McNutt, "Locomotion dynamics of hunting in wild cheetahs. Nature **498**(7453), 185–189 (2013)
14. H. Hayati, F. Mahdavi, D. Eager, Analysis of agile canine gait characteristics using accelerometry. Sensors **19**(20), 4379 (2019)
15. J.P. Zbilut, N. Marwan, The Wiener–Khinchin theorem and recurrence quantification. Phys. Lett. A **372**(44), 6622–6626 (2008)
16. N. Marwan, M.C. Romano, M. Thiel, J. Kurths, Recurrence plots for the analysis of complex systems. Phys. Rep. **438**(5–6), 237–329 (2007)
17. J.W. Cooley, P.A. Lewis, P.D. Welch, The fast Fourier transform and its applications. IEEE Trans. Educ. **12**(1), 27–34 (1969)

18. M.H. Hayes, *Statistical Digital Signal Processing* (Wiley, New York, 2009)
19. C. Torrence, G.P. Compo, A practical guide to wavelet analysis. Bull. Am. Meteorol. Soc. **79**(1), 61–78 (1998)
20. E. Bradley, H. Kantz, Nonlinear time-series analysis revisited. Chaos Interdiscip. J. Nonlinear Sci. **25**(9), 097610 (2015)
21. F. Takens, Detecting strange attractors in turbulence, in *Dynamical Systems and Turbulence, Warwick 1980* (Springer, Berlin, 1981), pp. 366–381
22. C. Frazier, K.M. Kockelman, Chaos theory and transportation systems. Transp. Res. Rec. **1897**(1), 9–17 (2004)
23. B. Goswami, A brief introduction to nonlinear time series analysis and recurrence plots. Vibration **2**, 332–368 (2020)
24. H. Kantz, T. Schreiber, *Nonlinear Time Series Analysis*, vol. 7 (Cambridge University Press, Cambridge, 2004)
25. S. Oberst, J. Lai, T. Evans, Key physical wood properties in termite foraging decisions. R. Soc. Interface **15**(149), 20180505 (2018)
26. S. Oberst, J. Baetz, G. Campbell, F. Lampe, J.C. Lai, N. Hoffmann, M. Morlock, Vibro-acoustic and nonlinear analysis of Cadavric femoral bone impaction in cavity preparations. Int. J. Mech. Sci. **144**, 739–745 (2018)
27. S. Oberst, S. Marburg, N. Hoffmann, Determining periodic orbits via nonlinear filtering and recurrence spectra in the presence of noise. Procedia Eng. **199**, 772–777 (2017)
28. S. Oberst, R.K. Niven, D. Lester, A. Ord, B. Hobbs, N. Hoffmann, Detection of unstable periodic orbits in mineralising geological systems. Chaos Interdiscip. J. Nonlinear Sci. **28**(8), 085711 (2018)
29. M. Stender, S. Oberst, M. Tiedemann, N. Hoffmann, Complex machine dynamics: Systematical recurrence analysis of disk brake vibration data. Nonlinear Dyn. **97**(4), 2483–2497 (2019)

Towards a High-Performance Foucault Pendulum

Matthew P. Cartmell (iD)**, Nicholas A. Lockerbie** (iD)**, and James E. Faller**

1 Introduction

1.1 Mathematical Modelling of the Foucault Pendulum Dynamics

There are many models of the Foucault pendulum to be found in the literature, see [1] for a substantial review, but not all are directly useful for accurate performance prediction. The model summarised here is taken from a previous study [1] and based on the system shown in Fig. 1, in which there is an Earth fixed frame, *EXYZ*, and a local frame *pxyz*. The unit vectors in each frame are represented by the following, where ϕ is the latitude:

$$\bar{e}_Z = \sin\phi.\bar{e}_z + \cos\phi.\bar{e}_y \tag{1}$$

The equations of motion can be expressed in local Cartesian coordinates, and include aerodynamic dissipation, Coriolis terms, and parametric excitation of the length [1]:

M. P. Cartmell (✉)
Department of Mechanical & Aerospace Engineering, University of Strathclyde, Glasgow, Scotland, UK
e-mail: matthew.cartmell@strath.ac.uk

N. A. Lockerbie
Institute for Gravitational Research, School of Physics & Astronomy, University of Glasgow, Glasgow, Scotland, UK

Emeritus Professor of Physics, University of Strathclyde, Glasgow, Scotland, UK

J. E. Faller
JILA, University of Colorado, Boulder, CO, USA
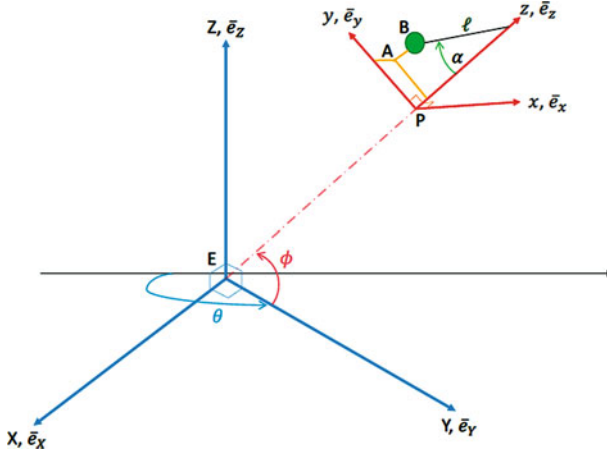
Fig. 1 Earth-centred frame *EXYZ* and local frame *pxyz*, showing pendulum deflected through α and located at a latitude defined by ϕ, [1]

$$\ddot{x} + \eta\,|\dot{x}|\,\dot{x} - 2\dot{y}\Omega sin\phi - x\Omega^2 + \frac{gx}{l(t)\sqrt{1 - \frac{x^2+y^2}{l(t)^2}}} = 0, \qquad (2)$$

$$\ddot{y} + \eta\,|\dot{y}|\,\dot{y} + 2\dot{x}\Omega sin\phi - y\Omega^2 sin^2\phi + r\Omega^2 sin\phi cos\phi + \frac{gy}{l(t)\sqrt{1 - \frac{x^2+y^2}{l(t)^2}}} = 0. \qquad (3)$$

The time-variant length due to the parametric excitation is defined by $l(t) = l_0 + l_1 Cos(\omega_1 t)$, where $\omega_1 = 2\omega_n + \epsilon\sigma$, to permit the conditions for principal parametric resonance (PPR), excited at frequency ω_1. We note that ω_n and $\epsilon\sigma$ are the undamped natural frequency of free vibration, and detuning from the perfect resonance condition, respectively. The lengths l_0 and l_1 are the nominal pendulum length and the imposed parametric excitation amplitude, respectively, and $l_1 \leq 0.01l_0$ in order to establish a region for the parametric resonance [1]. Equations (2) and (3) can be numerically integrated to obtain the pendulum's response as a result of the Newtonian rotation of the Earth, local radius r, at angular rate Ω. The aerodynamic damping is $\eta = \rho C_d \pi \frac{R_{bob}^2}{2m}$, where R_{bob} and m are the radius and mass of the bob, respectively. One should minimise η, by shielding the pendulum and introducing a partial vacuum around it. It is shown in [1] that the aerodynamic damping will greatly exceed the pivot friction in a well-designed system. There is a large literature on Foucault pendulums, and a consistent theme is the profound need to remove *all ellipticity* from the motion [1].

1.2 Theoretical Response Predictions to the Rotation of the Earth

Equations (2) and (3) are numerically integrated for pragmatic data, and the integrations may be performed within *Mathematica* using stringent accuracy controls. Results are presented in Figs. 2, 3, 4, and 5, for a 4 m pendulum, with all data shown in the captions. This data is derived from official physical data for two chosen locations, and pendulum design data extrapolated from experience gained from [1]. Two locations are considered: North Pole (NP) and Glasgow, Scotland, with the North Pole taken to benchmark the predicted results for the rotation of the Earth, over the same time period at Glasgow. The x, y responses of the pendulum are calculated with respect to the Earth-fixed frame *EXYZ*, confirming that the pendulum remains fixed in inertial space relative to the fixed stars, whilst the laboratory attached to the Earth rotates below it (displacements in m).

The effect of parametrically exciting the pendulum is very clear from the results shown in Fig. 2 (*left* and *right*), and that the magnification can be calculated in terms of the ratio of the Euclidean distances between the red and blue points of the two cases.

Principal parametric resonance gives a magnification, or gain, k, which can reach up to at least 6, and potentially higher, with some cyclical variation during each oscillation as the pendulum precesses round. This has some very significant advantages, as discussed in Sect. 1.3. Table 1 shows the precession predicted over $\Delta t = t_{end} - t_0$ equals one hour (3600 s) in the second and third rows for the pendulum without and with principal parametric resonance (PPR), located at the North Pole, and then extrapolated linearly over one sidereal day (SD). The data in the lowest row is for precession over 4 hours (14400 s) at the North Pole, see Fig. 3 for the (x, y) precessions, with a much larger initial displacement condition in the x direction, and which is then extrapolated linearly again over one sidereal day.
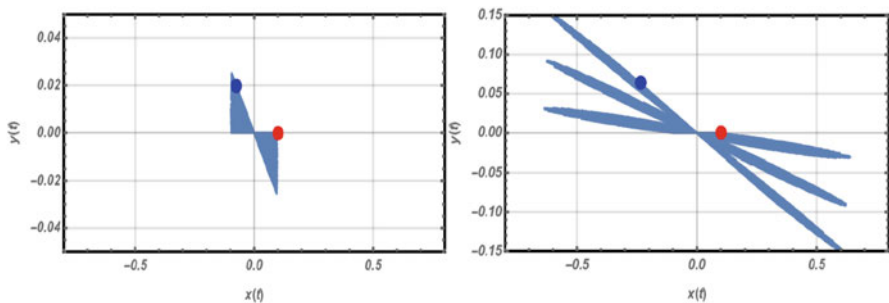
Fig. 2 Pendulum response over 1 hour at the North Pole for no parametric excitation, $l_1 = 0$ (*left*) and for parametric excitation, $l_1 = 0.040\ m$ (*right*). Red dots: displ. ICs $(x_0, y_0) = (0.1, 0)\ m$, blue dots: end points (x_{tend}, y_{tend}), vel ICs are $\dot{x}_0 = \dot{y}_0 = 0\ m/s$. Data: $l_0 = 4\ m$, $g = 9.8320 m/s^2$, $\Omega = 7.2921150 * 10^{-5}\ rad/s$, $\phi = 1.5705\ rad$, $r = 6357.00 * 10^3\ m$, $m = 5\ kg$, $\rho = 1.189\ kg/m^3$, $C_D = 10^{-6}$, $R_{bob} = 0.0463134\ m$, $t_{end} = 3600\ s$, $\epsilon\sigma = 0$
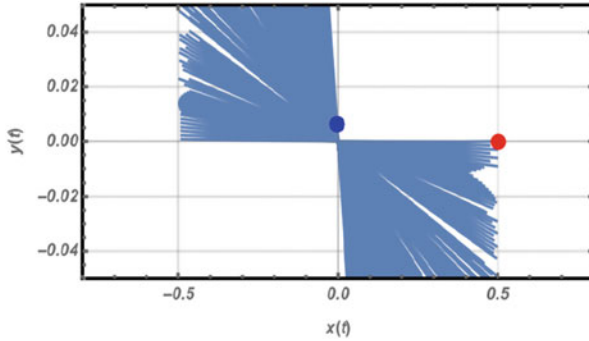
Fig. 3 Pendulum response over 4 hours at the North Pole for no parametric excitation, same data as for Fig. 2 (*left*) except for $x_0 = 0.5 \, m$ and $t_{end} = 14400 \, s$
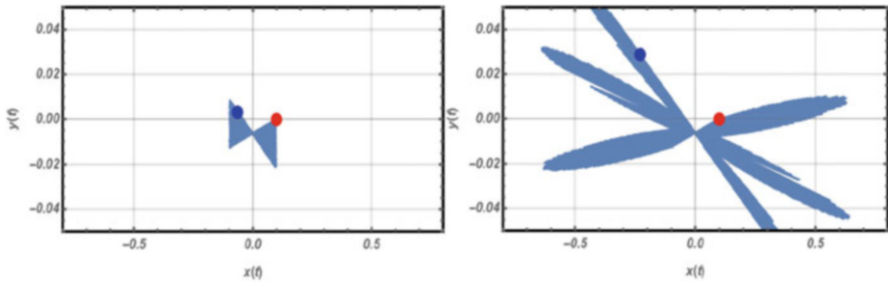
Fig. 4 Pendulum responses over 1 hour at Glasgow for no parametric excitation, $l_1 = 0$ (*left*) and for parametric excitation, $l_1 = 0.040 \, m$ (*right*). Red dots: displ. ICs $(x_0, y_0) = (0.1, 0) \, m$, blue dots: end points (x_{tend}, y_{tend}), velocity ICs are $\dot{x}_0 = \dot{y}_0 = 0 \, m/s$. Data: $l_0 = 4 \, m$, $g = 9.8156 m/s^2$, $\Omega = 7.2921150 * 10^{-5} \, rad/s$, $\phi = 0.9750 \, rad$, $r = 6363.18 * 10^3 \, m$, $m = 5 \, kg$, $\rho = 1.189 \, kg/m^3$, $C_D = 10^{-6}$, $R_{bob} = 0.0463134 \, m$, $t_{end} = 3600 \, s$, $\epsilon\sigma = 0$
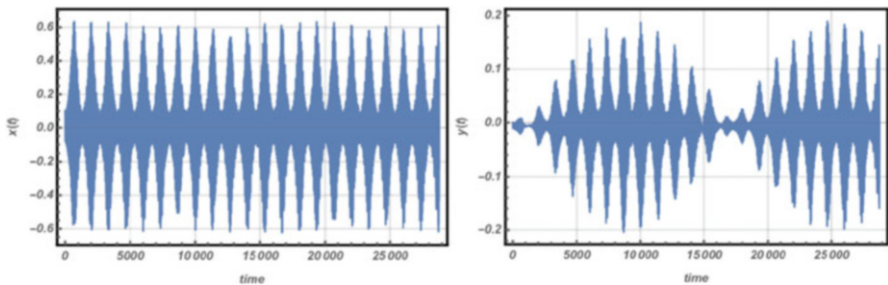
Fig. 5 Time responses over 8 hours at Glasgow for the parametrically excited case, $l_1 = 0.040 \, m$, same data as for Fig. 4 except for $t_{end} = 28800 \, s$, showing the persistence of lobing

Clearly, one should generally expect a precession of exactly 360° over one sidereal day at the North Pole, indicating that the biggest error (for the parametrically excited case) obtained here is 0.09%. The results for precession are almost entirely

Table 1 Precessions over Δt (see text) at NP

PPR	3,600 s	Sidereal day
off	15.042 °	360.029 °
on	15.027 °	359.671 °
PPR	14,400 s	Sidereal day
off	60.016°	360.095°

Table 2 Precessions over Δt at Glasgow

PPR	3,600 s	Sidereal day
off	12.420 °	297.265 °
on	12.358 °	296.503 °

independent of initial conditions [1], and as long as suitable accuracy controls are in place for the numerical integration, they can also be made to be largely independent of the integration time, defined as $\Delta t = t_{end}$, when $t_0 = 0$. It is significant to note from Fig. 2 (*right*) that the parametrically excited results display large lobes in the (x, y) responses, and these are extremely prominent in the time responses for x and y for this case as large, low-frequency amplitude modulations. The amplitude modulation depths in x and y can be reduced when the principal parametric resonance is slightly detuned, noting that this also reduces the available gain somewhat. It is evident from the basic results shown here for the North Pole that the Foucault pendulum will precess through exactly 360° over one sidereal day, as one would expect. These numerical results suggest that the North Pole can be a benchmark location for validating the numerical integration routine, and therefore predicting the operation of the pendulum in other places. See [1] for a fuller exploration of locations.

The remaining discussion in this section is based on the latitude of 55.86° N (0.975 rad N) for Glasgow, Scotland, UK, noting that the local values for the acceleration due to gravity, g, and the radius of the Earth, r, vary from those for the North Pole, all other data maintained except where specifically indicated. The results in Fig. 4 are without and with the same level of parametric excitation as for the cases in Fig. 2 for Glasgow.

In Fig. 4, the lobed response phenomenon is as evident for Glasgow as it was for the NP and wider analysis shows this to be a persistent feature of Foucault pendulum response when under principal parametric excitation of the length, and this is also dependent on the phase between the excitation and the response. However, the advantage of a positive gain ($k > 0$) and the beneficial effects of parametric resonance on ellipticity (Sect. 1.3) can outweigh the effect of the lobing. The lobes are very clearly depicted as a persistent feature over time in Fig. 5, for the responses in x and y, over 8 hours.

Precession data for Glasgow (Fig. 4) is given in Table 2 above, over 1 hour and then extrapolated over one sidereal day, and there is reasonable consistency between the cases for no parametric excitation and parametric excitation.

The results of Figs. 2, 3, 4, and 5 are developments of a wider study into Foucault pendulum response [1] and the main conclusion is that although numerical

accuracy has to be tightly controlled, the aggregated numerical error can potentially be <0.1%.

1.3   Discussion of General Foucault Pendulum Performance

A fundamental problem with all Foucault pendulums is a tendency for the planar motion to degenerate into ellipticity over time. This phenomenon is associated with a frequency anisotropy effect, specifically manifesting as increasingly different periods of each axis of the developing elliptical response. This effect is triggered in practice by structural asymmetries, and is greatly exacerbated in shorter pendulums. This is why Foucault's 67-metre installation in the Panthéon operated quite successfully over time, given the very long length of that pendulum [1]. There are several ways to overcome this inherent problem, starting with symmetrical design and high-quality manufacture and installation, together with mechanical and electro-mechanical mitigation measures (the Charron ring and various electromagnetic pusher drives [2, 3]). It was suggested by Pippard [4] in 1988 that parametric excitation of the length could mitigate this effect.

We start with 'self-sustaining' passive pendulums which depend for their subsequent motion on the launch that they get from suitable initial conditions. Olsson [5] analysed Foucault pendulum ellipticity and obtained a precession rate from structural asymmetry-driven frequency anisotropy, based on the lowest order Lindstedt-Poincaré perturbation solution to the ellipticity problem. This is defined by

$$\Omega_{ep} = \frac{3\omega_0 ab}{8}, \tag{4}$$

where the subscript denotes ellipticity precession. We note that $\omega_0 = \text{sign}\sqrt{\frac{g}{l}}$, and a and b are, respectively, the semi-major and semi-minor axes of the elliptical motion which are nondimensionalised in [5] and in equation (4), by dividing by l. Clearly, if the pendulum is working exactly as intended, then $b = 0$ and so $\Omega_{ep} = 0$. Ellipticity precession is most certainly not the only source of error within Foucault pendulum systems, but is the most significant because of the inherent difficulty in controlling b over time and the generally high magnitude of the subsequent ellipticity precession rate. Equation (4) shows that the ellipticity precession is linearly proportional to both a and b. Plewes [6] defines a useful metric for Foucault pendulum performance, described in [6] as 'error sensitivity', in the form of $d\Omega_{ep}/db$. It is interesting to compare the ellipticity error sensitivity for Foucault's original pendulum (which performed rather well due to its very long length and high bob momentum), at 0.00013, with a higher value of 0.00917 calculated for the 4 metre pendulum considered here, showing that the shorter pendulum is 70 times more sensitive to ellipticity error, assuming a constant l/a ratio of 16 for both designs. Taking

an *l/a* ratio of 40 instead, we get ellipticity error sensitivities of 0.00005 and 0.00367 respectively, which show that for this *l/a* ratio too, the shorter pendulum is still almost 70 times more sensitive to ellipticity error precession than Foucault's original pendulum. This confirms that longer Foucault pendulums are inherently less sensitive to ellipticity error than shorter pendulums, and so, it is logical to try to maximise pendulum length as far as possible. Using equation (4) to obtain $\frac{d\Omega_{ep}}{db}$ shows that the dependence on length is proportional to $\frac{1}{l^{5/2}}$.

This discussion emphasises the great importance of minimising the natural propensity of shorter Foucault pendulums to frequency anisotropy, at source, by means of good design, manufacture, installation, and also by means of active mitigation measures which we discuss next. The usual approach for providing a continuous excitation of a Foucault pendulum in order to confine its long-term motion within a stable response region has been to use some form of timed electromagnetic pulse which pushes or pulls the magnetised pendulum bob as it passes over an exciter coil. The exciter coil couples electromagnetically in a carefully timed manner, with a powerful magnet set into the bob [2, 3, 6]. There are various designs for such systems, with the 'pusher' installation of Schumacher and Tarbet [3] offering effective reduction in *b*. The penalties for adopting this approach are that the electromagnetic and mechanical properties of the bespoke exciter coil and bob magnet must be very precisely matched to ensure perfect and appropriate alignment of the electromagnetic field. The installation of these components directly under the bob may preclude the use of a highly accurate direct-view imaging system for tracking the motion of the pendulum.

Returning to the application of a parametric resonance in a Foucault pendulum, we start by considering the general benefit obtained by introducing this feature into a simple pendulum system. It is very well known that an 'unstable' parametrically excited pendulum or beam will in practice always display a softening response that is bounded due to the effect of the prevailing large deflection nonlinearity [7], noting the full analysis of a simple non-precessing pendulum in section 3.1.2 (pp. 139-145) in that reference. A cursory visual analysis of the results for principal parametric resonance (PPR) in the Foucault pendulum, in Fig. 2 (*right*), Fig. 4 (*right*), and Fig. 5, shows that the response is of large magnitude and certainly bounded. According to [7] such nonlinear parametrically resonant systems are strongly stable to small perturbations, and in practice, the smallness of such perturbations depends on the physical scale of the system. So, in the case of the 4-metre Foucault pendulum, the perturbation that would be necessary to knock the system out of its stable, nonlinear, precessing planar response would be of the order of several tens of cm. This tends to underpin the effectiveness of the use of PPR as a stabilising form of excitation, which may be applicable to the Foucault pendulum. Pippard [4, 8] examined this in some detail, starting with the premise that any pendulum motion normal to the precessing swing plane is in phase quadrature with the oscillation in the swing plane. So, if the excitation reaches its maximum velocity when the pendulum swing is at zero, maximum energy is transferred to the pendulum. This will strongly amplify the planar response and attenuate any normal motion. The

parametric excitation also counteracts dissipative effects within the system, in order to maintain the oscillating and precessional motions of the system, so *a* is naturally amplified and *b* is similarly attenuated. This effect was usefully quantified for the location of Cambridge, England, UK, in [4]. Pippard [4] also gives one of the most complete accounts of error sources in Foucault pendulum systems, discussing three principal sources in detail: suspension design, dissipation (as this may cause secondary anharmonicity leading to growth in *b*), and noise effects.

2 Frame-Dragging

2.1 Lense-Thirring Precession of a Test Mass due to the Rotation of the Earth

General Relativity states that inertial frames are 'influenced and dragged by the distribution and flow of mass–energy in the universe', noting the relativistic equivalence of mass and energy [9]. A theory for frame-dragging was proposed by Thirring and Lense in 1918, in which inertial frames are dragged around a central *rotating* mass due to the effect of its gravity on the surrounding spacetime [10]. The rotation of the central mass twists the surrounding spacetime, and this perturbs the orbits of other masses nearby. This effect is now known as Lense-Thirring precession, and henceforth as LT. The Earth's gravitational field is capable of generating frame-dragging and this is generally considered to be demonstrable in three gravitomagnetic manifestations: the precession of a gyroscope in orbit around the Earth, the precession of orbital planes where a mass orbiting the Earth constitutes a gyroscope whose orbital axis will precess, and the precession of the pericentre of the orbit of the test mass about the Earth.

GP-B measured the first two [11], and the LAGEOS satellites measured the second one only [12]. LAGEOS measured the LT drag of their orbital planes to ~0.031 arcsecs/year [9] which is ~ 8.611×10^{-6} °/year. This was subject to error due to uncertainty in the Earth's mass distribution, and there is still some debate about the true size of the error in LAGEOS's LT measurement, but it mainly derived from the low eccentricity of the LAGEOS orbits and the difficulties in eliminating Earth multipoles. GP-B measured LT to ~0.039 arcsecs/year [9], which is 10.833×10^{-6} °/year. GP-B used *IM Pegasi HR 8703* as the guide star and operated on a circular polar orbit of 642 km altitude [9]. The spin axes of GP-B's gyroscopes drifted, so the Geodetic precession [13] (due simply to the presence of the mass of Earth rather than its presence *and* its rotation) was only measured to a precision of 1.5%, which had a relatively significant knock-on effect on the measurement of LT. The relationships between the directions of the LT and the Geodetic precessions are orthogonal, and the total relativistic precession on the body is therefore the vector sum of the LT and Geodetic precessions. Our main interest is the LT component. The analysis behind LT, in terms of (weak) gravitomagnetic

effects on an accelerating mass, can be considered analogously with an accelerating charge producing a magnetic field. Specifically, the analogy is between the equations that govern the forces on a spinning electric charge with magnetic moment μ which moves through a magnetic field, and the forces of a spinning mass moving through the gravitational field of a rotating mass [9], and this analogy is made through Maxwell's equations. Fortunately, in exploring LT in the vicinity of the Earth, we are dealing with weak fields and non-relativistic velocities, so the full form of general relativity is not necessary and a linearised version of the theory is sufficient [14]. An analogy between weak-field, low-velocity general relativity and Maxwellian electrodynamics offers a simple basis for gravitoelectromagnetism (GEM), and Lense-Thirring precession can be shown to be one manifestation of that. The background for this can be found in [14], leading to an expression for LT precession of a test mass about the Earth:

$$\Omega_{LT} = \frac{G}{c^2 R^3} L' \left| 1 - 3 \left| \overline{Z} \cdot \overline{r} \right| \right|, \tag{5}$$

where the scalar angular momentum L' is given by $L' = I_{\oplus}\Omega_{\oplus}$, G is Newton's gravitational constant, c is the speed of light, and considering the Earth initially as a non-oblate sphere, then $I_{\oplus} = \frac{2}{5}Mr^2$. But the actual radius of gyration of the Earth [15, 16] is 0.576 r, so the factor of $\frac{2}{5}$ becomes 0.576^2 which is 0.3316. Therefore, $I_{\oplus} = 0.3316\, Mr^2$. We note also that the test mass, which is actually going to be the bob of the Foucault pendulum, is elevated at h from the surface of the Earth (therefore at radius R, where $R = r + h$, and r denotes the radius of the Earth at the location), and also $\overline{Z} \cdot \overline{z} = cos\theta$ and $R \approx r$ for h very small (assuming that the bob is hanging at approximately a metre above the ground). This result does not include the Geodetic precession and is purely the LT component. The angle θ is the colatitude which is the included angle between $\overline{Z}$ and $\overline{z}$ (the spin axis of Earth, Fig. 1, and the vertical axis at the location, respectively), so $\theta = \frac{\pi}{2} - \phi$, where ϕ is the latitude as measured from the equator.

2.2 Numerical Predictions for Frame-Dragging at the North Pole and Glasgow

Based on the following data, the LT precessions at the NP and Glasgow can both be calculated: $G = 6.67408 \times 10^{-11}$ m^3 kg^{-1} s^{-2}, $M = 5.972 \times 10^{24}$ kg, $\Omega_{\oplus} = 7.2921150 \times 10^{-5}$ rad/s, $c = 2.99792488 \times 10^8$ m/s, $R = 6358.00 \times 10^3$ m at the NP, $R = 6364.18 \times 10^3$ m at Glasgow, $\phi = 1.5707963$ rad at the NP, and $\phi = 0.9750$ rad at Glasgow. The prediction for LT at the NP is 219.5 mas/year (noting it is 220 mas/year in [4]), and at Glasgow, the prediction is 162.8 mas/year. For the NP, the LT prediction is 2.15×10^9 times smaller than the Newtonian rotation of the Earth, as is also discussed in the seminal paper [17].

2.3 An Experimental Challenge

A precursor Foucault pendulum experiment has been undertaken by the authors [1] and the effectiveness of parametric excitation on minor axis minimisation, and response gain amplification and stabilisation, has been explored. Work is currently in progress to complete the preparations for a further experiment capable of resolving LT precession in the laboratory. This will require an exceptional increase in mechanical and instrumentation precision, and outstanding noise rejection capability. This analysis and design work will be reported on in detail in the literature in due course.

3 Conclusions

It has been shown that a laboratory Foucault pendulum with parametric excitation of the length can be modelled to track the Newtonian rotation of the Earth to an accuracy of <0.1%. A precursor experiment has verified the effectiveness of parametric excitation in stabilising the motion of a practical mid-length pendulum of ~ 4 metres. Measurement of LT requires an increase in resolution of $>2 \times 10^9$, as shown by the modelling in this paper, putting great reliance on mechanical accuracy and exceptional signal processing capability. A very high-resolution optical imaging system specification and novel designs for the pendulum, fixturing, and shielded installation are under way.

References

1. M.P. Cartmell, J.E. Faller, N.A. Lockerbie, E. Handous, On the modelling and testing of a laboratory-scale Foucault pendulum as a precursor for the design of a high-performance measurement instrument. Proc. R. Soc. A **476**(20190680), 26 (2020). https://doi.org/10.1098/rspa.2019.0680
2. H.R. Crane, Short Foucault pendulum: a way to eliminate the precession due to ellipticity. Am. J. Phys. **49**, 1004–1006 (1981)
3. R.A. Schumacher, B. Tarbet, A short Foucault pendulum free of ellipsoidal precession. arXiv, 0902.1829v2 (2009)
4. A.B. Pippard, The parametrically maintained Foucault pendulum and its perturbations. Proc. R. Soc. A **420**, 81–91 (1988)
5. M.G. Olsson, The precessing spherical pendulum. Am. J. Phys. **46**, 1118 (1978)
6. D.B. Plewes, Magnetic monitoring of a small Foucault pendulum. Can. Rev. Sci. Instrumen. **89**, 065112 (2018)

7. M.P. Cartmell, *Introduction to linear, parametric and nonlinear vibrations*, 1st edn. (Chapman and Hall, London, 1990)
8. A.B. Pippard, *The physics of vibration, vol 1* (Cambridge University Press, Cambridge, 1978)
9. G. Chartas, Frame Dragging, Department of Physics & Astronomy, College of Charleston, SC 29424, USA, http://chartasg.people.cofc.edu/chartas/Teaching.html. Last accessed 18 Nov 2020.
10. Lense-Thirring precession, Wikipedia, https://en.wikipedia.org/wiki/Lense%E2%80%93Thirring_precession. Last accessed 18 Nov 2020.
11. B. Gravity Probe, Wikipedia, https://en.wikipedia.org/wiki/Gravity_Probe_B. Last accessed 18 Nov 2020.
12. B. Tapley, I. Ciufolini, Measuring the Lense-Thirring precession using a second Lageos satellite, Report No. CSR-89-3, Center for Space research, The University of Texas at Austin, TX 78712, USA, September 30 (1989)
13. The Geodetic effect, Wikipedia, https://en.wikipedia.org/wiki/Geodetic_effect. Last accessed 18 Nov 2020.
14. O. Chashchina, L. Iorio, Z. Silagadze, Elementary derivation of the Lense-Thirring precession. Acta. Physica. Polonica B **40**(8), 2363–2378 (2009)
15. J.B. Hartle, *Gravity: An Introduction to Einstein's General Relativity* (Addison-Wesley, San Fransisco, 2003)
16. N.A. Lockerbie, Gravitational quadrupolar coupling to equivalence principle test masses: the general case. Class. Quantum Grav. **19**, 2063–2077 (2002)
17. V.B. Braginsky, A.G. Polnarev, K.S. Thorne, Foucault pendulum at the South Pole: proposal for an experiment to detect the Earth's general relativistic gravitomagnetic field. Phys. Rev. Letters **53**(9), 863–866 (1984)

Part IV
System Identification and SHM

Identification of Nonpolynomial Forms of Damping Nonlinearity in Dynamic Systems Using Harmonic Probing and Higher Order FRFs

Hari Prasad Chintha and **Animesh Chatterjee**

1 Introduction

The identification of nonlinear dynamic systems from input-output data is often represented through the Volterra series, which provides an efficient mathematical platform for parametric and nonparametric modeling of various physical systems in many engineering applications. Nonlinearity in the system can result in extensive behavior; hence, prediction of nonlinear behavior in dynamic models is significant, to understand the nature of nonlinearity, whether it is in stiffness or in damping. If the nonlinearity is present in damping, it is classified as symmetric and asymmetric damping nonlinearity and further classification is extended to polynomial and nonpolynomial.

Nayfeh [1] has discussed various physical models with a damped unforced single degree of freedom such as hysteretic damping, Coulomb damping, and bilinear oscillators etc., and also studied quadratic damping of an immersed body when it moves through a fluid at high Reynolds numbers. The nonlinear quadratic form is also associated with many physical models such as the motion of swinging spring, the motion of the ship, the motion of the fluid interface, the motion of the rotating shaft, the vibration of shells and composite plates, and coupled longitudinal and transverse oscillation of column, etc. Dixon [2] studied the bilinear model with two coefficients for the two directions of motion because the asymmetry in operation is a significant feature of real suspension dampers.

Damping is inherently present in all dynamic systems and more often in a nonlinear form which can be symmetric or asymmetric and further of polynomial form or nonpolynomial form as given below.

H. P. Chintha · A. Chatterjee (✉)
Department of Mechanical Engineering, Visvesvaraya National Institute of Technology, Nagpur, Maharashtra, India
e-mail: harichintha@students.vnit.ac.in; achatterjee@mech.vnit.ac.in

(i) Cubic damping with $F_D[\dot{x}(t)] = c_1\dot{x}(t) + c_3\dot{x}^3(t)$ is symmetric and polynomial form.

(ii) Quadratic damping with $F_D[\dot{x}(t)] = c_2\dot{x}(t)|\dot{x}(t)|$ is symmetric and nonpolynomial form.

(iii) Square damping with $F_D[\dot{x}(t)] = c_1\dot{x}(t) + c_2\dot{x}^2(t)$ is asymmetric and polynomial form.

(iv) Bilinear damping $F_D[\dot{x}(t)] = \lambda c\dot{x}(t)$ for $\dot{x}(t) > 0$ and $F_D[\dot{x}(t)] = c\dot{x}(t)$ for $\dot{x}(t) < 0$ is asymmetric and nonpolynomial form.

Although identification work has been done for polynomial forms of damping by the earlier researchers Balachandran et al. [3], Adhikari et al. [4] Chatterjee and Chintha [5], it is not yet done for nonpolynomial forms. Here, we present the identification of nonpolynomial forms, i.e., case ii) and case iv).

In this paper, the proposed work consists of the identification of nonpolynomial form damping nonlinearity such as quadratic and bilinear damping forms. This presentation attempts an approximate analytical method to a model with nonpolynomial function through the Volterra series. In Sect. 2, nonlinear response formulation through the Volterra series and its higher order FRFs has been presented. In Sect. 3, coefficients of nonpolynomial function with a single degree of freedom system can be obtained through an analytical approximate solution. The identification of nonpolynomial form damping nonlinearity through the response spectrum and harmonic amplitude characteristic behavior has been studied (Sect. 4).

2   Volterra Series Representation of Nonlinear Structure

Volterra series representation for a general physical model with input excitation force as $f(t)$ and output response as $x(t)$ can be in the form of

$$x(t) = \int_{-\infty}^{\infty} h_1(\tau_1) f(t - \tau_1) d\tau_1$$

$$+ \ldots \int_{-\infty}^{\infty} \ldots \int_{-\infty}^{\infty} h_n(\tau_1, \tau_2, \ldots, \tau_n) f(t - \tau_1) \ldots f(t - \tau_n) d\tau_1 \ldots d\tau_n$$

$$= x_1(t) + x_2(t) + \cdots + x_n(t)+ \tag{1}$$

where $h_n(\tau_1, \tau_2, \ldots, \tau_n)$ are known as n[th] order Volterra kernels and its Fourier transform gives the nth order frequency response functions (FRFs)

$$H_n(\omega_1, \omega_2, \ldots, \omega_n) = \int\limits_{-\infty}^{\infty} \cdots \int\limits_{-\infty}^{\infty} h_n(\tau_1, \tau_2, \ldots, \tau_n) \prod_{i=1}^{n} e^{-j\omega_i \tau_i} \, d\tau_1 \ldots d\tau_n$$

(2)

For a single-degree-of-freedom system with a polynomial from in damping nonlinearity under harmonic excitation force with $f(t) = A\cos(\omega t) = \frac{A}{2}e^{j\omega t} + \frac{A}{2}e^{-j\omega t}$, the governing equation of motion is in the form

$$m\ddot{x}(t) + c_1\dot{x}(t) + c_2\dot{x}^2(t) + c_3\dot{x}^3(t) + \cdots + k_1x(t) = f(t)$$

(3)

The first three response components obtained to follow Eq. (3), becomes

$$x_1(t) = \frac{A}{2}H_1(\omega)e^{j\omega t} + \frac{A}{2}H_1(-\omega)e^{-j\omega t}$$

(4)

$$x_2(t) = \frac{A^2}{2}H_2(\omega, -\omega) + \frac{A^2}{4}H_2(\omega, \omega)e^{j2\omega t} + \frac{A^2}{4}H_2(-\omega, -\omega)e^{-j2\omega t}$$

(5)

$$x_3(t) = \frac{A^3}{8}H_3(\omega, \omega, \omega)e^{j3\omega t} + \frac{3A^3}{8}H_3(\omega, \omega, -\omega)e^{j\omega t}$$
$$+ \frac{3A^3}{8}H_3(\omega, -\omega, -\omega)e^{-j\omega t} + \frac{A^3}{8}H_3(-\omega, -\omega, -\omega)e^{-j3\omega t}$$

(6)

The total response, $x(t)$, in the form

$$x(t) = x_1(t) + x_2(t) + \cdots = \sum_{n=1}^{\infty} \left(\frac{A}{2}\right)^n \sum_{p+q=n} {}^nC_q H_n^{p,q}(\omega)e^{j\omega_{p,q}t}$$

(7)

where $H_n^{p,q}(\omega) = H_n\left(\underbrace{\omega, \omega, \ldots,}_{p \ times}\underbrace{-\omega, -\omega, \ldots}_{q \ times}\right)$, $\omega_{p,q} = (p-q)\omega$ and ${}^nC_q = \frac{n!}{(n-q)!q!}$

The response amplitude of mth harmonic $X(m\omega)$ can be obtained as

$$X(m\omega) = \sum_{i=1}^{\infty} 2\left(\frac{A}{2}\right)^{m+2i-2} {}^{m+2i-2}C_{i-1}H_{m+2i-1}^{m+i-1,i-1}(\omega)$$

(8)

Using Eq. (8), the first three harmonic amplitudes in addition with excitation frequency in the form of series as

$$X(\omega) = AH_1(\omega) + \frac{3}{4}A^3 H_3(\omega, \omega, -\omega) + \frac{5}{8}A^5 H_5(\omega, \omega, \omega, -\omega, -\omega) + \dots \tag{9}$$

$$X(2\omega) = \frac{A^2}{2}H_2(\omega, \omega) + \frac{A^4}{2}H_4(\omega, \omega, \omega, -\omega) + \dots \tag{10}$$

$$X(3\omega) = \frac{A^3}{4}H_3(\omega, \omega, \omega) + \frac{5}{16}A^5 H_5(\omega, \omega, \omega, \omega, -\omega) + \dots \tag{11}$$

By substituting Eqs. (7) in (3), functional series is synthesized into higher order FRFs in terms of first-order FRFs and nonlinear parameters as given as

$$\frac{{}^n c_q H_n^{p,q}(\omega)}{H_1(\omega_{p,q})} =$$

$$\left\{ \begin{array}{l} -c_2 \displaystyle\sum_{\substack{p_i + q_i = n_i \\ n_1 + n_2 = n}} \left\{ j\omega_{p_1,q_1}{}^{n_1} c_{q_1} H_{n_1}^{p_1,q_1}(\omega) \right\} \left\{ j\omega_{p_2,q_2}{}^{n_2} c_{q_2} H_{n_2}^{p_2,q_2}(\omega) \right\} \\[2em] -c_3 \displaystyle\sum_{\substack{p_i + q_i = n_i \\ n_1 + n_2 + n_3 = n}} \left\{ j\omega_{p_1,q_1}{}^{n_1} c_{q_1} H_{n_1}^{p_1,q_1}(\omega) \right\} \left\{ j\omega_{p_2,q_2}{}^{n_2} c_{q_2} H_{n_2}^{p_2,q_2}(\omega) \right\} \\[2em] \left\{ j\omega_{p_3,q_3}{}^{n_3} c_{q_3} H_{n_2}^{p_3,q_3}(\omega) \right\} \end{array} \right\} \tag{12}$$

From Eq. (12), second- and third-order FRFs are

$$H_2(\omega, \omega) = c_2 \omega^2 H_1^2(\omega) H_1(2\omega) \tag{13}$$

$$H_3(\omega, \omega, \omega) = H_1^3(\omega) H_1(3\omega) \left[4c_2^2 \omega^4 H_1(2\omega) + jc_3 \omega^3 \right] \tag{14}$$

3   Mathematical Models and Approximate Solution

3.1   Bilinear Damping

Considering the system with bilinear damping under harmonic excitation force, and the governing equation of motion in the form of

$$m\ddot{x}(t) + g\left[\dot{x}(t)\right] + kx(t) = A\cos wt \tag{15}$$

where

$$g\left[\dot{x}(t)\right] = \begin{cases} \lambda c\dot{x}(t), & \dot{x}(t) < 0, \quad\;\; \lambda = 1 \\ \lambda c\dot{x}(t), & \dot{x}(t) \geq 0, \;\; \lambda < 1 \end{cases} \tag{16}$$

where m is the mass of the system, k is the stiffness, and c is the damping coefficient of a system. The bilinear damping force function $g\left[\dot{x}(t)\right]$ is a nonpolynomial nonlinear, asymmetric, function which varies over a velocity range $-\dot{X}(t) \leq \dot{x}(t) \leq \dot{X}(t)$, with two-liner elements shown in Fig. 1. From Eq. (16), if $\lambda = 1$, the system is considered as linear damping oscillator and for $\lambda < 1$, then the system is represented as bilinear damping form. In order to obtain response analysis through the Volterra series, asymmetric bilinear damping form can be approximated with polynomial form as $\hat{g}\left[\dot{x}(t)\right]$ that is assumed as

$$\hat{g}\left[\dot{x}(t)\right] = g_0 + c_1\dot{x}(t) + c_2\dot{x}^2(t) + c_3\dot{x}^3(t) + \ldots \tag{17}$$
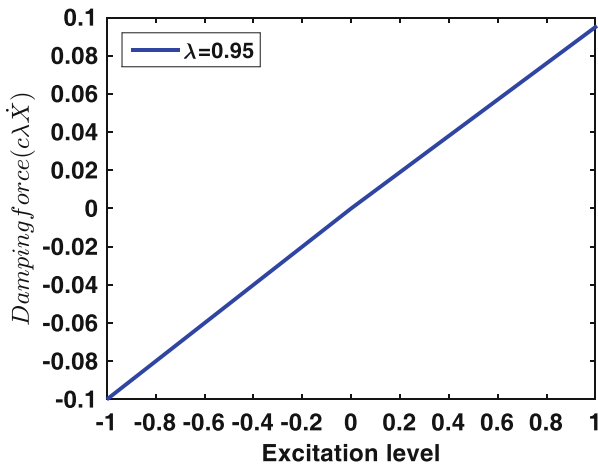
Fig. 1   Bilinear damping force function variation over velocity range for $\lambda = 0.95$

Since $\hat{g}\left[\dot{x}(t)\right]$ is a continuous nonlinear function with an appropriate number of powers over the interval of $\left(-\dot{X}(t), \dot{X}(t)\right)$, the approximate solution in Eqs. (17) can be simplified by truncating the polynomial form up to cubic terms. In order to solve approximate solution it is convenient to replace the velocity $\dot{x}(t)$ by introducing a new independent variable that is $y(t) = \dot{x}(t)$ and Eqs. (16 and 17) can be expressed in terms of new independent variable in the form of $g[y(t)]$ and $\hat{g}\left[y(t)\right]$. The coefficients of the polynomial c_i (where i=1, 2, 3..,) are determined by minimizing the integral

$$E\left(c_1 c_1, c_2, c_3\right) = \int_{-Y}^{Y} \left\{g\left[y(t)\right] - \hat{g}\left[y(t)\right]\right\}^2 dy \tag{18}$$

where Y denotes the maximum velocity. The minimization of the function of Eq. (18) requires

$$\frac{\partial E}{\partial c_i} = 0 \ for \ i = 1, 2, 3, ..n \tag{19}$$

Eq. (19) represents a system of "n" algebraic equations that can be solved simultaneously to obtain the coefficients of polynomials c_i ($c_1, c_2, c_3..$), but we limit the discussion up to case i=3, which can be determined as

$$c_1 = \frac{(\lambda + 1) c}{2}, c_2 = -\frac{15c(1 - \lambda)}{32Y} = -\frac{15c(1 - \lambda)}{32 \ \omega X_{max}}, c_3 = 0 \tag{20}$$

where $Y = \omega X_{max}$, ω is the excitation frequency, X_{max} is the maximum amplitude.

3.2 Quadratic Damping

Similarly, the governing equation of motion of quadratic damping under harmonic excitation force is in the form of

$$m\ddot{x}(t) + k_1 x(t) + g\left[\dot{x}(t)\right] = A cos(\omega t) \tag{21}$$

Here $g\left[\dot{x}(t)\right] = c\dot{x}(t)\left|\dot{x}(t)\right|$

$$g\left[\dot{x}(t)\right] = \begin{cases} -c\dot{x}^2(t), & \dot{x}(t) < 0 \\ c\dot{x}^2(t), & \dot{x}(t) \geq 0 \end{cases} \tag{22}$$

Here $g\left[\dot{x}(t)\right]$ is the quadratic damping force function, which varies over a velocity range $-\dot{X}(t) \leq \dot{x}(t) \leq \dot{X}(t)$. Quadratic damping form is also a nonpolynomial nonlinear function but symmetric.

The approximate solution is assumed as

$$\hat{g}\left[\dot{x}(t)\right] = c_1\dot{x}(t) + c_2\dot{x}^2(t) + c_3\dot{x}^3(t) \tag{23}$$

Solving for $y(t) = \dot{x}(t)$, similar to bilinear damping, the coefficients of polynomial c_i (where i=1, 2, 3..,) are determined by minimizing the integral

$$E\left(c_1, c_2, c_3\right) = \int_{-Y}^{Y}\left\{g\left[y\left(t\right)\right] - \hat{g}\left[y\left(t\right)\right]\right\}^2 dy \tag{24}$$

The minimization of function of Eq. (24) applies

$$\frac{\partial E}{\partial c_i} = 0 \; for \; i = 1, 2, 3, ..n \tag{25}$$

Eq. (25) consists of the system of equations, which can be solved simultaneously to determine the values of c_1, c_2, c_3.

$$c_1 = \frac{5}{16}cY = \frac{5}{16}c\omega X_{max}, c_2 = 0, c_3 = \frac{35}{48}\frac{c}{\omega Y} = \frac{35}{48}\frac{c}{\omega X_{max}} \tag{26}$$

4 Identification of Nonpolynomial Nonlinear Damping

4.1 Bilinear Damping Form

Figure 2a. shows the response spectrum of bilinear damping in which a second harmonic is present and it shows that bilinear damping is in the group of asymmetric nonlinearity forms. But a similar spectrum is exhibited by square damping also. Further classification is provided by the variation of second harmonic amplitude with excitation level as shown in Fig. 2b. This distinctive behavior has been explained by second harmonic amplitude, and which is formulated using Volterra series and second-order Frequency Response Functions. From the Volterra series and FRF synthesis formula, it can be explained that the second-order FRF $H_2(\omega, \omega)$ can be obtained by truncating Eq. (10) up to the first term of second harmonic amplitude $X(2\omega)$, which is also a function of the nonlinear parameter c_2. For square damping nonlinearity,

$$X\left(2\omega\right) = \frac{A^2}{2}H_2\left(\omega, \omega\right) = \frac{A^2}{2}c_2\omega^2 H_1^2\left(\omega\right) H_1\left(2\omega\right) \tag{27}$$
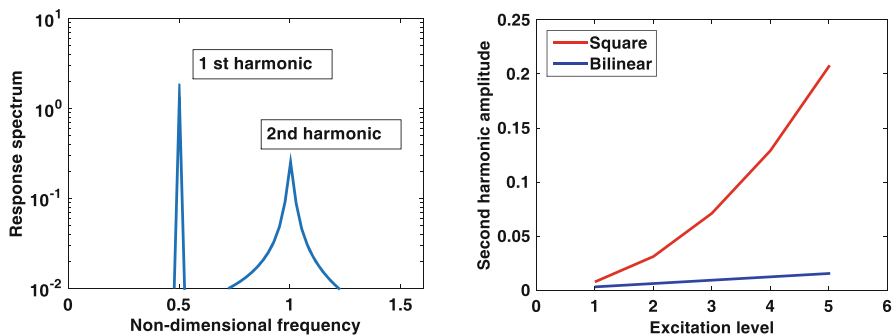
Fig. 2 (**a**) Response spectrum for bilinear damping ($\omega/\omega_n = 0.5$) (**b**) Second harmonic amplitude variation with excitation level($\omega/\omega_n = 0.33$)

$$X(2\omega) \propto A^2 \tag{28}$$

Similarly for bilinear damping, nonlinear parameter c_2 becomes

$$c_2 = -\frac{15c(1-\lambda)}{32\dot{X}} = -\frac{15c(1-\lambda)}{32\,\omega X} \approx -\frac{15c(1-\lambda)}{32\,\omega A H_1(\omega)} \tag{29}$$

where $X \approx X(\omega) = A H_1(\omega)$ is obtained by truncating the first term of the first harmonic amplitude of Eq. (9). If Eq. (29) is substituted in Eq. (27), then second harmonic amplitude $X(2\omega)$ for bilinear damping becomes

$$X(2\omega) = -\frac{15}{64} Ac(1-\lambda) H_1(\omega) H_1(2\omega) \tag{30}$$

$$X(2\omega) \propto A \tag{31}$$

From Eq. (28), it can be shown that second harmonic amplitude varies as a square function of excitation level for square nonlinearity, whereas it varies linearly (Eq. 31) for bilinear form. Although the bilinear function is a nonpolynomial function, it is approximated by a polynomial function which shows that the polynomial coefficients are amplitude dependent, which in turn is dependent on the excitation level. Thus, the second harmonic for bilinear damping behaves differently from a square damping form.
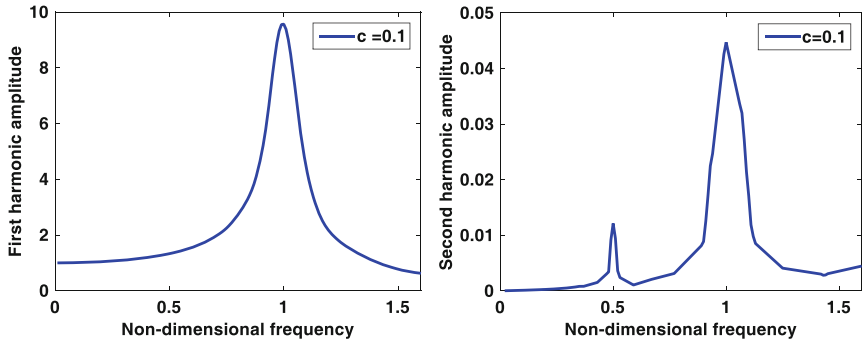
Fig. 3 Response harmonic amplitudes for bilinear damping ($\lambda = 0.95$) (**a**) First harmonic amplitude (**b**) Second harmonic amplitude

4.1.1 Response Characteristic Behavior of Bilinear Damping Form

The response characteristic variation of the harmonic amplitudes over the excitation frequency range is computed through numerical simulation using Runge-Kutta fourth-order method with $m = 1.0$, $k1 = 1.0$ and $c = 0.1$.

From Fig. 3, the following distinctive features have been observed in the bilinear damping form.

- The first harmonic amplitude in bilinear damping (Fig. 3a): the response variation is seen as a smooth curve over the frequency range.
- The second harmonic amplitude in bilinear damping (Fig. 3b): it will have two peaks. The first peak occurs around 50% of natural frequency, whereas the second peak occurs near the resonance. The first peak is smaller than the second peak. As λ decreases, amplitude increases in both harmonic amplitudes.

4.2 Quadratic Damping Form

Similarly, Fig. 4a shows the response spectrum of quadratic damping in which a third harmonic is present and it shows that quadratic damping is falling under the group of symmetric nonlinearity form. But, a similar spectrum is also exhibited by the cubic damping nonlinearity. Quadratic damping also further classifies by variation of third harmonic amplitude with excitation level shown in Fig. 4b. One can notice here that third harmonic amplitude varies as a square function for quadratic damping form, whereas it varies cubic function for cubic damping. This distinct behavior is explained through the Volterra series. The third harmonic amplitude can be obtained from the Volterra series synthesis formulae and its higher
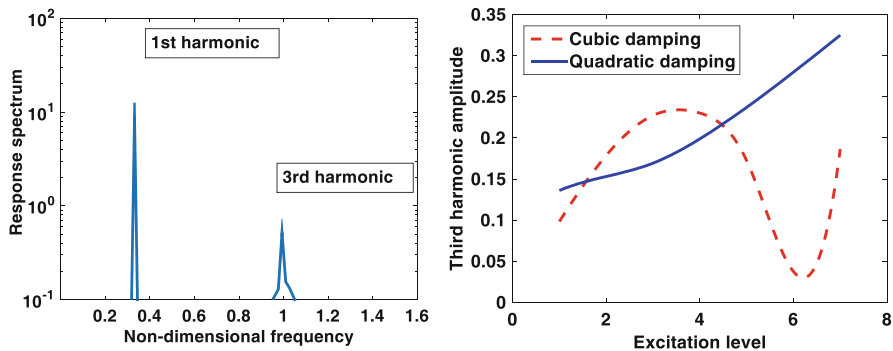
Fig. 4 (**a**) Response spectrum for quadratic damping ($\omega/\omega_n = 0.33$) (**b**) Third harmonic amplitude variation with excitation level($\omega/\omega_n = 0.33$)

order FRFs as given in Eq. (11). For cubic damping nonlinearity, c_2 is zero, then from Eq. (14), $H_3(\omega, \omega, \omega)$ is defined as

$$H_3(\omega, \omega, \omega) = jc_3\omega^3 H_1^3(\omega) H_1(3\omega) \tag{32}$$

Let us consider a first term of third harmonic amplitude

$$X(3\omega) = \frac{A^3}{4} H_3(\omega, \omega, \omega) \approx \frac{A^3}{4} jc_3\omega^3 H_1^3(\omega) H_1(3\omega) \tag{33}$$

$$X(3\omega) \propto A^3 \tag{34}$$

From Eq. (26), nonlinear parameter c_3 for quadratic damping is

$$c_3 = \frac{35}{48} \frac{c}{\omega A H_1(\omega)} \tag{35}$$

By substituting c_3 in Eq. (32)

$$X(3\omega) = j\omega^2 A^2 \frac{35}{192} H_1^2(\omega) H_1(3\omega) \tag{36}$$

$$X(3\omega) \propto A^2 \tag{37}$$

From Eq. (34), it is clearly shown that third harmonic amplitude varies as a cubic function of excitation level for cubic damping nonlinearity, whereas it varies square function for quadratic damping nonlinearity form (Eq. 37). The quadratic damping
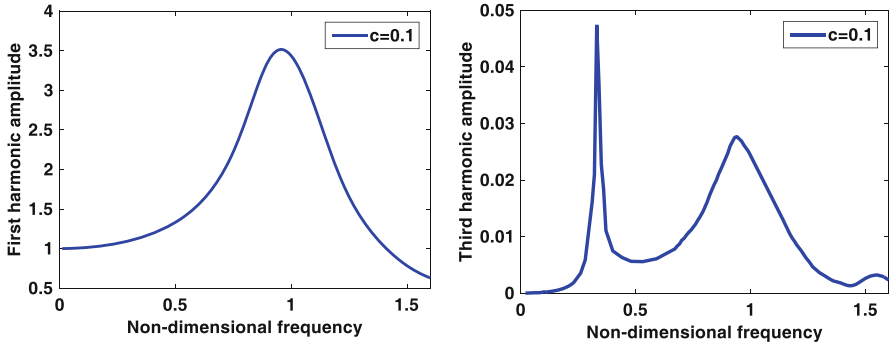
Fig. 5 Response harmonic amplitudes for quadratic damping (**a**) First harmonic amplitude (**b**) Third harmonic amplitude

nonlinearity function is also a nonpolynomial function, and it is approximated by a polynomial function which shows that the polynomial coefficients are amplitude dependent, which in turn is dependent on the square of excitation level. Thus, the third harmonic for quadratic damping behaves differently from a cubic damping form.

4.2.1 Response Characteristic Behavior of Quadratic Damping Form

From Fig. 5, the following distinctive features have been observed in the quadratic damping form.

- The first harmonic amplitude in quadratic damping appears similar to bilinear damping that is the response variation is along a smooth curve over the frequency range as shown in Fig. 5a.
- The third harmonic amplitude (Fig. 5b) in quadratic damping: it will also have two peaks. The first peak occurs around 33% of natural frequency, whereas the second peak occurs near the resonance. The first peak is bigger than the second peak.

5 Conclusions

The identification procedure is presented here to classify nonpolynomial form damping nonlinearity from polynomial form damping nonlinearity. It is illustrated that Volterra series synthesis formulation and its frequency response functions are employed to explicate the distinct response characteristic behavior of bilinear damping form and quadratic damping form qualitatively. The advantage of the Volterra series is higher order harmonic amplitudes obtained in the form of explicit

series, which is easy to compute and the disadvantage is an error due to series truncation that can be overcome by proper selection of excitation frequency and excitation level in order to accurately estimate nonlinear damping parameters. Estimation errors in can be decreased employing a higher order polynomial approximation; however, this involves exhaustive computational work of response harmonic amplitude since it requires higher order FRFs. Three independent methods such as response spectrum and its harmonic amplitude characteristic behavior and variation of harmonic amplitude with excitation level have been provided to identify the presence of bilinear form and quadratic form in a physical system with a damping force.

References

1. A.H. Nayfeh, D.T. Mook, *Nonlinear Oscillations* (John Willey, New York, 1979)
2. J.C. Dixon, *The Shock Absorber Handbook* (John Willey, New York, 1999)
3. B. Balachandran, A.H. Nayfeh, S.W. Smith, R.S. Pappa, On identification of nonlinear interactions in structures. AIAA J. Guid. Control Dyn. **17**(2), 257–262 (1994)
4. S. Adhikari, J. Woodhouse, Identification of damping: Part 2, non-viscous damping. J. Sound Vib. **243**(1), 43–61 (2001)
5. A. Chatterjee, H.P. Chintha, Identification and parameter estimation of cubic nonlinear damping using harmonic probing and volterra series. Int. J. Nonlinear Mech. **125**, 103518 (2020)

Identification of Nonlinear Damping Using Nonlinear Subspace Method

Rui Zhu, Stefano Marchesiello, Dario Anastasio, Dong Jiang, and Qingguo Fei

1 Introduction

In engineering, structures often exhibit nonlinear behavior. Nonlinear damping [1] is a common nonlinear type, which may lead to difficulties in predicting the system response [2]. Therefore, it is essential to identify the nonlinear damping parameters from the measured vibration data [3].

The reader can refer to the extensive review of Noël et al. [4] about the developments in nonlinear system identification during the past ten years, emphasizing the progress realized over that period. As for nonlinear damping, an identification method based on the harmonic balance analysis was implemented in [5], considering softening and hardening behaviors. Amabili et al. [6] identified the nonlinear damping at each excitation level in the nonlinear regime from the experimental data of a rubber plate. Moreover, it should be highlighted that damping identification can be a tricky task also in the linear case, as studied by Naylor et al. [7], characterizing the nonproportional damping distribution of a multi-degrees-of freedom system using the resonant decay method.

Among the several publications about the nonlinear system identification of structures, Marchesiello et al. [8] adopted the perspective of nonlinearities as internal feedback forces and proposed the nonlinear subspace identification technique (NSI). Given the robustness and efficacy of the subspace method, these nonlinear

R. Zhu · Q. Fei (✉)
Southeast University, Nanjing, Jiangsu, People's Republic of China
e-mail: qgfei@seu.edu.cn

S. Marchesiello · D. Anastasio
Politecnico di Torino, Torino, Italy

D. Jiang
Nanjing Forestry University, Nanjing, Jiangsu, People's Republic of China

369

subspace algorithms open up new horizons for the identification of nonlinear mechanical systems.

In this paper, NSI is extended to identify the nonlinear damping. Two numerical examples are used to verify the proposed method.

2   Nonlinear Subspace Method Considering Friction

The nonlinear damping is considered. The equation of the system can be written as follows:

$$M\ddot{x}(t) + C\dot{x}(t) + Kx(t) + f_d = f(t) \tag{1}$$

where M is the mass matrix, C is the damping matrix, and K is the linear stiffness matrix.

The system can be viewed as subjected to the external forces $f(t)$ and the internal feedback forces due to nonlinearities f_d as shown in Fig. 1.

A one-degree-of-freedom mass-spring system with the Coulomb friction is used to elaborate the nonlinear subspace method.

$$m\ddot{x}(t) + c\dot{x}(t) + kx(t) + \alpha \, \text{sgn}\,(\dot{x}(t)) = f(t) \tag{2}$$

By moving the nonlinear term of Eq. (2) to the right-hand side

$$m\ddot{x}(t) + c\dot{x}(t) + kx(t) = f(t) - \alpha \, \text{sgn}\,(\dot{x}(t)) = f(t) - f_d \tag{3}$$

A state vector is used by $z = [x \ \dot{x}]^T$, the state-space formulation of the equation of motion can be expressed as

$$\begin{Bmatrix} \dot{x} \\ \ddot{x} \end{Bmatrix} = \underbrace{\begin{bmatrix} 0 & 1 \\ -\frac{k}{m} & -\frac{c}{m} \end{bmatrix}}_{A_c} \begin{Bmatrix} x \\ \dot{x} \end{Bmatrix} + \underbrace{\begin{bmatrix} 0 & 0 \\ \frac{1}{m} & \frac{\alpha}{m} \end{bmatrix}}_{B_c} \begin{Bmatrix} f(t) \\ -Sgn\,(\dot{x}) \end{Bmatrix} \tag{4}$$
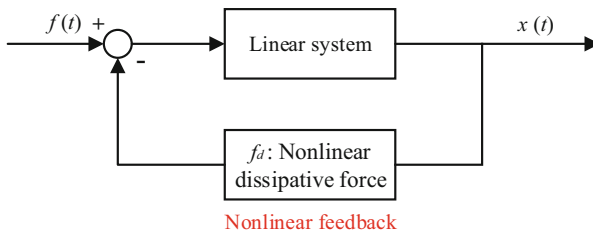
Fig. 1 Closed-loop representation with nonlinear damping

$$y = \underbrace{\begin{bmatrix} 1 & 0 \end{bmatrix}}_{C} \begin{Bmatrix} x \\ \dot{x} \end{Bmatrix} + \underbrace{\begin{bmatrix} 0 & 0 \end{bmatrix}}_{D} \begin{Bmatrix} f(t) \\ - Sgn(\dot{x}) \end{Bmatrix} \tag{5}$$

where A_c, B_c, C, and D are the continuous state-space matrix.

The "extended" frequency response function can be derived based on authors' previous work about the nonlinear subspace identification.

$$H_E(\omega) = D + C(i\omega I - A_c)^{-1} B_c \tag{6}$$

where I is the unit matrix, and ω is the angular frequency and $i = \sqrt{-1}$.

Substituting Eqs. (4) and (5) into Eq. (6), one can obtain

$$H_E(\omega) = \begin{bmatrix} H & H\alpha \end{bmatrix} \tag{7}$$

where H is the underlying linear system receptance matrix. The nonlinear damping coefficients can be identified based on Eq. (7).

3 Simulation

3.1 Single-degree-of-freedom System with 'Cubic Stiffness and Quadratic Friction

The SDOF system with cubic stiffness and coulomb friction is described in Fig. 1, whose motion is described by the following equation (Fig. 2):

$$m\ddot{x}(t) + c\dot{x}(t) + kx(t) + \alpha\dot{x}(t)|\dot{x}(t)| = f(t) \tag{8}$$

with system parameters summarized in. Assume that the type and the location of the nonlinearity are unknown (Table 1).

The SDOF system is excited by a zero-mean Gaussian random input, whose root-mean-square (r.m.s) value is 5. The response is calculated by Runge-Kutta. The effect of the measurement noise on the parameter estimation results is investigated

Fig. 2 A mass-spring system with quadratic friction
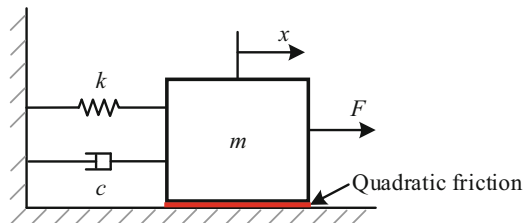
Table 1 System parameters
of the SDOF system

m (kg)	k (N/m)	c (Ns/m)	α(N)
2	1000	1	0.5
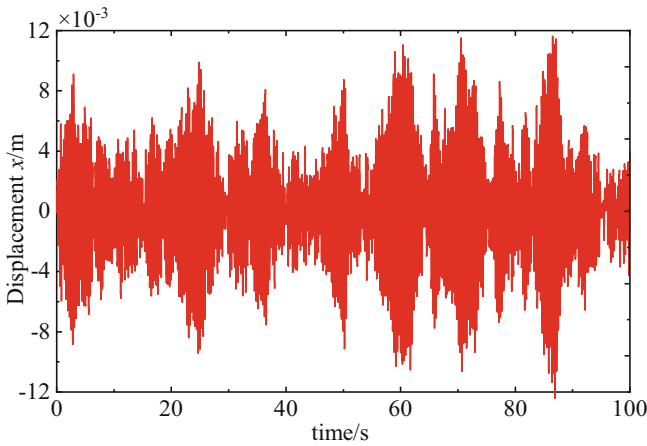
Fig. 3 The displacement of the system
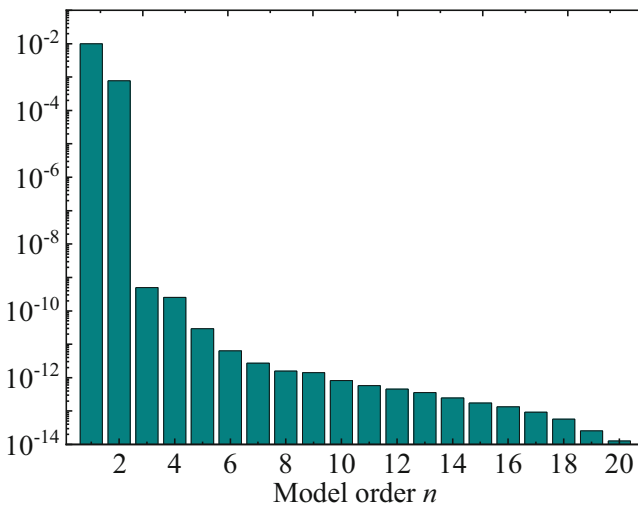
Fig. 4 Singular value plot with 5% measurement error and $i = 20$

by corrupting the previously generated output by adding 5% Gaussian zero-mean noise. The displacement is shown in Fig. 3.

The model order $n = 2$ is determined by inspecting the singular value plot in Fig. 4 (with $i = 20$ block rows), where a jump of seven orders of magnitude between model order two and three is observed.
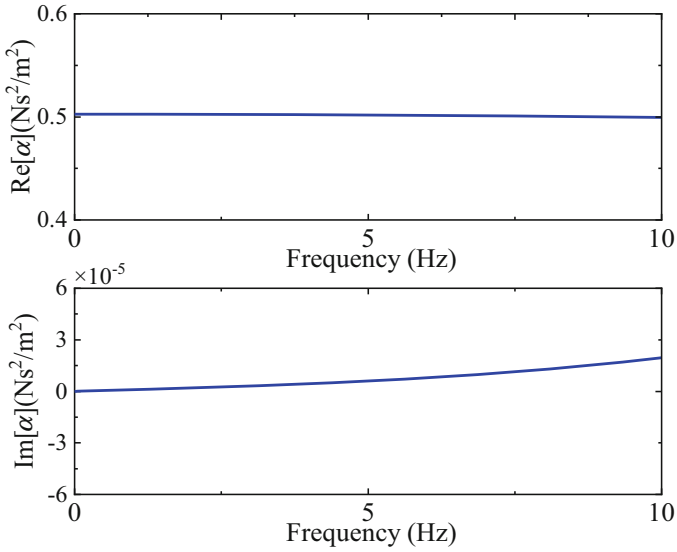
Fig. 5 Real and imaginary parts of the identified coefficients
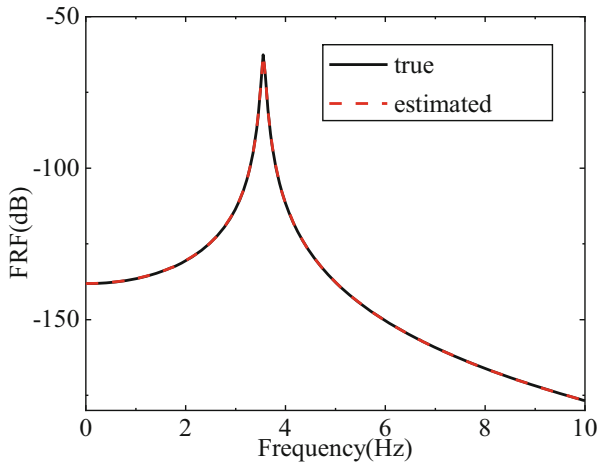
Fig. 6 Underlying linear FRF h_{11}

The determined coefficients are shown in Fig. 5. The error of the nonlinear damping coefficient α is only 1.2%. As shown in Fig. 6, the underlying estimated FRF h can be obtained by the NSI. Results show that the underlying estimated FRF h is in quite good agreement with the true value.

3.2 Three-degrees-of-freedom System with Coulomb and Quadratic Friction

The three-degree-of-freedom nonlinear system shown in Fig. 5 is excited by a zero-mean Gaussian random force at DOF 3 only. The system parameters are summarized in Table 2 (Fig. 7).

The system is excited by a zero-mean Gaussian random input, whose root-mean-square (r.m.s) value is 5 at node 3. The response is calculated by fourth Runge-Kutta. The effect of the measurement noise on the parameter estimation results is investigated by corrupting the previously generated output by adding 2% Gaussian zero-mean noise. The displacement is shown in Fig. 8.

The model order $n = 6$ is determined by inspecting the singular value plot in Fig. 4 (with $i = 40$ block rows), where a jump of four orders of magnitude between model order six and seven is observed (Fig. 9).

The determined coefficients are shown in Figs. 10 and 11. It is worth highlighting that the imaginary part is always much lower than the absolute value of the real part in the selected frequency range, which assesses the goodness of the identification. The identified damping coefficients are reported in Table 3. The max error is only 0.18%.

As shown in Fig. 12, the underlying estimated FRF h_{13} can be obtained by the NSI. Results show that the underlying estimated FRF h_{13} is in quite good agreement with the true value.

Table 2 System parameters of the 3-DOF system

Mass (kg)	Linear stiffness (N/m)	Damping (Ns/m)	Nonlinear damping
$m_1 = m_2 = 1$	$k_1 = k_3 = 800$	$c_1 = c_2 = 2$	$\alpha_1 = 5$
$m_3 = 1.5$	$k_2 = 1000$	$c_3 = 1$	$\alpha_2 = 0.2$
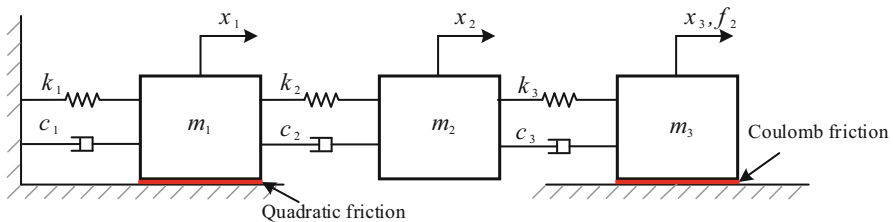
Fig. 7 Three-degree-of-freedom nonlinear system with quadratic friction to ground at DOF 1 and the Coulomb friction to ground at DOF 3
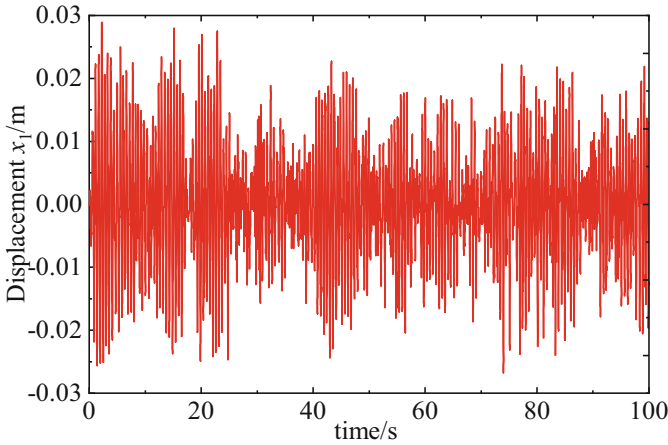
Fig. 8 The displacement of the system
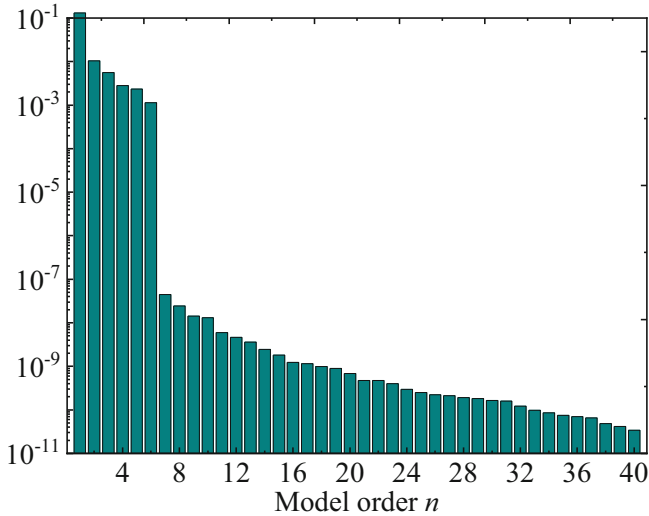
Fig. 9 Singular value plot with 2% measurement error and $i = 40$

4   Conclusions

Two common kinds of nonlinear damping are successfully identified by nonlinear subspace method. The effect of the measurement noise on the parameter estimation results is investigated by corrupting the previously generated output adding different Gaussian zero-mean noise. Results show that the proposed method can fully characterize the nonlinearities in the structure and effectively identify the nonlinear damping parameters.
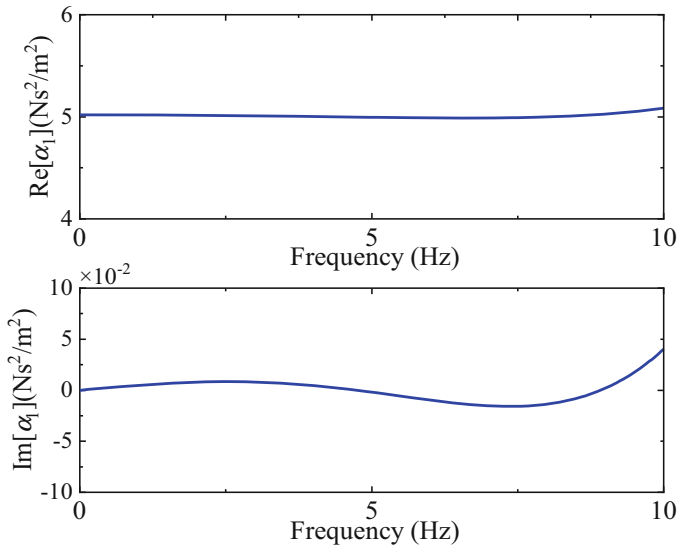
Fig. 10 Real and imaginary parts of the identified coefficient α_1
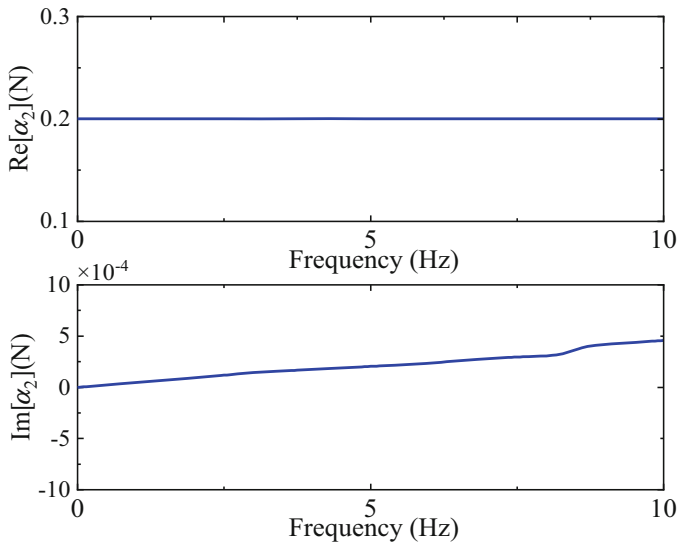
Fig. 11 Real and imaginary parts of the identified coefficient α_2

Table 3 Identified results

Nonlinear damping coefficients	Exact value	Identified value	Error/%
α_1	5	5.010	0.18
α_2	0.2	0.199	0.11
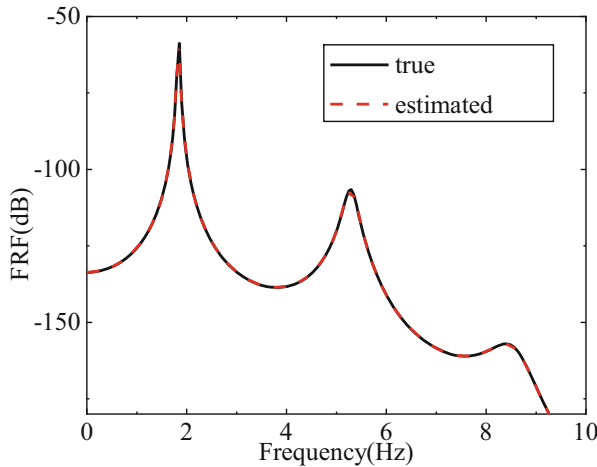
Fig. 12 Underlying linear FRF h_{13}

References

1. M. Amabili, Derivation of nonlinear damping from viscoelasticity in case of nonlinear vibrations. Nonlinear Dyn. **97**, 1785–1797 (2019)
2. R. Zhu, Q. Fei, D. Jiang, et al., Dynamic sensitivity analysis based on Sherman–Morrison–Woodbury formula. AIAA J. **57**(11) (2019)
3. R. Zhu, Q. Fei, D. Jiang, et al., Removing mass loading effects of multi-transducers using Sherman-Morrison-Woodbury formula in modal test. Aerosp. Sci. Technol. **93** (2019)
4. J.P. Noël, G. Kerschen, Nonlinear system identification in structural dynamics: 10 more years of progress. Mech. Syst. Signal Process. **83**, 2–35 (2017)
5. J. Delannoy, M. Amabili, B. Matthews, et al., *Non-Linear Damping Identification in Nuclear Systems under External Excitation[C]// ASME 2015 International Mechanical Engineering Congress and Exposition* (2015)
6. P. Balasubramanian, G. Ferrari, M. Amabili, Identification of the viscoelastic response and nonlinear damping of a rubber plate in nonlinear vibration regime. Mech. Syst. Signal Process. **111**, 376–398 (2017)
7. S. Naylor, M.F. Platten, J.R. Wright, Identification of multi-degree of freedom systems with nonproportional damping using the resonant decay method. J. Vibrat. Acoust. **126**(2), 298–306 (2004)
8. S. Marchesiello, L. Garibaldi, A time domain approach for identifying nonlinear vibrating structures by subspace methods. Mech. Syst. Signal Process. **22**(1), 81–101 (2008)

Nonlinear Restoring Force Subspace Identification of Negative Stiffness Nonlinear Oscillators

Qinghua Liu, Fangyuan Hu, Junyi Cao, and Xingjian Jing

1 Introduction

In recent years, many negative stiffness structures have been developed to enhance the ability of energy harvesting or vibration control [1–4]. Harne and Wang investigated the engineering application status of bistable structure dynamics in their book [1]. Daqaq et al. made a critical review and discussion on energy harvester using a bistable beam [2]. Jing et al. proposed a class of X-shaped structures for vibration isolation [3]. Yan et al. utilized symmetric permanent magnets to construct a bistate nonlinear vibration isolator [4]. The basic principle of these structures is to couple nonlinear negative stiffness on linear oscillators.However, it is hard to obtain the accurate nonlinear restoring force (NRF) in negative stiffness oscillators for dynamic analysis. In recent decades, much effort has been devoted to investigating the governing model derivation and the effect of NRF, such as analytical theory and direct measurement using a dynamometer, which are only suitable for ideal conditions [5–7]. Leng et al. utilized equivalent magnetizing current theory to calculate the potential wells function and Santon et al. calculated magnetic force based on the magnetic dipoles theory [5, 6]. The limitation of these two models is magnet's dimensions must be much less than the magnet interval. Zhou et al. measured the magnetic force and then fitted it with empirical polynomial function [7]. It will lead to failure when considering large deformation and asymmetric conditions. Therefore, modeling based on system identification of NRF is necessary.

Q. Liu · F. Hu · J. Cao (✉)
Key Laboratory of Education Ministry for Modern Design and Rotor-Bearing System, Xi'an Jiaotong University, Xi'an, China
e-mail: caojy@mail.xjtu.edu.cn

X. Jing
Department of Mechanical Engineering, The Hong Kong Polytechnic University, Hong Kong, China

For the identification of restoring force in nonlinear oscillators, many identification algorithms have been proposed [8]. Marchesiello et al. proposed a time-domain subspace identification algorithm to simulate the identification of NRF in an oscillator with the cubic stiffness and clearance type nonlinearity [9]. Noël, Filippis, and Anastasio et al. had improved this method to identify impact stiffness in SmallSat spacecraft [10], contact stiffness in bolted connected solar array structure and aircraft [11, 12], and distributed nonlinearities in slender beam [13]. Moreover, Zhang et al. investigated a two-stage time-domain approach based on the subspace method to identify multiple degree-of-freedom nonlinear structures [14]. Liu et al. proposed a novel nonlinear separation subspace identification algorithm to get contact stiffness in the cantilever beam system [15, 16]. It's attractive that this identification technology is used to identify NRF in negative stiffness oscillators, because of its robustness and high numerical performances.

2   Subspace Identification Method

2.1   Linear Subspace Identification

For the linear subspace identification method, the calculation process is conducted on the discrete-time state-space model of the dynamic system and can be expressed as

$$
\begin{aligned}
x_{r+1} &= Ax_r + Bu_r + p_r \\
y_r &= Cx_r + Du_r + q_r
\end{aligned}
\tag{1}
$$

where A, B, C, and D are, respectively, system matrix, input matrix, output matrix, and direct feedthrough matrix. u_r, y_r, and x_r are input, output, and state vector at time instant r. p_r and q_r represent the process error and measurement error and are all considered to be the zero-mean Gaussian white noises in this paper.

The goal of the subspace identification problem is to estimate the model order and the system matrices A, B, C, and D based on the input and output matrix. By iterating the two equations in Eq. (1) yields

$$
\begin{aligned}
y_k &= CA^{r-1}x_1 + CA^{r-2}Bu_1 + CA^{r-3}Bu_2 + \cdots CBu_{k-1} \\
&+ CA^{r-2}p_1 + CA^{r-3}p_2 + \cdots Cp_{k-1} + Du_k + q_k
\end{aligned}
\tag{2}
$$

Then extended observability matrix Γ and two triangular Toeplitz matrix Θ and Λ are defined as follows:

$$
\Gamma = \begin{bmatrix} C & CA & \cdots & CA^r \end{bmatrix}^T
\tag{3}
$$

$$\Theta = \begin{bmatrix} D & 0 & \cdots & 0 \\ CB & D & \cdots & 0 \\ \vdots & \vdots & \ddots & \vdots \\ CA^{r-2}B & CA^{r-3}B & \cdots & D \end{bmatrix} \tag{4}$$

$$\Lambda = \begin{bmatrix} 0 & 0 & \cdots & 0 & 0 \\ C & 0 & \cdots & 0 & 0 \\ CA & C & \cdots & 0 & 0 \\ \vdots & \vdots & \ddots & 0 & 0 \\ CA^{r-2} & CA^{r-3} & \cdots & C & 0 \end{bmatrix} \tag{5}$$

Then Eqs. (2) can be rearranged as

$$Y = \Gamma X + \Theta U + \Lambda P + Q \tag{6}$$

Finally, the input and output data should be gathered in the block Hankel matrix, and matrix projection theory should be utilized to calculate the estimated matrices [17].

$$A = T\hat{A}T^{-1}; \quad B = T\hat{B}; \quad C = \hat{C}T^{-1}; \quad D = \hat{D} \tag{7}$$

where ˆ denotes estimated matrics, T is an invertible matrix.

2.2 Nonlinear Subspace Identification

According to Newton's second law of motion, the mechanical equation of multi-stable oscillator with magnetic coupling can be written as follows:

$$M\ddot{w}(t) + C\dot{w}(t) + Kw(t) + \sum_{n=1}^{p} k_n w^n(t) = F(t) \tag{8}$$

where M, C, and K are equivalent linear mass, viscous damping, and stiffness, $w(t)$ is negative stiffness oscillator's displacement vector, and $F(t)$ is the input force. The nonlinear magnetic force can often be defined as high-order polynomial form $\sum_{n=1}^{p} k_n w^n(t)$ and can be seen as a feedback force on the underlying linear system, then the nonlinear term in Eq. (8) can be moved to the right-hand side.

$$M\ddot{w}(t) + C\dot{w}(t) + Kw(t) = F(t) - \sum_{n=1}^{p} k_n w^n(t) \tag{9}$$

The Eq. (9) can be converted into a continuous-time state-space model

$$
\dot{x} = A_c x + B_c u
$$
$$
y = C_c x + D_c u
$$
(10)

where A_c, B_c, C_c, and D_c are system matrices, input matrics, output metrics, and direct feedthrough term. The continuous model can be converted into a discrete state-space model and a discrete state vector is defined as $x_r = x(r\Delta t)$. Then the following discrete state-space model is obtained:

$$
x_{r+1} = A x_r + B u_r
$$
$$
y_r = C x_r + D u_r
$$
(11)

where $A = e^{A_c \Delta t}$, $B = \left(e^{A_c \Delta t} - I\right) A_c^{-1} B_c$.

Assuming that the displacement w at the end of the cantilever beam can be measured, the state-space formulation of the Eq. (9), corresponding to a state vector chosen as $x = [w \ \dot{w}]^T$ and to an input vector $u = [F(t) - k_1 w(t) \cdots - k_n w^n(t)]^T$, is.

$$
\left\{ \begin{matrix} \dot{w} \\ \ddot{w} \end{matrix} \right\} = \left[\begin{matrix} 0_{h \times h} & I_{h \times h} \\ -M^{-1}K & -M^{-1}C \end{matrix} \right] \left\{ \begin{matrix} w \\ \dot{w} \end{matrix} \right\} + \left[\begin{matrix} 0_{h \times h} & \cdots & 0_{h \times 1} \\ M^{-1} & \cdots & M^{-1}k_n \end{matrix} \right] \left\{ \begin{matrix} F \\ -w \\ \vdots \\ -w_n \end{matrix} \right\}
$$

$$
y = [I_{h \times h} \quad 0_{h \times h}] \left\{ \begin{matrix} w \\ \dot{w} \end{matrix} \right\} + \left[0_{h \times h} \ 0_{h \times 1} \cdots 0_{h \times 1} \right] \left\{ \begin{matrix} F \\ -k_1 \\ \vdots \\ -k_n w^n \end{matrix} \right\}
$$
(12)

The "extended" frequency response function (FRF) matrix $H_E(\omega)$ of the nonlinear system is

$$
\begin{aligned}
\hat{H}_E(\omega) &= \hat{D} + \hat{C}\left(i\omega I - \hat{A}_c\right)^{-1} \hat{B}_c \\
&= D + CTT^{-1}(i\omega I - A_c)^{-1} TT^{-1} A_c (A - I)^{-1} B \\
&= D + C(i\omega I - A_c)^{-1} B_c = H_E(\omega)
\end{aligned}
$$
(13)

It's obvious that the "extended" FRF contains the parameters of the system (include M, C, K, and k_n). Taking into account Eq. (12), the "extended" FRF becomes

$$
\begin{aligned}
H_E(\omega) &= (i\omega I - A_c)^{-1} M^{-1} \left[I \ k_1 \ \cdots \ k_n \right] \\
&= \left(K + i\omega C - \omega^2 M\right)^{-1} \left[I \ k_1 \ \cdots \ k_n \right]
\end{aligned}
$$
(14)

and particularly, in the case $\omega = 0$,

$$H_E(0) = \begin{bmatrix} K^{-1} & K^{-1}k_1 & \cdots & K^{-n}k_n \end{bmatrix} \tag{15}$$

Then the NRF function can be characterized as

$$f_{non} = \left(K^{-1}k_1 - K^{-1} \right) w + K^{-1}k_2 w^2 + \cdots + K^{-1}k_n w^n \tag{16}$$

3 Numerical Examples

Considering the simplest negative stiffness nonlinear oscillator, the NRF is at least third-order polynomial, where $K + k_1$ is negative and k_3 is positive. If k_2 is not zero, the system is asymmetric. This kind of oscillator is often called a bistable oscillator, which has two steady states and one unstable state. When designing a bistable oscillator, three equilibrium points w_1, w_2, and w_3 must be given first and unstable point w_2 is often designed as zero. Decompose the NRF into the following equation

$$f_{non} = k_3 \left(w - w_1 \right) \left(w - w_3 \right) \tag{17}$$

where $K + k_1 = k_3 w_1 w_3$ and $k_2 = -k_3(w_1 + w_3)$.

The tristable oscillator has five equilibrium points and three of them are stable. Similarly, five equilibrium points w_1, w_2, w_3, w_4, and w_5 must be given first and unstable point w_3 is often designed as zero. Then, the NRF can be expressed by

$$f_{non} = k_5 \left(w - w_1 \right) \left(w - w_2 \right) w \left(w - w_4 \right) \left(w - w_5 \right) \tag{18}$$

where

$$k_5 = K + k_1/w_1 w_2 w_4 w_5$$
$$k_2 = -k_5 \left((w_1 + w_2) w_4 w_5 + (w_4 + w_5) w_1 w_2 \right)$$
$$k_3 = k_5 \left((w_1 + w_2)(w_4 + w_5) + w_1 w_2 + w_4 w_5 \right)$$
$$k_4 = -k_5 \left(w_1 + w_2 + w_4 + w_5 \right)$$

Four types of oscillators' parameters are listed in Table 1.

The linear stiffness K of the beam and first-order polynomial coefficient of nonlinear magnetic force must be given first. In this paper, K is chosen to be 75 N/m, and k_1 is an interval value be designed between -120 N/m to -20 N/m. As can be seen in Fig. 1, k_1 can determine the depth of the potential wells of the bistable or tristable oscillators.

In the following simulations, $k_1 = -120$ N/m was considered for symmetric bistable and asymmetric bistable oscillator, $k_1 = -60$ N/m was considered for symmetric tristable and asymmetric tristable oscillator. Equivalent mass M and

Table 1 The parameter of four different types of negative stiffness oscillators

Types	NRF function	Equilibrium points w(m)				
Symmetric bistable	$f_{non} = (K + k_1)w + k_3w^3$	−0.005		0	0.005	
Asymmetric bistable	$f_{non} = (K + k_1)w + k_2w^2 + k_3w^3$	−0.007		0	0.005	
Symmetric tristable	$f_{non} = (K + k_1)w + k_3w^3 + k_5w^5$	−0.01	−0.005	0	0.005	0.01
Asymmetric tristable	$f_{non} = (K + k_1)w + k_2w^2 + k_3w^3 + k_4w^4 + k_5w^5$	−0.012	−0.006	0	0.005	0.01
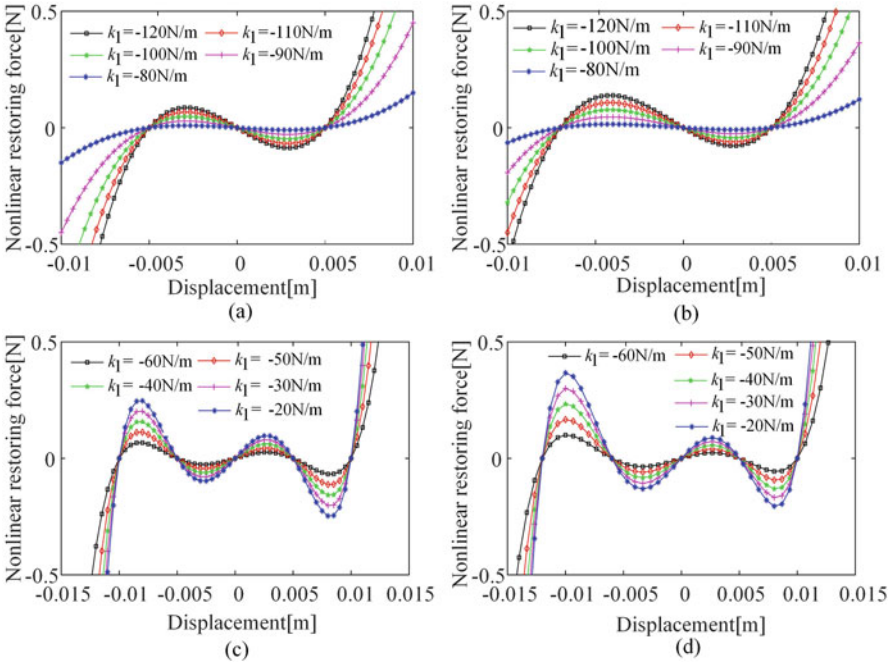
Fig. 1 (**a**) Symmetric bistable with k_1 from −120 N/m to −80 N/m; (**b**) asymmetric bistable with k_1 from −120 N/m to −80 N/m; (**c**) symmetric tristable with k_1 from -60 N/m to -20 N/m; (**d**) asymmetric tristable with k_1 from −60 N/m to −20 N/m

viscous damping C of the cantilever beam are 0.006 kg and 0.01 N • (s/m). In Table 2, the four types of NRF are simulated in Newton's second law of motion.

It is important to note that the bistable and tristable oscillator can behave interwell or intrawell oscillation, the selection of identification data sets is particularly important. The numerical examples show that the selected output displacement signal must contain both interwell or intrawell oscillation. In this paper, a sweep signal with constant excitation acceleration was chosen, it ensures that the amplitude of input excitation force is constant. Moreover, the sweep frequency range is determined by the natural frequency of the underlying linear system derived from

Table 2 Numerical simulation equations

Types	NRF function
Symmetric bistable	$f_{non} = -45w + 1.8 \times 10^6 w^3$
Asymmetric bistable	$f_{non} = -45w + 2.6 \times 10^3 w^2 + 1.29 \times 10^6 w^3$
Symmetric tristable	$f_{non} = 15w - 7.5 \times 10^5 w^3 + 6 \times 10^9 w^5$
Asymmetric tristable	$f_{non} = 15w - 750w^2 - 6.2 \times 10^5 w^3 + 1.25 \times 10^7 w^4 + 4.2 \times 10^9 w^5$

the nonlinear oscillator. Based on these principles, the frequency-swept response of Fig. 2(a, c, e, g) was used to make an identification simulation. Considering the noise pollution in real applications, signal-to-noise ratio 40 dB, 30 dB, and 20 dB gradually enhanced white Gaussian noise signal was added to the data set. Because the difference in the identification accuracy under different noises is not very big, it is not necessary to compare all of them. Here, only the case with the maximum noise of 20 dB is selected and all results show that the identified NRFs are all above 93% compared to the theoretical curve in Fig. 2(b, d, f, h).

Though the identified accuracy is slightly different between the four types of the oscillator, it must be noted that these differences depend on many factors like the optimal order of system matrix or selected identification signal. So, the comparison of identification ability between these four types of oscillators is unnecessary.

4 Experimental Verification

In this section, experiments are carried out to validate the ability of the nonlinear subspace identification method. The experimental system shown in Fig. 3 is set up and excited under constant and sweep frequency excitations by a vibration exciter (JZK-50) controlled by a signal generator (VT-9002-1) and a power amplifier (YE5874A). A displacement sensor (HL-G112-A-C5) is applied to measure the absolute displacement of the beam's displacement response and an oscilloscope (TBS2000) is used to collect the experimental data.

It's hard to achieve a completely symmetric condition because of the cantilever beam's internal stress, inhomogeneity of two rotating magnets, or installation conditions. So, if the position accuracy of the two steady-state points is higher than 95%, it will be regarded as symmetric.

The four different types of multistable oscillators' equilibrium points and other experimental parameters are listed in Table 3.

The restoring force surface (RFS) method can be used to verify the accuracy of NRF identified by the nonlinear subspace identification method. So, the multistable beams' displacement response was processed to get velocity and acceleration and then construct their RFS. The comparison between identified NRF and experimental RFS is illustrated in Fig. 4(a–d). It can be seen from Fig. 4 that the errors in the four types of oscillators are slightly different. However, it cannot explain that identifi-
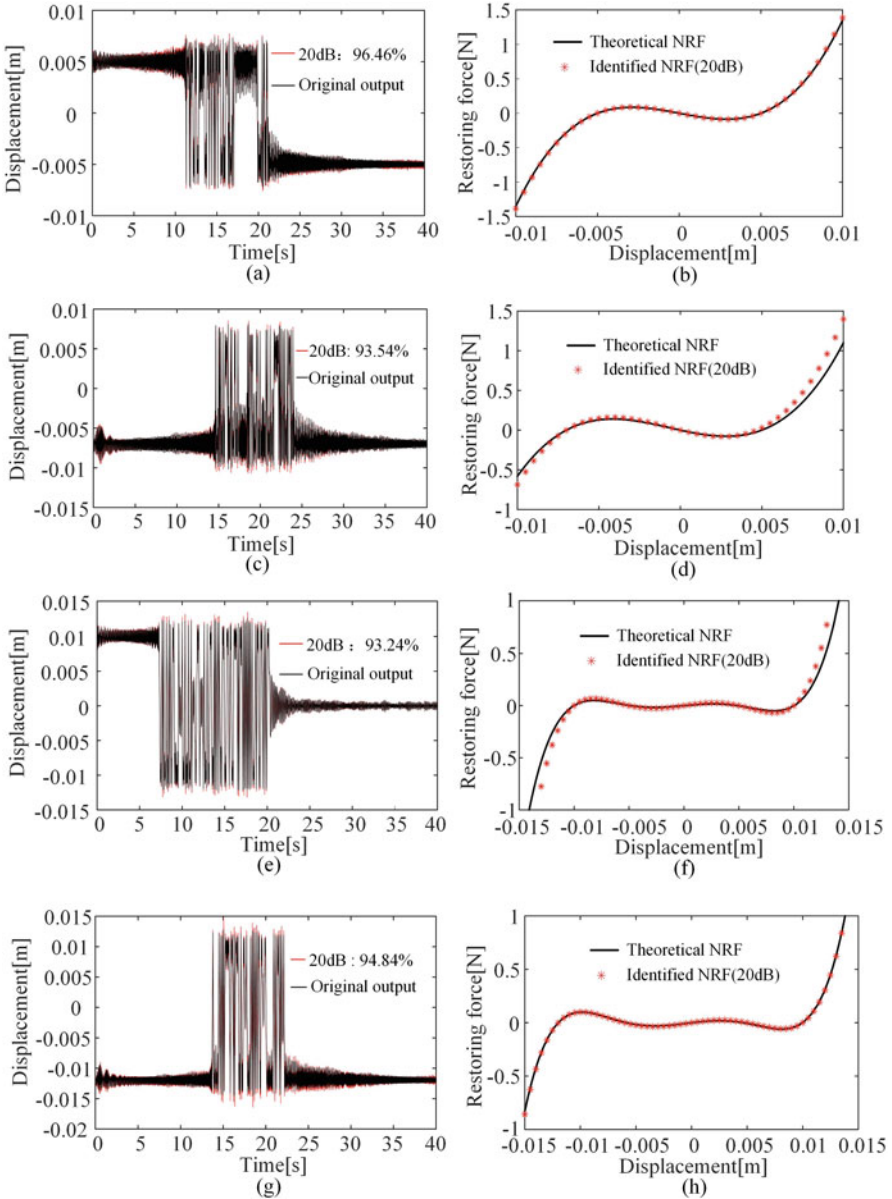
Fig. 2 (**a**) Symmetric bistable, (**c**) asymmetric bistable, (**e**) symmetric tristable, and (**g**) asymmetric tristable frequency-swept displacement response and identified results under 20 dB noise; (**b**, **d**, **f**, **h**) Comparsion between the identified NRF (20 dB) and theoretical NRF

cation accuracy is affected by different types of NRF. Through a large number of simulation data and experimental data sets identification results, it can be concluded
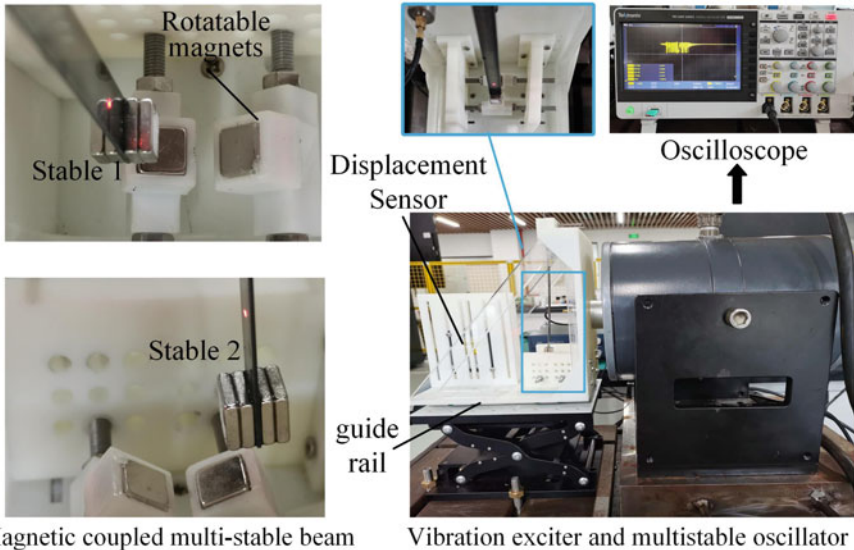
Fig. 3 Photo of the experimental test rig

Table 3 The experimental parameters of four different types of multistable oscillators

Types	Equilibrium points w(mm)	Sweep amplitude (m/s^2)	Sweep time (s)	Sweep range (Hz)
Symmetric bistable	-6.69; 0; 6.73	3	40	5 ~ 25
Asymmetric bistable	-8.81; 0; 6.21	10	40	15 ~ 35
Symmetric tristable	-10.95; 0; 11.09-5.3; 5.2	5.5	40	10 ~ 30
Asymmetric tristable	-12.50; 0; 9.60-6.3; 4.0	9	40	10 ~ 30

that the accuracy identified by the nonlinear subspace identification method strongly depends on the selection of excitation signal and measurement noises. Anyway, the identified NRF always keeps good agreement with the measured RFS.

5   Conclusions

In this paper, the four types of negative stiffness nonlinear oscillators were constructed by using a magnetically coupled multistable cantilever beam. To verify the identification ability of the nonlinear subspace identification algorithm, the sweep response signals of the multistable oscillator under different noises are selected. The simulation results show that at least above 93% accuracy was guaranteed though 20 dB noise was added. Moreover, the oscillators' Frequency-Sweeping response signal must contain both interwell oscillation and intrawell oscillation. In other words, the selection of the excitation signal is significant. In real experimental
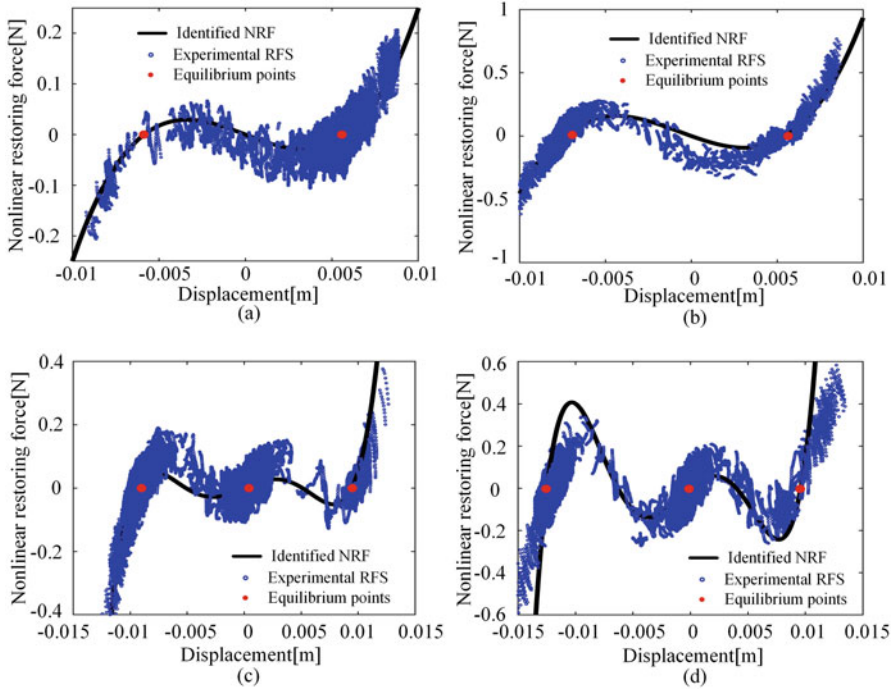
Fig. 4 The comparison between identified NRF and experimental RFS. (**a**) bistable oscillator; (**b**) asymmetric bistable; (**c**) tristable oscillator; (**d**) asymmetric tristable

conditions, the theoretical NRF is not known. So, experimental RFS was constructed to compare with the NRF identified by the nonlinear subspace algorithm. From the experimental results, four multistable oscillators' NRF are in good agreement with the measured RFS.

References

1. R. Harne, K. Wang, *Harnessing Bistable Structural Dynamics: For Vibration Control, Energy Harvesting, and Sensing* (John Wiley and Sons, 2017)
2. M.F. Daqaq, R. Masana, A. Erturk, D.D. Quinn, Closure: On the role of nonlinearities in energy harvesting: A critical review and discussion. Appl. Mech. Rev. **66**(4), 045501 (2014)
3. X. Jing, L. Zhang, G. Jiang, X. Feng, Z. Xu, Critical factors in designing a class of X-shaped structures for vibration isolation. Eng. Struct. **199**, 109659 (2019)
4. B. Yan, H. Ma, B. Jian, K. Wang, C. Wu, Nonlinear dynamics analysis of a bi-state nonlinear vibration isolator with symmetric permanent magnets. Nonlinear Dyn. **97**, 2499–2519 (2019)

5. Y. Leng, D. Tan, J. Liu, Y. Zhang, S. Fan, Magnetic force analysis and performance of a tri-stable piezoelectric energy harvester under random excitation. J. Sound Vib. **406**, 146–160 (2017)
6. S.C. Stanton, C.C. McGehee, B.P. Mann, Nonlinear dynamics for broadband energy harvesting: Investigation of a bistable piezoelectric inertial generator. Physica D. **239**, 640–653 (2010)
7. S. Zhou, J. Cao, A. Erturk, J. Lin, Enhanced broadband piezoelectric energy harvesting using rotatable magnets. Appl. Phys. Lett. **102**(17), 101301-R21 (2013)
8. J.P. Noël, G. Kerschen, Nonlinear system identification in structural dynamics: 10 more years of progress. Mech. Syst. Signal Process. **83**, 2–35 (2017)
9. S. Marchesiello, L. Garibaldi, A time-domain approach for identifying nonlinear vibrating structures by subspace methods. Mech. Syst. Signal. Process. **22**(1), 81–101 (2008)
10. J.P. Noël, L. Renson, G. Kerschen, Complex dynamics of a nonlinear aerospace structure: experimental identification and modal interactions. J. Sound. Vib. **333**(12), 2588–2607 (2014)
11. J.P. Noël, G. Kerschen, E. Foltete, S. Cogan, Grey-box identification of a non-linear solar array structure using cubic splines. W **67**, 106–119 (2014)
12. G.D. Filippis, J.P. Noël, G. Kerschen, L. Soria, C. Stephan, Experimental nonlinear identification of an aircraft with bolted connections. IMAC XXXIV. **1**, 263–278 (2016)
13. D. Anastasio, S. Marchesiello, G. Kerschen, J.P. Noël, Experimental identification of distributed nonlinearities in the modal domain. J. Sound Vib. **458**, 426–444 (2019)
14. M. Zhang, S. Wei, Z. Peng, X. Dong, W. Zhang, A two-stage time domain subspace method for identification of nonlinear vibrating structures. Int. J. Mech. Sci. **120**, 81–90 (2017)
15. B. Li, L. Han, W. Jin, S. Quan, Theoretical and experimental identification of cantilever beam with clearances using statistical and subspace-based methods. J. Comput. Nonlin. Dyn. **11**(3), 031003 (2016)
16. J. Liu, B. Li, H. Miao, X. Zhang, M. Li, A modified time domain subspace method for nonlinear identification based on nonlinear separation strategy. Nonlinear Dyn. **94**(4), 2491–2509 (2018)
17. P. Van Overschee, B.L. De Moor, *Subspace Identification for Linear Systems: Theory, Implementation, Applications* (Kluwer Academic Publishers, Boston, 1996)

Accurate Model Identification of Quadcopters with Moments of Inertia Uncertainty and Time Delay

Marzieh Ghani (iD) **and Afshin Banazadeh** (iD)

1 Introduction

Unmanned Aerial Vehicles (UAVs) have a wide range of applications in both military and commercial areas as they can hover, land and take off vertically; move in any direction and also fly at both high and low speed. Remote monitoring, surveillance and transportation of small packages are some of the applications of UAVs. Quadcopters are the most popular UAVs [1] due to their advantages: one of them is the lack of need for complex mechanical controller as they are controlled with the variation of rotor speed. Moreover, they can fly indoor and outdoor in light wind conditions. With the increase of interest in Quadcopters, the necessity of establishing a precise and fast mathematical model has increased in order to simulate dynamic behaviour and estimate dynamic characteristics with the aid of computers which lead to the cost and time reduction in the development of flight controllers [2].

Mathematical model of quadcopters can be derived in traditional way using Newton-Euler [3, 4] or Euler-Lagrange formalism [5] which is followed by a comparison between flight test data and simulation results for additional fine-tuning to enhance the accuracy of the model [2]. On the top of that is the system identification or the art of extracting mathematical model from measured input and output data [6–8] which not only is used to establish the dynamic model equations but also is useful to determine the constant parameters in the equations [9–12] or to obtain the dynamic of the subsystem of quadcopter like its rotors [13]. In [14] moment of inertia and thrust parameters of a hexacopter are evaluated by time domain system identification method. Inertia tensor of a quadcopter is investigated using test benches in [4]. A real-time estimator determining the inertia tensor of

M. Ghani · A. Banazadeh (✉)
Department of Aerospace Engineering, Sharif University of Technology, Tehran, Iran
e-mail: banazadeh@sharif.edu

391

a three degrees of freedom quadcopter hover platform is designed in [15]. System identification of quadcopters is accomplished also by employing frequency domain methods commonly applied to large-scale rotorcrafts and fixed wing aircraft [16–18]. Also, bare airframe dynamics is extracted in hover flight condition [19].

With regard to controller design, however, it is necessary that the main parameters to be known especially the moment of inertia, since it is not measurable through static tests [1]. However, analytical methods or CAD software can be used for geometrically simple objects which are impractical for quadcopters due to complexity in the equations and also the possibility of change from one mission to another due to payload requirements. Therefore, flight tests would be more convenient to obtain moments of inertia.

This paper proposes a method to obtain accurate moments of inertia of quadcopters with the aid of frequency domain system identification technique which is a fast and precise technique and also directly applicable to control system design. There are other methods to identify or simulate moments of inertia of quadcopters, but the advantage of frequency domain system identification technique is its high accuracy, low computational workload and capability to be implemented in different dynamic modes. Moreover, it can be easily used in control system design with regard to the extraction of the transfer function. The process has been firstly applied in a captive form to a quadcopter attached to the laboratory test stand with three degrees of freedom. Afterwards, the tests are repeated for F450 quadcopter and the extracted dynamic models are verified. Moreover, delay of the rotors as an important criterion in controller design is also identified.

2   Mathematical Model

Quadcopter consists of four identical motors with cross- or plus-form structure, as shown in Fig. 1. It is typically controlled by the speed of its motors. The equations of motion of this vehicle, with respect to the body reference frame, is expressed as follows:

$$F = m \frac{d(V)}{dt} + m(\boldsymbol{\omega} \times V) \tag{1}$$

$$M = [I] \frac{d(V)}{dt} + \boldsymbol{\omega} \times ([I]\,\boldsymbol{\omega}) \tag{2}$$

where $V = [V_x \ V_y \ V_z]^T$ and $\boldsymbol{\omega} = \begin{bmatrix} p \ q \ r \end{bmatrix}^T$ are translational and angular velocities in body reference frame, respectively. $F = \begin{bmatrix} F_x \ F_y \ F_z \end{bmatrix}^T$ is the external force vector, $M = \begin{bmatrix} M_x \ M_y \ M_z \end{bmatrix}^T$ is the external moment vector and $[I]$ is the matrix of moments of inertia which is a diagonal matrix and m is the mass of the vehicle.
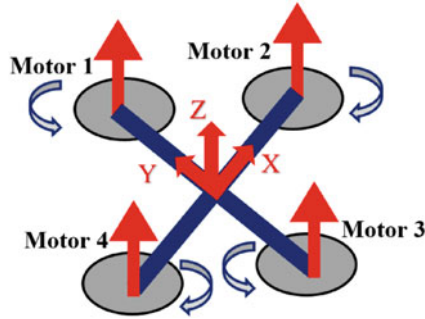
Fig. 1 Schematic of a quadcopter

External forces and moments are calculated based on the thrust force of each rotor, T_i, $i = 1, 2, 3, 4$ [3]:

$$F_z = -(T_1 + T_2 + T_3 + T_4) \tag{3}$$

$$M_x = (T_1 - T_3)\, D \tag{4}$$

$$M_y = (T_4 - T_2)\, D \tag{5}$$

$$M_z = (T_1 + T_3 - T_2 - T_4)\, K \tag{6}$$

where D is the distance from propellers to the Quadcopter's center of gravity and K is a constant that relates propeller's thrust to the yaw moment. The transformation matrix from the inertial reference frame to the body reference frame is written as follows:

$$[T]^{BI} = \begin{bmatrix} c\phi c\psi & c\theta c\psi & -s\theta \\ s\phi s\theta c\psi - c\phi s\psi & c\phi c\psi + s\phi s\theta s\psi & s\phi c\theta \\ c\phi s\theta c\psi + s\phi s\psi & s\theta c\phi s\psi - s\phi c\psi & c\theta c\phi \end{bmatrix} \tag{7}$$

2.1   3- and 6-DOF Newton-Euler Formalism

As shown in Fig. 2, the Quadcopter that is attached to a laboratory stand has only three rotational degree of freedom and its state vector consists of Euler angles and angular velocities as: $x = \begin{bmatrix} p & q & r & \phi & \theta & \psi \end{bmatrix}^T$. According to (2) and (7), the mathematical model of the 3-DOF Quadcopter is as follows:

Fig. 2 The captive test stand

$$
\dot{x} =
\begin{bmatrix}
\frac{M_x}{I_{xx}} - \frac{(I_{zz}-I_{yy})qr}{I_{xx}} \\
\frac{M_y}{I_{yy}} - \frac{(I_{xx}-I_{zz})pr}{I_{yy}} \\
\frac{M_z}{I_{zz}} - \frac{(I_{yy}-I_{xx})pq}{I_{zz}} \\
p + q\tan\theta\sin\phi + r\tan\theta\cos\phi \\
q\cos\phi - r\sin\phi \\
\frac{q\sin\phi}{\cos\theta} + \frac{r\cos\phi}{\cos\theta}
\end{bmatrix}
\tag{8}
$$

In case of considering both translational and rotational motion, the state vector is extended as: $x = \begin{bmatrix} p\ q\ r & V_x\ V_y\ V_z & \phi\ \theta\ \psi \end{bmatrix}^T$ and three differential equations are also added to (8), so the mathematical model of 6-DOF Quadcopter is as follows:

$$
\dot{x} =
\begin{bmatrix}
\frac{M_x}{I_{xx}} - \frac{(I_{zz}-I_{yy})qr}{I_{xx}} \\
\frac{M_y}{I_{yy}} - \frac{(I_{xx}-I_{zz})pr}{I_{yy}} \\
\frac{M_z}{I_{zz}} - \frac{(I_{yy}-I_{xx})pq}{I_{zz}} \\
\frac{F_x}{m} - g\sin\theta - (qV_z - rV_y) \\
\frac{F_y}{m} + g\cos\theta\sin\phi - (rV_x - pV_z) \\
\frac{F_z}{m} + g\cos\theta\cos\phi - (pV_y - qV_x) \\
p + q\tan\theta\sin\phi + r\tan\theta\cos\phi \\
q\cos\phi - r\sin\phi \\
\frac{q\sin\phi}{\cos\theta} + \frac{r\cos\phi}{\cos\theta}
\end{bmatrix}
\tag{9}
$$

3   System Identification

System identification or the art of extracting mathematical model of a system from measured input and output time history data has been developing since 1965 [6]. It is well suited to obtain a low-cost dynamic model of a quadcopter [2]. Firstly, a generic mathematical model is considered for the system that is enriched by processing flight test data to derive aerodynamic coefficients. Generally, enormous methods are presented for system identification, one of which is frequency domain identification [20].

Frequency domain system identification not only represents a linear dynamical model of the system, but also gives a relative robust model due to reduction in errors associated with bias effects and process noise [20]. Comprehensive Identification from FrEquency Response (CIFER) program is used to obtain a closed-loop dynamical model of quadcopters. CIFER has been successfully applied in the system identification of various aircraft and rotorcraft such as the XV-15, Bell-214ST and UH-60 [2]. It is possible to check the validity of frequency response data in CIFER after acquiring it by evaluating its coherence which is an indication of how well the output and input data are correlated. Coherence is given as follows:

$$Y_{xy}^2(\omega) = \frac{\left|\hat{G}_{xy}(f)\right|^2}{\left|\hat{G}_{xx}(f)\right|\left|\hat{G}_{yy}(f)\right|} \tag{10}$$

where $\hat{G}_{xx}(f)$, $\hat{G}_{yy}(f)$ and $\hat{G}_{xy}(f)$ are auto-spectral densities of the input, output and cross-spectral density of the input and output, respectively. A perfect correlation between input and output would result in a coherence value of unity, whilst poor coherence typically falls below a value of 0.6 [20]. After validating the coherence of the data, decoupling must be implemented such that the inputs provided by off-axis commands are removed from the output of the axis of interest. The frequency response function can be directly estimated as follows:

$$\hat{H}(f) = \hat{G}_{xx}^{-1}(f)\hat{G}_{xy}(f) \tag{11}$$

The cost function to optimize a single-input single-output (SISO) transfer function is defined as follows:

$$J = \frac{20}{n_\omega} \sum_{\omega_1}^{\omega_{n_\omega}} W_\gamma \left[W_g \left(\left|\hat{T}_c\right| - |T| \right)^2 + W_p \left(< \hat{T}_c - < T \right)^2 \right] \tag{12}$$

where n_ω is the number of frequency points, ω_1 and ω_{n_ω} define the starting and ending frequencies of interest, || and < are the magnitude (dB) and phase (degree) at each frequency, W_γ, W_g and W_p are the total, magnitude and phase weights,

and as $\hat{T}_c$ and T represent the estimated and actual values of each frequency point, respectively.

4   Results and Discussion

Experimental tests for transfer function extraction of both quadcopters are presented here. Single-input single-output (SISO) system identification is just implemented with regard to the cross control talk in control mechanism which results in an intense control coupling because of gyroscopic effects. However, multi-input single-output (MISO) analysis can be neglected due to great difference between the main or on-axis input and other correlated off-axis inputs. Specification of the quadcopter attached to the laboratory stand is described in Table 1.

The process of identification starts with the chirp signal known as a frequency sweep which consists of a sinusoidal function. In order to excite all different modes of the system, this signal starts at a low frequency and slowly increases to higher frequencies [16]. After performing experimental tests with different frequency sweeps for this quadcopter, it is found that inputs above 8 rad/sec are not followed by the system. Therefore, the maximum frequency of the input is set to be 10 rad/sec. Furthermore, regarding to the coherence, the minimum frequency of the input is defined to be 1.2 rad/sec. Thus, the frequency sweep input covers the frequency range of [1.2 10] rad/sec. In frequency domain system identification, the minimum identifiable frequency of the system depends on the data record duration, T_{rec}, that should be $\geq \frac{8\pi}{\omega_{min}}$. Hence, the input that is applied to the system is a frequency sweep illustrated in Fig. 3.

The dynamic model of the lateral mode is extracted from CIFER in the form of transfer function. The resulting magnitude, phase and coherence of the lateral transfer function is shown in Fig. 4. An examination of this figure shows a good coherence ($Y_{xy}^2 \geq 0.6$) for the frequency range of identification that confirms the dynamic is well excited. Therefore, the system is well representable by a linear model. The resulting transfer function of the lateral mode is as follows:

$$G(s) = \frac{\theta}{T_c} = \frac{8948.57}{s^3 + 7.3494s^2} \left(\frac{\deg}{N} \right) \tag{13}$$

Table 1 The laboratory stand specification

Arm length	25 cm
Stand height	150 cm
Type of motor	Brushless motor
Limited range (Pitch & Roll)	$\pm 50^\circ$
Limited range (yaw)	$\pm 180^\circ$
Sampling frequency	50 Hz
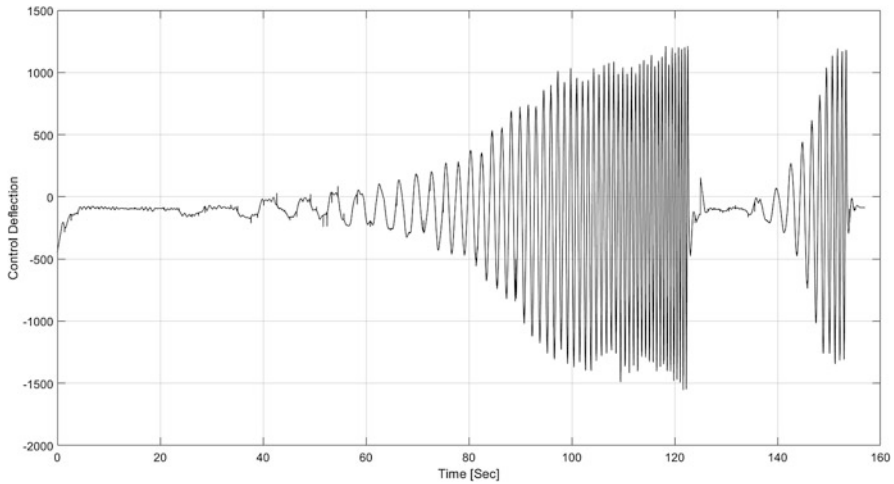
Fig. 3 The frequency sweep input, designed for the captive quadcopter
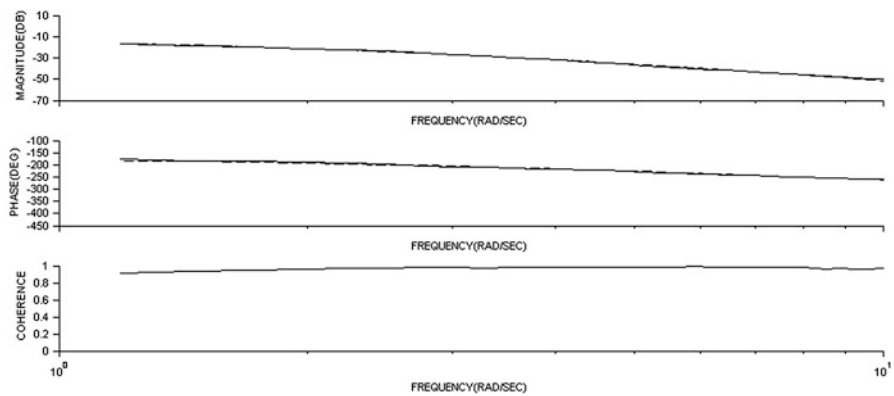
Fig. 4 Bode diagram of the lateral mode dynamics for the captive quadcopter

This is a low order transfer function of the quadcopter [17] that is convertible to a specific layout in order to obtain parameters such as inertia and motor latency based on theoretical basis and Padé approximation. From the theoretical basis, the transfer function for the longitudinal and lateral axes of the quadcopter is written as follows [21]:

$$G(s) = \frac{\theta}{T_c} = \frac{D}{Is^2} \tag{14}$$

where D is the arm length and I is defined as I_{xx} or I_{yy} depending on which axis the manoeuvre is done about it. Due to the time lag between a change of an input and output in real dynamic systems, it is necessary to approximate this time delay for a

precise model identification. This is usually done through Padé approximation of the exponential function [22]. Here, the time delay is approximated as follows:

$$e^{-Ts} = \frac{1}{1 + Ts} \tag{15}$$

where, T is the motor lag. Using (14) and (15), estimation of the phase lag and the moment of inertia of the motors about the lateral axis can be made by the following equation:

$$G(s) = \frac{\theta}{T_c} = \frac{D}{Is^2} \frac{1}{Ts + 1} \tag{16}$$

where D, I and T are the arm length, the moment of inertia and the motor lag, respectively. Comparing (13) and (14), the motor lag and the moment of inertia are estimated to be 0.136 sec and 0.03 kg.m², which is well matched with the moment of inertia calculated by SolidWorks for this quadcopter.

For the F450 quadcopter which is shown in Fig. 5, the frequency sweep input is applied with regard to the aforementioned rules in the previous part. Specification of this F450 quadcopter is described in Table 2. The data record duration is set to be 60 sec. An examination of Fig. 6 shows a good coherence for the frequency range of [6.0 15.0] rad/sec, so the system can be well identified in this range of frequency.

The resulting transfer function about the longitudinal axes is as follows:

Fig. 5 F450 quadcopter

Table 2 The F450 quadcopter specification

Arm length	25 cm
Weight	1.1 kg
Type of motor	Brushless motor Emax 2213
Blade size	8045
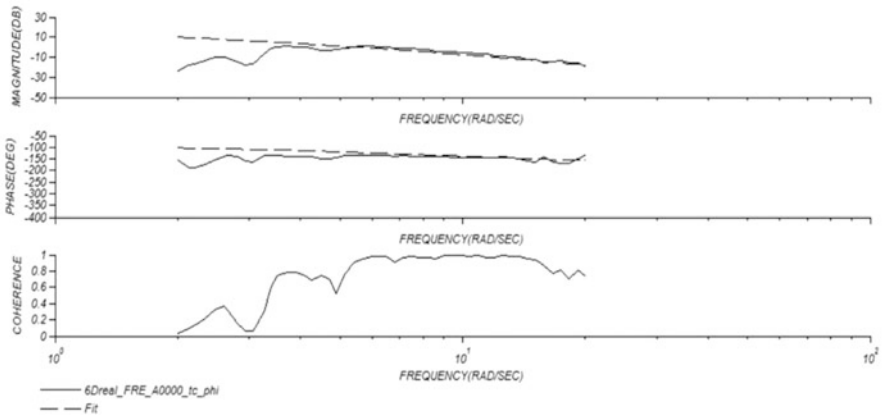
Fig. 6 Bode diagram of the longitudinal mode dynamics for the F450 quadcopter

$$G(s) = \frac{\theta}{T_c} = \frac{5128.04}{s^2 + 7.226s} \left(\frac{\text{deg}}{N} \right) \tag{17}$$

Estimation of the phase lag and the moment of inertia of the motors about the lateral axes for this system can also be done using the following equation:

$$G(s) = \frac{\theta}{T_c} = \frac{D}{Is} \frac{1}{Ts + 1} \tag{18}$$

Comparing (15) and (16), the motor lag and the moment of inertia are estimated to be 0.1384 sec and 0.0242 kg.m^2, which is sensible with regard to the parameters estimated by SolidWorks modelling.

5   Model Verification

Following to identification results, extracted models are needed to be verified in time domain with doublet manoeuvres. Both the extracted model and the real system should be in the same but separate control loop as shown in Fig. 7. The upper part of this figure belongs to the actual flight test data and the lower part belongs to the simulation of the identified model. It is seen that both parts are excited by the same input for comparison purposes and to validate the obtained transfer function.

It is seen that the extracted dynamic model has an excellent agreement with the flight test data in Fig. 8; thus, the closed-loop dynamic model of the quadcopters is successfully identified and accurately compared with the actual system.
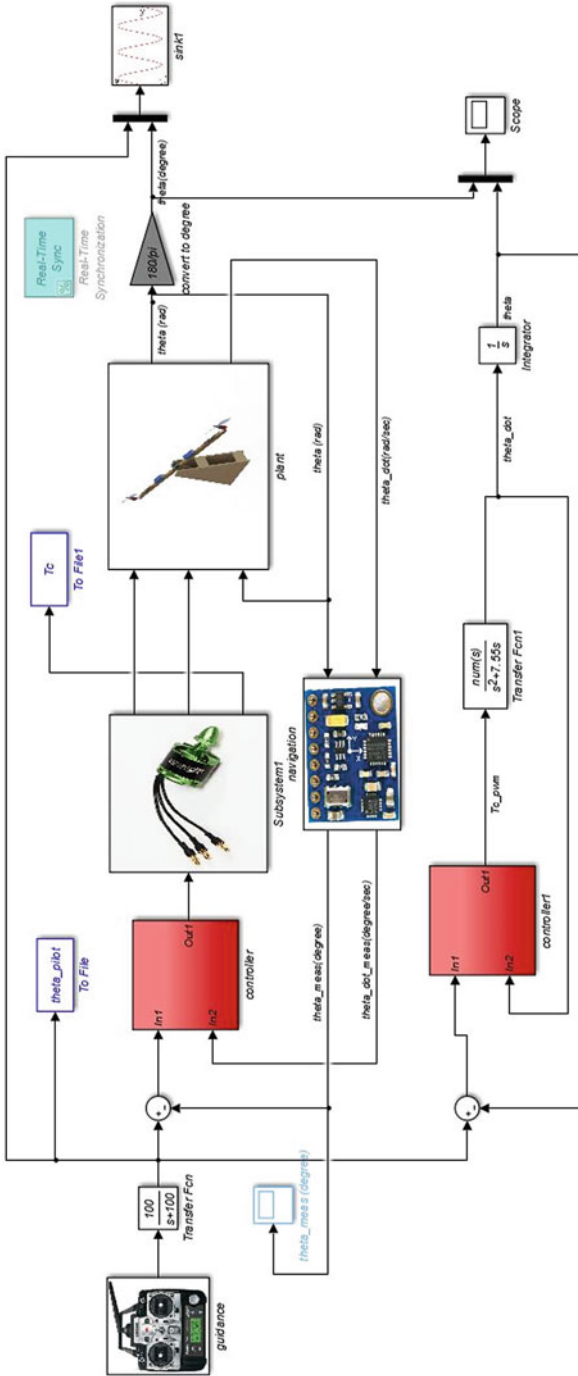
Fig. 7 Block diagram for model verification
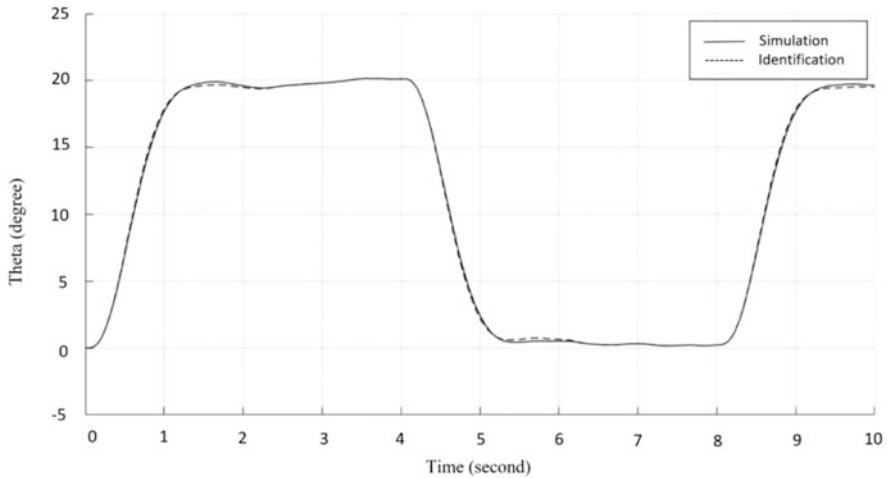
Fig. 8 Response about the longitudinal axis of the extracted transfer function compared to the flight test data

6 Concluding Remarks

In this study, a fast and practical method for identification of the critical parameters such as the moment of inertia and the motor lag of quadcopters has been successfully implemented. This method is based on the system identification in frequency domain. CIFER program is used to extract a bare airframe model using the motor speed as an input and orientation angle as an output with the control system in the loop due to marginal stability/instability of the system. Therefore, the extracted model was compared against flight test data in a manoeuvre not used in the process of system identification to examine the validity and accuracy.

Moreover, identified moment of inertia shows the same result as the outcome acquired from the SolidWorks modelling. It is found that the proposed method is precise, fast and simple compared to traditional modelling techniques. Here, the data acquisition rate plays a key role in the identification process and should not be less than 10 HZ for common quadcopters. It is notable that dynamics identification of quadcopters in frequency domain is immense because applying the periodic input is tough on these systems. Hence, identification of a captive quadcopter attached to the laboratory stand is a more attractive option.

References

1. M. Khan, Quadcopter flight dynamics. Int. J. Sci. Technol. Res. **3**(8), 130–135 (2014)
2. W. Wei, M.B. Tischler, K. Cohen, Frequency-domain system identification and simulation of a quadrotor controller, in *AIAA Modeling and Simulation Technologies Conference*, (2014, no. January)
3. I.M. Salameh, E.M. Ammar, T.A. Tutunji, Identification of quadcopter hovering using experimental data, in *IEEE Jordan Conference on Applied Electrical Engineering and Computing*, (2015), pp. 3–8
4. J. Gutemberg, B.F. Filho, C.E.T. Dórea, W.M. Bessa, J.L.C.B. Farias, Modeling , test benches and identification of a quadcopter modeling, test benches and identification of a quadcopter ∗, in *XIII Lat. Am. Robot. Symp. IV Brazilian Robot. Symp., No. May 2018*, (2016)
5. P. Castilli, R. Lozano, A. Dzul, Stabilization of a mini-rotorcraft having four rotors, in *IEEE/RSJ International Conference on Intelligent Robots and Systems*, (2004)
6. H. Shraim, A. Awada, R. Youness, A survey on quadrotors : Configurations, modeling and identification, control, collision avoidance, fault diagnosis and tolerant control, in *IEEE Aerospace and Electronic Systems Magazine, No. 10*, (2018), pp. 14–33
7. Z. Yang et al., System identification of an unmanned quadcopter system using MRAN neural system identification of an unmanned quadcopter system using MRAN neural. IOP Conf. Ser. Mater. Sci. Eng. (2017)
8. L. Wang, X. Chen, C. Liuping, L. Wang, Q. Uav, Step response of a quadcopter UAV using frequency-sampling filters filters. IFAC-PapersOnLine **48**(28), 122–127 (2015)
9. Z. Mustapa, S. Saat, S.H. Husin, T. Zaid, Quadcopter physical parameter identification and altitude system analysis, in *IEEE Symposium on Industrial Electronics and Applicatons*, (2014), pp. 130–135
10. A.R. Kim, A. Blevins, A. Sizemore, I. Sheppard, Dynamic modeling and simulation of a quadcopter with motor dynamics, in *AIAA Modeling and Simulation Technologies Conference, No. January*, (2017), pp. 1–16
11. D. Ho, J. Linder, G. Hendeby, M. Enqvist, Vertical modeling of a quadcopter for mass estimation and diagnosis purposes, in *Work. Res. Educ. Dev. Unmanned Aer. Syst*, (2017)
12. M.A. Khodja, M. Tadjine, M.S. Boucherit, Experimental dynamics identification and control of a, in *6th International Conference on Systems and Control*, (2017), pp. 498–502
13. P. Kantue, Nonlinear identification of an unmanned quadcopter rotor dynamics using RBF neural networks, in *22nd Int. Conf. Syst. Theory, Control Comput*, (2018), pp. 292–298
14. E. Capello, H. Park, B. Tavora, G. Guglieri, M. Romano, Modeling and experimental parameter identification of a multicopter via a compound pendulum test rig, in *2015 Work. Res. Educ. Dev. Unmanned Aer. Syst. RED-UAS 2015*, (2016), pp. 308–317
15. M. Dhaybi, N. Daher, Real-time estimation of the inertia tensor elements of a quadcopter hover platform, in *IEEE/ASME Int. Conf. Adv. Intell. Mechatronics, AIM, Vol. 2019-July*, (2019), pp. 1347–1352
16. A. Ji, K. Turkoglu, Development of a low-cost experimental quadcopter testbed using an Arduino controller for video surveillance, in *AIAA Infotec, No. January*, (2015), pp. 1–12
17. S. Sakulthong, S. Tantrairatn, W. Saengphet, Frequency response system identification and flight controller tuning for quadcopter UAV, in *Third International Conference on Engineering Science and Innovative Technology (ESIT)*, (2018), pp. 1–6

18. G. Cai, T. Taha, J. Dias, L. Seneviratne, A framework of frequency-domain flight dynamics modeling for multi-rotor aerial vehicles. P. I. Mech. Eng. G-J. Aer. *231*(1), 30–46 (2016)
19. C.F. Testing, F. Holzapfel, P. Niermeyer, T. Ra, F. Holzapfel, Open-loop quadrotor flight dynamics identification in frequency domain via open-loop quadrotor flight dynamics Identi cation in frequency domain via closed-loop flight Testing, in *AIAA Guidance, Navigation, and Control Conference*, (2015 July)
20. X. Zhang, X. Li, K. Wang, Y. Lu, A survey of modelling and identification of quadrotor robot. Abstr. Appl. Anal., 2014 (2014)
21. V. Praveen and A. S. Pillai, Modeling and simulation of quadcopter using PID controller. Int. J. Control Theory Appl. *9*(15), 7151–7158 (2016)
22. V. Hanta, A. Procházka, Rational Approximation of Time Delay, (2009)

Nonparametric Identification of a Nonlinear MEMS Resonator

Rodrigo T. Rocha (iD)**, Feras Alfosail** (iD)**, Wen Zhao** (iD)**,
Mohammad I. Younis** (iD)**, and Sami F. Masri**

1 Introduction

Accurate mathematical models bring many advantages, such as enabling predictions, and allowing the optimization of a system without the need to fabricate it, which reduces the cost and improves prototyping new designs. However, a mathematical model is different for each case of a different system. Thus, the challenge to obtain dynamical equations of motion for system with high complexity behavior due to the presence of nonlinearities becomes very high.

Nonparametric identification methods have shown to be a valuable strategy for formulating accurate models [1–5]. These methods can obtain a function from data measurements that may provide physical representation of a system without prior knowledge of the nature of the system restoring force or nonlinearities. In addition, these techniques have been recently implemented in machine learning applications through neural networks and optimization algorithms [4, 5].

Dynamical structures usually exhibit nonlinear behavior due to geometric, material, and external forces nonlinearities when undergoing large deformations. Microelectromechanical systems (MEMS) are well known to exhibit various non-

R. T. Rocha · W. Zhao · M. I. Younis (✉)
Physical Sciences and Engineering Division, King Abdullah University of Sciences and
Technology – KAUST, Thuwal, Saudi Arabia
e-mail: Mohammad.Younis@kaust.edu.sa

F. Alfosail
Physical Sciences and Engineering Division, King Abdullah University of Sciences and
Technology – KAUST, Thuwal, Saudi Arabia

Consulting Services Department, Saudi Aramco, Dharan, Saudi Arabia

S. F. Masri
Department of Civil Engineering, University of Southern California, Los Angeles, CA, USA

linear behaviors. Mainly, when microsystems are excited near resonance conditions by electrostatic DC and AC voltages, geometric and/or electrostatic nonlinearities can be activated. Among the common nonlinear dynamical phenomena in MEMS are jumps of hardening and softening type, and internal resonance among vibration modes. In addition, MEMS systems have been extensively studied in the past two decades due to their wide range of applications [6–10].

Therefore, the formulation of accurate mathematical models for MEMS systems is very important due to the need for a better understanding of their features. Hence, this work aims to extend the application of the nonparametric identification technique demonstrated in [2] to identify the dynamic response behavior of the first symmetric mode of a nonlinear MEMS resonator through experimental data.

2 MEMS Resonator

The MEMS resonator utilized for data measurement is a clamped-clamped microbeam (CC-microbeam), illustrated in Fig. 1a and b. The microbeam is made of SiN_3 and is fabricated using conventional surface micromachining processes [10]. It has Young's modulus $E = 160$ GPa, mass density $\rho = 2500$ kg/m^3, length $L = 253.6$ μm, depth $b = 49.2$ μm, and width $h = 2.7$ μm. A stationary actuation electrode is located under the microbeam, which is separated from it at a distance $d = 2.5$ μm.
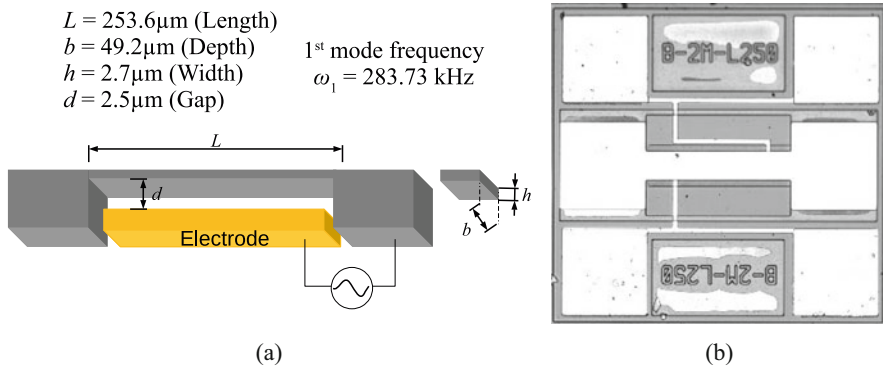
Fig. 1 (a) A schematic of the microbeam resonator. (b) Top view of the fabricated microbeam made of SiN_3

2.1 Mathematical Modelling

The microbeam is modeled as an Euler-Bernoulli beam accounting for nonlinear midplane stretching. The developed equation of motion accounts only for one mode of vibration of the microbeam, and it is used for validating the experimental data. In addition, it provides an analytical restoring force function that is used along with the nonparametric identification method, which is necessary for extracting the coefficients using the experimental data. The equation that governs the transverse motion w of the microbeam along length $\hat{x}$ and in time t is written as

$$EI\frac{\partial^4 w}{\partial \hat{x}^4} + m\frac{\partial^2 w}{\partial t^2} + c\frac{\partial w}{\partial t} - N\frac{\partial^2 w}{\partial \hat{x}^2} - \frac{EA}{2L}\left(\int_0^L \left(\frac{\partial w}{\partial \hat{x}}\right)^2 dx\right)\frac{\partial^2 w}{\partial \hat{x}^2}$$
$$= \frac{b\varepsilon(V_{DC}+V_{AC}\cos\Omega t)^2}{2(d-w)^2} \tag{1}$$

where m is mass per unit length, I is the area moment of inertia defined as $I = (bh^3/12)$, c is the viscous damping, N is the axial load, A is the cross-section area of the beam, ε is the dielectric constant, V_{DC} is the DC electrostatic voltage, V_{AC} is the amplitude of the harmonic electric voltage of frequency Ω.

We write the fixed-fixed boundary conditions as $w(0,t) = 0; \quad w(L,t) = 0$.

The new dimensionless variables are written as

$$y = \frac{w}{d}; \quad x = \frac{\hat{x}}{L}; \quad \tau = t\sqrt{\frac{EI}{L^4 m}} \tag{2}$$

Substituting Eqs. (2) into (1) yields

$$\frac{\partial^4 y}{\partial x^4} + \frac{\partial^2 y}{\partial t^2} + 2\mu\frac{\partial y}{\partial t} - N_{non}\frac{\partial^2 y}{\partial x^2} - \alpha_1\left(\int_0^1 \left(\frac{\partial y}{\partial x}\right)^2 dx\right)\frac{\partial^2 y}{\partial x^2} = \frac{\beta(V_{DC} + V_{AC}\cos\Omega\tau)^2}{(1-y)^2} \tag{3}$$

where the dimensionless coefficients in Eq. (3) are defined as

$$2\mu = c\sqrt{\frac{EI}{L^4 m}}; \quad N_{non} = \frac{NL^2}{EI}; \quad \alpha_1 = 6\left(\frac{d}{h}\right)^2; \quad \beta = \frac{bL^4\varepsilon}{2d^3 EI} \tag{4}$$

Accounting for the influence of electrostatic actuations V_{DC} and V_{AC}, the equation governing the static deflection y_s is obtained by dropping the time dependent terms, which yields

$$\left[\frac{d^4 y_s}{dx^4} - N_{non}\frac{d^2 y_s}{dx^2} - \alpha_1\left(\int_0^1 \left(\frac{dy_s}{dx}\right)^2 dx\right)\frac{d^2 y_s}{dx^2}\right](1-y_s)^2 = \beta\left(V_{DC}^2 + \frac{V_{AC}^2}{2}\right) \tag{5}$$

Next, Eq. (3) is perturbed around the equilibrium state by assuming the solution y composed of the static part and the dynamic part y_d as $y = y_d + y_s$. Omitting

the static equation, Eq. (5), and further simplifying the equation governing y_d, the nonlinear beam equation reduces to

$$
\left(\frac{\partial^4 y_d}{\partial x^4} + \frac{\partial^2 y_d}{\partial t^2} + 2\mu \frac{\partial y_d}{\partial t} - N \frac{\partial^2 y_d}{\partial x^2} \right) \left(1 - \frac{2y_d}{(1-y_s)} + \frac{y_d{}^2}{(1-y_s)^2} \right)
$$
$$
- \left(\alpha_1 \left(\int_0^1 \left[\left(\frac{dy_s}{dx} \right)^2 + 2\frac{dy_s}{dx}\frac{\partial y_d}{\partial x} + \left(\frac{\partial y_d}{\partial x} \right)^2 \right] dx \right) \frac{\partial^2 y_d}{\partial x^2} \right) \left(1 - \frac{2y_d}{(1-y_s)} + \frac{y_d{}^2}{(1-y_s)^2} \right)
$$
$$
- \left(\alpha_1 \left(\int_0^1 \left[2\frac{dy_s}{dx}\frac{\partial y_d}{\partial x} + \left(\frac{\partial y_d}{\partial x} \right)^2 \right] dx \right) \frac{d^2 y_s}{dx^2} \right) \left(1 - \frac{2y_d}{(1-y_s)} + \frac{y_d{}^2}{(1-y_s)^2} \right)
$$
$$
- \beta \frac{(2V_{DC}{}^2 + V_{AC}{}^2)}{(1-y_s)^3} y_d + \beta \frac{(2V_{DC}{}^2 + V_{AC}{}^2)}{2(1-y_s)^4} y_d{}^2
$$
$$
= 2\beta \frac{V_{DC} V_{AC} \cos(\Omega\tau)}{(1-y_s)^2} + \beta \frac{V_{AC}{}^2 \cos(2\Omega\tau)}{2(1-y_s)^2}
$$

$$(6)$$

The linear free vibration problem of Eq. (6) is obtained by dropping the forcing, damping, and nonlinear terms, which yields

$$
\frac{\partial^4 y_d}{\partial x^4} + \frac{\partial^2 y_d}{\partial t^2} - \left[N_{non} + \left(\alpha_1 \int_0^1 \left(\frac{dy_s}{dx} \right)^2 dx \right) \right] \frac{\partial^2 y_d}{\partial x^2}
$$
$$
- 2\alpha_1 \left(\int_0^1 \frac{dy_s}{dx}\frac{\partial y_d}{\partial x} dx \right) \frac{d^2 y_s}{dx^2} - \beta \frac{(2V_{DC}{}^2 + V_{AC}{}^2)}{(1-y_s)^3} y_d = 0
$$

$$(7)$$

The eigenvalue solution of the linear dynamic equation is assumed as $y_d = \phi(x)e^{i\omega t}$. Substituting this form into Eq. (7), and using the orthogonality of the modes, the mode shape and the natural frequency are identified. Further, the nonlinear dynamic equation is solved by assuming the solution to be $y_d(x,t) = \phi(x)u(t)$ under a single mode assumption. Then, substituting $y_d(x,t)$ into Eq. (6) and using the orthogonality of the mode shapes, it results in the below equation of the modal coordinate $u(t)$

$$
\ddot{u} + 2\mu\dot{u} + \omega^2 u + \alpha_{21}u^2 + \alpha_{22}\ddot{u}u + \alpha_{23}\dot{u}u + \alpha_{31}u^3
$$
$$
+ \alpha_{32}\ddot{u}u^2 + \alpha_{33}\dot{u}u^2 + \alpha_4 u^4 + \alpha_5 u^5 = F_1 \cos(\Omega t) + F_2 \cos(2\Omega t)
$$

$$(8)$$

where the equation is written in terms of dimensionless coefficients, and the dot denotes diferentiation with respect to time. For the dynamic simulations, Eq. (8) is integrated in time using a Runge-Kutta numerical scheme.

3   Experimental Setup and Validation of the Model

The validation of the mathematical model is carried out along with the simulated and experimental frequency response curves.
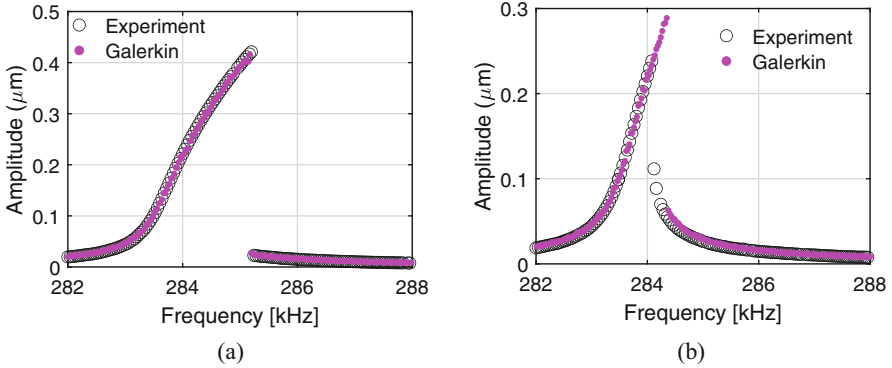
Fig. 2 Frequency-response curves of the microbeam, numerical simulation and experimental data. (**a**) Forward sweep, (**b**) backward sweep

The resonance frequencies are measured using the laser Doppler vibrometer of the Micro System Analyzer (MSA) from Polytec. Due to the small gap between the resonator and the electrode, a vacuum chamber is required to minimize the squeeze-film damping effect [9], with a pressure of 50mTorr set throughout the experiments.

To capture the frequency-response of the microbeam, a data acquisition card NI PXIe-1073 from National Instruments is used to excite the resonator and record the output from the Laser Doppler Vibrometer. The excitation signal is generated using the LabView software. The measurements are acquired by the laser and then postprocessed. Finally, the measurements are presented in the form of frequency-response curves plotted in MATLAB. The first resonance frequency was initially measured as 283.73 kHz at $V_{AC} = 1$ V and $V_{DC} = 0$ V to avoid frequency shift due to the electrostatic effect.

For the numerical simulations, the axial load is estimated to be $N_{non} = -4.365$ and the damping coefficient is $\mu = 3 \times 10^{-4}$ due to vacuum conditions. The frequency-response curves of Eq. (8) and the experimental data around the first mode of vibration are depicted in Fig. 2a and b, for $V_{AC} = 5.0$ V and no DC load. A nonlinear hardening behavior is noted, from both experiments and numerical simulations, with good agreement observed between them for both forward and backward sweeps. The agreement justifies that the analytical model can be used as a representation of the experiment, which is used for the identification process in the following sections.

4 The Nonparametric Identification Technique and Application

The nonparametric identification technique uses the state variables of a system to be identified, expressing its characteristics in terms of orthogonal functions [2]. The main purpose of the procedure is to find a restoring force $f(u, \dot{u})$ using Chebyshev polynomials, which for the current MEMS device and based on Eq. (8) can be expressed as

$$f(u, \dot{u}, \ddot{u}) = F_1 \cos(\Omega t) + F_2 \cos(2\Omega t) - \ddot{u} \tag{9}$$

where the restoring force is expressed as

$$\begin{aligned} f(u, \dot{u}, \ddot{u}) = {} & 2\mu\dot{u} + \omega^2 u + \alpha_{21} u^2 + \alpha_{22} \ddot{u} u + \alpha_{23} \dot{u} u \\ & + \alpha_{31} u^3 + \alpha_{32} \ddot{u} u^2 + \alpha_{33} \dot{u} u^2 + \alpha_4 u^4 + \alpha_5 u^5 \end{aligned} \tag{10}$$

The restoring force of the resonator has linear terms, nonlinear terms up to the fifth order, and cross-terms of the displacement, velocity, and acceleration. As the Laser Doppler Vibrometer uses a module that only can measure displacement and velocity, it is not possible to obtain the accelerations experimentally using the current setup. Hence, assuming that these cross-terms have no major influences on the system, they are neglected. Then, the restoring force of the microresonator reduces to

$$f(u, \dot{u}) = 2\mu\dot{u} + \omega^2 u + \alpha_{21} u^2 + \alpha_{23} \dot{u} u + \alpha_{31} u^3 + \alpha_{33} \dot{u} u^2 + \alpha_4 u^4 + \alpha_5 u^5 \tag{11}$$

We aim to identify the analytical restoring force of Eq. (11) from the identification procedure without any prior knowledge of the system. Based on Eq. (11), the extraction of data for displacement and velocity through the experimental system is carried out. The experimental data must be nondimensionalized according to Eq. (3), and $y_d = y - y_s$. The nondimensional data are normalized to generate the surface of the restoring in a normalized interval to be least-square fit with Chebyshev polynomials $T_n(q)$, where n is the order of the Chebyshev polynomial for a generic variable q [2]. The least-square method using Chebyshev polynomials is utilized to yield the restoring force in the form

$$f(u', \dot{u}') = \sum_{i=0}^{n} \sum_{j=0}^{m} C_{ij} T_i(u') T_j(\dot{u}') \tag{12}$$

where n and m are the order of the Chebyshev polynomials for u' and $\dot{u}'$, respectively.

(a) (b)
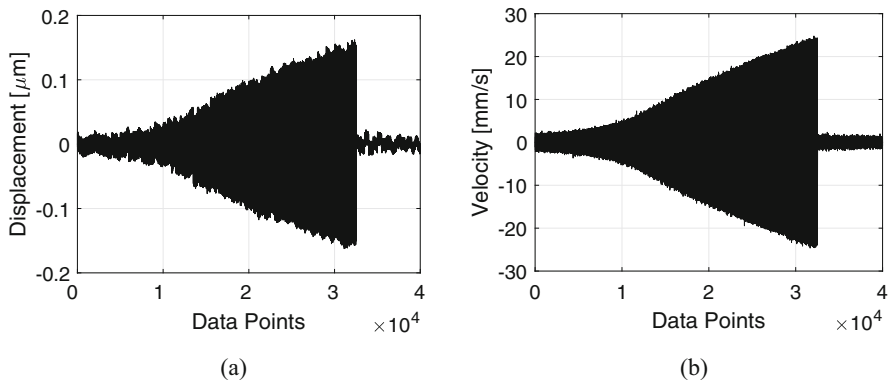
Fig. 3 Measured time histories of (**a**) displacement, (**b**) velocity versus the number of data points of the microbeam under $V_{AC} = 5$ V and $V_{DC} = 0$ V

The convergence of the C_{ij} coefficients depends directly on the values of n and m, and the complexity of the restoring force surface to be least-square fitted. If the restoring force is complex enough, higher order Chebyshev polynomials are required so that all the needed coefficients are fitted to the restoring force. However, the increase of the number of higher order terms increases the computational cost. Therefore, an efficient interpolation scheme is highly recommended in order to increase the convergence of the coefficients and, consequently, reduces the computation cost. In addition, the convergence also depends on the values of n and m to be sufficient to identify the most effective C_{ij} coefficients, and reduce the noneffective ones at negligible orders.

Considering an electrostatic excitation of $V_{AC} = 5$ V and no DC load, the restoring force of the microbeam based on the model is given by

$$f(u, \dot{u}) = 446.82u - 1163.68u^2 + 1828.68u^3 - 3189.86u^4 + 2351.32u^5$$
$$+ 6.00 \times 10^{-4}\dot{u} - 15.95 \times 10^{-4}u\dot{u} + 111.13 \times 10^{-5}u^2\dot{u}$$
(13)

Figure 2 shows the frequency response obtained through experiments with forward and backward sweeps, where hardening behavior is noted.

Then, the time history of displacement and velocity are extracted around the resonance region of Fig. 2. Figure 3a and b depict the time histories of the displacement and velocity, respectively. Each time history was obtained within 8×10^5 points, and for each consecutive 10^4 points, the frequency is changed.

The measured data are nondimensionalized and normalized with the function below
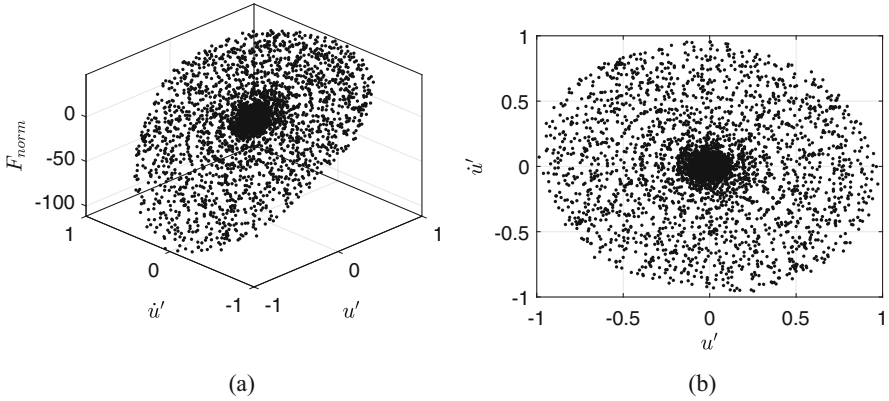
Fig. 4 (**a**) Surface of the normalized restoring forces of Eq. (15) using FND for the case of $V_{AC} = 5$ V, and $V_{DC} = 0$ V. (**b**) Displacement vs velocity

$$u' = \left[\frac{u - (u_{\max} + u_{\min})}{2}\right] / \left[\frac{(u_{\max} - u_{\min})}{2}\right]$$
$$\dot{u}' = \left[\frac{\dot{u} - (\dot{u}_{\max} + \dot{u}_{\min})}{2}\right] / \left[\frac{(\dot{u}_{\max} - \dot{u}_{\min})}{2}\right] \tag{14}$$

where $u_{max} = 0.16$, $u_{min} = -0.16$, $\dot{u}_{\max} = 25169.8$, and $\dot{u}_{\min} = -25093.6$. To reduce the computational cost and keep an acceptable accuracy of the data, the vectors for displacement and velocity are normalized for each 100 points, yielding 8000 data points for each vector. In addition, substituting Eqs. (14) into (13), the restoring force is given in the normalized form as

$$f_{norm}\left(u', \dot{u}'\right) = -0.20 + 73.31u' - 31.25u'^2 + 8.05u'^3 - 2.29u'^4 + 0.28u'^5$$
$$+ 15.10\dot{u}' - 6.57u'\dot{u}' + 0.75u'^2\dot{u}' \tag{15}$$

Since we do not have an experimental way of measuring the restoring force, we resort here to calculate it as based on Eq. (15) and the full normalized data (FND). Hence, the surface of the normalized restoring force is obtained, as shown in Fig. 4a, which represents the "measured" restoring force. The restoring force for a microbeam is quite distinctive and due to the nonlinearities presented in the system, the surfaces are curved and very complex.

To guarantee a precise convergence of the restoring force, an efficient interpolation scheme is required. It is noted that the restoring force data points only allow certain pairs of displacement and velocity that are obtained due to the nature of the problem. However, equally spaced increments for each pair of data points are required. Therefore, it is possible to create an interpolated surface by using one-dimensional least-square fit using Chebyshev polynomials, which is given by

$$f_{1D}\left(u', \dot{u}'\right) = \sum_{i=0}^{n} a_i T_i\left(u'\right) + \sum_{i=0}^{m} b_j T_j\left(\dot{u}'\right) = g\left(u'\right) + h\left(\dot{u}'\right) \tag{16}$$

where a_i and b_j are the Chebyshev polynomial coefficients for a one-dimensional (1D) least-square fit obtained from

$$\begin{aligned}
a_0 &= \frac{1}{M(u')} \sum_{i=1}^{M(u')} f\left(\xi_i, 0\right) & a_k &= \frac{2}{M(u')} \sum_{i=1}^{M(u')} f\left(\xi_i, 0\right) T_k\left(\xi_i\right) \\
b_0 &= \frac{1}{N(\dot{u}')} \sum_{i=1}^{N(\dot{u}')} f\left(0, \xi_i\right) & b_k &= \frac{2}{N(\dot{u}')} \sum_{i=1}^{N(\dot{u}')} f\left(0, \xi_i\right) T_k\left(\xi_i\right)
\end{aligned} \tag{17}$$

where the abscissa variables u' and $\dot{u}'$ are transformed to satisfy the normalized interval as

$$\xi_i = \cos\left[\frac{(2i+1)\pi}{2n}\right] \qquad i = 0, 1, \ldots, n-1 \tag{18}$$

In addition, the cross-terms are approximated by applying 2D least-square fit directly in the cross-term subregions. From Eq. (17), the 1D least-square fit of the restoring force surface of Fig. 4 is carried out. To maximize the convergence of the C_{ij}'s coefficients, short intervals for displacements and velocities are set to select data points that yield independent condensed displacement and velocity vectors, for their respective values of the restoring force. Setting the intervals to $-0.08 \leq u' \leq 0.08$ and $-0.5 \leq \dot{u}' \leq 0.5$, the least-square fit for each vector is given by

$$\begin{aligned}
g\left(u'\right) &= -16.69 T_0 + 79.52 T_1 - 16.77 T_2 + 2.10 T_3 - 0.28 T_4 + 0.01 T_5 \\
&\quad + 3.10 \times 10^{-3} T_6 - 2.49 \times 10^{-3} T_7 + 1.55 \times 10^{-3} T_8 - 2.98 \times 10^{-4} T_9 \\
h\left(\dot{u}'\right) &= -0.35 T_0 + 14.81 T_1 - 0.28 T_2 - 0.27 T_3 - 0.25 T_4 - 0.23 T_5 \\
&\quad - 0.21 T_6 - 0.18 T_7 - 0.15 T_8 - 0.12 T_9 \\
C_r\left(u', \dot{u}'\right) &= -4.39 T_{u'_1} T_{\dot{u}'_1} + 0.10 T_{u'_2} T_{\dot{u}'_1} + 0.47 T_{u'_3} T_{\dot{u}'_1} - 0.13 T_{u'_4} T_{\dot{u}'_1} \\
&\quad - 0.07 T_{u'_5} T_{\dot{u}'_1} + 0.01 T_{u'_6} T_{\dot{u}'_1} + 0.32 T_{u'_7} T_{\dot{u}'_1} - 0.16 T_{u'_8} T_{\dot{u}'_1}
\end{aligned} \tag{19}$$

Substituting the Chebyshev polynomials in Eq. (19), and from Eq. (16) added to the cross-terms C_r, the 2D least-square fit using Chebyshev polynomials is carried out, obtaining the restoring force of Eq. (20), where $H.O.T$ are higher order terms with very small coefficients below than 10^{-8}. The obtained surface using Eq. (20) is shown in Fig. 5 by the red surface.

Figure 5 shows the comparison between the normalized restoring force surfaces from the one obtained through Galerkin (Eq. 15) to the identified one (Eq. 20) using FND. It is clear that the identified surface converges to the original one, including for large deformations of the system $((u', \dot{u}') \approx -1 \text{ and } 1)$. It is also important
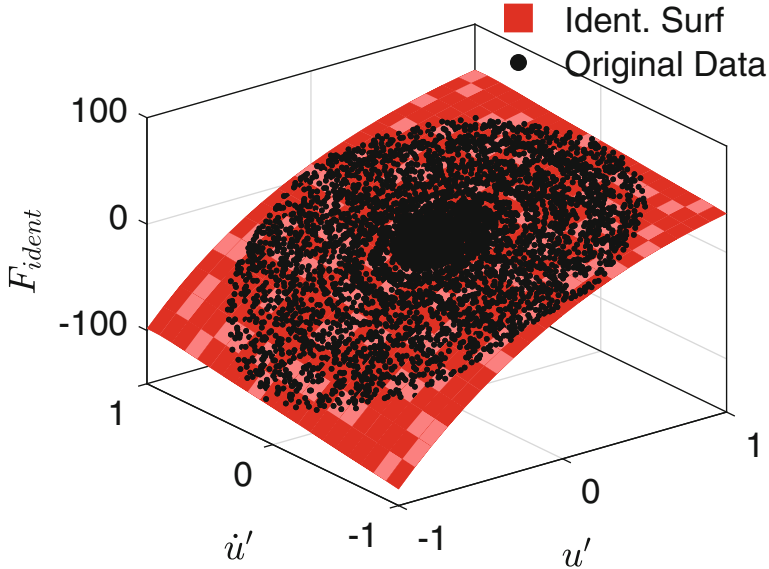
Fig. 5 Surface of the original normalized restoring force obtained using the Galerkin (Eq. 20), and the one (extrapolated red surface) identified based on the 2D least square fit with Chebyshev polynomials for V_{AC}=5V, V_{DC}=0V

to highlight that Eq. (20) can extrapolate very accurately the original values of the restoring force, which is made possible by the 1D interpolation scheme.

Accounting for the FND points for both surfaces, the relative error [2] between both of them is around 1.06%, showing a very close agreement of the identified restoring force through the least square fit with Chebyshev polynomials.

$$
\begin{aligned}
f_{ident}\left(u', \dot{u}'\right) = {} & -0.31 + \mathbf{73.30u'} - \mathbf{31.25u'^2} + \mathbf{8.11u'^3} - \mathbf{2.38u'^4} \\
& + \mathbf{0.22u'^5} + 0.10u'^6 + \mathbf{14.22\dot{u}'} - \mathbf{6.14u'\dot{u}'} + \mathbf{1.46u'^2\dot{u}'} \\
& + 3.28u'^3\dot{u}' - 1.61u'^4\dot{u}' - 1.13u'^4\dot{u}' + 0.37u'^6\dot{u}' - 2.27\dot{u}'^2 \\
& + 3.51\dot{u}'^3 + 7.86\dot{u}'^4 - 3.67\dot{u}'^5 - 6.56\dot{u}'^6 + H.O.T
\end{aligned}
$$

$$(20)$$

5   Conclusions

This work presented the nonparametric identification of an MEMS resonator by using experimental data measurements. The analytical modeling of the resonator was needed to construct a restoring force surface dependent on the displacement and velocities, whose data were experimentally acquired, as it is not possible to measure

the restoring force in the current experimental setup. Therefore, the validation of the analytical model with the experimental data was carried out.

Once the restoring force is obtained, the nonparametric identification method was used. It proved to be very efficient to identify all the linear and nonlinear features of the system without prior knowledge of them. To show the strength of the method, we plan to carry out the identification of the MEMS resonator for different DC and AC actuations.

References

1. J. He, B. Xu, S.F. Masri, Restoring force and dynamic loadings identification for a nonlinear chain-like structure with partially unknown excitations. Nonlinear Dyn. **69**(1–2), 231–245 (2012)
2. S.F. Masri, T. Caughey, A nonparametric identification technique for nonlinear dynamic problems. J. Appl. Mech. **46**(2), 433–447 (1979)
3. G. Birpoutsoukis, A. Marconato, J. Lataire, J. Schoukens, Regularized nonparametric Volterra kernel estimation. Automatica **82**, 324–327 (2017)
4. R.A. Sandler, S.A. Deadwyler, R.E. Hampson, D. Song, T.W. Berger, V.Z. Marmarelis, System identification of point-process neural systems using probability based Volterra kernels. J. Neurosci. Methods **240**, 179–192 (2015)
5. G. Song, V. Chaudhry, C. Batur, A neural network inverse model for a shape memory alloy wire actuator. J. Intell. Mater. Syst. Struct. **14**(6), 371–377 (2003)
6. M.I. Younis, A.H. Nayfeh, A study of the nonlinear response of a resonant microbeam to an electric actuation. Nonlinear Dyn. **31**(1), 91–117 (2003)
7. A.M. Tusset, J.M. Balthazar, D.G. Bassinello, B.R. Pontes, J.L.P. Felix, Statements on chaos control designs, including a fractional order dynamical system, applied to a "MEMS" comb-drive actuator. Nonlinear Dyn. **69**(4), 1837–1857 (2012)
8. A.Z. Hajjaj, N. Jaber, S. Ilyas, F.K. Alfosail, M.I. Younis, Linear and nonlinear dynamics of micro and nano-resonators: Review of recent advances. Inter J Non-Linear Mech **119**, 103328 (2020)
9. M.I. Younis, *MEMS Linear and Nonlinear Statics and Dynamics* (Springer Science and Business Media, New York, 2011)
10. S. Saghir, M.L. Bellaredj, A. Ramini, M.I. Younis, Initially curved microplates under electrostatic actuation: Theory and experiment. J. Micromech. Microeng. **26**(9), 095004 (2016)

Mine Clearance through an Artificial Intelligence Flying Drone

Federica Mezzani, Gianluca Pepe [ID], Nicola Roveri, and Antonio Carcaterra

1   Introduction

Landmines, heritage of the wars spreading between 1990 and 2000, are disseminated in more than 10 countries, with numbers far beyond tens of millions. The dramatic effects do not only involve victims, whose number reaches 6000 per year children included, but also the economic development based on an agricultural sector which is brutally jeopardized. The produced social impact is hard to estimate accounting for public health costs and psychological effects as post-traumatic stress disorder and depression. Thanks to the recent progresses in increasingly performing and portable sensors, the automation of the landmine searches through autonomous robots became possible, preventing the exploitation of traditional demining techniques, which still rely on human intervention and trained animals.

The present investigation focuses on the development of machine learning techniques for the identification and the localization of mines spread over an unknown territory. This is only an initial phase of a larger project, named MINOR, MINe Overall Recognition, which is aimed at generating a real-time map of the territory completed with the exact position of the mines, localized through a swarm of autonomous flying drones, equipped with a set of advanced sensors, as Ground Penetrating Radar (GPR) [1], high-sensitivity MEMS gravimeters, able to detect tiny variations of the local gravitational acceleration, tomography [2, 3], X-rays [4], infrared [5], metal detector [6], acoustic waves [7, 8], ultrasounds [9, 10], and thermal image camera. The autonomous vehicles are equipped with a co-operative driving and control system recently developed by the Sapienza research group

F. Mezzani (✉) · G. Pepe · N. Roveri · A. Carcaterra
Department of Mechanical and Aerospace Engineering, Sapienza University of Rome, Rome, Italy
e-mail: federica.mezzani@uniroma1.it

under the name of variational feedback controls (VFCs) that allow a detailed and optimized soil scan [11, 12].

The GPR has frequently been used in sub-soil examinations, given its upgraded capacity to separate little metal components [13]. Its slightest invasiveness, security, and speed point as a usually favourite apparatus for mine clearance investigation and UXOs (unexploded arms) localization [14]. However, in spite of the viable points of interest, mine location through GPR is frequently influenced by clutter defilement due to wire coupling, ground reflection, and other conceivably covered-up objects [15], which might sabotage the application of an automated discovery strategy. Indeed, clutter effect, primarily due to ground reflections, might produce a signature of the target barely recognizable. In this sense, the implementation of anti-clutter strategies [16] are needed to mitigate the effect of ground surface roughness [17] and to include the reduced number of metal components in the mines and the limited depth of burial.

The present work illustrates a two-step technique to precisely identify the nearness of a mine and to distinguish mines from other covered-up objects. At first, an off-line algorithm is used to train and tune a deep learning neural network by auto-generated GPR-like data. The produced network selects those data characterized by alike mine reflection signature, hence to recognize potential buried mines. A second algorithm, which relies on Symbolic Data Analysis (SDA), automatically clusters data and dividing mines from other objects. A convolutional neural network (CNN) is introduced to appropriately cluster the signals in the radargrams; however, the reliability can be ensured only by an extremely broad and various database. Moreover, data can be considered accurate only if the elements of the dataset are generated by experimental acquisitions. The combination of these two elements implies a time-consuming and costly experimental campaign. On the other hand, SDA is an unsupervised process and does not need a pre-defined database. This aspect makes SDA one of the most powerful tools to reduce the detection of false positives, that is, objects which are not mines however recognized as though they were. A still rough experimental campaign, carried out to validate the procedure, concludes this preliminary phase of the project.

2 MINOR Project

The entire project is based on three main key points: i) drones equipped with a complex network of sensors scan the surface; ii) innovative post-processing data techniques are implemented for the mine identification procedure by data fusion from the several sensors; iii) feasibility analysis completes the investigation through a comparison with other existing technologies.

The use of larger number of drones guarantees the enhancement of the accuracy, the reduction of the scanning time and optimize the drone's path. The drones fly at different heights; higher they fly, wider the scanned surface (Fig. 1), even though it leads to a reduction in the sensitivity. The flying logic includes only few master
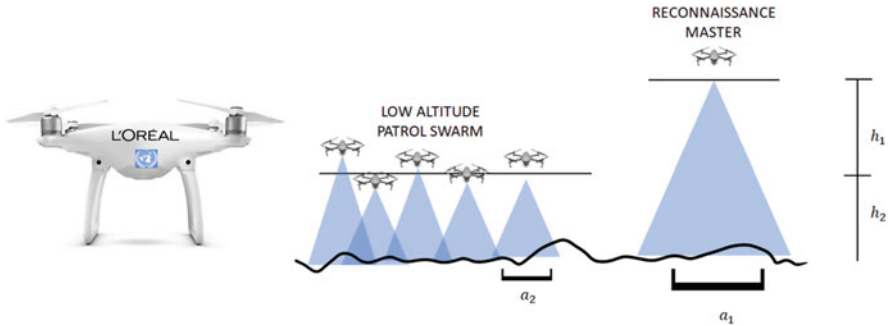
Fig. 1 Drone prototype and flying levels are determined based on a compromise between the scanned area and the sensitivity

drones which fly at h_1 covering in little time a broad area, according to a chessboard geometry, and detecting the areas that might contain mines; in a second phase, a larger swarm flies at the lower level h_2 over the regions detected as containing mines, indicated by the master drones, and find the exact location of the mines.

3 First Step Post-Processing Data Algorithm: Numerical Data Generation

The two-step algorithm relies on a convolutional neural network for the first item classification. An existing CNN, AlexNet, has been used. The choice of an already trained CNN is driven by the large amount of data and time that would be required to prepare a neural network from the beginning. AlexNet has been trained on a more than a million of images and can classify about 1000 objects. More than the input and output layers, constituted by 1000 neurons devoted to the classification, AlexNet is composed of 23 hidden layers meant to compute convolutional processes.

The CNN is implemented so to identify objects buried underground; accordingly, only two classification outputs, namely "Target," related to any detected object, and "Free areas," are returned by the CNN. The network has been trained through numerically generated radargrams, typical of GPR acquisitions. Buried objects produce a signal in the shape of a hyperbola. Figure 2 compares the signatures of a "Target" and "Free area." These radargrams have been created by GprMax [18], a Finite-Difference Time-Domain software that simulates the propagation of an electromagnetic wave inside a medium. The medium is discretized in a grid and each element of the grid has the physical parameters of the medium assigned, such as dielectric constant and magnetic permeability. At each section of the grid, the electromagnetic field is computed in time. The hyperbola training radargram is produced by providing to the software a precise model of the searched object, in this case a mine. The model considers the specific geometry as well as material
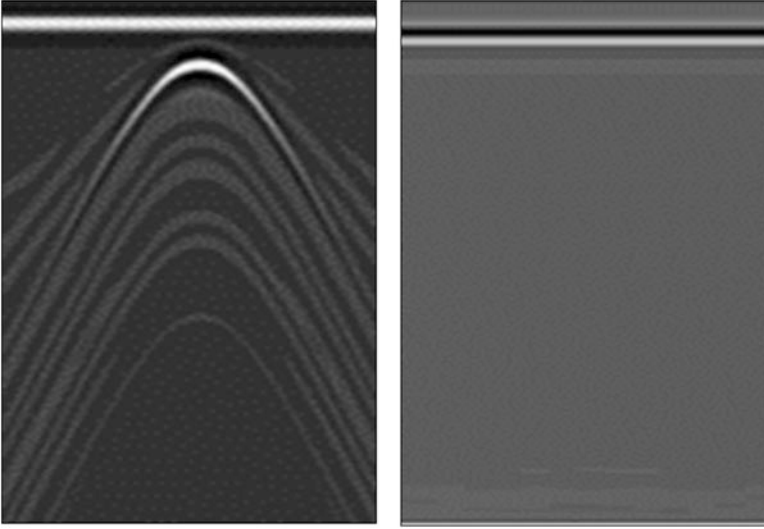
Fig. 2 Radargrams numerically generated by GPRMax: "target" on the left and "Free area" on the right

properties. The "Free area" instead includes only the ground interface signature. 2400 radargrams have been generated, of which 1200 are "Free area" and the remaining 1200 are "Target" with objects placed at different positions and depths.

The trained convolutional neural network is then applied to the experimental radargrams which does not consist of a single frame, but it is long as the length of the acquisition. To investigate the presence of mines, the algorithm generates a window which translates along the radargram, scanning all the frames. Each frame is compared with the reference radargrams in Fig. 2. The level of match defines the probability the detected object is a mine: indeed, the higher the probability, the more likely the target is a mine, even though the possibility of false positive is not cancelled yet. In the same way, low probability values indicate "Free areas."

4 Second Step Post-Processing Data Algorithm: Symbolic Data Analysis

Symbolic data analysis (SDA) is part of data mining techniques; in particular, it belongs to the data clustering methods. In data clustering, an entire set of data is divided into sub-groups according to the level of similarity of its composing elements. The classification does not require any a priori information about the common features of the data which are gathered only according to their level of homogeneity [19]. This technique, processing an unlabelled dataset, unveils

the hidden main structure/feature of each group. The data can appear as either time-series or space-series. In both cases, data are dynamics, implying each value of the dataset varies with either the space or the time coordinate. Besides, it is easy to notice how space and time series are high-dimensional data since each point of the series can be considered as an observation sequentially made. This technique praises two advantages [20]: the hidden information and the main features lost in the space-series are disclosed; secondly, SDA return images which facilitate the cluster understanding, the outliers, and the structures.

Among the several existing clustering algorithms [20, 21], such as hierarchical, partitioning clustering, and multi-step clustering, here, only a hierarchical one is used. In hierarchical methods, the cluster hierarchy is obtained either with agglomerative or divisive algorithms. The former, here used, considers each symbolic component of the data as a cluster, and consecutively combines the groups; the result is a nested hierarchy of similar clusters. A dendrogram, a tree-like diagram that records the sequences of merges [22], displays the generated groups. This method is surely effective given the fact it does not need a priori information about properties and number of the groups to be generated. However, applications to large amount of data set are prevented given its quadratic computational complexity. Moreover, when agglomerative cluster is used, no cluster adjustment is possible after the group generation, limiting the accuracy of the method.

5 Experiments and Results

The experimental campaign, which is only at its preliminary phase, is here devoted to validating the algorithm that must identify buried mines via GPR data acquisitions. To prove the reliability of the proposed technique, three types of mine prototypes as well as other metallic and non-metallic objects have been buried in the prepared terrain at the locations shown in Fig. 3. The grid has overall dimensions of $2\ m \times 0,\ 6\ m$, being the objects at distance of $1\ m$ along the x axis and of $0,\ 3\ m$ along the y axis. The depth of burial varies from $15\ cm$ for h_1 up to $7\ cm$ for h_3. The grid dimensions are set so as to ensure a space wide enough in between targets, a region that the GPR antenna can identify as uncontaminated, which should apparently appear in the radargrams.

The terrain, mixture of clay and topsoil, simulates woods conditions. The acquisition system consists of a commercial 1.6-GHz GPR antenna, RIS MF Hi-Mod model, which moves along both x and y directions and produces radargrams as reported in Figs. 4 and 5. In particular, Fig. 4 is related to the transverse acquisition in correspondence of the three mines M3, M4, and M7. Indeed, the different burials depths are clearly recognizable. It is noteworthy how the simulated mine signature shown in Fig. 2 well mimics the experimental curves here displayed. Figure 5 refers to the longitudinal acquisition at h_2 and is another interesting example since it shows how different objects produce different characteristic signatures. The first detected object is a brick and as it contains no metal components is barely detectable. Vice
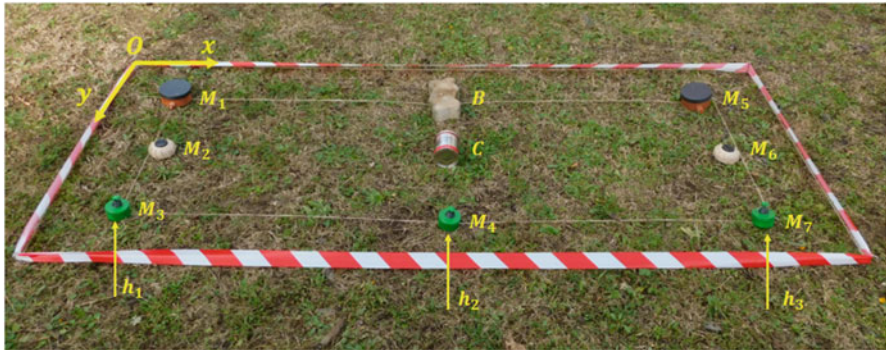
Fig. 3 Experimental grid
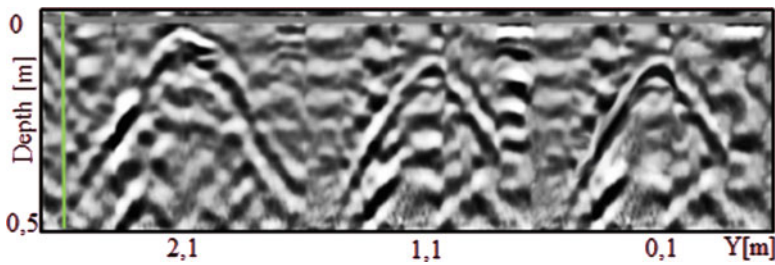
Fig. 4 Example of transverse acquisition
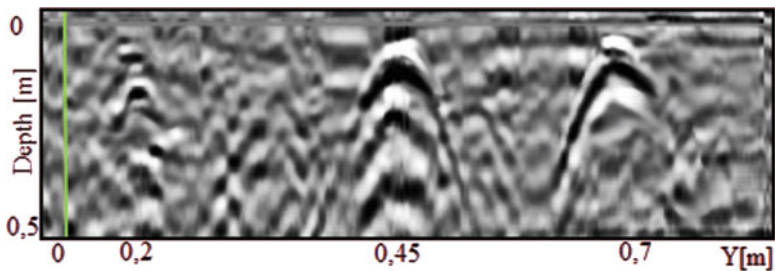
Fig. 5 Example of longitudinal acquisition at h_2

versa, being the two following objects a metal can and a mine, respectively, the antenna clearly detects them. Indeed, in general the higher the metal content, the clearer the signature, whilst what regards the depth depends upon the frequency of the antenna. In this specific example, 1.6 GHz prevents a good acquisition of objects just underneath the surface.

The greatest difference between numerical and experimental signature stands in the clutter effect related to ground reflections, as apparent in Fig. 4 and Fig. 5. Clutter noise is highly affected by the terrain composition and especially to moisture. A clayish terrain, as the one used in this experimental camping, though it depicts a

more realistic scenario with respect to other investigations [23, 24], which instead uses sandy soil, induces a slower drying and consequently less defined radargrams. Eventually, this aspect compromises the neural network training, which should rely on a vast image dataset, hardly acquirable in these conditions. Furthermore, the employed antenna with a frequency of 1.6 GHz is not extremely accurate for shallow buried objects. Its resolution in depth is as high as at least 10 cm. Accordingly, the radargram in Fig. 4 is more readable that the one in Fig. 5.

All the obtained radargrams are inputs for the CNN. Since the CNN returns the probability the detected object is a mine, that is, the higher the value of the probability, the more likely the target is a mine, the algorithm is practically able to distinguish targets from free areas, whose probability is nearly zero. As mentioned in Sect. 3, a window slides rightward along the radargram frame by frame. At each frame, the probability is computed as results of the comparison between the selected frame and the numerical signature. For easiness of reading, the "Free area," corresponding to an almost zero probability, is encircled in green; the target is encircled in red, as shown in Fig. 6, which reports few exemplifying frames of the transversal acquisition of Fig. 4.

Figure 7 reports only two frames as distinguishing of the clustering process on the acquisition at h_2, corresponding to Fig. 5. In the first sub-plot, the first signature corresponds to the brick and it is correctly labelled as "Free area," given the value of probability of only 21%. The second sub-plot shows the result of the clustering in correspondence of the metal can. Given the large amount of metal, even higher than the mine, the target is recognized as a mine, with a probability of 98%. This is a clear example of "false positive," namely, when objects are identified as mines even though they are not.

It is apparent how the clustering process via CNN correctly tells apart "Free areas" and non-metallic objects from "Targets"; however, among all the metallic objects, the accuracy is not sufficient to distinguish mines. This implies the need of a more intense training and the employment of an SDA algorithm, which is still in progress.

6 Conclusions

The present work is part of a larger research project, named MINOR, MINe Overall Recognition, which has the ambition to generate a real-time map with the exact location of anti-personnel mines. Mines will be detected through a swarm of autonomous drones and the data will be processed via a complex set of algorithms. Here, a two-step strategy is described as applied to GPR acquisition, being this sensor of the possible candidate to equip the drones. The algorithm, aimed at identifying buried antipersonnel mines, is the combination of a convolutional neural network and a symbolic data analysis process. The experimental campaign proved the effectiveness of the algorithm, which appears as a powerful tool to automatically detect buried objects with even small metal content. The inevitable clutter noise,
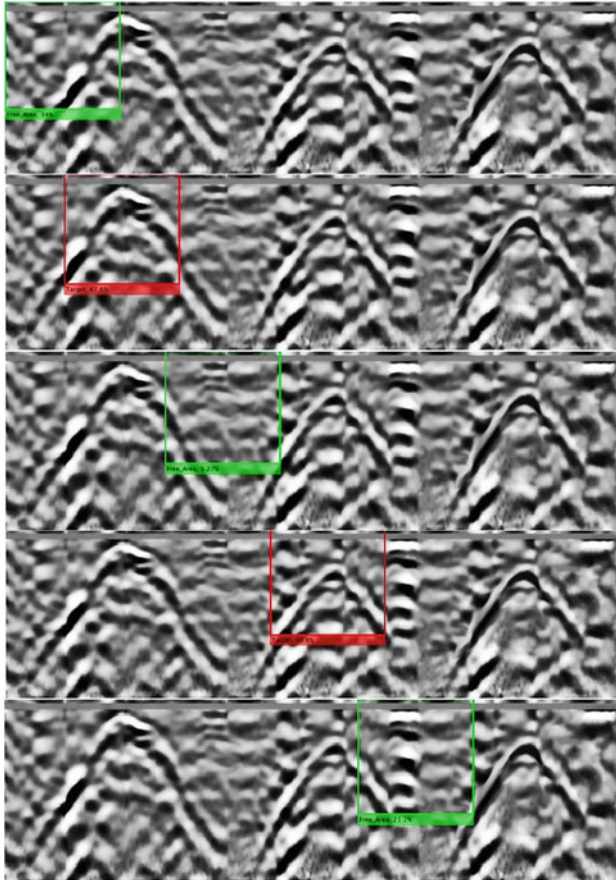
Fig. 6 Target estimation of transverse radargram

affecting all the measurements, does not compromise the results and the CNN algorithm correctly distinguishes "Free areas" and non-metal objects from mine-like targets. However, uncertainty is still high among the metallic objects. The SDA, which has the great advantage of not requiring a predefined dataset and which is still in progress, would solve the issue related to "false positives," that is, objects identified as mines, even though they are not.
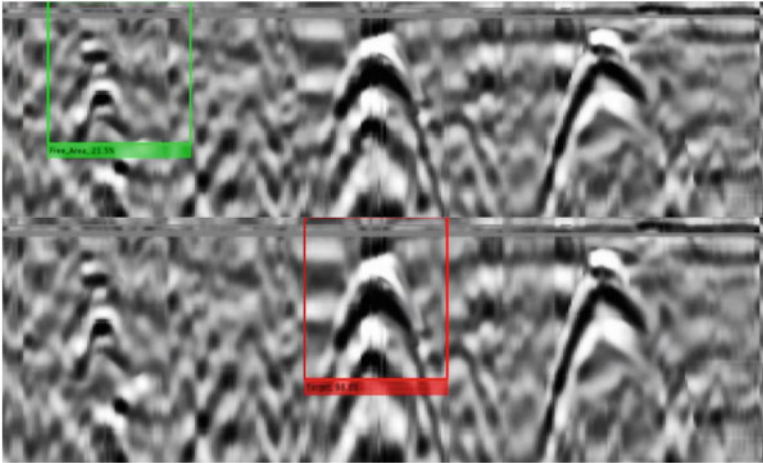
Fig. 7 Target estimation of h_2

References

1. O.L.L. Tellez, B. Scheers, Ground penetrating radar for close in mine detection, in *Mine Action, the Research Experience of the Royal Military Academy of Belgium*, (IntechOpen, 2017)
2. P. Church, J.E. McFee, S. Gagnon, P. Wort, Electrical impedance tomographic imaging of buried landmines. IEEE Trans. Geosci. Remote Sens. **44**(9), 2407–2420 (2006)
3. M. Metwaly, G. El-Quady, J. Matsushima, S. Szalai, N.S.N. Al-Arifi, Contribution of 3-D electrical resistivity tomography for landmines detection. Nonlinear Process. Geophys. **15**, 977–986 (2008)
4. G. Zentai, X-ray imaging for homeland security. Inter. J. Signal Imaging Syst. Eng. **3**(1), 13–20 (2010)
5. S. Kaya, U.M. Leloglu, Buried and surface mine detection from thermal image time series. IEEE J. Select. Topics Appl. Earth Observat. Remote Sens. **10**(10), 4544–4552 (2017)
6. K. Takahashi, H. Preetz, J. Igel, Soil properties and performance of landmine detection by metal detector and ground-penetrating radar—Soil characterisation and its verification by a field test. J. Appl. Geophys. **73**(4), 368–377 (2011)
7. M.S. Korman, J.M. Sabatier, Nonlinear acoustic techniques for landmine detection. J. Acoust. Soc. Am. **116**(6), 3354–3369 (2004)
8. C. Mc Caffrey, N. Pesonen, I. Marttila, K. Nummila, Towards an Acousto-Ultrasonic Landmine Detector
9. J.S. Martin et al., Ultrasonic displacement sensor for the seismic detection of buried land mines. Inter. Soc. Optics Photon. **4742**, 606–616 (2002)
10. A.G. Petculescu, J.M. Sabatier, Doppler ultrasound techniques for landmine detection. Inter. Soc. Optics Photon. **5415**, 30–34 (2004)
11. L. Nesi, G. Pepe, M. Bibuli, E. Zereik, A. Carcaterra, M. Caccia, A new tow maneuver of a damaged boat through a swarm of autonomous sea drones. IFAC-PapersOnLine **52**(21), 360–366 (2019)
12. N. Roveri, A. Carcaterra, L. Molinari, G. Pepe, Safe and secure control of swarms of vehicles by small-world theory. Energies **13**(5), 1043 (2020)
13. D.J. Daniels, P. Curtis, Minehound TM trials in Cambodia, Bosnia, and Angola. Inter. Soc. Optics Photon. **6217**, 62172N (2006)

14. P.D. Gader, M. Mystkowski, Y. Zhao, Landmine detection with ground penetrating radar using hidden Markov models. IEEE Trans. Geosci. Remote Sens. **39**(6), 1231–1244 (2001)
15. V. Kovalenko, A.G. Yarovoy, L.P. Ligthart, A novel clutter suppression algorithm for landmine detection with GPR. IEEE Trans. Geosci. Remote Sens. **45**(11), 3740–3751 (2007)
16. R. Solimene, A. Cuccaro, A. Dell'Aversano, I. Catapano, F. Soldovieri, Ground clutter removal in GPR surveys. IEEE J. Select. Topics Appl. Earth Observat. Remote Sens. **7**(3), 792–798 (2013)
17. O. Lopera, E.C. Slob, N. Milisavljevic, S. Lambot, Filtering soil surface and antenna effects from GPR data to enhance landmine detection. IEEE Trans. Geosci. Remote Sens. **45**(3), 707–717 (2007)
18. C. Warren, A. Giannopoulos, I. Giannakis, gprMax: Open source software to simulate electromagnetic wave propagation for ground penetrating radar. Comput. Phys. Commun. **209**, 163–170 (2016)
19. P. Rai, S. Singh, A survey of clustering techniques. Inter. J. Comput. Appl. **7**(12), 1–5 (2010)
20. H.-H. Bock and E. Diday, Analysis of Symbolic Data: Exploratory Methods for Extracting Statistical Information from Complex Data. Springer Science & Business Media, 2012
21. K. Leonard, J.R. Peter, Finding groups in data: An introduction to cluster analysis, in *Probability and Mathematical Statistics: Applied Probability and Statistics*, (Wiley Series, 1990)
22. J.J. Van Wijk, E.R. Van Selow, *Cluster and Calendar Based Visualization of Time Series Data* (IEEE, 1999), pp. 4–9
23. X. Song, T. Liu, D. Xiang, Y. Su, GPR antipersonnel mine detection based on tensor robust principal analysis. Remote Sens. **11**(8), 984 (2019)
24. X. Núñez-Nieto, M. Solla, P. Gómez-Pérez, H. Lorenzo, GPR signal characterization for automated landmine and UXO detection based on machine learning techniques. Remote Sens. **6**(10), 9729–9748 (2014)

A New Approach for Structural Health Monitoring: Damage Detection on Large Structures through a Swarm of Moving Sensors

Manuel Pinto, Nicola Roveri, Gianluca Pepe (ID), and Antonio Carcaterra

1 Introduction

Identification problems have been highly investigated over the past decades and represent a common topic of different disciplines, such as structural engineering, acoustic, environmental analysis. The key point is the ability of identifying the environment parameters. Indeed, the major task of this research branch is the characterization of an observed system, i.e. the environmental field, according to the set of data perceived by sensors array.

One peculiar category of these kind of problems takes place in the context of structural monitoring and deals with the identification of structural anomalies. In this type of applications, indeed, the possibility of monitoring the temporal behaviour of mechanical structures has a considerable importance since it can unveil conditions that can rapidly turn into critical. In the past years, several studies have been performed using time-frequency analysis techniques based on Wavelet transform [1–3]. The monitoring procedure consists of measurements acquired through conventional sensors, such as strain gauges, accelerometers and FBG optical sensors held at a fixed position [4–6].

The innovation of the presented approach lies in the chance to optimally move the used sensors along a defined trajectory.

In several parameter estimation and control theory application, the concept of the optimal observability plays a key role. The effects of the measurement location and the number of sensors have been studied in several works [7, 8], with the aim to develop strategies to determine a set of measurement locations which lead to the best state estimates [9].

M. Pinto (✉) · N. Roveri · G. Pepe · A. Carcaterra
Department of Mechanical and Aerospace Engineering, Sapienza University of Rome, Rome, Italy
e-mail: manuel.pinto@uniroma1.it

In the present paper, the possibility of optimally control sensors dynamics is investigated, in order to obtain infomation regarding the state of the observed system (e.g. stress state) and to obtain point information about the presence of an irregularity along the structure (e.g. localized damage).

The control of the sensors motion and the consequent damage identification are achieved through a two-step strategy. The first step is based on creating a set of equations containing both models for the dynamics of the structure and for the dynamics of the sensors; a linear quadratic regulator (LQR) control logic is developed to define the optimal trajectory of the swarm. The second step includes the identification of the damage module: the process of data analysis is investigated through the use of the technique based on Ensemble Empirical Mode Decomposition, combined with the Hilbert-Huang Transform (HHT) [10, 11].

The analysis is also focused on the evaluation of the possible advantages of having, instead of an array of fixed measurement stations, one or few moving sensors able to explore the whole system.

The statement of the problem is formulated as follows: a set of moving sensors can explore a space region R characterized by the presence of a propagating scalar field in the space and time coordinates ξ and t. Each of the sensors can move autonomously with an associated state variable x_i, whose dynamics can be written in the form $\dot{x}_i = f_i(x_i, u_i)$, where $x_i = \begin{Bmatrix} \xi_i \\ v_i \end{Bmatrix}$ is the state vector associated to the sensors dynamics, in which ξ_i is the spatial position, and v_i is its velocity.

The observed system, i.e. the observed field, can be generally described by a differential operator $D_{\xi, t}(w)$, with respect both to the space and the time variables. The field w obeys indeed to a known partial differential equation $D_{\xi, t}(w) = 0$. Given the premises, we can describe the problem with the following set of equations:

$$\begin{cases} \dot{x}_i = Ax_i + Bu_i + n_{x_i} \\ \quad D_{\xi,t}(w) = 0 \\ s_i = g_i w(x_i, t) + n_{s_i} \end{cases} . \tag{1}$$

2 Beam Dynamics and Damage Modelling

The general elastic shape $w(x, t)$ is expressed in terms of an expansion of know eigenfunctions $\phi_n(x)$, combined through a set of weighting unknown time-dependent coefficients $q_n(t)$. The general response of the beam deflection, according to Euler-Bernoulli theory, is a linear combination from all vibration modes:

$$w(x, t) = \sum_{n=1}^{N_{modes}} \phi_n(x) \cdot q_n(t). \tag{2}$$

The crack has been modelled as a torsional spring acting at the junction between the two segments of the beam. At that point, the continuity of the shear force and bending moment needs to be guaranteed through the compatibility conditions. The stiffness of the modelled spring is related to the geometrical characteristics of the crack [10, 12], namely, its depth, through the parameter k:

$$k = \left(6\pi \mu^2 f(\mu) h \right)^{-1}, \tag{3}$$

where $f(\mu)$ is a polynomial relation, function of the non-dimensional parameter $\mu = \frac{d}{\mu}$:

$$\begin{cases} f(\mu) = 0.6384 - 1.035\,\mu + 3.7201\mu^2 - 5.1773\mu^3 + 7.553\mu^4 - 7.332\mu^5 + 2.4909\mu^6 \\ \mu = \frac{d}{h} \end{cases} \tag{4}$$

3 Compact Form Including the Sensor's Dynamics

For the sake of simplicity in the present section, the following notation will be adopted: the state vector for sensor dynamics is $x = \begin{Bmatrix} \xi_{(j)} \\ v_{(j)} \end{Bmatrix}$; $\tilde{\xi}_{(j)} = \xi_{(j)} - L_1$, with $\xi_{(j)}$ being the j-th sensor along the longitudinal coordinate ξ, and L_1 being the position of the crack. The modal shapes are $\phi_{n,j}^{(i)}$.

Dynamic equations of sensors have been represented through a moving mass system subjected to external forces acting on the ξ axes, as $m\dot{v}_{j\xi} = F_{j\xi}$.

All these relations can be reduced to a set of matrix equations that includes the carrier dynamics, the mechanical structure model, and the sensor model equation. As a preliminary study, the effect of external noise will not be considered, so that Eq. (1) becomes:

$$\begin{cases} \dot{x} = Ax + Bu \\ y = \dot{q} \\ \dot{y} = -\Lambda q - D\dot{q} + \Psi \\ s = G(x)\,q \end{cases} \tag{5}$$

Where the vector $Y = \begin{Bmatrix} q \\ \dot{q} \end{Bmatrix}$ contains the principal coordinates of the decoupled time-dependent equation of the beam dynamics: $\ddot{q}_n + \omega_n q_n + \zeta_n \dot{q}_n = \int_0^L \Phi(x) P(x,t)\, dx$. $\Lambda = \text{diag}\left[\omega_1^2, \omega_2^2, \ldots, \omega_{N_{modes}}^2 \right]$ is the natural frequencies matrix of the structure and Ψ is the input vector. The damping factors are contained in the diagonal matrix $D = diag\,[\zeta_n \omega_n]$, where $\zeta_n = \frac{c}{2\omega_n\,\rho S}$. Proceeding as for Kalman's filter approach, let's consider a unique state vector in which we write the

assembly of the first three theoretical models, that is $r^T = [x, q, y]^T$, the problem can be rewritten in a compact form:

$$\begin{cases} \dot{r} = \widetilde{A}r + \widetilde{B}u + \widetilde{\Psi} \\ \quad s = \widetilde{G}(x)\,r \end{cases}. \tag{6}$$

With state space augmented matrices and vectors $\widetilde{A}, \widetilde{B}, \widetilde{\Psi}, \widetilde{n}, \widetilde{G}$ of dimension respectively: $\widetilde{A} = (2 \cdot N_S + 2 \cdot N) \times (2 \cdot N_S + 2 \cdot N); \widetilde{B} = (2 \cdot N_S + 2 \cdot N) \times 1;$ $\widetilde{\Psi} = (2 \cdot N_S + 2 \cdot N) \times 1$; rectangular measure matrix $\widetilde{G} = N_s \times (2 \cdot N_S + 2 \cdot N)$.

The observation equation considers the rectangular matrix $\widetilde{G}$ containing the modal eigenfunctions $\phi_n(\xi)$, so that it is a time-variant matrix depending on the state (i.e. position) of the moving sensor.

4   Simulations

Simulations have been carried out considering a simply supported beam with length $L = 20\ m$, with rectangular cross section of $S = 0.04\ m^2$, Young modulus $E = 200\ GPa$ and moment of inertia $I = 1.33 \cdot 10^{-4} m^4$. Referring to Eqs. (3) and (4), the damage has been modelled as a torsional spring of stiffness $k = 1.55 \frac{N}{m}$, while the crack depth is half of the beam height, i.e. $\mu = 0.5$. Since the presence of the damage, compared to the case of the undamaged beam, has a noticeable effect on the beam dynamics in terms of natural frequencies with modes higher than fourth, the first six modes have been considered in the simulations.

In order to test the strategy, different scenarios have been considered, in which the crack has been positioned respectively at the coordinates $\xi_c = 0.7L$ and $0.8L$. The source exciting the beam is a moving load $|P| = 1000N$ crossing the beam with velocity $v_L = 40 \frac{Km}{h}$.

Two main groups of tests have been performed. The first case considers four accelerometers moving along the beam; the second case considers the same four accelerometers held at fixed position. Differences between both cases in terms of accuracy and efficiency will be compared in order to evaluate advantages of the proposed strategy.

The measurement stations have been modelled as four accelerometers moving along the structure within four different constrained regions.

The motion of the set of sensors is regulated through the development of a Linear Quadratic Regulator algorithm (i.e. LQR). The request to move along a specific region of the beam is formulated using the optimal control theory by the minimization or maximization of a given cost functions J:

$$J = \min_{\substack{\boldsymbol{u} \in U \\ \boldsymbol{x} \in X}} \int_0^T E\left(\boldsymbol{x}, \boldsymbol{u}\right) dt \tag{7}$$

The objective function $E(\boldsymbol{x}, \boldsymbol{u})$ indicates the distance (i.e. the target position) that must be reached by the sensor carrier, satisfying state and control constraints $\boldsymbol{u} \in U$, $\boldsymbol{x} \in X$ respectively. That leads to the equation of the control vector:

$$\boldsymbol{u} = -\boldsymbol{K}_{LQR}\left(\boldsymbol{x} - \boldsymbol{x}_T\right), \tag{8}$$

where $\boldsymbol{K}_{LQR}$ and $\boldsymbol{S}$ are the optimal gain of the control action and the solution matrix of the Riccati equation, respectively, defined as follows:

$$\boldsymbol{K}_{LQR} = \boldsymbol{R}^{-1}\boldsymbol{B}^T\boldsymbol{S}, \tag{9}$$

$$-\dot{\boldsymbol{S}} = \boldsymbol{A}^T\boldsymbol{S} + \boldsymbol{S}\boldsymbol{A} + \boldsymbol{Q} - \boldsymbol{S}\boldsymbol{B}\boldsymbol{R}^{-1}\boldsymbol{B}^T\boldsymbol{S}. \tag{10}$$

In Table 1 are reported the chosen initial and target state vectors (position and velocity), respectively, of the four accelerometers, that will lead to the four trajectories. Trajectories are chosen so that each sensor covers the entire constrained regions during the time of acquiring (crossing time of the moving load). Namely, through the selection of the matrices $\boldsymbol{Q}$ and $\boldsymbol{R}$, as the sensors approach their target position, the control action is adjusted so that the sensors smoothly reach the target points with velocity equal to zero.

For what it concerns the location of the fixed sensors, they were respectively positioned at the coordinates: $\boldsymbol{\xi}_{s1} = \mathbf{0.15L}$, $\boldsymbol{\xi}_{s2} = \mathbf{0.3L}$, $\boldsymbol{\xi}_{s3} = \mathbf{0.6L}$, $\boldsymbol{\xi}_{s4} = \mathbf{0.8L}$.

5   Data Processing with EMD and HHT

Once simulations have been performed, all the collected data goes under the processing through the Hilbert-Huang Transform (HHT), which is based on the

Table 1 Chosen trajectories of the moving sensors

Sensor #	Initial condition $[\xi_0, v_0]$	Target point $[\xi_T, v_T]$
Accelerometer 1	[0,0]	[0.3 L,0]
Accelerometer 2	[0.3 L,0]	[0.6 L,0]
Accelerometer 3	[0.6 L,0]	[0.8 L,0]
Accelerometer 4	[L,0]	[0.8 L,0]

analysis of monocomponent signals obtained through the Empirical Mode Decomposition (EMD) of the original acquired acceleration signals and the subsequent Hilbert Transform (HT). The method of EMD, described ahead, is a tool for multicomponent nonlinear signal analysis, highly investigated over the past decades in the context of damage identification [13–17].

The EMD method is developed from the assumption that any non-stationary and non-linear time series consists of different simple intrinsic modes of oscillation. Given an observation of a multicomponent signal $x(t)$, it could be essentially represented as a superposition of several components of different scales, i.e. the superposition of high-frequency oscillation over-low frequency oscillation. The presence of the damage causes a discontinuity in the vibration response of the excited beam which may result in the variation of structural stiffness and hence enable structures to vibrate nonlinearly.

The EMD is an adaptive time-frequency data analysis method; its aim is to identify proper time scales that reveals physical characteristics of the processed signals, decomposing them into a finite number of components which are referred to as Intrinsic Mode Functions (i.e. IMF). Every obtained IMF is basically mono-component and has to satisfy two main conditions:

(i) In the whole data set, the number of extrema and the number of zero-crossings must either be equal or differ at most by one.
(ii) At any point, the mean value of the envelope defined by the local maxima and the envelope defined by the local minima is zero.

Based on the previous conditions, the procedure to extract the IMFs from a given signal $x(t)$ is called sifting process, which consists of the following steps:

1. Identification of all the local extrema and interpolation through a cubic spline function of all the local maxima and local minima, respectively.
2. Once the upper and the lower envelopes (x_{max} and x_{min}) are obtained, compute the envelope mean between the two functions, i.e. $m_1(t) = \frac{x_{max}(t) + x_{min}(t)}{2}$.
3. Extract the estimation of the first IMF by subtracting $m_1(t)$ from the original signal: $h_1(t) = x(t) - m_1(t)$.
4. Using $h_1(t)$ as new input signal, iterate steps from 1 to 3 until the IMF is obtained through the verifying of a proper stopping criterium [14]. The original signal is so decomposed in the first Intrinsic Mode Function $IMF_1(t)$ and a residue $r_1(t)$. Update the residue $r_1(t) = x(t) - IMF_1(t)$.
5. Using the residue $r_1(t)$ as the new input signal, iterate steps from 1 to 4 until the final residue $r_k(t)$ becomes monotone.

At the end of the process, the original signal is a combination of all the computed IMFs plus the last residue, i.e. $x(t) = \sum_1^k IMF_k(t) + r_k(t)$.

The damage identification process is performed through the analysis of the first Instantaneous Frequency functions, computed through the use of the Hilbert Transform (HT), applied to each IMF around the first natural frequency of the system.

Considering $x(t)$ as the $IMF(t)$ to be processed, the Hilbert Transform is defined:

$$y(t) = H(x(t)) = \frac{1}{\pi} \int \frac{x(t)}{t - \tau} d\tau. \tag{11}$$

The Hilbert transform applies a phase shift of $\frac{\pi}{2}$ to the signal and leads to its analytical representation as a complex-valued function:

$$z(t) = x(t) + i y(t). \tag{12}$$

From Eq. (12) the phase $\varphi(t)$ is defined:

$$\varphi(t) = atan \frac{y(t)}{x(t)}. \tag{13}$$

The Instantaneous Frequency function is then computed:

$$IF(t) = \frac{1}{2\pi} \frac{d\varphi(t)}{dt}, \tag{14}$$

where $\omega(t) = \frac{d\varphi(t)}{dt}$ is the instantaneous angular frequency. Note that the phase of Eq. (13) has to be the unwrapped phase angle of the signal, in order to avoid discontinuities in the resulting IFs.

6 Results and Discussions

Results of the methodology are here presented. The presence of the damage causes a noticeable effect in the frequency response of the excited beam: in particular, the crack induces a local change in frequency well enhanced in the Instantaneous Frequency functions so that, as the load crosses the damaged section of the structure, they show a narrow peak.

In Figs. 1 and 2 the Instantaneous Frequency (IF) functions versus the normalized beam length are reported, for different positions of the crack, extrapolated from the processing through EMD of the acceleration signals measured by the sensors, according to the setup described in Sect. 4. For a moving load with velocity of $v_L = 40 \frac{Km}{h}$, three scenarios are presented: the cases in which the damage is located at $\xi_c = 0.8L$ and $0.7L$, respectively.

In details blue plots represent the response for the case of moving sensors, while the red graphs are referred to the case in which the sensors don't have any actuation ($\boldsymbol{u} = 0$), so that they are held at fixed location.

The general response of the method is the same in every curve: the presence of the damage causes a discontinuity in the frequency content around the first fundamental frequency f_1 ($f_1 \approx 1.13\ Hz$). The global effect is a general frequency modulation
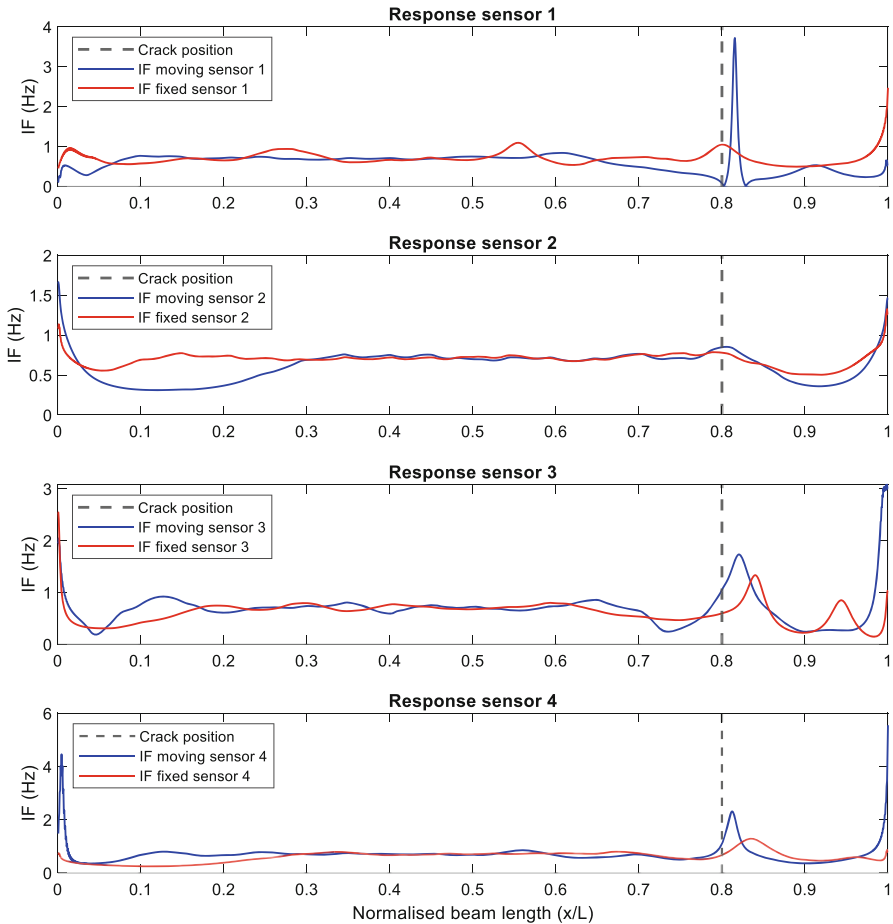
Fig. 1 Instantaneous Frequency functions of the acquired signals for the case of a moving load with velocity $v = 40\frac{km}{h}$. Dashed line represents the crack position located at $L_{crack} = 0.8L$

below the value of f_1; there is also a local effect enhanced by the IF: in proximity of the damage (as the load crosses the crack), the IF curves show a narrow peak generally above f_1, allowing a direct and effective crack identification.

The comparison between the scenarios shows the method provides a general better response for the cases of moving sensors. In particular, as shown in Fig. 1, the peaks of the blue IFs are well sharp and narrow and they are able to identify, except for a small spatial error, the position of the damage. The use of moving sensors seems to have a relevant influence on the accuracy of the method, especially for the sensors located in proximity to the external boundaries of the beam (Accelerometers #1 and #4): as it is shown in the first and the last subplot of Fig. 1, indeed, the poor
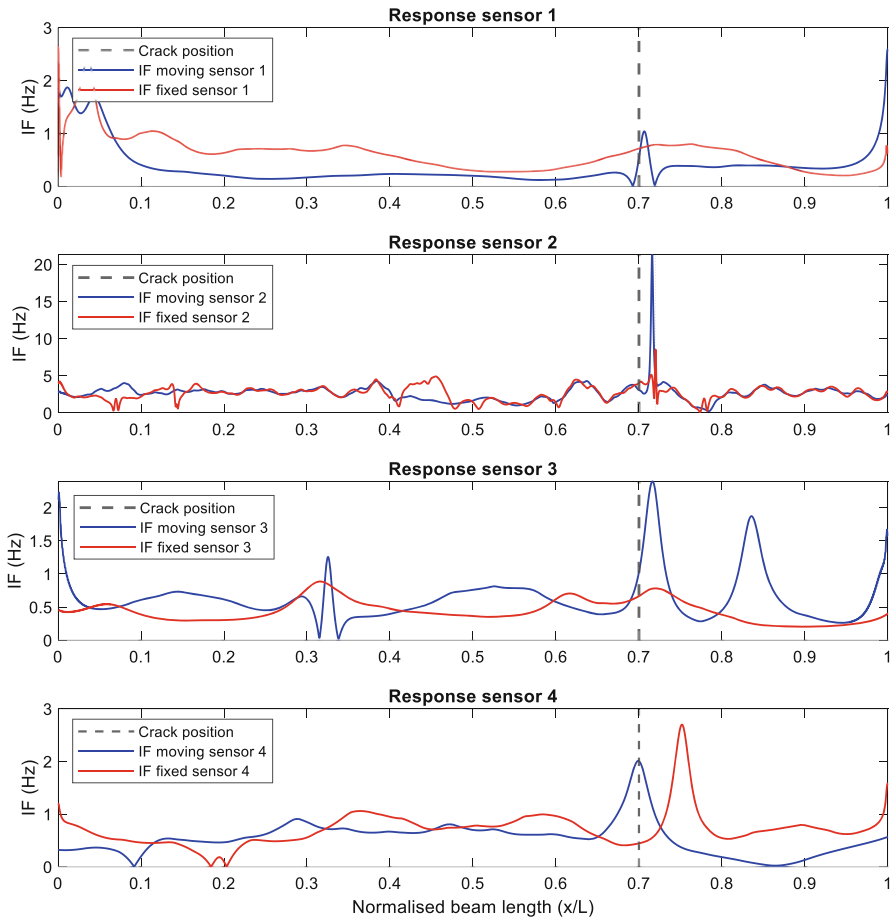
Fig. 2 Instantaneous Frequency function of the acquired signals for the case of a moving load with velocity $v = 40 \frac{km}{h}$. Dashed line represents the crack position located at $L_{crack} = 0.7L$

response enhanced by the red curves has been overcome through the deployment of the sensors towards more sensible location of the structure.

Similar considerations can be made for the other set of results reported in Fig. 2, in which the moving sensors allow to identify the damage position all the time with the minimum error, even if in some cases, some false-positive peaks occur (subplot #3 of Fig. 2). Few cases of noisy response occurred, as reported for example in subplot #2 of Fig. 2 both for moving and fixed sensors. Although the response shows a peak, or at least a local maximum at the crack location, the general trend is not sharp, but shows several noisy oscillations. These phenomena could be caused by some inaccuracy of the sifting process which did not allow a perfect monocomponent decomposition of the original signals, leading to a noisy and not precise response in the resulting Instantaneous Frequency functions.

7 Conclusions

In the present paper, a methodology for damage deduction in large structures is presented. The method, instead of using a classical set of fixed measurement stations, proposes the use of an array of moving accelerometers, able to explore specific constrained regions of the structure. The whole procedure involves a two-step strategy: i) through the development of an LQR control logic, it is possible to establish the trajectories of the moving sensors and ii) the identification procedure involves data processing based on Empirical Mode Decomposition, combined with the Hilbert-Huang Transform.

The crack estimation procedure has been performed through direct analysis of the Instantaneous Functions around the value of the first fundamental frequency of the system. The frequency changes induced by the presence of the damaged result in a global effect, i.e. a frequency modulation below the first natural frequency value. A more important local effect is shown at the crack location, where, as the load crosses the damage, the IFs show a narrow peak above the fundamental frequency, allowing a direct identification of the crack.

Our results show the potential of the strategy: the possibility of heading the measurement stations to more optimal and sensitive positions leads to an enhancement of the crack identification.

The comparison between the results performed with moving sensors and fixed sensors shows that the motion of the measurement station improves the accuracy of the estimation, and an increase of the sensitivity of the sensors occurs, especially for the first and last accelerometers of the array. In the specific instantaneous functions, indeed, the peaks of the curves are well enhanced.

The strategy is still under investigation. Further analysis will concern the influence of the sensors velocity and the influence of noise corrupting the acquired data, leading to the development of an estimator based on Extended Kalman Filter in order to reconstruct the elastic shape of the observed structure.

References

1. W.L. Bayissa, N. Haritos, S. Thelandersson, Vibration-based structural damage identification using wavelet transform. Mech. Syst. Signal Process. **22**(5), 1194–1215 (July 2008)
2. M. Cao, W. Xu, W. Ostachowicz, S. Zhongqing, Damage identification for beams in noisy conditions based on Teager energy operator-wavelet transform modal curvature. J. Sound Vib. **333**(6), 1543–1553 (2014)
3. Y. Yang, S. Nagarajaiah, Blind identification of damage in time-varying systems using independent component analysis with wavelet transform, mechanical systems and signal processing, volume 47. Issues **1–2**(3), 3–20 (2014)
4. M. Pinto, N. Roveri, G. Pepe, A. Nicoletti, G. Balconi, A. Carcaterra, *Embedded Optical Sensors for Vibration Monitoring of Large Structures, ISMA 2018 and 7th International Conference on Uncertainty in Structural Dynamics, USD 2018 Leuven* (Belgium, 2018), pp. 3875–3886

5. N. Roveri, A. Carcaterra, A. Sestieri, Real-time monitoring of railway infrastructures using fibre Bragg grating sensors. Mech. Syst. Signal Process. **60-61**, 14–28 (2015)
6. S. Villalba, J.R. Casas, Application of optical fiber distributed sensing to health monitoring of concrete structures. Mech. Syst. Signal Process. **39**, 441–451 (2013)
7. C.S. Kubrously, H. Malebranche, Sensors and controllers location in distributed systems – A survey. Automatica **21**(2), 117 (1985)
8. L. Carotenuto, G. Raiconi, Identifiability and identification of a Galerkin approximation for a class of distributed parameter systems. Int. Journal Syst. Sci. **11**, 1035 (1980)
9. T.K. Yu, J.H. Seinfeld, Observability and optimal measurement location in linear distributed parameter systems. Int. J. Control., 785–799 (1973).
10. N. Roveri, A. Carcaterra, Damage detection in structures under traveling loads by Hilbert–Huang transform. Mech. Syst. Signal Process. **28**, 128–144 (2012)
11. N. Roveri, A. Carcaterra, Unsupervised identification of damage and load characteristics in time-varying systems. Contin. Mech. Thermodyn. **27**, 531–550 (2015)
12. N. An, H. Xia, J. Zhan, Identification of beam crack using the dynamic response of a moving spring-mass unit. Interaction and Multiscale Mechanics **3**(4), 321–331 (2010)
13. G. Kerschen, A.F. Vakakis, Y.S. Lee, D.M. McFarland, L.A. Bergman, Toward a fundamental understanding of the Hilbert–Huang transform in nonlinear structural dynamics. J. Vib. Control. **14**(1–2), 77–105 (2008)
14. G. Rilling, P. Flandrin, P. Goncalves, On empirical mode decompositions and its algorithms, in *Proceedings of IEEE-EURASIP Workshop on Nonlinear Signal and Image Processing NSIP-03*, (Grado, Italy, 2003)
15. J. N. Yang; Y. Lei; S. Lin, N. Huang. Hilbert-Huang based approach for structural damage detection. J. Eng. Mech. **130**(1), 85–95 (2004).
16. S. Lin, J.N. Yang, L. Zhou. Smart materials and structures damage identification of a benchmark building for structural health monitoring. Smart Mater. Struct. **14**(3), S162 (2005).
17. T.B. Roy, S. Banerji, S.K. Panigrahi, A. Chourasia, L. Tirca, A. Bagchi, *A Novel Method for Vibration-Based Damage Detection in Structures Using Marginal Hilbert Spectrum. Recent Advances in Structural Engineering, Volume 1. Lecture Notes in Civil Engineering, Vol 11* (Springer, 2019)

Gait Optimization Method for Quadruped Locomotion

Maicol Laurenza, Gianluca Pepe (iD), and Antonio Carcaterra

1 Introduction

Nature has always been a source of inspiration for engineers and scientists who have always tried to replicate or at least develop systems that resemble it. This is because nature, in its many forms, is a system that in millions of years of evolution has selected and perfected beings that excel in specific tasks. However, often nature operates a selection characterized by constraints that modern technology can partially overcome, and possible innovative solutions emerge even looking in the groove of nature bioinspired mechanisms.

In this context, the present paper follows a twofold inspiration in the investigation of quadrupedal robots. On one hand, it is scientifically interesting to explore how quadrupedal locomotion, suitably modelled, can produce gaits that resemble results to which nature arrived over a long evolution. On the other hand, the investigation tries to go beyond the solutions proposed by nature: is it possible to disclose different kind of gaits for a quadrupedal mechanism as the product of a strict optimization process, making these gaits solutions for the best desirable performances?

To obtain a natural and efficient gait for legged robots, two kinds of strategies for sequencing or coordination of the leg movements can be followed. The first strategy assumes that the gaits of animals are optimal, as otherwise they would not have been able to survive the competition and natural selection proposed by Darwin's Theory of Evolution [1]. However, biological locomotion data cannot be used directly for a legged robot due to kinematic and dynamic inconsistencies between animals and legged robots. Today's mechanisms are heavy and have large energy consumption, since they need large number of actuators to move multiple degree-of-freedom legs [2]. The second strategy formulates the gait generation problem of the legged robot

M. Laurenza (✉) · G. Pepe · A. Carcaterra
Sapienza University of Rome, Rome, Italy
e-mail: maicol.laurenza@uniroma1.it

as an optimal optimization problem with multiples constraints [3–7]. It generates the optimal gait cycle by minimizing some performance indexes, like motion speed, stability criteria, actuating forces, energy consumption, etc. Evolutionary computation, including the Genetic Algorithm (GA), is a natural choice for the gait optimization of legged robots, since it uses optimization methods based on Darwin's Theory of Evolution [8–10]. The result of the optimal trajectories is then tracked through feedback controllers. Typical controls are Hybrid Zero Dynamics or the simplest PD [11–13]. Nonlinear variational optimal controls have been analyzed and studied to include nonquadratic penalty function and nonlinear affine systems [14–19] to better chase the trajectories.

The main idea of this paper is based on an optimal optimization process where only the forces transmitted to the ground are considered, without imposing no leg elements or kinematic constraints. The force profiles are morphologically modified through a parametric optimization to guarantee the body attitude, moving at a certain speed. The optimization is performed by GA. The optimum is determined, over a time period, to minimize the Cost of Transport (COT), i.e., the amount of energy used over time.

The paper is organized as follows: Section 2 describes the dynamic model and definition of the ground reaction forces. Section 3 defines the optimization variables and discusses the objective functions and stability constraints of the optimization. Section 4 provides the optimization results and a comparison between different natural gaits.

2   Mathematical Model for the Gait Optimization

The optimization model, proposed in this paper, consists of identifying an optimal gait capable of moving a suspended body through the succession of four alternating thrusts generated by legs. The innovation of this approach lies in the absence of a specific kinematic configuration of the legs, thus leaving room for possible free solutions that maybe nature hasn't found. It will then be a later problem identifying the best kinematic configurations that best approximate the optimal solution found. The quadrupedal model is illustrated in Fig. 1, where the body is suspended on four legs, transmitting forces and moments, thanks to the interaction with the ground.

The legs are labelled as *FL* (front left), *FR* (front right), *HL* (hind left), *HR* (hind right) and the period in which the legs are in contact with the ground is called *conctact phase* (*CP*), while the one in which the legs are in the air is called *swing phase* (*SP*).

Newton-Euler equations that govern the rigid body dynamics can be expressed in the fixed reference frame for the translational components and in the body reference frame for the rotational components:
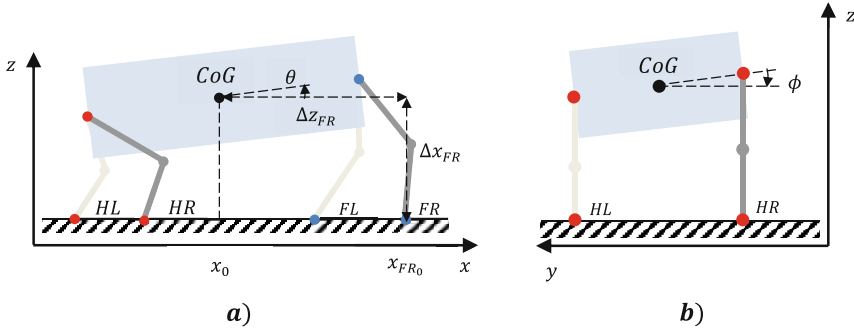
Fig. 1 Lateral (**a**) and rear (**b**) view of the model

$$m\,\ddot{\boldsymbol{r}} = \boldsymbol{f}_e,$$

$$\boldsymbol{I}\dot{\boldsymbol{\omega}} = \boldsymbol{m}_e - \boldsymbol{\omega} \times (\boldsymbol{I}\boldsymbol{\omega})\,, \tag{1}$$

where $\boldsymbol{r}$ identify the centre of gravity (CoG) of mass m, $\boldsymbol{f}_e$ the external forces, with respect to the fixed reference frame, while inertia matrix $\boldsymbol{I}$, angular velocity $\boldsymbol{\omega}$, and external moments $\boldsymbol{m}_e$ are computed in the body reference frame. Assuming $\boldsymbol{I}$ as principal inertia matrix and small pitch and roll angles, we can approximate the equations of motion in the fixed reference frame for a 4 dof rigid body in longitudinal motion x, vertical motion z, roll ϕ, and pitch θ (Fig. 1):

$$\begin{array}{ll} m\ddot{x} = F_x & I_x\ddot{\phi} = M_x \\ m\ddot{z} = F_z & I_y\ddot{\theta} = M_y \end{array}, \tag{2}$$

where I_x, I_y are the inertias along the two axes; F_x, F_z, M_x, M_y are the total forces and moments in the fixed frame coming from the four legs FR, FL, HR and HL.

From Fig. 2, the duration of the entire locomotion cycle, in which the four legs follow one another, is defined by T and leg contact duration by T_i. The time at which each leg touches the ground is $t_i \in [0, T]$, where $i = FR, FL, HR, HL$.

When an animal moves on the ground, its limb contacts and pushes against the ground, so expressing a ground reaction force. The vertical component F_z of the ground reaction force serves to support the animal's weight, while the horizontal component F_y allows the animal to accelerate and decelerate. Even when an animal moves at a steady speed, its limbs exert decelerating and accelerating horizontal forces to control the balance. In this paper, the focus of the work is to find compatible contact forces for each leg that allows the body to move at a certain speed and keep a stable attitude. Considering a single leg, the vertical force F_{zi} is bound to act only during the CP and it must start and end with zero value to represent the arriving and leaving phases [20]. The shape is defined through a spline function passing
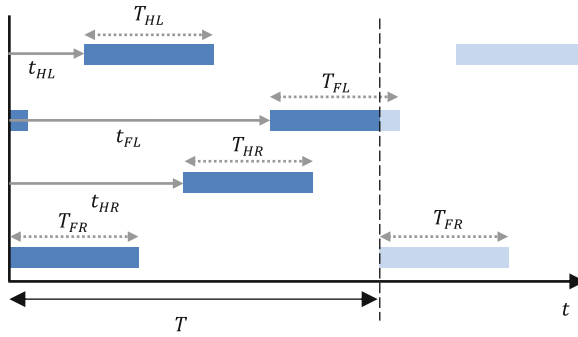
Fig. 2 Temporal diagram of the entire period of locomotion of the quadruped
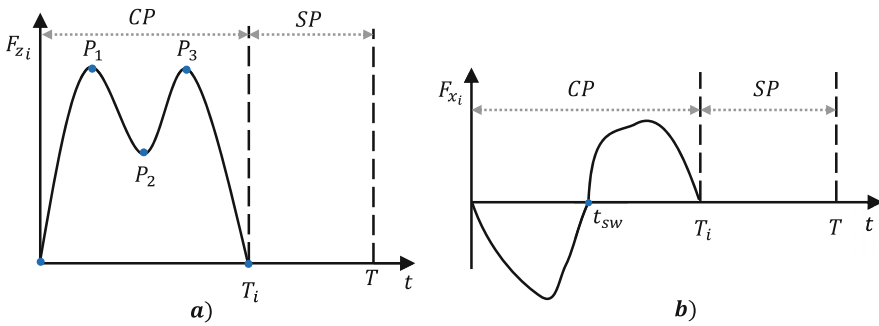
Fig. 3 Vertical (**a**) and longitudinal (**b**) ground force for one leg during the gait period

across three unknown points $[P_1, P_2, P_3]$ which have to be optimized (Fig. 3a). The longitudinal ground reaction for each leg F_{x_i} is instead identified by the Coulomb expression (Fig. 3b). The force is defined as the product of the grip coefficient μ and the vertical force F_{z_i} with the hyperbolic tangent that allows to consider the acceleration and deceleration grip phase of the foot.

$$F_{x_i} = -\mu F_{z_i} \tanh \left(\gamma \left(t_i - t_{sw} \right) \right). \tag{3}$$

The *tanh* function is translated with a parameter $t_{sw} \in [t_i, t_i + T_i]$ that identifies the time at which the foot switch from decelerating to accelerating grip. This model excludes the possibility of foot slipping, as it is a dissipative action that lowers the efficiency of the motion.

Moreover, the transition phase is governed by the parameter γ that considers the characteristics of the actuators. Eventually, moments M_x and M_y on CoG can be computed by identifying the foot force arm. From Fig. 1a, let's consider the *FR* foot at the beginning of the contact phase $t_{FR} = 0$ with a position x_{FR0}. Given the lack of slipping, the horizontal arm between CoG and the foot contact point is

$\Delta x_{FR}(t) = x_{FR_0} - x$. In the same way, the vertical arm component can be evaluated as $\Delta z_{FR}(t) = z_{FR_0} - z$, giving the opportunity to express the two moments like:

$$\begin{aligned} M_{y_i} &= F_{x_i} \Delta z_i - F_{z_i} \Delta x_i \\ M_{x_i} &= F_{z_i} \Delta y_i \end{aligned}, \tag{4}$$

where Δy_i, in our case, is a constant parameter stating the mounting spacing of the legs along the y axis. Clearly, the two moments $M_{x_i}(t)$ and $M_{y_i}(t)$ are nonnull only during the contact phase where $t \in [t_i, t_i + T_i]$.

3 Optimization Model

Usually, in the quadruped legged locomotion, the stability of a gait is guaranteed using criteria such as Zero-Moment Point [21, 22]. Other studies face the stability problem with Poincare map [23, 24] or ground reference points [25]. In this paper, unlike the classical approaches, the gait stability is guaranteed by satisfying periodic limit cycle conditions.

The optimization is performed over a single period which begins and ends when the *FR* leg meets the ground. The algorithm selected is the well-known genetic algorithm (GA) which has been used to find not only the stride length, frequencies, and velocities but also the quantity and form of the forces exchanged on the ground compatibly with the constraints. The parameters p_{GA} serve as inputs for the optimization algorithm to minimize a specific objective function. The optimization is designed to find the optimal gait to maintain constant the initial speed and height, selecting the relative phases of each legs t_i, the time duration of the contact phase, which is here imposed the same for all the legs $T_i = T_{CP}$, and the shape of the normal force through P_j points (see Fig. 3).

$$p_{GA} = \left[t_i, T_{CP}, P_j\right] \tag{5}$$

The entire cycle duration T is an imposed parameter as it depends directly on the actuator's technology and hardware available. Sure enough, reducing the time T will raise the cost of technology to be used. Higher computational costs and power density of the actuators are required, along with high accuracy and sensitivity of sensors.

Once the p_{GA} parameters have been assigned, the solution provides an iterative resolution scheme that resolves independently first the vertical dynamics, then the horizontal dynamics, and then ends with the rotational dynamics.

Over the single stride, the average vertical force exerted on the ground by all the limbs must equal the body weight m multiplying the gravity force g:

$$\frac{1}{T}\int_0^T \sum_i F_{z_i}\left(P_j\right)\alpha\, dt = mg \tag{6}$$

The force shape is randomly defined by the GA with a spline interpolation through P_j points. The parameter α rescales the normal force to satisfy the constraint eq. (6) for the entire cycle. The condition (6) involves that the initial velocity along the z axis will be the same at the time T.

$$\dot{z}(0) = \dot{z}(T) \tag{7}$$

However, another condition is needed to assure that the cyclic motion along z axis doesn't diverge. At the end of the cycle, the body needs to return to the initial height:

$$z(0) = z(T). \tag{8}$$

Identifying the initial vertical speed as the double integral of the vertical acceleration allows to satisfy the requirement (8):

$$\dot{z}(0) = -\frac{1}{mT}\int_0^T \int_0^\tau \left(\sum_i F_{z_i}\left(P_j\right)\alpha - mg\right) dt d\tau. \tag{9}$$

The same strategy can be used to maintain a periodic longitudinal speed, as long as the following integral is satisfied:

$$\int_0^T \sum_i F_{x_i}\left(t_{sw}\right) dt = 0, \tag{10}$$

which depends on the parameter t_{sw}, the time at which the transition between acceleration and deceleration grip phase is realized. The eq. (10) is solved by a nonlinear numerical solver to guarantee the periodicity of the speed:

$$\dot{x}(0) = \dot{x}(T). \tag{11}$$

This doesn't assure that the average speed is the desired one, but at least we guarantee a certain stability of the velocity.

On the other hand, also the resulting moments must assure a stable attitude during the stride cycle, similarly to what has been stated for vertical and longitudinal motion. The following constraints are consequently required:

$$\int_0^T M_y\left(x_{FR_0}\right) dt = 0,$$

$$\int_0^T M_x\left(\Delta_y\right) dt = 0\, dt = 0. \tag{12}$$

Solving the eq. (12), through the identification of the maximum stride span x_{FR_0} and the mounting spacing Δ_y, allows to find the initial and final velocity of roll and pitch that guarantees a periodic motion:

$$\dot{\theta}(0) = \dot{\theta}(T) = -\frac{1}{I_y T} \int_0^T \int_0^\tau M_y \left(x_{FR_0} \right) \, dt d\tau,$$

$$\dot{\phi}(0) = \dot{\phi}(T) = -\frac{1}{I_x \left(\Delta_y \right) T} \int_0^T \int_0^\tau M_x \left(\Delta_y \right) \, dt d\tau. \tag{13}$$

Eventually, the objective function, that has to be minimized for identifying the most efficient gait, can be expressed. The energy cost E should be defined as the integral of the absolute value of the power, given the periodicity of the motion and the absence of non-conservative forces:

$$E = \frac{1}{T} \int_0^T |P_{ower}| \, dt. \tag{14}$$

Equation (14) must consider kinetic and potential power of the CoG during the entire cycle. Computing the integral of the power absolute value allows a correlation with possible dissipative forces of real applications. In fact, it is reasonable considering dissipative power dependent from quadratic speed and so proportional to $|P_{ower}|$.

4 Results

The mass properties of the body are selected considering the characteristic parameters of quadrupeds in nature, in particular horses. Consequently, the optimization is performed with the purpose of finding the energy-efficient gait that moves the body at an average speed of 1.35 m/s, with a gait period T of 1s, which are common parameters of horses walking gait. In nature, walking gaits involve overlapping contact phase such that $\frac{T_{CP}}{T} > 0.5$, i.e., each leg remains in contact more time than in the air, providing a stable base of support. The results show that the optimal gait found by GA follows the characteristics of a classical walking gait for a quadruped animal. In fact, the sequence of the legs is shown to be $FR - HL - FL - HR$, with a $t_i = [0.25; 0.5; 0.75; 1]$ multiples of ¼ and the time of contact phase of $\frac{T_{CP}}{T} = 0.58$. In Fig. 4, the numerical results of the optimization problem are presented. It can be seen how the body keeps a steady longitudinal speed $\dot{x}$, around the target speed of 1.35 m/s, maintaining a stable and restrained attitude and assuring the periodical constraints. What we are showing is one of the possible solutions, as the genetic algorithm can also find points of local optimum, depending on the weights of the objective function.
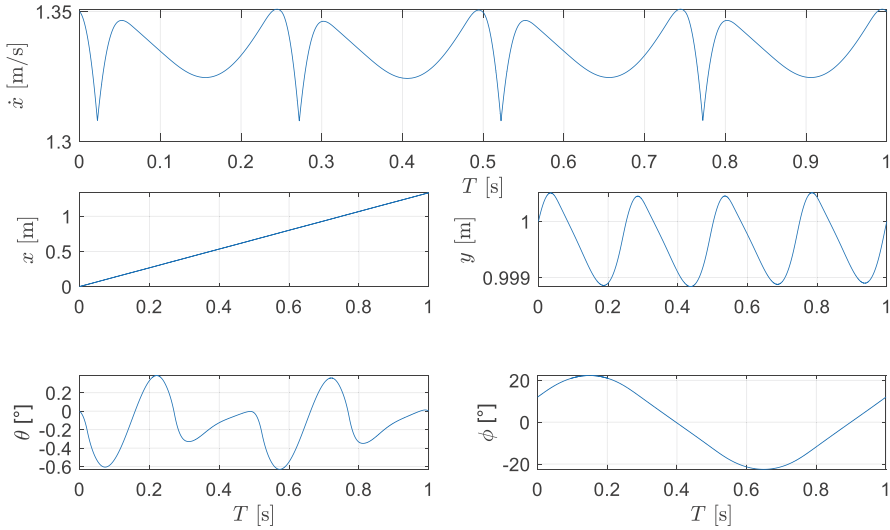
Fig. 4 Motion and attitude of the body during the single stride

Consequently, we decided to investigate other gaits, existing in nature, and find out how much energy they consume to make the body move at the same target speed. In a quadrupedal trot, for example, the diagonal forelimb and hindlimb move in phase, while, in pacing, the forelimb and hindlimb on the same side of the body are in phase. Instead, when the forelimbs and hindlimbs each move together in phase, the gait is considered a "full-bound." To assure the selection of these gaits, we imposed only the time t_i between the legs as constraints:

$$Trot : \begin{matrix} t_{FR} = t_{HL} \\ t_{FL} = t_{HR} \end{matrix} \quad Pace : \begin{matrix} t_{FR} = t_{HR} \\ t_{FL} = t_{HL} \end{matrix}$$

$$Full - bound : \begin{matrix} t_{FR} = t_{FL} \\ t_{HL} = t_{HR} \end{matrix} \tag{15}$$

In Fig. 5a are shown the resulting ratios $\frac{T_{CP}}{T}$ for each of the analyzed gaits. Trotting and running gaits are typically characterized by $\frac{T_{CP}}{T} \leq 0.5$; however, we can see that the optimization isn't consistent to what happens in nature. That's because animals change gait from a walk to a trot or a run only to move at increasing speed, instead we imposed the same target velocity to the body.

Eventually, comparing the energy consumption of these analyzed gaits with the optimal one, we can confirm how the walking gait is the most efficient one for a quadruped at the target speed of 1.35 *m/s* and a gait period of 1 *s* (Fig. 5b).
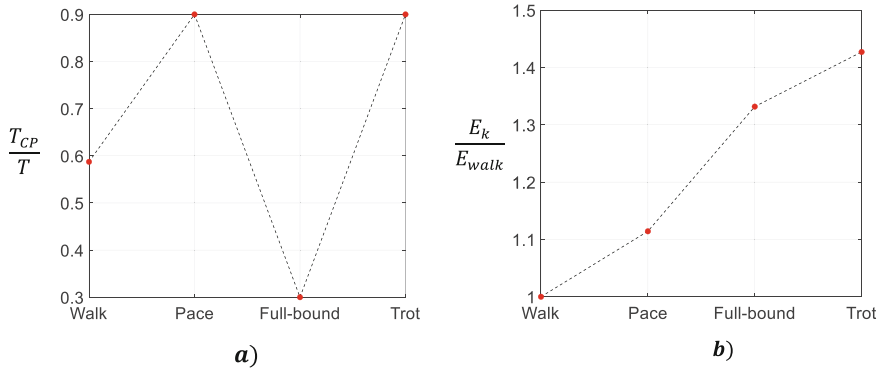
Fig. 5 Ratios of the contact time (**a**) and energy consumption (**b**) over cycle time for imposed gaits

5 Conclusions

In this work, a legged optimization model is proposed to identify different gaits of a quadruped system regardless of the physical characteristics of the system itself. The advantage is to be able to find optimal features of the gait without the constraint of any kinematic mechanism for the legs, body, etc., allowing a free search of the optimum. Preimposed forces profiles are shaped to guarantee stability of the motion, at a constant speed. The scope is to find optimal gaits that move a body in the most efficient way, and then compare them to the ones resulting from natural evolution to see if there exist more efficient ones.

The optimal gait was found to be consistent to that found in nature, suggesting that energy consumption is one of the factors contributing to the evolution of gaiting patterns in quadrupeds. Future works will consist in finding a kinematic mechanism compatible with the optimal gait and using nonlinear feedback controls to control the quadruped robot.

References

1. M. Srinivasan, A. Ruina, Computer optimization of a minimal biped model discovers walking and running. *Nature* **439**, 72–75 (2006). https://doi.org/10.1038/nature04113
2. X. Meng, S. Wang, Z. Cao, L. Zhang, A review of quadruped robots and environment perception, in *2016 35th Chinese Control Conference (CCC), 27–29 July 2016*, (2016), pp. 6350–6356. https://doi.org/10.1109/ChiCC.2016.7554355
3. L. Hu, C. Zhou, EDA-based optimization and learning methods for biped gait generation. Lect. Notes Control Informat. Sci. **362**, 541–549 (2007)
4. A. Masuri, O. Medina, S. Hacohen, N. Shvalb, Gait and trajectory optimization by self-learning for quadrupedal robots with an active back joint. J. Robot. **2020**, 8051510 (2020). https://doi.org/10.1155/2020/8051510

5. T. Kato, K. Shiromi, M. Nagata, H. Nakashima, K. Matsuo, Gait pattern acquisition for four-legged mobile robot by genetic algorithm, in *IECON 2015 - 41st Annual Conference of the IEEE Industrial Electronics Society, 9–12 Nov. 2015*, (2015), pp. 004854–004857. https://doi.org/10.1109/IECON.2015.7392860

6. E. Koco, S. Glumac, Z. Kovacic, Multiobjective optimization of a quadruped robot gait, in *22nd Mediterranean Conference on Control and Automation, 16–19 June 2014*, (2014), pp. 1520–1526. https://doi.org/10.1109/MED.2014.6961591

7. M. Focchi, A. Del Prete, I. Havoutis, R. Featherstone, D. Caldwell, C. Semini, High-slope terrain locomotion for torque-controlled quadruped robots. Autonomous Robots **41**, 259–272 (2016)

8. S.N. Miandoab, F. Kiani, E. Uslu, Generation of automatic six-legged walking behavior using genetic algorithms, in *2020 International Conference on INnovations in Intelligent SysTems and Applications (INISTA), 24–26 Aug. 2020*, (2020), pp. 1–5. https://doi.org/10.1109/INISTA49547.2020.9194620

9. S. Zhai, B. Jin, Y. Cheng, Mechanical design and gait optimization of hydraulic hexapod robot based on energy conservation. Appl. Sci. **10**(11), 3884 (2020). https://doi.org/10.3390/app10113884

10. C. Cai, H. Jiang, Performance comparisons of evolutionary algorithms for walking gait optimization, in *2013 International Conference on Information Science and Cloud Computing Companion, 7–8 Dec. 2013*, (2013), pp. 129–134. https://doi.org/10.1109/ISCC-C.2013.100

11. M. Neunert, F. Farshidian, A. W. Winkler, and J. Buchli, Trajectory Optimization through Contacts and Automatic Gait Discovery for Quadrupeds, 2016

12. W.-L. Ma, K.A. Hamed, A.D. Ames, *First Steps Towards Full Model Based Motion Planning and Control of Quadrupeds: A Hybrid Zero Dynamics Approach* (IEEE, 2019), pp. 5498–5503

13. A. Srisuchinnawong et al., *Neural Control for Gait Generation and Adaptation of a Gecko Robot* (IEEE, 2019), pp. 468–473

14. D. Antonelli, L. Nesi, G. Pepe, A. Carcaterra, Mechatronic control of the car response based on VFC, in *Proceedings of the ISMA2018, Leuven, Belgium*, (2018), pp. 17–19

15. G. Pepe, D. Antonelli, L. Nesi, A. Carcaterra, *Flop: Feedback Local Optimality Control of the Inverse Pendulum Oscillations* (Presented at the ISMA, Leuven, 2018)

16. D. Antonelli, L. Nesi, G. Pepe, A. Carcaterra, A novel approach in Optimal trajectory identification for Autonomous driving in racetrack, in *2019 18th European Control Conference (ECC), 25–28 June 2019*, (2019), pp. 3267–3272. https://doi.org/10.23919/ECC.2019.8795637

17. D. Antonelli, L. Nesi, G. Pepe, A. Carcaterra, A novel control strategy for autonomous cars, in *2019 American Control Conference (ACC), , 10–-12 July 2019*, (2019), pp. 711–716. https://doi.org/10.23919/ACC.2019.8814944

18. G. Pepe, M. Laurenza, D. Antonelli, A. Carcaterra, A new optimal control of obstacle avoidance for safer autonomous driving, in *2019 AEIT International Conference of Electrical and Electronic Technologies for Automotive (AEIT AUTOMOTIVE), 2–4 July 2019*, (2019), pp. 1–6. https://doi.org/10.23919/EETA.2019.8804549

19. M. Laurenza, G. Pepe, D. Antonelli, A. Carcaterra, Car collision avoidance with velocity obstacle approach: Evaluation of the reliability and performace of the collision avoidance maneuver, in *5th International Forum on Research and Technologies for Society and Industry: Innovation to Shape the Future, RTSI 2019 - Proceedings*, (2019), pp. 465–470. https://doi.org/10.1109/RTSI.2019.8895525.

20. J. Dentinger, G. Street, Animal locomotion (second edition). Andrew a. Biewener and Sheila N. Patek. 2018. Oxford university press, Oxford, U.K. 240 pp. $95.00 hardcover. ISBN: 978-019874316. J. Wildl. Manag. **83**, 07/01 (2019). https://doi.org/10.1002/jwmg.21713

21. Z. Yu et al., Disturbance rejection for biped walking using zero-moment point variation based on body acceleration. IEEE Transactions on Industrial Informatics, Industrial Informatics, IEEE Transactions on, IEEE Trans. Ind. Inf., Periodical **15**(4), 2265–2276 (2019). https://doi.org/10.1109/TII.2018.2890195

22. A.S. Baskoro, M.G. Priyono, *Design of humanoid robot stable walking using inverse kinematics and zero moment point* (IEEE, 2016), pp. 335–339

23. H. Gritli, S. Belghith, Walking dynamics of the passive compass-gait model under OGY-based state-feedback control: Analysis of local bifurcations via the hybrid Poincaré map, in *Chaos, Solitons and Fractals: the interdisciplinary journal of Nonlinear Science, and Nonequilibrium and Complex Phenomena*, vol. 98, (2017), pp. 72–87. https://doi.org/10.1016/j.chaos.2017.03.004
24. W. Znegui, H. Gritli, and S. Belghith, Stabilization of the Passive Walking Dynamics of the Compass-Gait Biped Robot by Developing the Analytical Expression of the Controlled Poincare Map, 2020
25. P.R. Roan, A. Burmeister, A. Rahimi, K. Holz, D. Hooper, *Real-world validation of three tipover algorithms for mobile robots* (2010), pp. 4431–4436

Early Detection of Cracks in a Gear-Train System Using Proper and Smooth Orthogonal Decompositions

Zihan Liu, T. Haj Mohamad, Shahab Ilbeigi, and C. Nataraj

1   Introduction

In rotating machinery, gears are common components, which interconnect mechanical parts and allow them to be engaged in a mechanical system. They play the role of transmitting kinetic energy and transforming rotation. Due to the importance of gears, any degradation of its performance affects the function of the whole system and leads to machine breakdown. In general, gear faults are the most prevailing causes of transmission system failure, which makes the diagnostic technology of gear faults significant in improving safety, reducing breakdown and economic losses.

In modern industry, there are three main maintenance strategies including Breakdown Maintenance, Time-Based Maintenance, and Condition-Based Maintenance (CBM). Breakdown Maintenance is performed on a machine that has broken down and cannot operate. Time-Based Maintenance is routine maintenance performed on a machine at fixed time intervals regardless of its condition. On the other hand, CBM relies on implementing online assessments of the current machine condition without interrupting normal machine operation. This chapter focuses on developing a CBM algorithm for early detection of gear cracks.

A successful fault detection at an early stage is of paramount importance as most of the catastrophic machinery failures are caused by undetected minute faults that are aggravated over time. Furthermore, early detection can also help in avoiding expensive repair costs. The difficulty in detecting cracks at early stages is due to the fact that minute faults cause changes in the vibration signal at a very low energy that are barely detectable [1] and obscured by more prominent frequency components.

Z. Liu · T. H. Mohamad · S. Ilbeigi · C. Nataraj (✉)
Villanova Center for Analytics of Dynamic Systems, Villanova University, Villanova, PA, USA
e-mail: zliu5@villanova.edu; thajmoha@villanova.edu; ilbeigi@uri.edu; c.nataraj@villanova.edu
http://vcads.org

In gear trains, cracks occurring on the gear tooth surface during gear meshing are prevalent damage in early stages.

In the field of vibration monitoring of rotating machinery, more and more techniques based on extracting features of vibrational signals are developed [2, 3]. In earlier work, we introduced the Phase Space Topology (PST) family of methods to diagnose nonlinear systems by describing the topology of the phase space trajectory quantitatively [4–8]. In this chapter, we extract features by using Proper Orthogonal Decomposition (POD) and a newly developed method called Smooth Orthogonal Decomposition (SOD) [9]. POD and SOD are techniques used to map multi-dimensional data into basis vectors. POD, also known as principal component analysis (PCA), finds orthogonal basis vectors such that the projection of the data onto these basis vectors has maximum variance. SOD can be viewed as an extension to POD, which alters these basis vectors in a way that the evolution of data, or in other words the dominant flow, has the maximum smoothness, which releases the condition of basis orthogonality.

The rest of this chapter is organized as follows: Sect. 2 introduces the experimental setup and gear tooth cracks. Section 3 presents the diagnostic method and the proposed feature extraction techniques. In Sect. 4, extracted features are plotted and fault detection results are presented. Finally, Sect. 5 summarizes and concludes this chapter.

2   Experimental Setup

In this research, the proposed method is applied to a mock-up of a helicopter gearbox system, which is a 5 m large-scale machine shown in Fig. 1. As is shown in the figure, its main structure consists of a motor, a dynamometer, and four gearboxes. The system schematic diagram is illustrated in Fig. 2. For this study, gear defects are introduced by replacing the gear located in gearbox number 3 and shown in green color in Fig. 2, while the remaining gears are kept unchanged. The defective gear with a root crack of 2 mm size located on one tooth is shown in Fig. 3.

The triaxial accelerometer is equipped on the gearbox number 3 to record the vibrational signal of the gearbox at a sampling frequency of 102,400 Hz. Two encoders are mounted on shafts A and C to measure rotational speeds of shafts A and C with a resolution of 360 pulse /rev. A tachometer is installed on shaft B to measure the shaft rotational speed at a rate of 1 pulse/rev. The recording of the vibrational signal lasts 64 s for both healthy, and the cracked tooth conditions, which can ensure the same data capacity of two conditions.

Fig. 1 Gear-train experimental setup, four gray metal boxes denote 4 gearboxes
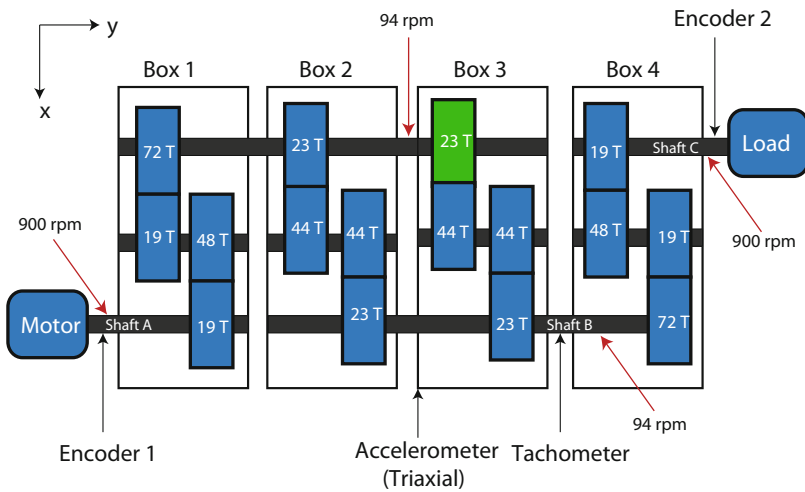
Fig. 2 Gear-train schematic. The number in every gear represents the number of teeth for each gear. Shafts *A* and *C* are connected to the motor and load, respectively

3 Diagnostic Method

Figure 4 demonstrates the overall flow of the proposed diagnostic strategy. First, the vibrational signal of the shaft is collected by the accelerometer for two gear

Fig. 3 Gear defects: crack on
one tooth with 2 mm depth
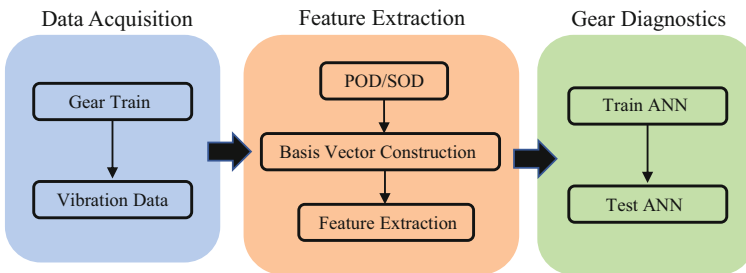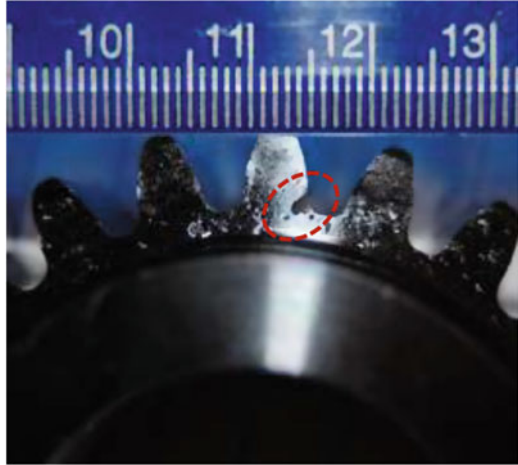
Fig. 4 Diagnostic approach

conditions such as healthy and cracked tooth. Then POD and SOD methods are
implemented to establish the construction of basis vectors. Second, the projection
of data on these basis vectors can be obtained as features of each data set, and more
details on this step will follow. Finally, extracted features are employed as an input
to develop a classification model using ANN. This section will proceed to provide a
brief theory and mathematics of POD and SOD methods.

3.1 Proper Orthogonal Decomposition

Proper Orthogonal Decomposition (POD) [10, 11], also referred to as principal
component analysis (PCA), is a statistical approach that can be used to represent
multi-dimensional data as orthogonal base vectors while retaining the dominant

components of the original data set. Suppose we have a sampled scalar filed in the form of a matrix $X \in \mathbb{R}^{r \times n}$, which contains r snapshots of n scalar time series. The linear projection of X can be obtained using $Q = X\Phi$, where $\Phi = [\phi_1, \phi_2, \ldots, \phi_n] \in \mathbb{R}^{n \times n}$ are the orthogonal basis vectors. We are looking for a basis vector $\phi_k \in \mathbb{R}^n$ such that there is maximum variance in a projection of the data matrix on this vector. The problem of finding such a basis vector ϕ_k can be translated into the following restricted problem of maximization:

$$\max_{\phi_k} \|X\phi_k\|^2 \quad \text{while} \quad \|\phi_k\| = 1 . \tag{1}$$

The solution to the POD problem is obtained by solving the eigenvalue problem of the auto-covariance matrix Σ_{xx}.

$$\Sigma_{xx}\phi_k = \lambda_k\phi_k . \tag{2}$$

The corresponding auto-covariance matrices Σ_{xx} can be obtained by

$$\Sigma_{xx} = \frac{1}{r-1}X^\mathrm{T}X \quad . \tag{3}$$

In this form, λ_k are proper orthogonal values (POVs), $\phi_k \in \mathbb{R}^n$ are proper orthogonal modes (POMs), and columns of Q are proper orthogonal coordinates (POCs). POVs are ordered such that $\lambda_1 \geq \lambda_2 \geq \ldots \geq \lambda_n$ and reflect the variances in X data along the corresponding POMs.

3.2 Smooth Orthogonal Decomposition

Smooth Orthogonal Decomposition (SOD) [10, 11] can be seen as an extension to POD. Assume we have a projection of the data matrix $P = X\Psi$, where $\Psi = [\psi_1, \psi_2, \ldots, \psi_n] \in \mathbb{R}^{n \times n}$. We are looking for a basis vector $\psi_k \in \mathbb{R}^n$, such that a projection of the data onto this vector has both maximal variance and minimal roughness (i.e., maximal smoothness). Roughness can be defined as the squared L_2 norm of the data change rate. Thus, the roughness of a scalar field X is equal to $\|\dot{X}\psi_k\|$, where $\dot{X} \in \mathbb{R}^{r \times n}$ is the derivative of X, which corresponds to the rate of changes in data or information.

Therefore, the description of SOD can be translated into maximizing the following function:

$$\max_{\psi_k} \|X\psi_k\|^2 \quad \text{while} \quad \min_{\psi_k} \|\dot{X}\psi_k\|^2 . \tag{4}$$

By defining $\lambda(\psi_k)$ as the ration of $\|X\psi_k\|$ and $\|\dot{X}\psi_K\|$, Eq. (4) can be translated into

$$\max_{\psi_K} \lambda(\psi_k) = \frac{\|X\psi_k\|^2}{\|\dot{X}\psi_k\|^2}. \tag{5}$$

We can rewrite the above equation in the following form:

$$\max_{\psi_k} \lambda(\psi_k) = \frac{\psi_k^T \Sigma_{xx} \psi_k}{\psi_k^T \Sigma_{\dot{x}\dot{x}} \psi_k}, \tag{6}$$

where the auto-covariance matrix Σ_{xx} is from Eq. (3), and the auto-covariance matrix of $\dot{X}$ can be obtained by

$$\Sigma_{\dot{x}\dot{x}} = \frac{1}{r-1}\dot{X}^T\dot{X}. \tag{7}$$

In order to maximize $\lambda(\psi_k)$, we make the first derivative equal to zero:

$$\frac{\partial \lambda(\psi_k)}{\partial \psi_k} = \frac{2(\psi_k^T \Sigma_{\dot{x}\dot{x}} \psi_k)\Sigma_{xx}\psi_k - 2(\psi_k^T \Sigma_{xx}\psi_k)\Sigma_{\dot{x}\dot{x}}\psi_k}{(\psi_k^T \Sigma_{\dot{x}\dot{x}}\psi_k)^2} = 0. \tag{8}$$

After simplification by using Eq. (6), we can obtain

$$\Sigma_{xx}\psi_k = \lambda_k \Sigma_{\dot{x}\dot{x}}\psi_k. \tag{9}$$

Equation (9) is a generalized eigenvalue problem of the matrix pairs Σ_{xx} and $\Sigma_{\dot{x}\dot{x}}$. The solution to the SOD problem can be obtained by solving the above eigenvalue problem. In this equation, λ_k are smooth orthogonal values (SOVs), and $\psi_k \in \mathbb{R}^n$ are *smooth projection modes* (SPMs). Simplifying Eq. (9) further, the equation can be summarized into the following matrix form:

$$\Sigma_{xx}\Psi = \Sigma_{\dot{x}\dot{x}}\Psi\Lambda. \tag{10}$$

In the above equation, each column of Ψ denotes an SPM. Λ is a matrix in the form of $\Lambda = \mathrm{diag}([\lambda_1, \lambda_2, \ldots, \lambda_{2n}]) \in \mathbb{R}^{n \times n}$, which contains all the SOVs. To define the degree of smoothness of the coordinates, the magnitude of the corresponding SOV can be used. This implies that the larger the SOV in magnitude, the smoother the related coordination is in time. A matrix of *smooth orthogonal modes* (SOMs) Φ can be defined to satisfy orthogonality as follows:

$$\Phi^T\Psi = I \quad \text{and} \quad \Phi = \Psi^{-T}. \tag{11}$$

To sum up, POD and SOD are techniques used to map multi-dimensional data into basis vectors. POD takes the spatial or geometric consequences of this mapping into account, while the temporal structure of state evolution is ignored. In contrast, in terms of total spatial variation and temporal smoothness of the related
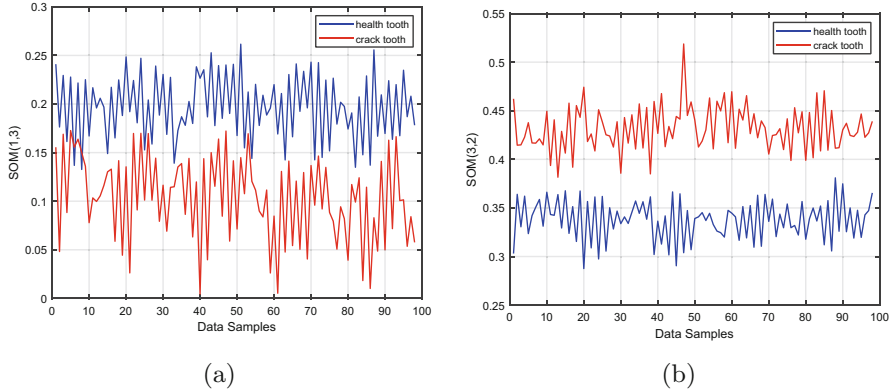
Fig. 5 Smooth orthogonal mode features for healthy gear condition (blue) and cracked tooth condition (red). (**a**) The third coordinate of the first smooth orthogonal mode. (**b**) The second coordinate of the third smooth orthogonal mode

coordinates, SOD considers both the geometrical characteristics of states and their time evolution.

3.3 Feature Extraction and Supervised Learning

The most striking advantage of both POD and SOD techniques is their optimality: they offer efficient way to capture the dominant components of an high-dimensional process by projecting the original data flow onto only a few numbers of "modes." This projection *preserves the nonlinearity* of the original data flow in the form of basis vectors; therefore, POD and SOD techniques are able to characterize nonlinear dynamical systems and identify trends in the data.

In this chapter, POD and SOD methods are used as feature extraction techniques for detection of gear system defects. For the POD technique, a feature set is extracted from each data sample including: (1) the proper orthogonal modes, (2) proper orthogonal values, and (3) the angle lying between each proper orthogonal mode and the positive x-axis. For the SOD technique, the feature set from each data set consists of: (1) the smooth orthogonal modes, (2) smooth orthogonal values, and (3) the angle lying between each smooth orthogonal mode and the positive x-axis.

In Fig. 5, two mode features obtained by the SOD technique are demonstrated. Y-axis denotes the smooth orthogonal mode, and the x-axis is the number of samples. In Fig. 5a, the average values of healthy tooth and cracked tooth are about 0.2 and 0.1, while in Fig. 5b, the mean values for healthy and cracked gear are 0.35 and 0.45, respectively. The significant difference of average values ensures that the two states are separable. Two mode features obtained by the POD technique are exhibited in Fig. 6. As seen in Fig. 6a, the values of the proper orthogonal modes are overlapping,
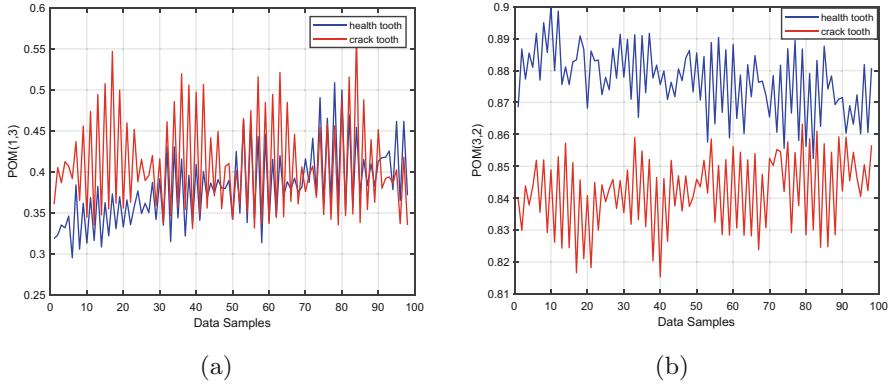
Fig. 6 Proper orthogonal mode features for healthy gear condition (blue) and cracked tooth condition (red). (**a**) The third coordinate of the first proper orthogonal mode. (**b**) The second coordinate of the third proper orthogonal mode
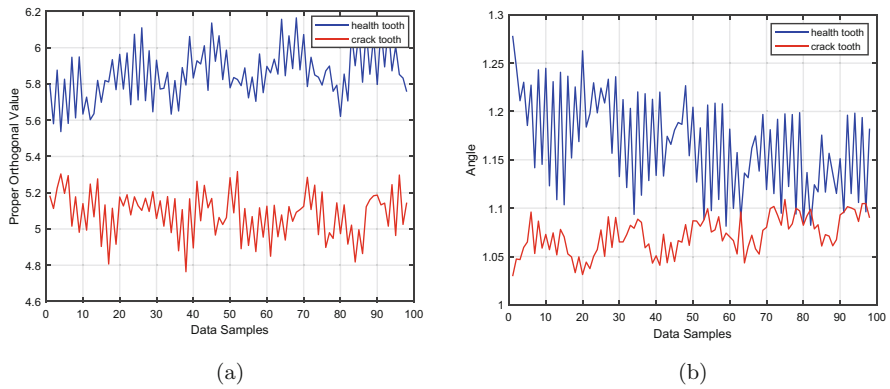
Fig. 7 Features extracted by POD technique. Blue plot is for the healthy tooth, and red plot is for the cracked tooth. (**a**) Proper orthogonal value. (**b**) Angle between proper orthogonal mode and the positive x-axis

which makes it difficult to distinguish different gear conditions. In Fig. 6b, although the two plots only overlap in a few sample points, the mean values of healthy tooth and cracked tooth are 0.88 and 0.84, which are too close to separate two different conditions. In Fig. 7, two different features obtained by the POD technique are exhibited. Figure 7a demonstrates proper orthogonal values, and the two different states are perfectly separated. Figure 7b shows the angle lying between the proper orthogonal mode and the positive x-axis. In spite of the angle fluctuation for the healthy tooth condition, a large mean difference still ensures that the two conditions can be separated, which is proved by subsequent experiment results.

In the last step, an Artificial Neural Network (ANN) is developed in order to find the relationship between the extracted features (input) and the gear conditions

(output). A two-layer neural network with a single hidden layer is chosen to map those features in order to predict gear health conditions. The total number of selected neurons is twenty, and the back-propagation algorithm is used to train the ANN. In the trained ANNs, the activation functions for the neurons of hidden and output layers are Tansig (a hyperbolic tangent sigmoid transfer function) and Softmax (a smooth approximation to the arguments of the maxima function), respectively.

4 Fault Detection Results

The effectiveness of the classification model is demonstrated by a confusion matrix. A confusion matrix can compare the predicted classes with the actual classes and help in analyzing the performance of the classification model by certain evaluation matrices such as accuracy, sensitivity, and precision [12]. In both Tables 1 and 2, each column of the confusion matrix corresponds to the result of the prediction of a certain class, while each row represents the actual class. The elements placed in the main diagonal exhibit the correct classified prediction for each corresponding class. In each element of the confusion matrix, the upper number represents the number of cases and the lower number represents the absolute percentage of these cases with respect to the total number of cases.

Table 1 indicates the test performance of the classification model trained by the SOD-based features. A total of 196 data points are collected, 50% of the total data are set as training set, 20% are validation set, and 30% are testing set. As can be seen, the SOD-based classifier is capable of predicting all the health conditions with 100% accuracy, 100% precision, and 100% sensitivity with no misclassification.

Table 2 shows the testing performance of the POD-based classifier, the same total data capacity and the same training and testing ratio are implied to this classifier, and 100% accuracy, 100% precision, and 100% sensitivity are also observed. All of these indicate the validity of the SOD and POD techniques in diagnostics.

Table 1 ANN testing results and confusion matrices of SOD (**H**: healthy tooth **C**: cracked tooth)

Output	Target		Recall	Precision
	H	C		
H	25	0	100.0%	100.0%
	42.4%	0.0%		
C	0	34	100.0%	100.0%
	0.0%	57.6%		
			Overall accuracy 100.0%	

Table 2 ANN testing results and confusion matrices of POD (**H**: healthy tooth **C**: cracked tooth)

Output	Target		Recall	Precision
	H	C		
H	30	0	100.0%	100.0%
	50.8%	0.0%		
C	0	29	100.0%	100.0%
	0.0%	49.2%		
			Overall accuracy 100.0%	

5   Conclusions

In this chapter, a mock-up of a helicopter gearbox system with two conditions is studied in order to detect and identify a gear with a cracked tooth in the early stage. The POD and SOD methods are introduced as feature extraction techniques in the study. The diagnostic result validates that the POD- and SOD-based features adequately portray the nonlinear behavior of the helicopter gearbox system by preserving the nonlinearity of the original data flow. By extracting only 15 features from the gearbox vibration data, we are able to achieve 100% accuracy. This high detection accuracy ensures the timely and effective detection of gear cracks at the early stage of mechanical operation. It is known that the shaft rotational speed can have a big effect on the behavior of dynamics systems. Thus, these experiments can be extended to consider various known and unknown operating speeds in future studies.

References

1. J. Mączak, M. Jasiński, Model-based detection of local defects in gears. Arch. Appl. Mech. **88**(1–2), 215–231 (2018)
2. M.S. Safizadeh, S.K. Latifi, Using multi-sensor data fusion for vibration fault diagnosis of rolling element bearings by accelerometer and load cell. Inf. Fusion **18**, 1–8 (2014)
3. R. Yuan, Y. Lv, G. Song, Fault diagnosis of rolling bearing based on a novel adaptive high-order local projection denoising method. Complexity **2018** (2018)
4. T.H. Mohamad, F. Nazari, C. Nataraj, A review of phase space topology methods for vibration-based fault diagnostics in nonlinear systems. J. Vib. Eng. Tech. **8**(3), 393–401 (2020).
5. M. Samadani, T.H. Mohamad, C. Nataraj, Feature extraction for bearing diagnostics based on the characterization of orbit plots with orthogonal functions, in *International Design Engineering Technical Conferences and Computers and Information in Engineering Conference*, vol. 50206 (American Society of Mechanical Engineers, New York, 2016), p. V008T10A026

6. T.H. Mohamad, C. Nataraj, An overview of PST for vibration based fault diagnostics in rotating machinery, in *MATEC Web of Conferences*, vol. 211 (EDP Sciences, Les Ulis, 2018), p. 01004

7. T.H. Mohamad, C. Nataraj, Gear fault diagnostics using extended phase space topology, in *Annual Conference of the Prognostics and Health Management Society* (2017)

8. T.H. Mohamad, C. Nataraj. Fault identification and severity analysis of rolling element bearings using phase space topology. J. Vib. Control **27**(3–4), 295–310 (2021)

9. T.H. Mohamad, S. Ilbeigi, C. Nataraj, Proper and smooth orthogonal decompositions for detection of inner race defects in rolling element bearings with variable rotational speeds, in *Nonlinear Dynamics of Structures, Systems and Devices* (Springer, Berlin, 2020), pp. 493–501

10. D. Chelidze, W. Zhou, Smooth orthogonal decomposition-based vibration mode identification. J. Sound Vib. **292**(3-5),461–473 (2006)

11. K. Lu, Y. Jin, Y. Chen, Y. Yang, L. Hou, Z. Zhang, Z. Li, C. Fu, Review for order reduction based on proper orthogonal decomposition and outlooks of applications in mechanical systems. Mech. Syst. Signal Process. **123**, 264–297 (2019)

12. T.H. Mohamad, Y. Chen, Z. Chaudhry, C. Nataraj, Gear fault detection using recurrence quantification analysis and support vector machine. J. Softw. Eng. Appl. **11**(5), 181–203 (2018)

On the Physical Consistency of Evolution Laws Obtained with Sparse Regression

Diego Matos Silva Lopes and Americo Cunha Jr

1 Introduction

Most classical dynamic systems, such as a harmonic oscillator and a simple pendulum, have their evolution law inferred through the first principles [1, 2]. However, some modern dynamical systems, such as those that appear in areas like epidemiological modeling [3, 4] and neuroscience [5–7], have the basic evolution laws not well understood or even unknown so that the use of first principles to obtain the governing equations is unfeasible. In other applications, structural health monitoring [8, 9], for instance, it may be possible that the basic principles of dynamics are well understood, but some peculiarities not, which make it difficult to construct high-fidelity predictive models.

In this context, discovering the evolution law for this kind of dynamical system in an analytical way becomes an almost impossible task. However, with the emergence of the information age, where data are exponentially generated and stored, it is natural to try to use information embedded in datasets associated with the dynamical system of interest to infer its underlying evolution law.

Neural networks (NNs) [10–12] have a high capacity to learn complex patterns, which makes them at first glance natural candidates to be used in the search for mathematical expressions that represent the desired evolution law. However, despite having incredible power of prediction (interpolation) in the domain spanned by the training data, several NN architectures lack in providing interpretable expressions for the identified dynamic model, which makes it difficult to generalize (extrapolate) system behavior for unknown conditions.

D. M. S. Lopes (✉) · A. Cunha Jr
Rio de Janeiro State University – UERJ, Rio de Janeiro, Brazil
e-mail: diego.matos@uerj.br; americo.cunha@uerj.br

Alternatively, regression techniques are more proper for providing the interpretability that NN does not have, which makes them an attractive tool to extract dynamic evolution laws from datasets [13]. Considering that, the technique known as sparse identification of nonlinear dynamics (SINDy) [13–16], a sparse regression method to identify evolution equations from data that proven to be efficient in different areas and problems, and stands out for three aspects: (1) interpretability of the obtained equation, (2) excellent generalization (extrapolation) capability, and (3) computational efficiency. As several dynamic systems have evolution laws with only a few terms, SINDy looks for a sparse and parsimonious differential equation that best fits the known data.

If the method is applied in a system where the first principles are unknown, it is interesting to have some guarantee that the identified evolution law respects fundamental physical laws since their violation can translate into a dynamic behavior that is divergent from the original one. For instance, if the balance of momentum is not respected, mass or velocity is affected, potentially changing the inertial effects. When the energy balance is violated, the contribution from kinetic/potential energy to the mechanical energy can be in a proportion far from the original system, which can imply changes in the displacement/velocity. Even when a qualitatively good result is observed, small differences in the system parameters can significantly change quantitatively the long-term behavior.

This work aims to verify the physical consistency of the evolution law obtained by SINDy, checking if the identified dynamical system respects physical principles such as the balance of momentum and energy and if the underlying balance of these quantities is an accurate approximation for those associated with the original system. For this purpose, the Duffing oscillator is used as a benchmark, where the underlying evolution equation is obtained from synthetic data that emulate experimental measurements for the displacement time series of this dynamical system.

The rest of this manuscript is organized as follows. In Sect. 2, it is presented a brief explanation of the Duffing oscillator and the methodology used to identify the dynamic evolution laws. Some examples and test results are presented in Sect. 3. Finally, in Sect. 4, the final remarks are highlighted.

2 Methodology

The dynamical system chosen to test the physical consistency of the identified dynamic laws obtained with SINDy is the Duffing oscillator, once this kind of oscillator has many possible applications, such as structural dynamics and energy harvesting [17–22], and a very rich and well-known dynamic behavior. Figure 1 shows a schematic of a vibratory system that behaves like a Duffing oscillator, in which the dynamic behavior evolves according to

$$\ddot{x} + \delta\,\dot{x} + \alpha\,x + \beta\,x^3 = \gamma\,\cos(\omega t)\,, \tag{1}$$

Fig. 1 Schematic of a Duffing oscillator driven by a sinusoidal external excitation
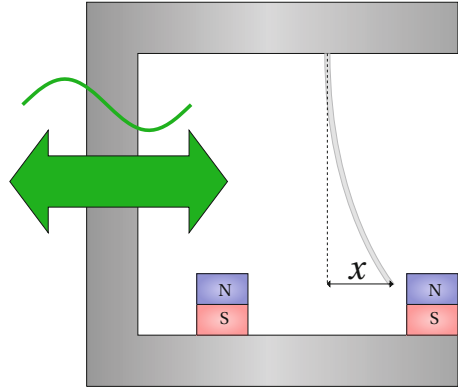
where the function $x = x(t)$ is the displacement of the beam tip, and the $\dot{x}$ and $\ddot{x}$ are, respectively, the first and second derivatives of x, i.e., the velocity and acceleration [23]. The parameters in the equation of motion are the damping coefficient δ, the linear stiffness α, the nonlinear stiffness β, the external excitation amplitude γ, and the external excitation frequency ω.

2.1 Sparse Identification of Nonlinear Dynamics

The SINDy method can handle first-order dynamical systems of form

$$\dot{\mathbf{x}} = \mathbf{f}(\mathbf{x}) \,, \tag{2}$$

where $\mathbf{x}$ is the state vector, $\dot{\mathbf{x}}$ is the time derivative of the state vector, and $\mathbf{f}(\mathbf{x})$ is the unknown evolution law. Higher order systems may be written as a first-order system by increasing the state dimension. For instance, the Duffing oscillator in Eq. (1) can be rewritten as

$$
\begin{aligned}
\dot{x}_1 &= \phi \, x_2, \\
\dot{x}_2 &= -\delta \, x_2 - \alpha \, x_1 - \beta \, x_1{}^3 + \gamma \, \cos x_3, \\
\dot{x}_3 &= \omega.
\end{aligned}
\tag{3}
$$

To determine the dynamic evolution law $\mathbf{f}$, it is necessary to have observations (time series) of the system state $\mathbf{x}$ and velocity $\dot{\mathbf{x}}$, which are organized as follows:

$$
\mathbf{X} \;=\; \begin{bmatrix} \mathbf{x}^T(t_1) \\ \mathbf{x}^T(t_2) \\ \vdots \\ \mathbf{x}^T(t_m) \end{bmatrix} = \begin{bmatrix} x_1(t_1) & x_2(t_1) & \dots & x_n(t_1) \\ x_1(t_2) & x_2(t_2) & \dots & x_n(t_2) \\ \vdots & \vdots & \ddots & \vdots \\ x_1(t_m) & x_2(t_m) & \dots & x_n(t_m) \end{bmatrix}, \tag{4}
$$

$$
\dot{\mathbf{X}} \;=\; \begin{bmatrix} \dot{\mathbf{x}}^T(t_1) \\ \dot{\mathbf{x}}^T(t_2) \\ \vdots \\ \dot{\mathbf{x}}^T(t_m) \end{bmatrix} = \begin{bmatrix} \dot{x}_1(t_1) & \dot{x}_2(t_1) & \dots & \dot{x}_n(t_1) \\ \dot{x}_1(t_2) & \dot{x}_2(t_2) & \dots & \dot{x}_n(t_2) \\ \vdots & \vdots & \ddots & \vdots \\ \dot{x}_1(t_m) & \dot{x}_2(t_m) & \dots & \dot{x}_n(t_m) \end{bmatrix}. \tag{5}
$$

After having the data arranged in a matrix form, it is possible to build a library (dictionary) of candidate functions $\Theta(\mathbf{X})$ to construct the evolution law terms. In general, this library includes polynomials, trigonometric, exponential, and logarithmic functions (among other possibilities), i.e.,

$$
\Theta(\mathbf{X}) = \begin{bmatrix} \vert & \vert & \vert & \vert & \vert & & \vert & \vert & \vert & \vert \\ 1 & \mathbf{X} & \mathbf{X^{P_2}} & \mathbf{X^{P_3}} & \mathbf{X^{P_4}} & \dots & \mathbf{X^{P_k}} & \sin(\mathbf{X}) & \cos(\mathbf{X}) & e^{\mathbf{X}} \\ \vert & \vert & \vert & \vert & \vert & & \vert & \vert & \vert & \vert \end{bmatrix}, \tag{6}
$$

where each column in this matrix represents a candidate function, the $\mathbf{X^{P_n}}$ notation indicates all possible n-order polynomials formed by combining the state variables.

What SINDy does is to solve the following regression problem:

$$
\dot{\mathbf{X}} \approx \Theta(\mathbf{X})\varXi, \tag{7}
$$

where the coefficient matrix $\varXi$ is determined by minimizing a misfit function that measures the discrepancy between $\Theta(\mathbf{X})\varXi$ and $\dot{\mathbf{X}}$, i.e.,

$$
\varXi^* = \arg \min_{\varXi} ||\dot{\mathbf{X}} - \Theta(\mathbf{X})\,\varXi||_2 + \lambda\,||\varXi||_1\,, \tag{8}
$$

where $||\cdot||_2$ and $||\cdot||_1$ denote the norm-2 and norm-1, respectively.

Note that, to produce a sparse solution, a user-controlled λ parameter is introduced, which acts as a threshold. A first least squares regression results in a vector with estimated values for $\varXi$. Coefficients that represent the exact evolution law have more meaningful value than those that are not. After that, the absolute values of the coefficient vectors $\varXi$, which is smaller than a λ, have their values changed to zero. This process, known as sequential thresholded least squares, is repeated until a parsimonious evolution law is discovered [13]. For systems where the best parameter λ is unknown, machine learning techniques for model validation are necessary to ensure a good result, e.g., cross-validation, among others [24].

2.2 Training Dataset

In a typical scenario, the dataset used to infer the evolution law of the dynamic system is observations obtained with some type of sensor, in the field or in the laboratory. To emulate a set of displacement and velocity measurements for the Duffing oscillator, synthetic data are considered in this work. The corresponding time series are generated with the aid of the numerical integrator ODE45 from MATLAB, fixing the time step as $\Delta t = 0.01$. Concretely, a dataset with 151 equally spaced samples between 0 and 15 s is obtained with the numerical integrator and polluted with a zero-mean Gaussian white noise (with variance η^2) to emulate the fluctuations in experimental measurements.

2.3 Balance of Energy and Momentum

The total energy, for both the original and the identified system, is the sum of the kinetic and potential energy

$$E = \frac{1}{2} x_2^2 + \frac{1}{2} \alpha\, x_1^2 + \frac{1}{4} \beta\, x_1^4. \tag{9}$$

Although this scalar quantity is not conserved, as the considered dynamics is dissipative, the balance between the mechanical energy of the system and the work done by external and dissipation forces must be respected, i.e.,

$$\left[\frac{1}{2} x_2^2 + \frac{1}{2} \alpha\, x_1^2 + \frac{1}{4} \beta\, x_1^4 \right]_0^t = \int_0^t \left[-\delta\, x_2^2(\tau) + \gamma\, \cos(\omega\tau)\, x_2(\tau) \right] d\tau. \tag{10}$$

Similarly, the linear momentum variation has to balance the impulse of the forces acting on the system

$$x_2(t) - x_2(0) = \int_0^t \left[-\delta\, x_2(\tau) - \alpha\, x_1(\tau) - \beta\, x_1^3(\tau) + \gamma\, \cos(\omega\tau) \right] d\tau. \tag{11}$$

Therefore, if SINDy identifies the correct candidate functions, the balance of energy and momentum is respected by construction. However, even in this case, a question persists: compared to the original dynamics, how representative (in quantitative terms) are these balance principles?

3 Results and Discussion

Two parameter settings are used to evaluate the balance of energy and momentum in the SINDy method, nominally, the unforced conservative case, and the forced dissipative dynamics. For all the numerical experiments done and the database used, SINDy obtained enough parsimonious results to activate just the right candidate functions.

In the first case, the unforced conservative dynamics, 151 equally spaced time samples are used in the training step, with a library of polynomial functions up to third order without trigonometrical terms, with $\lambda = 0.2$, and initial conditions $x_0 = 2$ and $v_0 = -2$. Table 1 shows the values that SINDy inferred for two different noise intensities. The more the noise, the less similar is the identified dynamics to their original counterpart.

In Fig. 2, the reader can see a verification test that estimates if the identified dynamics present an energy/momentum balance that is compatible with the invariances intrinsic to the original dynamics. The right side of Eqs. (10) and (11) is computed for both the identified dynamics and the original dynamics, and the differences between the respective quantities are computed, to estimate the balance error due to deviations in the identified coefficients. It is possible to notice that the error in the momentum balance is directly proportional to the noise intensity, emphasizing the importance of obtaining good quality data.

Therefore, despite identifying candidate functions correctly and with coefficients close to the original, the difference in both balances is a sinusoidal growing function over time. For the two noise intensities, the coefficients identified for the linear stiffness are lower than the original, while the nonlinear stiffness is slightly higher. Both systems after a long time become out of phase with the original one. For the systems with $\eta = 0.010$, this is achieved early than the case where $\eta = 0.001$, with time for that bigger than 300.

In Fig. 3, a case without noise is considered, to assess the fundamental limit of noiseless measures. Note that, for different initial conditions, the error in the momentum balance is comparable to floating point noise, so that for any practical effect, SINDy can be considered to respect the linear momentum balance.

Now, the dissipative forced Duffing oscillator is considered. Two different noise intensities, $\eta = 0.001$ and $\eta = 0.010$, are employed once again, as well as the library of polynomial functions up to third order with trigonometrical terms, 151 equally spaced time samples, $\lambda = 0.02$, and initial conditions $x_0 = 2$ and $v_0 = -2$.

Table 1 Parameters of the original and identified dynamics in the conservative unforced case, with noise intensities equal to $\eta = 0.001$ and $\eta = 0.010$

	δ	α	β	γ	ω	ϕ
Original value	0.0	1.0	−1.0	0.0	0.0	1.0
Identified value ($\eta = 0.001$)	0.0	0.9998	−0.9999	0.0	0.0	1.0000
Identified value ($\eta = 0.010$)	0.0	0.9976	−0.9993	0.0	0.0	1.0002
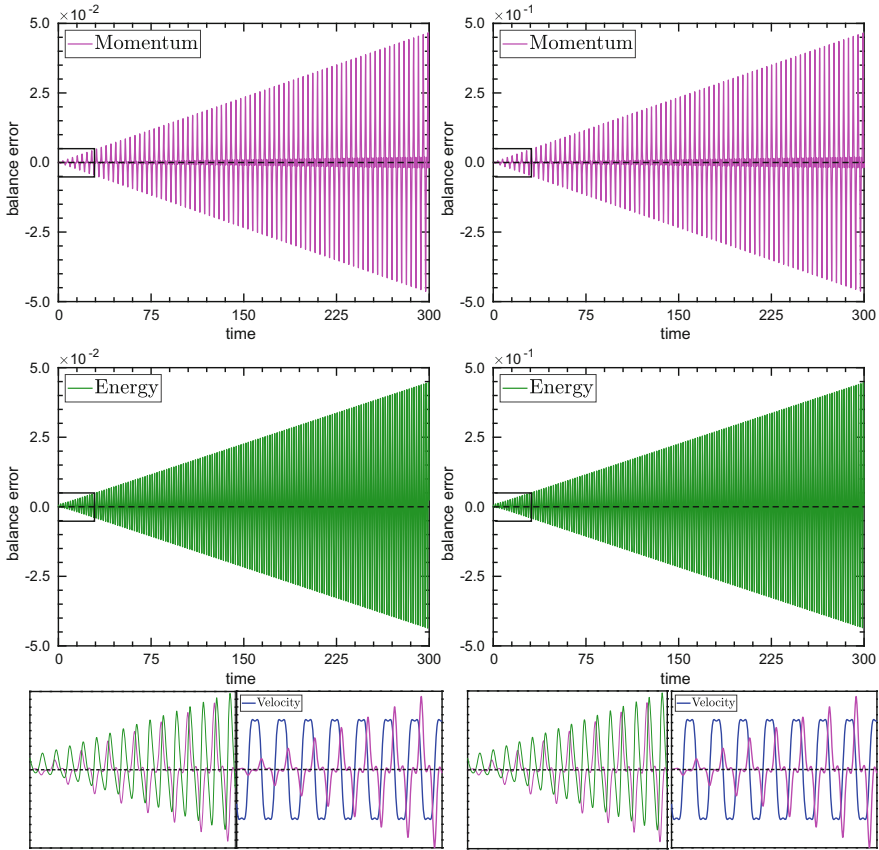
Fig. 2 The difference in the balance of energy and momentum between the original and identified dynamics for the unforced conservative case, with $\eta = 0.001$ (left) and $\eta = 0.010$ (right). The two insets below each graph show a zoom from the upper rectangles, where it is possible to see the symmetrical format of the curve. The velocity is plotted together with the momentum error, to show that the error in the momentum is a local maximum whenever the oscillator velocity is zero

The SINDy is able to identify the correct terms with great accuracy, despite the small amount of data, as can be seen in Table 2, which shows the system parameters for the original and the identified dynamics.

The balance of energy and momentum is plotted for this second case in Fig. 4, where it is possible to notice a richer oscillatory pattern, for both the momentum and energy errors, when compared to the first case. Looking at the energy error, initially, the local pikes and valleys are coinciding with those from the momentum error curve, but after some time, they become out of phase.

The difference in the balance of momentum and energy both has the same asymptotic behavior as in the conservative case, but now it is possible to observe an oscillatory pattern that is completely different from the conservative unforced case.
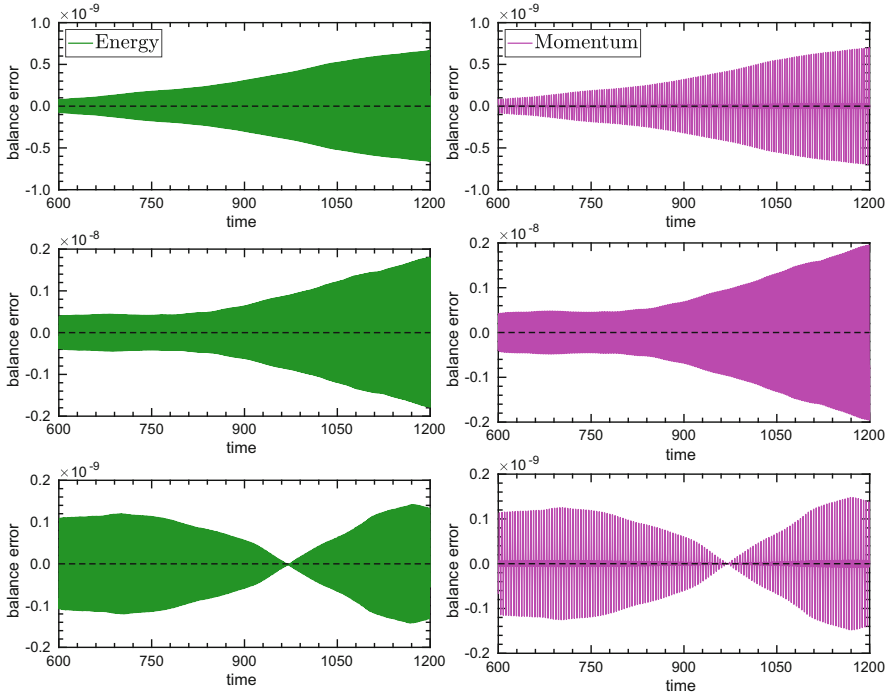
Fig. 3 The difference in the balance of energy and momentum between the original and identified dynamics with noise-free data, for different initial conditions. On the top, the initial conditions are $x_0 = 2$ and $v_0 = -2$, on the middle $x_0 = 3$ and $v_0 = 2$, and for last, on the bottom $x_0 = 1$ and $v_0 = 2.5$

Table 2 Parameters of the original and identified dynamics in the dissipative forced case, with noise intensities equal to $\eta = 0.001$ and $\eta = 0.010$

	δ	α	β	γ	ω	ϕ
Original value	-0.1	1.0	-1.0	1.0	2.0	1.0
Identified value ($\eta = 0.001$)	-0.0999	1.0001	-1.0000	0.9998	2.0000	1.0000
Identified value ($\eta = 0.010$)	-0.0992	1.0006	-1.0001	0.9976	1.9996	1.0003

A transient is noticed that is quickly dampened giving rise to a periodic stationary response, with an amplitude that increases (very slowly) with time.

4   Conclusions

This work presented a study on the physical consistency of the evolution law inferred from a given dataset employing the SINDy method. Two configurations of the Duffing oscillator are used to investigate the difference in energy and momentum
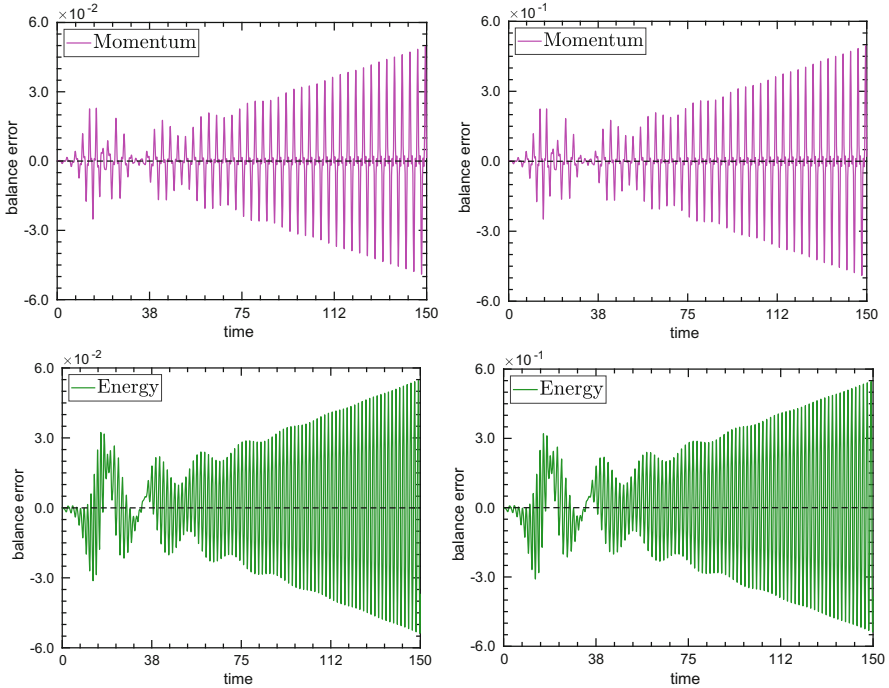
Fig. 4 The difference in the balance of energy and momentum between the original and identified dynamics for the dissipative forced case, with $\eta = 0.001$ (left) and $\eta = 0.010$ (right)

balance with respect to the original dynamics. In all cases, SINDy identified the right candidate functions, and therefore the balance of energy and momentum is respected. However, analyzing the difference in the energy and momentum balance identified, in relation to the original, that function is growing rapidly over time. This implies that for long time periods, the identified dynamic will be out of phase to the original.

References

1. H.C. Corben, M.S. Stehle, *Classical Mechanics*, 2nd ed. (Dover, New York, 1994)
2. L. Meirovitch, *Methods of Analytical Dynamics* (Dover, New York, 2003)

3. E. Dantas, M. Tosin, A. Cunha Jr, Calibration of a SEIR-SEI epidemic model to describe the Zika virus outbreak in Brazil. Appl. Math. Comput. **338**, 249–259 (2018). https://doi.org/10.1016/j.amc.2018.06.024

4. E. Dantas, M. Tosin, A. Cunha Jr, An uncertainty quantification framework for a Zika virus epidemic model. J. Comput. Interdisc. Sci. **10**(2), 91–96 (2019). https://doi.org/10.6062/jcis.2019.10.02.0163

5. A.H. Marblestone, G. Wayne, K.P. Kording, Toward an integration of deep learning and neuroscience. Front. Comput. Neurosci. **10**, 94 (2016). https://doi.org/10.3389/fncom.2016.00094

6. J.I. Glaser, A.S. Benjamin, R. Farhoodi, K.P. Kording, The roles of supervised machine learning in systems neuroscience. Prog. Neurobiol. **175**, 126–137 (2019). https://doi.org/10.1016/j.pneurobio.2019.01.008

7. B.A. Richards, T.P. Lillicrap, P. Beaudoin, A deep learning framework for neuroscience. Nat. Neurosci. **22**, 1761–1770 (2019). https://doi.org/10.1038/s41593-019-0520-2

8. L.G.G. Villani, S. Silva, A. Cunha Jr, Damage detection in uncertain nonlinear systems based on stochastic Volterra series. Mech. Syst. Signal Process. **125**, 288–310 (2019). https://doi.org/10.1016/j.ymssp.2018.07.028

9. L.G.G. Villani, S. Silva, A. Cunha Jr, M.T. Todd, Damage detection in an uncertain nonlinear beam based on stochastic Volterra series: An experimental application. Mech. Syst. Signal Process. **128**, 463–478 (2019). https://doi.org/10.1016/j.ymssp.2019.03.045

10. F. Hasssanibesheli, N. Boers, J. Kurths, Reconstructing complex system dynamics from time series: a method comparison. New J. Phys. **22**, 073053 (2020). https://doi.org/10.1088/1367-2630/ab9ce5

11. Y. LeCun, Y. Bengio, G. Hinton, Deep learning. Nature **521**, 436–444 (2015). https://doi.org/10.1038/nature14539

12. D. Zhang, L. Guo, G.E. Karniadakis, Learning in modal space: solving time-dependent stochastic PDEs using physics-informed neural networks. SIAM J. Sci. Comput. **42**(2), A639–A665 (2020). https://doi.org/10.1137/19M1260141

13. S.L. Brunton, J.L. Proctor, J.N. Kutz, Discovering governing equations from data by sparse identification of nonlinear dynamical systems. PNAS **113**(15), 3932–3937 (2016). https://doi.org/10.1073/pnas.1517384113

14. E. Kaiser, J.N. Kutz, S.L. Brunton, Sparse identification of nonlinear dynamics for model predictive control in the low-data limit. Proc. R. Soc. A **474**, 20180335 (2018). https://doi.org/10.1098/rspa.2018.0335

15. B. Bhadriraju, M.S.F. Bangi, A. Narasingam, J.S.I. Kwon, Operable adaptive sparse identification of systems: Application to chemical processes. AIChE J. **66**, e16980 (2020). https://doi.org/10.1002/aic.16980

16. L. Zhang, H. Schaeffer, On the convergence of the SINDy algorithm. Multiscale Model. Simul. **17**(3), 948–972 (2019). https://doi.org/10.1137/18M1189828

17. F. Cottone, L. Gammaitone, H. Vocca, Nonlinear energy harvesting. Phys. Rev. Lett. **102**(8), 080601 (2009). https://doi.org/10.1103/PhysRevLett.102.080601

18. V.G. Lopes, J.V.L.L. Peterson, A. Cunha Jr, Numerical study of parameters influence over the dynamics of a piezo-magneto-elastic energy harvesting device, in *XXXVII Congresso Nacional de Matemática Aplicada e Computaciona*, Proceeding Series of the Brazilian Society of computational and Applied Mathematics, vol. 6, n. 1, S.J. dos Campos-SP (2017). https://doi.org/10.5540/03.2018.006.01.0407

19. V.G. Lopes, J.V.L.L. Peterson, A. Cunha Jr, Nonlinear characterization of a bistable energy harvester dynamical system, in *Topics in Nonlinear Mechanics and Physics*. Springer Proceedings in Physics, ed. by M. Belhaq, vol. 228 (Springer, Singapore, 2019). https://doi.org/10.1007/978-981-13-9463-8_3

20. J.V.L.L. Peterson, V.G. Lopes, A. Cunha Jr, Maximization of the electrical power generated by a piezo-magneto-elastic energy harvesting device, in *XXXVI Congresso Nacional de Matemtica Aplicada e Computacional*. Proceeding Series of the Brazilian Society of Computational and Applied Mathematics, vol. 5, n. 1, Gramado-RS (2016). https://doi.org/10.5540/03.2017.005.01.0200

21. D. Guyomar, C. Richard, A. Badel, E. Lefeuvre, M. Lallart, Energy harvesting using non-linear techniques, in *Energy Harvesting Technologies*, ed. by S. Priya, D.J. Inman (Springer, Boston, 2009). https://doi.org/10.1007/978-0-387-76464-1_8
22. L. De la Roca, J.V.L.L. Peterson, M. Pereira, A. Cunha Jr, Control of chaos via OGY method on a bistable energy harvester, in *25th ABCM International Congress on Mechanical Engineering, Uberlândia-MG* (2019)
23. M.J. Brennan, I. Kovacic, Examples of physical systems described by the Duffing equation, in *The Duffing Equation: Nonlinear Oscillators and Their Behaviour*, ed. by I. Kovacic, M.J. Brennan (Wiley, Chichester, 2011)
24. C.M. Bishop, *Pattern Recognition and Machine Learning* (Springer, Berlin, 2006)

Part V
Multibody Dynamics

Linear Stability Analysis of a Bicycle Multibody Model with Toroidal Wheels

A. G. Agúndez, D. García-Vallejo, and E. Freire

1 Introduction

From the work of Whipple [1] to the present day, the stability analysis of bicycles has been a subject of great interest. In 2007, a benchmark bicycle model was presented by Meijaard et al. [2], which has been widely used in numerous theoretical [3–5] and experimental works [6]. The discussion of the linear stability of this benchmark along relevant trajectories, such as the straight and circular motions with constant velocity, was thoroughly made by Basu-Mandal et al. [3] and Xiong et al. [5, 7]. Moreover, this bicycle benchmark model recently allowed the validation of novel linearization procedures for constrained multibody systems [8].

Some developments of the bicycle benchmark have been introduced in recent times [9–12], consisting in more advanced models of frames, riders and tires, aimed to further understanding the bicycle dynamics and stability. The multibody model of this work presents toroid-shaped wheels, which are assumed to roll without slipping, and the linearization of the equations of motion is performed resorting to one of the procedures of Ref. [8]. The stability results of the benchmark showed the accuracy and efficiency of this procedure with respect to the conventional symbolic approaches. To perform an eigenvalue sensitivity analysis, the Jacobian matrix is obtained as function of the dynamic and geometric parameters of the multibody system. The influence of the steer axis tilt and the tori aspect ratios on the stability of the bicycle is studied considering different scenarios.

A. G. Agúndez (✉) · D. García-Vallejo
Department of Mechanical Engineering and Manufacturing, Universidad de Sevilla, Seville, Spain
e-mail: agarciaagundez@us.es; dgvallejo@us.es

E. Freire
Department of Applied Mathematics II, Universidad de Sevilla, Seville, Spain
e-mail: efrem@us.es

2 Description of the Model and Equations of Motion

The bicycle multibody model presents five rigid bodies: the inertial frame is designated as body 1; the rear and front wheels, modelled as tori rolling without slipping, are bodies R and F, respectively; the rear body and frame assembly, including the rider, is designated as B and the front handlebar is represented by H. The centres of mass G_j, with $j = \{B, H, R, F\}$, correspond to the origins of the body frames. The $n \times 1$ set of coordinates x, which belongs to a domain of $\mathbb{R}^n$, is given by

$$x = \begin{pmatrix} x_b & y_b & z_b & \psi_b & \theta_b & \phi_b & \delta & \theta_R & \theta_F & \xi_R & \xi_F & \eta_R & \eta_F \end{pmatrix}^{\mathrm{T}}. \tag{1}$$

The coordinates x_b, y_b and z_b locate G_B; the angles $\{\psi_b, \theta_b, \phi_b\}$, which correspond to a yaw–pitch–roll (3–2–1) sequence, orient body B in space; the steering angle δ represents the rotation of the handlebar with respect to body B and θ_R and θ_F correspond to the rotations of the rear and front wheels with respect to bodies B and H, respectively (Fig. 1).

The numbering of the bodies, the coordinates of the system, the body frames and the main geometric parameters of the multibody model are shown in Fig. 2. As in Ref. [13], the toroidal geometry of the wheels is described by means of four non-generalized coordinates: ξ_R, ξ_F, η_R and η_F. The position vector of the contact points P and Q can be expressed in the body frames of the rear and front wheels, respectively, with these non-generalized coordinates. Denoting the minor and major radii of the toroidal wheel by a_i and b_i, with $i = \{R, F\}$, the tori aspect ratios can be defined as follows:

$$\mu_R = \frac{a_R}{b_R}, \ \mu_F = \frac{a_F}{b_F}. \tag{2}$$

The minor and major radii can be related with the radius R_i of the hoop-shaped wheels by means of the following relations:

$$a_R + b_R = R_R, \ a_F + b_F = R_F. \tag{3}$$

The local frames and the non-generalized coordinates of the toroidal wheel are shown in Fig. 2a. The middle plane of the torus, which contains the hoop of equivalent radius R_i, is designated as π_m, and the torus tube centre is C_i. Furthermore, Fig. 2b depicts a front view of the wheel.

The equations of motion of the bicycle, constrained by holonomic and nonholonomic constraints, are given by the following differential-algebraic system:

$$M(x)\ddot{x} + D^{\mathrm{T}}(x)\lambda = Q(x, \dot{x}), \tag{4}$$

$$C(x) = 0, \tag{5}$$

$$C_{nh}(x, \dot{x}) = B(x)\dot{x} = 0. \tag{6}$$
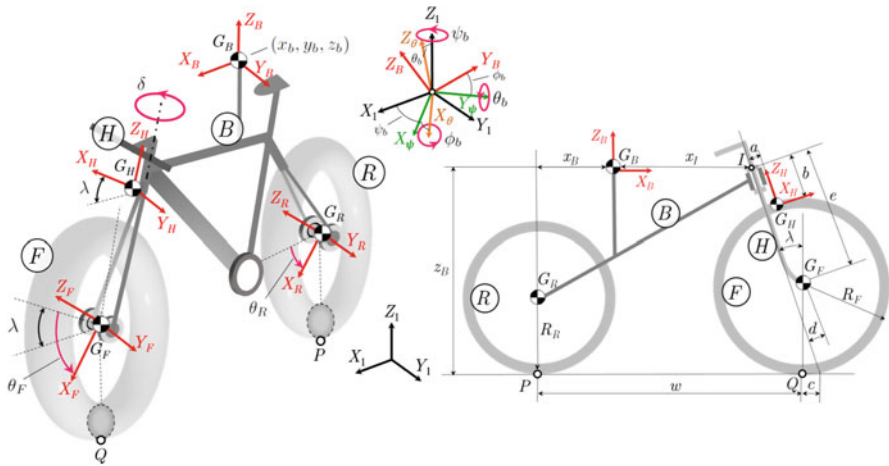
Fig. 1 Bicycle multibody model with toroidal wheels: coordinates of the system, numbering of the bodies, body frames and main geometric parameters
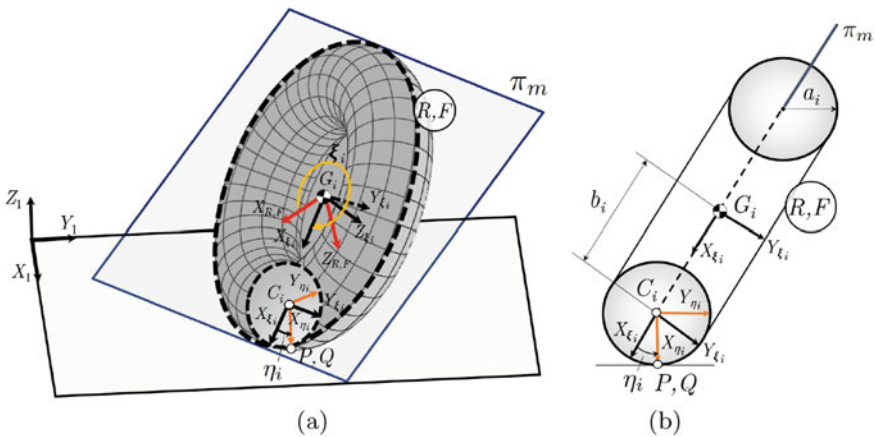
Fig. 2 Model of the toroidal wheels. (**a**) Toroidal wheel: local frames and non-generalized coordinates. (**b**) Toroidal wheel: front view

In Eqs. (4)–(6), $M(x)$ represents the $n \times n$ mass matrix; the $n \times 1$ vector of generalized forces is denoted by $Q(x, \dot{x})$; $C(x)$ corresponds to the $m \times 1$ set of holonomic constraints; $C_{nh}(x, \dot{x})$ is the $l \times 1$ set of nonholonomic constraints, linearly dependent on velocities and the $(m + l) \times 1$ vector of Lagrange multipliers is denoted by λ. The matrices $B(x)$ and $D(x)$, whose dimensions are $l \times n$ and $(m + l) \times n$, respectively, are given by

$$B\left(x\right) = \frac{\partial C_{nh}\left(x, \dot{x}\right)}{\partial \dot{x}}, \quad D\left(x\right) = \begin{pmatrix} C_x\left(x\right) \\ B\left(x\right) \end{pmatrix}, \tag{7}$$

where $C_x = \frac{\partial C}{\partial x}$. All the terms in Eqs. (4)–(6) are smooth functions. The Newton–Euler equilibrium equations (4) can be symbolically derived using Ref. [14]. Due to the wheel–ground contact, the holonomic constraints are

$$C\left(x\right) = \left(r_{P_Z}, r_{Q_Z}, n \cdot t_{L_R}, n \cdot t_{T_R}, n \cdot t_{L_F}, n \cdot t_{T_F}\right)^{\mathrm{T}} = 0, \tag{8}$$

where r_{P_Z} and r_{Q_Z} are the Z-components of the contact points position vectors r_P and r_Q; t_{T_i} and t_{L_i} represent the transversal and longitudinal tangent vectors to P and Q and n is the normal vector to the ground surface. These vectors can be computed as follows:

$$r_P = r_{G_R} + R_R \bar{r}_{G_R P}^{R}, \quad r_Q = r_{G_F} + R_F \bar{r}_{G_F Q}^{F},$$

$$\bar{r}_{G_R P}^{R} = R_{\xi_R}\left(\begin{pmatrix} b_R \\ 0 \\ 0 \end{pmatrix} + R_{\eta_R}\begin{pmatrix} a_R \\ 0 \\ 0 \end{pmatrix}\right), \quad \bar{r}_{G_F Q}^{F} = R_{\xi_F}\left(\begin{pmatrix} b_F \\ 0 \\ 0 \end{pmatrix} + R_{\eta_F}\begin{pmatrix} a_F \\ 0 \\ 0 \end{pmatrix}\right),$$

$$t_{L_R} = R_R \frac{\partial \bar{r}_{G_R P}}{\partial \xi_R}^{R}, \quad t_{T_R} = R_R \frac{\partial \bar{r}_{G_R P}}{\partial \eta_R}^{R}, \quad t_{L_F} = R_F \frac{\partial \bar{r}_{G_F Q}}{\partial \xi_F}^{F}, \quad t_{T_F} = R_F \frac{\partial \bar{r}_{G_F Q}}{\partial \eta_F}^{F},$$
$$\tag{9}$$

where R_R and R_F are the orientation matrices of the body frames $R \langle X_R Y_R Z_R \rangle$ and $F \langle X_F Y_F Z_F \rangle$, respectively; the rotations corresponding to ξ_i and η_i are given by the matrices R_{ξ_i} and R_{η_i} and $\bar{r}_{G_R P}^{R}$ and $\bar{r}_{G_F Q}^{F}$, expressed in the body frames R and F, respectively, are local position vectors.

Moreover, since the wheels are assumed to roll without slipping, one obtains four nonholonomic constraints:

$$C_{nh}\left(x, \dot{x}\right) = \left(v_{P_x}, v_{P_y}, v_{Q_x}, v_{Q_y}\right)^{\mathrm{T}} = 0, \tag{10}$$

where v_P and v_Q are the velocity of the contact points P and Q, respectively.

Therefore, $n = 13$, $m = 6$ and $l = 4$ in the bicycle multibody model. The combination of the time derivative of the holonomic constraints with the nonholonomic constraints leads to the following index-2 DAE system:

$$M\left(x\right)\ddot{x} + D^{\mathrm{T}}\left(x\right)\lambda = Q\left(x, \dot{x}\right), \tag{11}$$

$$D\left(x\right)\dot{x} = 0. \tag{12}$$

3 Linearization of the Equations of Motion

The rectilinear motion with constant velocity of the bicycle can be expressed as

$$\mathbf{x}^0 = \left(x_b^0, \ y_b^0, \ z_b^0, \ \psi_b^0, \ \theta_b^0, \ \phi_b^0, \ \delta^0, \ \theta_R^0, \ \theta_F^0, \ \xi_R^0, \ \xi_F^0, \ \eta_R^0, \ \eta_F^0 \right)^{\mathrm{T}},$$

$$= \left(vt, \ 0, \ z_B, \ 0, \ 0, \ 0, \ 0, \ \frac{v}{R_R}t, \ \frac{v}{R_F}t, \ \frac{5\pi}{2} - \theta_R^0, \ \lambda + \frac{5\pi}{2} - \theta_F^0, \ 0, \ 0 \right)^{\mathrm{T}}.$$

(13)

Particularizing Eq. (11) for the equilibrium solution (13), the Lagrange multipliers associated with this reference motion are given by $\boldsymbol{\lambda}^0 = \left(\lambda_1^0, \ \lambda_2^0, \ \mathbf{0}_{1\times 8} \right)^{\mathrm{T}}$, with

$$\lambda_1^0 = -\frac{g}{w} \left(m_B \left(w - x_B \right) + m_H \left(z_B \tan \left(\lambda \right) - a \cos \left(\lambda \right) - b \sin \left(\lambda \right) - c \right) + m_R w \right),$$

$$\lambda_2^0 = -\frac{g}{w} \left(m_B x_B + m_H \left(w - z_B \tan \left(\lambda \right) + a \cos \left(\lambda \right) + b \sin \left(\lambda \right) + c \right) + m_F w \right).$$

(14)

The linearization approach is based on the implicit differentiation of the constraint equations (12), which avoids the problem of explicit solution of Eq. (12) at the linearization. Defining the variations $\tilde{\mathbf{x}}$, $\dot{\tilde{\mathbf{x}}}$, $\ddot{\tilde{\mathbf{x}}}$ and $\tilde{\boldsymbol{\lambda}}$, the following relations can be introduced:

$$\mathbf{x} = \tilde{\mathbf{x}} + \mathbf{x}^0, \ \dot{\mathbf{x}} = \dot{\tilde{\mathbf{x}}} + \dot{\mathbf{x}}^0, \ \ddot{\mathbf{x}} = \ddot{\tilde{\mathbf{x}}} + \ddot{\mathbf{x}}^0 \text{ and } \boldsymbol{\lambda} = \tilde{\boldsymbol{\lambda}} + \boldsymbol{\lambda}^0.$$

(15)

Computing the Taylor expansion of Eqs. (11)–(12) with respect to the equilibrium (13), and neglecting second-order and higher terms, yields

$$\mathbf{M}\left(\mathbf{x}^0 \right) \ddot{\tilde{\mathbf{x}}} + \left. \frac{\partial \left(\mathbf{M}\left(\mathbf{x} \right) \ddot{\mathbf{x}}^0 \right)}{\partial \mathbf{x}} \right|_0 \tilde{\mathbf{x}} + \mathbf{D}^{\mathrm{T}}\left(\mathbf{x}^0 \right) \tilde{\boldsymbol{\lambda}} + \left. \frac{\partial \left(\mathbf{D}^{\mathrm{T}}\left(\mathbf{x} \right) \boldsymbol{\lambda}^0 \right)}{\partial \mathbf{x}} \right|_0 \tilde{\mathbf{x}}$$

$$= \left. \frac{\partial \mathbf{Q}}{\partial \mathbf{x}} \right|_0 \tilde{\mathbf{x}} + \left. \frac{\partial \mathbf{Q}}{\partial \dot{\mathbf{x}}} \right|_0 \dot{\tilde{\mathbf{x}}},$$

(16)

$$\mathbf{D}\left(\mathbf{x}^0 \right) \dot{\tilde{\mathbf{x}}} + \left. \frac{\partial \left(\mathbf{D}\left(\mathbf{x} \right) \dot{\mathbf{x}}^0 \right)}{\partial \mathbf{x}} \right|_0 \tilde{\mathbf{x}} = \mathbf{0},$$

(17)

where $\left. \dfrac{\partial \left(\cdot \right)}{\partial \mathbf{x}} \right|_0 = \left. \dfrac{\partial \left(\cdot \right)}{\partial \mathbf{x}} \right|_{\mathbf{x}^0, \dot{\mathbf{x}}^0}$ and $\left. \dfrac{\partial \left(\cdot \right)}{\partial \dot{\mathbf{x}}} \right|_0 = \left. \dfrac{\partial \left(\cdot \right)}{\partial \dot{\mathbf{x}}} \right|_{\mathbf{x}^0, \dot{\mathbf{x}}^0}$ are used for simplicity.

A coordinate split, consisting in $m + l$-dependent and $n - m - l$-independent velocities, will be considered to reduce the linearized equations of motion: $\dot{\tilde{\mathbf{x}}} = \left(\dot{\tilde{\mathbf{x}}}_{ai} \ \dot{\tilde{\mathbf{x}}}_{dd} \right)^{\mathrm{T}}$. In the same way, the following partition at position level is used: $\tilde{\mathbf{x}} =$

$\left(\tilde{\boldsymbol{x}}_{ai} \ \tilde{\boldsymbol{x}}_{dd} \right)^{\mathrm{T}}$. Choosing as independent coordinates x_b, ϕ_b and δ, these sets are given by

$$\tilde{\boldsymbol{x}}_{ai} = \left(\tilde{x}_b \ \tilde{\phi}_b \ \tilde{\delta} \right)^{\mathrm{T}}, \ \tilde{\boldsymbol{x}}_{dd} = \left(\tilde{y}_b \ \tilde{z}_b \ \tilde{\psi}_b \ \tilde{\theta}_b \ \tilde{\theta}_R \ \tilde{\theta}_F \ \tilde{\xi}_R \ \tilde{\xi}_F \ \tilde{\eta}_R \ \tilde{\eta}_F \right)^{\mathrm{T}}. \tag{18}$$

The use of the matrix $\boldsymbol{D}\left(\boldsymbol{x}^0 \right)$ allows the elimination of the variation of the Lagrange multipliers in Eq. (16). The following transformation matrix is defined:

$$\boldsymbol{T}_0 = \begin{pmatrix} \boldsymbol{I}_{(n-m-l)} \\ -\left(\boldsymbol{D}_{dd} \left(\boldsymbol{x}^0 \right) \right)^{-1} \boldsymbol{D}_{ai} \left(\boldsymbol{x}^0 \right) \end{pmatrix}, \tag{19}$$

where $\boldsymbol{D}_{dd}\left(\boldsymbol{x}^0 \right)$ is a square matrix of dimension $m + l$. Since the term $\boldsymbol{T}^{\mathrm{T}} \left(\boldsymbol{x}^0 \right) \boldsymbol{D}^{\mathrm{T}} \left(\boldsymbol{x}^0 \right) \tilde{\boldsymbol{\lambda}}$ fades away, Eq. (16) becomes

$$\boldsymbol{T}_0^{\mathrm{T}} \left(\boldsymbol{M} \left(\boldsymbol{x}^0 \right) \ddot{\tilde{\boldsymbol{x}}} + \left. \frac{\partial \left(\boldsymbol{M}\left(\boldsymbol{x}\right) \ddot{\boldsymbol{x}}^0 \right)}{\partial \boldsymbol{x}} \right|_0 \tilde{\boldsymbol{x}} + \left. \frac{\partial \left(\boldsymbol{D}^{\mathrm{T}}\left(\boldsymbol{x}\right) \boldsymbol{\lambda}^0 \right)}{\partial \boldsymbol{x}} \right|_0 \tilde{\boldsymbol{x}} \right)$$
$$= \boldsymbol{T}_0^{\mathrm{T}} \left(\left. \frac{\partial \boldsymbol{Q}}{\partial \boldsymbol{x}} \right|_0 \tilde{\boldsymbol{x}} + \left. \frac{\partial \boldsymbol{Q}}{\partial \dot{\boldsymbol{x}}} \right|_0 \dot{\tilde{\boldsymbol{x}}} \right). \tag{20}$$

Equation (20) can be written in terms of $\tilde{\boldsymbol{x}}_{ai}$ and $\tilde{\boldsymbol{x}}_{dd}$ and their time derivatives. To that end, the time derivative of Eq. (12) is used:

$$\boldsymbol{D}\left(\boldsymbol{x}\right) \dot{\boldsymbol{x}} = \boldsymbol{0} \ \xrightarrow{\mathrm{d}(\cdot)/\mathrm{d}t} \ \boldsymbol{D}\left(\boldsymbol{x}\right) \ddot{\boldsymbol{x}} + \boldsymbol{d}\left(\boldsymbol{x}, \dot{\boldsymbol{x}} \right) = \boldsymbol{0}, \tag{21}$$

where $\boldsymbol{d}\left(\boldsymbol{x}, \dot{\boldsymbol{x}} \right) = \dfrac{\partial \left(\boldsymbol{D}\left(\boldsymbol{x}\right) \dot{\boldsymbol{x}} \right)}{\partial \boldsymbol{x}} \dot{\boldsymbol{x}}$. Equation (21) can be linearized with respect to the equilibrium (13), leading to

$$\boldsymbol{D}\left(\boldsymbol{x}^0 \right) \ddot{\tilde{\boldsymbol{x}}} + \left. \frac{\partial \left(\boldsymbol{D}\left(\boldsymbol{x}\right) \ddot{\boldsymbol{x}}^0 \right)}{\partial \boldsymbol{x}} \right|_0 \tilde{\boldsymbol{x}} + \left. \frac{\partial \boldsymbol{d}}{\partial \boldsymbol{x}} \right|_0 \tilde{\boldsymbol{x}} + \left. \frac{\partial \boldsymbol{d}}{\partial \dot{\boldsymbol{x}}} \right|_0 \dot{\tilde{\boldsymbol{x}}} = \boldsymbol{0}. \tag{22}$$

The expression (22) enables the obtaining of $\ddot{\tilde{\boldsymbol{x}}}_{dd}$ in terms of $\ddot{\tilde{\boldsymbol{x}}}_{ai}$, which results in the acceleration relation:

$$\ddot{\tilde{\boldsymbol{x}}} = \boldsymbol{T}_0 \ddot{\tilde{\boldsymbol{x}}}_{ai} + \boldsymbol{U}_0 \dot{\tilde{\boldsymbol{x}}} + \boldsymbol{V}_0 \tilde{\boldsymbol{x}}, \tag{23}$$

with

$$
U_0 = \begin{pmatrix} \mathbf{0}_{(n-m-l) \times n} \\ -\left(D_{dd}\left(x^0\right)\right)^{-1} \left.\dfrac{\partial d}{\partial \dot{x}}\right|_0 \end{pmatrix},
$$

$$
V_0 = \begin{pmatrix} \mathbf{0}_{(n-m-l) \times n} \\ -\left(D_{dd}\left(x^0\right)\right)^{-1} \left(\left.\dfrac{\partial \left(D\left(x\right)\ddot{x}^0\right)}{\partial x}\right|_0 + \left.\dfrac{\partial d}{\partial x}\right|_0 \right) \end{pmatrix}.
\tag{24}
$$

Moreover, one resorts to Eq. (17) to write the set $\dot{\tilde{x}}_{dd}$ as

$$
\dot{\tilde{x}}_{dd} = T^0_{dd}\dot{\tilde{x}}_{ai} + \bar{V}_0\tilde{x},
\tag{25}
$$

where

$$
T^0_{dd} = -\left(D_{dd}\left(x^0\right)\right)^{-1} D_{ai}\left(x^0\right), \quad \bar{V}_0 = -\left(D_{dd}\left(x^0\right)\right)^{-1} \left.\dfrac{\partial \left(D\left(x\right)\dot{x}^0\right)}{\partial x}\right|_0.
\tag{26}
$$

The following velocity relation is obtained using Eq. (25):

$$
\dot{\tilde{x}} = T_0\dot{\tilde{x}}_{ai} + \bar{\bar{V}}_0\tilde{x},
\tag{27}
$$

where $\bar{\bar{V}}_0 = \begin{pmatrix} \mathbf{0}_{(n-m-l) \times n} \\ \bar{V}_0 \end{pmatrix}$. Furthermore, the coordinate partition of Eq. (18) allows the obtaining of the following expression:

$$
\tilde{x} = E_{ai}\tilde{x}_{ai} + E_{dd}\tilde{x}_{dd},
\tag{28}
$$

with E_{ai} and E_{dd} given by

$$
E_{ai} = \begin{pmatrix} I_{(n-m-l)} \\ \mathbf{0}_{(m+l) \times (n-m-l)} \end{pmatrix}, \qquad E_{dd} = \begin{pmatrix} \mathbf{0}_{(n-m-l) \times (m+l)} \\ I_{(m+l)} \end{pmatrix}.
\tag{29}
$$

Substituting Eqs. (23), (27) and (28) in Eq. (20), and resorting to Eq. (25), one obtains the resulting linear ODE system:

$$
m_0\ddot{\tilde{x}}_{ai} = \left(R_0\bar{\bar{V}}_0 + S_0\right)E_{ai}\tilde{x}_{ai} + \left(R_0\bar{\bar{V}}_0 + S_0\right)E_{dd}\tilde{x}_{dd} + R_0T_0\dot{\tilde{x}}_{ai},
\tag{30}
$$

$$
\dot{\tilde{x}}_{dd} = \bar{V}_0E_{ai}\tilde{x}_{ai} + \bar{V}_0E_{dd}\tilde{x}_{dd} + T^0_{dd}\dot{\tilde{x}}_{ai},
\tag{31}
$$

where

$$m_0 = T_0^{\mathrm{T}} M\left(x^0\right) T_0, \quad R_0 = T_0^{\mathrm{T}}\left(\left.\frac{\partial Q}{\partial \dot{x}}\right|_0 - M\left(x^0\right) U_0\right),$$

$$S_0 = T_0^{\mathrm{T}}\left(\left.\frac{\partial Q}{\partial x}\right|_0 - M\left(x^0\right) V_0 - \left.\frac{\partial\left(M\left(x\right)\ddot{x}^0\right)}{\partial x}\right|_0 - \left.\frac{\partial\left(D^{\mathrm{T}}\left(x\right)\lambda^0\right)}{\partial x}\right|_0\right).$$

$$(32)$$

Finally, introducing $\tilde{X} = \left(\tilde{x}_{ai}\ \dot{\tilde{x}}_{ai}\ \tilde{x}_{dd}\right)^{\mathrm{T}}$, the system of equations (30) and (31) is expressed as $\dot{\tilde{X}} = J\tilde{X}$, with J being the Jacobian matrix:

$$J = \left(\begin{array}{c|c|c} \mathbf{0}_{(n-m-l)} & I_{(n-m-l)} & \mathbf{0}_{(n-m-l)\times(m+l)} \\ \hline m_0^{-1}\left(R_0\bar{\bar{V}}_0 + S_0\right)E_{ai} & m_0^{-1}R_0T_0 & m_0^{-1}\left(R_0\bar{\bar{V}}_0 + S_0\right)E_{dd} \\ \hline \bar{V}_0 E_{ai} & T_{dd}^0 & \bar{V}_0 E_{dd} \end{array}\right). \qquad (33)$$

Note that J is a square matrix of dimension $2n - m - l = 16$.

4 Results and Discussion

Due to the translational nature of the equilibrium solution (13), the Jacobian matrix of Eq. (33) exhibits time-independent coefficients, expressed in terms of the parameters of the bicycle benchmark. This allows the performance of the stability analysis by directly computing its set of eigenvalues. To illustrate the effect of the steer axis angle and the rear and front tori aspect ratios on the eigenvalues of the system, a sensitivity analysis will be made. The chart of Fig. 3 shows all the considered scenarios.

The results of the bicycle benchmark [2] showed that, when the weave speed v_w is reached, the stabilization of the weave mode occurs and the uncontrolled bicycle becomes stable. Conversely, when the capsize speed v_c is achieved, the uncontrolled bicycle becomes unstable. Therefore, the self-stability range of the bicycle is $v_w < v < v_c$. The inclusion of torus-shaped wheels greatly impacts on this self-stability velocity range, being highly sensitive to the tori aspect ratios. Figure 4a shows the influence of the front torus aspect ratio μ_F for $\lambda = \{10°, 18°, 30°\}$. An increase of the minor radius of the front tire decreases the width of the stability regions, which finally fade out. The speeds v_w and v_c are reduced as μ_F increases, being more pronounced the decrease of v_c. By contrast, Fig. 4b shows, for the velocity range 0–15 m/s, the stabilizing effect of the rear aspect ratio μ_R, since the widths of the stability regions grow as μ_R rises. As for μ_F, the change in v_c is more significant than in v_w. These results are in agreement with those of Ref. [10], where the finite-cross-sectional radii of the tires are considered by including an overturning moment in each of the tires of the benchmark model. When both wheels are modelled with the same aspect ratio, $\mu_R = \mu_F = \mu$, the destabilizing effect of the front tire
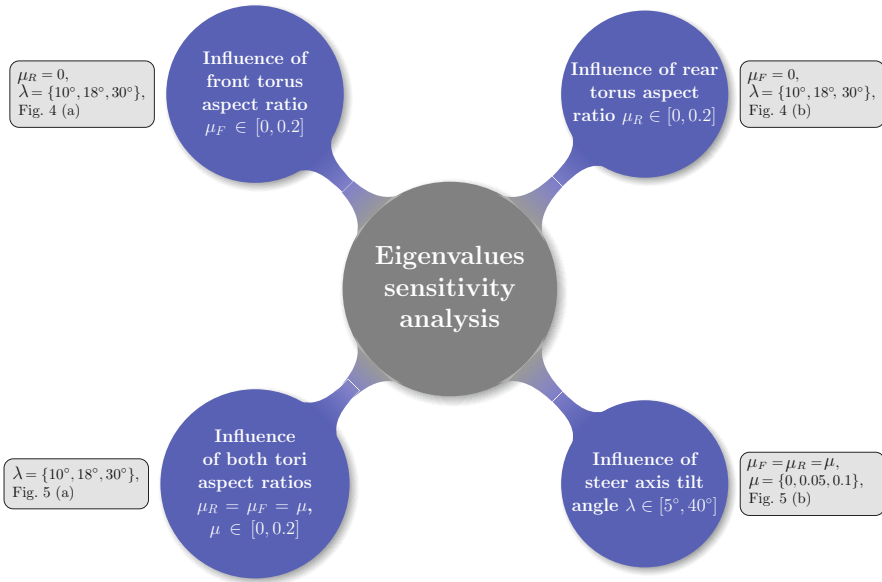
Fig. 3 Sensitivity analysis: combinations of the design parameters considered
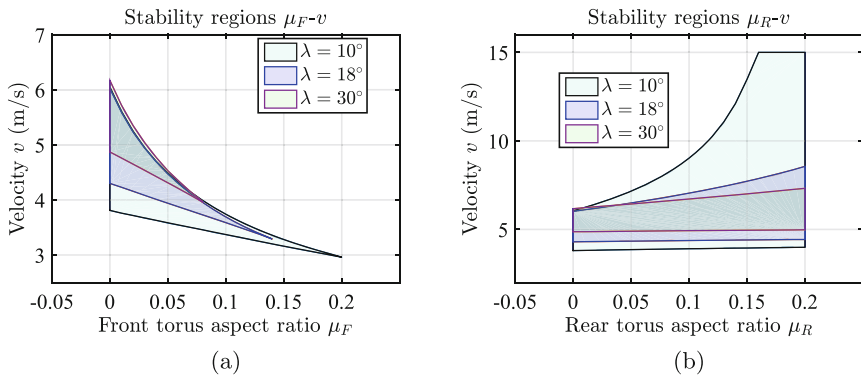
Fig. 4 Influence of μ_F and μ_R on the stability range. (**a**) Stability regions μ_F-v, with $\mu_R = 0$. (**b**) Stability regions μ_R-v, with $\mu_F = 0$

prevails, being the stability regions of Fig. 5a very similar to those of Fig. 4a. The size of the stability regions decreases as the steer axis tilt λ increases. Lastly, Fig. 5b shows the effect of λ, in the range $\lambda \in [5°, 40°]$, for $\mu_R = \mu_F = \mu = \{0, 0.05, 0.1\}$. In the hoop-shaped wheels case, with $\mu = 0$, the capsize speed v_c initially decreases as λ rises until $\lambda \simeq 17.5°$ and then increases. This tendency of v_c can also be seen for $\mu = 0.05$. The consideration of the toroidal wheels shrinks the stability regions, as can be seen for $\mu = 0.05$ and $\mu = 0.1$.
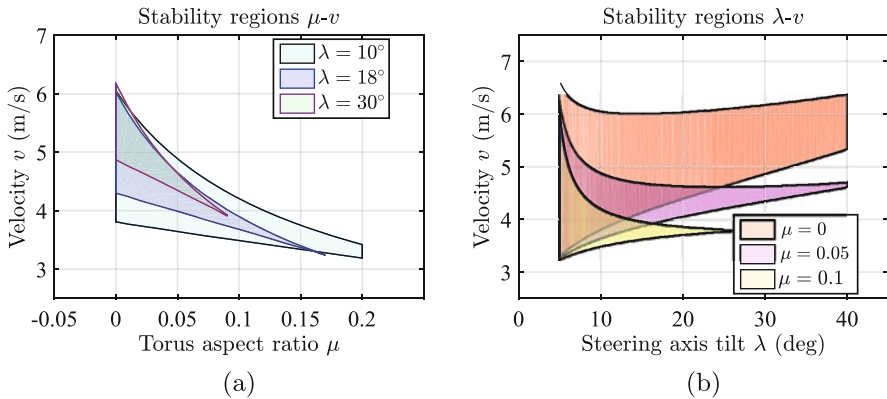
Fig. 5 Influence of μ and λ on the stability range. (**a**) Stability regions μ-v. (**b**) Stability regions λ-v

5 Conclusions

In this work, the stability of a bicycle with toroid-shaped wheels, based on the benchmark of Meijaard et al. [2], is analysed. The equations of motion of the multibody system are linearized resorting to a novel numerical linearization approach, which exhibits an excellent efficiency with constrained multibody systems of high complexity. With this approach, the Jacobian matrix is expressed in terms of the dynamic and geometric parameters of the multibody system. A wide variety of scenarios (see Fig. 3) is considered in the stability analysis, studying the effect of the tori aspect ratios and the steer axis tilt on the self-stability of the bicycle. The obtained results are consistent with those of the literature.

In future work, the multibody model will be extended by adding suspensions and more realistic models of tires and riders, and the stability analysis of more complex trajectories will be addressed resorting to the linearization approach here described.

References

1. F.J.W. Whipple, The stability of the motion of a bicycle. Q. J. Pure Appl. Math. **30**(120), 312–321 (1899)
2. J.P. Meijaard, J.M. Papadopoulos, A. Ruina, A.L. Schwab, Linearized dynamics equations for the balance and steer of a bicycle: a benchmark and review. Proc. R. Soc. A Math. Phys. Eng. Sci. **463**(2084), 1955–1982 (2007)
3. P. Basu-Mandal, A. Chatterjee, J.M. Papadopoulos, Hands-free circular motions of a benchmark bicycle. Proc. R. Soc. A Math. Phys. Eng. Sci. **463**(2084), 1983–2003 (2007)
4. J.L. Escalona, A.M. Recuero, A bicycle model for education in multibody dynamics and real-time interactive simulation. Multibody Syst. Dyn. **27**(3), 383–402 (2012)

5. J. Xiong, N. Wang, C. Liu, Stability analysis for the Whipple bicycle dynamics. Multibody Syst. Dyn. **48**(3), 311–335 (2020)
6. J.D.G. Kooijman, A.L. Schwab, J.P. Meijaard, Experimental validation of a model of an uncontrolled bicycle. Multibody Syst. Dyn. **19**(1–2), 115–132 (2008)
7. J. Xiong, N. Wang, C. Liu, Bicycle dynamics and its circular solution on a revolution surface. Acta Mech. Sin. **36**(1), 220–233 (2020)
8. A. García-Agúndez, D. García-Vallejo, E. Freire, Linearization approaches for general multibody systems validated through stability analysis of a benchmark bicycle model. Nonlinear Dyn. **103**(1), 557–580 (2021)
9. A.L. Schwab, J.P. Meijaard, J.D.G. Kooijman, Some recent developments in bicycle dynamics, in *Proceedings of the 12th World Congress in Mechanism and Machine Science* (2007), pp. 1–6
10. R.S. Sharp, On the stability and control of the bicycle. Appl. Mech. Rev. **61**(6), 1–24 (2008)
11. J.K. Moore, *Human Control of a Bicycle* (University of California, Davis, 2012)
12. V.E. Bulsink, A. Doria, B. van de Belt, B. Koopman, The effect of tyre and rider properties on the stability of a bicycle. Adv. Mech. Eng. **7**(12), 1687814015622596 (2015)
13. A. García-Agúndez, D. García-Vallejo, E. Freire, Study of the forward locomotion of a three-dimensional multibody model of a waveboard by inverse dynamics. Mech. Mach. Theory **149**, 103826 (2020)
14. W. Schiehlen, Multibody system dynamics: Roots and perspectives. Multibody Syst. Dyn. **1**(2), 149–188 (1997)

Co-Simulation in Mechanical Systems with Non-linear Components

Evangelos Koutras, Elias Paraskevopoulos, and Sotirios Natsiavas

1 Introduction

Co-simulation or solver coupling has already been applied extensively to various engineering fields [1, 2]. The basic idea is founded on a decomposition of the global model into two or more sub-models. The different sub-systems are connected by coupling variables which are exchanged only at the macro-time (or communication) points. Between these points, the sub-systems are integrated independently, using their own solver. Generally, the sub-systems can be coupled by physical force/torque laws (applied forces/torques) or by algebraic constraint equations (reaction forces/torques) [3, 4]. Here, solver coupling by applied forces/torques is considered only. Also, two well-known co-simulation approaches are used. More specifically, a parallel and a sequential scheme is applied, known as Jacobi and Gauss-Seidel scheme, respectively. Furthermore, co-simulation approaches can be sub-divided into explicit, implicit and semi-implicit methods. Finally, concerning the decomposition of the overall system into sub-systems, three different possibilities can be distinguished. Namely, force/force, force/displacement and displacement/displacement decomposition.

In the present work, the attention is focused on starting a systematic investigation on the effect of non-linearities in the convergence and numerical error behavior of various co-simulation schemes, which are available in the literature. For this, a two degree of freedom weakly non-linear system is employed as a model. This system consists of two oscillators, interconnected by a linear damper and a non-linear Duffing type spring, involving linear and cubic displacement terms. In addition, the external forcing possesses a component with frequency close to one of the natural

E. Koutras · E. Paraskevopoulos · S. Natsiavas (✉)
Department of Mechanical Engineering, Aristotle University, Thessaloniki, Greece
e-mail: natsiava@auth.gr

frequencies of the linearized model. Despite the fact that the model examined has a simple structure, the dynamics is sufficiently complex. Moreover, the co-simulation techniques used can be extended and applied to arbitrary multibody or structural dynamics systems.

The main emphasis of this study is placed on developing a formulation with general validity, providing information that will help in starting the process of revealing global dynamics of non-linear systems, by employing reliable and efficient co-simulation techniques. In the next section, the example dynamical system is introduced and an analytical solution is derived by applying the method of multiple scales. This solution is then used as a guide for the numerical results obtained by co-simulation. These results illustrate the effectiveness and accuracy of the co-simulation techniques employed.

2   Example Mechanical Model

The main objective of the present work is to investigate effects caused in a general co-simulation process, related to the presence of non-linearities, in a systematic way. The example model selected is shown in Fig. 1. It consists of a two-degree of freedom oscillator, including an interconnecting spring with a Duffing type non-linearity. Specifically, the spring force connecting masses m_1 and m_2 equals $k_0 x + \hat{k}_0 x^3$, where x is their relative displacement. This model was chosen since it is simple enough but possesses the main ingredients of a co-simulation model involving non-linearities. Namely, it has two distinct mechanical components coupled through a non-linear connection. Moreover, the resulting dynamical system is amenable to analysis. That is, when the system is weakly non-linear, the method of multiple scales can be applied for capturing its dynamics in an analytic manner.

The equations of motion of the system examined are first derived and put in the form of a set of two coupled non-linear ordinary differential equations (ODEs)

$$M \underline{\ddot{x}} + C \underline{\dot{x}} + K \underline{x} + \underline{g}\left(\underline{x}\right) = \underline{F}(t) \tag{1}$$
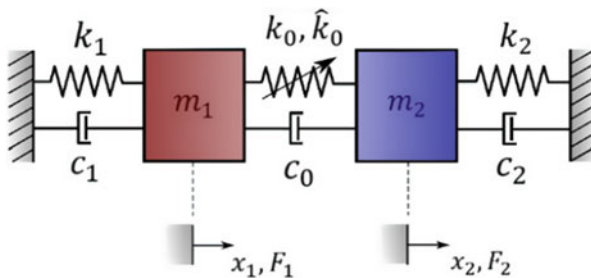
Fig. 1 Example mechanical model

with

$$\underline{x} = \begin{pmatrix} x_1 \\ x_2 \end{pmatrix}, M = \begin{bmatrix} m_1 & 0 \\ 0 & m_2 \end{bmatrix}, C = \begin{bmatrix} c_1 + c_0 & -c_0 \\ -c_0 & c_2 + c_0 \end{bmatrix}, K = \begin{bmatrix} k_1 + k_0 & -k_0 \\ -k_0 & k_2 + k_0 \end{bmatrix}$$

$$\underline{g}(\underline{x}) = \hat{k}_0 (x_1 - x_2)^3 \begin{pmatrix} 1 \\ -1 \end{pmatrix}, \quad \underline{F}(t) = \begin{pmatrix} F_1(t) \\ F_2(t) \end{pmatrix}$$

These equations are first put in a normalized form, by introducing the parameters

$$\hat{\omega}_n = \sqrt{k_n/m_n}, \zeta_n = c_n / \left(2\sqrt{k_n m_n} \right), n = 0, 1, 2$$

with $m_0 = m_2$. Then, selecting the normalized time and displacement by

$$\tau = \hat{\omega}_1 t, y_n(\tau) = x_n(t)/x_c, n = 1, 2$$

where x_c is a characteristic length, Eq. (1) appears in the normalized form

$$\hat{M} \underline{\ddot{y}} + \hat{C} \underline{\dot{y}} + \hat{K} \underline{y} + \underline{\hat{g}}(\underline{y}) = \underline{\hat{F}}(\tau) \tag{2}$$

for harmonic forcing $F_n(t) = \hat{F}_n \cos(\Omega t - \varphi_n)$, with

$$\hat{M} = \begin{bmatrix} 1 & 0 \\ 0 & \mu \end{bmatrix}, \hat{C} = \begin{bmatrix} \hat{\delta}_1 + \hat{\delta}_0 & -\hat{\delta}_0 \\ -\hat{\delta}_0 & \hat{\delta}_2 + \hat{\delta}_0 \end{bmatrix}, \underline{\hat{g}}(\underline{y}) = \hat{k}_0 (y_1 - y_2)^3 \begin{pmatrix} 1 \\ -1 \end{pmatrix},$$

$$\underline{\hat{F}}(\tau) = \begin{pmatrix} \hat{f}_1 \cos(\omega\tau - \varphi_1) \\ \hat{f}_2 \cos(\omega\tau - \varphi_2) \end{pmatrix}$$

$$\mu = m_2/m_1, \rho = \hat{\omega}_2/\hat{\omega}_1, \rho_0 = \hat{\omega}_0/\hat{\omega}_1, \delta = \mu\rho^2, \delta_0 = \mu\rho_0^2, \hat{\delta}_1 = 2\zeta_1, \hat{\delta}_2 = 2\mu\rho\zeta_2$$

$$\hat{\delta}_0 = 2\mu\rho_0\zeta_0, \hat{k}_0 = \left(\hat{k}_0/k_1 \right) x_c^2, \hat{f}_1 = \hat{F}_1/(k_1 x_c), \hat{f}_2 = \mu\hat{F}_2/(k_1 x_c), \omega = \Omega/\hat{\omega}_1$$

The study focuses on primary resonance of the first linear mode, that is

$$\omega = \omega_1 + \varepsilon\sigma_1 \tag{3}$$

where ω_1 is the lower natural frequency of the linear system. This makes necessary an appropriate ordering in the terms appearing in the equations of motion [5]. For this, set

$$\varepsilon = 2\mu\rho_0\zeta_0, \hat{\delta}_n = \varepsilon\delta_n, \hat{k}_0 = \varepsilon\kappa_0, \hat{f}_n = \varepsilon f_n, n = 1, 2$$

Then, the equations of motion appear in the following normalized form

$$\hat{M}\ddot{\underline{y}} + \hat{K}\underline{y} = \varepsilon\underline{p}\left(\tau, \underline{y}, \dot{\underline{y}}\right) \tag{4}$$

with

$$\underline{p}\left(\tau, \underline{y}, \dot{\underline{y}}\right) = \begin{pmatrix} f_1\cos(\omega\tau - \varphi_1) - (1+\delta_1)\dot{y}_1 + \dot{y}_2 - \kappa_0(y_1 - y_2)^3 \\ f_2\cos(\omega\tau - \varphi_2) + \dot{y}_1 - (1+\delta_2)\dot{y}_2 - \kappa_0(y_2 - y_1)^3 \end{pmatrix} \tag{5}$$

Next, employ the modal transformation

$$\underline{y}(\tau) = \underline{Y}\,\underline{u}(\tau) \tag{6}$$

where the 2x2 matrix $\underline{Y} = [\underline{y}_1\ \underline{y}_2]$ is formed by the two linear modes of the system. Then, using the appropriate orthonormality conditions, Eq. (4) takes the form

$$\ddot{\underline{u}} + \Lambda\underline{u} = \varepsilon\left[\underline{h}_0(\tau) + \underline{h}\left(\underline{y}, \dot{\underline{y}}\right)\right] \tag{7}$$

with

$$\underline{h}_0(\tau) = Y^T\begin{pmatrix} f_1\cos(\omega\tau - \varphi_1) \\ f_2\cos(\omega\tau - \varphi_2) \end{pmatrix} \equiv \begin{pmatrix} \hat{\xi}_1\cos(\omega\tau + \theta_1) \\ \hat{\xi}_2\cos(\omega\tau + \theta_2) \end{pmatrix} \tag{8}$$

and

$$\begin{aligned}
\underline{h}\left(\underline{y}, \dot{\underline{y}}\right) &= Y^T\begin{pmatrix} -(1+\delta_1)\dot{y}_1 + \dot{y}_2 - \kappa_0(y_1 - y_2)^3 \\ +\dot{y}_1 - (1+\delta_2)\dot{y}_2 - \kappa_0(y_2 - y_1)^3 \end{pmatrix} \\
&\equiv \begin{pmatrix} \alpha_{11}\dot{u}_1 + \alpha_{12}\dot{u}_2 + \gamma_{11}u_1^3 + \gamma_{12}u_1^2 u_2 + \gamma_{13}u_1 u_2^2 + \gamma_{14}u_2^3 \\ \alpha_{21}\dot{u}_1 + \alpha_{22}\dot{u}_2 + \gamma_{21}u_1^3 + \gamma_{22}u_1^2 u_2 + \gamma_{23}u_1 u_2^2 + \gamma_{24}u_2^3 \end{pmatrix}
\end{aligned} \tag{9}$$

The values of the constants $\hat{\xi}_i$, θ_i, α_{ij} $(i, j = 1, 2)$ and γ_{ij} $(i, j = 1 - 4)$ in Eqs. (8) and (9) are easily determined with respect to the system parameters defined before [5]. Then, for small values of the parameter ε, application of the method of multiple time scales provides approximate analytical solutions with asymptotic form

$$\underline{u}(\tau; \varepsilon) = \underline{u}_0(\tau_0, \tau_1) + O(\varepsilon) \tag{10}$$

where $\tau_0 = \tau$ is the fast time scale and $\tau_1 = \varepsilon\tau$ is the slow time scale of the system examined. Specifically, this solution is obtained in the form

$$\underline{u}_0(\tau_0, \tau_1) = \begin{pmatrix} a_1(\tau_1)\cos(\omega\tau_0 + \theta_1 - \gamma_1(\tau_1)) \\ a_2(\tau_1)\cos\left(\hat{\omega}\tau_0 - \gamma_2(\tau_1)\right) \end{pmatrix} \tag{11}$$

with $\gamma_1 = \sigma_1\tau_1 + \theta_1 - \varphi_1$, $\gamma_2 = \hat{\sigma}_2\tau_1 - \varphi_2$ and $\hat{\omega} = \omega_2 + \varepsilon\hat{\sigma}_2$. For the resonance considered, the amplitudes and phases satisfy the following set of slow flow ODEs

$$a_1' = c_1 a_1 + c_4 \sin \gamma_1, \, a_1 \gamma_1' = \sigma_1 a_1 + c_5 a_1^3 + c_6 a_1 a_2^2 + c_4 \cos \gamma_1, \tag{12}$$

$$a_2' = e_1 a_2, \, a_2 \gamma_2' = \hat{\sigma}_2 a_2 + e_5 a_1^2 a_2 + e_6 a_1^2 a_2 \tag{13}$$

Among all the possible solutions of these equations, constant solutions, with

$$a_1' = \gamma_1' = a_2' = \gamma_2' = 0 \tag{14}$$

possess a prominent place. The last conditions lead immediately to $\alpha_2 = 0$, which corresponds to motions involving the directly excited mode only, with amplitude and phase determined by the modulation equations

$$a_1' = c_1 a_1 + c_4 \sin \gamma_1, \tag{15}$$

$$a_1 \gamma_1' = \sigma_1 a_1 + c_5 a_1^3 + c_4 \cos \gamma_1 \tag{16}$$

These equations have identical structure with the modulation equations obtained for the single degree of freedom Duffing oscillator [5]. Based on Eqs. (6), (10) and (11), constant solutions correspond to harmonic response of the original system, with

$$\underline{y}(\tau) = a_1 \cos(\omega \tau_0 + \theta_1 - \gamma_1) \, \underline{y}_1 \tag{17}$$

Finally, the stability properties of these solutions can also be determined [5].

3 Description of the co-Simulation Method

In this work, the example mechanical system shown in Fig. 1 is examined [5, 6]. The basic idea of co-simulation consists in a decomposition of the overall system into two (or more) sub-systems, which are connected through appropriate coupling variables. Communication of sub-systems takes places at pre-defined time points. In the meanwhile, they are integrated independently from each other using their own solver.

A separate sub-system is responsible for the proper communication between the sub-systems, called master (or orchestrator). The way this is accomplished is through appropriate (based on decomposition approach) coupling conditions G_j ($j = 1, \ldots, k$) that need to be satisfied at the macro-time points. Specifically, solving from T_N to T_{N+1}, master initially provides sub-systems with input (coupling) variables $\underline{U}_i$ ($i = 1, \ldots, n$). The sub-systems are then responsible for solving from T_N to T_{N+1} using their own solver. As a next step, the orchestrator collects the output variables $\underline{Y}_i$ of the submodels at communication point T_{N+1}. Based
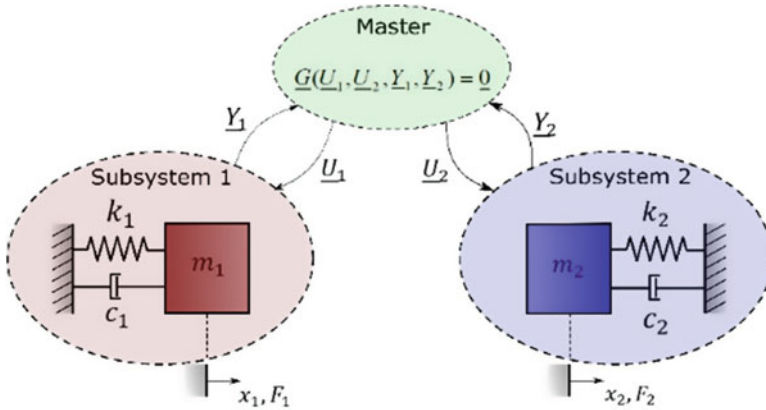
Fig. 2 Co-simulation procedure

on these variables and the coupling conditions, improved predictions for the input variables are provided to the sub-systems (Fig. 2).

Co-simulation approaches can be subdivided into explicit, implicit and semi-implicit methods. Using an implicit approach, the methodology explained previously is accomplished through a predictor-corrector approach until the coupling conditions are fully satisfied. Using a semi-implicit approach, the corrector step has to be repeated only once. As a consequence, solver re-initialization is necessary in both cases. On the contrary, in explicit methods, only matching of the coupling variables takes place based on the coupling conditions and the simulation proceeds on to the next macro-time step H.

Regarding implicit and semi-implicit methods, the core idea is to formulate the Newton method at the interface level to find corrected coupling variables [3, 7]. By collecting the vector of input and output variables and the residuals' vector

$$\underline{U} = \begin{pmatrix} \underline{U}_1 \\ \vdots \\ \underline{U}_n \end{pmatrix}, \underline{Y} = \begin{pmatrix} \underline{Y}_1 \\ \vdots \\ \underline{Y}_n \end{pmatrix}, \underline{R} = \begin{pmatrix} G_1\left(\underline{U}, \underline{Y}\right) \\ \vdots \\ G_k\left(\underline{U}, \underline{Y}\right) \end{pmatrix} \tag{18}$$

the corrected coupling variables can be calculated by solving the linear system

$$\frac{\partial \underline{G}}{\partial \underline{U}} \Delta \underline{U} = -\underline{R}, \Delta \underline{U} = \underline{U}^{m+1} - \underline{U}^m \tag{19}$$

For the predictor part, extrapolation of coupling variables based on previous converged values takes place during initialization of a macro-time step H. Constant, linear and quadratic Lagrange polynomials can be used. For the decomposition of the global model into sub-models, three different techniques can be used. Namely, force-force, force-displacement and displacement-displacement approaches.

3.1 Force-Force Decomposition

In this case, both sub-systems are force-driven single-mass oscillators, excited by the coupling force $\tilde{\lambda}$, as shown in Fig. 3. The input variable $U_{1,2} = \tilde{\lambda}$ is given by

$$G = \tilde{\lambda} - c_0 \left(u_2 - u_1\right) - k_0 \left(x_2 - x_1\right) - \hat{k}_0 (x_2 - x_1)^3 \tag{20}$$

3.2 Force-Displacement Decomposition

In this approach, the first sub-system is excited by the coupling force $\tilde{\lambda}$, while the second is a base-point excited single-mass oscillator, as shown in Fig. 4. The input variables

$$U_1 = \tilde{\lambda}, \underline{U}_2 = \begin{pmatrix} \tilde{x}_1 \\ \tilde{u}_1 \end{pmatrix} \tag{21}$$
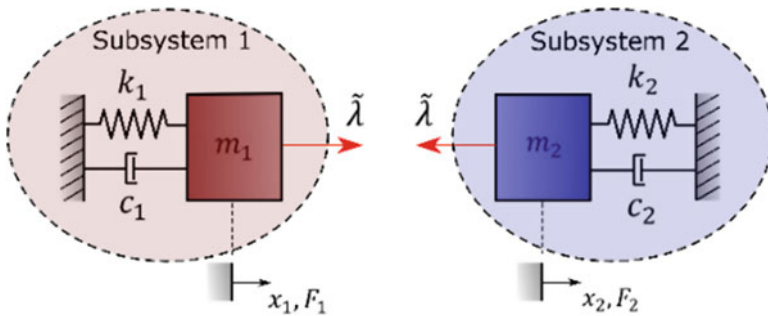
Fig. 3 Force-force decomposition
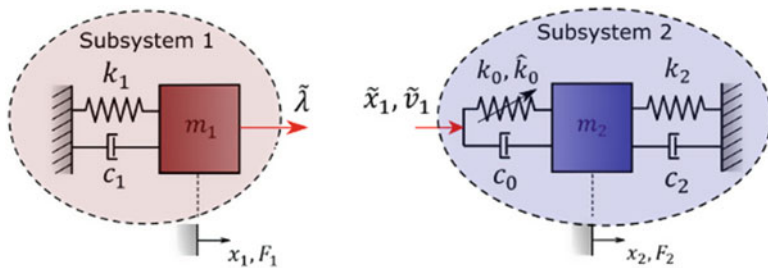
Fig. 4 Force-displacement decomposition

are given by the coupling conditions

$$
\underline{G} = \begin{pmatrix} \tilde{\lambda} - c_0 (u_2 - u_1) - k_0 (x_2 - x_1) - \hat{k}_0 (x_2 - x_1)^3 \\ \tilde{x}_1 - x_1 \\ \tilde{u}_1 - u_1 \end{pmatrix}
\tag{22}
$$

3.3 Displacement-Displacement

In a displacement-displacement decomposition approach, both sub-systems are base-point excited single-mass oscillators, as depicted in Fig. 5. The input variables

$$
\underline{U}_1 = \begin{pmatrix} \tilde{x}_2 \\ \tilde{u}_2 \end{pmatrix}, \underline{U}_2 = \begin{pmatrix} \tilde{x}_1 \\ \tilde{u}_1 \end{pmatrix}
\tag{23}
$$

are given by the coupling conditions

$$
\underline{G} = \begin{pmatrix} \tilde{x}_1 - x_1 \\ \tilde{u}_1 - u_1 \\ \tilde{x}_2 - x_2 \\ \tilde{u}_2 - u_2 \end{pmatrix}
\tag{24}
$$

Communication between sub-systems at macro-time points is necessary. As a consequence, the choice of the way that the information is exchanged between the different models is another important property of the co-simulation method. There are mainly two possibilities, which correspond to a parallel (Jacobi) and a serial (Gauss-Seidel) data exchange, as their properties are similar to the linear iterative solvers.

In the Jacobi pattern, each sub-system integrates its own dynamics in parallel and independently, as shown in Fig. 6(a). Hence, there is no data flow dependency within the time step and also no need for sub-models to wait each other. The disadvantage of this communication pattern lies in its accuracy which is usually
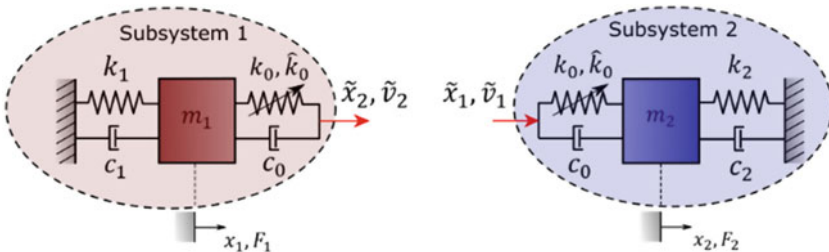
Fig. 5 Displacement-displacement decomposition
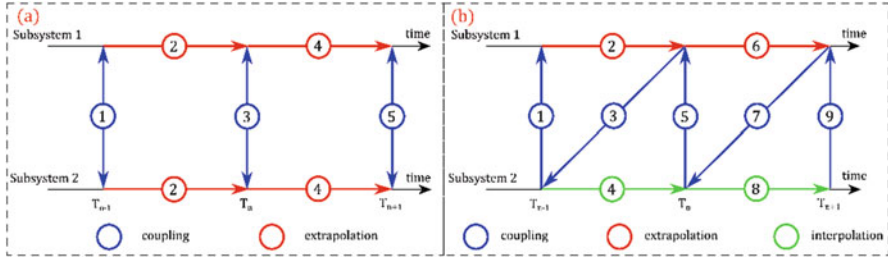
Fig. 6 Jacobi (**a**) and Gauss-Seidel (**b**) communication patterns

worse in comparison with Gauss-Seidel, due to extrapolation of coupling variables in both sub-systems.

In the Gauss-Seidel approach, the coupled sub-systems integrate their own dynamics sequentially, as depicted in Fig. 6(b). The advantage of this pattern is its higher accuracy compared with the Jacobi pattern due to the fact that a better prediction for the coupling variables is provided to the second sub-system through interpolation. However, the different sub-systems need to wait each other resulting in a higher computational cost. Furthermore, as the number of sub-systems increases, this drawback gets even worse.

4   Numerical Results and Discussion

Initially, emphasis was placed on activating the non-linear behaviour of the oscillator through proper selection of the system parameters. Using their numerical values,

$$\mu=0.5,\ \zeta_0=0.1,\ \zeta_1=0.01=\zeta_2,\ \rho=1.8,\ \rho_0=0.6,\ \varepsilon=0.06,\ \kappa_0=1/3,\ \hat{f}_1=0.55$$

led to the results of Fig. 7. Two regions are of interest, one near $\sigma_1=0$ and the other around $\sigma_1=4$. In this work, the focus was placed on the first of these two regions.

As usual, multiple solutions exist within a frequency range in Fig. 7. Consequently, a pure numerical solution would be dangerous to use. However, the non-linear analysis described previously revealed approximate analytical solutions of the system examined which were then used as a basis for producing accurate co-simulation results.

To examine the convergence behaviour of the co-simulation schemes, a proper measure of the global error was first established. The error at each macro-time point was set as

$$\underline{\varepsilon}_p(t) = \underline{x}_{cs}(t) - \underline{x}_{ref}(t),\ \underline{\varepsilon}_v(t) = \underline{\dot{x}}_{cs}(t) - \underline{\dot{x}}_{ref}(t)$$
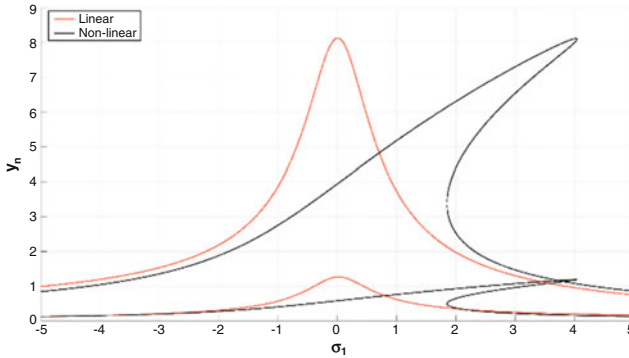
Fig. 7 Normalized displacement amplitude for linear and non-linear system

where a numerical solution of Eq. (1) is used as reference. Then, the global error in the position and the velocity is calculated by taking the RMS value of the quantities

$$\underline{\varepsilon}_{pos}(t) = \sqrt{\underline{\varepsilon}_p^T M \underline{\varepsilon}_p}, \ \underline{\varepsilon}_{vel}(t) = \sqrt{\underline{\varepsilon}_v^T M \underline{\varepsilon}_v}$$

Figure 8 shows the position and velocity error for the Jacobi pattern and force-force decomposition of the system. A comparison of the explicit (constant extrapolation) and implicit co-simulation approach reveals that the latter provides more accurate results, due to its iterative nature. Also, for the same system parameters, use of the Gauss-Seidel pattern and/or different decomposition approaches leads to quite similar behaviour.

In Fig. 9, the convergence behaviour of Jacobi and Gauss-Seidel patterns is under investigation. The decomposition of the global system is displacement-displacement, while an explicit co-simulation approach is used. The extracted results are in agreement with the theoretical background. Specifically, the Gauss-Seidel pattern provides more accurate results due to its sequential nature. Similar results are also observed for the cases of force-force and force-displacement decomposition of the overall system.

Finally, a detailed analysis of the convergence behaviour of explicit co-simulation approaches for different extrapolation orders is carried out, as depicted in Fig. 10. For higher approximation orders, the accuracy is improved which usually comes with the drawback of reduced stability. In this case, a Jacobi communication pattern and a force-force decomposition is used, while the corresponding results using a Gauss-Seidel pattern and/or different decomposition types show a similar behaviour.
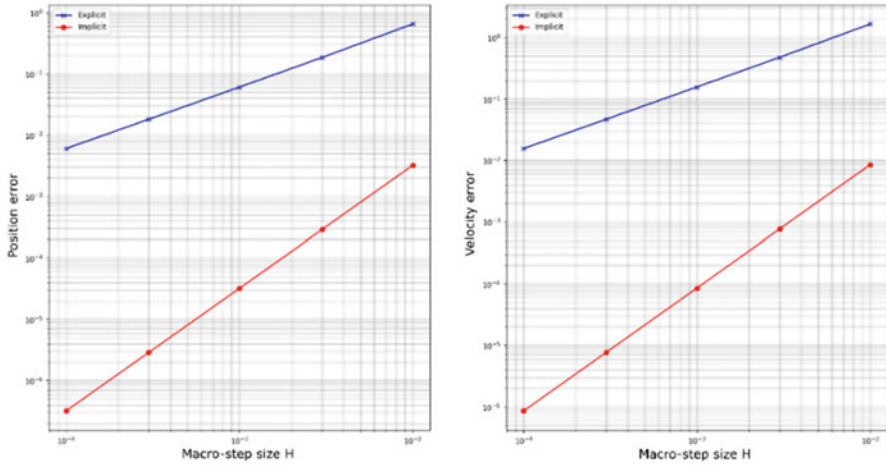
Fig. 8 Convergence plots for Jacobi communication pattern and force-force decomposition (constant extrapolation)
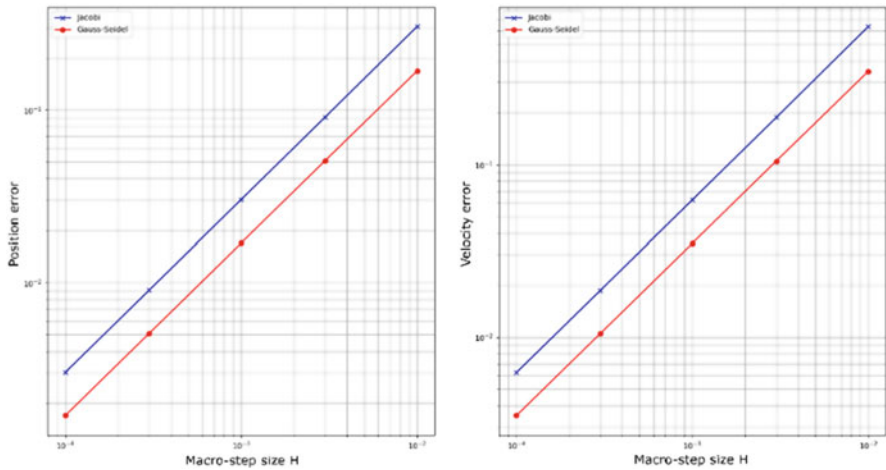
Fig. 9 Convergence plots for explicit communication approach and displacement-displacement decomposition (constant extrapolation)

5 Synopsis and Future Work

A co-simulation approach has been developed and applied to a (weakly) non-linear system. A detailed analysis of the convergence behaviour has also been carried out. Four different categories were examined, namely communication pattern, decomposition type, extrapolation order and numerical scheme (implicit/explicit). The main emphasis was placed on the accuracy of the schemes. However, a detailed
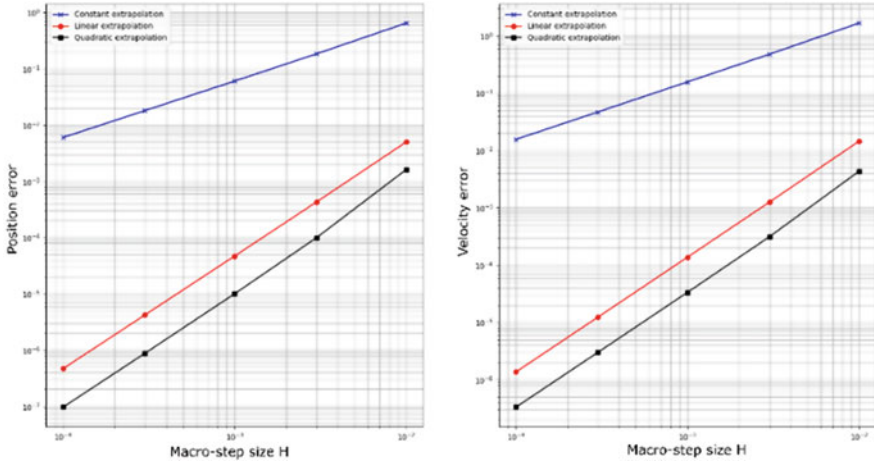
Fig. 10 Convergence plots for Jacobi communication pattern and force-force decomposition

analysis of the stability behaviour must be carried out in order to create a complete picture. Finally, the new approach will be applied to complex mechanical problems [2], in order to demonstrate its effectiveness to arbitrary multibody or structural dynamics systems.

References

1. C. Gomes, C. Thule, P.G. Larsen, H. Vangheluwe, Co-simulation: State of the art. arXiv preprint **arXiv**, 1702.00686 (2017)
2. E. Paraskevopoulos, S. Stefanidou, S. Natsiavas, A novel approach for the analysis of a coupled train-railway bridge system: Basic principles and methodology. COMPDYN2019 (2019)
3. B. Schweizer, D. Lu, Semi-implicit co-simulation approach for solver coupling. Arch. Appl. Mech. **84**(12), 1739–1769 (2014)
4. B. Schweizer, D. Lu, Predictor/corrector co-simulation approaches for solver coupling with algebraic constraints. ZAMM-Journal of Applied Mathematics and Mechanics/Zeitschrift für Angewandte Mathematik und Mechanik **95**(9), 911–938 (2015)
5. S. Natsiavas, Modal interactions in self-excited oscillators under external primary resonance. J. Sound Vib. **184**(2), 261–280 (1995)
6. S. Natsiavas, P. Metallidis, External primary resonance of self-excited oscillators with 1: 3 internal resonance. J. Sound Vib. **208**(2), 211–224 (1997)
7. Sicklinger, S. A.: Stabilized Co-Simulation of Coupled Problems Including Fields and Signals (Doctoral Dissertation, Technische Universität München). (2014)

A Novel Time-Stepping Method for Multibody Systems with Frictional Impacts

Sotirios Natsiavas, Panagiotis Passas, and Elias Paraskevopoulos

1 Introduction

Dynamics of mechanical systems with impact and friction is a challenging research topic [1]. The strongly nonlinear and numerically stiff nature of the equations of motion necessitates application of special techniques. In engineering, numerical integration techniques were developed along two main avenues. First, a large group of publications focused on models arising by application of the finite element method to elastodynamic problems [2, 3]. Also, a lot of research was devoted to multibody systems [4, 5]. A combination of the methods developed in both of these areas is needed in solving complex engineering problems, like in the discipline of flexible multibody dynamics.

In this study, the attention focused on developing an efficient time-stepping method for the integration of the equations of motion of multibody systems subject to a single unilateral and a set of bilateral motion constraints. This was achieved by seeking a better modeling of the dynamics process. First, a consistent application of Newton's law is performed in both the impact-free and the impact phases, using concepts of Analytical Dynamics [6, 7]. Moreover, once a potential impact event is detected, an appropriate return map is applied, bringing the state of the system back to the allowable domain [8]. This avoids interpenetration and provides the preimpact conditions. Then, the postimpact state of a system involving frictional impacts is determined by solving a system of three ODEs (Ordinary Differential Equations) only, obtained through a suitable change of coordinates [7]. In this way, the problem of numerical stiffness, which is inherent to impact problems and is

S. Natsiavas (✉) · P. Passas · E. Paraskevopoulos
Department of Mechanical Engineering, Aristotle University, Thessaloniki, Greece
e-mail: natsiava@auth.gr

related to the large difference in the timescales associated with the dynamics during the free and the impact phase of the motion, is handled in an efficient manner.

Here, the methodology presented in [6] is extended to systems involving a unilateral constraint. The presence of a unilateral constraint, arising from an impact or a friction event (like slip or stick), causes additional difficulties [9, 10]. In essence, the relatively small duration of an impact event induces severe numerical stiffness in the equations of motion. Due to these inherent difficulties, an accurate and efficient numerical integration requires development of special techniques. Here, this is achieved by developing an appropriate time-stepping scheme, involving a return map, which is activated when an impact event is detected. The idea of a return map is similar to that applied earlier to other problems of mechanics [11, 12]. Here, a large modification is necessary since the configuration space is non-Euclidean [8, 13]. In addition, following the detection of an impact, the equations of motion are transformed into a set of three equations, evolving over a much smaller timescale than the others, which are solved separately, until the end of the impact event. This is based on theory presented in earlier work [7] and is a key to overcome numerical stiffness problems in an efficient manner.

The material of this paper is organized as follows. First, the governing equations of motion are presented briefly in Sec. 2. Next, the basic ingredients of the new numerical integration scheme, including the incorporation of a suitable return mapping, are presented in Sec. 3. Selected numerical results are then presented in Sec. 4.

2 Equations of Motion

The configuration of the class of systems examined is described by a set of generalized coordinates, $q = (q^1, \ldots, q^n)$. Their motion is represented by a point p, moving along the configuration manifold M as a function of time t [14]. The generalized velocity $\underline{v}$ belongs to a vector space T_pM. Using the summation convention on repeated indices, $\underline{v} = v^I \underline{e}_I$, with $I = 1, \ldots, n$, where $\mathfrak{B}_e = \{\underline{e}_1 \ \ldots \ \underline{e}_n\}$ is a basis of T_pM. Employing the duality pairing $\underline{u}^* (\underline{w}) \equiv \langle \underline{u}, \underline{w} \rangle$, $\forall \underline{w} \in T_pM$, where $\langle \cdot, \cdot \rangle$ is the inner product of T_pM selected based on the kinetic energy of the system, the elements of the cotangent space T_p^*M represent generalized momenta. These elements can be expressed in the form $\underline{u}_M^* = u_I \underline{e}^I$, with respect to a dual basis $\mathfrak{B}_e^* = \{\underline{e}^1 \ \ldots \ \underline{e}^n\}$.

When there are no motion constraints, the solution is determined by Newton's law

$$\underline{h}_M^* \equiv \nabla_{\underline{v}} \underline{p}_M^* - \underline{f}_M^* = \underline{0}. \tag{1}$$

Covectors $\underline{f}_M^* = f_I \underline{e}^I$ and $\underline{p}_M^* = p_I \underline{e}^I$ represent applied forces and generalized momenta, respectively, with $p_I = g_{IJ} v^J$, where g_{IJ} represent the components

of the metric tensor at point p. Also, the covariant differential of covector p_M^*, corresponding to tangent vector $\underline{v}$, takes the form $\nabla_{\underline{v}} p^*(t) = \left(\dot{p}_I - \Lambda_{JI}^K p_K v^J \right) \underline{\tilde{e}}^I$, with $I, J, K = 1, \ldots, n$, where the quantities Λ_{IJ}^K are known as affinities [15].

The presence of a contact event is signaled by an inequality

$$\rho(p) \geq 0 \tag{2}$$

This establishes a new n-dimensional manifold $X = \{p \in M \mid \rho(p) \geq 0\}$, so that the motion of point p is restricted to one side of a hypersurface ∂X of M, defined by $\rho = 0$ and known as the boundary of X. This makes possible the application of results from the theory of manifolds with a boundary [16]. First, among all smooth vector fields on X, only those tangent to ∂X are allowable. Moreover, the metric and the connection (affinities) are virtually unaffected at points away from the boundary, but they are affected significantly at points near the boundary [7].

The presence of equality motion constraints is expressed in the general form.

$$\dot{\psi}^R \equiv a_I^R(q) v^I = 0, I = 1, \ldots, n \text{ and } R = 1, \ldots, k. \tag{3}$$

When a constraint is holonomic, the corresponding equation becomes $\phi^R(q) = 0$. Then, the equations of motion are obtained by

$$\underline{h}^* \equiv \underline{h}_M^* - \underline{h}_C^* = \underline{0}, \tag{4}$$

in place of Eq. (1), where.

$$\underline{h}_C^* = \sum_{R=1}^{k} h_R a_I^R \underline{\tilde{e}}^I \text{ with } h_R = (\overline{m}_{RR} \dot{\lambda}^R)^{\cdot} + \overline{c}_{RR} \dot{\lambda}^R + \overline{k}_{RR} \lambda^R - \overline{f}_R. \tag{5}$$

The convention on repeated indices does not apply to index R, while the quantities $\overline{m}_{RR}$, $\overline{c}_{RR}$, $\overline{k}_{RR}$, and $\overline{f}_R$ are determined by the constraints (for details, see [17]). Also,

$$\underline{h}_M^* = h_I \underline{\tilde{e}}^I \text{ with } h_I = (g_{IJ} v^J)^{\cdot} - \Lambda_{LI}^K g_{KJ} v^J v^L - f_I \tag{6}$$

Finally, substitution of Eqs. (5) and (6) into (4) leads to a set of n second-order ODEs in the $n + k$ unknowns $q^{I'}$ and λ^R. The formulation is completed after including the k equations of the constraints (3), which are also put eventually in a second-order ODE form, providing a natural stabilization effect on the constraints. Namely,

$$g_R = (\overline{m}_{RR} \dot{\psi}^R)^{\cdot} + \overline{c}_{RR} \dot{\psi}^R = 0 \text{ or } g_R = (\overline{m}_{RR} \dot{\phi}^R)^{\cdot} + \overline{c}_{RR} \dot{\phi}^R + \overline{k}_{RR} \phi^R = 0, \tag{7}$$

for a nonholonomic and a holonomic constraint, respectively [17].

In the absence of significant friction effects, the dominant dynamics during the contact phase is captured by a single ODE with form

$$(\overline{g}_{11}v^1)^{\cdot} - \overline{\Lambda}_{11}^1 \overline{g}_{11} v^1 v^1 - \overline{f}_1 = 0, \tag{8}$$

along the direction of a special coordinate x^1, starting from the boundary, with a direction normal to it [7]. All terms in Eq. (8) are of order $O(1/x^1)$, while the terms in the remaining equations of motion are $O(1)$. This separation of scales in the equations of motion is exploited to avoid stiffness problems during numerical integration. Finally, the introduction of friction effects causes the appearance of two more equations.

$$(\overline{g}_{22}v^2)^{\cdot} - \overline{f}_2 = 0 \text{ and } (\overline{g}_{33}v^3)^{\cdot} - \overline{f}_3 = 0, \tag{9}$$

representing action along the tangential directions of the physical space. Then, Eqs. (8) and (9) constitute a set of three coupled ODEs (Ordinary Differential Equations), capturing the dominant dynamic behavior, which is confined in the three-dimensional cotangent distribution in the configuration space affected by the contact action [7].

3 Numerical Integration of the Equations of Motion

The presence of strongly nonlinear terms in the equations of motion and the numerical stiffness in these equations necessitate application of a numerical integration method. In this work, a new time-stepping method is developed, which is set up in a way to avoid them. The basic steps of this numerical procedure are briefly summarized next.

In the absence of impact and friction, a three-field augmented Lagrangian formulation is available [6]. The process starts by putting the equations of motion in a suitable weak form, leading to an efficient temporal discretization. When an impact is detected, some modifications are in order. Figure 1 is used to illustrate the scenario followed in such a case. Specifically, at time t_m, the system configuration in the physical space is represented by a point p_m, which lies in the interior X^o of the
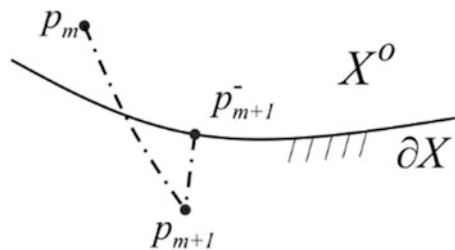
Fig. 1 Illustration of the total action of the return map

constrained configuration manifold X. At the next time t_{m+1}, the new configuration point p_{m+1} is located outside X, indicating that an impact event may have occurred during the current time step. In practice, this is verified by using a suitable contact detection algorithm, which determines both the location of the contact point and the normal contact direction in the physical space [18]. The next step is to return to a point on the boundary ∂X, representing the configuration of the system where the impact event took place. This is achieved through the development and application of an appropriate return mapping (for details, see [6]). Similar maps have also been constructed in other situations [11, 12]. In this work, this step is performed with more care, by taking into account that the configuration manifold M is nonflat [13], in general, as explained briefly next.

The boundary ∂X is locally convex. Then, the task of returning from p_{m+1} back to a point on the boundary ∂X in a unique way is reduced to finding the autoparallel starting from point p_{m+1} and ending on ∂X, having the shortest length. The iterations are stopped when the final point of this process, say p_{m+1}^-, is located inside X and sufficiently close to the boundary ∂X. Symbolically, these can be represented by

$$p_{m+1}^- = \mathfrak{P}\left(p_{m+1}\right). \tag{10}$$

The overall equations of motion are solved in a block-wise manner. This means that, assuming a fixed position, the system's velocity is calculated, followed by an update to the positions. If the updated positions lead the system's position outside the boundary, an iteration of the return map procedure takes place, driving the position back to the boundary. This is repeated until both the overall residual and the returned positions converge. The final point p_{m+1}^- lies inside the constrained configuration manifold X, sufficiently close to the boundary ∂X. This result provides the updated values at the position level and the equations of motion are solved to provide the corresponding velocity vector $\underline{v}_{m+1}^-$. If this vector points toward the interior X^o of the constrained manifold, the solution process continues without considering occurrence of an impact. However, if vector $\underline{v}_{m+1}^-$ points toward the boundary ∂X of the constrained manifold, its value is used as a preimpact velocity and the solution process is continued in the next step, which leads to determination of the postimpact state, say $(p_{m+1}^+, \underline{v}_{m+1}^+)$.

The equations of motion within the boundary layer are first put in a weak form. For their numerical discretization, special curves are selected to approximate the natural trajectory near the boundary of manifold X. The first natural choice is the autoparallel curves [15]. However, using such curves for the geometric discretization of the natural trajectory inside the boundary layer leads to numerical problems since the value of v^1 takes relatively small values. Consequently, such curves tend to become tangent and stay close to the boundary ∂X. For this reason, a higher order set of curves on X is considered, giving rise to a geometric cubic spline on manifold X in the vicinity of the boundary ∂X [19]. The numerical integration advances up until the value of x_{m+1}^1 becomes equal to the value of the boundary layer width b. At that point, the velocity of the system is first transformed

from the *x*-coordinate system, which was employed for performing the evaluations within the boundary layer, back to the original *q*-coordinate system. In addition, the position of the system is assumed to remain virtually equal to the preimpact position $\underline{q}_{m+1}^-$. Using these values as initial conditions, the numerical integration continues according to the process described for impact-free motions.

4   Numerical Results

A set of numerical results is presented next, illustrating the accuracy and effectiveness of the new methodology, applied to systems with rigid members. First, dynamics of the classical problem of a ball bouncing on a rigid plane is considered. Next, a more involved problem, considering impact dynamics of a die with a rigid ground, is examined.

4.1   Bouncing Sphere

The first example is a rigid sphere of unit mass and radius $r = 0.1$ m, bouncing on a rigid plane. The sphere motion starts with a zero initial velocity when its center is located at a height $h = 0.5$ m, under the action of gravity, with gravity acceleration $g = -9.81$ m/s^2. The position of its center is determined by a single Cartesian coordinate, χ^1, having its origin on the ground. For this case, an analytical solution is available for both the impact-free phase and the impact phase.

Some typical results are presented in Fig. 2, obtained by employing the new time-stepping scheme. First, Fig. 2a shows the histories of the vertical displacement of the lowest point of the sphere, for two values of the kinematic coefficient of restitution e. Likewise, Fig. 2b depicts the histories of the corresponding mechanical energies. As expected, there is no energy dissipation for the value $e = 1$, corresponding to an elastic impact and leading to an infinite number of contact events. However, this picture changes for $e = 0.8$, leading to a gradual loss of mechanical energy at each impact. This is demonstrated by Fig. 2b and is reflected by the decreasing amplitude of the displacement in Fig. 2a.

The results of Fig. 2 were compared and found to be in virtual coincidence with the results from the exact solution, in both the free and the impact phases. For example, Fig. 3 presents results determined during the first impact phase. These results were obtained for a value of a maximum penetration ratio $\delta = 0.8$. In general, the values of the parameters δ and e are needed in order to determine the force $\overline{f}_1$ in Eq. (8). First, Fig. 3a shows histories of the vertical displacement of the sphere, while Fig. 3b depicts the corresponding histories of the vertical velocity, determined for $e = 1$. The results obtained reveal that application of the new numerical discretization procedure leads to a virtual coincidence with the analytical solution by using a relatively small number of time steps. More specifically, this was
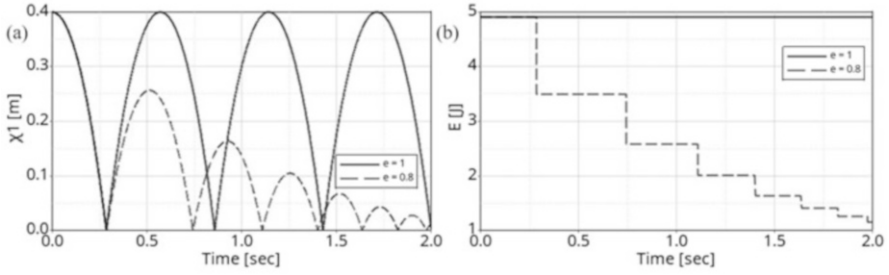
Fig. 2 A sphere bouncing on a rigid ground: (**a**) vertical displacement and (**b**) mechanical energy, for $e = 1$ and 0.8
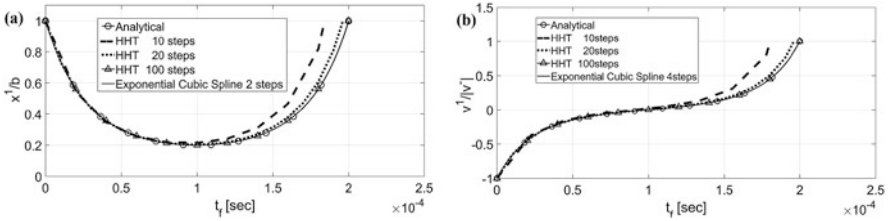
Fig. 3 Histories obtained during the first impact phase by the analytical solution, the new geometric method and the HHT-α method for (**a**) the vertical displacement and (**b**) the vertical velocity of the sphere, with $e = 1$

achieved by using only two time steps in the case examined. Next, the emphasis was put on a comparison with classical integration methods. In particular, results obtained by employing the HHT-α method are presented next. Several values of the numerical dissipation parameter α were tried, in the range $0 \leq \alpha \leq 1/3$, with $\beta = (1 + \alpha)^2/4$ and $\gamma = \alpha + 1/2$. The results presented next were obtained for $\alpha = 0$, but no noticeable differences were detected for other values of α. First, it was found that the impact phase interval should be split to at least seven steps, before the HHT-α method can run and yield a solution. Also, quite a large number of time steps are required in order for the numerical results to be of a reasonable accuracy. This comparison illustrates that the new integration method is more effective, since it leads to the exact solution with a much bigger time step. This, instead, is attributed to the fact that the new method exploits the geometric properties of the system examined during its dynamic evolution in the impact phase.

4.2 Die Tossing

The next set of numerical results was obtained for the motion of a die thrown over a rigid ground. This motion is viewed from a coordinate system $Oxyz$, which is fixed on the ground. It is affected by gravity, acting along the negative z-axis and
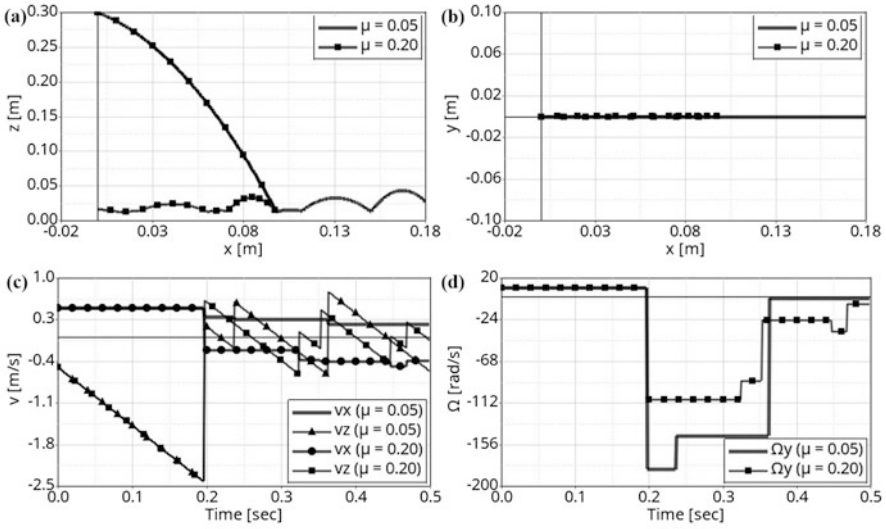
Fig. 4 Plane die tossing. Projection of the trajectory of the cube center on: (**a**) the vertical Ozx and (**b**) the horizontal plane Oxy. Histories of (**c**) the velocity components of the mass center and (**d**) the angular velocity of the cube

involves frictional impacts. The die considered is a homogeneous rigid cube, with a mass of 0.016 kg and edge length of 0.02 m. It starts from a position above the ground, with the cube edges parallel to the axes of the $Oxyz$ coordinate system. Moreover, the initial position and velocity are chosen to satisfy two scenarios. In the first, the cube executes a planar motion, taking place in the vertical plane Ozx. In the second scenario, the initial conditions are modified so that the cube exhibits a spatial motion and hits the ground with one of its vertices. In all cases, the value of the kinematic restitution parameter was chosen as $e = 0.5$ [20]. Moreover, the maximum penetration ratio was selected as $\delta = 0.20$, while the value of the coefficient of friction between the die and the ground was chosen as $\mu = 0.05$ or 0.20.

First, in the results presented in Fig. 4, the initial position of the cube center is at (0, 0, 0.3) m, while its initial velocity is (0.5, 0, −0.5) m/s. Moreover, the initial angular velocity of the cube is (0, 10, 0) rad/s. These initial conditions lead to a subsequent planar motion of the cube. First, Fig. 4a shows the projection of the trajectory executed by the cube center of mass on the vertical plane Ozx for the values selected for μ. Likewise, Fig. 4b shows the projection of the same trajectory on the horizontal plane Oxy. Then, the histories of the two nonzero velocity components of the mass center are shown in Fig. 4c. Finally, the history of angular velocity of the cube is presented in Fig. 4d. A remarkable result is that, for the case with $\mu = 0.20$, the cube starts moving in the opposite direction than it was thrown after the first impact, as it becomes clear by Figs. 4a and c.

Next, in the set of results presented in Fig. 5, the initial position of the cube center and its initial velocity are kept the same as in the previous case. However,
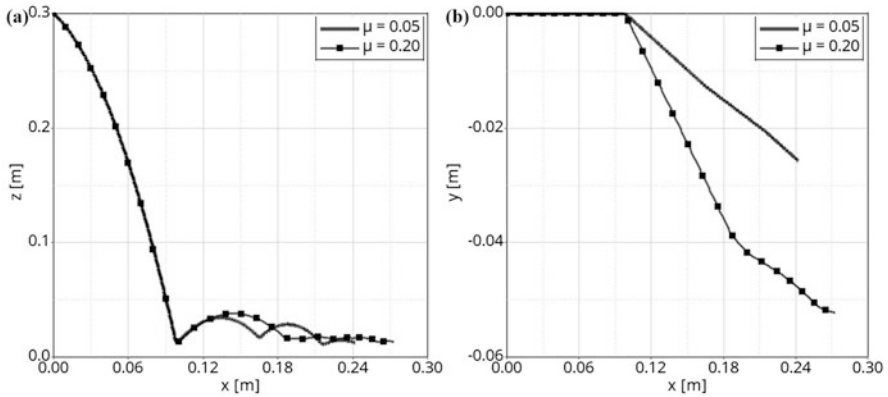
Fig. 5 Spatial die tossing. Projection of the trajectory of the cube center on (**a**) the vertical plane *Ozx* and (**b**) the horizontal plane *Oxy*

an angular velocity component about the *x*-axis is added, so that the initial cube angular velocity is (10, 10, 0) rad/s. These initial conditions lead to a general spatial motion of the cube. First, Fig. 5a shows the projection of the trajectory executed by the cube center of mass on plane *Ozx* for the two values selected for the coefficient of friction. Likewise, Fig. 5b shows the projection of the same trajectory on plane *Oxy*.

Finally, the emphasis was placed on investigating the dynamics of the cube arising during the first impact phase. Specifically, the history of the tangential velocity component V_x of the cube contact point is presented in Fig. 6a, while the corresponding histories of the tangential velocity V_y and the normal velocity V_z are included in Fig. 6b, for the plane motion of the die. Similar results were also obtained for the spatial motion of the die. In all cases examined, a smooth change is observed to occur in the velocity components throughout the impact phase.

5 Synopsis and Extensions

In the first part of this study, the basic steps of a new time stepping scheme were presented, for capturing dynamics of multibody systems involving impacts and friction. A vital part of that scheme was the development of a new return map. This need arises from the fact that the configuration space of the class of systems examined is non-Euclidean. Specifically, application of this map in order to return a point from the outside to the boundary of the constrained manifold, defined by a unilateral constraint, leads to a curve with the shortest length among a special set of curves emanating from the outer point. In addition, the final curve selected crosses the boundary of the allowable motions in a normal way. In this way, the new return
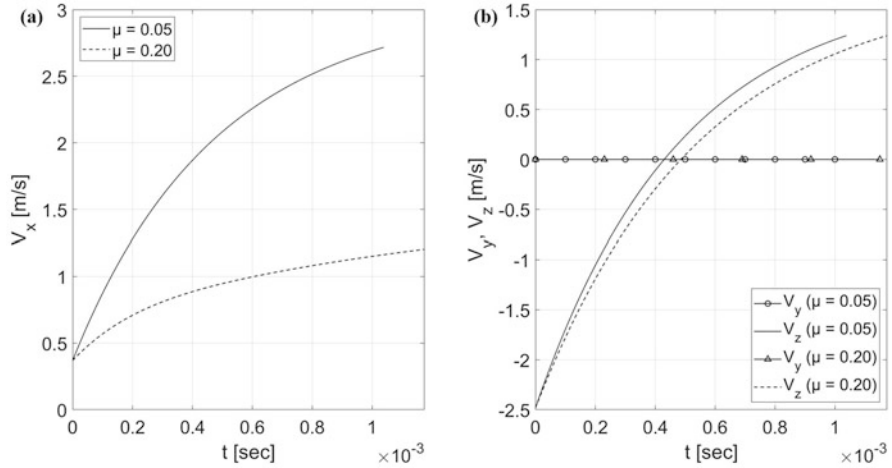
Fig. 6 Velocity components of the cube contact point during the first impact phase: (**a**) tangential component V_x (plane motion), (**b**) tangential component V_y and normal component V_z (plane motion)

map is a generalization of the classical orthogonal projection operation performed in Euclidean spaces. Based on these ideas, a complete numerical algorithm was set up, providing the means to capture dynamics of multibody systems involving a single impact and several bilateral constraints. Finally, the accuracy and effectiveness of the new time stepping scheme were verified in the second part of this work, by presenting numerical results for two representative mechanical examples.

The methodology developed can be applied to discrete mechanical systems subject to a set of bilateral motion constraints and a single unilateral constraint. A first possible step is to extend it in order to cover cases involving permanent contact. In such cases, the contact is modeled as a bilateral constraint up to a point where separation of the contacting bodies occurs. Another useful extension of this study is to cases with multiple impacts. This is a theoretically challenging subject, involving consideration of configuration manifolds with corners, having a significant engineering importance [5, 16].

References

1. S. Natsiavas, Analytical modeling of discrete mechanical systems involving contact, impact and friction. ASME J. Appl. Mech. Reviews **71**, 050802–050825 (2019)
2. T.A. Laursen, *Computational Contact and Impact Mechanics: Fundamentals of Modeling Interfacial Phenomena in Nonlinear Finite Element Analysis* (Berlin, Springer, 2002)
3. P. Wriggers, *Computational Contact Mechanics*, 2nd edn. (Springer, Berlin, 2006)
4. W.J. Stronge, *Impact Mechanics* (Cambridge Univ Press, Cambridge, UK, 2000)

5. B. Brogliato, *Nonsmooth Mechanics: Models, Dynamics and Control*, 3rd edn. (Springer, London, 2016)
6. N. Potosakis, E. Paraskevopoulos, S. Natsiavas, Application of an augmented Lagrangian approach to multibody systems with equality motion constraints. Nonlinear Dyn. **99**, 753–776 (2020)
7. S. Natsiavas, E. Paraskevopoulos, A boundary layer approach to multibody systems involving single frictional impacts. ASME J. Comput. Nonlinear Dyn. **14**, 011002–011016 (2019)
8. E. Paraskevopoulos, P. Passas, S. Natsiavas, A novel return map in non-flat configuration spaces of multibody systems with impact. Int. J. Solids Struct. **202**, 822–834 (2020)
9. J.J. Moreau, Numerical aspects of the sweeping process. Comput. Methods Appl. Mech. Eng. **177**, 329–349 (1999)
10. V. Acary, B. Brogliato, Numerical methods for nonsmooth dynamical systems, lecture notes, in *Appl. Comput. Mech. 35*, (Springer, Berlin, 2008)
11. A.E. Giannakopoulos, The return mapping method for the integration of friction constitutive relations. Comput. Struct. **32**, 157–167 (1989)
12. J.C. Simo, T.J.R. Hughes, *Computational Inelasticity* (Springer, New York, 1998)
13. C. Udriste, *Convex Functions and Optimization Methods on Riemannian Manifolds, Mathematics and its Applications*, vol 297 (Kluwer Academic Publishers Group, Dordrecht, 1994)
14. A.M. Bloch, *Nonholonomic Mechanics and Control* (Springer, NY, 2003)
15. T. Frankel, *The Geometry of Physics: An Introduction* (Cambridge University Press, New York, 1997)
16. R.B. Melrose, *The Atiyah-Patodi-Singer Index Theorem, Research Notes in Mathematics, Vol. 4* (A.K. Peters Ltd., Wellesley, MA, 1993)
17. S. Natsiavas, E. Paraskevopoulos, A set of ordinary differential equations of motion for constrained mechanical systems. Nonlinear Dyn. **79**, 1911–1938 (2015)
18. A. Pournaras, F. Karaoulanis, S. Natsiavas, Dynamics of mechanical systems involving impact and friction using a new contact detection algorithm. Int. J. Non-Linear Mech. **94**, 309–322 (2017)
19. M. Camarinha, F. Silva Leite, P. Crouch, On the geometry of Riemannian cubic polynomials. Differential Geometry Appl. **15**, 107–135 (2001)
20. M. Kapitaniak, J. Strzalko, J. Grabski, T. Kapitaniak, The three-dimensional dynamics of the die throw. Chaos **22**, 047504–047508 (2012)

A Generalized Spring-Loaded Inverted Pendulum Model for Legged Robots

Guangrong Chen, Sheng Guo, Bowen Hou, Junzheng Wang, and Huafeng Lu

1 Introduction

Spring-loaded inverted pendulum (SLIP) model has been verified to be an effective model to simulate the locomotion of legged robots [1], including walking and running [2] and bipeds and quadrupeds [3].

Unfortunately, the analytical solutions of SLIP model are difficult to obtain since there exist some coupling terms or nonlinear stance equations. Schwind and Koditschek proposed Picard iterative method to generate closed-form approximations to the return map associated with a family of non-integrable Hamiltonian systems [4]. Geyer et al. derived an approximate solution in elementary functions assuming a small angular sweep and a small spring compression during stance [5]. Arslan et al. introduced a novel gravity correction scheme that extends on one of the more recent analytic approximations to the SLIP dynamics and achieves good accuracy even for highly non-symmetric trajectories [6]. Yu et al. presented a novel method of perturbation to obtain the analytic approximate solution to the SLIP dynamics in stance phase with considering the effect of gravity from sagittal hopping [7] into spatially running [1].

However, the classical SLIP model only considers the axial force along the equivalent leg. This disadvantage limits the potential of SLIP when it is employed

G. Chen (✉) · S. Guo · H. Lu
Robotics Research Center, Beijing Jiaotong University, Beijing, China
e-mail: grchen@bjtu.edu.cn

B. Hou
Beijing Engineering and Technology Research Center of Rail Transit Line Safety and Disaster Prevention, Beijing, China

J. Wang
State Key Laboratory of Intelligent Control and Decision of Complex Systems, School of Automation, Beijing Institute of Technology, Beijing, China

to do the locomotion control for legged robots even though it is simple. Therefore, an improved SLIP model considering both axial and tangential forces along the equivalent leg should be issued to tap the potential of modified SLIP model.

2 Generalized SLIP Model

2.1 SLIP Model

The classical SLIP model is shown in Fig. 1a. The mathematical model of SLIP model contains flight and stance phases, as shown in Fig. 1b.

The dynamics of flight phase of SLIP model can be simplified as

$$
\begin{cases}
\ddot{x} = 0 \\
\ddot{z} = -g
\end{cases}
\tag{1}
$$

where x and z are the horizontal and vertical position of CoM of SLIP model, respectively, and g is the acceleration of gravity.

The dynamics of stance phase of SLIP model can be expressed as

$$
\begin{cases}
\ddot{\alpha} = \frac{g \sin \alpha - 2\dot{\rho}\dot{\alpha}}{\rho} \\
\ddot{\rho} = \rho \dot{\alpha}^2 - g \cos \alpha - \frac{k}{m}(\rho - \rho_0)
\end{cases}
\tag{2}
$$

where α is the angle between the leg and the vertical direction, ρ is the leg length, m is the mass of load, and k is the stiffness of spring.

As shown in Fig. 1a, the equivalent system of classical SLIP model is constructed between the point of hip joint (H) and the foot end effector (E). However, the actual spring is configured between the point of ankle joint (A) and point E, as shown in Fig. 2a. There exists an inconsistence in the direction of spring between the
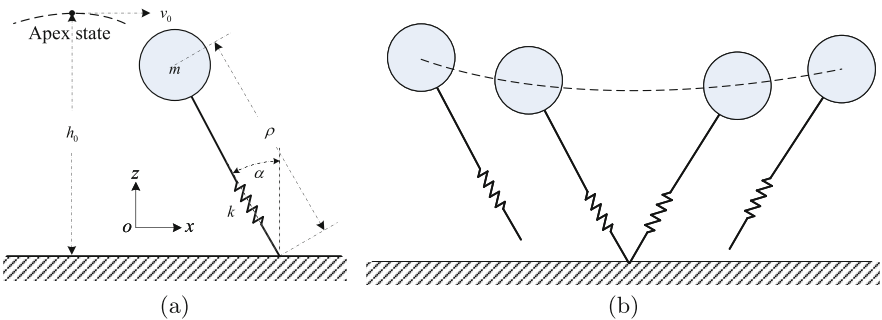
Fig. 1 The SLIP model and its flight and stance phases. (**a**) The classical SLIP model. (**b**) The flight and stance phases of SLIP model
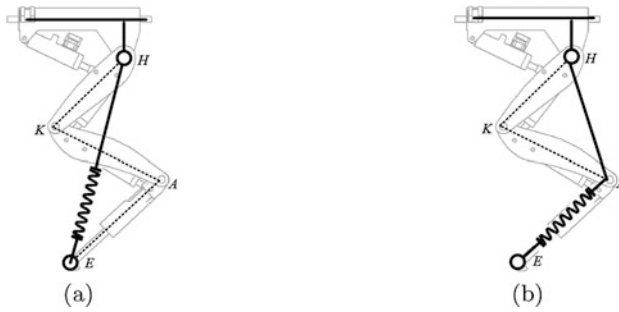
Fig. 2 The equivalent systems of classical and articulated/generalized SLIP models. (**a**) The equivalent system of classical SLIP. (**b**) The equivalent system of articulated/generalized SLIP

Fig. 3 The proposed GSLIP model
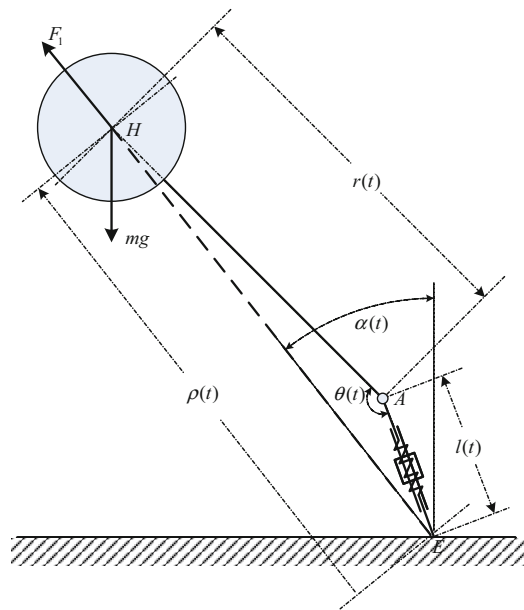
equivalent and actual springs. Thus, the equivalent system of articulated/generalized SLIP is proposed to handle this problem. The GSLIP model is shown in Fig. 2b.

Based on the SLIP model in Fig. 1a and its mathematical model in (1) and (2), the proposed GSLIP model can be shown in Fig. 3, where $r(t)$ is the length of link HA, $l(t)$ is the length of spring or AE, $\rho(t)$ is the length of HE or the equivalent leg length, $\theta(t)$ is the joint angle $\angle HAE$, $\alpha(t)$ is the contact angle of GSLIP model, mg is the gravity of load, and F_l is the axial force of load along HE.

Since the dynamics of flight phase of GSLIP model is the same as that of SLIP model, it can also be written as (1). As for the dynamics of stance phase of GSLIP model, it can be reformulated as

$$
\begin{cases}
\ddot{\alpha} = \dfrac{g\sin\alpha - 2\dot{\rho}\dot{\alpha}}{\rho} \\
\ddot{\rho} = \rho\dot{\alpha}^2 - g\cos\alpha - \dfrac{k}{m}\dfrac{\rho\left(r\cos\theta + \sqrt{\rho^2 - r^2\sin^2\theta} - l_0\right)}{\sqrt{\rho^2 - r^2\sin^2\theta}}
\end{cases}
\tag{3}
$$

Compare (3) with (2), the main difference is the second equation, which mainly reflects the differential equation of axial length.

2.2 Normalization

Defining the time scale as s, the dimensionless time $\bar{t}$ and the actual time t under the time scale s satisfy $t = s\bar{t}$. Under the definition, the differential operation $\frac{d}{dt}(\bullet)$ can be represented as $\frac{d}{dt}(\bullet) = \frac{1}{s}\frac{d}{d\bar{t}}(\bullet) = \frac{1}{s}(\bullet)'$, where $(\bullet)'$ is the differential operation under the new time scale s. Through this definition, the dimensionless form of the parameters in (3) can be written as follows:

$$
\begin{aligned}
\rho &= \rho_0\bar{\rho}, & \dot{\rho} &= \frac{\rho_0\bar{\rho}'}{s}, & \ddot{\rho} &= \frac{\rho_0\bar{\rho}''}{s^2} \\
r &= r_0\bar{r}, & \dot{r} &= \frac{r_0\bar{r}'}{s}, & \ddot{r} &= \frac{r_0\bar{r}''}{s^2} \\
\alpha &= \bar{\alpha}, & \dot{\alpha} &= \frac{\bar{\alpha}'}{s}, & \ddot{\alpha} &= \frac{\bar{\alpha}''}{s^2} \\
\theta &= \bar{\theta}, & \dot{\theta} &= \frac{\bar{\theta}'}{s}, & \ddot{\theta} &= \frac{\bar{\theta}''}{s^2}
\end{aligned}
\tag{4}
$$

where $\bar{\bullet}$ is the dimensionless form of $\bullet$, and $\bar{\bullet}'$ and $\bar{\bullet}''$ are the dimensionless derivative and the second derivative of $\bar{\bullet}$, respectively.

The choice of time scale s directly affects the simplicity of GSLIP model in dimensionless form. Therefore, based on the Froude constant used by Alexander [8], the time scale is set as $s = \sqrt{\frac{\rho_0}{g}}$. Substituting (4) into (3), it yields

$$
\begin{cases}
\bar{\rho}\bar{\alpha}'' + 2\bar{\rho}'\bar{\alpha}' - \sin\bar{\alpha} = 0 \\
\bar{\rho}'' = \bar{\rho}\bar{\alpha}'^2 - \cos\bar{\alpha} - \dfrac{k\rho_0}{mg}\dfrac{\bar{\rho}\left(\frac{r_0}{\rho_0}\bar{r}\cos\theta + \sqrt{\bar{\rho}^2 - \left(\frac{r_0}{\rho_0}\right)^2\bar{r}^2\sin^2\theta} - \frac{l_0}{\rho_0}\right)}{\sqrt{\bar{\rho}^2 - \left(\frac{r_0}{\rho_0}\right)^2\bar{r}^2\sin^2\theta}}
\end{cases}
\tag{5}
$$

Define the dimensionless stiffness of spring of leg as $\bar{k} = \frac{k\rho_0}{mg}$, and define the ratio of leg length as $\eta = \frac{r_0}{\rho_0}$. Based on the geometric relationships, it yields

$$\frac{l_0}{\rho_0} = \eta \cos \theta + \sqrt{1 - \eta^2 \sin^2 \theta} \tag{6}$$

Substituting (6) into (5), it yields

$$\begin{cases} \bar{\rho} \bar{\alpha}'' + 2 \bar{\rho}' \bar{\alpha}' - \sin \bar{\alpha} = 0 \\ \bar{\rho}'' = \bar{\rho} \bar{\alpha}'^2 - \cos \bar{\alpha} - \bar{k} \dfrac{\bar{\rho} \left(\eta \bar{r} \cos \theta + \sqrt{\bar{\rho}^2 - \eta^2 \bar{r}^2 \sin^2 \theta} - \eta \cos \theta - \sqrt{1 - \eta^2 \sin^2 \theta} \right)}{\sqrt{\bar{\rho}^2 - \eta^2 \bar{r}^2 \sin^2 \theta}} \end{cases} \tag{7}$$

3 Approximate Analytic Solutions to GSLIP Model

Some reasonable assumptions and simplifications should be set to make it easier to get the approximate analytic solutions even through these assumptions and simplifications will increase the errors of solutions.

Assumption 1 Small spring compression: if the spring compression in the stance phase is assumed as a zeroth-order small quantity, then $0 < \frac{l_0 - l}{l_0} \ll 1$ and $0 < \frac{\rho_0 - \rho}{\rho_0} \ll 1$.

Assumption 2 Small scanning angle: if the scanning angle of leg in the stance phase is assumed as a first-order small quantity, then $\sin \theta \approx \theta$ and $\cos \theta \approx 1$.

Assumption 3 Conservation of angular momentum: this assumption is used in the process of solving the axial length, but not in the process of solving the scanning angle, so as to improve the accuracy of the solution in the case of asymmetric scanning angle.

3.1 Approximations for Axial Length $\bar{\rho}$

Based on Assumption 3, the angular momentum is constant when solving the axial length $\bar{\rho}$ and it can be defined as $p_\theta = \bar{\rho}^2 \bar{\alpha}'$. Then, it yields $\bar{\rho} \bar{\alpha}'^2 = \frac{p_\theta^2}{\bar{\rho}^3}$. Combining Assumption 2, the second equation of (7) can be rewritten as

$$\bar{\rho}'' = \frac{p_\theta^2}{\bar{\rho}^3} - 1 - \bar{k} \frac{\bar{\rho} \left(\delta \left(\bar{r}, \eta, \theta \right) + \sqrt{\bar{\rho}^2 - \tau \left(\bar{r}, \eta, \theta \right)} \right)}{\sqrt{\bar{\rho}^2 - \tau \left(\bar{r}, \eta, \theta \right)}} \tag{8}$$

where $\delta \left(\bar{r}, \eta, \theta \right) = \eta \bar{r} \cos \theta - \eta \cos \theta - \sqrt{1 - \eta^2 \sin^2 \theta}$ and $\tau \left(\bar{r}, \eta, \theta \right) = \eta^2 \bar{r}^2 \sin^2 \theta$ are known parameters.

Based on Assumption 1, the Taylor series expansion of $\frac{1}{\bar{\rho}^3}$ at $\bar{\rho} = 1$ can be written as

$$\left.\frac{1}{\bar{\rho}^3}\right|_{\bar{\rho}=1} = 1 - 3\left(\bar{\rho} - 1\right) + o\left(\left(\bar{\rho} - 1\right)^2\right) \tag{9}$$

And, the Taylor series expansion of $\dfrac{\bar{\rho}}{\sqrt{\bar{\rho}^2 - \tau(\bar{r}, \eta, \theta)}}$ at $\bar{\rho} = 1$ can be written as

$$\left.\frac{\bar{\rho}}{\sqrt{\bar{\rho}^2 - \tau(\bar{r}, \eta, \theta)}}\right|_{\bar{\rho}=1} = \frac{1}{\sqrt{(1-\tau)^3}} - \frac{\tau}{\sqrt{(1-\tau)^3}}\bar{\rho} + o\left(\left(\bar{\rho} - 1\right)^2\right) \tag{10}$$

Omitting the higher order terms in (9) and (10), and substituting them into (8), it yields

$$\bar{\rho}'' = \left(-3p_\theta^2 - \bar{k} + \frac{\bar{k}\delta\tau}{\sqrt{(1-\tau)^3}}\right)\bar{\rho} + \left(4p_\theta^2 - 1 - \frac{\bar{k}\delta}{\sqrt{(1-\tau)^3}}\right) \tag{11}$$

Solving the second-order ordinary differential equation shown in (11), the expression of axial length $\bar{\rho}$ of GSLIP model can be obtained as

$$\bar{\rho} = \bar{\rho}_m + a\cos\left(\omega_0 \bar{t} + \varphi\right) \tag{12}$$

where $\omega_0 = \sqrt{\bar{k} + 3p_\theta^2 - \dfrac{\bar{k}\delta\tau}{\sqrt{(1-\tau)^3}}}$ is the vibration frequency in the axial

direction, $\bar{\rho}_m = \dfrac{\left(4p_\theta^2 - 1 - \frac{\bar{k}\delta}{\sqrt{(1-\tau)^3}}\right)}{\sqrt{\bar{k} + 3p_\theta^2 - \frac{\bar{k}\delta\tau}{\sqrt{(1-\tau)^3}}}}$ is the mean value of vibration, and $a =$

$\sqrt{\left(1 - \bar{\rho}_m\right)^2 + \left(\dfrac{\bar{\rho}_{TD}'}{\omega_0}\right)^2} > 0$ and $\varphi = \arctan\left(\dfrac{\bar{\rho}_{TD}'}{(\bar{\rho}_m - 1)}\right) \in [0, \pi]$ are, respectively, the amplitude and initial phase of vibration. And, a and φ are determined by initial values of stance phase.

3.2 Approximations for Scanning Angle $\bar{\alpha}$

Based on Assumption 2, the first equation in (7) can be rewritten as

$$\bar{\alpha}'' + \frac{2\bar{\rho}'}{\bar{\rho}}\bar{\alpha}' - \frac{1}{\bar{\rho}}\bar{\alpha} = 0 \tag{13}$$

where the axial length $\bar{\rho}$ and its differential $\bar{\rho}'$ have been solved and can be regarded as known variables.

In order to solve (13), the first-order differential term $\bar{\alpha}'$ should be eliminated first. Introducing auxiliary variables $p\left(\bar{t}\right)$ and $u\left(\bar{t}\right)$ to satisfy

$$\bar{\alpha}\left(\bar{t}\right) = p\left(\bar{t}\right)u\left(\bar{t}\right), \tag{14}$$

(13) can be rewritten as

$$pu'' + \left(2p' + \frac{2\bar{\rho}'p}{\bar{\rho}}\right)u' + \left(p'' + \frac{2\bar{\rho}'p'}{\bar{\rho}} - \frac{1}{\bar{\rho}}\right)u = 0 \tag{15}$$

Letting the coefficient of the first-order differential term u' be zero, it yields

$$p' + \frac{\bar{\rho}'p}{\bar{\rho}} = 0 \tag{16}$$

Integrating (16) can obtain

$$p = \frac{c}{\bar{\rho}} \tag{17}$$

where c is an undetermined constant, and p is an auxiliary variable. Taking $c = 1$ directly and substituting (17) into (15) yield

$$u'' = \left(1 + \frac{\bar{\rho}''}{\bar{\rho}}\right)u \tag{18}$$

Substituting the axial length (12) into (18) yields

$$u'' - \left(1 - \frac{\omega_0^2 \varepsilon \cos \psi}{1 + \varepsilon \cos \psi}\right)u = 0 \tag{19}$$

where $\varepsilon = \frac{a}{\bar{\rho}_m}$, $\psi = \omega_0 \bar{t} + \varphi$. Noting that the definition of ε owns real clear physical meaning, which is the length ratio of axial vibration amplitude of CoM of GSLIP model to the equilibrium position of vibration. Based on Assumption 1, it can be found that ε is a small quantity. Since $\cos \psi$ is bounded, the Taylor series expansion of the fraction containing ε in (19) at $\varepsilon = 0$ can be written as

$$\frac{\varepsilon \cos \psi}{1 + \varepsilon \cos \psi} = \varepsilon \cos \psi + o\left(\varepsilon^2\right) \tag{20}$$

Ignoring the second-order small quantity in (20) and substituting (20) into (19), the differential equation with Mathieu function format can be obtained as

$$u'' - \left(1 - \omega_0^2 \varepsilon \cos \psi\right)u = 0 \tag{21}$$

Using the conventional perturbation method and choosing ε as the perturbation parameter, the power series perturbation solution of the above Mathieu equation

(21) can be obtained as

$$u\left(\bar{t}, \varepsilon\right) = u_0\left(\bar{t}\right) + \varepsilon u_1\left(\bar{t}\right) + \varepsilon^2 u_2\left(\bar{t}\right) + \cdots \tag{22}$$

where u_i is the perturbed solution of each order, which is corresponding to the perturbation parameter ε.

Substituting (22) into (21) and combining the terms with the same order of ε, it yields

$$\begin{cases} \varepsilon^0 : u''_0 - u_0 = 0 \\ \varepsilon^1 : u''_1 - u_1 = -\omega_0^2 u_0 \cos\psi \\ \varepsilon^2 : \cdots \end{cases} \tag{23}$$

The general solution of u_0 can be obtained directly through the differential equation corresponding to the zero power of ε and that is

$$u_0 = c_1 e^{\bar{t}} + c_2 e^{-\bar{t}} \tag{24}$$

where the coefficients c_1 and c_2 are determined by initial values.

Substituting (24) into the first power expression in (23), it yields

$$u_1 = \frac{\omega_0^2 c_1}{\omega_0^2 + 4} e^{\bar{t}} \left(\cos\psi - \frac{2}{\omega_0}\sin\psi\right) + \frac{\omega_0^2 c_2}{\omega_0^2 + 4} e^{-\bar{t}} \left(\cos\psi + \frac{2}{\omega_0}\sin\psi\right) \tag{25}$$

In order to balance the simplicity and the accuracy of approximate analytical solutions, the second-order and other higher order terms in (23) are ignored, and only the zeroth-order term (24) and the first-order term (25) are retained. As thus, the final perturbation solution of Mathieu equation (22) is obtained as

$$\begin{aligned} u &= u_0 + \varepsilon u_1 \\ &= c_1 e^{\bar{t}} + c_2 e^{-\bar{t}} + \frac{\omega_0^2 c_1}{\omega_0^2 + 4} e^{\bar{t}} \left(\cos\psi - \frac{2}{\omega_0}\sin\psi\right) + \frac{\omega_0^2 c_2}{\omega_0^2 + 4} e^{-\bar{t}} \left(\cos\psi + \frac{2}{\omega_0}\sin\psi\right) \end{aligned} \tag{26}$$

When the initial state of GSLIP model at the touchdown $\{\bar{\rho}_{TD}, \bar{\rho}_{TD}', \alpha_{TD}, \alpha_{TD}'\}$ is known, the undetermined coefficients in (26) can be obtained as

$$\begin{bmatrix} \sigma_{11} & \sigma_{12} \\ \sigma_{21} & \sigma_{22} \end{bmatrix} \begin{bmatrix} c_1 \\ c_2 \end{bmatrix} = \begin{bmatrix} \bar{\rho}_{TD}\alpha_{TD} \\ \bar{\rho}_{TD}'\alpha_{TD} + \bar{\rho}_{TD}\alpha_{TD}' \end{bmatrix} = \begin{bmatrix} u_{TD} \\ u_{TD}' \end{bmatrix} \tag{27}$$

where

$$\sigma_{11} = 1 + \frac{\omega_0^2 \varepsilon}{\omega_0^2 + 4} \left(\cos \varphi - \frac{2}{\omega_0} \sin \varphi \right)$$
$$\sigma_{12} = 1 + \frac{\omega_0^2 \varepsilon}{\omega_0^2 + 4} \left(\cos \varphi + \frac{2}{\omega_0} \sin \varphi \right)$$
$$\sigma_{21} = 1 + \frac{\omega_0^2 \varepsilon}{\omega_0^2 + 4} \left(- \cos \varphi - \left(\omega_0 + \frac{2}{\omega_0} \right) \sin \varphi \right) \tag{28}$$
$$\sigma_{22} = -1 + \frac{\omega_0^2 \varepsilon}{\omega_0^2 + 4} \left(\cos \varphi - \left(\omega_0 + \frac{2}{\omega_0} \right) \sin \varphi \right)$$

Substituting (28) into (27) yields

$$c_1 = \frac{\sigma_{22} u_{TD} - \sigma_{12} u_{TD}{}'}{\sigma_{11} \sigma_{22} - \sigma_{12} \sigma_{21}}$$
$$c_2 = \frac{-\sigma_{21} u_{TD} + \sigma_{11} u_{TD}{}'}{\sigma_{11} \sigma_{22} - \sigma_{12} \sigma_{21}} \tag{29}$$

Combining (14), (17), and (26), the approximate analytic solutions for scanning angle $\bar{\alpha}$ can be obtained as

$$\bar{\alpha} \left(\bar{t} \right) = \frac{u \left(\bar{t} \right)}{\bar{\rho} \left(\bar{t} \right)} \tag{30}$$

Thus, approximate analytic solutions to the GSLIP model are (12) and (30).

4 Simulation Results and Performance Analysis

The system parameters of SLIP and GSLIP models are shown in Table 1.

Table 1 System parameters of SLIP and GSLIP models

Parameter	Symbol	Value
Mass of load	m	80 kg
Equivalent leg length	ρ_0	1 m
Joint angle	θ	135°
Spring length	l_0	0.1 m
Ratio of leg length	η	0.89
Acceleration of gravity	g	9.8 m/s^2
Spring stiffness	k	$20 \sim 50$ kN/m
Initial apex height of CoM	h_0	$0.95 \sim 1.05$ m
Initial forward velocity	v_0	$2 \sim 6$ m/s
Contact angle	α	$5 \sim 25°$

4.1   Prediction Performance of Approximations

Taking the relative error of the apex state of system in flight phase, including forward velocity v_{apex} and apex height of CoM h_{apex}, as the main index to evaluate the prediction performance of approximate solution, it yields

$$e_{apex}\left(s_{appr}\right) = \frac{\left|s_r - s_{appr}\right|}{s_r} \times 100\% \tag{31}$$

where e_{apex} is the relative error of prediction of apex state of flight phase, s_{appr} is the prediction of apex state of approximate solution (forward velocity v_{apex} or apex height h_{apex}), s_r is the prediction of apex state of (2) or (3) without approximation, and it is calculated by the fourth-order Runge–Kutta method. The relative errors of SLIP model in (2) and GSLIP model in (3) are calculated via the index (31), respectively.

For two system models, the relative errors of forward velocity v_{apex} and apex height h_{apex} are calculated separately. And, the statistics of $e_{apex}\left(v_{appr}\right)$ and $e_{apex}\left(h_{appr}\right)$, error mean μ_e, standard deviation σ_e, and maximum prediction error M_e, are calculated as

$$\begin{aligned}
\mu_e &= \frac{1}{N}\sum_{j=1}^{N} e_{apex-j} \\
\sigma_e &= \sqrt{\frac{1}{N}\sum_{j=1}^{N}\left(e_{apex-j} - \mu_e\right)^2} \\
M_e &= \max\left(e_{apex-j}\right)
\end{aligned} \tag{32}$$

where N is the size of test groups. A different test is with different initial states: k, h, v_0, and α, as shown in Table 1.

4.2   Simulation Results

The overall errors of two models for apex state prediction are shown in Fig. 4.

It can be found that both the models can achieve high prediction performance of apex state in the approximations by using perturbation method, and the mean errors of predictions are all smaller than 5%, which provides a high prediction accuracy for locomotion control for legged robot. By comparison between SLIP model and GSLIP model, the error mean μ_e, standard deviation σ_e, and maximum prediction error M_e, of the relative errors of apex state of the approximations based on GSLIP model, including forward velocity v_{apex} and apex height h_{apex}, are all smaller than those based on SLIP model. That means that the approximations based on the GSLIP model have higher prediction accuracy than the approximations based on SLIP model. That is, the prediction accuracy of approximations is model-dependent.
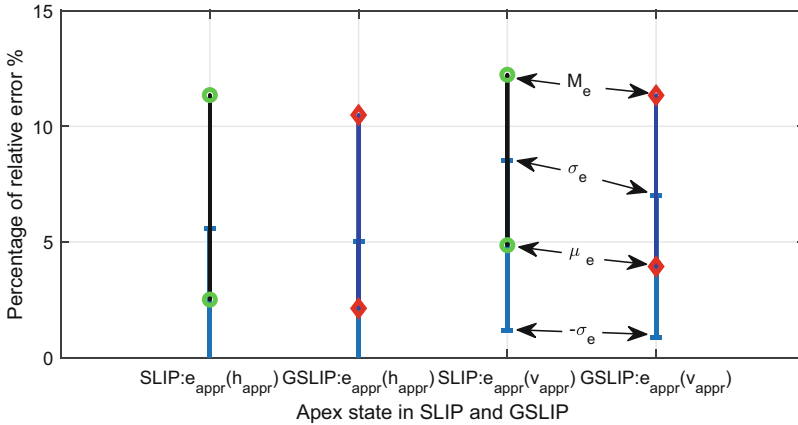
Fig. 4 The overall errors of two models for apex state prediction

5 Conclusions

In this chapter, an approximate analytic solution to a generalized SLIP model is proposed and investigated for legged robots. Firstly, an articulated/generalized SLIP model is proposed, in which both axial and tangential forces along the equivalent leg are considered. Secondly, the analytical approximation of proposed GSLIP model is addressed through the method of perturbation. Thirdly, the prediction performances of approximations of proposed GSLIP model are discussed. Finally, comparative simulations show that the GSLIP model would achieve better prediction performance than the classical SLIP model. This research provides an insight for the locomotion control of hydraulic legged robots. Future works will focus on the advantages and disadvantages between GSLIP and classical SLIP.

References

1. H. Yu, H. Gao, Z. Deng, Toward a unified approximate analytical representation for spatially running spring-loaded inverted pendulum model. IEEE Trans. Robot. **37**, 691–698 (2020)
2. G. Chen, J. Wang, S. Wang, J. Zhao, W. Shen, Compliance control for a hydraulic bouncing system. ISA Trans. **79**, 232–238 (2018)
3. H. Yudong, Research on servo control and stable walking for a hydraulic quadruped robot. PhD thesis, Beijing Institute of Technology (2016)
4. W.J. Schwind, D.E. Koditschek, Approximating the stance map of a 2-DOF monoped runner. J. Nonlinear Sci. **10**(5), 533–568 (2000)

5. H. Geyer, A. Seyfarth, R. Blickhan, Spring-mass running: simple approximate solution and application to gait stability. J. Theor. Biol. **232**(3), 315–328 (2005)
6. O. Arslan, U. Saranli, O. Morgul, An approximate stance map of the spring mass hopper with gravity correction for nonsymmetric locomotions, in *2009 IEEE International Conference on Robotics and Automation* (IEEE, Piscataway, 2009), pp. 2388–2393
7. H. Yu, M. Li, P. Wang, H. Cai, Approximate perturbation stance map of the slip runner and application to locomotion control. J. Bionic Eng. **9**(4), 411–422 (2012)
8. R. Alexander, Optimization and gaits in the locomotion of vertebrates. Physiol. Rev. **69**(4), 1199–1227 (1989)

On the Mobility of a Robot-Trajectory Process

Friedrich Pfeiffer

1 Introduction

A machine possesses a kinematic and a dynamic structure, so does the process. One art of engineering consists in matching both as optimally possible. An example is a robot following a prescribed path by one degree of freedom only, namely the curvilinear coordinate s along that path. All robot degrees of freedom are projected to this single path coordinate coming out with a linear system of ordinary differential equations of motion in the square of the path velocity. Many applications of trajectory planning and comparisons with measurements were carried out through [1–5]. By analyzing various types of processes, we find an astonishingly large number being defined by one trajectory only, from manufacturing to transport technologies. Therefore, the one-dimensional robot example represents some amount of generality.

2 General Equations

For technological processes, kinematics and possibly some forces are known, and the machine dynamics is unknown. This requires a multibody dynamical model of the machine with the necessity, that all machine components follow the prescribed process. Constraints resulting from that requirement will be expressed by some gradients $(\frac{\partial z}{\partial s})$ and $(\frac{\partial s}{\partial z})$, where z and s are machine and process coordinates, respectively. We start with models for the machine, represented by a robot.

F. Pfeiffer (✉)
Lehrstuhl fuer Angewandte Mechanik, TU-Muenchen, Munich, Germany
e-mail: friedrich.pfeiffer@tum.de, http://www.amm.mw.tum.de

In a first step and for later definitions, we consider Jourdain's principle of lost power for a rigid multibody system [6]

$$\sum_{i=1}^{n} \delta \underbrace{\begin{pmatrix} \boldsymbol{v}_{O'} \\ \omega \end{pmatrix}^{T}}_{\dot{z}^{T}} \left\{ \underbrace{\begin{pmatrix} m\boldsymbol{I} & m\tilde{\boldsymbol{r}}_{O'S}^{T} \\ m\tilde{\boldsymbol{r}}_{O'S} & \Theta_{O'} \end{pmatrix}}_{\boldsymbol{M}} \underbrace{\begin{pmatrix} \boldsymbol{a}_{O'} \\ \dot{\omega} \end{pmatrix}}_{\ddot{z}} + \underbrace{\begin{pmatrix} m\tilde{\omega}\tilde{\omega}\boldsymbol{r}_{O'S} \\ \tilde{\omega}\Theta_{O'}\omega \end{pmatrix}}_{f^{g}} \right.$$

$$\left. - \underbrace{\begin{pmatrix} \boldsymbol{F}^{e} + \boldsymbol{F}^{a} + \boldsymbol{F}^{p} \\ \boldsymbol{M}_{O'}^{e} + \boldsymbol{M}_{O'}^{a} + \boldsymbol{M}_{O'}^{p} \end{pmatrix}}_{f^{e}+f^{a}+f^{p}} - \underbrace{\begin{pmatrix} \boldsymbol{F}^{c} \\ \boldsymbol{M}_{O'}^{c} \end{pmatrix}}_{f^{c}} \right\}_{i} = 0 \qquad (1)$$

($\boldsymbol{v}_{O'}$ and ω are translational and rotational velocities, $\boldsymbol{a}_{O'}$ and $\dot{\omega}$ translational and rotational accelerations, m, $\boldsymbol{I}$, $\Theta_{O'}$ masses and mass moments of inertia, O' and S reference point and center of gravity, and f^{g}, f^{e}, f^{a}, f^{p}, f^{c} gyroscopic, applied, driving, process and constraint forces and torques).

The virtual velocities $\delta\dot{z}$ cannot be chosen arbitrarily, but they must satisfy side conditions in form of constraints. In the following, we shall focus on non-holonomic and scleronomic constraints, which means no loss of generality [2]. Following the ideas of Jacobi [7] in the form given in [8], we come out with the well-known *non-minimal form* as a typical example [9, 10].

$$\boldsymbol{M}\ddot{z} + \boldsymbol{f} - \boldsymbol{f}^{c} = \boldsymbol{0}, \quad \text{with} \quad \boldsymbol{f} = \boldsymbol{f}^{g} - \boldsymbol{f}^{e} - \boldsymbol{f}^{a} - \boldsymbol{f}^{p}, \qquad \boldsymbol{f}^{c} = -\boldsymbol{W}(z,t)\lambda,$$

$$\dot{\Phi} = \boldsymbol{W}^{T}\dot{z} + \bar{\boldsymbol{w}} = \boldsymbol{0}, \quad \ddot{\Phi} = \boldsymbol{W}^{T}\ddot{z} + \left[\left(\frac{d\boldsymbol{W}^{T}}{dt} \right)\dot{z} + \left(\frac{d\bar{\boldsymbol{w}}}{dt} \right) \right] = \boldsymbol{W}^{T}\ddot{z} + \hat{\boldsymbol{w}} = \boldsymbol{0},$$

$$(2)$$

where $\ddot{\Phi}$ follows from $\frac{d}{dt}(\boldsymbol{W}^{T}\dot{z} + \bar{\boldsymbol{w}})$. The mass matrix is positive definite and symmetric. The constraints $\dot{\Phi}$ may include the machine and process constraints Φ, but they may also include the machine constraints alone or the process constraints alone depending on the specific model under consideration. The non-minimal coordinates depend on the minimal ones $z = z(\boldsymbol{q})$. Therefore, $\dot{z} = (\frac{\partial z}{\partial \boldsymbol{q}})\dot{\boldsymbol{q}}$, which gives for the constraints of equations (2) the well-known relation $\frac{\partial \dot{\phi}}{\partial \dot{\boldsymbol{q}}} = \boldsymbol{W}^{T}(\frac{\partial z}{\partial \boldsymbol{q}}) = (\frac{\partial z}{\partial \boldsymbol{q}})^{T}\boldsymbol{W} = \boldsymbol{0}$, very convenient for eliminating constraint forces (example $\boldsymbol{F}_{i}$ from Fig. 4 and [8]).

In many cases of practical relevancy, the minimal coordinates $\boldsymbol{q}$ are known. For this case, we project the vector z directly to $\boldsymbol{q}$ and in a second step from $\boldsymbol{q}$ to the path coordinates (see [1, 3–5, 11]). With the help of the derivatives

$$\dot{z} = \left(\frac{\partial z}{\partial \boldsymbol{q}} \right)\dot{\boldsymbol{q}}, \quad \ddot{z} = \left[\frac{\partial}{\partial \boldsymbol{q}} \left(\frac{\partial z}{\partial \boldsymbol{q}} \right)\dot{\boldsymbol{q}} \right]\dot{\boldsymbol{q}} + \left(\frac{\partial z}{\partial \boldsymbol{q}} \right)\ddot{\boldsymbol{q}}, \quad \dot{\boldsymbol{q}} = \left(\frac{\partial \boldsymbol{q}}{\partial s} \right)\dot{s}, \quad \ddot{\boldsymbol{q}} = \left(\frac{\partial \boldsymbol{q}}{\partial s} \right)\ddot{s} + \left(\frac{\partial^{2} \boldsymbol{q}}{\partial s^{2}} \right)\dot{s}^{2},$$

$$(3)$$

and following equations (2), we come out with

$$M_q\ddot{q} + \left(\frac{\partial z}{\partial q}\right)^T M\left[\frac{\partial}{\partial q}\left(\frac{\partial z}{\partial q}\right)\dot{q}\right]\dot{q} + \left(\frac{\partial z}{\partial q}\right)^T (f^g - f^e - f^a - f^p) = 0,$$

$$M_q = \left[\left(\frac{\partial z}{\partial q}\right)^T M\left(\frac{\partial z}{\partial q}\right)\right]. \tag{4}$$

These are the equations of motion in terms of the minimal coordinates q. Using the relations (3) and applying additionally the abbreviations $\frac{dq}{ds} = q'$, $\ddot{q} = \frac{1}{2}q'(\dot{s}^2)' + q''(\dot{s}^2)$, and $\ddot{s} = \frac{d\dot{s}}{dt} = (\frac{d\dot{s}}{ds})\dot{s} = \frac{1}{2}(\dot{s}^2)'$, we may project them directly onto the given trajectory, which comes out with the following form:

$$A(s)(\dot{s}^2)' + B(s)(\dot{s}^2) + C(s) = T(s), \qquad (A, B, C, T) \in R^{n_q},$$

$$B(s) = M_q q'' + (\frac{\partial z}{\partial q})^T M[\frac{\partial}{\partial q}(\frac{\partial z}{\partial q})q']q',$$

$$A(s) = \frac{1}{2}M_q q', \qquad C(s) = f_q^e, \qquad T(s) = f_q^a, \tag{5}$$

with the abbreviations:

$$f_q = (\frac{\partial z}{\partial q})^T (f^g - f^e - f^a - f^p)_q, \qquad f_q^g = (\frac{\partial z}{\partial q})^T M[\frac{\partial}{\partial q}(\frac{\partial z}{\partial q})\dot{q}]\dot{q}. \tag{6}$$

Note that f_q^g is already part of the coefficient $B(s)$. Equation (5) represents a quadratic form being linear in $(\dot{s}^2)$. Note also that Eq. (4) represents only one form to produce the first equation (5), there exist related ways to come from (2) to (5) with a gradient $(\frac{\partial z}{\partial q})$ expressed by W [2, 8].

A remark concerning Cartesian and joint spaces: the strength of the method presented consists in a tool for design and layout, where the Cartesian space of the machine components represents simply geometrical position and orientation as known for example from CAD analysis. For dynamical analysis, the minimal coordinates, for example the joint space of robots, concentrate dynamics to a minimum as given by the constraints. This is not a must, but an advantage.

For numerical simulations, it sometimes makes sense to use dimensionless magnitudes. Referring all geometrical parameters to some length, all masses to some mass and time to gravity and length give $\bar{z} = \frac{z}{l}$, $\bar{s} = \frac{s}{l}$, $\bar{q} = q$, $\bar{m}_i = \frac{m_i}{m}$, $\bar{t} = \sqrt{\frac{g}{l}}t$, $\bar{f} = \frac{f}{mg}$, $l = \sqrt{\sum_j l_j^2}$, and $m = \sqrt{\sum_j m_j^2}$. These modifications have to be included into the equations above, which is straightforward.

3   Mobility Space by Ruled Surfaces

The general mobility problem for a machine consists in an initial value problem or in a stationary operation situation, usually accompanied by some performance criteria. Such criteria might be minimum time, minimum energy, maximum mobility, and the like. The solution of this problem is constrained, where the most important constraints are as follows:

The constraining torques or forces are limited, which means (Eq. 5)

$$T_{i,min} \leq [A_i(s)(\dot{s}^2)' + B_i(s)(\dot{s}^2) + C_i(s)] \leq T_{i,max},$$

$$(\dot{s}^2)' = \frac{-B_i(s)(\dot{s}^2) - C_i(s) + \begin{pmatrix} T_{i,max} \\ T_{i,min} \end{pmatrix}}{A_i(s)}, \qquad (\dot{s}^2)_{A=0} = \frac{-C_i(s) + \begin{pmatrix} T_{i,max} \\ T_{i,min} \end{pmatrix}}{B_i(s)}, \tag{7}$$

where the last equation can be seen as an additional constraint. Further possible constraints are the following: the angular or translational velocities of constraining elements may be limited due to some maximum speeds of the drive train components ($\dot{q}_{i,min} \leq [q_i'\dot{s}] \leq \dot{q}_{i,max}$), and the path velocity itself might become constrained by some manufacturing process ($-v_{max} \leq |\mathbf{r}'|\dot{s} \leq +v_{max}$) with the vector $\mathbf{r}$ from the constrained machine element under consideration to a process path point. These relations define together a limiting velocity $\dot{s}_L$ along the path which must not be exceeded:

$$0 \leq (\dot{s}^2) \leq (\dot{s}^2)_L, \quad \text{with} \quad (\dot{s}^2)_L = \min\left[\left(\frac{\dot{q}_{i,max}}{q_i'}\right)^2, \quad \left(\frac{v_{max}}{|\mathbf{r}'|}\right)^2, \quad (\dot{s}^2)_{A=0} \right]. \tag{8}$$

Extremum mobility can be achieved by applying in equations (7) the maximum and minimum torques (forces) ($T_{i,min}, \ T_{i,max}$). Operation at the torque limits takes place for

$$(\dot{s}^2)'_{max} = \frac{-B_i(s)\dot{s}^2 - C_i(s) + T_{i,max}}{A_i(s)}, \quad (\dot{s}^2)'_{min} = \frac{-B_i(s)\dot{s}^2 - C_i(s) - T_{i,min}}{A_i(s)}, \tag{9}$$

which define two straight lines in the $[(\dot{s}^2)', (\dot{s}^2)]$-plane. The altogether ($2f_D$) straight lines ($f_D \leq f$) form a polygon confined at the left side by the axis $(\dot{s}^2) = 0$ and at the right side by the ($T_{i,min}, T_{i,max}$)-straight-lines or by the constraint $(\dot{s}^2)_L$ given by Eq. (8). Without violating the constraints, which may be extended without many problems, motion can take place only within or on the polygons, which contain the following information: the maximum possible velocity $\dot{s}_{max}^2$ and for each point $(\dot{s}^2)$ a maximum and a minimum acceleration or deceleration
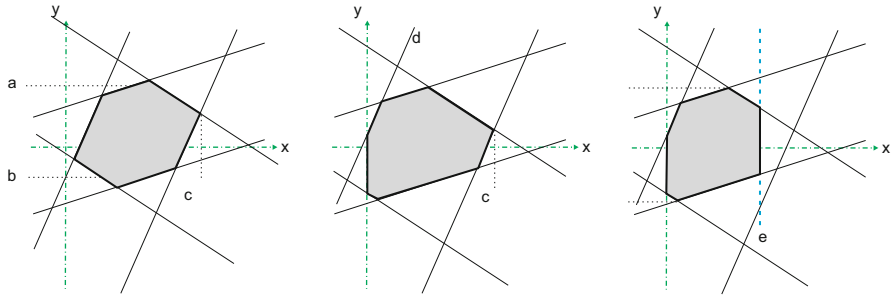
Fig. 1 Polygons of possible motion for s = constant [1, 3]

$[(\dot{s}^2)'_{max}, (\dot{s}^2)'_{min}]$. For finding time-optimal solutions, we have to go along the assemblage of these polygons and generate what we call extremals (Fig. 1).

Combining all polygons for all path points s, we obtain a constrained phase space bounded by ruled surfaces due to the straight-line characteristics of the polygons [12]. We call this phase space motion or mobility space. These polygons appear as plain cuts perpendicular to the s-axis, Fig. 6. The evaluation of these polygons with the help of equations (7) to (9) is difficult. From many trials, a numerical procedure is chosen, being the most efficient at the time being.

4 Example Multi-DOF Robot with Revolute Joints

Kinematics and Initial Conditions We consider a robot with n links and (n+1) revolute joints and a corresponding number of degrees of freedom. These links have the length l_i, the center of mass C_i, and the distance d_i from the link joint i to the center of mass C_i (see Figs. 2 and 3). A typical example with five DOFs is depicted by Fig. 2. The robot can move around a vertical z-axis with an angular coordinate q_0, and each of the links moves in one plane with relative angular coordinates q_i. With respect to the coordinate systems, we shall use an inertial reference.

We project the equations of motion to minimal coordinates. From kinematics, we need the derivatives $(\frac{\partial z}{\partial q})$ and $\left[\left(\frac{\partial}{\partial q}(\frac{\partial z}{\partial q})\dot{q} \right)\dot{q} \right]$, which we evaluate in the following, considering also Eq. (1) and keeping in mind that any $\dot{x} = (x)'\dot{s}$. Additionally, we define

$$_I\dot{z} = (_I\dot{z}_i \ _I\dot{z}_2 ...._I\dot{z}_{n_m})^T, \qquad q = (q_0 \ q_1 \ q_2.........q_{n_q})^T,$$

$$_I\dot{z}_i = (\dot{r}_i^T \ \omega_i^T)^T, \quad \dot{r}_i = (\dot{x} \ \dot{y} \ \dot{z})^T, \quad _B\zeta_i = (\xi \ \eta \ \zeta)^T, \quad \dot{\omega}_i = (\dot{\omega}_x \ \dot{\omega}_y \ \dot{\omega}_z)^T,$$

$$z \in \mathrm{R}^{n_m}, \quad q \in \mathrm{R}^{n_q} \ z_i \in \mathrm{R}^6, \quad r_i \in \mathrm{R}^3, \quad \zeta_i \in \mathrm{R}^3 \ \omega_i \in \mathrm{R}^3. \tag{10}$$
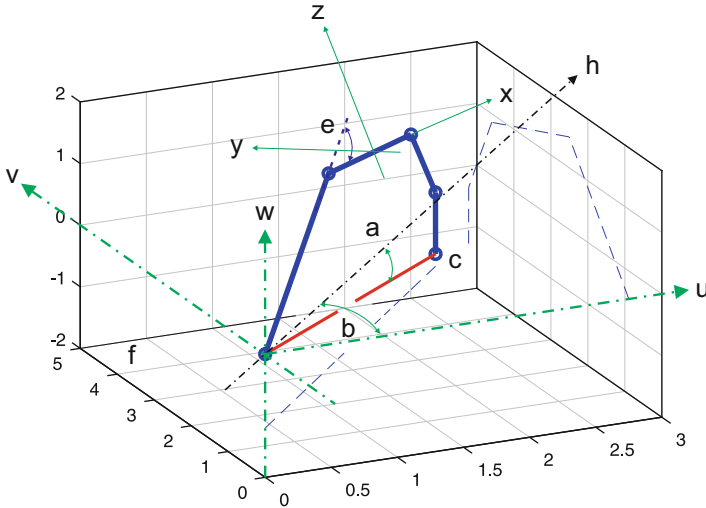
Fig. 2 Geometry of a multi-DOF robot

The Cartesian coordinates z depend on a set of angular joint coordinates q or $\bar{q}$. They represent the minimal coordinates of the system. The indices I and B stand for "inertial" and "body." Two sets of angles are needed, the relative link angles q_i as already defined above and the absolute link angles $\bar{q}_i$ indicated by Fig. 3.

$$\bar{q}_i = \frac{\pi}{2} - \sum_{j=1}^{i} q_j = \bar{q}_{i-1} - q_i, \qquad q_i = \bar{q}_{i-1} - \bar{q}_i, \qquad \bar{q}_0 = \frac{\Pi}{2}. \qquad (11)$$

With these definitions, the joint vectors z_{Ji} and the center of mass vectors z_{Ci} possess the following elements:

$$r_{Ji} = \sum_{j=1}^{i-1} l_j \begin{pmatrix} \cos\bar{q}_j \cos q_0 \\ \cos\bar{q}_j \sin q_0 \\ \sin\bar{q}_j \end{pmatrix}, \quad r_{Ci} = \sum_{j=1}^{i-1} l_j \begin{pmatrix} \cos\bar{q}_j \cos q_0 \\ \cos\bar{q}_j \sin q_0 \\ \sin\bar{q}_j \end{pmatrix} + d_i \begin{pmatrix} \cos\bar{q}_i \cos q_0 \\ \cos\bar{q}_i \sin q_0 \\ \sin\bar{q}_i \end{pmatrix}. \qquad (12)$$

It should be noted that for the rotation around the vertical inertial z_1-axis (Fig. 2), the above vectors are zero, $r_{Ji} = 0$, and $r_{Ci} = 0$. The angular velocities ω_i are determined by the well-known relations $_I\tilde{\omega}_i = \dot{A}_{IB}A_{BI} = \dot{A}_{IB}A_{IB}^T$ with the result [2]

$$_I\omega_i = \begin{pmatrix} -\dot{\bar{q}}_i \sin q_0 \\ +\dot{\bar{q}}_i \cos q_0 \\ \dot{q}_0 \end{pmatrix}, \quad _B\omega_i = \begin{pmatrix} -\dot{q}_0 \sin\bar{q}_i \\ \dot{\bar{q}}_i \\ +\dot{q}_0 \cos\bar{q}_i \end{pmatrix}, \quad A_{IB} = \begin{pmatrix} \cos q_0 \cos\bar{q}_i & -\sin q_0 & \cos q_0 \sin\bar{q}_i \\ \sin q_0 \cos\bar{q}_i & +\cos q_0 & \sin q_0 \sin\bar{q}_i \\ -\sin\bar{q}_i & 0 & \cos\bar{q}_i \end{pmatrix}. \qquad (13)$$
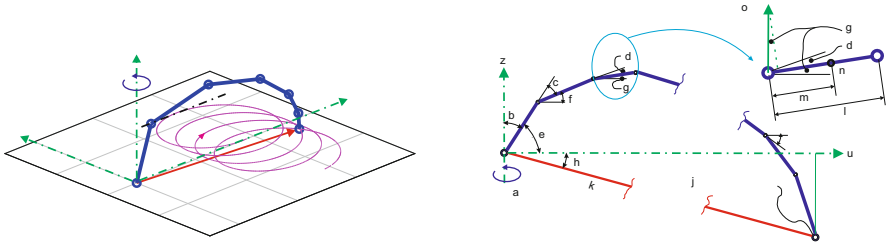
Fig. 3 Robot tracking a path and corresponding joint angles in the u–z plane, see Fig. 2

The matrix A_{IB} follows from two rotations, first around the inertial z-axis and second around the body-fixed y-axis. For i = 1 (first degree of freedom with q_0), the angular velocity is $_I\omega_1 = _B\omega_1 = (0 \ 0 \ \dot{q}_0)^T$.

For positioning the robot end effector at the target point, we apply formula (12) and require (Fig. 3)

$$
r_{Jn} = r(q(s)) = \sum_{j=1}^{n} l_j \begin{pmatrix} \cos \bar{q}_j \cos q_0 \\ \cos \bar{q}_j \sin q_0 \\ \sin \bar{q}_j \end{pmatrix} = \begin{pmatrix} x \\ y \\ z \end{pmatrix}_{trajectory} . \tag{14}
$$

This represents a nonlinear set of equations for the determination of robot coordinates q. It is solved by an optimization algorithm, where for an estimate of the starting position of the robot, all joints are approximately assembled along a circular line.

Gradients and Derivatives Equations (12) and (13) together with (10) form the vector z with its time derivative

$$
_I\dot{z}_{Ji} = \begin{pmatrix} \sum_{j=1}^{i-1} l_j[-\cos q_0 \sin \bar{q}_j \dot{\bar{q}}_j - \sin q_0 \cos \bar{q}_j \dot{q}_0] \\ \sum_{j=1}^{i-1} l_j[-\sin q_0 \sin \bar{q}_j \dot{\bar{q}}_j + \cos q_0 \cos \bar{q}_j \dot{q}_0] \\ \sum_{j=1}^{i-1} l_j[+\cos \bar{q}_j \dot{\bar{q}}_j] \\ -\dot{\bar{q}}_i \sin q_0 \\ +\dot{\bar{q}}_i \cos q_0 \\ \dot{q}_0 \end{pmatrix}, \qquad _I\dot{z}_{J1} = _I\dot{z}_{C1} = \begin{pmatrix} 0 \\ 0 \\ 0 \\ 0 \\ 0 \\ \dot{q}_0 \end{pmatrix} . \tag{15}
$$

According to the definitions in (10) and the relation $(\frac{\partial z}{\partial q}) = (\frac{\partial \dot{z}}{\partial \dot{q}})$, we construct from the time derivatives (Eqs. (15)) and from the formula $\frac{dz_i}{dt} = (\frac{\partial z_i}{\partial q})\dot{q}$ all first and second derivatives being needed in the following.

The gradients above need the first derivative $(q') = (\frac{\partial q}{\partial s})$ and the second one $(q'') = (\frac{\partial^2 q}{\partial s^2})$. The trajectory with the path coordinate s is prescribed, we know all path points, for example in an inertial frame, and we know all derivatives of the path itself. According to the solution of Eqs. (14), we also know the robot angles $q = q(r(q(s)))$, which then allows the application of a numerical procedure

$$q' = \frac{q(s_{i+1}) - q(s_{i-1})}{s_{i+1} - s_{i-1}}, \qquad q'' = \frac{q(s_{i+1}) - 2q(s_i) + q(s_i)}{[\frac{1}{2}(s_{i+1} - s_{i-1})]^2}. \qquad (16)$$

To evaluate the same information for the angle q_0, we start with the (x,y,z)-position of each trajectory point and calculate q_0 and its derivatives (Fig. 2)

$$\tan q_0 = (\frac{y}{x})_{path}, \qquad q_0' = \frac{y'x - yx'}{x^2 + y^2},$$

$$q_0'' = \left[\frac{y''x - yx''}{x^2 + y^2} + 2\frac{x'y'(y^2 - x^2) - xy((y')^2 - (x')^2)}{(x^2 + y^2)^2} \right]. \qquad (17)$$

For our specific case of an n-link robot following a trajectory we determine $q = q(r(s))$ by an optimization algorithm, see above.

Equations of Motion Following Eq. (1), the mass matrix and its derivatives write

$$M_i = \begin{pmatrix} mE & m\tilde{r}_{O'S}^T \\ m\tilde{r}_{O'S} & \Theta_{O'} \end{pmatrix}_i \in R^{n_m, n_m}, \quad \text{with} \quad \Theta_{O'i} = -\sum_{\Delta m}[\tilde{r}_{O'S}\tilde{r}_{O'S}\Delta m]_i$$

$$\frac{dM_i}{dt} = \begin{pmatrix} 0 & m\dot{\tilde{r}}_{O'S}^T \\ m\dot{\tilde{r}}_{O'S} & \dot{\Theta}_{O'} \end{pmatrix}_i, \qquad \frac{d\Theta_{O'i}}{dt} = -\sum_{\Delta m}[\dot{\tilde{r}}_{O'S}\tilde{r}_{O'S} + \tilde{r}_{O'S}\dot{\tilde{r}}_{O'S}]_i \Delta m_i.$$

$$(18)$$

For some link i, we choose as a reference point the center of mass S, which makes $r_{O'S} = 0$ and $\dot{r}_{O'S} = 0$. A special case is the first coordinate q_0, where the reference point O' is the coordinate origin with $(r_{O'S})_i \neq 0$ being the distance to the mass centers of each link i. For this case and according to the equations (12), we have $(r_{O'S})_i = r_{Ci}$. The moment of inertia for the bar-like links alone is $\dot{\Theta}_{Si} = \frac{1}{3}m_i l_i^2[1 - 3(\frac{d}{l}) + 3(\frac{d}{l})^2]$.

As a second step, we have to evaluate the forces and torques considered in an inertial system. The external and applied forces and torques (Fig. 4) are
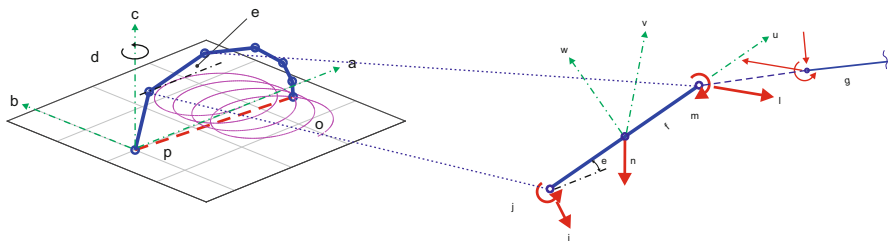
Fig. 4 Trajectory, torques, and forces at link i

$$_I\boldsymbol{f}_i^e = [0 \ \ 0 \ \ (-m_i g) \ \ 0 \ \ 0 \ \ 0]^T, \quad _I\boldsymbol{f}_1^e = \boldsymbol{0}, \qquad _I\boldsymbol{f}_1^a = [0 \ \ 0 \ \ 0 \ \ 0 \ \ 0 \ \ (T_1)]^T,$$

$$_I\boldsymbol{f}_{i>1}^a = [0 \ \ 0 \ \ 0 \ \ (-(T_{a(i+1)} - T_{ai})\sin q_0) \ \ (+(T_{a(i+1)} - T_{ai})\cos q_0) \ \ 0]^T.$$
(19)

According to the relations in (4), the equations of motion (5) will be used for further evaluations.

5 Some Results

Larger scale applications have been performed in the framework of a collaborative research center of the German research foundation [1, 3] and in the USA by Bobrow et al. [4] and Dubowsky and Shiller [5]. These findings cannot be presented here. The following results are given by dimensionless magnitudes, see the end of Sect. 2, for example, $s \to (sl)$, $(\dot{s}^2) \to (gl)(\dot{s}^2)$, $(\dot{s}^2)' \to g(\dot{s}^2)'$. Bars are omitted.

Horizontal Circle Trajectory Evaluating equations (5) for each trajectory point results in Fig. 5, which depicts on the left side the horizontal circle with a robot indication and in addition polygons for six trajectory points. These polygons are scaled equally, giving some feeling for the motion capabilities of the robot around the circle. The points furthest away from the robot base show relatively small motion areas due to the fact that the robot being there in a stretched position has to counterbalance its own weight by the given drives, leaving less power for velocity and acceleration. At the position of start level and of the position 180°, opposite velocities are largest but accelerations diminished. Motion at these points is dominantly performed by the arm drives and not so much by the vertical drive with angular velocity $\dot{q}_0$. Another situation is illustrated by the two points nearest to the robot base, exhibiting large acceleration capabilities and medium-sized velocities. They are dominated by the drive around z with $\dot{q}_0$. The right side of Fig. 5 depicts six polygons as illustrated in the middle graph. Considering more of these polygons gives the left picture of Fig. 6 and arranging them along the path coordinate s the right picture. We call this structure motion or mobility space.

Altogether it is a mountain-like construct generated by straight-lines forming ruled surfaces as an exterior boundary. Motion can only take place on these ruled surfaces originating from the extremum drive torques or forces, or it can take place in the space bounded by these ruled surfaces. For ruled surfaces, see [12] or elsewhere. The motion space of Fig. 6 represents a convenient tool for studying various solution and motion concepts. For example, to go with constant velocity within the free space, we put $(\dot{s}^2)' = 0$ and get immediately the necessary torques from equations (5), namely $\boldsymbol{T}(s) = \boldsymbol{B}(s)(\dot{s}^2) + \boldsymbol{C}(s)$. A more interesting case is that of time-minimum motion requiring to find trajectories on the ruled surfaces only. From Sect. 3, these extremals can be constructed on both sides of the motion space, the side with maximum accelerations $(\dot{s}^2)'_{max}$ containing the max-extremals and the
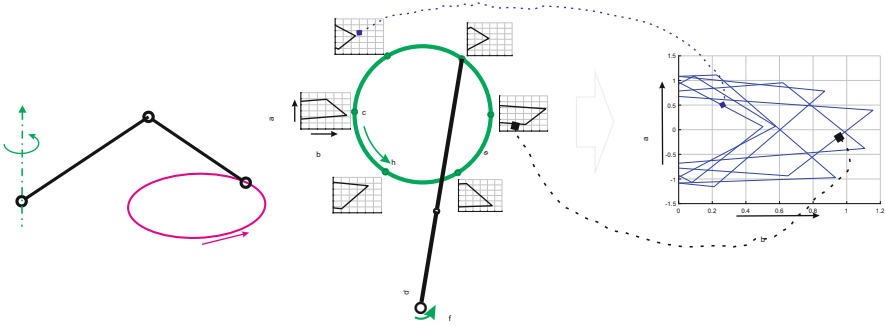
Fig. 5 Motion areas (polygons) along a horizontal circular trajectory
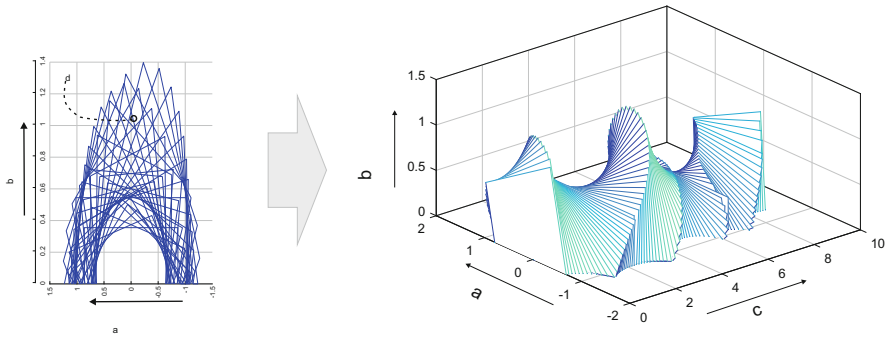
Fig. 6 Generation of motion space

side with minimum accelerations $(\dot{s}^2)'_{min}$ containing the min-extremals. Figure 7 illustrates the projections of these extremals together with the maximum velocities from motion space onto the $[\dot{s}^2 - s]$-plane.

A time-optimal solution, for example, must be composed by several of these extremals for following reasons. Requiring $\dot{s}^2 = 0$ at s=0 and $s = s_F$ makes it necessary to follow a certain combination of extremals for arriving at the final point. Such a procedure needs an integration of the equations of motion along the ruled surfaces and thus from polygon at s to the next one at $(s + \Delta s)$. Integration on polygons excludes normally a progress along the rim of the motion space, exceptions are possible.

Figure 7 illustrates that procedure. The blue extremal at the beginning connects s=0 with the maximum velocity curve at $s \approx 1.7$, and the green extremal at the end connects $s = s_E \approx 8.8$ with $s \approx 6.9$. Note that the blue extremals are on the motion space side with maximum accelerations and the green on the side with minimum accelerations. As a further step, we construct all extremals originating from the saddle point (minimum points) at $s \approx 2.2$ and at $s \approx 6.7$. These are
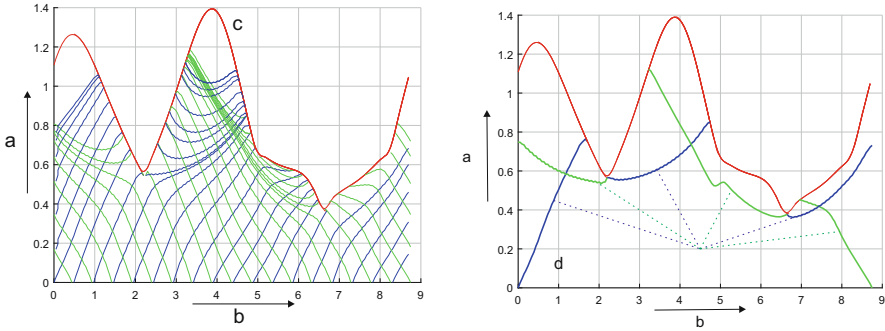
Fig. 7 Field of extremals (blue lines are max-extremal and green lines are min-extremals) and an extremal selection forming the time-optimal solution

points, where at least one coefficient A_i of the equations (5) vanishes, thus allowing a smooth step from one side of the motion space to the other one. The extremals from these points intersect the extremals coming from the beginning and from the end. The ensemble of the six curves forms the time-optimal solution for the motion under consideration, avoiding any limits and integration problems.

Considering the driving torques along the time-optimal solution confirms qualitatively the algorithm, comparisons with measurements in [2].

6 Conclusions

The sense of the method lies in providing some tool for design of machines performing processes, especially with respect to parameter studies. The results give all motion possibilities for the drive structure of the machine, modifications and additional limits or constraints can easily be implemented. Within the resulting motion space, any dynamics might be realized.

For the system considered, multibody equations of motion with constraints are mapped to the trajectories by Jacobians or gradients resulting in quadratic form relations, the solution space of which can be directly evaluated, addressed motion space. As an example, a robot following some path is considered, and the results are discussed.

Further research will concentrate on more general machines including existing problems of mechanical engineering. Evaluation options will be expanded. In detail, the numerical algorithms connected with all aspects of the polygons and the motion space must be improved, especially with respect to numerical stability. Contact forces will be included and constrained forces evaluated. Larger examples will be investigated. Studies up to now confirm the potential of the method concerning design evaluations and design improvements.

References

1. F. Pfeiffer, *Optimal Trajectory Planning for Manipulators*, Systems and Control Encyclopedia (Pergamon Press, Oxford, 1990)
2. F. Pfeiffer, *Mechanical System Dynamics* (Springer, Heidelberg, 2008)
3. R. Johanni, *Optimale Bahnplanung bei Robotern*, Fortschritt-Berchte VDI, Reihe 18, Nr. 51 (VDI-Verlag Düsseldorf, 1988)
4. J.E. Bobrow, S. Dubowsky, J.S. Gibson, Time optimal control of robotic manipulators along specified paths. Int. J. Robot. Res. **4**, 3–17 (1985)
5. S. Dubowsky, Z. Shiller, Optimal dynamic trajectories for robotic manipulators, in *Proc. 5th Symp. on Theory and Practice of Robotics and Manipulators* (1985)
6. F. Pfeiffer, Th. Schindler, *Introduction to Dynamics* (Springer, Berlin, 2015)
7. C.G.J. Jacobi, *Vorlesungen über Dynamik*, ed. by A. Clebsch (Georg Reimer, Berlin, 1866)
8. H. Bremer, *Elastic Multibody Dynamics* (Springer Science +Business Media, B.V., Dordrecht, 2008)
9. A. Shabana, *Dynamics of Multibody Systems*, 3rd ed. (Cambridge University Press, Cambridge, 2005)
10. Chr. Woernle, *Mehrkörpersysteme*, 2 Auflage (Springer, Berlin, 2016)
11. F. Pfeiffer, Motion spaces of machine-process combinations. Arch. Appl. Mech. **89**(10), 2115–2132 (2019). Springer
12. J. Hoschek, *Liniengeometrie* (B. I. Hochschulskripten, Bibliographisches Institut Zürich, 1971)

Multiple Sommerfeld Effects in Vehicle Dynamics

Walter V. Wedig

1 Introduction

Vertical vibrations of a vehicle driven by a constant force on sinusoidal road surface are coupled with its horizontal drift motion effecting that the travel velocity fluctuates around a speed mean. The coupling between both planar motions is caused by the permanent direction change of the contact force to ground along the contour of the road profile. The paper explains the non-linear model of this dynamic problem applying averaging methods to calculate stationary solutions before and after the resonance speed. Numerical integrations are applied to obtain limit cycles around the averaged solutions plotting the changing car acceleration against the true velocity. The stationary solutions are stable in mean when the slope of the force speed characteristic is positive. This leads to the so-called Sommerfeld effect [1] that for a given driving force, the car gets stuck before the resonance speed and can only pass over the resonance to reach stable higher travel velocities by increasing the driving force, considerably [2]. First investigations of velocity jumps and turbulent speeds in non-linear vehicle road dynamics are given by Wedig in [3–7] applying sinusoidal and random road models introduced by Robson and al. in [8–10]. The first-order road model in [11, 12] is extended in [3, 4] to a second-order one which includes sinusoidal models. Blekhman and Kremer studied the same vehicle road system in [13, 14] for the special case of small road excitations to calculate the averaged response of driving cars, only (see also [15]). In [2, 7], these investigations are extended to sinusoidal road surfaces and limit cycles in the phase plane of driving cars.

W. V. Wedig (✉)
KIT - Karlsruher Institut für Technologie, Karlsruhe, Germany

2 Models of Non-linear Vehicle Road Dynamics

Figure 1 shows the applied quarter car model rolling on a wavy road with level z and slope u that generates vertical car vibrations y and coupled velocity v described by

$$\dot{\mathsf{v}} = \left[\omega_1^2 (y - z) + 2D\omega_1 (\dot{y} - \dot{z})\right] \tan \alpha + f/m, \tag{1}$$

$$\ddot{y} + 2D\omega_1 (\dot{y} - \dot{z}) + \omega_1^2 (y - z) = 0, \mathsf{v} = \dot{s}. \tag{2}$$

In Eqs. (1) and (2), $\omega_1^2 = c/m$ determines the natural frequency ω_1 of the vehicle, $2D\omega_1 = b/m$ denotes its damping, f is the driving force which is constant when travelling on way s. The non-linear term in Eq. (1) represents the damper and spring force multiplied by $\tan\alpha$ that takes the horizontal component by $\tan\alpha = dz/ds$.

The road surface is given by $z(s) = z_0 \cos (\Omega s)$ and $u(s) = -z_0 \sin (\Omega s)$ where z_0 is the amplitude of the road level and Ω is the road frequency calculated by the wave length $L = 2\pi/\Omega$. We differentiate level z and slope u with respect to s in order to obtain $dz = -z_0\Omega \sin (\Omega s)ds$ and $du = -z_0\Omega \cos (\Omega s)ds$ that leads to the oscillator

$$\dot{z} = \mathsf{v}\Omega u, \dot{u} = -\mathsf{v}\Omega z. \tag{3}$$

Eq. (3) is obtained when both increments above are divided by dt and ds/dt is replaced by v. Furthermore, $dz/ds = -z_o\Omega \sin (\Omega s) = \Omega u$ is valid so that Eq. (1) reads
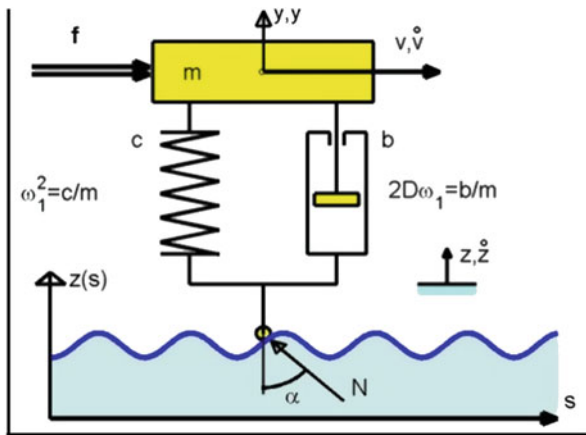
Fig. 1 Quarter vehicle model on a wavy road with vertical vibrations and speed fluctuations

$$\dot{v} = \left[\omega_1^2 (y - z) + 2D\omega_1 (\dot{y} - \dot{z})\right]\Omega u + f/m. \tag{4}$$

Eqs. (2), (3) and (4) describe a five-dimensional problem with the following five unknowns [4, 7]: the horizontal velocity v(t) of the vehicle, its vertical vibration by displacement $y(t)$ and velocity $\dot{y}(t) = \omega_1 x(t)$ and the road level $z(t)$ and slope $u(t)$. For analytical and numerical investigations, it is appropriate to introduce the dimensionless time $\tau = \omega_1 t$ and the related velocity $v = v\Omega/\omega_1$ as well as the co-ordinates $(\bar{z}, \bar{u}) = (z, u)/z_0$ and $(\bar{y}, \bar{x}) = \Omega(y, x)$. The insertion into Eqs. (4) and (3) gives

$$v' + 2D(z_0\Omega)^2\bar{u}^2 v = z_0\Omega(\overline{uy} + 2D\overline{ux}) - (z_0\Omega)^2\,\overline{zu} + f\Omega/c, \tag{5}$$

$$\bar{z}' = v\bar{u}, \bar{u}' = -v\bar{z}, \text{IC.} : \bar{z}(0) = 1, \bar{u}(0) = 0. \tag{6}$$

Derivatives with respect to the time $\tau = \omega_1 t$ are denoted by $(\bullet)'$. The initial conditions (IC) of the related road level and slope are given in Eq. (6). Note that the velocity eq. (5) is determined by the co-variances of the two vibration co-ordinates y and $x = y'$ multiplied by level z and slope u of the road. The road equations in Eq. (6) and the dimensionless first-order form of Eq. (2) are applied to derive the differential equations of these co-variances with the 4x4 matrix of the skew-symmetric form

$$\begin{bmatrix} \overline{zy}' \\ \overline{uy}' \\ \overline{zx}' \\ \overline{ux}' \end{bmatrix} + \begin{bmatrix} 0 & -v & -1 & 0 \\ v & 0 & 0 & -1 \\ 1 & 0 & 2D & -v \\ 0 & 1 & v & 2D \end{bmatrix} \begin{bmatrix} \overline{zy} \\ \overline{uy} \\ \overline{zx} \\ \overline{ux} \end{bmatrix} = z_0\Omega \begin{bmatrix} 0 \\ 0 \\ \bar{z}^2 + 2Dv\overline{zu} \\ \overline{zu} + 2Dv\bar{u}^2 \end{bmatrix}. \tag{7}$$

Since the related level and slope of the road are given by $\bar{z} = \cos(v\tau)$ and $\bar{u} = -\sin(v\tau)$, averaging methods can be applied to Eqs. (7) and (5) by introducing $\overline{zu} = 0$ and $\bar{z}^2 = \bar{u}^2 = 1/2$ that leads to time-invariant co-variances in Eq. (7). The insertion of these co-variances into Eq. (5) gives the driving force in dependence on the averaged speed, as follows:

$$f\Omega/c = (z_0\Omega)^2 \frac{Dv^5}{\left(1 - v^2\right)^2 + (2Dv)^2}, v = v\Omega/\omega_1. \tag{8}$$

In Fig. 2, the driving force (8) is marked by red color and plotted against the related velocity $v = v\Omega/\omega_1$ for the damping $D = 0.2$ and the road level $z_o\Omega = 1$. Note that the loss of energy per time in the damper is balanced by the driving force times speed.
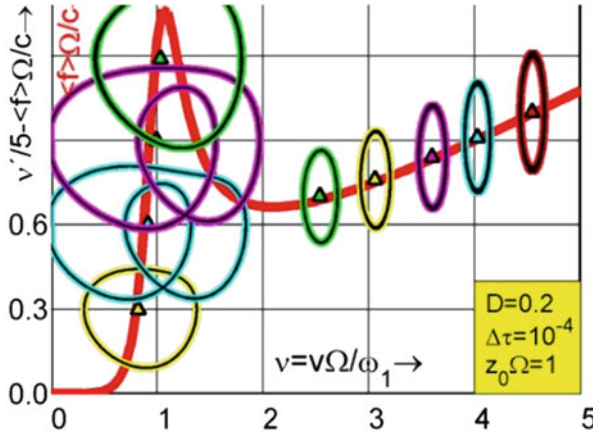
Fig. 2 Limit cycles of acceleration versus travel velocity around driving speed mean

3 Stabilized Integration by Means of Polar Co-ordinates

To improve numerical integration [2, 7] in Eqs. (5), (6) and (7), the polar co-ordinates $\overline{z} = \overline{r} \cos\varphi$ and $\overline{u} = \overline{r} \sin\varphi$ are introduced into the road eqs. (6) that leads to

$$\overline{r}' = 0, \overline{r} = 1, \varphi' = -v. \tag{9}$$

Obviously, the related radius $\overline{r}$ is integrated to $\overline{r} = 1$ and the derivative φ' of the polar angle φ is equal to the negative travel speed v. Both results are inserted to get

$$v' + 2D(z_0\Omega)^2\overline{u}^2 v = z_0\Omega\,(\overline{uy} + 2D\overline{ux}) - (z_0\Omega)^2 \sin\varphi \, \cos\varphi + f\Omega/c, \tag{10}$$

$$
\begin{bmatrix} \overline{zy}' \\ \overline{uy}' \\ \overline{zx}' \\ \overline{ux}' \end{bmatrix} +
\begin{bmatrix} 0 & -v & -1 & 0 \\ v & 0 & 0 & -1 \\ 1 & 0 & 2D & -v \\ 0 & 1 & v & 2D \end{bmatrix}
\begin{bmatrix} \overline{zy} \\ \overline{uy} \\ \overline{zx} \\ \overline{ux} \end{bmatrix}
= z_0\Omega
\begin{bmatrix} 0 \\ 0 \\ \cos^2\varphi + 2Dv \, \sin\varphi \, \cos\varphi \\ \sin\varphi \, \cos\varphi + 2Dv \sin^2\varphi \end{bmatrix}
\tag{11}
$$

Numerical integration of Eqs. (9), (10) and (11) is performed by means of Euler schemes applying the time step $\Delta\tau = 10^{-4}$. Figure 3 shows a first result of periodic limit cycles marked by yellow black line and plotted in the plane of the true travel velocity and acceleration. The latter is scaled by the factor 0.3 and shifted from the zero axis to the driving force $f\Omega/c$ marked by red line. This result is obtained for the driving force $f\Omega/c = 0.6$, the road level $z_o\Omega = 0.9$ and the damping $D = 0.2$. The numerical integration is started with an initial velocity marked by a blue square and
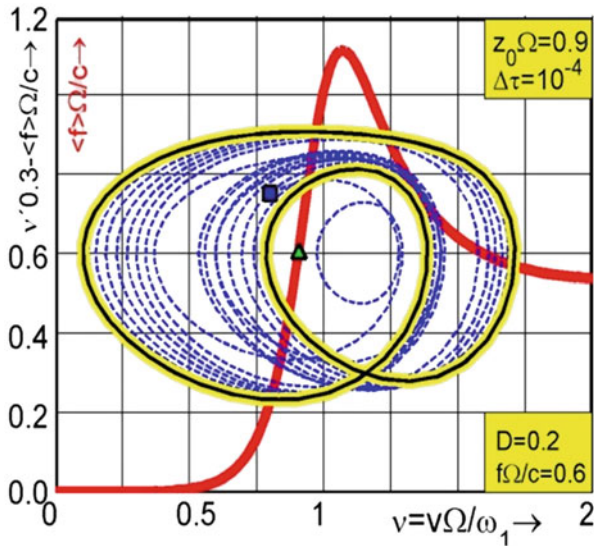
Fig. 3 Double periodic limit cycle of scaled and shifted acceleration vs. true travel speed

with initial co-variances calculated by means of the averaged eq. (7) for the same velocity. The subsequent integration results are marked by blue dashed lines. They are transients, which move clockwise in the phase plane and end in the periodic limit cycle after a sufficiently long integration time. Afterwards, the integration is continued in order to calculate the mean velocity and acceleration, both of which are marked by a green triangle.

Figure 4 shows a further limit cycle applying the extended integration routine

$$\bar{y}' = \bar{x}, \bar{x}' = -(\bar{y} + 2D\bar{x}) + z_o \Omega (\cos\varphi + 2D\nu\sin\varphi). \tag{12}$$

It is needed for the calculation of the vertical displacement and velocity of the vehicle vibrations. For this purpose, $\dot{y} = \omega_1 x$ is inserted into Eq. (2) to obtain the extended integration routine in Eq. (12), which is applied to calculate periodic limit cycles of the quarter car model with the same road level. As before, the blue square denotes the initial values by which the simulation is started. The results obtained, in the beginning, are transients, marked by blue dashed lines. After sufficiently many clockwise rotations, the transients end into a periodic limit cycle marked by a yellow black line. Note that the application of polar co-ordinates in Eq. (9) excludes wheel jumps in the numerical integration. In case of a weak spring pre-compression by weight, the numerical results should be checked stepwise in order to switch into the flight modus when the spring tension in the wheel suspension tends to zero.
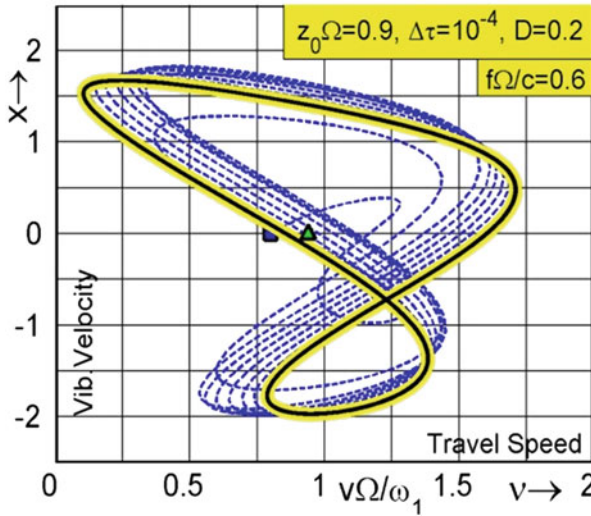
Fig. 4 Periodic limit cycle of the travel speed vs. vibration velocity with dashed transients

4   Multiple Sommerfeld Effects in Multi-Body Car Models

Figure 5 shows an example of multi-body quarter car models with two masses m rolling with velocity v on wavy road surfaces modelled by means of $z(s) = z_o \cos \Omega s$ in dependence on the travel way co-ordinate s. The speed frequency v Ω is related to the reference circle frequency ω_1 introduced by $\omega_1^2 = c/m$. The car model shown in Fig. 5 possesses 2 1/2 degrees of freedom described by the equations of motion

$$\ddot{y}_1 + 2d_1\omega_1 \left(\dot{y}_1 - \dot{y}_2 \right) + 2D\omega_1 \left(\dot{y}_1 - \dot{z} \right) + \omega_1^2 \left(y_1 - y_2 \right) = 0, \tag{13}$$

$$\ddot{y}_2 + 2d_2\omega_1 \left(\dot{y}_2 - \dot{z} \right) - 2d_1\omega_1 \left(\dot{y}_1 - \dot{y}_2 \right) + \omega_1^2 \left(2y_2 - y_1 - z \right) = 0, \tag{14}$$

$$2\dot{v} + \omega_1 \left[\omega_1 \left(z - y_2 \right) + 2d_2(\dot{z} - \dot{y}_2) + 2D \left(\dot{z} - \dot{y}_1 \right) \right] \tan \alpha = f/m. \tag{15}$$

As noted in Fig. 5, B, b_1 and b_2 are damping coefficients related to the reference circle frequency. Eqs. (13) and (14) are derived by means of the dynamic balance of all vertical forces acting at the upper and lower masses, respectively. Eq. (15) follows from the horizontal dynamic equilibrium $2m\dot{v} + N \sin\alpha = f$ with the horizontal component of the normal force. Its vertical component $N \cos \alpha$ is equal to the spring force c and damper forces D and d_2 that leads to $\tan \alpha = \Omega u$ times the spring damper force.
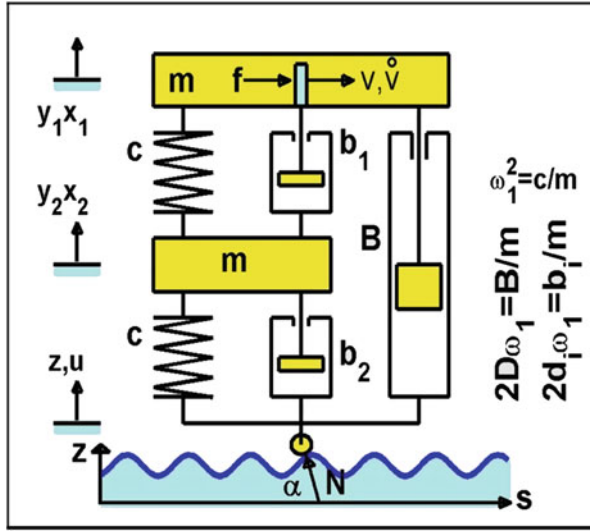
Fig. 5 Quarter car model (2 1/2 DOF) rollingon a wavy surface driven by force $f = const$

For numerical integration, the time $\tau = \omega_1 t$ and the velocity $v = v\Omega/\omega_1$ as well as the vibration velocities $\dot{y}_i = \omega_1 x_i$ are inserted with $i = 1, 2$ into Eq. (15) that leads to

$$2v' + (z_o\Omega)^2 2\,(d_2 + D)\,\bar{u}^2 v = \Omega z_o\left(\bar{y}_2 + 2d_2\bar{x}_2 + 2D\bar{x}_1\right)\bar{u} - (\Omega z_o)^2\overline{zu} + f\Omega/c. \tag{16}$$

In Eq. (16), the related co-ordinates $(\bar{z}, \bar{u}) = (z, u)\,/z_o$ and $(\bar{y}_i, \bar{x}_i) = (y_i, x_i)\,\Omega$, are inserted into the road equation for both masses $(i = 1, 2)$, respectively. The equations of motion are re-written into a first-order system. In this form, they are applied to derive the skew-symmetric matrix eq. (17) of all eight co-variances, as follows:

$$\begin{bmatrix}\overline{zy_1}\\\overline{uy_1}\\\overline{zy_2}\\\overline{uy_2}\\\overline{zx_1}\\\overline{ux_1}\\\overline{zx_2}\\\overline{ux_2}\end{bmatrix}' + \begin{bmatrix}0 & -v & 0 & 0 & -1 & 0 & 0 & 0\\ v & 0 & 0 & 0 & 0 & -1 & 0 & 0\\ 0 & 0 & 0 & -v & 0 & 0 & -1 & 0\\ 0 & 0 & v & 0 & 0 & 0 & 0 & -1\\ 1 & 0 & -1 & 0 & 2(d_1+D) & -v & -2d_1 & 0\\ 0 & 1 & 0 & -1 & v & 2(d_1+D) & 0 & -2d_1\\ -1 & 0 & 2 & 0 & -2d_1 & 0 & 2(d_1+d_2) & -v\\ 0 & -1 & 0 & 2 & 0 & -2d_1 & v & 2(d_1+d_2)\end{bmatrix}\begin{bmatrix}\overline{zy_1}\\\overline{uy_1}\\\overline{zy_2}\\\overline{uy_2}\\\overline{zx_1}\\\overline{ux_1}\\\overline{zx_2}\\\overline{ux_2}\end{bmatrix} = z_o\Omega\begin{bmatrix}0\\0\\0\\0\\2Dvzu\\2Dv\bar{u}^2\\2d_2v\overline{zu} + \bar{z}^2\\2d_2v\overline{zu}^2 + \overline{zu}\end{bmatrix}$$

$$\tag{17}$$

Eqns. (16) and (17) are averaged by means of $\overline{zu} = 0$ and $\bar{z}^2 = \bar{u}^2 = 1/2$ and solved in this form to obtain the driving force in dependence on the averaged car velocity. Fig. 6 shows this result marked by blue line which is calculated for the road level $z_o\Omega = 1$ and the damping values $D = d_1 = d_2 = 0.1$. In the middle range
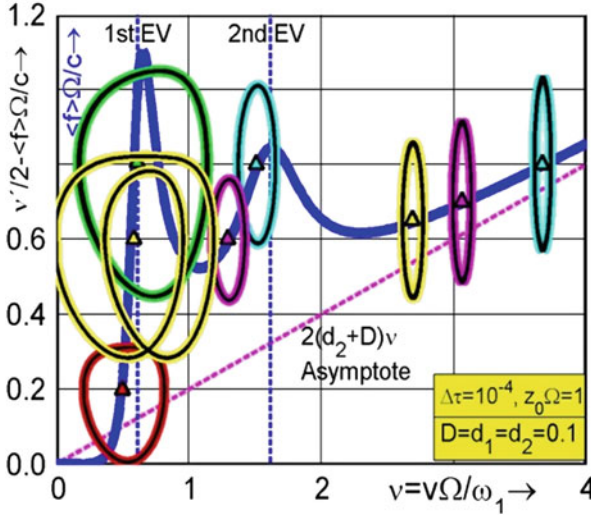
Fig. 6 Driving force (blue) of averaged speed and limit cycles of acceleration vs true velocity

of the driving force assumed to be constant and independent of speed, there are five stationary solutions: two solutions are unstable and three are stable. This stability behaviour is numerically confirmed by the limit cycles shown in Fig. 6 which are obtained by the above velocity and co-variance equations applying the polar co-ordinates $\bar{z} = \bar{r} \cos \varphi$ and $\bar{u} = \bar{r} \sin \varphi$ of the road contour with the amplitude $\bar{r} = 1$ and the angle velocity $\varphi' = -v$. Numerical results are calculated by means of Euler schemes with the step size $\Delta \tau = 10^{-4}$. Fig. 6 shows three limit cycles (red, yellow, green) before the first resonance, two further limit cycles (red, cyan) between the first and second resonance and the last three limit cycles (yellow, red, cyan) for overcritical speeds near the asymptote $f\Omega/c = 2(d_2 + D)v$ which is marked by dashed line in red.

5 Limit Cycle Flow of Vehicles Rolling on Noisy Roads

Figure 7 shows stochastic limit cycles obtained for the quarter car model in case that the angle motion on the sinusoidal road form is perturbed by additive noise given by

$$d\phi_\tau = -V_\tau d\tau + \sigma dW_\tau, \quad \Delta W_n = \sqrt{\Delta \tau} \, N_n. \tag{18}$$
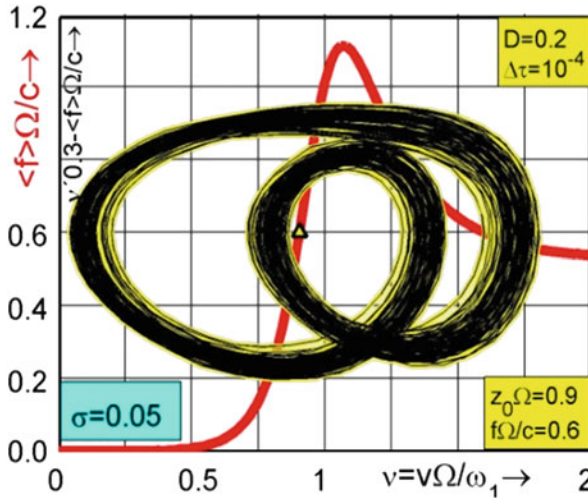
Fig. 7 Limit cycle flow with double period for quarter car models rolling on noisy road surface

In Eq. (18), capital letters with index τ denote set functions [16, 17] dependent on time. Noise is generated by normally distributed numbers N_n with zero mean [18].

The stochastic angle perturbation takes into account that the road surface is no longer sinusoidal but more realistically irregular and noisy with bounded realizations. This leads to response realizations which are bounded, as well. First results are shown in Fig. 7 where trajectories of stochastic limit cycles are plotted in the phase plane of travel velocity and acceleration multiplied by the factor 0.3 and shifted by the driving force, applied. The realizations are calculated by means of Eqs. (10), (11) and (18) for the damping $D = 0.2$, the driving force $f\Omega/c = 0.6$, the road level $z_o\Omega = 0.9$ and the noise intensity $\sigma = 0.05$ applying the Euler scheme with time step $\Delta\tau = 10^{-4}$. The mean value of scaled acceleration and velocity is marked by a yellow triangle on the red curve of the mean speed driving force indicating that the mean acceleration is vanishing and the mean travel speed coincides with Eq. (8). The comparison with the periodic limit cycle in Fig. 3 shows that the sharp line is widened to a bundle of realizations, the boundaries of which are double periodic with two loops and one node of two cross-free limit flows. Figure 8 shows its double crater like probability distribution density on the phase plane of velocity and acceleration. The clockwise rotation of the phase is slow when the density is high and vice versa fast for low densities.
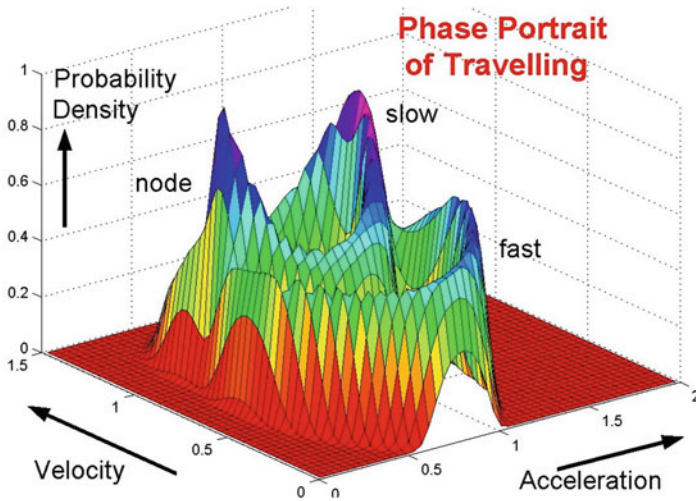
Fig. 8 Double crater like probability density with fast and slow motions in the phase plane

Fig. 9 Elastically supported unbalanced rotor with 2 DOF and driven by a constant moment
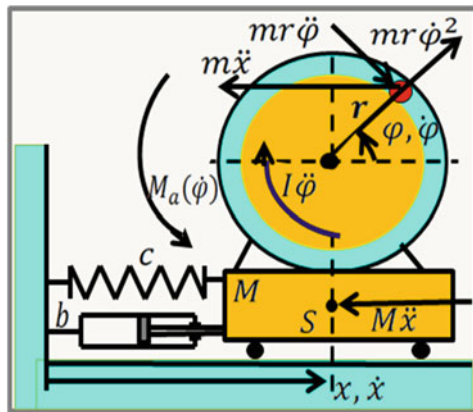
6 Limit Cycle Flows and Sommerfeld Effects in Rotor Dynamics

It is now interesting to compare the above results with corresponding ones, well known in rotor dynamics [19–26]. For these purposes, consider the unbalanced rotor, shown in Fig. 9. The rotor has the moment of inertia I and rotates with angle velocity $\dot{\varphi} = \omega$ driven by the moment M_a. The rotor with mass M is supported by spring c and damper b so that horizontal vibrations $\xi = x/r$ are possibly excited by the unbalanced mass m fixed at the radius r on the rotor. Rotation and translation of the rotor are described by the two equations of motion

$$\ddot{\xi} + 2D\omega_1\dot{\xi} + \omega_1^2\xi = \mu\left(\dot{\varphi}^2\cos\varphi + \ddot{\varphi}\,\sin\varphi\right), \tag{19}$$

$$\left(I + mr^2\right)\ddot{\varphi} = mr^2\ddot{\xi}\,\sin\varphi + M_a, \xi = x/r. \tag{20}$$

The frequency ω_1, the damping D and the mass ratio μ are introduced as follows:

$$\omega_1^2 = \frac{c}{M+m}, 2D\omega_1 = \frac{b}{M+m}, \mu = \frac{m}{M+m} \leq 1. \tag{21}$$

In a first investigation, the angle velocity of the rotor is assumed to be constant. With $\ddot{\varphi} = 0$. Eq. (19) becomes linear and can be solved. Its stationary solution is inserted into Eq. (20) that gives the periodic driving moment needed to keep the angle velocity constant. Its mean value [24–26], and is calculated as follows:

$$\frac{M_a}{cr^2} = \frac{D\mu^2\eta^5}{\left(1-\eta^2\right)^2 + (2D\eta)^2}, \eta = \frac{\omega}{\omega_1}. \tag{22}$$

In Eq. (22), η denotes the rotor speed ω related to the circle frequency ω_1 of the engine. Note that this result coincides with Eq. (8) when the force $f\Omega/c$ is replaced by the moment M_a/cr^2, the related translation velocity by the rotation speed ratio and the mass ratio μ replaced by $z_o\Omega$ that determines the strength of the road excitation. In order to improve numerical integrations, Eqs. (19) and (20) are rearranged to

$$\ddot{\xi} = \left[\mu\dot{\varphi}^2\cos\varphi - \omega_1^2\xi - 2D\omega_1\dot{\xi} + \mu\left(M_a/I_g\right)\sin\varphi\right]/\Delta, \tag{23}$$

$$\ddot{\varphi} = \left[\left(M_a/I_g\right) + \left(\mu\dot{\varphi}^2\cos\varphi - \omega_1^2\xi - 2D\omega_1\dot{\xi}\right)\rho\,\sin\varphi\right]/\Delta. \tag{24}$$

In Eq. (24), ρ is the ratio of moments of inertia and Δ is the determinant given by

$$\Delta = 1 - \mu\rho\sin^2\varphi > 0, \rho = mr^2/\left(I + mr^2\right) < 1. \tag{25}$$

For $\mu\rho < 1$, the determinant Δ is positive definite. In Eq. (24), the total mass of inertia is denoted by $I_g = I + mr^2$. Note that in Eqs. (23) and (24), both accelerations of interest are decoupled and isolated on the left side of both equations of motion. This corresponds to the iteration technique in classical non-linear equation systems.

Applying the dimensionless time $\tau = \omega_1 t$, Eqs. (23) and (24) are rewritten as follows:

$$\xi' = \zeta, \quad \zeta' = \left(\mu\,\eta^2\cos\varphi - \xi - 2D\zeta + \rho m_a\sin\varphi\right)/\Delta, \tag{26}$$

$$\varphi' = \eta, \quad \eta' = \rho\left[\left(\mu\,\eta^2\cos\varphi - \xi - 2D\zeta\right)\sin\varphi + m_a/\mu\right]/\Delta. \tag{27}$$
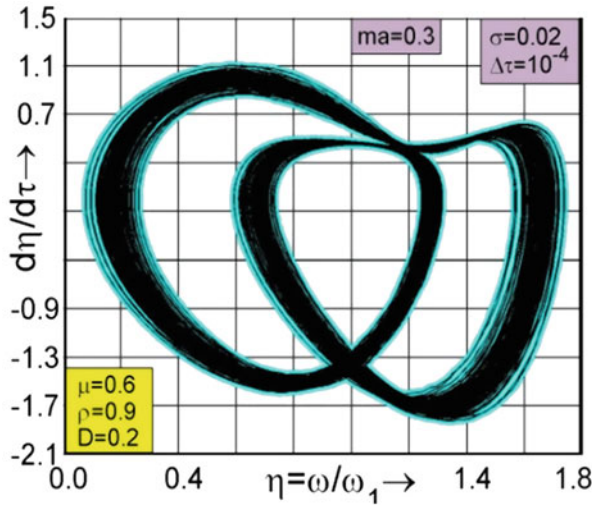
Fig. 10 Double periodic limit cycle flow in the phase plane of perturbed motions

In these equations, ζ and η are velocities of the translation and rotation co-ordinates ξ and φ, respectively. The dimensionless parameter m_a denotes the related driving moment given by $m_a = M_a/(cr^2)$. In Eq. (27), this driving moment is applied by m_a/μ which is proportional to μ when Eq. (22) is inserted. Similar to Sect. 5, it is assumed that the rotational speed of the rotor is perturbed by white noise of intensity $\sigma = 0.02$ effected, e.g., by flow turbulence and combustion in the engine. In correspondence to Eq. (18), $\varphi' = \eta$ in Eq. (27) is replaced by $d\varphi_\tau = \eta_\tau d\tau + \sigma dW_\tau$ so that the deterministic periodic limit cycle is widened to a bundle of non-periodic trajectories. Fig. 10 shows numerical evaluation for $D = 0.2$, $\mu = 0.6$, $\rho = 0.9$ and $m_a = 0.3$ when the rotor gets stuck before resonance. In the stochastic case, all non-periodic trajectories form a flow with inner and outer limits marked by green colour which are double periodic with a periodic probability density similar as shown in Fig. 8. Accordingly, the phase motion is fast when the flow is widened and it becomes slow in the upper right part in Fig. 10, where two different narrow flows are close to each other turning clockwise around. Finally, it is noted that in the book of Lin and Cai [27], noise perturbations in sinusoidal terms applied above to translation or rotation speeds are called Dimentberg-Wedig models.

7   Concluding Remarks

When vehicles are rolling on uneven roads driven by a constant force, vertical vibrations of the vehicle are induced which are coupled with the horizontal motions of the vehicle effecting that the travel velocity fluctuates around a stationary speed

with zero mean acceleration. The coupling between both planar motions is caused by the permanent direction change of the contact force to ground along the contour of the road profile. In case of sinusoidal road profiles, the vehicle gets stuck before the resonance speed and needs more power supply to overcome the resonance in order to reach higher speeds. This is desirable when on unpaved roadways, the resonance vibrations start with 30 km/h.

To enlighten these dynamic effects, the paper presents the following main new results:

1. Multiple Sommerfeld effects are shown between the resonances and before and after the peaks of all resonances. The periodic limit cycles in Fig. 6 are new results showing how the car speed gets stuck on positive force slopes.
2. In Figs. 7 and 8, non-periodic stochastic limit cycles are calculated with a bundle of realizations which are described by periodic probability density distributions of travel speed against acceleration in the phase plane.
3. New robust integration routines are introduced into rotor dynamics in order to derive non-periodic limit cycles of acceleration against rotation speed. All realizations together form a periodic flow as shown in Fig. 10.

In vehicle road dynamics, these results are derived by means of co-variance equations of the road times the vibration co-ordinates. They have skew symmetric forms and can be averaged in order to get the averaged co-variances and averaged vehicle speeds for given driving force. These results are applied as initial values of the Euler integration to obtain the true velocity against the acceleration plotted as periodic limit cycles around the averaged values. In [2], it is shown that the co-variance equations and the drift equation can be solved by means of Fourier expansions. In future, the same analytical technique should be introduced into rotor dynamics, where up to now, the paper presents numerical results, only. Note that the two equations of motion of the Sommerfeld model are ill conditioned in the sense that numerical integration by means of Euler schemes fails. Therefore, the paper proposes to re-arrange the equations of motion so that the unknown accelerations of translation and rotation are decoupled and isolated on the left side of the equations and can be integrated.

Conflict of Interest The author declares that he has no conflict of interest.

References

1. A. Sommerfeld, Beiträge zum dynamischen Ausbau der Festigkeitslehre. Zeitschrift des Vereins Deutscher Ingenieure **46**, 391–394 (1902) (in German)
2. W.V. Wedig, Turbulent travel speeds in nonlinear vehicle road dynamics. J. Nonlinear Dyn. **100**, 147–158 (2020)
3. W.V. Wedig, Velocity jumps in road-vehicle dynamics, in *12th International Conference on Vibration Problems (ICOVP 2015), Procedia Engineering 144*, (Elsevier, 2016), pp. 1076–1085. (available online at www.sciencedirect.com)

4. W.V. Wedig, Jump phenomena in road-vehicle dynamics. Int. J. Dyn. Control **4**, 21–28 (2016)
5. W.V. Wedig, New resonances and velocity jumps in nonlinear road-vehicle dynamics, in *Proceedings of IUTAM Symposium on Analytical Methods in Nonlinear Dynamics*, ed. by P. Hagedorn, (Frankfurt, Germany, 2016) July2015, Procedia IUTAM, Elsevier, 1-9 (available online at www.sciencedirect.com)
6. W.V. Wedig, Lyapunov exponents and rotation numbers in rotor- and vehicle dynamics. Procedia Engineer. **199**, 875–881 (2017) available at www.sciencedirect.com
7. W.V. Wedig, Velocity turbulences in stochastic road-vehicle dynamics, Proc. of the 15th international probabilistic workshop. Dresden TUD press **1**, 1–13 (2017)
8. C.J. Doods, J.D. Robson, The description of road surface roughness. J. Sound Vib. **31**, 175–183 (1973)
9. K. Sobczyk, D. MacVean, J. Robson, Response to profile-imposed excitation with randomly varying transversal velocity. J. Sound Vib. **52**, 37–49 (1977)
10. B.R. Davis, A.G. Thompson, Power spectral density of road profiles. Veh. Syst. Dyn. **35**(6), 409–415 (2001)
11. K. Popp, W.O. Schiehlen, *Fahrdynamik* (Teubner-Verlag, (in German), 1993)
12. W.V. Wedig, Dynamics of cars driving on stochastic roads, in *Computational Stochastic Mechanics CSM-4*, ed. by P. Spanos, G. Deodatis, (Millpress, Rotterdam, 2003), pp. 647–654
13. I. Blekhman, E. Kremer, Vertical-longitudinal dynamics of vehicles on road with uneveness. Procedia Engineer. **199**, 3278–3283 (2017) available at www.sciencedirect.com
14. I. Blekhman, E. Kremer, Vibrational resistance to vehicle motion due to road unevenness. J. Sound Vib. **405**, 306–313 (2017)
15. S.K. Barti, A. Sinha, A.K. Samantary, R. Bhattacharyya, *Sommerfeld Effect in a Single DOF System with Base Excitation from Motor Driven Mechanism, Mechanism and Machine Theory, Volume 148* (Elsevier, SciencesDirect, 2020)
16. L. Arnold, *Stochastic Differential Equations* (Wiley, New York, 1974)
17. W.V. Wedig, Simulation of road-vehicle systems. Prob. Eng. Mech. **27**, 82–87 (2012)
18. P. Kloeden, E. Platen, *Numerical Solution of Stochastic Differential Equations: A Review* (Springer, Heidelberg, 1995)
19. D.M. Smith, The motion of a rotor carried by a flexible shaft in flexible bearings. Proc. R. Soc. Lond. Ser. A **142**(846), 92–118 (1933)
20. M.F. Dimentberg, *Flexural Vibrations of Rotating Shaft* (Butterworths, London, 1961)
21. P.J. Brosens, S.H. Crandall, Whirling of unsymmetrical rotors, Tran. ASME J. Appl. Mech. **28**(3), 355–362 (1961)
22. A. Fidlin, O. Drozdetskaya, On the averaging in strongly damped systems: The general approach and its application to asymptotic analysis of the Sommerfeld effect. Procedia IUTAM **18**, 43–52 (2016)
23. A. Bisoi, A.K. Samantaray, R. Bhattacharyya, Sommerfeld effect in a two-disk rotor dynamic system at various unbalance conditions. Meccanica **53**(4–5), 681–701 (2018)
24. S.K. Bharti, A. Bisoi, A. Sinha, A.K. Samantaray, R. Bhattacharyya, Sommerfeld effect at forward and backward critical speeds in a rigid rotor shaft system with anisotropic supports. J. Sound Vib. **442**, 330–349 (2019)
25. M. Dimentberg, L. McGovern, R. Norton, J. Chapdelaine, R. Harrison, Dynamics of an unbalanced shaft interacting with a limited power supply. Nonlinear Dyn. **13**, 171–187 (1997)
26. S.K. Bharti, A. Sinha, A.K. Samantary, Bhattacharyya, The Sommerfeld effect of second kind: Passage through parametric instability in a rotor with non-circular shaft and anisotropic flexible supports. Nonlinear Dyn. **100**, 3171–3179 (2020)
27. Y.K. Lin, G.Q. Cai, *Probabilistic Structural Dynamics* (McGraw-Hill, 2004)

A Forward Dynamics Methodology to Study Nonlinear Dynamics and Wear of Total Knee Arthroplasties

Ehsan Askari and Michael S. Andersen

1 Introduction

Relative motion between the knee components, dynamic loading, and contact stresses in the knee joint play vital roles in the development and progression of wear occurrence in total knee arthroplasty (TKA), which can ultimately cause the implant to fail and require revision [1, 2]. Therefore, developing anatomical-based models to study the kinetic and kinematic behavior of substructures of TKAs while taking the real geometry and material properties of knee components is essential. Having a look at the scientific history of knee joint models, the pioneering successful work comes back to the anatomical and sophisticated three-dimensional (3D) quasi-static model Wismans et al. developed in 1980 [3]. During the last decades, many studies were carried out employing quasi-static knee models [4, 5]. However, quasi-static models do not allow to consider inertial loads and detailed studies of such a complex joint to determine, e.g., the tribological behavior of the joint [6, 7]. Much of the mathematical dynamic approaches of the joint available in the literature are two-dimensional, considering motions in the sagittal plane only [8]. One of the very first successful attempts to determine the 3D dynamic solution of knee joint was carried out by Abdel-Rahman and Hefzy [6], while the model did not account for the deformation of the articular surfaces and the real geometry of the tibial insert. Later, that model was improved by Caruntu and Hefzy [7] to take into account deformable contact at the articular surfaces. Although much of the available knee joint dynamic models just focused on the joint rather than whole body simulation, Piazza and

E. Askari (✉)
Department of Electromechanical, Systems and Metal Engineering, Ghent University, Zwijnaarde, Belgium

M. S. Andersen
Department of Materials and Production, Aalborg University, Aalborg, Denmark

Delp utilized a full-body dynamic model [9]. The drawback of that study, however, was to employ the rigid-contact theory to simulate the knee joint, which was not capable of calculating contact stresses. An efficient approach can be considered the one that links an in-detail forward dynamic methodology of the knee joint with a deformable contact model to a musculoskeletal system that is responsible to obtain physiological forces and moment from surrounding tissues, e.g., muscles and hip, for which commercial software is available [5].

The present study aims at developing a forward dynamics model of TKA being subjected to the boundary conditions obtained from a musculoskeletal modeling [4]. The real geometry of the bearing surfaces is used, which are smoothed using a Laplacian smoothing technique. A specific contact search procedure is developed that reduces computational time considerably. Ligaments are also modelled using a nonlinear elastic model, accounting for a realistic asymmetric nonlinear ligament behavior [4]. In addition, motion equations of the tibiofemoral joint are derived based on Newton's second law of motion and Euler's equations [7]. Archard wear law is then embedded in the present dynamic approach, which allows for the prediction of TKA wear. A mesh density analysis is performed and the developed approach is assessed comparing acquired outcomes with those available in the literature.

2 Patient-Specific Musculoskeletal Modeling

To estimate patient-specific TKA knee joint loads, an already validated patient-specific musculoskeletal model is employed [4]. Data for one male subject (age: 86, height: 1.80 m and mass: 75 kg) with an instrumented, posterior cruciate-retaining TKA prosthesis from the 5th Grand Challenge Competition to Predict In Vivo Knee Loads [4] is applied for the model development. Among others, the dataset contains pre- and postoperative Computed Tomography (CT) scans, trajectories of skin markers and ground reactions during standing reference trials and dynamic movement trials, including gait at a self-selected speed as well as measurements from the instrumented knee prosthesis. Additionally, Stereolithography (STL) 3D geometries of the femoral component, tibial tray and insert, patellar button, and segmentation of the postoperative CTs of the partial pelvis, femur, patella, tibia, fibula, partial talus, and partial calcaneus are also included in the dataset. For the dynamic analysis, the one gait trial of level walking at self-selected speed (PS_ngait_og_ss1) is utilized [4]. The musculoskeletal model is developed using the AnyBody Modeling System (AMS) v. 7.1 (AnyBody Technology A/S, Denmark) and based on the human model from the AnyBody Managed Model Repository (AMMR) v. 1.6.

3 Tribology and Forward Dynamics Modeling

We focus on an assembly consisting of the tibia and femur as the tibiofemoral joint's components along with its ligaments to develop a tribology and forward dynamic model. In the following, the developing process of such a model is described in detail. The bearing surfaces are constructed from a cloud of 3-D data points before being meshed. Then, a forward dynamics model is derived after developing an approach to compute contact stresses between articulating bodies. Finally, the tribology of the polyethylene tibia is formulated to predict wear.

3.1 Surface Treatment

The Laplacian smoothing technique is used to smooth the triangulated surfaces of the femoral part and tibial insert for which all vertices adjoining any vertex are determined, to which the umbrella operator is employed. The bearing surface of the tibial insert is constructed using the Non-Uniform Rational B-Spline (NURBS) surface methodology and is in turn meshed using a uniformly discretized domain A, shown in Fig. 1. Corresponding to each node on the tibial bearing surface, a node on the master body, i.e., the femoral part, is determined using a minimum normal distance approach. The technique to determine the minimum normal distance of a node, e.g., $Q_T^{k,j}$, with respect to the femoral body, is visualized in Fig. 2.
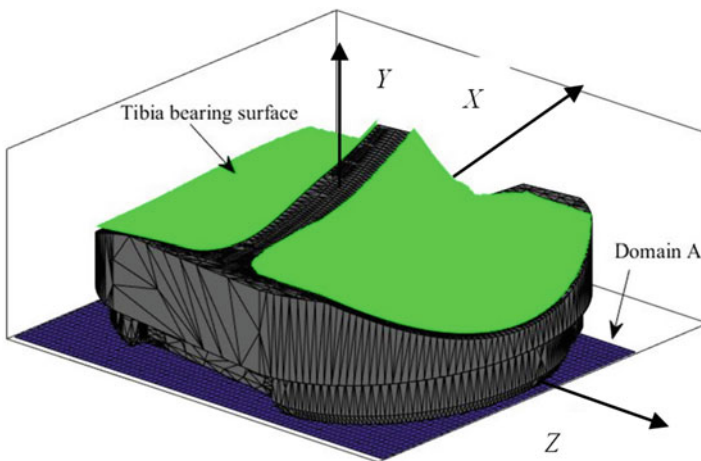
Fig. 1 The domain "A" that is discretized into a uniform mesh
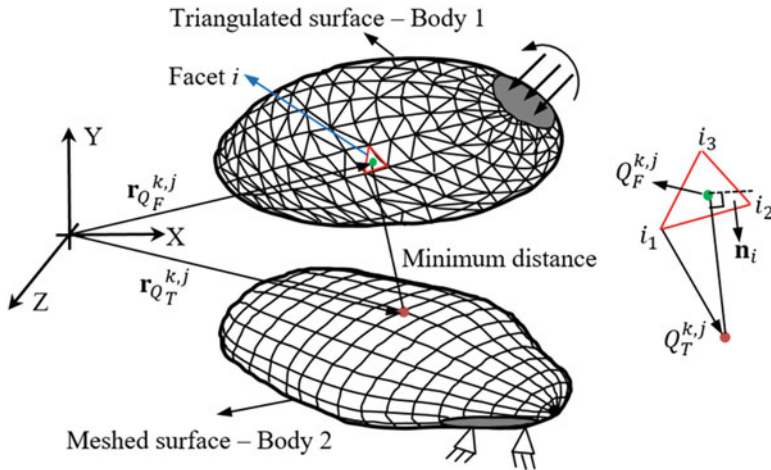
Fig. 2 Determination of the minimum distance of a node, $Q_T^{k,j}$, on the Body 2 to the Body 1

3.2 Contact Search and Detection

According to the translational and rotational motion of the knee components and their irregular geometries, a spatial search is required and one always has to check possible contacts at any time. The scheme developed in this study subdivides the domain where the contact is likely to take place, i.e., the tibial bearing surface, into uniform cells or bounding boxes, each of which includes several elements of the surface discretized in the first place [10]. The upper-bound value, i.e., y, of each bounding box is determined that is compared to the lower-bound value of the femoral bearing surface in the differential domain of the bounding box. If any intersection occurs, this bounding box gets opened to check all nodes herein. Thereafter, the normal minimum distance of each node (i, j) of elements inside the bounding boxes that is in contact is determined and is stored as the respective penetration depth, $D_{i,j}$.

3.3 Contact Formulation

The present study implements a concept proposed in [11] to evaluate the contact stresses in TKA. Knowing the penetration depth $D_{i,j}$ and computing its time derivative $\dot{D}_{i,j}$ from the dynamic motion of the knee, the normal contact pressure, $\sigma^{i,j}$, at any node can be evaluated based on the Kelvin-Voigt model as follows [11]:

$$\sigma^{i,j} = -K D_{i,j} - K \tau \dot{D}_{i,j}, \tag{1}$$

in which K is the contact stiffness and τ the relaxation time. K is obtained from $K = \Lambda/\Xi$ where $\Lambda = (1 - \upsilon)E/[(1 + \upsilon)(1 - 2\upsilon)]$ and Ξ is the tibia thickness. E and υ are Young's modulus and Poisson ratio of the polyethylene that are, respectively, 463 MPa and 0.46 as reported in [11, 12]. The resulting contact force imposed on the femur is computed from the following integration:

$$\mathbf{F}_{cont} = \iint_{A} \sigma \mathbf{n}\, dA, \tag{2}$$

where $\mathbf{n}$ indicates the normal unit vector of facets of the femur surface. The friction force, designated by $\mathbf{F}_{\mu}$, is also taken into account using the Coulomb law as $\mathbf{F}_{\mu} = -\mu \|\sigma \mathbf{n}\| \mathbf{t}$ where μ denotes the friction coefficient and $\mathbf{t}$ is the tangential vector along with the local motion occurring in the respective differential contact area.

3.4 Ligament Modeling

In this study, ligament forces are modeled using an asymmetric nonlinear elastic model. The force, $f(\varepsilon)$, each ligament, i.e., PCL, LCL, and MCL, imposes on the femur can be evaluated from the following formula, which also includes a slack region [4]:

$$f(\varepsilon) = \begin{cases} \frac{k\varepsilon^2}{4\varepsilon_1} & 0 \le \varepsilon \le 2\varepsilon_1 \\ k(\varepsilon - \varepsilon_1) & \varepsilon > 2\varepsilon_1 \\ 0 & \varepsilon < 0 \end{cases}, \tag{3}$$

where k is the ligament stiffness and ε depicts the strain while ε_1 is a constant with value of 0.03, which is associated with the transition phase between linear and nonlinear regions of the force-strain curve. Stiffness and reference strain assigned to each ligament bundles are adapted from the literature [4]. The resulting ligament force and moment imposed to the femur are computed by the following formula:

$$\begin{aligned} \mathbf{F}_{lig} &= \mathbf{F}_{LCL} + \mathbf{F}_{PCL} + \mathbf{F}_{MCL}, \\ \mathbf{M}_{lig} &= \mathbf{M}_{LCL} + \mathbf{M}_{PCL} + \mathbf{M}_{MCL}. \end{aligned} \tag{4}$$

3.5 Forward Dynamics Modeling

The constitutive motion equations of tibiofemoral joints can be written based on the general linear and angular momentum equations. The former is the so-called Newton's second law of motion, which is written as follows [13, 14]:

$$M\ddot{\mathbf{X}} = \mathbf{F}, \qquad \mathbf{F} = \mathbf{F}_{ext} + \mathbf{F}_{cont} + \mathbf{F}_{\mu} + \mathbf{F}_{lig}, \tag{5}$$

in which M is the femur mass, while $\ddot{\mathbf{X}}$ denotes the vector of translational acceleration and $\mathbf{F}$ is the vector sum of all force vectors applied to the femur, including the external forces, $\mathbf{F}_{ext}$, contact resultant forces, $\mathbf{F}_{cont}$, friction force, $\mathbf{F}_{\mu}$, and ligaments loads, $\mathbf{F}_{lig}$. The angular-momentum equation can also be given by:

$$\mathbf{M}_C^* = \mathbf{I}^{C*}\dot{\boldsymbol{\omega}}^* + \tilde{\boldsymbol{\omega}}^* \mathbf{I}^{C*}\boldsymbol{\omega}^*, \tag{6}$$

where $\mathbf{M}_C^* = \mathbf{R}^T \mathbf{M}_C$ is the sum of external moments that are computed with respect to the body coordinate system of the femoral part (xyz). Moreover, $\mathbf{M}_C$ is the sum of the externally applied moments that are determined with respect to the origin of the coordinate system (xyz), but computed in the global coordinate system. $\mathbf{R}^T$ is the transpose of the rotation tensor of the femur. $\mathbf{I}^{C*}$ and $\boldsymbol{\omega}^*$ stand for the tensor of inertia and the angular velocity of the femoral component in the body coordinate system, respectively. In the dynamic model, a rotation tensor with Euler angles of the z-x-y sequence is constructed with the array of Euler angles $q^T = \{\phi, \theta, \psi\}$ to determine the location of each node of the femur. The corresponding rotation tensor can be given by

$$
\begin{aligned}
\mathbf{R} &\equiv \mathbf{R}_{z-x-y} \\
&= \begin{bmatrix}
\cos\phi\cos\psi - \sin\phi\sin\theta\sin\psi & -\sin\phi\cos\theta & \cos\phi\sin\psi + \sin\phi\sin\theta\cos\psi \\
\sin\phi\cos\psi + \cos\phi\sin\theta\sin\psi & \cos\phi\cos\theta & \sin\phi\sin\psi - \cos\phi\sin\theta\cos\psi \\
-\cos\theta\sin\psi & \sin\theta & \cos\theta\cos\psi
\end{bmatrix},
\end{aligned}
\tag{7}
$$

where ϕ is the magnitude of the planar rotation around the axis z, which is the flexion-extension angle. The angular velocity in the body coordinate system can be written based on time derivatives of Euler angles as follows:

$$\boldsymbol{\omega}^* = \mathbf{H}_{z-x-y}^* \begin{Bmatrix} \dot{\phi} \\ \dot{\theta} \\ \dot{\psi} \end{Bmatrix}. \tag{8}$$

Operator $\mathbf{H}_{z-x-y}^*$ is the tangent operator, that is, tangent to the rotation manifold. The body coordinate system is set to coincide with the principal axes of the mass moment of inertia tensor and Eq. (6) is thus reduced to a diagonal form. The governing equations are further simplified to the so-called Euler's equations for the angular motion of a rigid body. In the analysis, the femur mass with all surrounding tissues of the male subject is 7.5 kg, while the tensor of inertia with respect to the body coordinate system is (0.4516 0 0; 0 0.0213 0, 0 0 0.4516) [4]. The numerical integration of Eqs. (5) and (6) is performed using the adaptive Runge-Kutta-Fehlberg method [15].

3.6 Polyethylene Damage: Wear and Creep

Archard's wear model is commonly used by the tribology community to describe adhesive and abrasive wear mechanisms, although it is often adopted for a wide range of applications as a result of its efficiency and simplicity [5]. Employing Archard's wear law, the linear wear rate can be computed using the following expression [13]:

$$\frac{dh}{ds} = k_W P, \tag{9}$$

in which h denotes the wear depth, while s stands for the sliding distance. The variable k_W is the wear factor with unit $mm^3 N^{-1} m^{-1}$. Kang and his colleagues proposed formulations to compute wear factor based on both cross-shear ratio, $\Im$, and the contact pressure of the UHMWPE tibial insert [16], which is given by

$$k_w (\Im, \overline{p}) = \exp \left[-13.1 + 0.19 \ln (\Im) - 0.29 \overline{p} \right], \tag{10}$$

where $\overline{p}$ is the average contact pressure for a given element, which is determined by averaging contact stress over one gait cycle, and the definition of the cross-shear ratio and the procedure to compute it is well described in [16]. Wear factor given in Eq. (10) is dependent on the contact pressure and is not easily implemented into computational wear modeling. Abdelgaied et al. [12] developed a wear model based on the idea that wear volume (W) is proportional to the contact area (A) and sliding distance (S) and a nondimensional wear coefficient (C) determined experimentally, as follows:

$$C = (a + b \times CS)^{-1/c}, \tag{11}$$

where CS is the cross-shear ratio, and parameters a, b, and c are constant and determined from the experimental measurements of a multidirectional pin-on-disk wear test [12] as $a = 8.5173e-65$, $b = 9.3652e-60$, and $c = -6.7454$.

4 Results and Discussion

To guarantee the accuracy and convergence of dynamics and contact simulations, a mesh density analysis is performed. Three different element sizes to discretize the domain A, Fig. 1, are considered, i.e., 0.2, 0.4, and 0.6 mm. Multiple system parameters that can be influenced by the mesh size are used to assess the mesh density, such as contact forces and moments on both medial and lateral condyles, and maximum contact pressures on both condyles. According to the outcomes obtained, the mesh size of 0.2 mm is deemed to produce accurate results and is used in this study to perform the computational analysis. The developed model is

Table 1 A comparative study of three techniques to compute wear: wear depth (W.D) (mm/mc); volumetric wear (V.W.) (mm^3/mc)

Method i[1]			Method ii[2]			Method iii[3]	
W.D.	V.W.		W.D.	V.W.		W.D.	V.W.
0.092[4] / 0.092[5]	9.1		0.036[4] / 0.052[5]	4.7		0.051[4] / 0.047[5]	6.7

[1]Method i: Constant wear factor; [2]Method ii: Kang et al. [16], Eq. (10); [3]Method iii: Wear coefficient [12], Eq. (11); [4]Medial condyle; [5]Lateral condyle

Table 2 Comparison of wear outcomes with those available in the literature

Study	Study type	Wear depth	Volumetric wear
Present study	Numerical	0.4590[1] / 0.4585[2]	9.1
Fregly et al. [5]	Numerical	0.5[1] / 0.5[2]	
Zhang et al. [17]	Exp. / Numerical	0.44[1] / 0.43[2]	7.8-8.5
Abdelgaed et al. [12]	Numerical		5.7-6.0[*] / 8.3-8.7[**]
Gill et al. [18]	Retrieval	0.50 (0.10 mm/mc)	

[1]Medial condyle; [2]Lateral condyle; [*]Intermediate kinematic input; [**]High kinematic inputs.

employed to compute linear and volumetric wear rates for one million cycles while using three available wear techniques, Table 1. The highest values of both linear and volumetric wear rates are reported employing Method i with a constant wear factor of 2.2×10^{-16} mm^{3}N^{-1}m [5]. Using the wear factor suggested by Kang et al. [16] gives less wear depth on the medial condyle than that on the lateral one, which opposes the outcomes associated with the other two methodologies.

Moreover, the outcomes acquired using the developed methodology are compared to those available in the literature as listed in Table 2 for comparison purpose. Maximum linear wear rates (mm/mc) are reported on both medial and lateral condyles that align with previous studies in terms of not only wear magnitudes but also approximately similar values acquired on both condyles. The volumetric wear (mm^3/mc) that the developed model produces is comparable well with those other researchers reported by either numerical, experimental, or retrieval studies.

4.1 Dynamics and Tribology of the Joint

The loci of the motion of the femur center with respect to the tibia on the transverse plane for four different friction coefficients are illustrated in Fig. 3. It can be seen that increasing friction coefficient leads to a significant change in the trajectory of the femur center in lateral-medial direction in particular. However, the friction influence is not that large in posterior-anterior direction, although some variations have been observed for the case study with friction coefficient 0.04 and 0.12 compared to others. This is also observed that the trajectory loops of all case studies are closed. Although friction and viscous contact lead to the energy loss in the
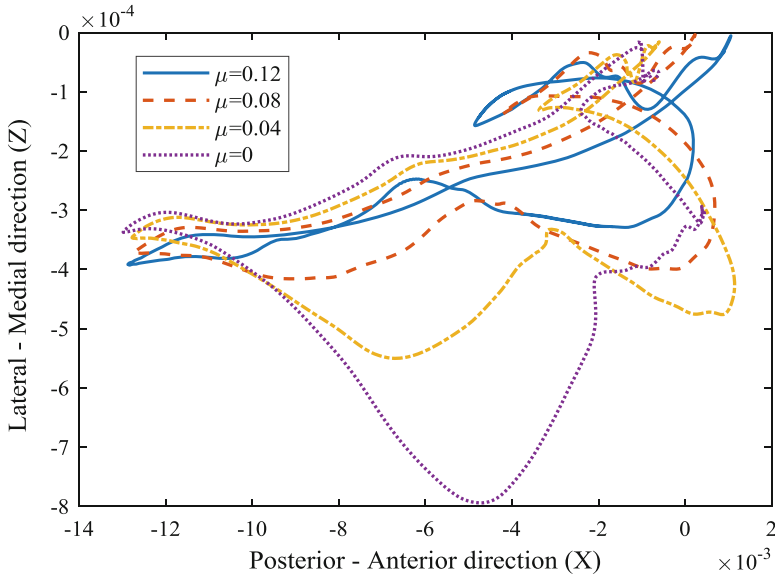
Fig. 3 Effects of friction coefficient (Coulomb's law) on trajectory of the tibiofemoral joint

system, energy is continuously introduced in the system due to the rheonomically constrained flexion-extension rotation and boundary conditions, e.g., loads and moments imposed on the femoral bone from muscles, hip joints, among others, which is why the femur center motion converges to a steady-state periodic motion.

The effect of friction on linear and volumetric wear rates is also investigated and acquired outcomes are listed in Table 3 using the wear coefficient [12]. It can be observed that the maximum linear wear rates are obtained in the case study with $\mu = 0.12$. Lateral linear wear value of the case study with friction coefficient 0.08 is lower than that with $\mu = 0.04$, which means it is not a direct relationship between the wear values and friction coefficient. The interesting outcome is the maximum volumetric wear rate occurs for the case study with $\mu = 0.04$, while the minimum volumetric and linear wear rates are associated with the frictionless joint. When the friction is higher, the greater linear wear can be expected as the worn area decreases due to the changes in the trajectory of the femoral part. However, there is another important contributing factor to wear occurrence, which can prevent the wear to increase. When UHMWPE slides against a metallic counter face, molecular chains preferentially become oriented along a so-called principal molecular orientation (PMO), resulting in a higher wear resistance of polyethylene, which is called orientation hardening in the direction of the PMO.

The wear map and distribution of four study cases considered in this article are illustrated in Fig. 4. It can be observed that the distribution of wear in the medial condyle shrinks in anterior-posterior direction once friction coefficient increases. Moreover, increasing friction gives rise to wear values on the lateral condyle as can

Table 3 Effects of friction coefficients on wear rates

Friction Co.	Medial linear wear rate (mm/mc)	Lateral linear wear rate (mm/mc)	Volumetric wear rate (mm^3/mc)
$\mu = 0.12$	0.066	0.051	7.06
$\mu = 0.08$	0.051	0.045	6.68
$\mu = 0.04$	0.043	0.049	7.16
$\mu = 0$	0.037	0.031	6.09
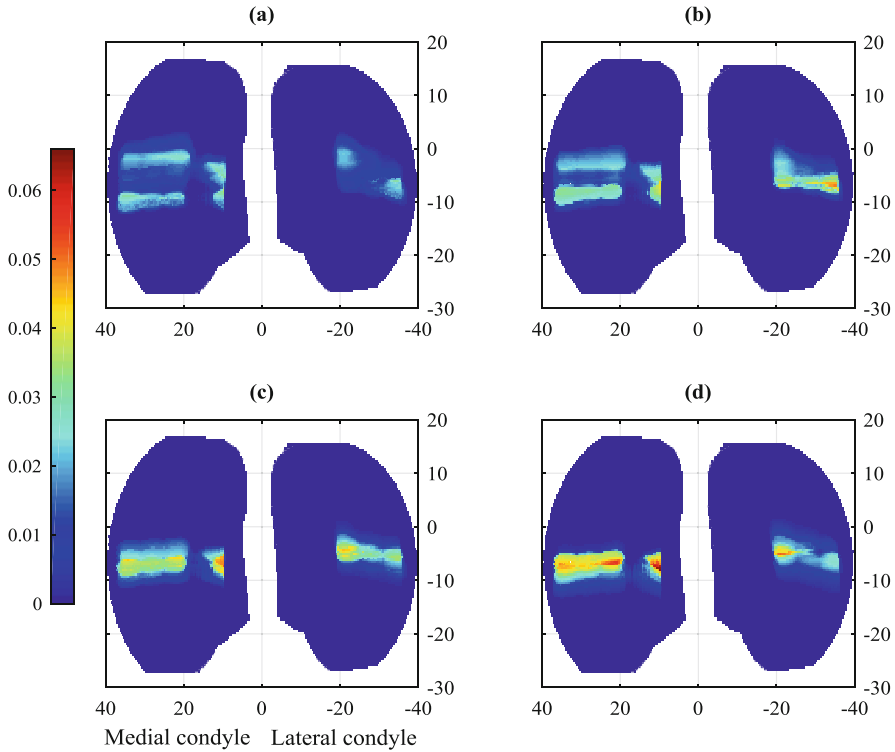
Fig. 4 Effect of friction coefficient on linear wear values (mm) of tibiofemoral joints after one million cycles: (a) $\mu = 0$; (b) $\mu = 0.04$; (c) $\mu = 0.08$; (d) $\mu = 0.12$.

be observed in Fig. 4 and more intense color of the wear map becoming red. The worn area on the lateral condyle of the knee joint is seen to be the same for all cases. The other finding is the maximum linear wear rate on the lateral side of the joint occurs close to the lateral periphery of the joint when $\mu = 0.04$, while it is shifted to the middle of the lateral condyle with increasing friction as is observable in Figs. 4c,d. The worn area on the medial condyle with high linear wear rates increases in the case study with $\mu = 0.12$ and is more uniform compared to others, Figs. 4a,b in particular.

5   Conclusions

A nonlinear forward dynamics approach was developed in which a tribology methodology was integrated to investigate friction effects on dynamics and wear of tibiofemoral joints. A mesh sensitivity was performed to come up with a mesh size that can guarantee the accuracy, convergence, and efficiency of the developed method. A comparison of acquired outcomes to those available in the literature allowed the assessment of the developed model. It was shown that friction influences the trajectory of the femoral part with respect to the tibial insert significantly in medial-lateral direction as well as the gross motion loci. The maximum linear wear rates occur for the case study with highest friction coefficient, while the maximum volumetric wear value is associated with $\mu = 0.04$, which is greater than those cases with higher friction. It was also observed that the distribution of wear in the medial condyle shrinks in anterior-posterior direction once friction coefficient increases. Moreover, increasing friction gives rise to wear values on the lateral condyle.

References

1. E. Hasler, W. Herzog, T. Leonard, A. Stano, H. Nguyen, In vivo knee joint loading and kinematics before and after ACL transaction in an animal model. J. Biomech. **31**, 253–262 (1998)
2. E. Askari, M.S. Andersen, Effect of ligament properties on nonlinear dynamics and wear prediction of knee prostheses. J. Biomech. Eng. **143**(2), 021014 (2020)
3. J. Wismans et al., A three-dimensional mathematical model of the knee joint. J. Biomech. **13**, 677–686 (1980)
4. M.A. Marra et al., A Subject-Specific Musculoskeletal Modeling Framework to Predict In Vivo Mechanics of Total Knee Arthroplasty. J. Biomech. Eng. **137**, 020904-1-12 (2015)
5. B.J. Fregly et al., Computational wear prediction of a total knee replacement from in vivo kinematics. J. Biomech. **38**, 305–314 (2005)
6. E.M. Abdel-Rahman, M.S. Hefzy, Three-dimensional dynamic behavior of the human knee joint under impact loading. Med. Eng. Phys. **20**, 276–290 (1998)
7. D.I. Caruntu, M.S. Hefzy, 3-D Anatomically based dynamic modeling of the human knee to include tibio-femoral and patello-femoral joints. J. Biomech. Eng. **126**, 44–53 (2004)
8. M.H. Moeinzadeh, A.E. Engin, N. Akkas, Two-dimensional dynamic modeling of human knee joint. J. Biomech. **16**(4), 253–264 (1983)
9. S.J. Piazza, S.L. Delp, Three-dimensional simulation of total knee replacement motion during a step-up task. J. Biomech. Eng. **123**, 599–606 (2001)
10. O. Wriggers, *Computational contact mechanics*, 2nd edn. (Springer, 2006)
11. E. Askari, Mathematical models for characterizing non-Hertzian contacts. Appl. Math. Model. **90**, 432–447 (2021)
12. A. Abdelgaied et al., Computational wear prediction of artificial knee joints based on a new wear law and formulation. J. Biomech. **44**, 1108–1116 (2011)

13. E. Askari, M.S. Andersen, A dynamic model of polyethylene damage in dry total hip arthroplasties: wear and creep. Multibody Syst. Dyn. **45**(4), 403–429 (2019)
14. O.A. Bauchau, Flexible multibody dynamics. Springer (2011)
15. E. Askari, M.S. Andersen, A modification on velocity terms of Reynolds equation in a spherical coordinate system. Tribol. Int. **131**, 15–23 (2019)
16. L. Kang et al., Enhanced computational prediction of polyethylene wear in hip joints by incorporating cross-shear and contact pressure in additional to load and sliding distance: effect of head diameter. J. Biomech. **42**(7), 912–918 (2009)
17. J. Zhang et al., A patient-specific wear prediction framework for an artificial knee joint with coupled musculoskeletal multibody-dynamics and finite element analysis. Tribol. Int. **109**, 382–389 (2017)
18. H.S. Gill, et al.: In vivo measurement of volumetric wear of a total knee replacement. Knee **13**, 312–317 (2006)

Solving Non-smooth Dynamic Problems Using the Alternating Direction Method of Multipliers

Alessandro Tasora, Dario Mangoni, and Simone Benatti

1 Introduction

Simulation of complex systems involving multiple contacts between mechanical parts can lead to problems of non-smooth dynamics. In such framework, contacts and frictional effects are represented by set-valued functions, thus leading to a more complex mathematical framework with respect to conventional smooth ordinary differential equations (ODEs) or differential-algebraic equations (DAEs). In the latter, in fact, frictional contacts are often approximated as smooth regularizations, hence, introducing spring-like penalty forces that allow the adoption of typical ODE or DAE time integrators, but at the same time incurring in low stability unless very small time steps are used.

Following the seminal works by Moreau [1, 2], most formulations for non-smooth dynamical problems are based on measure differential inclusions (MDIs): just like differential inclusions they allow set-valued force laws (such as the Coulomb–Amontons dry friction model) but also generalize to the case where velocity is assumed to be a possibly discontinuous function of bounded variation in order to allow impulsive events.

These problems can be solved by means of special time-stepping methods that offer superior robustness and stability at the cost of solving a complementarity problem, or more in general a variational inequality (VI), per each time step [3]. In this context, unknowns to be solved are velocity measures and reaction impulses at contact points and at joints: in cases of many parts with a lot of frictional contacts, the large dimension of the VI could lead to a bottleneck in the time-stepping process.

A. Tasora (✉) · D. Mangoni · S. Benatti
Department of Engineering and Architecture, University of Parma, Parma, Italy
e-mail: alessandro.tasora@unipr.it; http://digitaldynamicslab.unipr.it

This stimulated a lot of research on efficient numerical methods in the last three decades.

One of the former approaches, presented in [4], was based on solving a linear complementarity problem (LCP) per each time step. LCPs are sub-cases of VIs, for whom a direct method (Lemke's algorithm) does exist. However, direct LCP solvers offer exact solution at the cost of very expensive pivoting sub-iterations that scale badly with an increasing number of unknowns, and for these reasons, they are not much used nowadays.

On the other hand, approximate but efficient methods based on fixed-point iterations became popular in the area of real-time simulators and robotics [5]. In most cases, they are based on stationary methods like Gauss–Seidell or Jacobi iterations interleaved with projections on friction cones. They can be used to solve the LCP or the cone complementarity problem (CCP), another special case of the VI in which the multibody contact problem can be formulated. Attempts were made in order to parallelize them and to increase their convergence, such as over-relaxation, the Krasnoselskii–Mann smoothing, and warm-starting, [6, 7] but in general they perform poorly when there are odd mass ratios and when articulated mechanisms such as robots are added to the scenarios—in those cases convergence often stalls, and if the iteration is prematurely truncated, reaction impulses are badly estimated and mechanisms fall apart or bend, and objects might interpenetrate.

Another option is to solve the CCP as an optimization problem, using first-order optimization methods such as the Nesterov accelerated projected gradient descent [8] or the Barzilai–Borwein spectral projected gradient [9]. These methods are based on a simple projection operator, matrix-by-vector multiplications, and inner products. Their convergence is better than for fixed-point iterations, however they share with them the following issue: that they often require the building of a Delassus operator, that is, a Schur complement matrix that is easy to compute in efficient (factored and sparse) format if diagonal masses are used because these can be easily inverted, but hard to handle if finite elements are added to the problem, because they introduce stiffness and damping matrices whose inverse would be needed as well.

A further class of solvers is represented by non-smooth Newton methods, such as the one presented in [10] , that assume a generic nonlinear complemetarity problem (NCP), again a sub-case of a VI, and represent the NCP complementarity constraints using non-smooth functions like the Fisher–Burmeister function. A generalized non-smooth Newton method can be used to find the zero of the functions, at the cost of solving a linear system per each iteration.

Under mild assumptions, the VI can be stated as a convex CCP, which can be also cast as an optimization problem, namely a quadratic program (QP) with convex constraints [11]. For such a class of optimization problems, one can use interior-point methods (IPMs), a class of solvers that share some similarities with the abovementioned non-smooth Newton methods—for example, the solution of a saddle-point linear system is required at each iteration. IPMs offer the best theoretical convergence. However, their implementation is quite intricate, and

despite the encouraging theoretical properties, in practice they do not scale well for large problems. Also, there are no reliable ways to warm-start them [12] .

Recently, there has been a revival of alternating direction method of multipliers (ADMMs) and similar operator-splitting methods for solving constrained optimization problems [13]. Even if the theoretical convergence of such methods is worse than the one of IPMs, recent developments showed that in practical scenarios they offer superior speed, scalability, and robustness [14]. An attractive property of ADMM is that it requires the solution of a linear system per each iteration, but unlike IPMs, such linear system most often remains unchanged during the iterations, so a factorization can be reused multiple times with a great benefit in terms of speed.

A similar scheme, based on a sequential unconstrained minimization technique, has been proposed in [15] for non-smooth dynamics and robotics.

In [16], a specialized ADMM method for quadratic problems with conic constraints has been presented: on the top of this method, we develop a solver that can exploit the nature of non-smooth dynamical problems.

2   The Non-smooth Multibody Model

Different time-stepping schemes have been proposed for MDIs; here, we refer to the one discussed [7] without lack of generality. After regularization and convexification and discretization, the MDIs lead to a major numerical bottleneck to be solved at each time step: a (mixed) CCP with unknowns v and γ_ϵ:

$$\begin{cases} M\boldsymbol{v} - \boldsymbol{k} - D_\epsilon \boldsymbol{\gamma}_\epsilon = 0 & \text{(1a)} \\[2mm] D_\epsilon^T \boldsymbol{v} + \boldsymbol{b}_\epsilon = \boldsymbol{u}_\epsilon & \text{(1b)} \\[2mm] -\varUpsilon^\circ \ni \boldsymbol{u}_\epsilon \quad \perp \quad \boldsymbol{\gamma}_\epsilon \in \varUpsilon & \text{(1c)} \end{cases}$$

where

- unknown v is the speed at the end of the time step,
- unknown γ_ϵ is the reaction in contacts and bilateral joints, a vector-signed measure with the Lebesgue decomposition in atomic parts (impacts) and continuous parts (continuous reactions),
- M is a positive-definite block diagonal matrix containing masses and inertia tensors of the bodies,
- D_ϵ is a sparse matrix, the transpose Jacobian of all constraints,
- k is a vector containing terms proportional to applied forces, among other things,
- b is a vector containing constraint stabilization terms, among other things,
- $\varUpsilon$ is the Cartesian product of all cones of admissible constraint forces, $\varUpsilon = \times_i \varUpsilon_i$,
- if a frictional contact is added, $\varUpsilon_i \subset \mathbb{R}^3$ is a second-order Lorentz cone with aperture proportional to friction coefficient,

– if a bilateral constraint is added, $\Upsilon_i = \mathbb{R}$ and $\Upsilon_i^\circ = \{0\}$,
– if a unilateral constraint is added, $\Upsilon_i = \mathbb{R}^+$ and $\Upsilon_i^\circ = \mathbb{R}^-$, and
– Υ° is the polar cone, opposite of the dual cone, i.e., $\Upsilon^* = -\Upsilon^\circ$.

For more details on the model, we refer to [17].

Introducing the Schur complement

$$N = D_\epsilon^T M^{-1} D_\epsilon$$

and the vector

$$r_\epsilon = D_\epsilon^T M^{-1} k + b_\epsilon$$

such that

$$u_\epsilon = N\gamma_\epsilon + r_\epsilon$$

one can also write the problem as the following CCP:

$$-\Upsilon^\circ \ni N\gamma_\epsilon + r_\epsilon \quad \perp \quad \gamma_\epsilon \in \Upsilon \tag{2}$$

This CCP corresponds exactly to a first-order optimality condition of a convex quadratic program:

$$\min \quad \frac{1}{2}\gamma_\epsilon^T N\gamma_\epsilon + r_\epsilon^T \gamma_\epsilon \tag{3a}$$

$$\text{s.t.} \quad \gamma_\epsilon \in \Upsilon \tag{3b}$$

and in fact, the CCP (2) can be written in the more conventional language of the KKT optimality conditions on *dual variables* y multipliers, for $y = -u_\epsilon$ and *primal variables* γ_ϵ:

$$N\gamma_\epsilon + r_\epsilon + Iy = 0 \tag{4a}$$

$$\gamma_\epsilon = z \tag{4b}$$

$$\Upsilon \ni z \quad \perp \quad y \in \Upsilon^\circ \tag{4c}$$

After the convex program (3) is solved by ADMM, one can compute $v = M^{-1}(k + \bar{D}_\epsilon \gamma_\epsilon)$ with a quick post-processing step.

The ADMM method in [16] can be used to solve problems in the form

$$Px + q + A^T y = 0 \tag{5a}$$

$$Ax - b = z \tag{5b}$$

$$C \ni z \quad \perp \quad y \in \mathcal{N}_C(z) \tag{5c}$$

and one can see that (4) is a special case of (5), where $A = I$, $P = N$, $C = \Upsilon$, and $q = r$, $x = \gamma_\epsilon$, $b = 0$, where some optimizations can take place because of the structure of our problem.

We remark that the ADMM method just makes the assumption of Υ being convex, so the problem can be generalized to $\gamma_\epsilon \in C$, where C is a generic convex set, and at the same time, we assume an associated flow $u_\epsilon \in -\mathcal{N}_C(\gamma_\epsilon)$. For instance, C could be a capped friction cone to represent plasticization of contacts, or a cone translated downward to represent possible adhesion in contact up to a threshold, or the Von Mises yield region if γ_ϵ represent stresses in finite elements undergoing plasticization.

Also, in sake of highest generality, in presence of finite elements, one might need to use tangent stiffness matrices K and damping matrices D to accommodate an implicit integration scheme for stiff elements, and this means that the Schur complement would be computed as $N = D_\epsilon^T H^{-1} D_\epsilon$. Here, H, taking the place of the original M matrix, is rather a linear combination of M, K, and D (depending on the integration scheme) and in general is not diagonal anymore.

3 The ADMM Solver

For variables $(x, z) \in \mathbb{R}^m \times \mathbb{R}^n$, the ADMM methods solve constrained optimization problems with separable structure

$$\min \quad f(x) + g(z) \tag{6a}$$

$$\text{s.t.} \quad Ax + Bz - b = 0 \tag{6b}$$

by introducing an augmented Lagrangian

$$\mathcal{L}_\rho(x, z, y) = f(x) + g(z) + y^T(Ax + Bz - b) + \frac{\rho}{2}\|Ax + Bz - b\|^2 \tag{7}$$

and by iterating over two minimization problems as in the following loop:

$$x^{k+1} \in \operatorname{argmin}\mathcal{L}_\rho(x, z^k, y^k) \tag{8}$$

$$z^{k+1} \in \operatorname{argmin}\mathcal{L}_\rho(x^{k+1}, z, y^k) \tag{9}$$

$$y^{k+1} = y^k + \rho(Ax^{k+1} + Bz^{k+1} - b) \tag{10}$$

Although the convergence is fast in the first iterations, it tends to deteriorate later as in fixed-point iterations; however, in practical scenarios where loose tolerances can be accepted, the method proves to be very efficient and robust.

In order to rewrite (3) as a sum of two functions as in (6), we introduce the auxiliary variables $(\tilde{\boldsymbol{\gamma}}_\epsilon, \tilde{z})$, we state the $\boldsymbol{\gamma}_\epsilon \in \Upsilon$ constraint by adding a non-smooth penalty function given by the indicator function $\mathcal{I}_\Upsilon(\boldsymbol{\gamma}_\epsilon)$, where $\mathcal{I}_\Upsilon(\boldsymbol{\gamma}_\epsilon) = 0$ for $\boldsymbol{\gamma}_\epsilon \in \Upsilon$ and $= \infty$ otherwise, another indicator function $\mathcal{I}_{\boldsymbol{\gamma}_\epsilon=z}(\boldsymbol{\gamma}_\epsilon, z)$, and finally we have

$$\min \quad \frac{1}{2}\tilde{\boldsymbol{\gamma}}_\epsilon^T N \tilde{\boldsymbol{\gamma}}_\epsilon + \boldsymbol{r}_\epsilon^T \tilde{\boldsymbol{\gamma}}_\epsilon + \mathcal{I}_{\tilde{\boldsymbol{\gamma}}_\epsilon=\tilde{z}}(\tilde{\boldsymbol{\gamma}}_\epsilon, \tilde{z}) + \mathcal{I}_\Upsilon(\boldsymbol{\gamma}_\epsilon) \tag{11a}$$

$$\text{s.t.} \quad (\tilde{\boldsymbol{\gamma}}_\epsilon, \tilde{z}) = (\boldsymbol{\gamma}_\epsilon, z) \tag{11b}$$

We can write the augmented Lagrangian introducing two step size parameters σ and ρ and two vector of multipliers $\boldsymbol{w}$ and $\boldsymbol{y}$, obtaining

$$\mathcal{L}_{\sigma,\rho}\left((\tilde{\boldsymbol{\gamma}}_\epsilon, \tilde{z}), (\boldsymbol{\gamma}_\epsilon, z), (\boldsymbol{y}, \boldsymbol{w})\right) = \frac{1}{2}\tilde{\boldsymbol{\gamma}}_\epsilon^T N \tilde{\boldsymbol{\gamma}}_\epsilon + \boldsymbol{r}_\epsilon^T \tilde{\boldsymbol{\gamma}}_\epsilon + \mathcal{I}_{\tilde{\boldsymbol{\gamma}}_\epsilon=\tilde{z}}(\tilde{\boldsymbol{\gamma}}_\epsilon, \tilde{z}) + \mathcal{I}_\Upsilon(\boldsymbol{\gamma}_\epsilon)$$

$$+ \boldsymbol{w}^T(\tilde{\boldsymbol{\gamma}}_\epsilon - \boldsymbol{\gamma}_\epsilon) + \frac{\sigma}{2}\left\|\tilde{\boldsymbol{\gamma}}_\epsilon - \boldsymbol{\gamma}_\epsilon\right\|^2 + \boldsymbol{y}^T(\tilde{z} - z) + \frac{\rho}{2}\|\tilde{z} - z\|^2 \tag{12}$$

that is also, using the property $\boldsymbol{y}^T\boldsymbol{r} + \frac{\rho}{2}\|\boldsymbol{r}\|^2 = \frac{\rho}{2}\left\|\boldsymbol{r} + \frac{1}{\rho}\boldsymbol{y}\right\|^2 - \frac{1}{2\rho}\|\boldsymbol{y}\|^2$, the following:

$$\mathcal{L}_{\sigma,\rho}\left((\tilde{\boldsymbol{\gamma}}_\epsilon, \tilde{z}), (\boldsymbol{\gamma}_\epsilon, z), (\boldsymbol{y}, \boldsymbol{w})\right) = \frac{1}{2}\tilde{\boldsymbol{\gamma}}_\epsilon^T N \tilde{\boldsymbol{\gamma}}_\epsilon + \boldsymbol{r}_\epsilon^T \tilde{\boldsymbol{\gamma}}_\epsilon + \mathcal{I}_{\tilde{\boldsymbol{\gamma}}_\epsilon=\tilde{z}}(\tilde{\boldsymbol{\gamma}}_\epsilon, \tilde{z}) + \mathcal{I}_\Upsilon(\boldsymbol{\gamma}_\epsilon)$$

$$+ \frac{\sigma}{2}\left\|\tilde{\boldsymbol{\gamma}}_\epsilon - \boldsymbol{\gamma}_\epsilon + \frac{1}{\sigma}\boldsymbol{w}\right\|^2 - \frac{1}{2\sigma}\|\boldsymbol{w}\|^2 + \frac{\rho}{2}\left\|\tilde{z} - z + \frac{1}{\rho}\boldsymbol{y}\right\|^2 - \frac{1}{2\rho}\|\boldsymbol{y}\|^2 \tag{13}$$

The first step of ADMM requires to compute

$$(\tilde{\boldsymbol{\gamma}}_\epsilon^{k+1}, \tilde{z}^{k+1}) = \text{argmin}\mathcal{L}_{\sigma,\rho}\left((\tilde{\boldsymbol{\gamma}}_\epsilon, \tilde{z}), (\boldsymbol{\gamma}_\epsilon^k, z^k), (\boldsymbol{y}^k, \boldsymbol{w}^k)\right)$$

This can be simplified remembering that $\boldsymbol{w}^k$ will always be zero, that some terms are constant and can be left out, and that the $\mathcal{I}_{\tilde{\boldsymbol{\gamma}}_\epsilon=\tilde{z}}(\tilde{\boldsymbol{\gamma}}_\epsilon, \tilde{z})$ term can be elided to turn finally the unconstrained argmin$\mathcal{L}_{\sigma,\rho}$ into the equality constrained optimization problem:

$$\min \quad \frac{1}{2}\tilde{\boldsymbol{\gamma}}_\epsilon^T N \tilde{\boldsymbol{\gamma}}_\epsilon + \boldsymbol{r}_\epsilon^T \tilde{\boldsymbol{\gamma}}_\epsilon + \frac{\sigma}{2}\left\|\tilde{\boldsymbol{\gamma}}_\epsilon - \boldsymbol{\gamma}_\epsilon^k\right\|^2 + \frac{\rho}{2}\left\|\tilde{z} - z^k + \frac{1}{\rho}\boldsymbol{y}^k\right\|^2 \tag{14a}$$

$$\text{s.t.} \quad \tilde{\boldsymbol{\gamma}} = \tilde{z} \tag{14b}$$

For such problem, the KKT conditions lead to the following linear problem:

$$[N + (\sigma + \rho)I]\,\tilde{\boldsymbol{\gamma}}_\epsilon = \sigma\boldsymbol{\gamma}_\epsilon^k + \rho\boldsymbol{z}^k - \boldsymbol{r} - \boldsymbol{y}^k \tag{15}$$

The linear system (15) can be solved as it is, but in our case it would be better to exploit the fact that the Schur matrix N is a product $D_\epsilon^T H^{-1} D_\epsilon$. We would like to avoid computing H^{-1}, even storing a precomputed inverse for all iterations would be unpractical because often dense (except when H is a diagonal mass matrix M). So, we propose to replace (15) with the equivalent saddle-point problem:

$$\begin{bmatrix} H & D_\epsilon \\ D^T & -(\sigma + \rho)I \end{bmatrix} \left\{ \begin{matrix} \boldsymbol{v} \\ -\tilde{\boldsymbol{\gamma}}_\epsilon^{k+1} \end{matrix} \right\} = \left\{ \begin{matrix} \boldsymbol{k} \\ -\boldsymbol{b}_\epsilon + \sigma\boldsymbol{\gamma}_\epsilon^k + \rho\boldsymbol{z}^k - \boldsymbol{y}^k \end{matrix} \right\} \tag{16}$$

which, even if it introduces an auxiliary variable $\boldsymbol{v}$, is very sparse and does not require computing any H^{-1}.

A remarkable side effect of this approach is that its auxiliary variable $\boldsymbol{v}$ is also the velocity term in the original MDI (1), so one does not need to compute it as $\boldsymbol{v} = H^{-1}(\boldsymbol{k} + D_\epsilon\boldsymbol{\gamma}_\epsilon)$ after the iteration converged because it is a byproduct of the linear solver.

The second step of ADMM is a minimization problem too, but it can be rephrased in terms of a projection on the separable set Υ of the friction cones; note that this requires an inexpensive and parallelizable operation.

Using these results and adding a Krasnoselskii–Mann relaxation factor $\alpha \in (0, 2]$, one obtains the final algorithm:

$$\begin{bmatrix} H & D_\epsilon \\ D^T & -(\sigma + \rho)I \end{bmatrix} \left\{ \begin{matrix} \boldsymbol{v} \\ -\tilde{\boldsymbol{\gamma}}_\epsilon^{k+1} \end{matrix} \right\} = \left\{ \begin{matrix} \boldsymbol{k} \\ -\boldsymbol{b}_\epsilon + \sigma\boldsymbol{\gamma}_\epsilon^k + \rho\boldsymbol{z}^k - \boldsymbol{y}^k \end{matrix} \right\} \tag{17a}$$

$$\boldsymbol{\gamma}_\epsilon^{k+1} = \tilde{\boldsymbol{\gamma}}_\epsilon^{k+1} + (1 - \alpha)\boldsymbol{\gamma}_\epsilon^k \tag{17b}$$

$$\boldsymbol{z}^{k+1} = \Pi_\Upsilon \left(\alpha\tilde{\boldsymbol{\gamma}}_\epsilon^{k+1} + (1 - \alpha)\boldsymbol{z}^k + \frac{1}{\rho}\boldsymbol{y}^k \right) \tag{17c}$$

$$\boldsymbol{y}^{k+1} = \boldsymbol{y}^k + \rho \left(\alpha\tilde{\boldsymbol{\gamma}}_\epsilon^{k+1} + (1 - \alpha)\boldsymbol{z}^k - \boldsymbol{z}^{k+1} \right) \tag{17d}$$

$$\boldsymbol{r}_{\text{prim}} = \boldsymbol{\gamma}_\epsilon^{k+1} - \boldsymbol{z}^{k+1} \tag{17e}$$

$$\boldsymbol{r}_{\text{dual}} = N\boldsymbol{\gamma}_\epsilon^{k+1} + \boldsymbol{r} + \boldsymbol{y}^{k+1} \tag{17f}$$

The iteration is terminated when $\boldsymbol{r}_{\text{prim}}$ and $\boldsymbol{r}_{\text{dual}}$ fall under prescribed tolerances. We remark that setting proper values for ρ is of fundamental importance in order to obtain a good speed of convergence. In most cases, one can use heuristics and adjust ρ only one or two times during the iterations, hence allowing to reuse the factorization of the linear system. Also, σ acts similarly to a regularization term and can be left to low values anyway.

4 Results and Conclusions

We performed benchmarks involving multibody systems with contacts between multiple parts, showing that the performance of the ADMM method is capable of handling problems that would converge too slowly using conventional projected fixed-point methods (see Fig. 1) or even first-order SPG spectral methods [9]. An additional benefit of ADMM, when compared with those methods, is that it does not require the computation of a Schur complement, and hence it can be applied seamlessly to problems featuring a block-sparse matrix in place of the diagonal M in (1), such as when introducing stiffness and damping matrices for finite elements (see Fig. 2).

Our ADMM method requires few computational primitives: basically, a projection of dual variables on conic sets, a backward solve of a linear system, and a forward solve. The latter is a computational bottleneck, but it can be performed only once per run, as the matrix does not change often during the iterations. A good estimation of the ADMM step size proved to be fundamental in achieving good convergence: using some heuristics, we obtained an efficient auto-tuning algorithm. We noted that ADMM can be successfully applied to problems that exhibit temporal coherence because, unlike IPMs, it supports warm-starting.
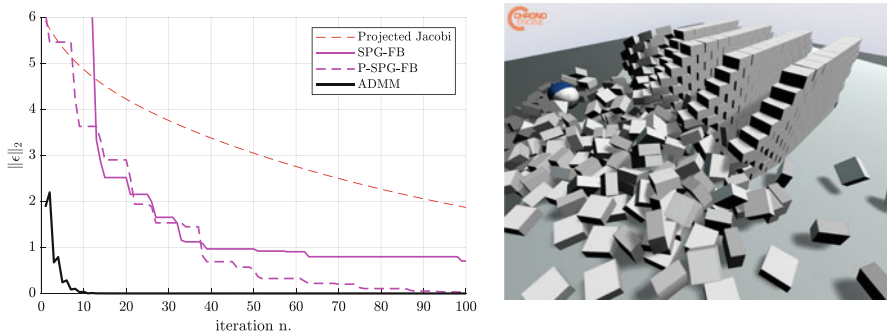
Fig. 1 Convergence of the ADMMM method within one time step of the wrecking ball benchmark (600 bricks in four walls): residual in frictional constraint violation compared to fixed-point Jacobi iterations and to first-order SPG methods

Fig. 2 Test 5. Large deformation of a finite element mesh colliding with a plane. Thanks to the non-smooth formulation, large time steps can be used (only ten steps have been used from start to end), and no penalty parameters must be used in contact points. Contacts between lugs and ground show zero interpenetration regardless of the stiffness of the mesh

References

1. J.J. Moreau, Unilateral constraints and dry friction in finite freedom dynamics, in *Nonsmooth Mechanics and Applications*, ed. by J. Moreau, P. Panagiotopoulos. CISM Courses and Lectures no. 302 (Springer, New York, 1988), pp. 1–82

2. M. Jean, J.J. Moreau, Unilaterality and dry friction in the dynamics of rigid body collections, in *1st Contact Mechanics International Symposium, Lausanne* (1992)

3. V. Acary, B. Brogliato, *Numerical Methods for Nonsmooth Dynamical Systems: Applications in Mechanics and Electronics*, vol. 35 (Springer Science & Business Media, New York, 2008)

4. D.E. Stewart, J.C. Trinkle, An implicit time-stepping scheme for rigid-body dynamics with inelastic collisions and Coulomb friction. Int. J. Numer. Methods Eng. **39**, 2673–2691 (1996)

5. J. Bender, M. Müller, M.A. Otaduy, M. Teschner, M. Macklin, A survey on position-based simulation methods in computer graphics. Comput. Graph. Forum **33**(6), 228–251 (2014). https://doi.org/10.1111/cgf.12346. https://onlinelibrary.wiley.com/doi/abs/10.1111/cgf.12346

6. R. Tonge, F. Benevolenski, A. Voroshilov, Mass splitting for jitter-free parallel rigid body simulation. ACM Trans. Graph. (TOG) **31**(4), 105 (2012)

7. A. Tasora, M. Anitescu, A matrix-free cone complementarity approach for solving large-scale, nonsmooth, rigid body dynamics. Comput. Methods Appl. Mech. Eng. **200**(5–8), 439–453 (2011). https://doi.org/10.1016/j.cma.2010.06.030

8. H. Mazhar, T. Heyn, A. Tasora, D. Negrut, Using Nesterov's method to accelerate multibody dynamics with friction and contact. ACM Trans. Graph. **34**(3), 32:1–32:14 (2015)

9. T. Heyn, M. Anitescu, A. Tasora, D. Negrut, Using Krylov subspace and spectral methods for solving complementarity problems in many-body contact dynamics simulation. IJNME **95**(7), 541–561 (2013). https://doi.org/10.1002/nme.4513

10. M. Macklin, K. Erleben, M. Müller, N. Chentanez, S. Jeschke, V. Makoviychuk, Non-smooth Newton methods for deformable multi-body dynamics. ACM Trans. Graph. **38**(5), 140:1–140:20 (2019). https://doi.org/10.1145/3338695

11. M. Anitescu, A. Tasora, An iterative approach for cone complementarity problems for nonsmooth dynamics. Comput. Optim. Appl. **47**(2), 207–235 (2010). https://doi.org/10.1007/s10589-008-9223-4

12. D. Mangoni, A. Tasora, R. Garziera, A primal–dual predictor–corrector interior point method for non-smooth contact dynamics. Comput. Methods Appl. Mech. Eng. **330**, 351–367 (2018). https://doi.org/10.1016/j.cma.2017.10.030. http://www.sciencedirect.com/science/article/pii/S004578251730703X

13. T. Goldstein, B. O'Donoghue, S. Setzer, R. Baraniuk, Fast alternating direction optimization methods. SIAM J. Imaging Sci. **7**(3), 1588–1623 (2014). https://doi.org/10.1137/120896219. https://epubs.siam.org/doi/abs/10.1137/120896219

14. M. Cannon, P. Goulart, M. Garstka, COSMO: A conic operator splitting method for large convex problems, in *European Control Conference* (2019). https://ora.ox.ac.uk/objects/uuid:25211347-1646-4d6b-9ad5-807d1c865e50

15. K. Yunt, C. Glocker, Trajectory optimization of mechanical hybrid systems using SUMT, in 9th *IEEE International Workshop on Advanced Motion Control*. (IEEE, Piscataway, 2006), pp. 665–671. https://doi.org/10.1109/AMC.2006.1631739. ISSN: 1943-6580

16. B. Stellato, G. Banjac, P. Goulart, A. Bemporad, S. Boyd, OSQP: an operator splitting solver for quadratic programs. Math. Program. Comput. **12**(4), 637–672 (2020). https://doi.org/10.1007/s12532-020-00179-2

17. D. Negrut, R. Serban, A. Tasora, Posing multibody dynamics with friction and contact as a differential complementarity problem. ASME J. Comput. Nonlinear Dyn. **13**(1), 014,503 (2017). https://doi.org/10.1115/1.4037415

PyChrono and gym-chrono: A Deep Reinforcement Learning Framework Leveraging Multibody Dynamics to Control Autonomous Vehicles and Robots

Simone Benatti, Aaron Young, Asher Elmquist, Jay Taves, Radu Serban, Dario Mangoni, Alessandro Tasora, and Dan Negrut

1 Introduction

Reinforcement Learning (RL) [1] is a Machine Learning technique based on agent–environment interactions: at each interaction, the agent performs an *action* and collects the *state* of the system and a *reward* measuring its performance in solving some task; the goal of RL is, given the state, picking the action that maximizes the expected sum of reward, thus solving the task. In the last few years [2], Deep Learning used in conjunction with RL [called Deep Reinforcement Learning (DRL)] has demonstrated to be a viable approach to solve complex real-world robotic tasks [3]. DRL methods, like any other Deep Learning approach, require a large dataset to optimize the Neural Networks, and this dataset can be collected by sampling from real robots or through simulation, the latter being safer, cheaper, and easier to set up and parallelize.

The results obtained in DRL-based controls has arisen interest in physics engine providing a Python API. The DRL community heavily relies MuJoCo [4] and PyBullet [5] for robotics environments and on CARLA [6] and AirSim [7] for autonomous driving.

We provide in a single Python framework a set of reinforcement learning environments that feature

– Multibody Dynamics simulation with constraints and smooth or non-smooth contacts,
– deformable bodies simulation through Finite Element Analysis simulation,

S. Benatti (✉) · D. Mangoni · A. Tasora
Department of Engineering and Architecture, University of Parma, Parma, Italy
e-mail: simone.benatti@studenti.unipr.it

A. Young · A. Elmquist · J. Taves · R. Serban · D. Negrut
University of Wisconsin – Madison, Madison, WI, USA

– vehicle dynamics simulation tools, and
– sensor simulation.

2 PyChrono

2.1 *Interpreted Language*

Python is an interpreted language. This brings obvious upsides in terms of ease of use but greatly limits the computational performance. Python has also limited parallelization capabilities, since each Python process is locked on a single thread (Global Interpreter Lock, also known as GIL).

The reason behind Python success in high performance computing is the interfacing with compiled libraries through *Bindings*. In this scenario, Python is used as high-level interface.

2.1.1 SWIG

To create a Python *Wrapper* for Chrono, we rely on SWIG [8] (Simplified Wrapper and Interface Generator). It generates bindings between C/C++ code and common scripting languages, such as Perl, C#, and Python, without need to modify the underlying code.

What the Python/C++ bindings do is creating hooks to call the compiled libraries, and therefore while the functions are called from the Python API, the computation, under the hood, calls the same libraries as the C++ API. By doing this, the computational overhead of using Python is minimal while getting the usage and compatibility benefits.

Besides allowing to solve the Python performance issues, Python bindings also allow to use multithreading when it is leveraged by the underlying code. This fits well into Python purpose, being a high-level programming language relying on binary libraries for computation. In Fig. 1, we show how PyChrono can still use multiple CPU cores while being used from Python in a simulation with finite elements and contacts.

2.2 *Package Features*

2.2.1 Multibody Dynamics

PyChrono wraps the Multibody Dynamics simulation classes of Project Chrono, providing
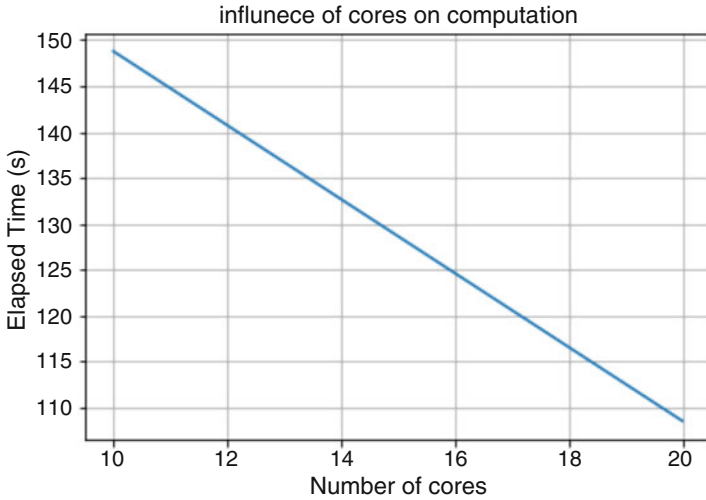
Fig. 1 Speedup in computation when parallelizing the task on two cores

– multibody constrained dynamics,
– smooth and non-smooth contacts,
– FEA-based deformable bodies: beams, shells, and 3D elements,
– various solvers and timesteppers, and
– 1D shaft systems simulation

These features are provided by three sub-modules: *core, fea,* and *mkl* (the latter only providing the interface to MKL PARDISO solver).

2.2.2 Modeling and Visualization Tools

The *irrlicht* and *post-process* sub-modules provide real-time 3D rendering and post-processing tools (such as POV-Ray scripts for higher quality rendering).

2.2.3 Vehicle Dynamics

Wrapping all of Project Chrono vehicle simulation classes, PyChrono supports template-based tools for modeling wheeled and tracked vehicles. The templates include wheeled vehicle parts (steering, suspension, wheel, etc.), tracked vehicle parts (track shoe, sprocket, idler, etc.), terrain, power train, and driver. For some of these classes have several sub-classes that represent different mechanisms or physics detail. For example, there are 19 different suspension mechanisms (double wishbone, multi-link, etc.) and 13 different tire models (rigid, Pacejka, deformable etc.). PyChrono vehicle also provides complete vehicle models that combined the

aforementioned parts to give the user a pre-cooked vehicle model. This feature is especially welcome in contexts, such as the topic of this work, in which the focus is not on a specific vehicle model, but rather testing an autonomous driving tool on a generic vehicle.

2.2.4   Sensor Simulation

The *sensor* sub-module wraps Chrono::Sensor functionalities, being

– support for exteroceptive sensing, which is the sensing providing scene information. More specifically, it uses NVIDIA OptiX library ray tracing to simulate camera and LiDAR sensors, whose process runs on the GPU;
– support for Interoceptive sensing, which is the sensing providing information from the simulation itself (although processed, such as converting positions to GPS coordinates). This family includes inertial measurement unit (IMU) sensors and GPS; and
– parametrization of sensors specifics (update rate, field of view, and lag) and noise models for every sensor supported.

Sensor Data Pipeline in Python API

Camera and LiDAR sensors outputs (RGB images and point clouds, respectively) memory footprint are large and in a vision-based control moving these data at each controller step might be a major bottleneck. To solve this, we cast map the data as NumPy arrays [9] using the NumPy SWIG interface. Doing so, the NumPy array class is wrapped around the raw array without instantiating new memory. This comes with no overhead, saving both time and memory.

2.2.5   Deployment of the Python Package

Anaconda is a Python distribution that creates *virtual environments* of Python to have various versions of Python and Python packages on the same machine. It also manages the installation and dependency management of Python packages through the Conda Package Manager. Through Anaconda toolchain, it is possible to create packages using *conda-build* and make it available to the public through the Anaconda Cloud platform.

For these reasons, we identified Anaconda packages as the right tool to deploy and distribute PyChrono. This deployment strategy makes the simulation tool more easily available for the user, and PyChrono had great benefited from this, having reached more than 3000 downloads at the time of writing this document.

3 gym-chrono

3.1 Motivations and Features

gym-chrono is a Python module that provides a set of Reinforcement Learning virtual environments that use PyChrono for physics simulation. This package is an extension of OpenAI gym package, and all its environments inherit from the OpenAI gym environment class. Since every third-party algorithm and DRL framework is compatible with OpenAI gym environments, they can be used for gym-chrono environments as well. The same goes for environments utilities, such as the subprocess environment parallelization provided by OpenAI Baselines. Moreover, once the package is installed through Pytohn package manager, its environments can be called from anywhere in the machine by their unique ID.

3.2 Environments

This is a list of the gym-chrono environments. We will refer to state as s and the action as a.

3.2.1 Benchmarking Environments

These two environments are the simplest of the set and are used to benchmark algorithms or hyperparameters tuning, without the pretense of modeling real-world robots. The first is a reversed pendulum to be balanced ($s \in \mathbb{R}^4$, $a \in \mathbb{R}$) and the second a 4-legged walker called *ant* ($s \in \mathbb{R}^{30}$, $a \in \mathbb{R}^8$) (Figs. 2 and 3).

3.2.2 Robotics Environments

These environments feature models of real robots created with our SolidWorks plugin. We provide a 6-DOF robotic arm (Fig. 4) that has to reach a random end-effector position without colliding with the floor or its own parts ($s \in \mathbb{R}^{18}$, $a \in \mathbb{R}^6$) and a hexapod (Fig. 6) that must learn to walk ($s \in \mathbb{R}^{53}$, $a \in \mathbb{R}^{18}$).

3.2.3 Autonomous Driving Environments

These environments leverage the *vehicle* and *sensor* modules to reproduce autonomous driving scenarios and are divided into two sub-categories:

– Vision-only:
  These environments observation is an RGB image, thus the cannot navigate if the
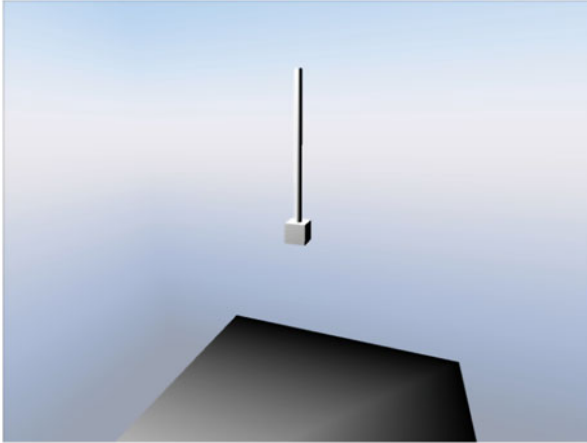
Fig. 2 Pendulum
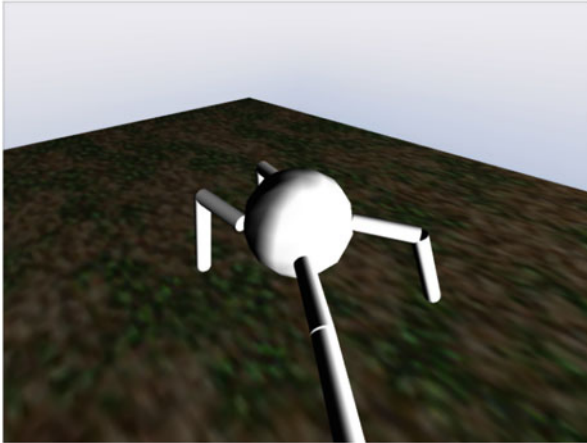
Fig. 3 Ant

direction is not encoded in the image (such as in the cone track). We provide an obstacle avoidance (Fig. 5) and a cone track environment (Fig. 8)
– Sensor Fusion:
These environments observation is a set (tuple) of heterogeneous tensors, usually an image and a vector. They are capable of autonomous navigation since the scene and the GPS information are encoded in the state. This family is composed of a convoy following and off-road navigation environments.
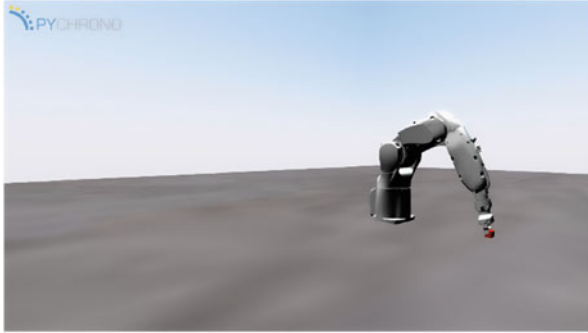
Fig. 4 Robotic arm environment
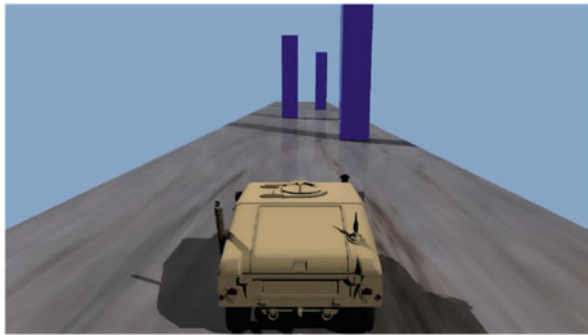
Fig. 5 Obstacle avoidance environment

4 DRL Algorithm Implementation

4.1 PPO Algorithm

To solve this environment, we wrote a custom PyTorch [10] implementation of the Clipped Objective version of the Proximal Policy optimization algorithm [11].

Let the ratio $r_t(\theta) = \frac{\pi_\theta(a_t|s_t)}{\pi_{\theta_k}(a_t|s_t)}$. Then, we can define the *Clipped Objective Function* that is to be maximized as follows:

$$\mathcal{L}_{\theta k}^{CLIP}(\theta) = \underset{\tau \sim \pi_k}{E} \left[\sum_{t=0}^{\infty} \left[\min\left(r_t(\theta)\hat{A}_t^{\pi_k}, clip\left(r_t(\theta), 1-\epsilon, 1+\epsilon\right)\right) \hat{A}_t^{\pi_k} \right] \right] \quad (1)$$

with

t timestep. The sum to ∞ is a generalization, in finite horizon scenarios the sum ends a t the terminal step. The data might be collected over multiple simulations; in this case, in the sum, there will be several initial and terminal timesteps;

a_t action at timestep t;

s_t state at timestep t;

θ policy NN parameters;

π_θ policy, the probability distribution of actions given the state. $\pi_\theta(a_t|s_t)$ is the probability of taking the action a_t in state s_t;

ϵ clipping ratio, ~ 0.2;

k the k-th parameter update. Before the update, the parameters are θ_k, and the Advantage Function is estimated on the Policy π_{θ_k}; and

$\hat{A}_t^{\pi_k}$ estimate of the Advantage Function at timestep t w.r.t. the policy π_{θ_k}

We mentioned the Advantage Function. To define it, we first need to introduce the *State Value Function* (or often only Value Function, also VF) as

$$V^\pi(s_t) \quad := \quad \mathbb{E}\left[\sum_{l=0}^\infty \gamma^l r_{t+l} \mid s_t\right] \tag{2}$$

where

– $r : t + l$ is the reward at timestep $t + l$, and
– γ is the discount factor.

The VF, being the expected value of the (discounted) sum of future reward given the current policy π, tells how much a state is *good* when following the current policy.

The Advantage Function (AF) is defined as

$$A^{\pi,\gamma} = \mathbb{E}_{s_{t+1}}\left[r_t + \gamma V^{\pi,\gamma}(s_{t+1}) - V^{\pi,\gamma}(s_t)\right] = E_{s_{t+1}}\left[\delta_t^{V^{\pi,\gamma}}\right] \tag{3}$$

Being affected by a lower variance, it is more convenient to estimate the VF through an NN rather than the AF, using the unbiased estimator proposed by Schulman et al. [12].

The generalized advantage estimator GAE(γ, λ) is defined as a λ exponentially weighted average:

$$\hat{A}_t^{GAE(\gamma,\lambda)} = \sum_{l=0}^\infty (\gamma\lambda)^l \delta_{t+l}^V \tag{4}$$

4.2   Continuous Control

When using a DRL technique with a stochastic policy, we must sample the action from a distribution determined by the NN. To do so, in continuous task, the typical solution is to sample the action from a multivariate Gaussian distribution. The means of the distributions are the NN outputs, while the variances are optimizable

parameters. Variances are high during the early stages of the training to encourage exploration and narrow down as the policy converges.

4.2.1 Implementation Details and Features

Our custom implementation of the PPO algorithm relies on PyTorch DL framework and uses Adam optimizer

Our algorithm is able to deal with vector, image, and image+vector tuple inputs, given that the right NN model is called (we also provide several NN architectures to accommodate different input shapes).

5 Results Obtained

Using the aforementioned algorithm, with different NN architectures according to the observation shape, we have been able to train the autonomous agents to solve all the tasks of gym-chrono, while we mention here just a couple of them for the sake of brevity (Fig. 6).

Hexapod The hexapod walker is the gym-chrono environment featuring the highest number of actions, thus being the hardest of robotics environments. In fact, as reported in Fig. 7, it took 6000 episodes to converge, being almost three times the number of policy updates required by the robotic arm.

Hallway Cone Track In this environment (Fig. 8), a model of an RC car has to drive in a reproduction of a real indoor hallway in a track delimited by red and green cones. The agent only controls one action (the steering) since the speed is feedback controlled to keep a constant value, and thus the convergence can be reached in a relatively short amount of iteration (as shown in Fig. 9). This being said, this
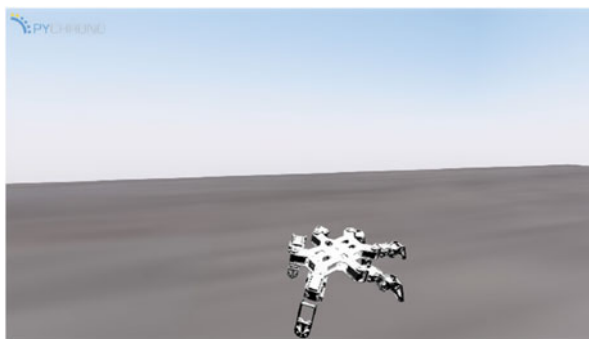
Fig. 6 Hexapod environment
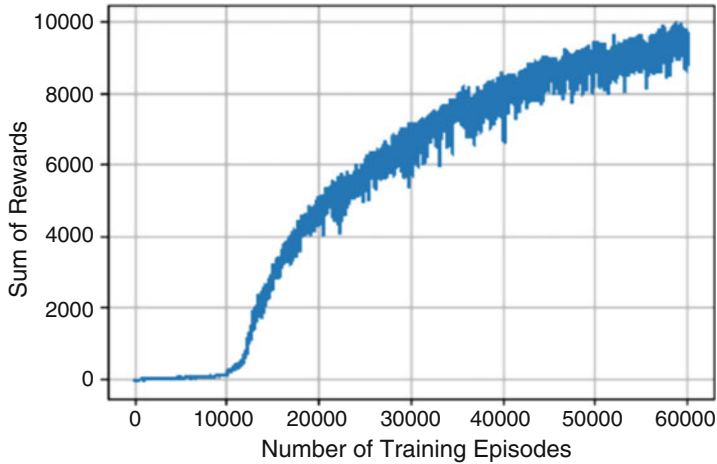
Fig. 7 Hexapod reward progression
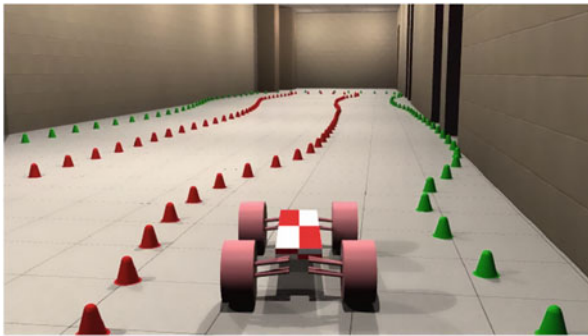
Fig. 8 Hallway cone track environment

scenario proves the capability of PyChrono of dealing with large scenarios (the hallway 3D mesh) and large dataset (the 160×90 image observation is the largest of the set). In addition, this environment could be solved only after the starting position was placed in proximity of a turn. Starting on a straight, with a 0 steering angle, means starting in a local maximum that the algorithm is likely to overfit.

6 Conclusions

Together with a concerted effort to improve the Python wrappers of Chrono, which lead to an Anaconda-distributed package with a good user base [13], we built a set of increasingly challenging DRL environments and used state-of-the-art continuous
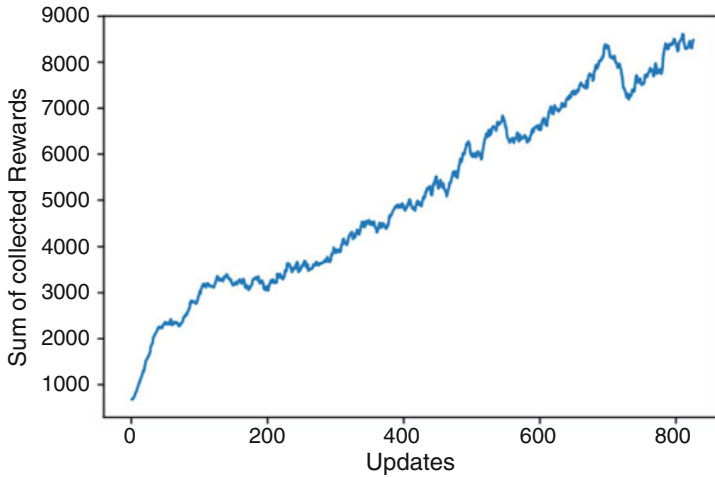
Fig. 9 Hallway cone track reward progression

action DRL algorithms to solve them. The first step has been building and solving benchmark environments such as the inverted pendulum and the 4-legged walker [14]. Then, we included models of real 6-DOF robots by leveraging the tools for 3D CAD parsing of Chrono [15] and more complex real-world robotic walkers. This feature proved to be useful by making changes in the model extremely easy to be passed to the training environment.

The latest development has been in the field of autonomous driving in off-road conditions, simulating vehicle dynamics and terrain deformation. In this context, we have been able to train autonomous agents to navigate in off-road unknown scenarios with obstacles and height irregularities to reach a target location. These results have been made possible by the capabilities of Chrono in vehicle and sensor simulation, whose API allows to model vehicle and attach sensors to them, easing the creation of autonomous driving virtual environments, while providing detailed models of vehicles and terrain for accurate physical simulation.

References

1. R. S. Sutton, A. G. Barto, *Introduction to Reinforcement Learning*, 1st ed. (MIT Press, Cambridge, MA, 1998)
2. V. Mnih, K. Kavukcuoglu, D. Silver, A. Graves, I. Antonoglou, D. Wierstra, M. A. Riedmiller, Playing Atari with deep reinforcement learning. *CoRR*, abs/1312.5602 (2013)
3. OpenAI, M. Andrychowicz, B. Baker, M. Chociej, R. Jozefowicz, B. McGrew, J. Pachocki, A. Petron, M. Plappert, G. Powell, A. Ray, J. Schneider, S. Sidor, J. Tobin, P. Welinder, L. Weng, W. Zaremba, Learning dexterous in-hand manipulation (2018)
4. E. Todorov, T. Erez, Y. Tassa, Mujoco: A physics engine for model-based control, in *2012 IEEE/RSJ International Conference on Intelligent Robots and Systems* (IEEE, Piscataway, 2012), pp. 5026–5033

5. E. Coumans, Y. Bai, Pybullet, a python module for physics simulation for games, robotics and machine learning (2016). http://pybullet.org, 2016–2019.
6. A. Dosovitskiy, G. Ros, F. Codevilla, A. Lopez, V. Koltun, CARLA: An open urban driving simulator, in *Proceedings of the 1st Annual Conference on Robot Learning* (2017), pp. 1–16
7. S. Shah, D. Dey, C. Lovett, A. Kapoor, Airsim: High-fidelity visual and physical simulation for autonomous vehicles, in *Field and Service Robotics* (Springer, Cham, 2018), pp. 621–635
8. D.M. Beazley, Swig: An easy to use tool for integrating scripting languages with c and c++, in *Proceedings of the 4th Conference on USENIX Tcl/Tk Workshop, 1996 - Volume 4*, TCLTK'96 (USENIX Association, 1996), p. 15
9. S. Van Der Walt, S.C. Colbert, G. Varoquaux, The numpy array: a structure for efficient numerical computation. Comput. Sci. Eng. **13**(2), 22 (2011)
10. A. Paszke, S. Gross, S. Chintala, G. Chanan, E. Yang, Z. DeVito, Z. Lin, A. Desmaison, L. Antiga, A. Lerer, Automatic differentiation in PyTorch (2017)
11. J. Schulman, F. Wolski, P. Dhariwal, A. Radford, O. Klimov, Proximal policy optimization algorithms. *CoRR*, abs/1707.06347 (2017)
12. J. Schulman, P. Moritz, S. Levine, M. I. Jordan, P. Abbeel, High-dimensional continuous control using generalized advantage estimation. *CoRR*, abs/1506.02438 (2015)
13. Project CHRONO Development Team. PyChrono: A Python wrapper for the Chrono multi-physics library. https://anaconda.org/projectchrono/pychrono. Accessed: 29 Apr 2020
14. S. Benatti, A. Tasora, D. Mangoni, Training a four legged robot via deep reinforcement learning and multibody simulation, in *Multibody Dynamics 2019. ECCOMAS 2019. Computational Methods in Applied Sciences* (2019)
15. S. Benatti, A. Tasora, D. Fusai, D. Mangoni, A modular simulation platform for training robots via deep reinforcement learning and multibody dynamics, in *Proceedings of the 2019 3rd International Conference on Automation, Control and Robots*, ICACR 2019, New York (Association for Computing Machinery, New York, 2019), pp. 7–11
16. G. Brockman, V. Cheung, L. Pettersson, J. Schneider, J. Schulman, J. Tang, W. Zaremba, Openai gym. *CoRR*, abs/1606.01540 (2016)
17. A. Tasora, R. Serban, H. Mazhar, A. Pazouki, D. Melanz, J. Fleischmann, M. Taylor, H. Sugiyama, D. Negrut, Chrono: An open source multi-physics dynamics engine, in *High Performance Computing in Science and Engineering – Lecture Notes in Computer Science*, ed. by T. Kozubek (Springer, Cham, 2016), pp. 19–49

Index